SAMSO-TR-68-90

[redacted]

8525-1-F

Copy 1

THE UNIVERSITY OF MICHIGAN

COLLEGE OF ENGINEERING

DEPARTMENT OF ELECTRICAL ENGINEERING

Radiation Laboratory

8525-1-F = RL-2179

Investigation of Coated Re-entry Vehicle Cross Sectior (U)

Final Report
18 December 1966 - 18 December 1967

By
R. F. GOODRICH, J. J. BOWMAN, B. A. HARRISON, E. F. KNOTT, T. B. A. SENIOR, T. M. SMITH, H. WEIL and V. H. WESTON

January 1968

Contract F 04694-67-C-0055

Contract With: **Hq. Space and Missile Systems Organization**
Air Force Systems Command
Norton Air Force Base, California 92409

[redacted]

Administered through:
OFFICE OF RESEARCH ADMINISTRATION • ANN ARBOR

MISSING
PAGE

FOREWORD

(U) This report, SAMSO-TR-68-90 was prepared by the Radiation Laboratory of the Department of Electrical Engineering of The University of Michigan under the direction of Dr. Raymond F. Goodrich, Principal Investigator and Burton A. Harrison, Contract Manager. The work was performed under Contract F 04694-67-C-0055, "Investigation of Re-entry Vehicle Surface Fields (SURF)". The work was administered under the direction of the Air Force Headquarters, Space and Missile Systems Organization, Norton Air Force Base, California 92409, by Capt. J. Wheatley, SMYSP, and was monitored by Mr. H.J. Katzman of the Aerospace Corporation.

(U) The studies presented herein cover the period 18 December 1966 through 18 December 1967.

(U) In addition to security requirements which must be met, this document is subject to special export controls and each transmittal to foreign governments or foreign nationals may be made only with prior approval of SAMSO, SMSDI, Air Force Station, Los Angeles, CA 90045.

(U) Information in this report is embargoed under the Department of State International Traffic in Arms Regulations. This report may be released to Foreign governments by departments or agencies of the U.S. Government subject to approval of Hq. Space and Missile Systems Organization (SMSDI), Air Forse Station, Los Angeles, Calif., 90045 or higher authority within the Department of the Air Force. Private individuals or firms require a Department of State export license.

(U) The publication of this report does not constitute Air Force approval of the report's findings or conclusions. It is published only for the exchange and stimulation of ideas.

SAMSO Approving Authority
William J. Schlerf BSYDR
Contracting Officer

ABSTRACT

(S) This is the final report on Contract F 04694-67-C-0055, an investigation of re-entry vehicle radar cross section, the third phase of a program designated Project SURF. The objective of the SURF program is (1) to achieve the capability to determine the radar cross section of metallic and coated re-entry vehicles which are sphere-capped-cones in shape, or modifications of that basic shape, (2) to determine the effect on radar cross section of the plasma re-entry environment and (3) to study methods for countering short pulse discrimination of these re-entry shapes. Parts (1) and (2) of this program are based upon the interpretation of surface field data obtained on models illuminated by radar in a specially designed facility. Radar backscatter measurements and computer programs are used to check theoretical conclusions. This final report discusses the work carried out in the fourth quarter of this contract and such formulas for radar cross section as were developed and which extend the results previously reported.

TABLE OF CONTENTS

Table of Contents (Cont'd)

Table of Contents (Cont'd)

I

INTRODUCTION

(S) This is the Final Report under Contract F 04694-67-C-0055. It reports the results of the third phase of Project SURF, a complex program to determine the radar cross section of cone-sphere-like re-entry vehicles under exoatmospheric and re-entry conditions. The investigation is part of the ABRES program. It was carried out under the auspices of Space and Missile Systems Organization (SAMSO) at the Radiation Laboratory of the Department of Electrical Engineering of The University of Michigan. The SAMSO project officer was Captain James Wheatley. The work was monitored for the Air Force by the Aerospace Corporation under the direction of Mr. H.J. Katzman.

(S) SURF made use of experimental methods of measuring the surface currents induced on metallic and coated models of re-entry shapes to obtain a basis for an analytical synthesis of radar cross section formulas. Inasmuch as the re-entry shapes being considered were of extremely low cross section, it would have been difficult to study them solely with radar range techniques or using full-scale models and it would have been impossible using these techniques to isolate in a practical or economical way, the effect on radar cross section of perturbations, coatings and antennas.

(S) The objectives of the SURF investigation were to achieve a capability to determine the radar cross section of metallic and coated re-entry vehicles taking into account variations in shape, particularly in the generally spherical termination of the conical portion of the body and the effect on radar cross section of slot and annular (ring) antennas. The study included a determination of the radar cross section of these bodies in the plasma re-entry environment and a determination of methods for countering short pulse discrimination techniques.

(U) The groundwork for meeting these objectives was laid in studies under contracts AF 04 (694)-683 and AF 04 (694)-834 under which radar reflectivity of metallic bodies was investigated and the studies to determine the effect of coatings, perturbations of shape and the effect of antennas were initiated. Included in the Final Reports on these earlier phases (Goodrich et al, 1965 and 1967), was a "Handbook" of radar cross section formulas for computation of the reflectivity of the shapes which were studied in those periods. The present report supplements that "handbook" in Section VII.

(U) Many of the radar cross section formulas which were constructed were checked with experimental measurements. The comparisons are described in Section 3.2 and were undertaken as a result of recommendations made by the Aerospace Corporation in a Technical Discussion meeting, one of the several technical meetings held by SAMSO, Aerospace Corporation and Radiation Laboratory personnel to review the progress of the program. However, the most recent results of the SURF programs embodied in the radar cross section formulas of Section VII have not been compared with experimental data and it would be desirable to do so in order to obtain a figure of merit and a range of validity for them.

(U) During the course of the SURF investigation, many computer programs were written for the machine calculation of the radar cross section of the various shapes which were studied. An independent programming effort was also undertaken at the Aerospace Corporation by Dr. Fred Meyers who produced programs for the radar cross section formulas of the first two "handbooks." However, it was believed to be desirable to have a very useful computational tool in the form of a general computer program for metallic and coated rotationally symmetric shapes. An attempt has been made to construct such a computer program and the results of this work are described

in Section VIII. The problem proved to be mucn more difficult than had been anticipated at the onset of the analysis. More time and effort have been put into it than had been initially planned and although at many times it seemed that the programming was completed, difficulties in numerical analysis continue to preclude a satisfactory solution to the problem.

(S) The plasma re-entry study was started during the second phase of SURF under Contract AF 04 (694)-834. It has as its objective the formation of a theoretical foundation to explain the data which was being obtained during flights carried out under other Air Force programs and to facilitate the calculation of the radar cross section of plasma embedded bodies. During this year, an experimental program was set up here to investigate the soundness of the assumptions on which the theory was based. As will be seen from the disucssions in Section V, the course of the experiments, more questions were raised than were answered. It had been expected that this would be a continuing study but with the termination of this program, the solution of some of these problems will have to be deferred. If a resumption of this work is undertaken in the future, it would be desirable to have more empirical data on the nature of flow fields.

(S) The short pulse study described in Section VI was based upon the need to investigate the feasibility of countering short pulse discrimination techniques which might be used distinguish between the radar echoes of a re-entry vehicle and decoy bodies by scrutiny of their short pulse radar returns. A method for studying perfectly conducting bodies has been developed and is described in Section VI. It can be made applicable to coated bodies for which impedance boundary conditions hold.

(U) A list of technical reports, in addition to the quarterly reports written under AF 04694-67-C-0055 is given in Section X.

II

EXPERIMENTAL INVESTIGATION

2.1 Introduction and Review of Program

(S) The experimental basis for the SURF program rests on two experimental techniques. One technique, radar backscatter measurements, is well-known and anechoic facilities for making these measurements were in operation at the Radiation Laboratory at the start of the investigation. The other technique, surface current measurements, was a relatively new technique. It was completely new in this application. A small facility has been constructed and operated before the SURF program began in order to test the feasibility of using this technique to obtain information which would be useful in devising methods for computing the radar cross section of extremely low cross section shapes. The technique was shown to be a valuable tool and upon the initiation of the SURF program, a working facility and special electromagnetic and electrostatic probes were designed and constructed so that it could be applied to models of the re-entry shape under investigation. The particular shape, of course, was that of the cone-sphere re-entry vehicle typified by the LORV series of missiles and perturbations of cone-sphere typified by the indented rear termination of the Mark-12 re-entry vehicle and by the antenna and rocket nozzle perturbations of the LORV and Mark-12 vehicles. It was necessary that the surface current measurement technique be applicable to both the metallic and the absorber coated models under study.

(U) The surface current facility which evolved is described in Knott (1965). A brief summary of the experimental program is given in the following pages along with typical results for the increasingly complicated experimental situations which were studied. Detailed analysis of the experimental results are given in Section III of this report. For added coherence, the re-entry plasma experimental work is described in Section V in conjunction with the theory and analysis of the plasma embedded re-entry vehicle.

(S) In retrospect we can enumerate items of special interest. For one, the "indentedness" of the base cannot be discerned from a flat back and this is because the radius of curvature immediately aft of the join, and not that of the indentation, is the most important contributor to the radar cross section. We also learned that in general sheets of absorbent material markedly decreased the effects from perturbed models. The absorbing material acts as a shield and hides the underlying model from the incident field. However, perturbations in the form of annular slots can be large and frequency dependent, because the impedance looking into a typical slot depends strongly on frequency.

(U) Probably the most important thing we learned during the last year was the importance of maintaining sets of experimental measurements which can be readily compared with each other. This is not always easy to plan in the beginning of a long program because one cannot always see the direction the research is going to take. Early in the program we began measuring surface fields on objects and recorded the data by hand from observations of meter readings. We plotted the data manually. We soon discovered how to do this efficiently and during the second year made a great deal of measurements this way by the third year it was apparent that linear, not logarithmic, plots of amplitude vs distance along the surface were more convenient. We had been measuring amplitude in decibels, which is a logarthmic system, and a hand conversion was required to compare data. Therefore, early in the third year we designed and built a semi-automatic recording system, constructed to index and probe, in small steps. The system permitted the probe to stop wobbling or dancing after indexing and after a short interval of about 3 seconds, the pen on the recorder was commanded to drop down onto the re-

corder chart paper to record a datum point. After the point had been recorded the system told the probe to index one more interval and the process was repeated. In addition, the recorded data was plotted linearly and not in decibels. The purpose was, of course, to provide plots that could be observed directly without the laborious hand conversion process from the logarthmic system. The system worked well but used a great deal of chart paper and later, to solve this problem, we halved the chart scale. This had the effect of putting the data on half as much paper and therefore consumed less space. The upshot of all these changes was that we had a series of hand-recorded data in decibels, some linear recordings at one distance scale and some linear recordings with half that distance scale. This made comparison of many sets of early and late measurements difficult.

(U) These variations in the recording format show up in this report. The reader will observe as we progress through some experimental results that the scales are sometimes logarthmic and sometimes linear and that the distance scales along the surface are not always the same. This is because we are comparing data taken over many months of the contract period and have had some trouble comparing all the data on this basis.

(S) In the remainder of the experimental section we will review the effects of coatings on cone spheres, work that was actually carried out late in 1966; the behavior of surface fields on coated cone spheres obliquely illuminated; show how coatings suppress the effects of perturbations on cone spheres, such as the annular tip antenna simulations and join antenna simulations; show that the slots in the absorber jacket of a cone can seriously perturb surface fields by exposure of the underlying structure and by the formation of surface discontinuities in the absorbent material itself. We will also show that the indentation of concave-capped models is not important if the object is coated

with absorber and, finally, will present surface field and backscatter data for flat-backed models which show that the radius of curvature at the join is a dominant influence on backscatter.

2.2 The Influence of Absorber on Cone Spheres

(S) The experimental results previously obtained are documented in quarterly reports and in the final reports for Phase I and Phase II of SURF. In this section we intend only to hit highlights and to point out major influences of coatings on cone spheres. It will be recalled that several coatings were examined by means of transmission line experiments and some of these coatings were applied to cone spheres. Thin, heavy resonant coatings, flexible urethane foam coatings, a thick, heavy, lossy coating called "Eccosorb CR" were used. In Fig. 2-1 is a photograph of a 3-inch diameter, 15^{o} total angle cone sphere covered with Eccosorb CR material and is probably the best model that we produced with a coating on it. The observer can see that the tip is a sharp one, that the surface is smooth, and that auxiliary distance scales appear on the side of the model to augment reading out probe position. This coating had magnetic, as well as dielectric, loss and the coating was about 3/8" thick. In Fig. 2-2 is a photograph of a model coated with LS-26 material. Observe that the coating was sewn on with thread and that we also have a scale on this model to indicate probe position. Note that near the tip the threads cause irregular, but unavoidable bumps on the surface; because of the flexible nature of the material and because of its thickness, the coating could not be wrapped very accurately around the tip. The model therefore is somewhat shorter than it would have been, had the coating been of uniform thickness all the way out to a sharp tip. This fact will be evident as we progress through the experimental plots. The coating on the model in Fig. 2-1 was not removable, but the coating jackets seen in Fig. 2-2 could be removed and replaced with other materials because of the sutures.

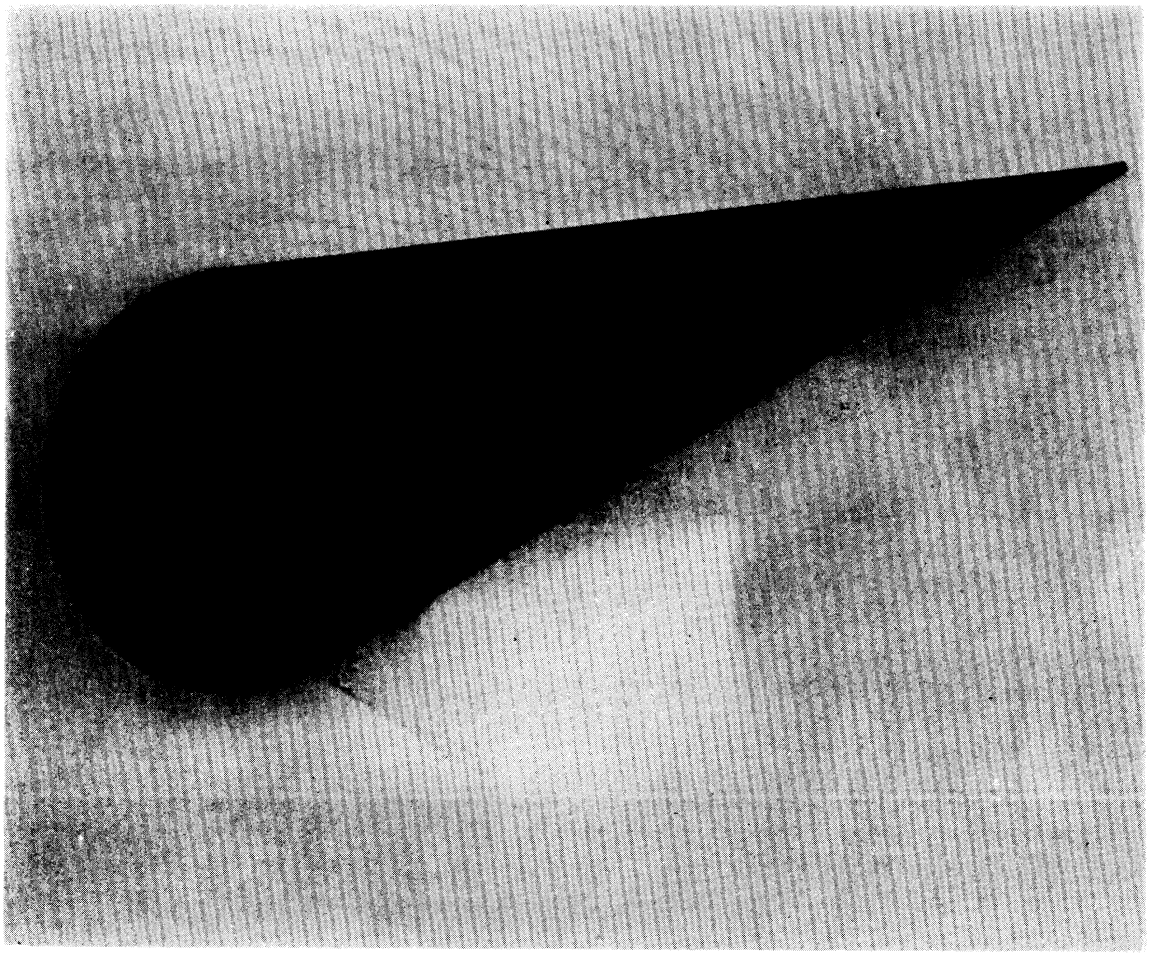

FIG. 2-1: OUR BEST ABSORBER-CLAD CONE-SPHERE HAD A MACHINED OUTER SURFACE; CONE HALF-ANGLE IS 7.5^{o}, BASE DIAMETER IS 3.000", COATING THICKNESS IS 3/8".

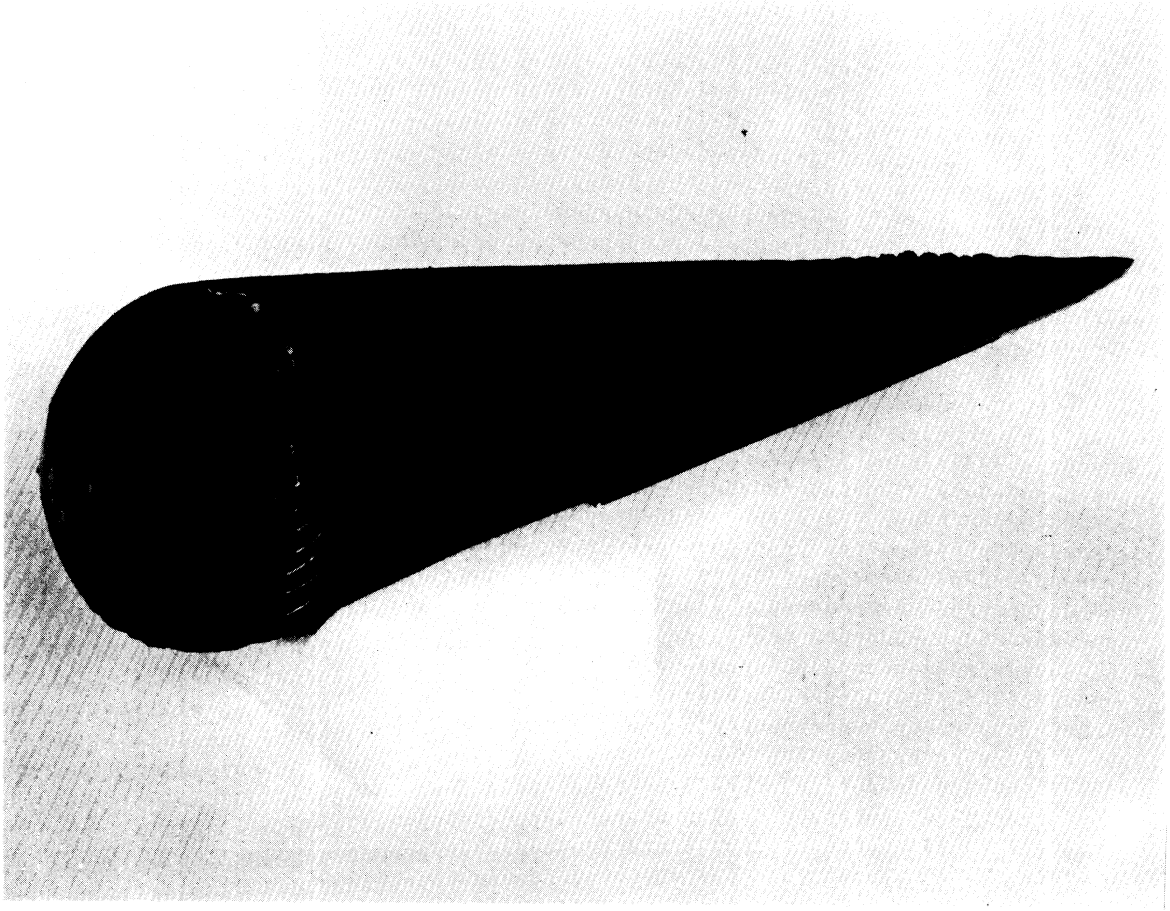

FIG. 2-2: FLEXIBLE ABSORBERS HAD SUTURED SEAMS; CONE HALF-ANGLE IS 7.5°, BASE DIAMETER IS 3.000", COATING IS APPROXIMATELY 1/4" THICK.

(S) In Fig. 2-3 we present the results of surface field measurements on three models for ka = 1, where a is the radius of metallic spherical base. The fields in the plot have been normalized with respect to the incident magnetic intensity, H_o . The underlying model in each case was a 3" diameter cone sphere with a 15^o total angle at the apex. We present amplitude in db and thus have a logarithmic scale. The results for three coatings are shown and it will be observed that two of the coatings behave nearly identically and, in fact, the curves tracing out the response for LS-22 and LS-26 coatings are nearly the same as that for a base model: this is because the coating is nearly transparent at this frequency. The Eccosorb CR coating, on the other hand, had a slightly better effect but not much near the side. The field intensity for the Eccosorb CR coating extends much further to the left than does the LS coating because the Eccosorb coating was more perfect and formed a more perfect, hence longer, tip. There is a sharp dip shortly aft of the tip but the intensity builds up to a value of about 2 db. The amplitude remains constant at about 2 db until one reaches the join and at the very antipode the intensity is 0 db. The marked oscillations for the LS coatings are spaced very nearly a half wavelength apart.

(S) Turning now to Fig. 2-4 we see the effect of much increased frequence upon the same models. Again we plot amplitude in db as a function of distance traversed along the surface aft from the tip and for this figure, ka = 5. Note that although the fields attained a maximum intensity of about 8 db as shown in Fig. 2-3, they fall to about - 5 db in Fig. 2-4. This is because the coatings were much more effective in attenuating the wave traveling along the conical portion. One can also see that the perturbations are much faster along the side, evidence that a higher frequency was being used. Note that once the join has been passed the fields decay quite rapidly until the antipode reached. The Eccosorb absorber is much more efficient in suppressing the wave near the tip than the LS materials, but after about 2 wavelengths

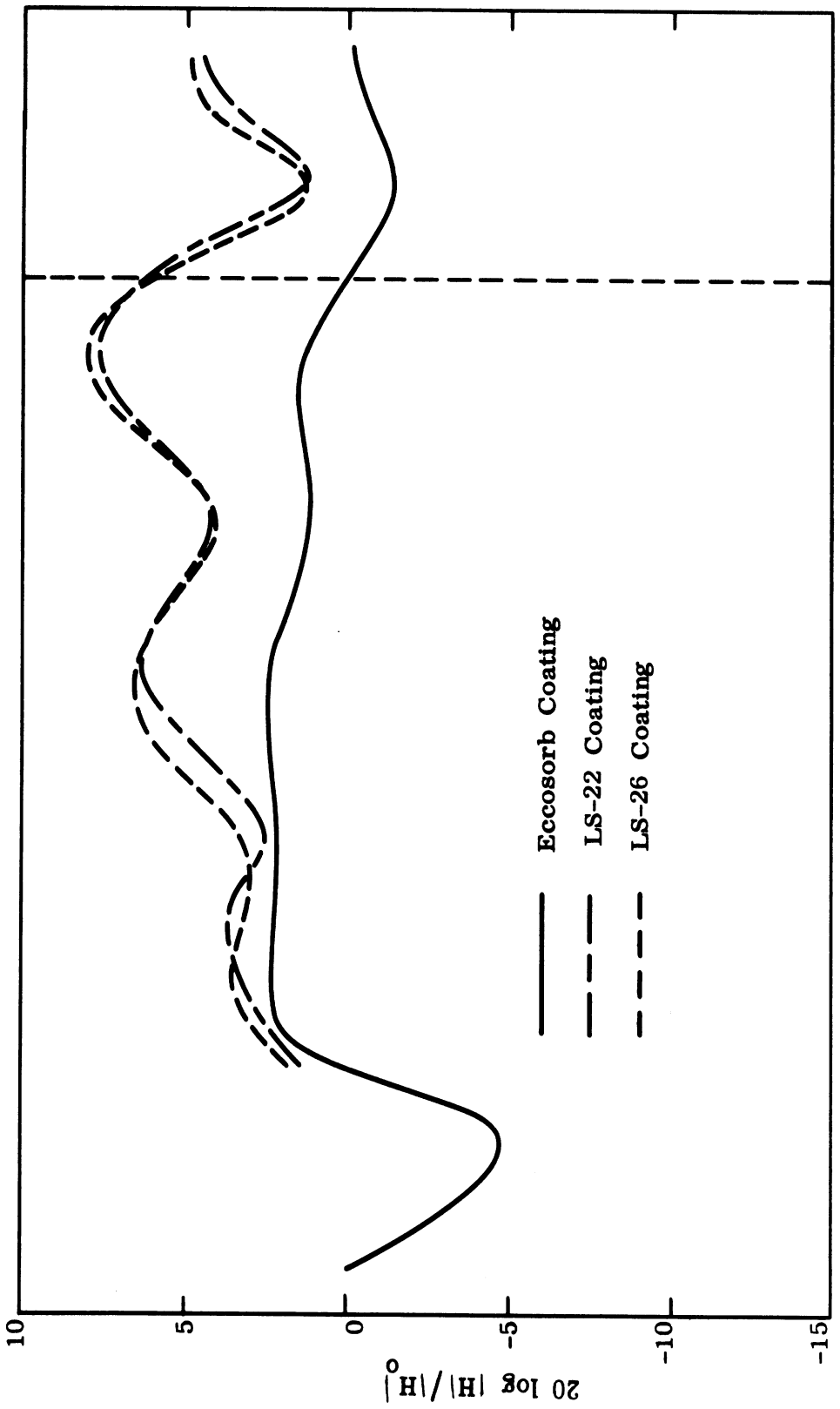

FIG. 2-3: SURFACE FIELDS ON CONE-SPHERES SUPPRESSED BUT SLIGHTLY AT LOW FREQUENCIES BY COATINGS.

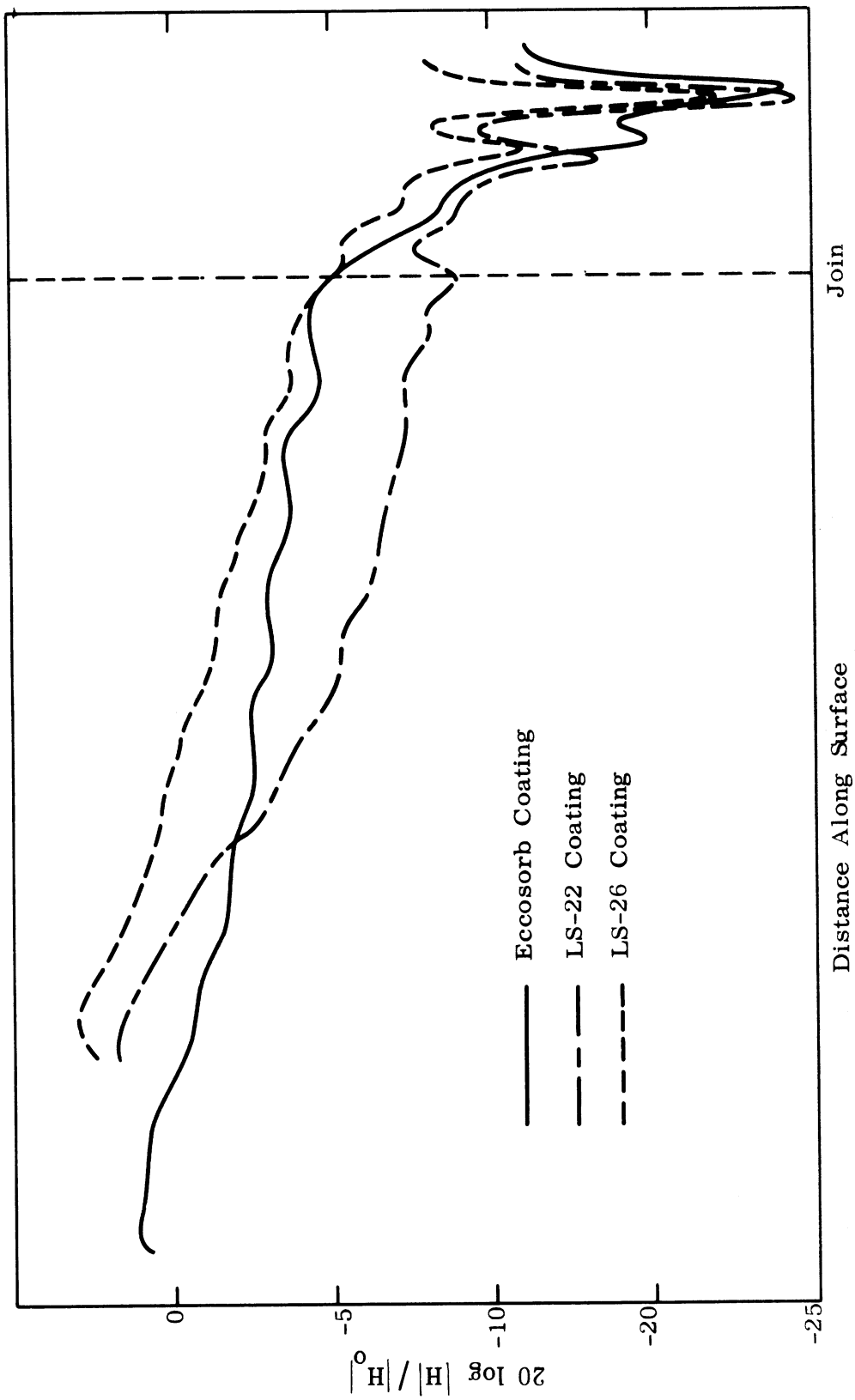

FIG. 2-4: COATINGS HAVE A BETTER CHANCE OF REDUCING FIELD INTENSITIES AT HIGHER FREQUENCIES:

aft of the tip the LS coatings proved to be more effective. It was once thought that the LS-22 coating was more efficient than the LS-26 but the data in Fig. 2-4 suggested this is not true. It may be possible that the technicians interchanged coatings and failed to note the change in the data. We note that both Figs. 2-3 and 2-4 are for nose-on incidence.

(S) In Fig. 2-5 we see the effect of changing the angle of incidence. There are four curves displayed here representing angles of incidence running from 0^{o}, which is nose-on, to 82.5^{o} which is broadside to the conical surface. The model in this case is coated with Eccosorb CR and ka = 5. Observe that we have a symmetrical pattern, with the tip lying near the left and right extremes of the figure and the antipode near the center. For nose-on incidence we would expect a symmetrical pattern and indeed we do get one as evidenced by the solid trace. If now the angle of incidence is changed to 7.5^{o} we see that the fields on the lit side (the left side) of the figure are more intense than on the shadowed side, which is the right side of the figure. If we change the angle of incidence to 37.5^{o} the fields on the lit side increase even more, approximately 5 db above the nose-on case, while on the right side the fields are reduced of the order of 15 db. Finally, as we go out to 82.5^{o}, the fields attain their maximum intensities on the lit side and their minimum on the shadowed side. There are small perturbations near the tip on the lit side which are about half a wavelength apart and they are evidence of waves traveling back and forth along the illuminated surface, despite the fact that the incident wave has no component in this direction.

(S) Note that on the illuminated side for the 82.5^{o} incidence angle, the field intensity is nearly constant at a level of about + 3 db. Ordinarily if the model has not been coated the intensity would have been very close to 6 db.

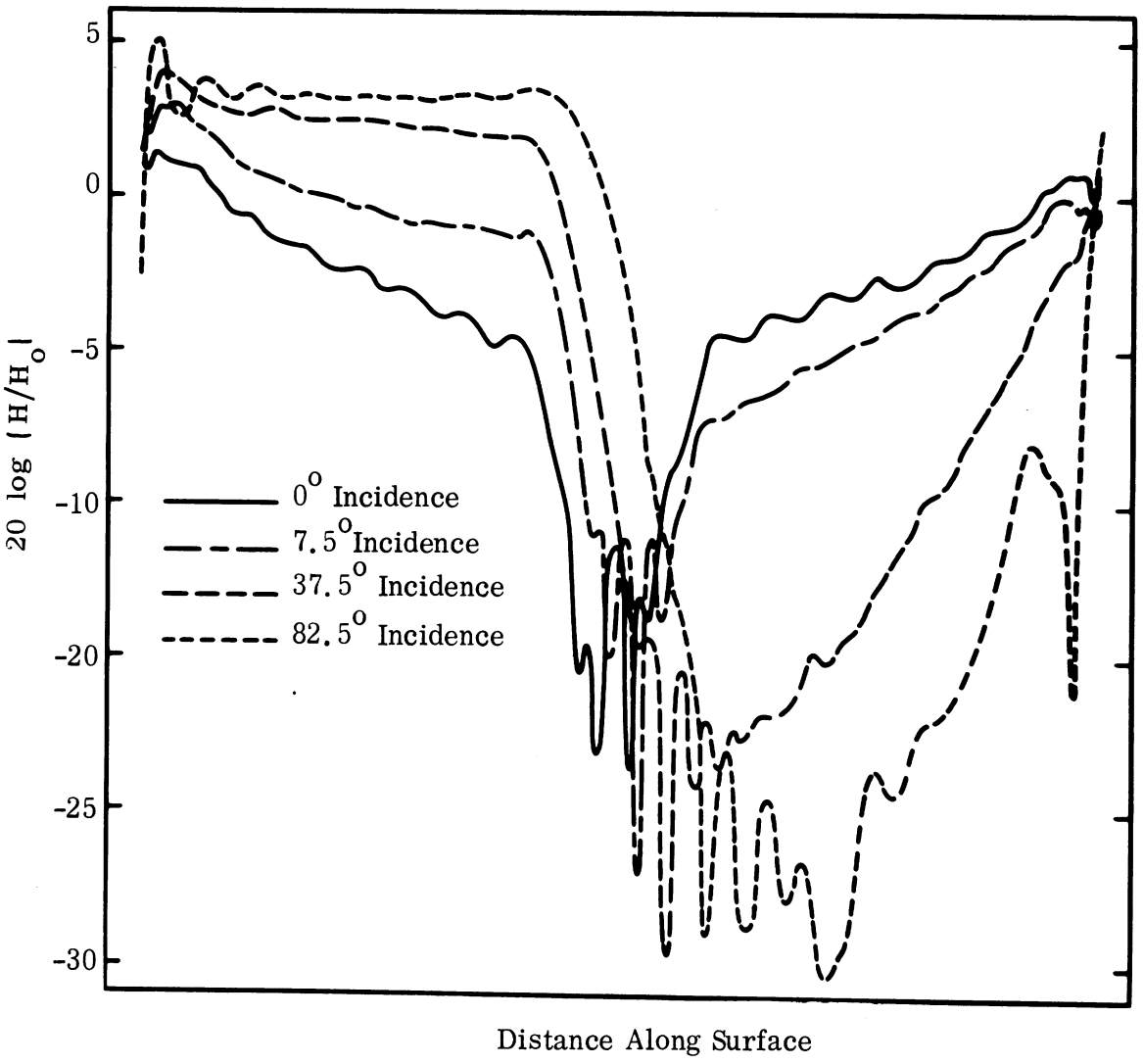

FIG. 2-5: FOR OBLIQUE INCIDENCE, FIELD INTENSITIES ON THE LIT SIDE ARE MUCH STRONGER THAN ON THE SHADOWED SIDE.

This suggests that the absorber is nominally at 3 db absorber. The data very graphically show that the absorber, although it may be a poor one for normal incidence, is a good one for attenuating waves traveling along the long slanted surface. One would expect that even though an absorber would be very poor, say only 2 or 3 db, it would be a reasonably good one if the body is a long one viewed nose-on.

2.3 Coated Perturbed Models.

(S) In this section we will show that if a smooth body, like a cone sphere, is perturbed by either tip antennas or antennas situated near the join, these can be large contributors to surface field perturbations and backscatter measurements. Then if these perturbed bodies are sheathed in an absorber jacket the perturbations will practically disappear and the cross sections of the bodies will be much reduced. Finally, we will show that if slots are cut in the coating just above the antenna simulations, that the perturbations will again arise and be relatively large contributors to the backscatter. Figures 2-6 and 2-7 are photographs of the perturbed models that we built in 1966 to aid surface field studies. The model in Fig. 2-6 is called LSP (Lucite Spacer, Point) while the model in Fig. 2-7 is called LSH (Lucite Spacer, Hemisphere). The antenna simulations were provided by lucite wafers, 1/4" thick. These two models form the models for which a great deal of experimental work was done.

(S) In Fig. 2-8 we present a composite trace of the surface field intensities for the two models and we compare them with a plain cone-sphere for which ka = 5. Observe that we again plot amplitude in db as a function of distance aft from the tip. The tip lies on the left side of the figure, the antipode lies at the right, and the join is clearly marked by a dashed line. The solid trace, the behavior of the surface fields on a plain cone-sphere, begins near 0 db at the tip and rises gradually to about 5 db two wavelengths aft,

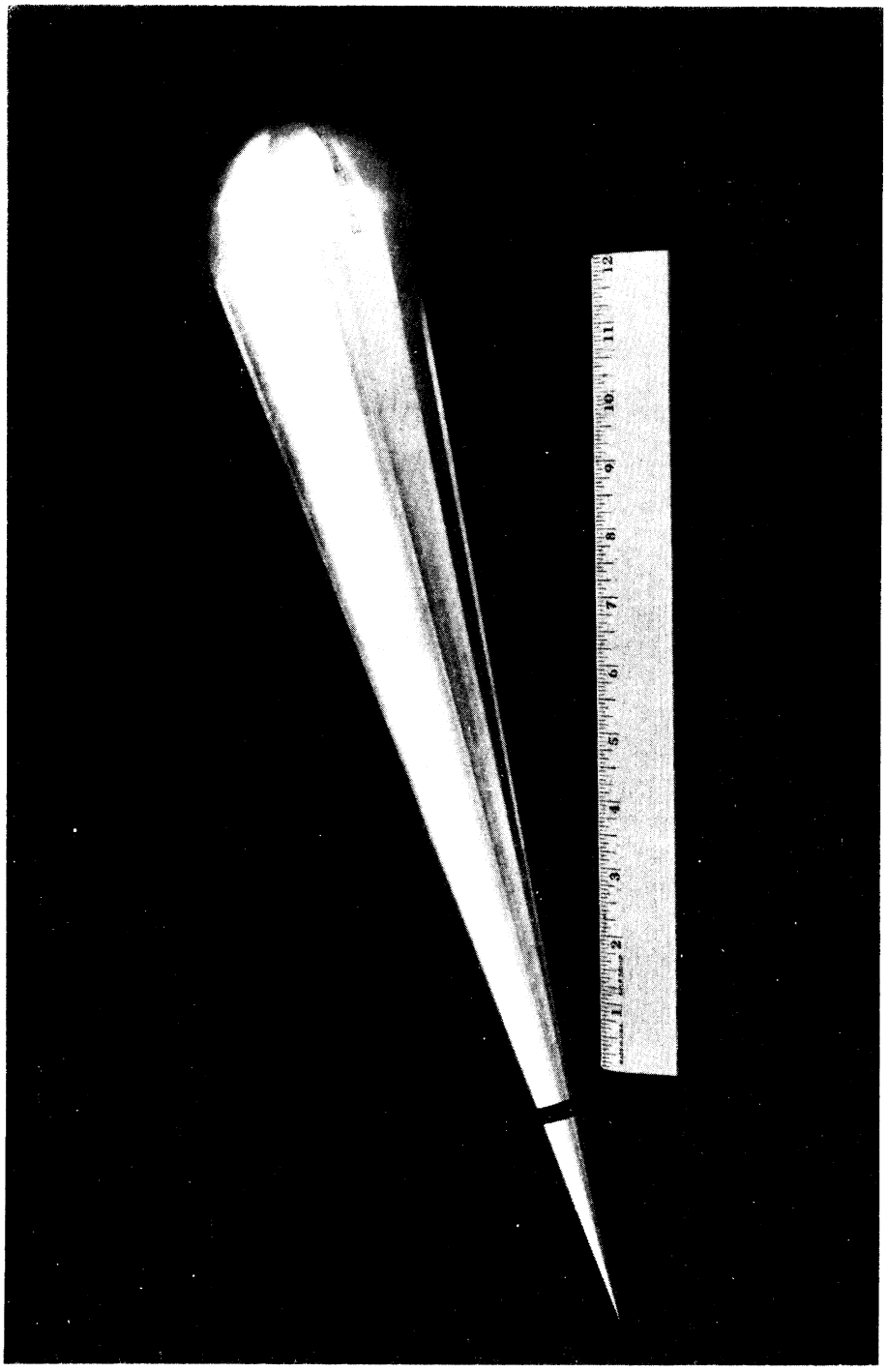

FIG. 2-6: MODEL LSP HAS A LUCITE SPACER NEAR THE TIP, OTHERWISE THE MODEL IS A 7.5^{o} HALF-ANGLE, 1.420" BASE DIAMETER CONE-SPHERE.

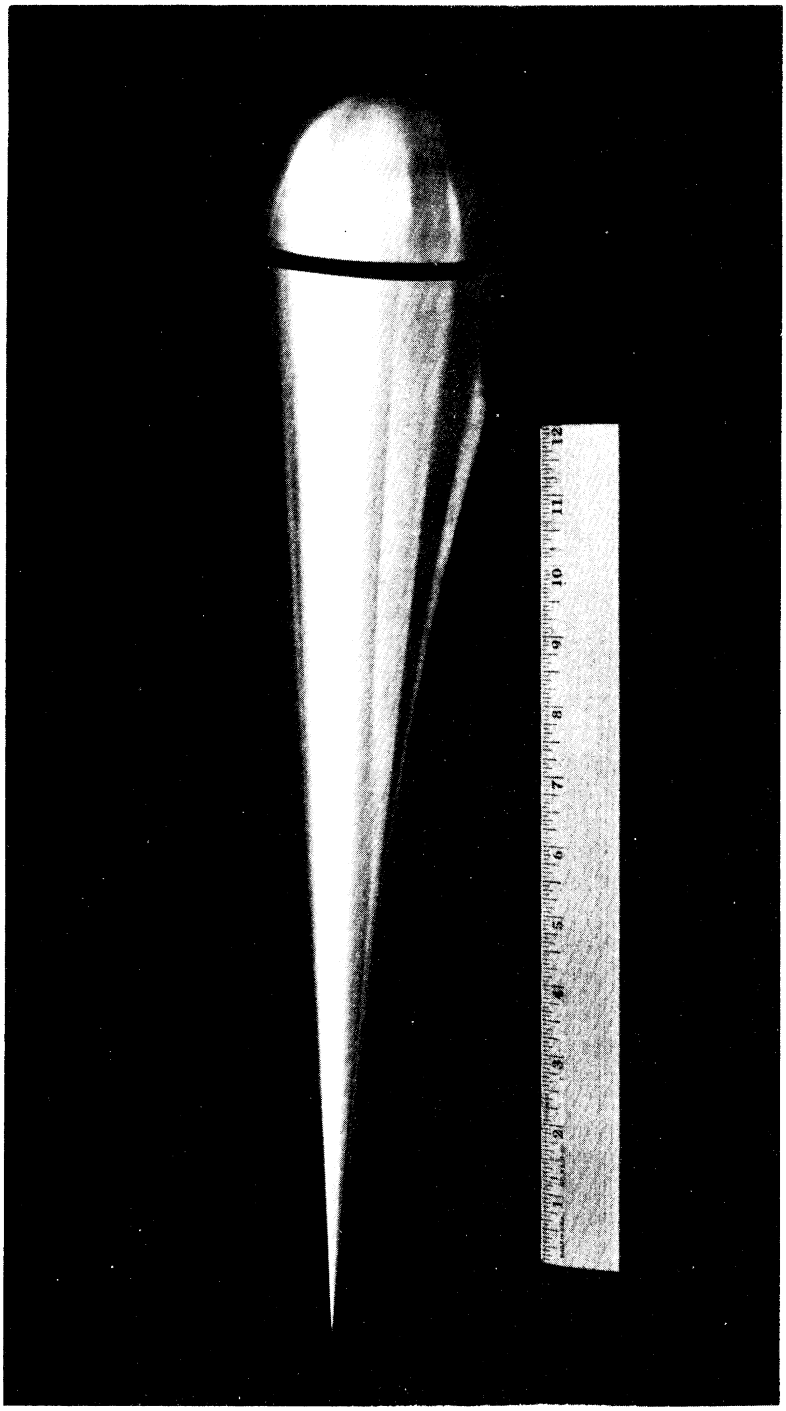

FIG. 2-7: MODEL LSH HAS A LUCITE SPACER JUST BEHIND THE JOIN, OTHERWISE IT IS A CONE-SPHERE OF THE SAME SIZE AS MODEL LSP.

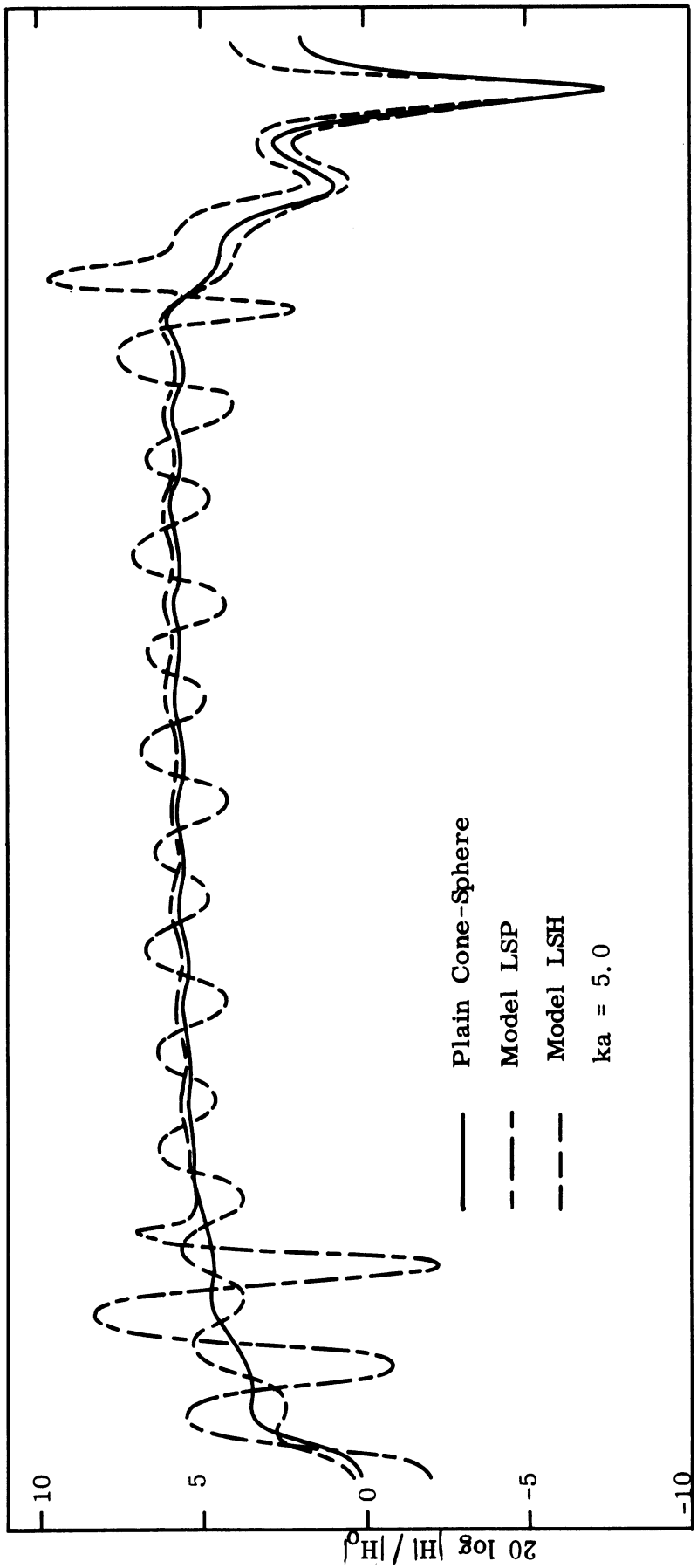

FIG. 2-8: THE DISCONTINUITIES OF MODELS LSP AND LSH HAVE DIFFERENT EFFECTS ON THE SURFACE FIELDS.

and finally near the join attains a value of about 6 db. If we now examine the trace comprized of the long dashes, we see that the fields begin at the tip slightly below that of the plain cone-sphere but have a series of very strong oscillations amounting to more than 10 db in amplitude. These oscillations are due to the spacer near the tip and once the spacer has been traversed, the trace is much like that of an ordinary cone-sphere. We conclude that the effects of the Lucite Spacer Point are felt only forward of the spacer and not aft. Finally, considering the trace comprised of the small short dashes, we see that the intensity begins again at 0 db and builds up to about 6 db near the join, but that the intensity has a series of quite regular perturbations amounting to about 2 db in amplitude. Since the spacer for this model was near the join and since the perturbations are largely along the conical surface, we can see that the LSH model perturbs the entire surface field structure. Near the spacer we can see the strong rise in intensity and the fields around the back are not the same as they were for a plane cone sphere. Bearing these characteristics in mind we now turn to Fig. 2-9 through 2-12 which illustrate the effects of covering the model with an absorber layer.

(S) In Fig. 2-9 we plot the results for ka = 1. Note that we plot the linear field intensity normalized to the incident field, not decibels, as a function of distance along the surface. All three models show very nearly the same behavior and we are led to conclude that the coating shields the spacers from the incident field. The fields on model LSP show a very small dip slightly inward from the tip and the fields from model LSH show another small dip very near the join. Aside from these tiny perturbations, the structures along all three models are practically identical. Figure 2-10 shows that for a ka = 3 the model LSH produces a phase inversion of the

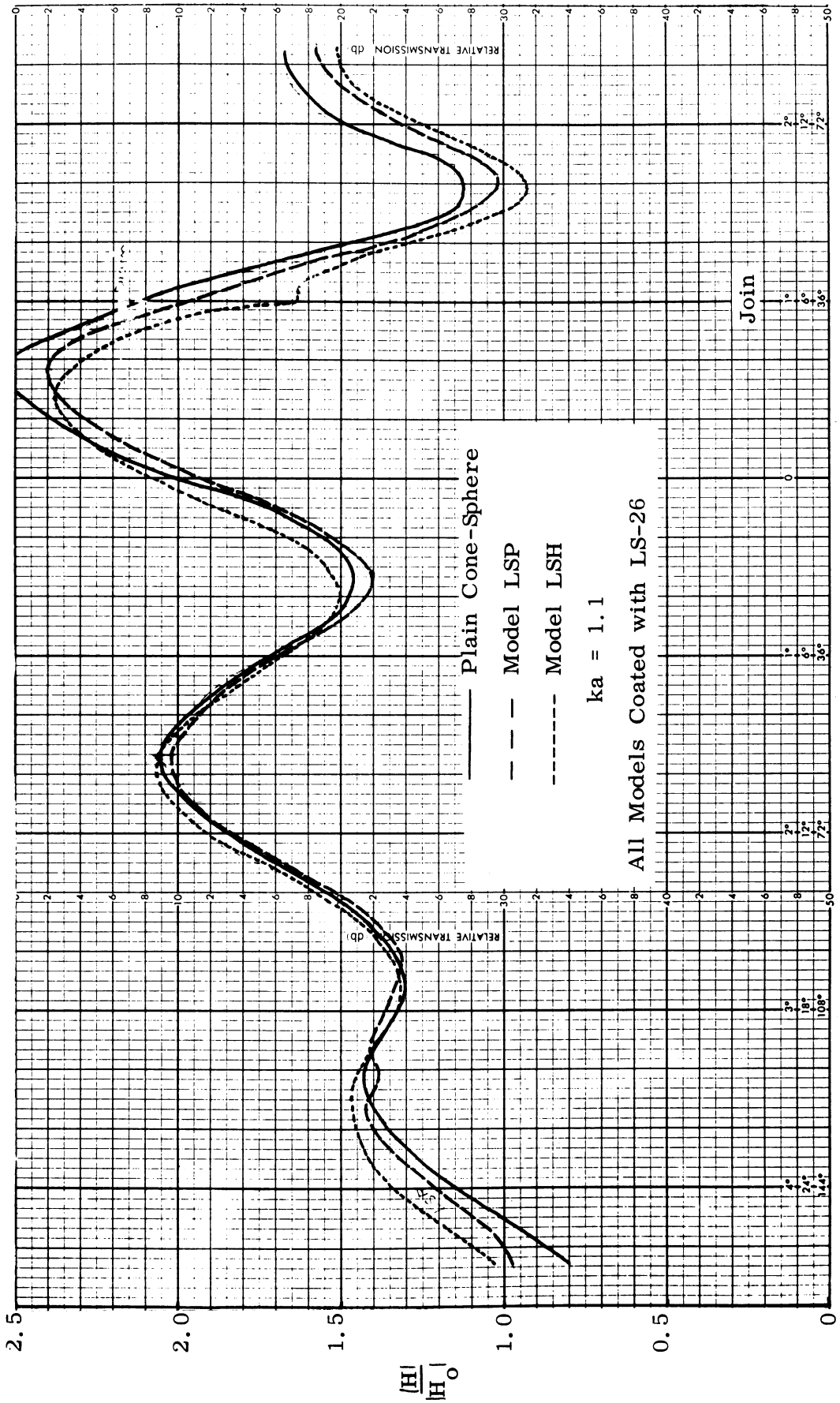

FIG. 2-9: EVEN FOR LOW FREQUENCIES, THE DISCONTINUITIES OF MODELS LSH AND LSP ARE HIDDEN WITH AN ABSORBER SHEATH, ka = 1.1.

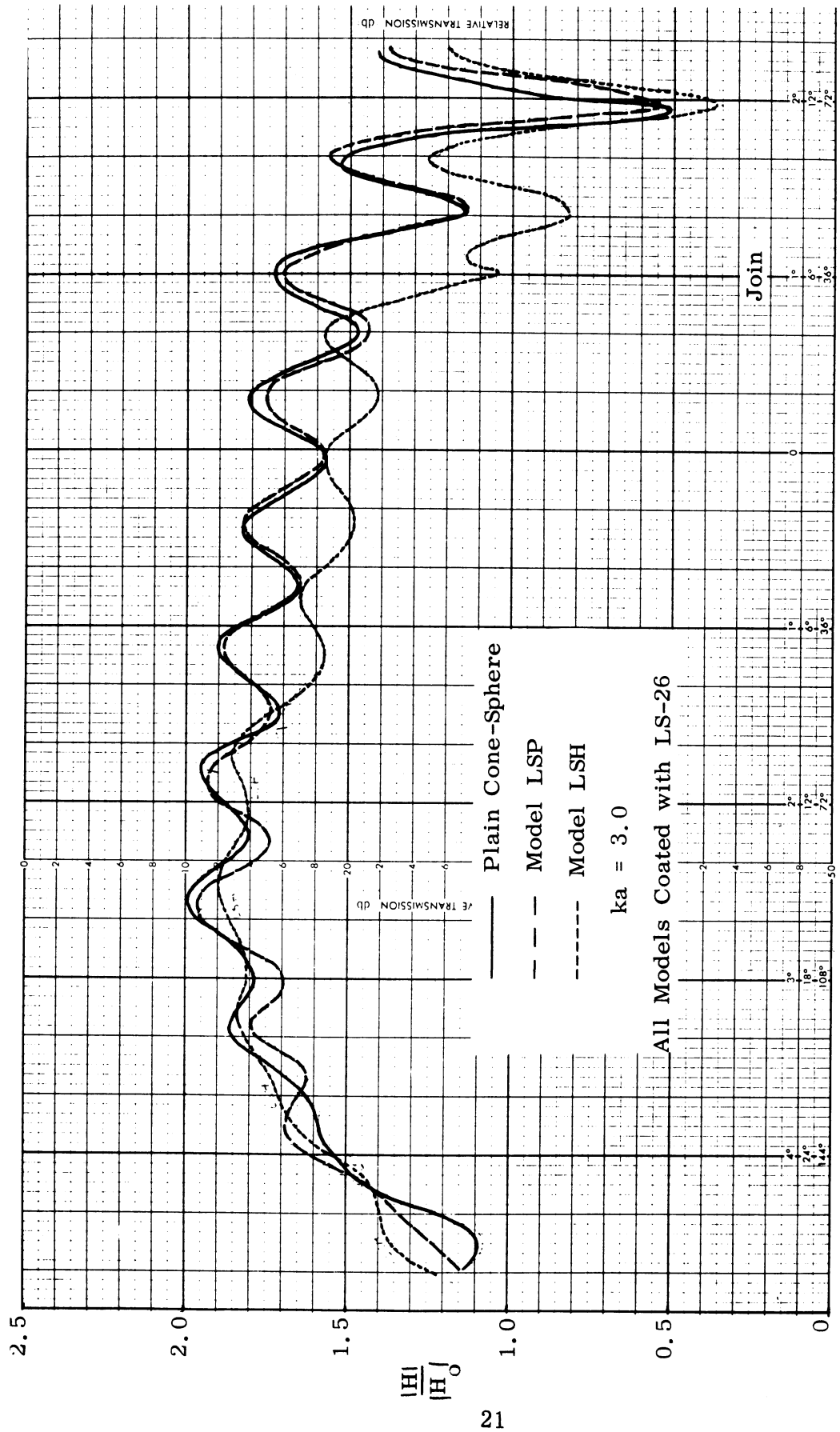

FIG. 2-10: FOR ka = 3.0, THE PERTURBING EFFECTS OF MODELS LSP AND LSH ARE NOT COMPLETELY SHIELDED.

surface fields; i.e., the reflections seem to peak up where previously there were nulls and to have nulls where there were previously peaks. Note that beyond the Lucite spacer the fields for the plain cone-sphere and for model LSP are practically identical. For this ka we see the strongest effect for the LSH model and the fields around the rear are some 2 db lower than for model LSP or for the plain cone-sphere.

(S) In Fig. 2-11 the fields are plotted for ka = 5. Notice that model LSP shows some perturbations but that the plain cone-sphere and model LSH also have these perturbations. We ascribe the similarity to the roughness of the tip because of the way the coating was sewn on. The fields for all three models decay to about 0.6 near the join and between the join and the tip the fields are about the same for all three models. Around the back there are small differences but again we ascribe these to experimental errors. In Fig. 2-12 appear the results taken for the highest ka (ka = 8). Again there are perturbations on both the LSH and LSP models due to irregularities in the coating near the tip and all three traces are very nearly coincident from tip to antipode. In reviewing Figs. 2-9 through 2-12 we conclude that the coating markedly suppresses the effects of the perturbations of the underlying model. If the model is long enough in terms of wavelengths, surface field intensities near the join will be very much those that would be found on an infinitely long cone, as will be brought out in later sections of this report.

(S) The above results show that an absorbent coating can reduce the surface fields, and therefore the backscatter, from long targets provided the coating covers the entire model. But if there are antennas on the object which must radiate, the coating will interfere or reduce the efficiency of that radiation. We therefore undertook to expose the underlying perturbations (the

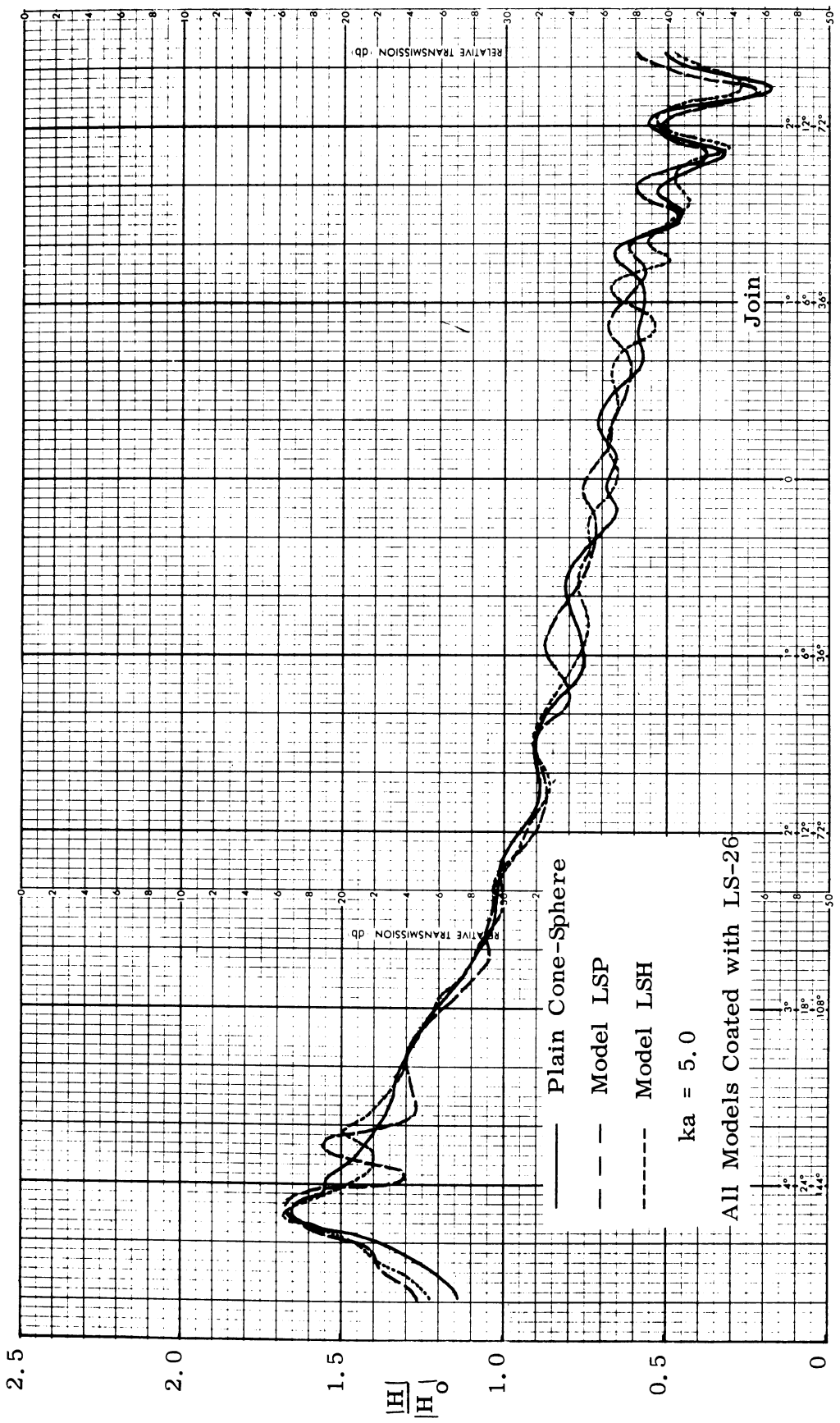

FIG. 2-11: FOR ka = 5.0, THE PERTURBED MODELS ARE FAIRLY WELL SHIELDED.

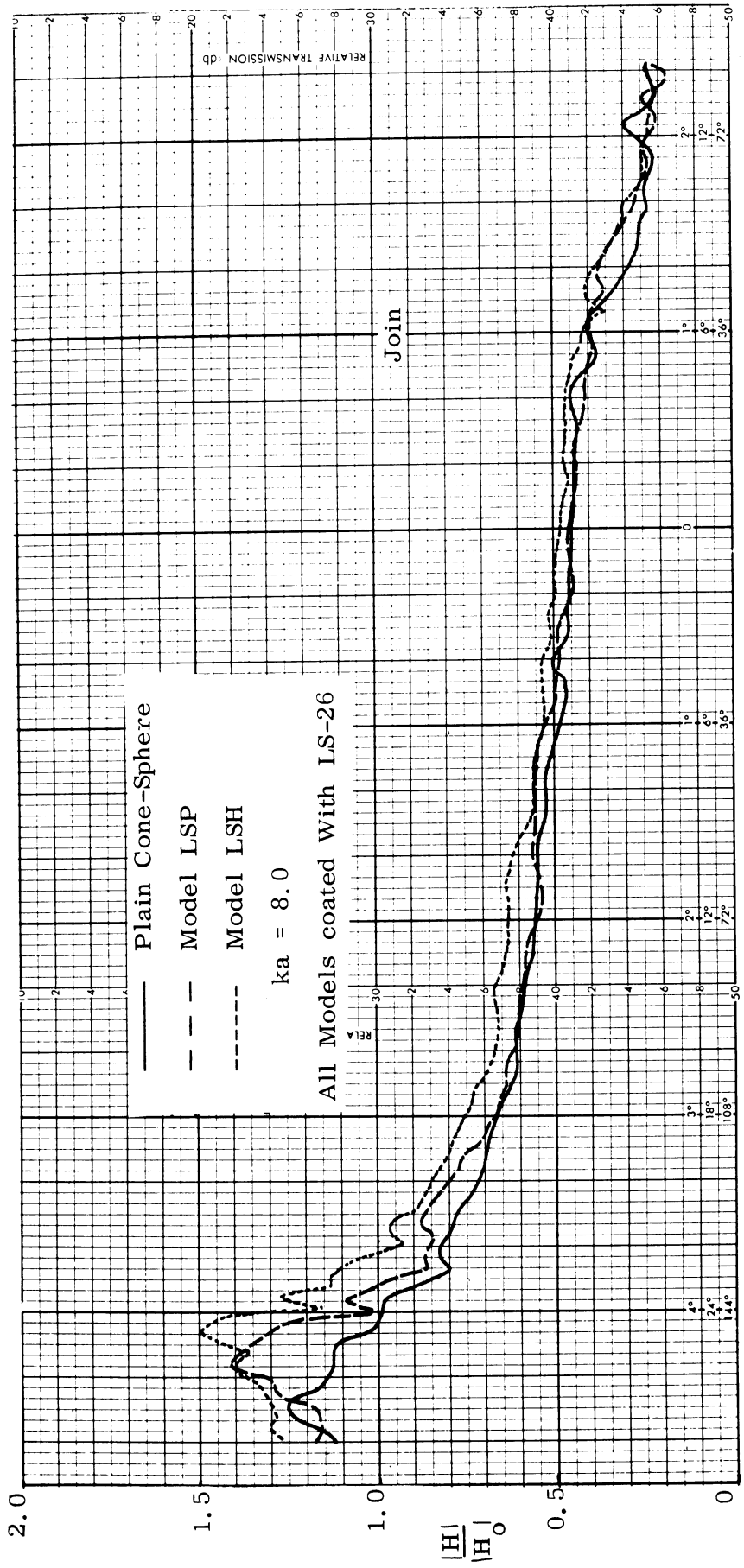

FIG. 2-12: FOR ka = 8, ONE CANNOT TELL THAT THE MODEL INSIDE THE ABSORBER SHEATH IS ANYTHING BUT PLAIN.

Lucite spacers), by cutting slots in the absorber coating directly above them. Two jackets of LS-26 were fabricated, one with the slot aligned at a point directly above the point where the spacer would be for the LSP model, and one having a slot in the coating directly above the point where the spacer for the LSH model would be. This is illustrated graphically in Fig. 2-13.

(S) To fully assess the effects of model and coating combinations, we alternately left the slots air-filled or we loaded them with Lucite. We inserted model LSP, as well as the plain cone-sphere, into the upper left hand jacket of Fig. 2-13 and used the air and Lucite loading in the slot. This had the effect of producing four different measurement situations. We also inserted model LSH and the plain cone-sphere in the absorber sheath shown in the upper right hand figure of Fig. 2-13. With the slot loaded with air or Lucite we produced four more model combinations. The total effect was 8 models which we examined for four ka values: we will not present the results for the ka values but instead have selected typical ones for ka's of 3, 5, and 8.

(S) Turning now to Fig. 2-14, there are four traces showing effects of the surface fields for the four models mentioned above for ka = 3. These curves were traced directly from the raw data and the quantity displayed is the amplitude of the surface field intensity as a function of distance along the surface, not db. Notice that the air and Lucite perturb the fields about equally, independent of which model is used inside the coating. On the other hand, the reader will note that the perturbations are much stronger if the underlying model is the LSP model and the perturbations seem to be largely on the forward side of the spacer. Aft of the spacer the field intensities are practically identical for all four model configurations, and although around the back there seems to be one trace that is much different from the other three, we ascribe it to experimental error.

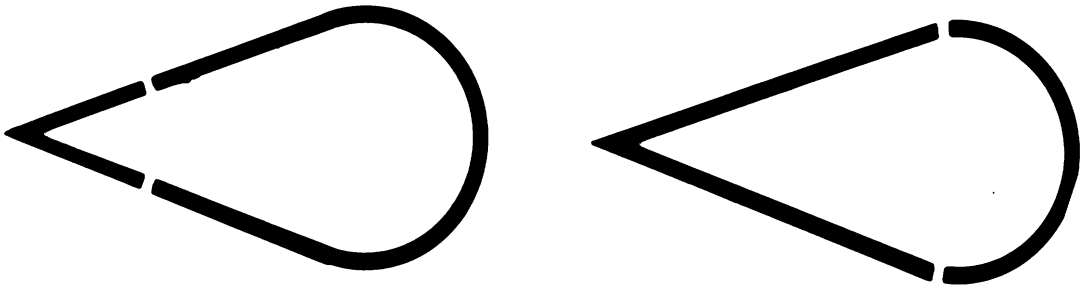

Absorbent Sheaths

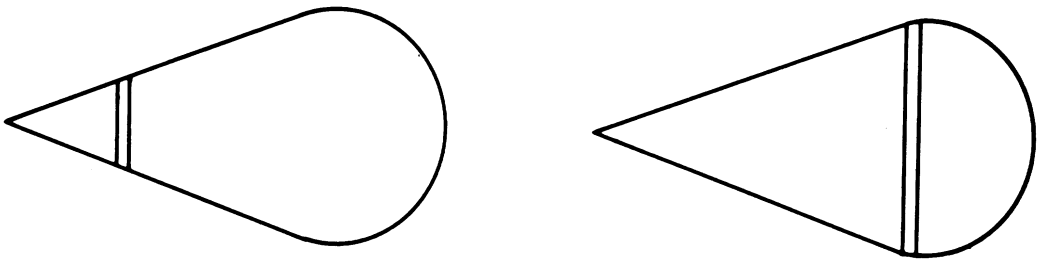

Model LSP Model LSH

Plain Cone-Sphere

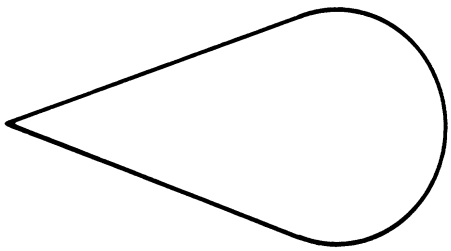

FIG. 2-13: VARIOUS COMBINATIONS OF MODELS AND SLOTTED ABSORBER SHEATHS PRODUCED EIGHT SEPARATE MEASUREMENT SITUATIONS.

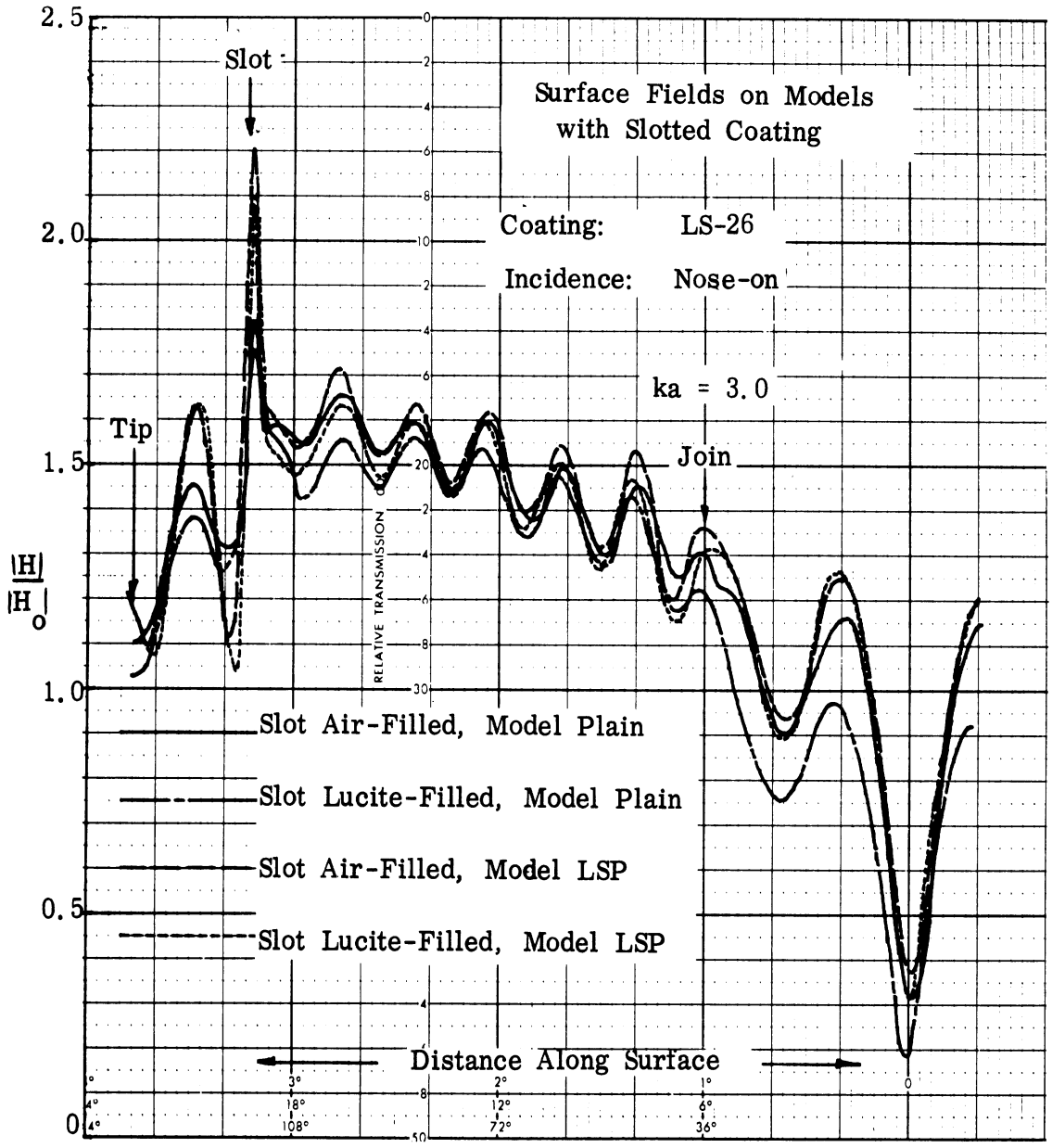

FIG. 2-14: A FORWARD SLOT IN THE COATING AFFECTS ONLY THE INTENSITIES IN FRONT OF THE SLOT.

(S) Turning now to Fig. 2-15, which is for the same ka as Fig. 2-14, we have shown model LSH and a plain cone-sphere inside the absorber coating. Again, notice that the air and Lucite seem to perturb the fields about the same but that if the underlying model is the LSH model, the perturbations are much stronger than if the model underneath is a plain one. Again, we see a phase inversion due to the presence of the LSH model, similar to that seen in an earlier figure. Observe that the fields around the back of the model are markedly different and that one would therefore have to know the impedance looking into the slot in order to predict the fields around the back.

(S) In passing to higher ka, Fig. 2-16, we have the results for a ka = 5. For this figure we have again studied the model LSP where the slot in the coating beam forward, and this time the air seems to perturb the fields more than the Lucite. In fact, the greatest perturbation occurs when the model underneath was model LSP and when the slot in the coating was filled with Lucite. The amplitude of the fields along the conical part between the spacer and the join decays in nearly the same behavior but with slightly different phases. Around the back of the model, from the join to the antipode, there is hardly any difference between the four models. It appears that some perturbing effects can be obtained even with a plain cone-sphere underneath, but if the underlying model is LSP, then the effects are much greater and they always appear forward of the spacer, and not aft. In Fig. 2-17 are displayed the effects of inserting model LSH inside the sheath. From the tip back very nearly to the join the fields are nearly the same, which we ascribe to the fact that the absorber is attenuating the incident wave much more than when the spacer is near the front. Careful examination shows the model LSH perturbs the field slightly more, especially aft of the spacer.

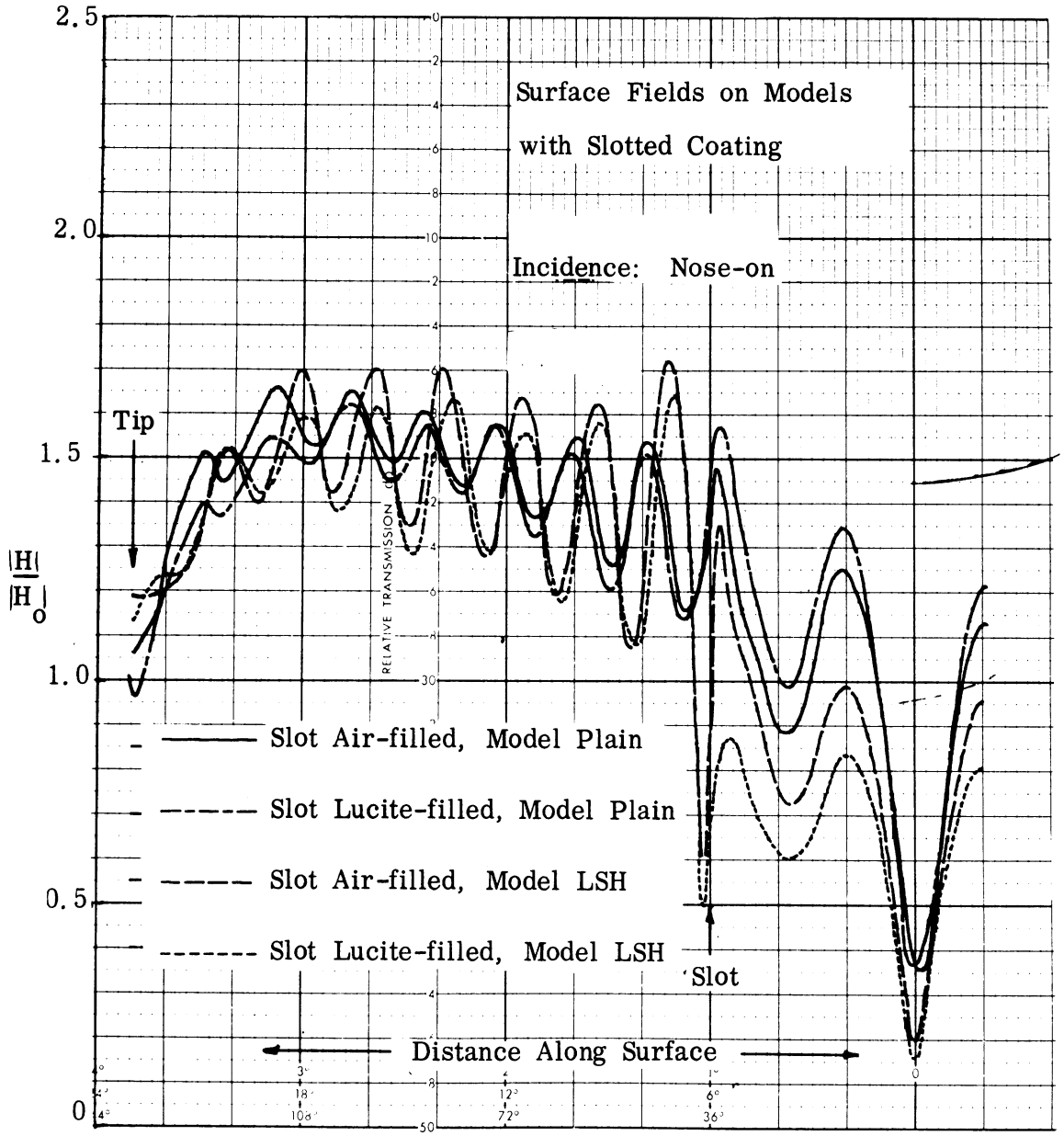

FIG. 2-15: A REAR SLOT AFFECTS THE FIELD INTENSITIES ON BOTH SIDES OF THE SLOT. ka = 3, Coating is LS-26.

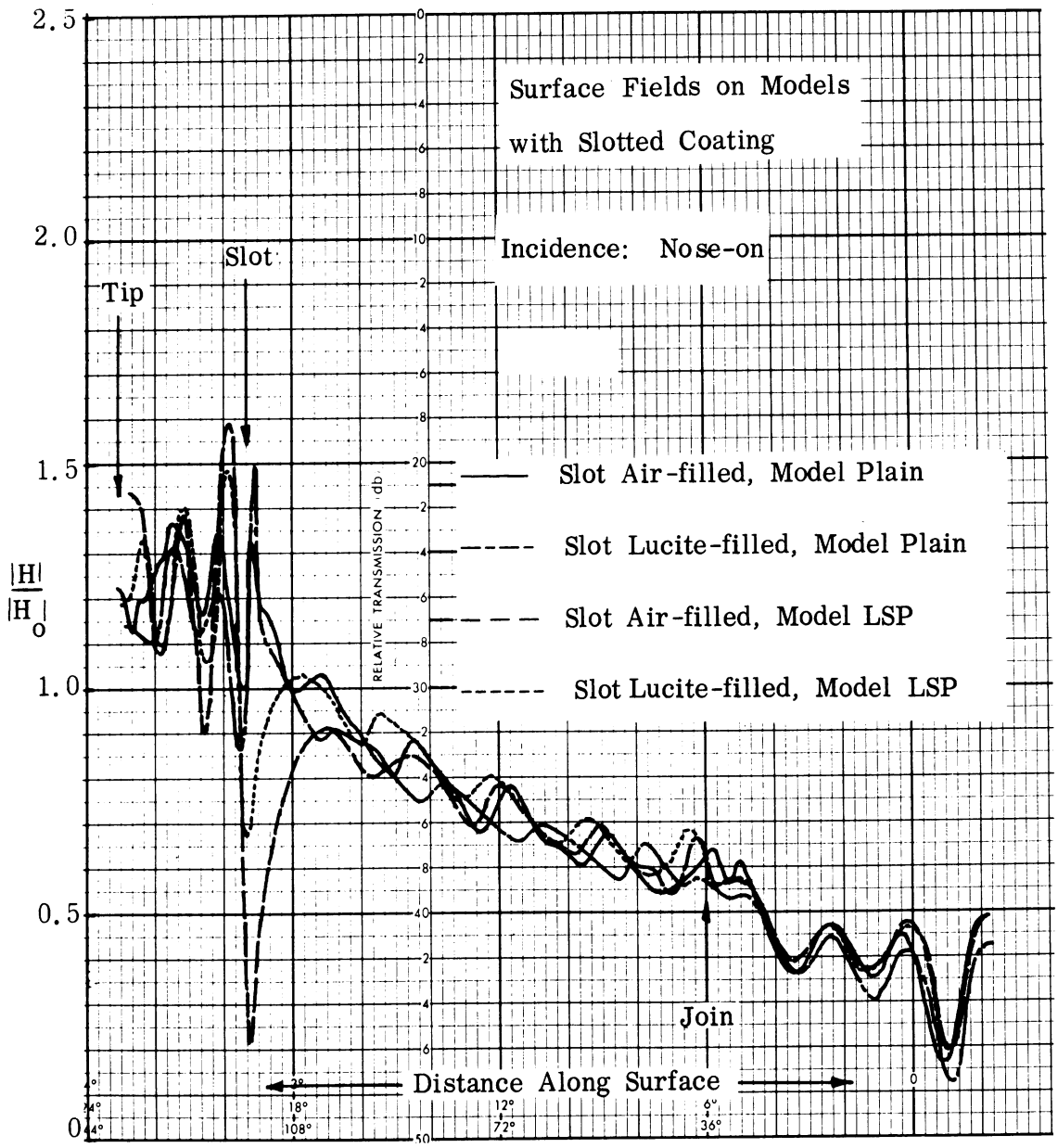

FIG. 2-16: STRONG PERTURBATIONS OCCUR IN FRONT OF A FORWARD SLOT FOR ka = 5.0. Coating: LS-26.

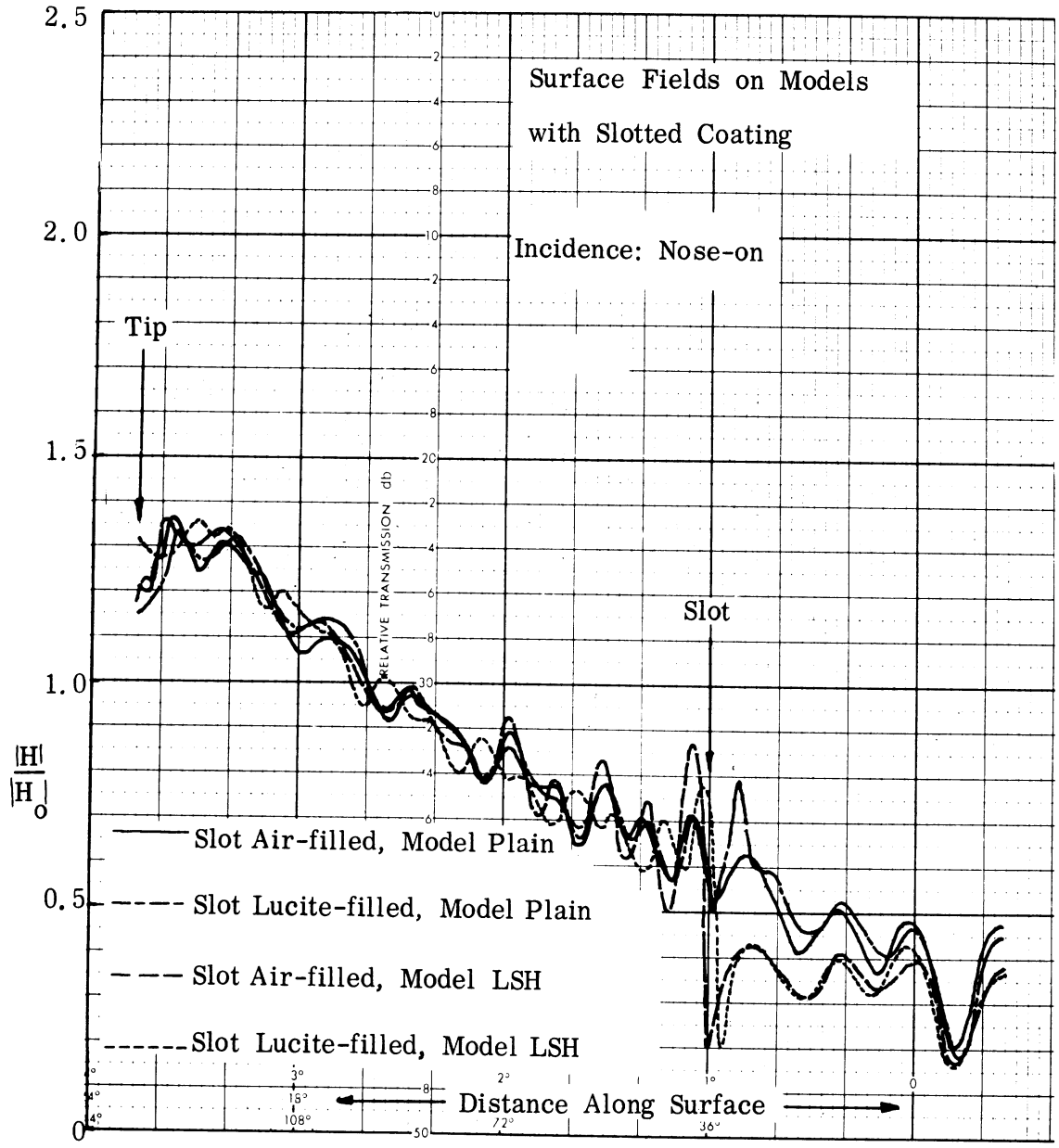

FIG. 2-17: A REAR SLOT SEEMS TO HAVE LESS PERTURBING EFFECT FOR ka = 5.0 THAN ka = 3.0. Coating: LS-26.

(S) Finally, turning to Fig. 2-18 we caution the reader that the scale has been expanded because the field intensities were very small. The frequency for this figure was such that ka = 8 and in this figure model LSH was slipped inside the sheath. Note that the fields are not perturbed on the front nor around the back but that a small local perturbation is centered near the slot. The perturbation seems to be about the same whether the model underneath it is LSH or a plain one, and it seems to be about as strong whether the slot is filled with air or filled with Lucite.

2.4 Indented Base Models

(S) Early in the contract we constructed a series of indented base models and measured the surface fields on them. Results of these measurements show that the surface fields were more or less independent of the depth of indentation on the back. In Fig. 2-19 is a sketch of the geometry of the terminating base and it can be seen that the base was formed from two circles, one near the join and another whose center lay on the axis of the model. These circles were tangent to each other and to the sides of the cone. The radius C was selected to give the variation in the depth of indentation while the radius just after the join was held fixed at 0.553". These models were given the names ID-1, ID-2 and ID-3 with the depth of indentation increasing with increasing model number. The models were coated with an absorbent jacket, as shown in Fig. 2-20, and because of the geometry of the base we found it difficult to glue the absorbent material onto the indentation. We therefore stretched the absorbing material directly across the back forming a void between the material itself and the surface at the indentation. We measured these models for four values of ka, but will present the results for only three ka's.

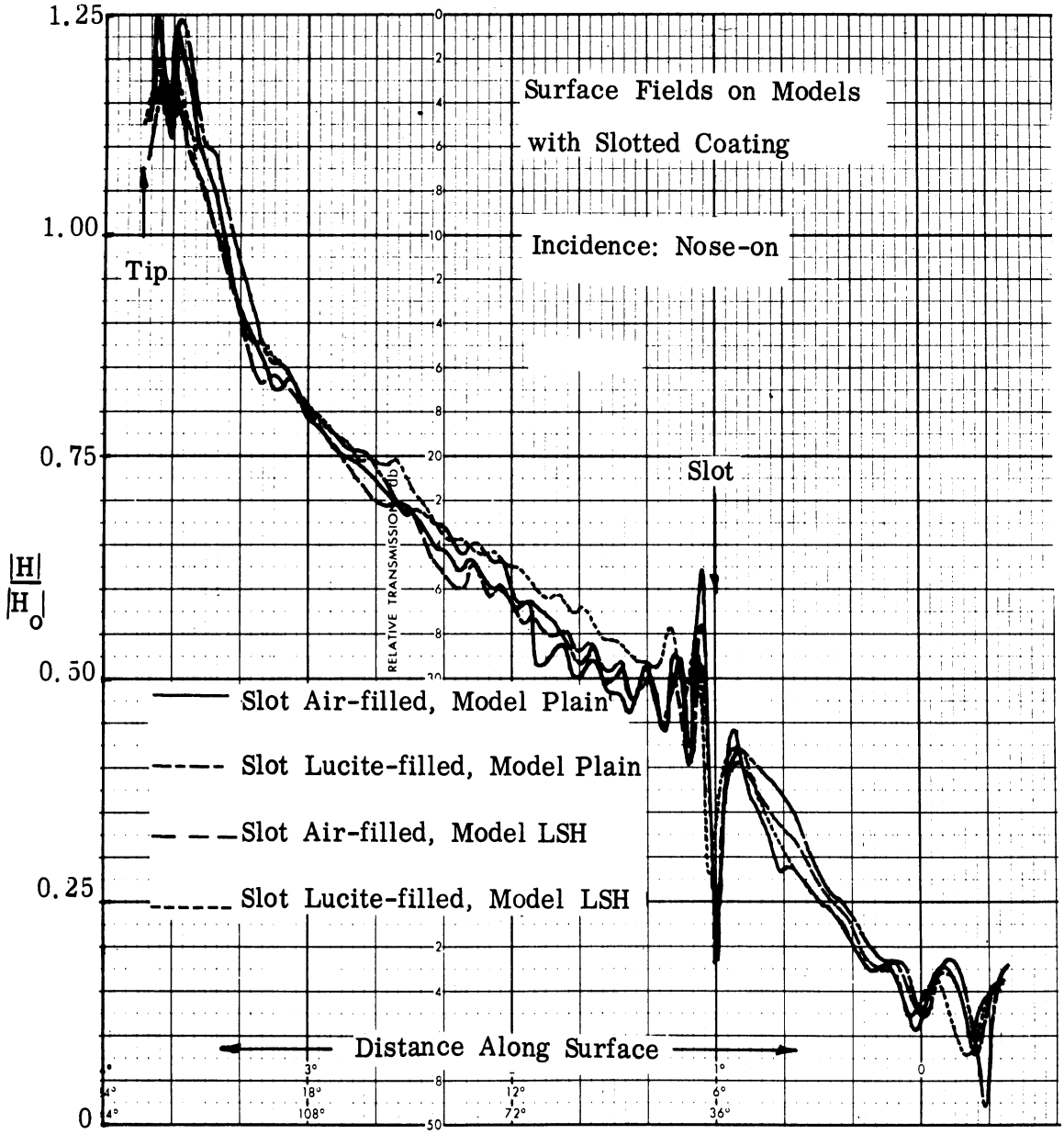

FIG. 2-18: FOR ka = 8.0, A REAR SLOT PRODUCED RELATIVELY LOCAL PERTURBATIONS. Coating: LS-26.

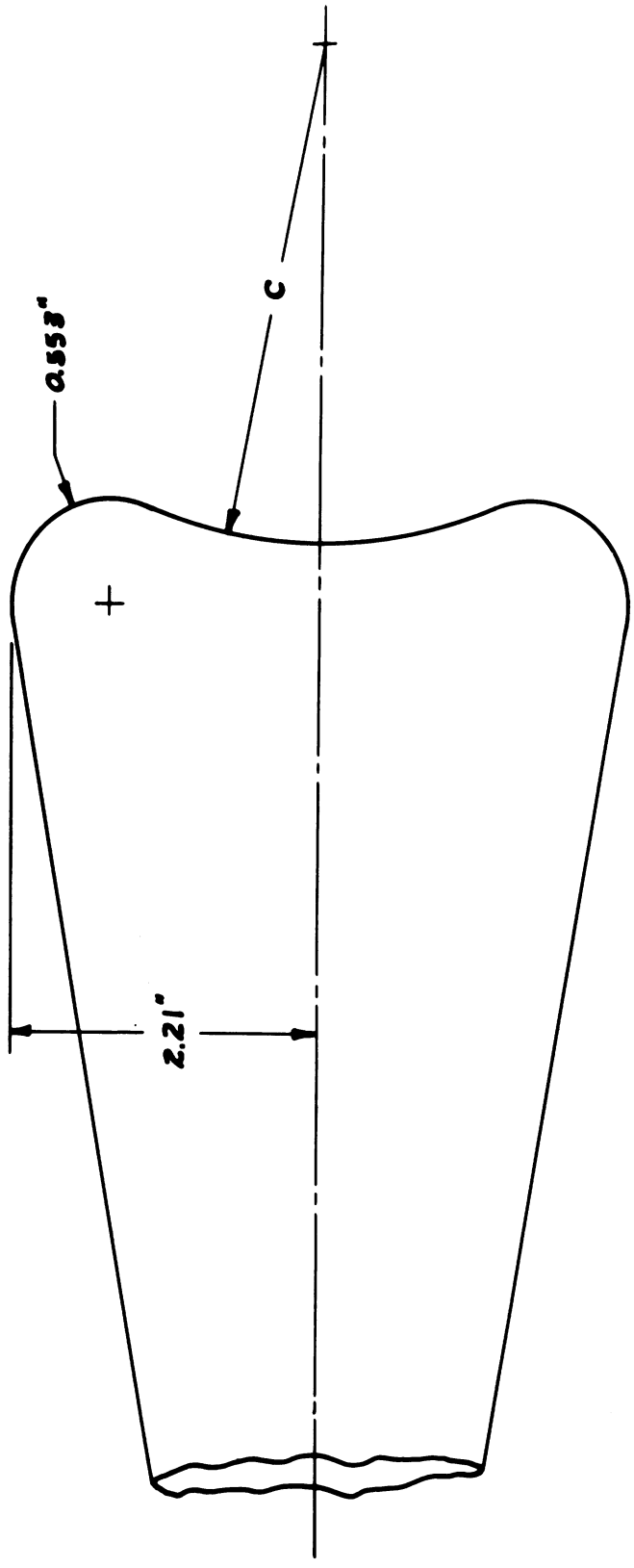

MODEL	C_1 INCHES
ID-1	4.558
ID-2	2.212
ID-3	1.519

FIG. 2-19: THREE INDENTED-BASE MODELS WERE FABRICATED.

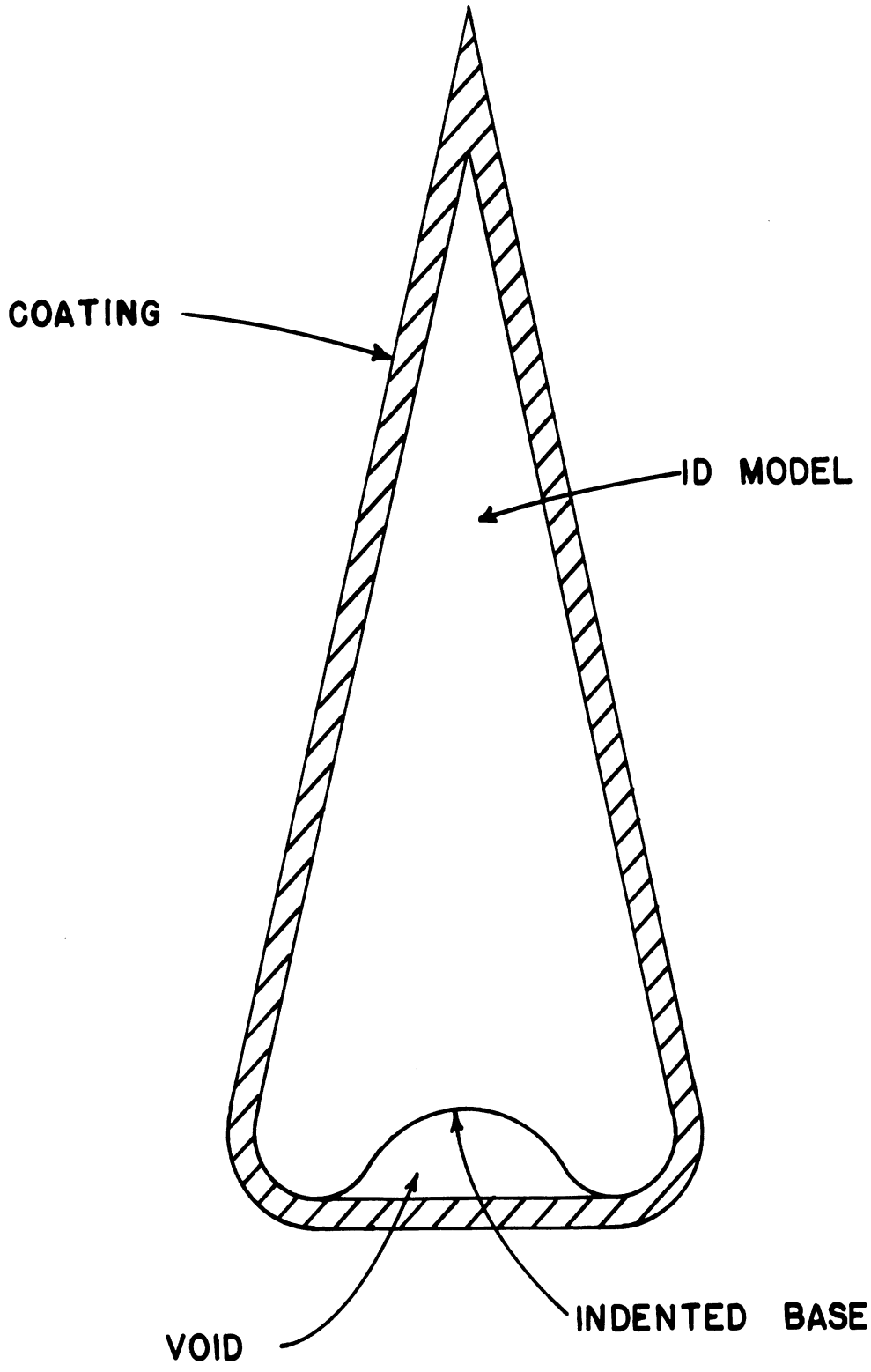

FIG. 2-20: THE ABSORBER JACKET WAS STRETCHED ACROSS THE INDENTED BASE AND CREATED A VOID.

(U) The results of the measurements are summarized in Fig. 2-21. There are three families of curves displayed, one for each ka value used: these were ka = 3, 5 and 8. The curves for each of the ID models are clearly identified as solid, alternate solid and dashed, and dashed traces. The coating was LS-26 and the angle of incidence was held at nose-on.

(S) Notice that for all three values of ka the field at the tip is the same. Considering firstly the uppermost curve, ka = 3, the three traces are nearly coincident. The incident field begins near unity, builds up to a value of 1.8, and then is nearly constant aft to the join. A series of small perturbations are spaced about half a wavelength apart and the intensities drop off beyond the join and around the back. For ka = 5, the center group of traces, the fields barely reach a value of 1.4 about a wavelength behind the tip and at the join they attain the value of about 0.6. For ka = 8, the lower group of traces, the fields drop off exponentially attaining a value of about 0.4 at the join, and the traces are substantially coincident.

(S) From Fig. 2-21 we can see two things. One is that, independent of ka, surface fields on all three models behave practically identically. Secondly, as ka increases the mean value of the intensity greatly decreases, showing that the absorber was more effective at higher frequencies. Since the three models had varying degrees of indentation and since the families of curves are very nearly coincident, we conclude that the nature of indentation is not important. We will see in a later presentation of data that it is not the depth of indentation, but the radius of the curvature near the join, that influences the backscatter.

2.5 Flat-Based Models

(S) In the foregoing description, we discovered that the radius of curvature near the join did not influence the measurements because that radius was

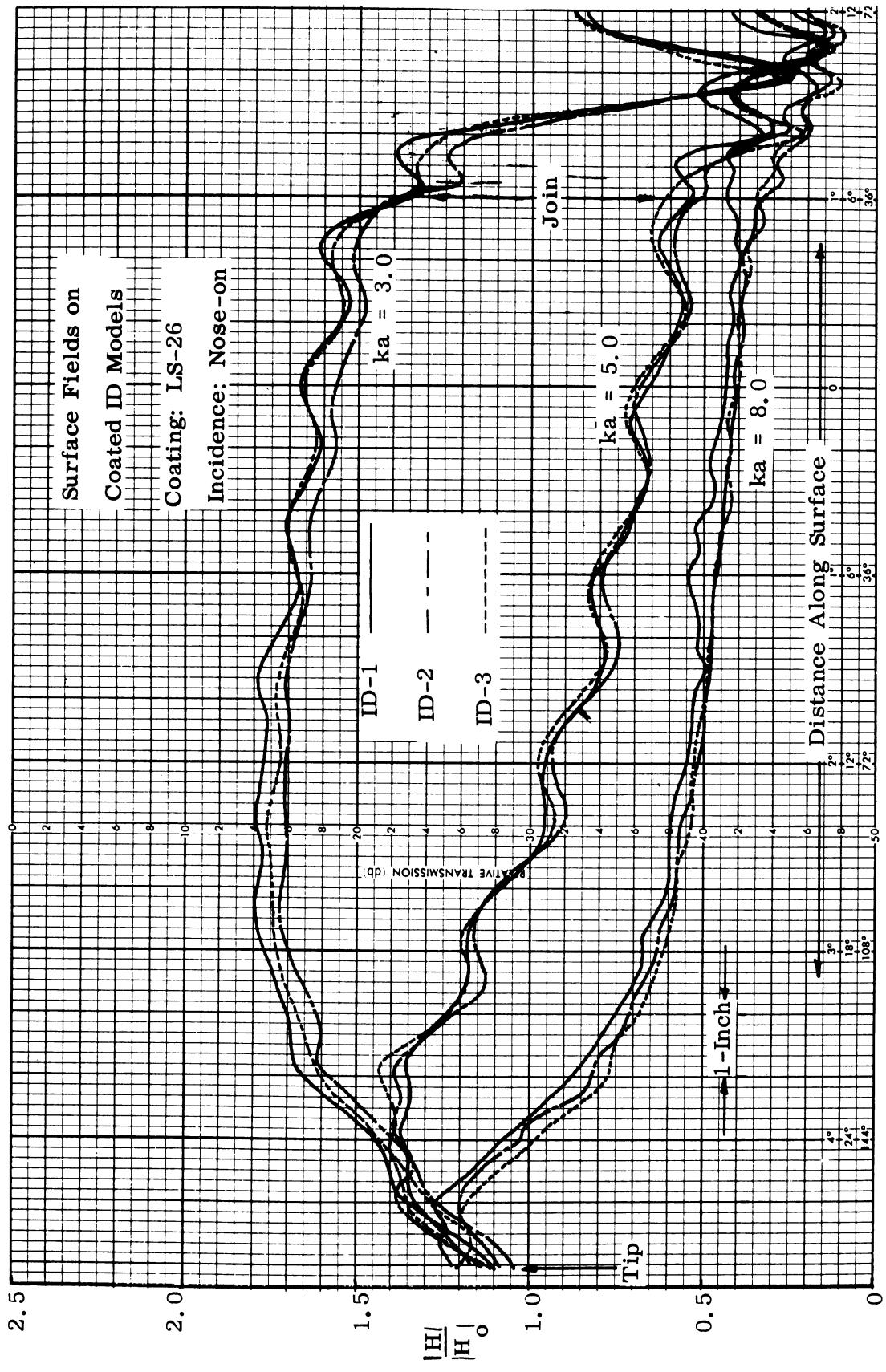

FIG. 2-21: MEASUREMENTS OF SURFACE FIELDS ON ABSORBER-CLAD INDENTED-BASE MODELS SHOW THE DEPTH OF INDENTATION HAS LITTLE OR NO EFFECT.

not changed. The depth of indentation was the only variable and we found that the indentation is not important. Therefore, we constructed a series of flat-backed models whose radius of curvature near the join varied from model to model. These models are shown in the photograph of Fig. 2-22. Notice that two conical front portions were used in conjunction with any of four caps to produce the four models. These models were labelled the FB series, FB standing for flat-backed. In Fig. 2-23 is a sketch of the models and we prudently selected the radius of the base of the cone to be 1.878" so that ka would be precisely the frequency expressed in GHz. Depending on the radius of curvature just after the join, the maximum model diameter could exceed 1.878" by a small amount, but this was of the order of half percent, at most. The small radius b was selected to provide ratios of b/a to 0.1, 0.2, 0.3 and 0.4.

(S) We measured the surface fields on the flat-based models for four values of ka, but will present only the data for ka's of 3 and 8 for illustration. The results for all four models are summarized on a single plot (Fig. 2-24) for ka = 3. Observe that the smallest radius of curvature, that of FB-1, gives rise to the largest perturbation on the side of the cone, and that the model with the largest radius of curvature, FB-4, has the smallest perturbation. In general the normalized fields attain a value of about 2.0 near the join, and the curve for model FB-4 is displaced downwards somewhat from the other three. This, we believe, is due to experimental error in the calibration of the data. Figure 2-25 shows the surface fields for these four models for ka = 8. Again, the strongest perturbation occurs for FB-1, and the slightest perturbation for FB-4. It seems that the strong effects of the smallest radius of curvature continue for relatively high frequencies.

(S) In examining Figs. 2-24 and 2-25, one notices that the curves for the larger radius of curvature extend farther to the right than the ones for the smaller radii. This is because the distance around the back of these models

FIG. 2-22: THE FB MODELS CAN BE ASSEMBLED FROM EITHER OF TWO IDENTICAL CONES AND ANY OF FOUR DIFFERENT REAR CAPS.

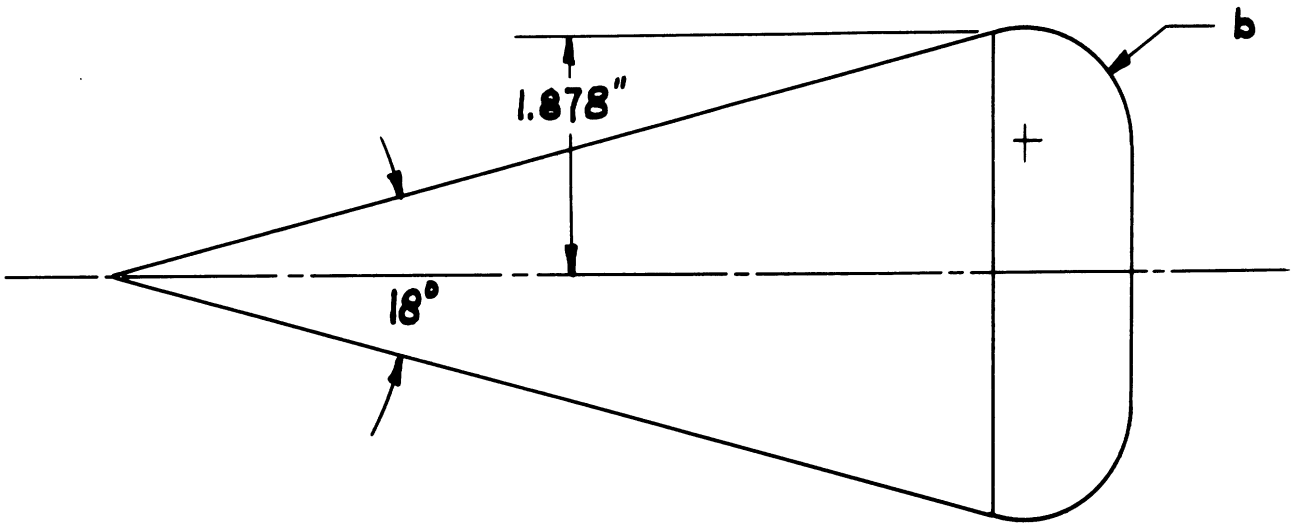

MODEL	b, INCHES	b/a
FB-1	0.188	0.1
FB-2	0.376	0.2
FB-3	0.564	0.3
FB-4	0.751	0.4

FIG. 2-23: THE FLAT BASED MODELS WERE BASICALLY 9° (HALF-ANGLE) CONES. Sketch is not to scale.

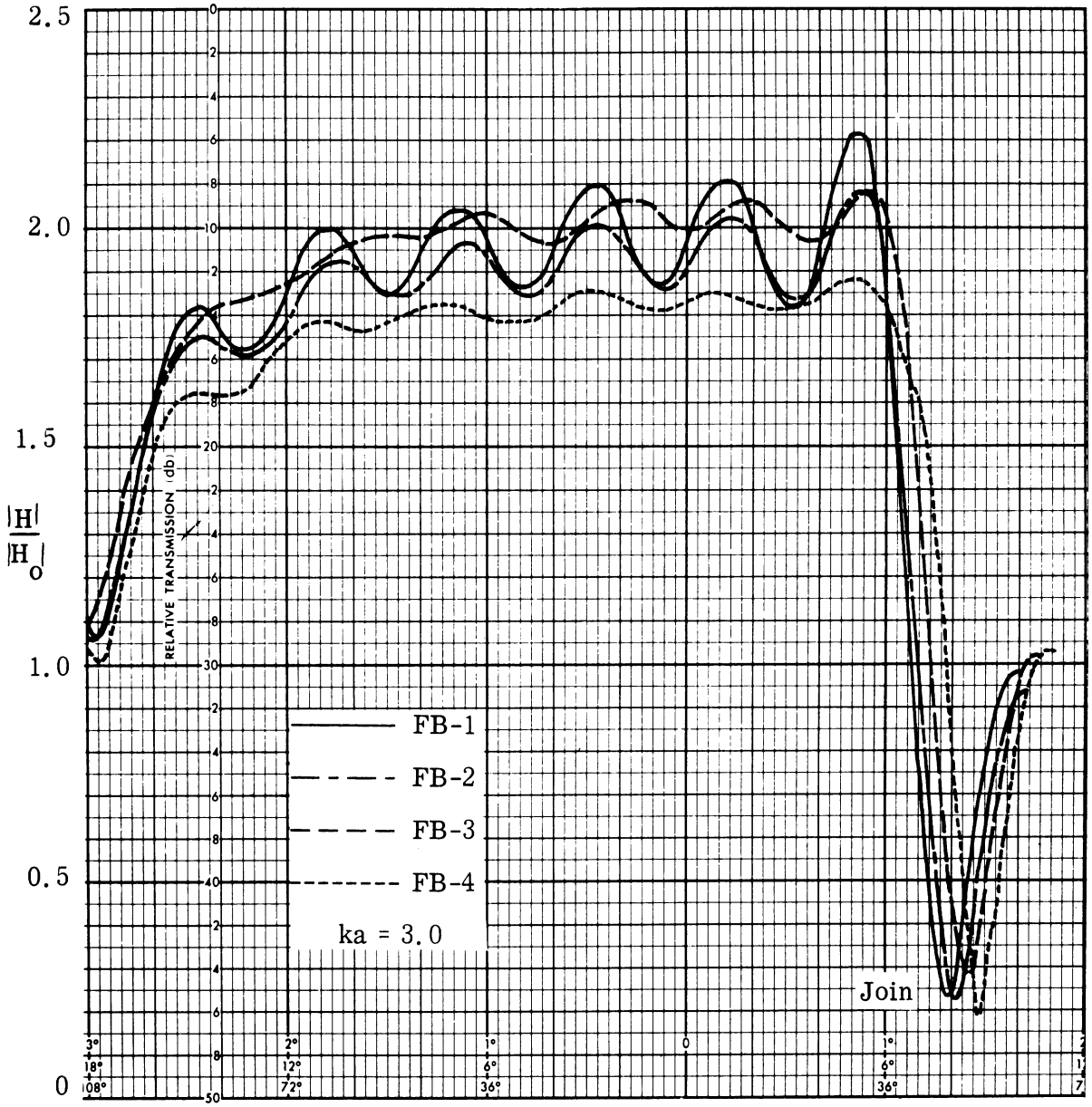

FIG. 2-24: SURFACE FIELDS SHOW STRONGER PERTURBATIONS FOR SMALLER RADII OF CURVATURE FOR ka = 3.0.

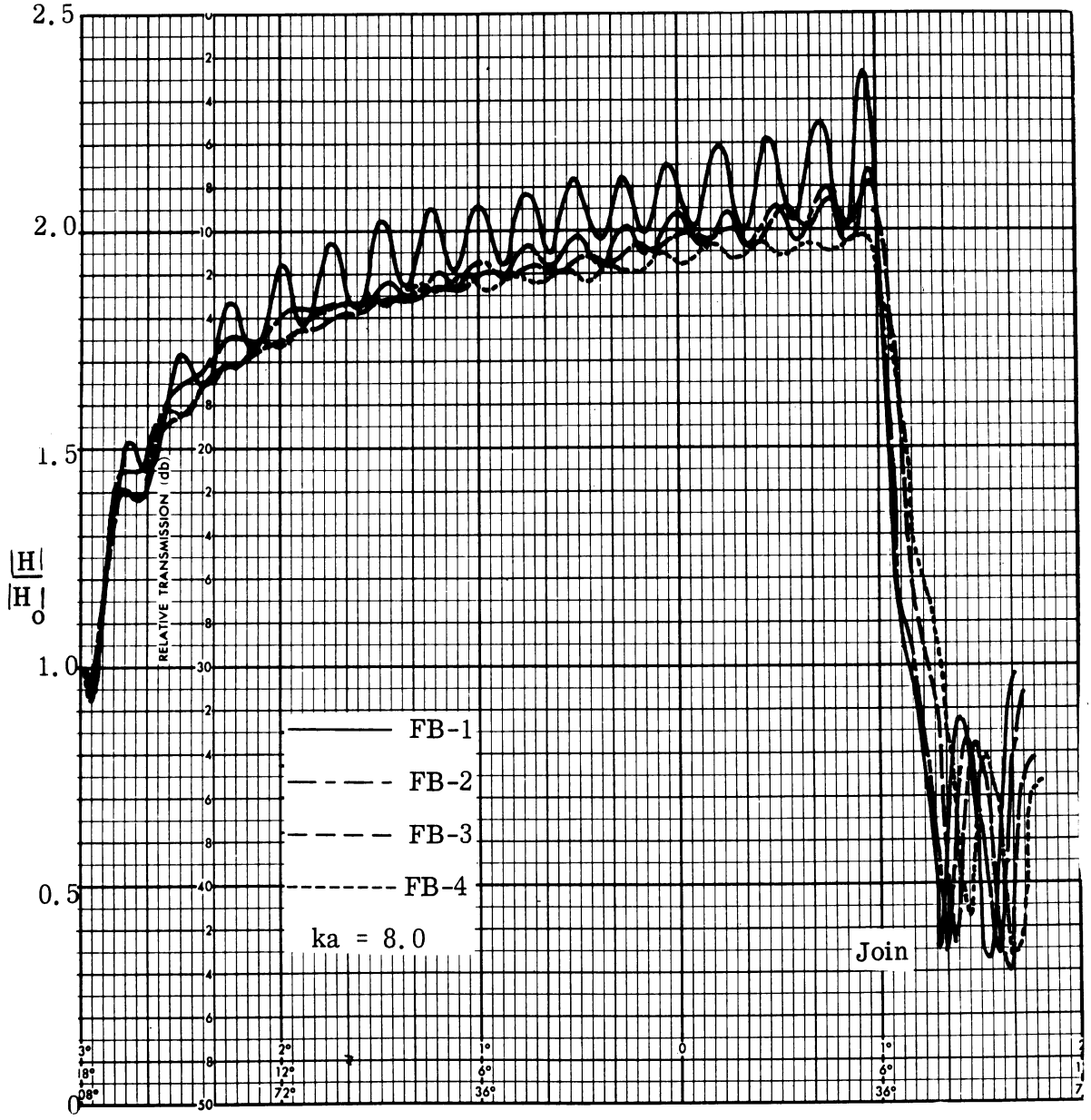

FIG. 2-25: PERTURBATIONS IN SURFACE FIELDS PERSIST FOR ka = 8.0.

was larger, and therefore, extends farther to the right by virtue of the increased radius of curvature. As the base of the model becomes flatter by virtue of sharper corners, the reflections due to the corner radii will be greater and the radar backscatter will be greater. As a confirmation of this we turn to Fig. 2-26. Here is plotted the radar cross section of the four FB models and we display, in addition, the results of a plain cone-sphere for comparison. The measurements were all made for nose-on incidence and although complete azimuthal scattering patterns were obtained, only the nose-on aspect was read from the patterns and plotted. Observe in Fig. 2-26 that radar cross section in db relative to a square meter, is plotted and if we are to strike averages through these curves we must do so cautiously because of the logarthmic scale.

(S) The data span quite a large difference in ka, running from about 1 on the left to 6 on the right. This required the use of both L-band and an S-band scattering systems. Note that there is a relatively shallow null for FB-1 and that this null increases in depth as we go to models FB-2, 3 and 4, and reach a maximum depth with model FB-4. Observe, also, that the position of the null has a tendency to shift gradually to the left, toward lower ka. If one were to carefully strike average values through each of these four patterns, one would see that the average cross section is creeping upwards slightly with decreasing radius. Notice that the average return is from 2 to 10 db higher than for a cone sphere, depending on the sharpness of the radius and upon ka.

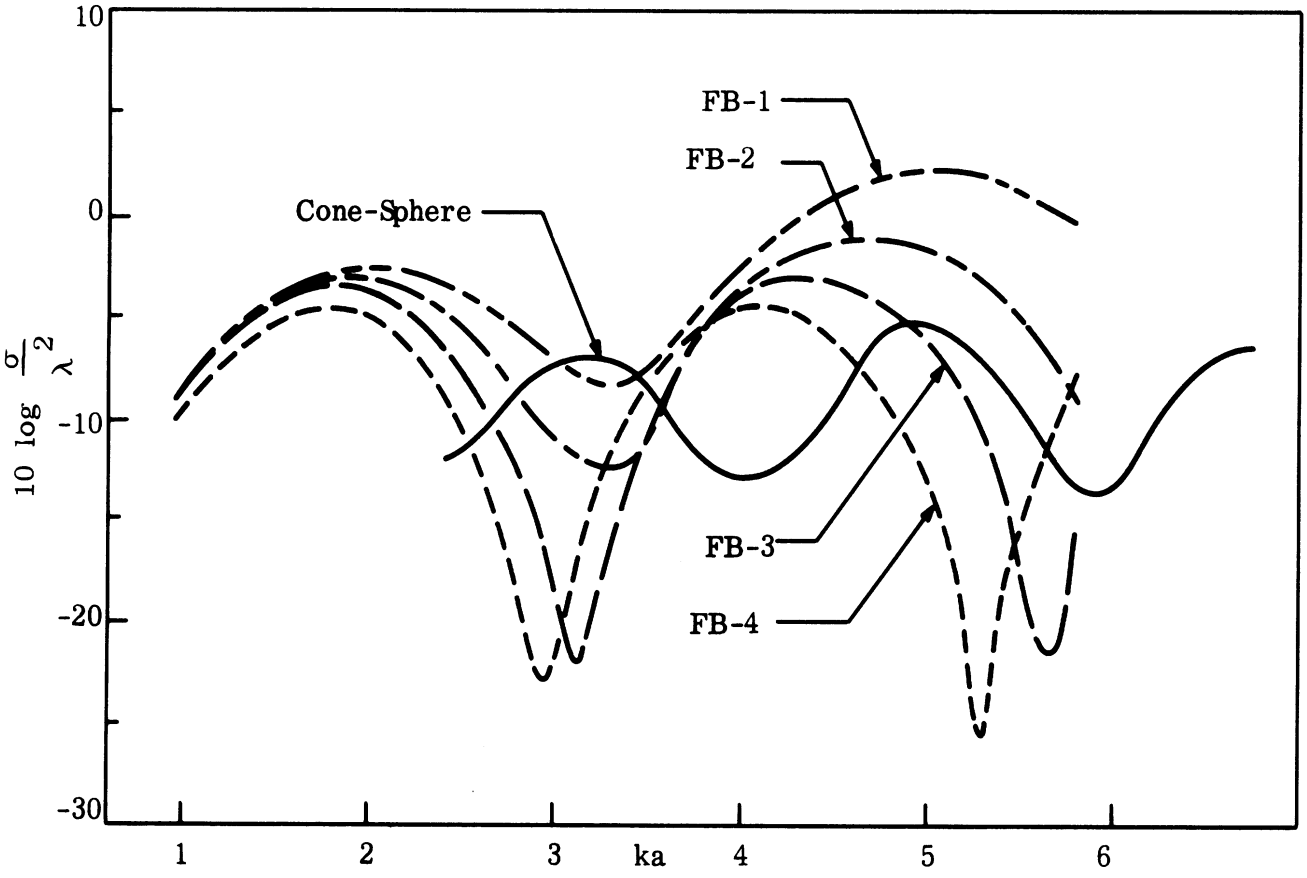

FIG. 2-26: NOSE-ON BACKSCATTER MEASUREMENTS SEEM TO QUALITATIVELY VERIFY PREDICTIONS BASED ON SURFACE FIELD DATA: Experiment datum points have been deleted and replaced with smooth curves.

III

INTERPRETATION OF EXPERIMENTAL DATA

3.1 Introduction

(U) This section contains an interpretation of the experimental data and gives comparisons between the computed (theoretical) and measured (experimental) values for the surface current and for the backscattering cross section for a variety of cone-sphere-like objects. Some of this interpretation and comparison has been grouped under the heading, "Agreement Item". This is the term given to work initiated and carried out as a result of recommendations made by Aerospace Corporation personnel at Technical Discussion meetings and agreed to by SAMSO and Radiation Laboratory representatives. The Agreement Item, Section 3.2 of this report, describes comparison between computed and measured values for the cone-sphere with a concavity at the back of the sphere (the ID models), the cone-sphere with a dielectric insert representing a ring antenna near the tip of the cone (the LSP models) and coated cone-spheres. In Section 3.3 is a further discussion of the backscattering behavior of the LSP type of vehicle.

(U) A study had been made of the effect on radar cross section of variation of the radius of curvature near the cone-sphere-join. Experimental data was obtained on metallic models with different radii of curvature. The conical portion of the models was terminated with a flat back (the FB models). An interpretation of the data on the FB models is given in Section 3.4.

(U) It is important to know the limitations of the theoretical approach. Although effective formulas for computation have been derived and comparisons with measured data show excellent agreement between theory and experiment, the formulas cannot be applied to all situations without understanding their limitations. Section 3.5 is a discussion of such limitations which we call a "failure" of a scattering estimate.

(U) The experimental investigation which accompanied the study of the radar cross section of a re-entry vehicle in a plasma environment is reported in Section IV which also includes a report on the theoretical investigations of the re-entry plasma.

(U) The formulas for the computation of radar cross section which were developed under SURF III are given in Handbook form in Section VI although some of them appear prior to Section VI in the various technical discussions, e.g., in the report of the Agreement Item.

3.2 Agreement Item (Task 3.1.1)

3.2.1 Introduction

(U) At the SURF Technical Direction Meeting held on 14 and 15 March 1967, it was agreed that a comparison would be made between predicted values for the backscattering cross section based on formulas originated under the SURF program and the results of experimental measurements that we have carried out. The bodies listed for this study were:

I A conducting shape (such as a cone-sphere)
   (a) with concavity
   (b) with ring-type antenna

II A coated shape (such as a cone-sphere)
   (a) with lossless coating
   (b) with lossy coating

and it was requested that the comparison be performed for all angles of incidence out to the specular glint, with (preferably) the same ka value (or frequency) employed in each case.

(U) Implicit in this agreement was that we would use experimental data already acquired (and reported) under the SURF program. As of March 1967 data was available for a bare (metallic) cone-sphere at 10 values of ka (15 patterns); the bare ID-1 model (indented base) at 4 values of ka; the bare LSP model (Lucite spacer point, simulating a nose-tip antenna) at four values of ka, and models coated with LS-22, LS-24, or LS-26 at seven values of ka each. In every case the polarization used was horizontal,* and the half-cone angle, α, was 7.5^{o}. Table III-1 gives a listing of the available data, and shows the variety of shapes and parameters for which the theoretical comparison could be made.

(U) In the following we present comparisons of the theoretically-predicted cross sections with a selection of the measured patterns, together with certain additional curves aimed at indicating the degree of correspondence of theory with experiment in those cases where no complete comparison is included. Although there was no express requirement for a consideration of the bare metallic body per se, it was felt desirable to make the comparison for this body also. In all cases the experimental curves are direct tracings of the measured pen recordings with the vertical scale expressed in db relative to a square wavelength. To convert this to dbsm it is merely necessary to add a constant to the ordinate, which constant depends of the frequency used. For four typical frequencies the constants are given on page 50.

---

*This negated the original intention that the theoretical comparison be carried out for vertical polarization, and because of the relatively low and irregular nature of the backscattering cross section for horizontal polarization in the aspect range between the backward cone and the specular glint, the resulting tests of the theory were more stringent than they would otherwise have been.

TABLE III-1: Available Backscatter Patterns

Base Cone-Sphere

ka	Freq. (GHz)	Radius, a (inches)	Pattern No.
2.976	2.53	2.21	3905
2.976	2.53	2.21	3970
3.010	3.77	1.50	3946
3.010	3.77	1.50	3948
3.494	2.97	2.21	4086
3.965	3.37	2.21	3898
4.506	3.83	2.21	3903
4.506	3.83	2.21	3904
4.655	5.83	1.50	3944
5.212	4.43	2.21	4090
6.318	5.37	2.21	4088
6.318	5.37	2.21	4089
6.732	8.43	1.50	3942
6.741	5.73	2.21	3891
6.741	5.73	2.21	3892

Base ID-1

ka	Freq. (GHz)	Radius, a (inches)	Pattern No.
2.976	2.53	2.21	3969
3.965	3.37	2.21	3978
4.5059	3.83	2.21	3980
6.741	5.73	2.21	3963

Base LSP Model

ka	Freq. (GHz)	Radius, a(inches)	Pattern No.
2.976	2.53	2.21	3967
3.965	3.37	2.21	3976
4.5059	3.83	2.21	3983
6.741	5.73	2.21	3965

Coated Cone-Spheres

ka	Freq. (GHz)	Radius, a (inches)	Pattern No.		
			LS-22	LS-24	LS-26
2.976	2.53	2.21	3914	3972	3911
3.010	3.77	1.50	4003	3935	3998
3.965	3.37	2.21	3912	3974	3900
4.51	3.83	2.21	3917	3949	3901
4.51	3.83	2.21	3924	3986	--
4.655	5.83	1.50	4006	3938	3995
6.732	8.43	1.50	4002	3939	3999
6.741	5.73	2.21	3918	3956	3889
6.741	5.73	2.21	3921	3987	--

Frequency (GHz)	Additive Constant (db)
2.53	-18.5
3.37	-21.0
3.83	-22.1
5.73	-25.6

3.2.2 Bare Cone-Sphere

(U) For a metallic cone-sphere of radius a and half-angle α viewed at an angle θ to nose-on with horizontal polarization, the expression for the theoretically predicted backscattering cross section given in Goodrich et al, (1967) is:

[A] within the backward cone ($0 \leq \theta < \alpha$):

$$\frac{\sigma}{\lambda^2} = \frac{1}{\pi} \left| S_1 + S_2 + S_3 \right|^2 \tag{3.1}$$

where S_1 is the tip contribution

$$S_1 = S_{tip} = \frac{-i}{4} \frac{\tan^2 \alpha}{(1 - \sin^2 \theta \sec^2 \alpha)^{3/2}} e^{-2ika \operatorname{cosec} \alpha \cos \theta}, \tag{3.2}$$

S_2 is the join contribution

$$S_2 = S_{join} = \frac{i}{4} \sec^2 \alpha \, J_o(2ka \cos \alpha \sin \theta) e^{-2ika \sin \alpha \cos \theta} \tag{3.3}$$

and S_3 is related to the sphere creeping wave contribution

$$S_{cw} = \left(\frac{ka}{2}\right)^{4/3} e^{i\pi/3} \left\{ 1 + \frac{e^{i\pi/3}}{60\beta_1^2} (32\beta_1^3 + 9) \left(\frac{2}{ka}\right)^{2/3} \right\} \frac{1}{\beta_1 \left\{ Ai(-\beta_1) \right\}^2}$$

$$\exp\left\{ i\pi ka - e^{-i\pi/6} \pi\beta_1 \left(\frac{ka}{2}\right)^{1/3} - e^{i\pi/6} \frac{\pi}{60\beta_1} (\beta_1^3 - 9) \left(\frac{2}{ka}\right)^{1/3} \right\} \qquad (3.4)$$

in which Ai(-x) is the Airy function with $\beta_1 = 1.018793$ and $Ai(-\beta_1) = 0.5356567$. The phase associated with each term in (3.1) is that appropriate to an origin at the shadow boundary.

(U) The contribution S_3 is related to S_{cw} as follows:

$$S_3 = \gamma S_{cw} \quad , \qquad (3.5)$$

where γ is an enhancement factor. Based on surface field measurements, an empirical curve showing the dependence of γ on ka for $\alpha = 7.5^o$ has been given by Senior and Zukowski (1965, Fig. 2-10). A theoretical (asymptotic) approximation to γ, is

$$\gamma \simeq \left[2\left(\frac{1}{3} + \int_0^{\beta_1} Ai(-x)\,dx\right) \left\{ 1 + \frac{1}{2}\left(\frac{ka}{2}\right)^{2/3} \alpha^2 \beta_1^2 e^{-i\pi/3} \right\} + \right.$$

$$\left. + \left(\frac{ka}{2}\right)^{2/3} \alpha^2 e^{-i\pi/3} Ai(-\beta_1) \right] \cdot \exp\left\{ -\left(\frac{ka}{2}\right)^{1/3} \alpha\beta_1 e^{-i\pi/6} \right\} \qquad (3.6)$$

(Hong and Weston, 1965), and it will be noticed that in this approximation γ is complex, albeit with only small imaginary part (phase of order 5^o). Eq. (3.6) fails when ka is amll, a fact which is evident from the comparison given in Fig. 3-1. Nevertheless, for all $ka > 3$ it may be adequate (and is computationally covenient) to use Eq. (3.6) in the theoreticaly prescription of the scattering.

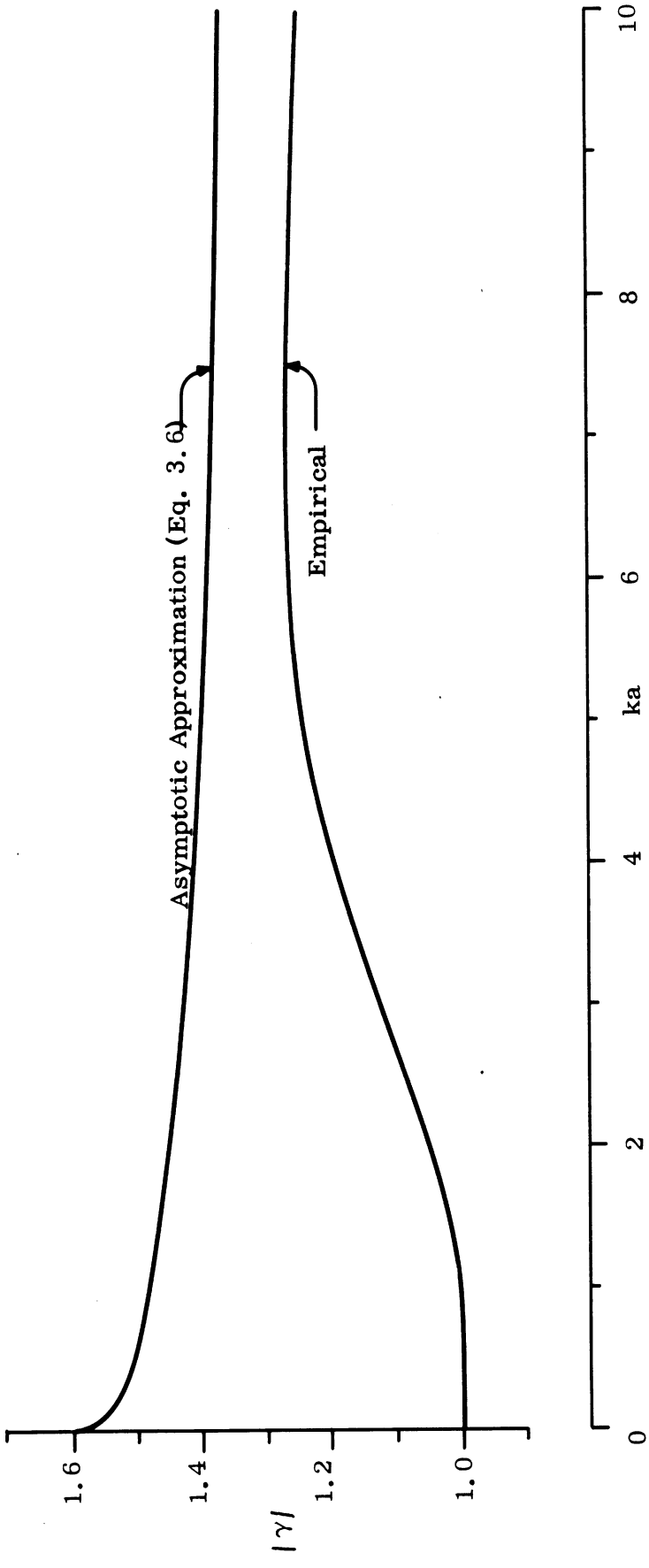

FIG. 3-1: MODULUS OF CREEPING ENHANCEMENT FACTOR FOR $\alpha = 7.5^{o}$: Empirical (Based on Surface Field Data) and Asymptotic Approximation (Eq. 3.6).

(U) To obtain an appreciation of the magnitude of the various contributors to the scattering, we show in Fig. 3-2 a plot of $|S_{tip}|$, $|S_{join}|$ and $|S_{cw}|$ for $\alpha = 7.5^0$ and $\theta = 0$. It will be observed that $|S_{cw}|$ is somewhat greater than $|S_{join}|$ throughout the range of ka considered, and that by comparison with these two contributors, $|S_{tip}|$ is negligible. The theoretical nose-on cross sections computed from Eq. (3.1) using the empirical and asymptotic enhancement factors for the creeping wave contribution are plotted as functions of ka in Figs. 3-3 and 3-4. The experimental values are those of Blore (1964), together with the one derived from the measured patterns listed in Table III-1. The agreement is excellent, bearing in mind the scatter of the experimental data particularly for the larger ka values and for ka < 3 (say) the superiority of the empirical enhancement factor over its asymptotic approximation (3.6) is clearly evident from Fig. 3-4.

[B] between the backward cone and the specular flash ($\alpha \leq \theta \leq \pi/2 - \alpha$):

$$\frac{\sigma}{\lambda^2} = \frac{1}{\pi} \left| S_{spec} \right|^2 \tag{3.7}$$

with

$$S_{spec} = 1/4\, e^{i\pi/4} \sqrt{\frac{ka \cos \alpha}{\pi \sin \theta}} \tan(\alpha + \theta) e^{2ika \cot\alpha \cos(\alpha + \theta)}$$

$$\times \left\{ 1 - F \left[\sqrt{2\, ka \cot\alpha \cos(\alpha + \theta)} \right] \right\} \tag{3.8}$$

where

$$F(\tau) = \frac{e^{-i\tau^2}}{\tau} \int_0^{\tau} e^{it^2}\, dt \tag{3.9}$$

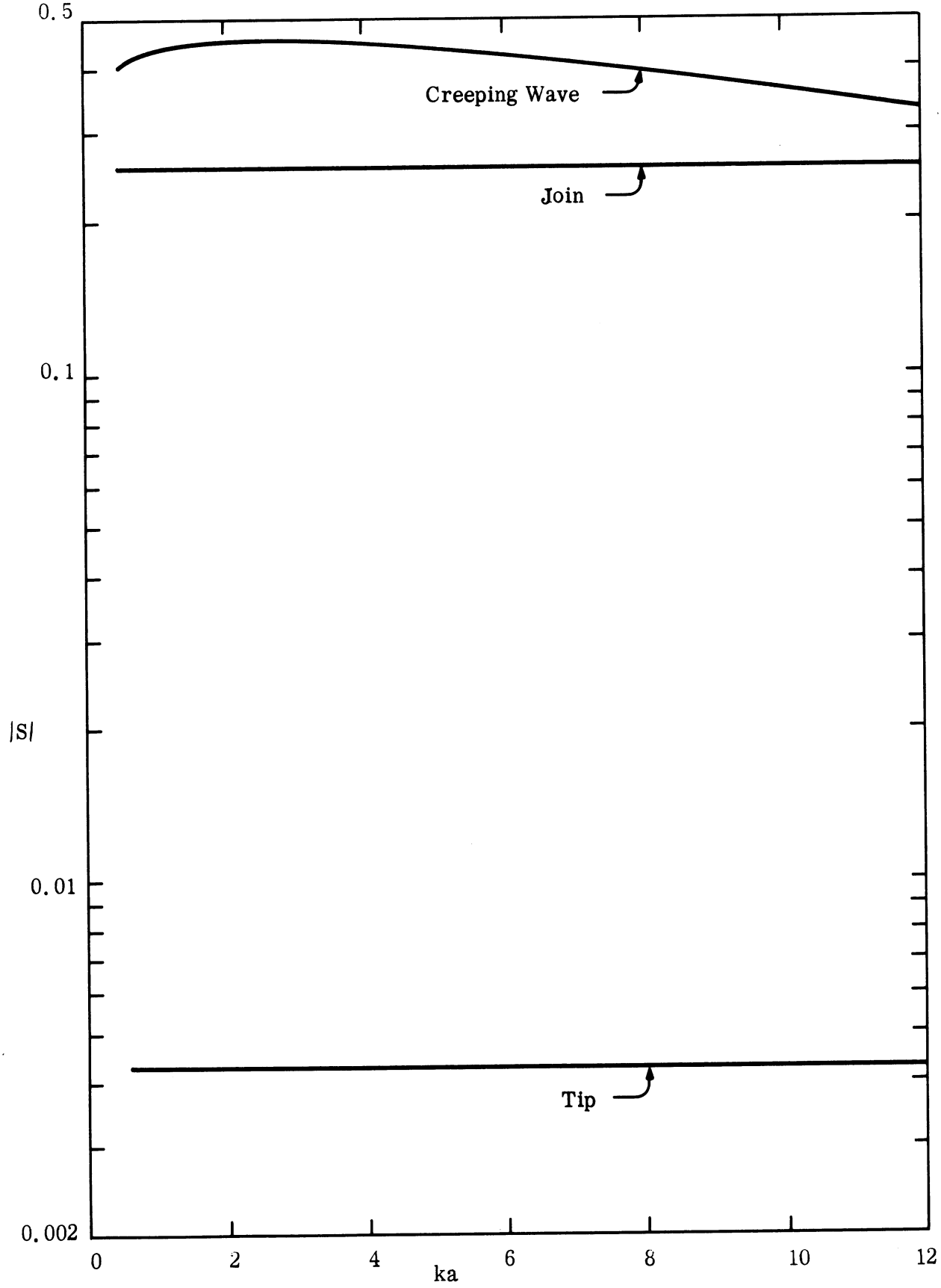

FIG. 3-2: COMPARISON OF TIP, JOIN AND UNENHANCED CREEPING WAVE SCATTERING AMPLITUDES FOR NOSE-ON INCIDENCE ON A CONE-SPHERE, $\alpha = 7.5^{o}$

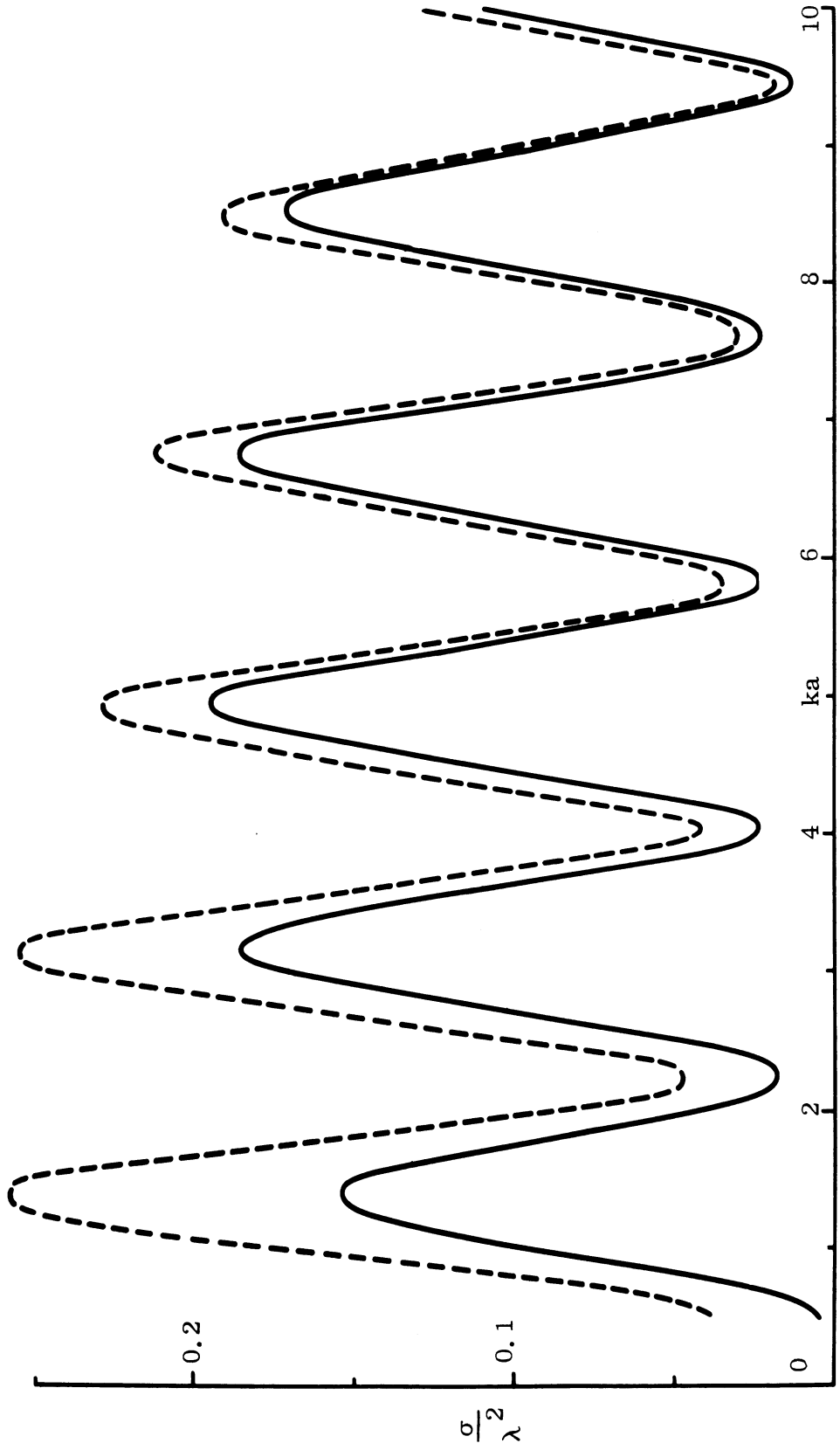

FIG. 3-3: THEORETICAL NOSE-ON BACKSCATTERING CROSS SECTION FOR A CONE-SPHERE WITH $\alpha = 7.5^{\circ}$, COMPUTED USING THE EMPIRICAL ENHANCEMENT FACTOR (——) AND ITS ASYMPTOTIC APPROXIMATION (---).

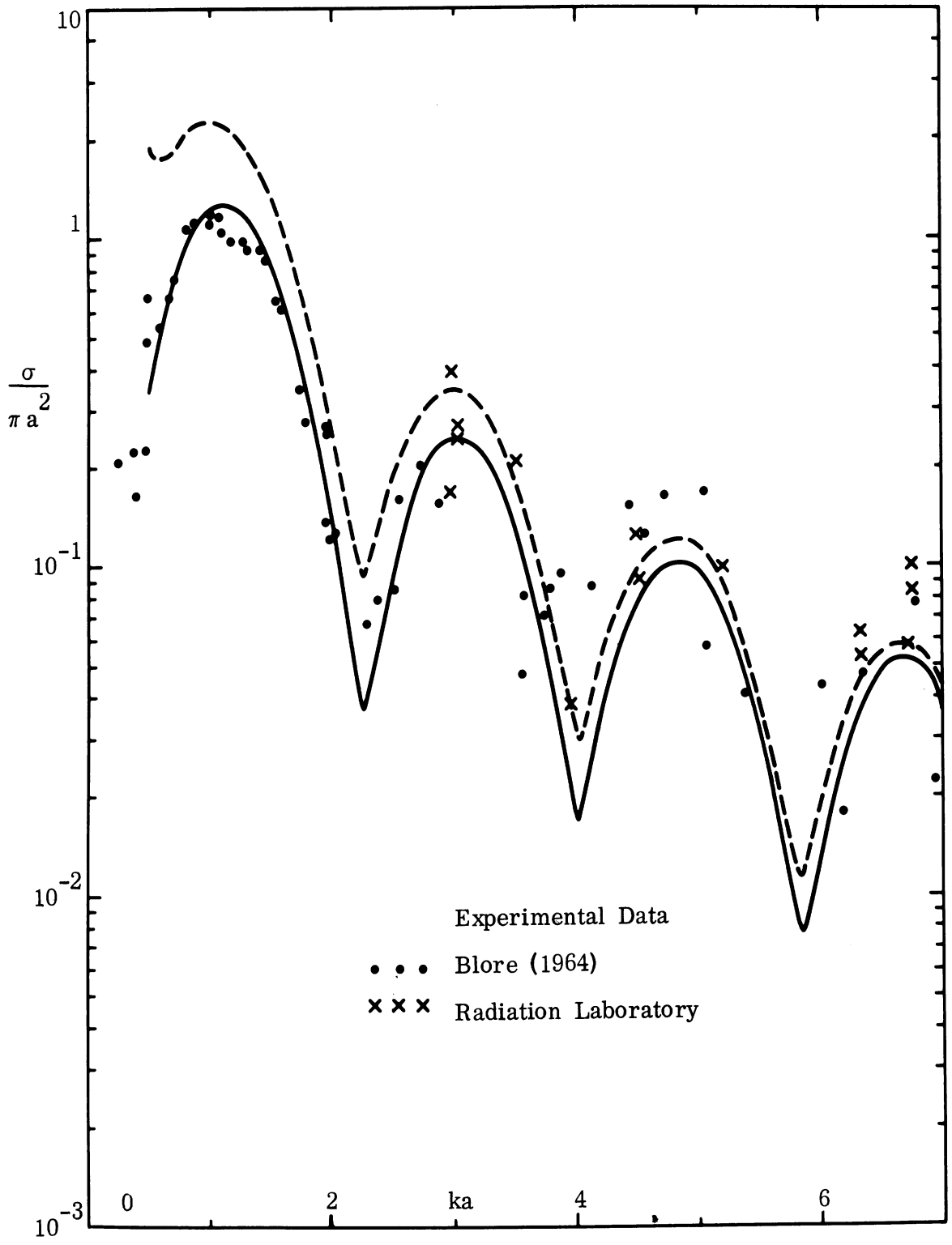

FIG. 3-4: THEORETICAL NOSE-ON BACKSCATTERING CROSS SECTION FOR A CONE-SPHERE WITH $\alpha = 7.5^{\circ}$, COMPUTED USING THE EMPIRICAL ENHANCEMENT FACTOR (——) AND ITS ASYMPTOTIC APPROXIMATION (---).

is related to the Fresnel integral. In the direction $\theta = \pi/2 - \alpha$ of the specular flash itself, Eq. (3.7) reduced to

$$\frac{\sigma}{\lambda^2} = \frac{\operatorname{cosec}^2 \alpha \sec \alpha}{9\pi^2} (ka)^3 \quad . \tag{3.10}$$

The cross section computed from this is plotted as a function of ka in Fig. 3-5, along with the experimental data points obtained from Blore (1964) and from our own measured patterns. The agreement is relatively good, though we do observe a tendency for the measured values (particularly those of Blore) to fall below the theoretical estimate by an amount which increases with ka. At least part of this seems attributable to near-zone effects in the measurements.

[C] Comments:

(U) When the backscattering cross section provided by Eqs. (3.1) and (3.7) is computed as a function of θ for given ka, the resulting curve has an abrupt discontinuity at the edge, $\theta = \alpha$, of the backward cone for all except the very largest values of ka. The discontinuity arises partly from the assumption of a reduced join contribution for $\theta > \alpha$, but more particularly from the assumed absence of any creeping wave return outside the backward cone. Inasmuch as the creeping wave contributor is the dominant contributor for ka = O(10) or less, the net effect is a jump of order 10 db or more for small ka, and only for ka > 100 (say) is the discontinuity * of no concern. It is clearly desirable that we attempt to bridge it.

(U) To this end, the first (and obvious) modification of the theoretical prescription is to retain the expressions for S_{tip} and S_{join} even outside the backward cone, and only transfer the formula (3.7) at such a value of θ as

* Note that the discontinuity does not appear with vertical polarization.

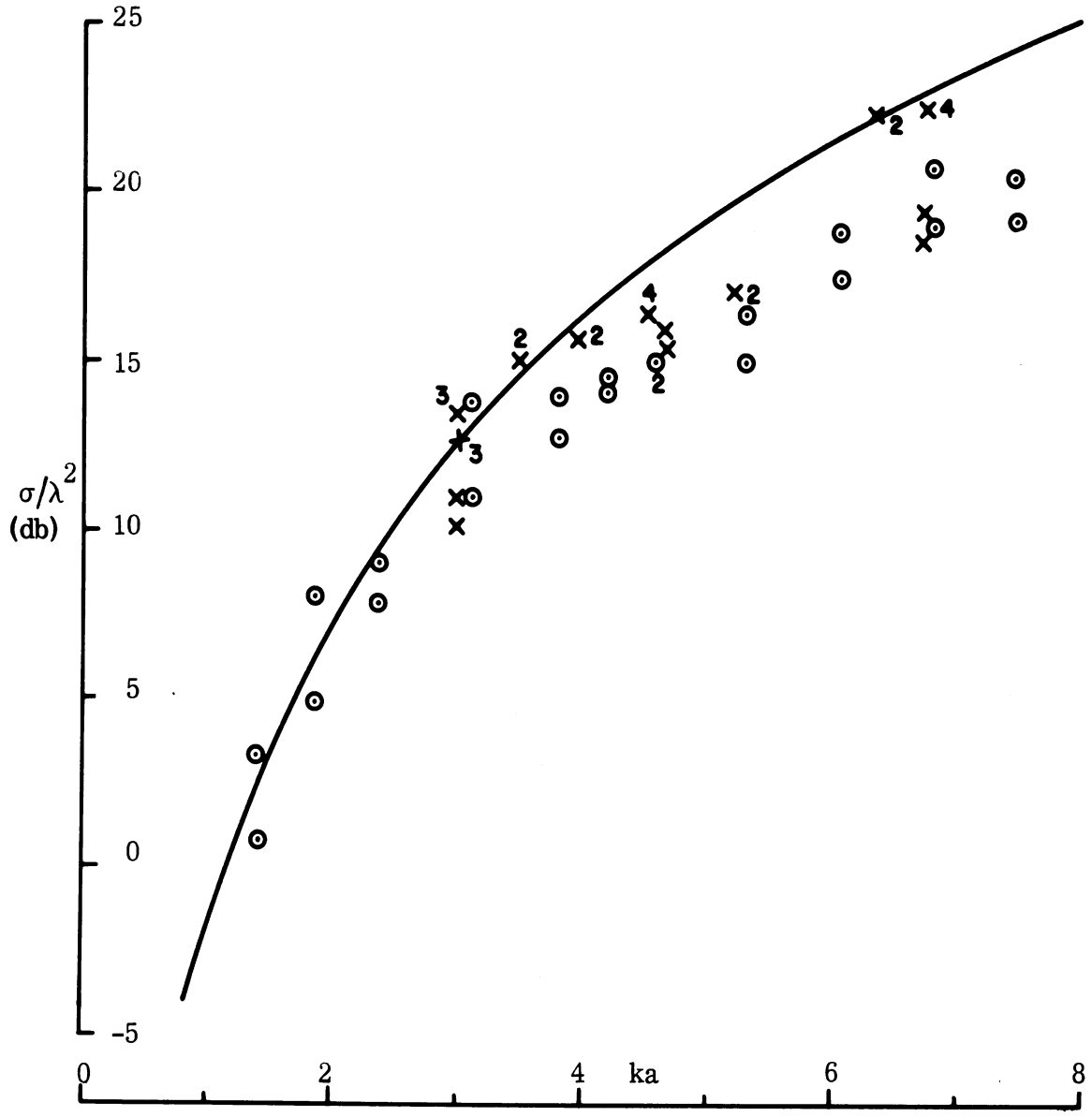

FIG. 3-5: THEORETICAL SPECULAR FLASH CROSS SECTIONS FOR A CONE-SPHERE WITH $\alpha = 7.5^{o}$, COMPUTED USING EQ. (3.10). Experimental Data, ⊙⊙⊙ Keys and Primich (1959), xxx Radiation Laboratory.

the use of the wide angle formula for the Bessel function is truly valid. Since the join continues to be excited outside the backward cone, the modification is theoretically defensible, and leads to some (but not a complete) reduction in the magnitude of the jump at $\theta = \alpha$.

(U) The second modification is more empirical in nature and is promoted partly from a consideration of the nature of the shadow boundary excitation (the origin of the creeping waves), but more from an examination of the measured patterns. It is found that (i) the width of the nose-on lobe in the patterns is in no degree equal to α, but does appear to decrease with increasing ka for given α; (ii) marked (single) side-lobes are apparent between the nose-on lobe and the commencement of the build-up to the specular flash; (iii) the widths and center (θ) values of these side lobes tend to decrease with increasing ka; and (iv) the heights of the side lobes relative to the nose-on lobe do not appear to depend on ka, and average -8 db or less. These facts are suggestive of a J_o dependence for the creeping wave return as well as for the join contribution, and by likening the shadow boundary to a (pseudo) ring singularity, it is apparent that the multiplicative factor should be $J_o(2ka \sin\theta)$. Note that within the backward cone ($0 \leq \theta < \alpha$), these modifications have only an infinitesimal effect on the cross section provided by Eq. (3.1).

(U) The resulting prescription for the backscattering cross section is now $0 \leq \theta \leq \beta$:

$$\frac{\sigma}{\lambda^2} = \frac{1}{\pi} \left| S_1 + S_2 + S_3 J_o(2\,ka\,\sin\theta) \right|^2 \qquad (3.11)$$

where S_1, S_2, and S_3 are as shown in Eqs. (3.2), (3.3) and (3.5) respectively.

$\beta \leq \theta \leq \pi/2 - \alpha$:

$$\frac{\sigma}{\lambda^2} = \frac{1}{\pi} \left| S_{spec} \right|^2 \qquad (3.12)$$

where S_{spec} is as shown in Eq. (3.8). The angle β at which the transition between the two formulae is made should be beyond the value of θ corresponding to the first zero of J_o (i.e. beyond $\sin^{-1} \frac{2.405}{2ka}$), and at the first subsequent intersection of (3.11) with (3.12).

(U) Comparisons between the measured and predicted values of the cross section for ka = 2.98 and 4.51 are given* in Figs. 3-6 and 3-7 respectively. The agreement is less good at the higher frequency, though we remark that the measured flash values are lower than for other (similar) models at the same frequency, and that the nose-on lobe width is atypically large..

3.2.3 Indented (ID) Models

(U) The basic ID Model is a metallic cone of half-angle 7.5^o terminated in a toroidal ring of radius 0.533 inches, which ring is itself joined to a concave spherical surface of radius c. The profile of the rear portion is shown below (Fig. 3-8.) At each junction in the profile the tangents are continuous, and the termination is therefore a smooth one simulating an indented base.

(U) Three ID models were constructed differing only in the values of the parameter c. In particular, the maximum radius, a, was the same for each and was insignificantly different (by less than one percent) from the value 2.210 inches appropriate to the corresponding cone-sphere. For the three bodies the parameter c was as follows:

*Here, and subsequently, all wide angle computations based on Eq. (3.12) were carried out on a digital computer, and the rest by hand.

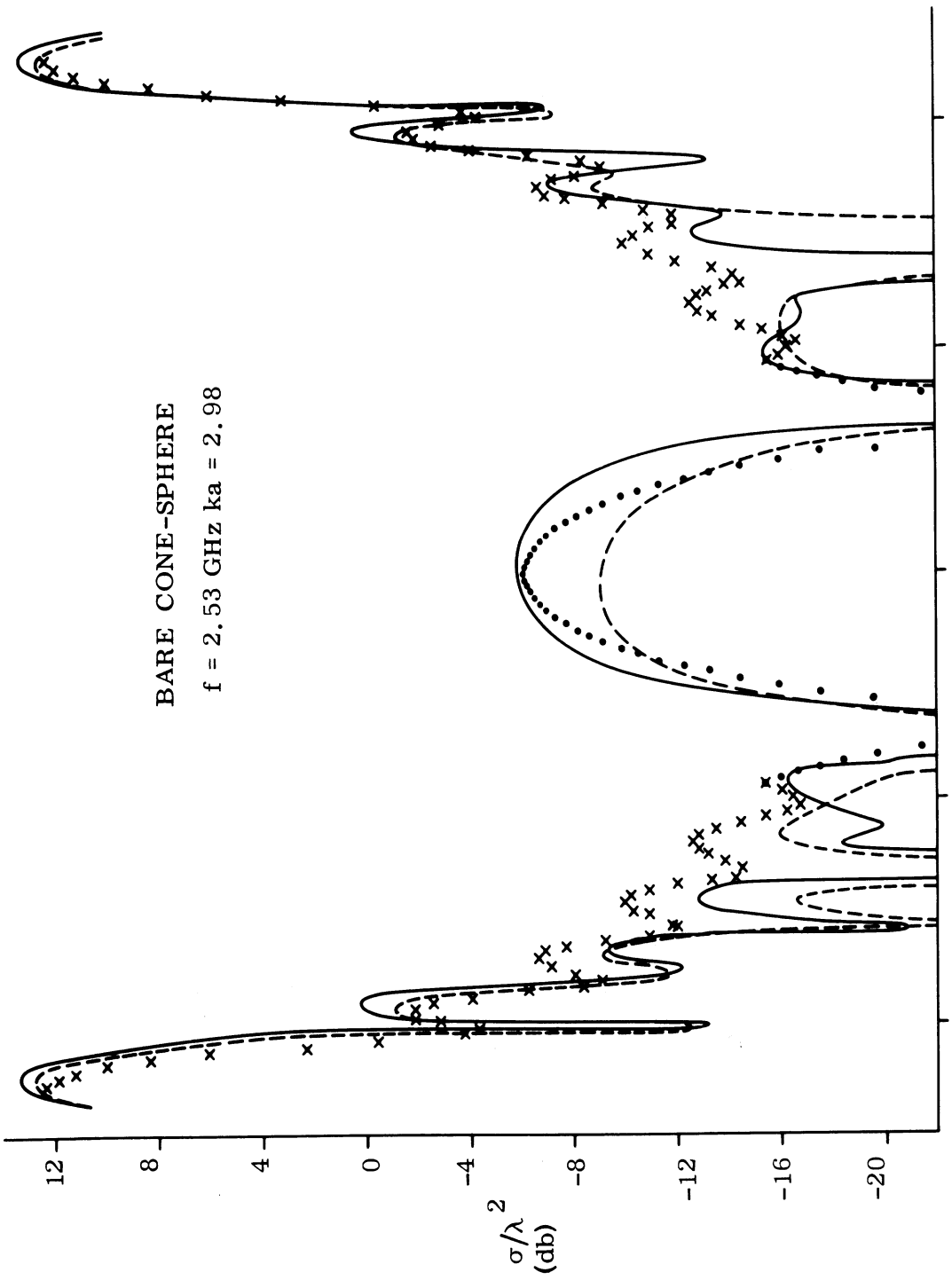

FIG. 3-6: COMPARISON BETWEEN THEORY AND EXPERIMENT. Solid line is experimental data.

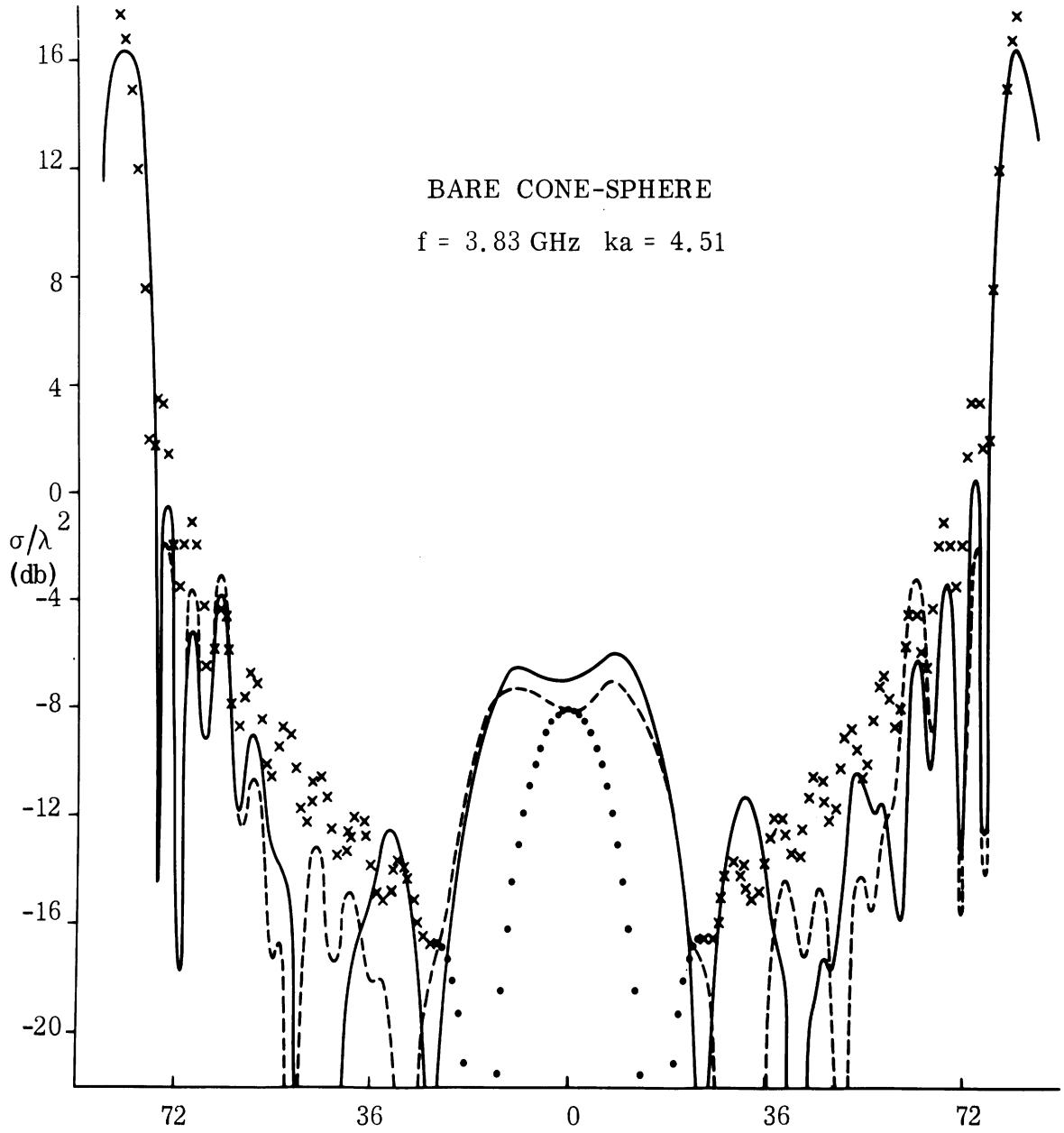

FIG. 3-7: COMPARISON BETWEEN THEORY AND EXPERIMENT. Solid line is experimental data.

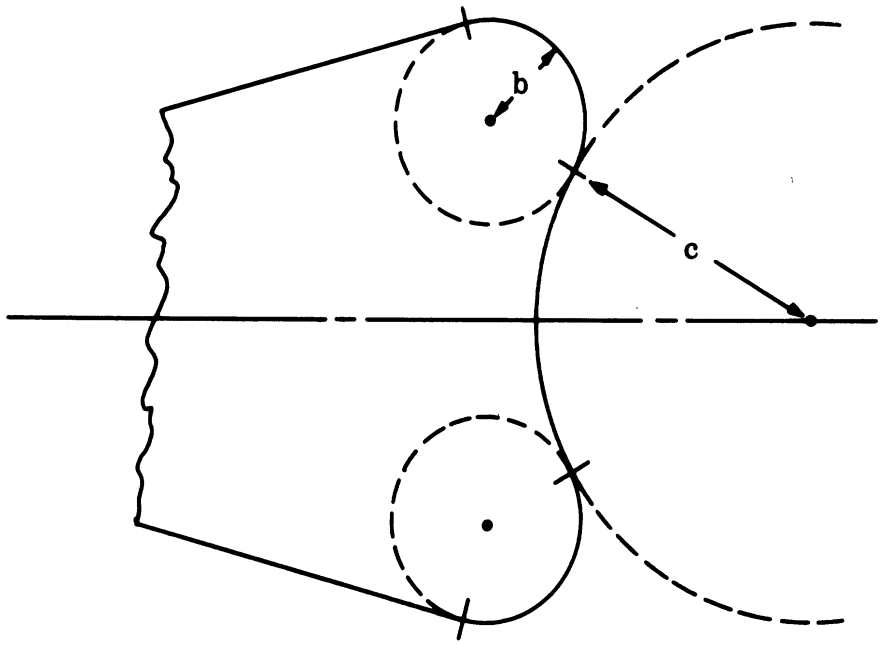

FIG. 3-8: TERMINATION OF ID MODEL.

ID-1, c = 4.558 inches

ID-2, c = 2.212 inches

ID-3, c = 1.519 inches

implying that the indentation was greatest for model ID-3. Surface field data was obtained for each of these models, but as of March 1967, backscatter patterns had been produced only at four isolated values of ka for model ID-1. Since that time, however, a much greater volume of more accurate data has been accumulated not only for model ID-2 but also for other shapes related to the ID series, and it is convenient to refer to (and reproduce some of) this later data in support of the theoretical estimates of the cross section. Nevertheless, in accordance with the ground rules, the oblique incidence comparison will be carried out using two of the initial (inferior) patterns for model ID-1.

(U) For incidence at or near to nose-on the contributors to the back scattering cross section are again the tip, the join and the creeping wave, but the last two are vitally affected by the nature of the termination. Taking first the creeping wave, this is born in a region which is non-spherical and, for nose-on incidence, starts out along a geodesic whose longitudinal radius of curvature is b. According to our philosophy under which the creeping wave is primarily determined by the local geometry, and leaks off energy in the tangential direction at all points of its path, the way in which the wave crosses the indentation is by means of this leaked energy and any contribution from energy which has followed the surface is negligible by comparison. Because of this, the backscattering cross sections of all three ID models should be indistinguishable, and this is confirmed by the results for models ID-1 and ID-2 shown in Fig. 3-9. The theory also implies that were we to cover the indentation with a (flat) metal disc the cross section would be unchanged, and this was verified by probe measurements following first a free space trajector across the indentation. In consequence, the scattering is determined only by the parameters a and b, and is independent of c, and in judging the efficacy of our theory we can therefore make use of the quite complete data for the FB models (having b/a varying from 0.4 to 0.1, and otherwise flat back, and $\alpha = 9^{o}$) in addition to that obtained explicitly with the ID models.

(U) The far field prescription for a body having half angle α and radii a and b as previously defined is as follows: $0 \leq \theta \leq \beta$:

$$\frac{\sigma}{\lambda^2} = 1/\pi \left| S_1 + S_2 + S_3 J_o (2 ka \sin \theta) \right|^2 \qquad (3.13)$$

where S_1 is the tip contribution shown in Eq. (3.2); S_2 is the join contribution whose specification is (see Section 3.4):

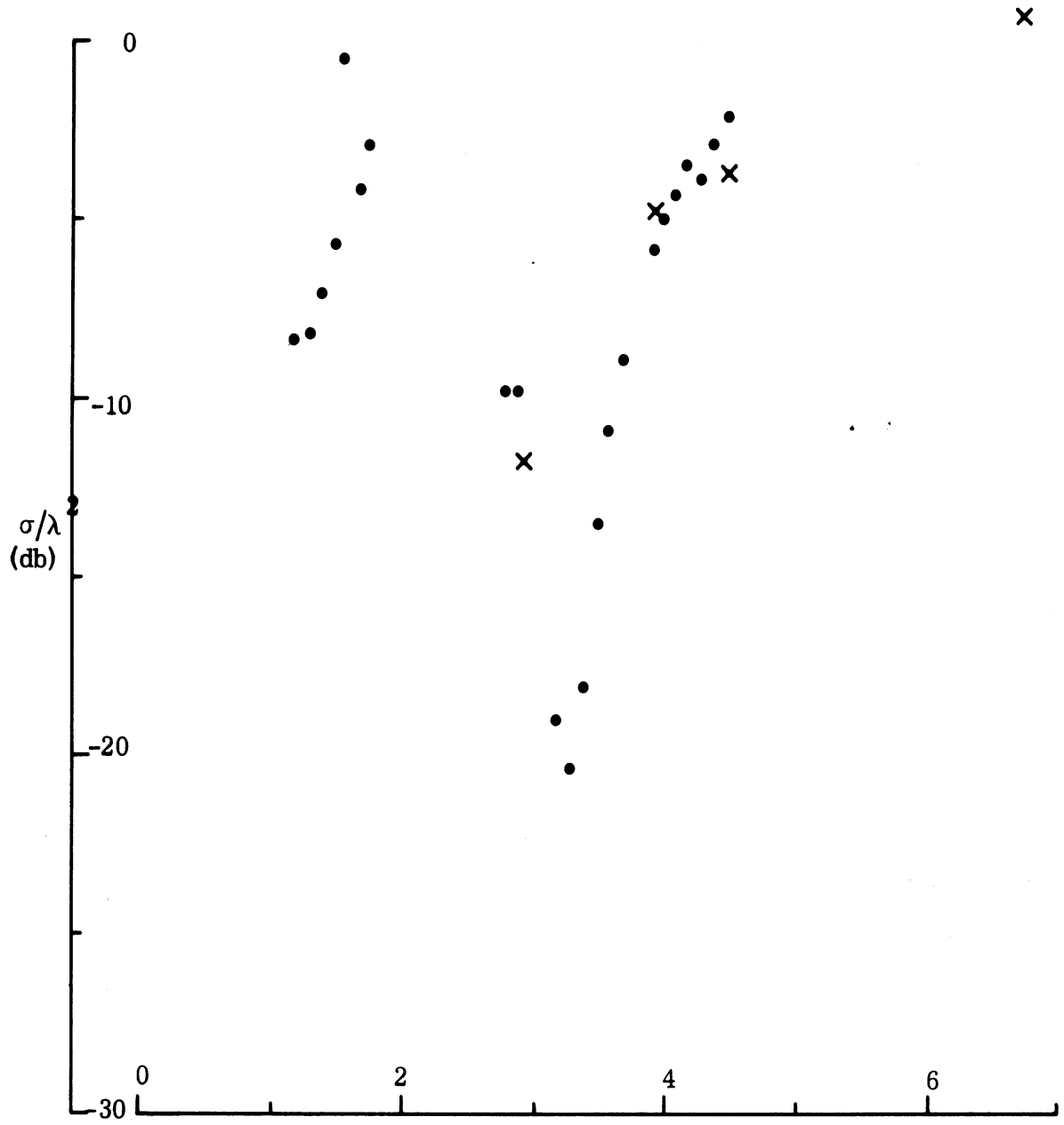

FIG. 3-9: MEASURED NOSE-ON BACKSCATTERING CROSS SECTIONS FOR MODELS ID-1 (x x x) AND ID-2 (● ● ●).

$$S_2 = \frac{i}{4} \sec^2 \alpha \, \frac{a}{b} \, B(kb) \, J_o (2ka \cos\alpha \sin\theta) \, e^{-2ikb \sin\alpha \cos\theta} \qquad (3.14)$$

for $kb_1 \leq kb \leq \infty$, where

$$kb_1 = - \frac{3n \sin 2\pi/n}{16 \cos^2 \alpha} \qquad (3.15)$$

with $n = 3/2 + \alpha/\pi$, and

$$B(kb) = 1 - \frac{C}{(kb)^{0.6}} \qquad (3.16)$$

with

$$C = 5/64 \left(- \frac{6n \sin 2\pi/n}{\cos^2 \alpha} \right)^{0.6} ; \qquad (3.17)$$

and

$$S_2 = - i \, \frac{ka}{2n} \operatorname{cosec} \frac{2\pi}{n} \, J_o (2ka \cos\alpha \sin\theta) e^{-2ikb \sin\alpha \cos\theta} \qquad (3.18)$$

for $kb \leq kb_1$; and S_3 is the creeping wave contribution

$$S_3 = \gamma(ka) \, B(kb) \, \frac{a}{2b} \left(\frac{kb}{2}\right)^{1/3} \frac{e^{2ik(a-b) + \frac{i\pi}{12}}}{\sqrt{2k(a-b)}}$$

$$\times \frac{1}{\beta_1 \left\{ Ai(-\beta_1) \right\}^2} \, S^{(1)}(kb) \qquad (3.19)$$

where

$$S^{(1)}(kb) = \left(\frac{kb}{2}\right)^{4/3} e^{i\pi/3} \left\{1 + \frac{e^{i\pi/3}}{60\tau^2\beta_1^2}(32\beta_1^3 + 9)\right\} \frac{1}{\beta_1\left\{Ai(-\beta_1)\right\}^2}$$

$$\times \exp\left\{i\pi kb - e^{-i\pi/6}\tau\pi\beta_1 - e^{i\pi/6}\frac{\pi}{60\tau\beta_1}(\beta_1^3 - 9)\right\} \qquad (3.20)$$

with $\tau = (kb/2)^{1/3}$. B(kb) is as defined in Eq. (3.16), and $\gamma(ka)$ is the enhancement factor appropriate to a cone-sphere of radius a. Note that $S^{(1)}(kb)$ is the (unenhanced) creeping wave contribution for a sphere of radius b and, as such, its expression is identical to that in Eq. (3.4) with a replaced by b. $\beta \leq \theta \leq \pi/2 - \beta$:

$$\frac{\sigma}{\lambda^2} = 1/\pi \left|S_{spec}\right|^2 \qquad (3.21)$$

(see Eq. 3.12).

(U) Plots of S_2 computed from Eqs. (3.14) and (3.15) for $\theta = 0$ and $\alpha = 9^o$ as functions of ka for various values of b/a are shown in Fig. 3-10. For this value of α, C = 0.2625 and $kb_1 = 0.2356$. Note the smooth continuation into the flat-backed cone result. It is our belief that the expression for the join contribution given in Eqs. (3.14) and (3.18) is valid and numerically effective for all a, b and α, and, as such, its derivation is a notable achievement. In contrast, the expression for the creeping wave contribution (see Eq. 3.19) is not quite so accurate, and though the results obtained from it are, as we shall see, more than adequate for almost all ka and b/a, the transition to the flat-backed cone result ($b \rightarrow 0$) is not correctly reproduced for small ka, and the transition to the pure sphere result ($b \rightarrow \alpha$) is discontinuous for all ka.

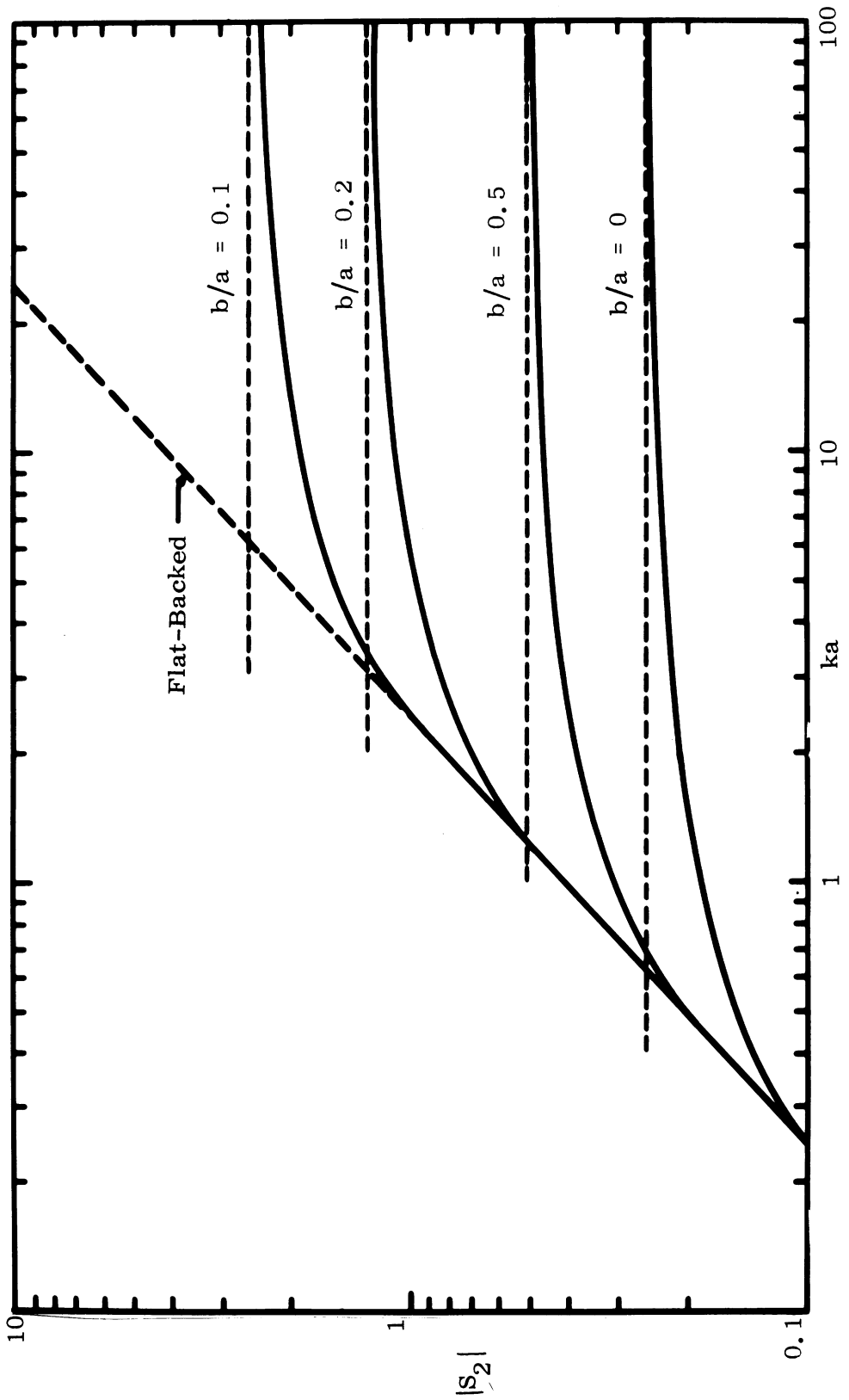

FIG. 3-10: MODULUS OF JOIN CONTRIBUTION S_2 FOR AN FB OR ID MODEL WITH $\alpha = 9^o$ FOR VARIOUS b/a RATIOS.

(U) A comparison between the predicted and measured nose-on back scattering cross sections of models ID-1 and ID-2 is shown in Fig. 3-11. For ease of computation we have here* omitted any tip contribution, and have neglected any creeping wave enhancement (i.e. taken $\gamma \equiv 1$). The fit is extremely good, and the slight discrepancy in the depths of the minima could almost certainly have been removed had we included a tip contribution. A similar comparison, but now for model FB-4 (b/a = 0.4, $\mu = 9^{o}$) is given in Fig. 3-12, and hence again the fit is excellent.

(U) The measured and theoretical backscatter patterns for model ID-1 at the frequencies 2.53 and 3.83 GHz, corresponding to ka = 2.98 and 4.51, are presented in Figs. 3-13 and 3-14 respectively. At the higher frequency the agreement is reasonably good, though there is some discrepancy in the structure of the pattern just outside the nose-on lobe. At the lower frequency, this discrepancy is much more marked, and there is not much agreement between theory and experiment in the aspect range between nose-on lobe and the side lobes of the specular flash. The discrepancy has its origin in the failure of the Bessel function factor J_0 to adequately reproduce the creeping wave behavior at oblique incidence and, as noted elsewhere (see Section 3.5), the measured patterns for the ID and FB models in this region are, for small ka, in closer agreement with the patterns for a true flat-backed cone than for a cone-sphere-like object. We also observe a slight discrepancy in level in Fig. 3-13, but since this occurs equally at broad-side and nose-on, it is believed due to an error in experimental calibration.

---

* As was done in all computations throughout this section.

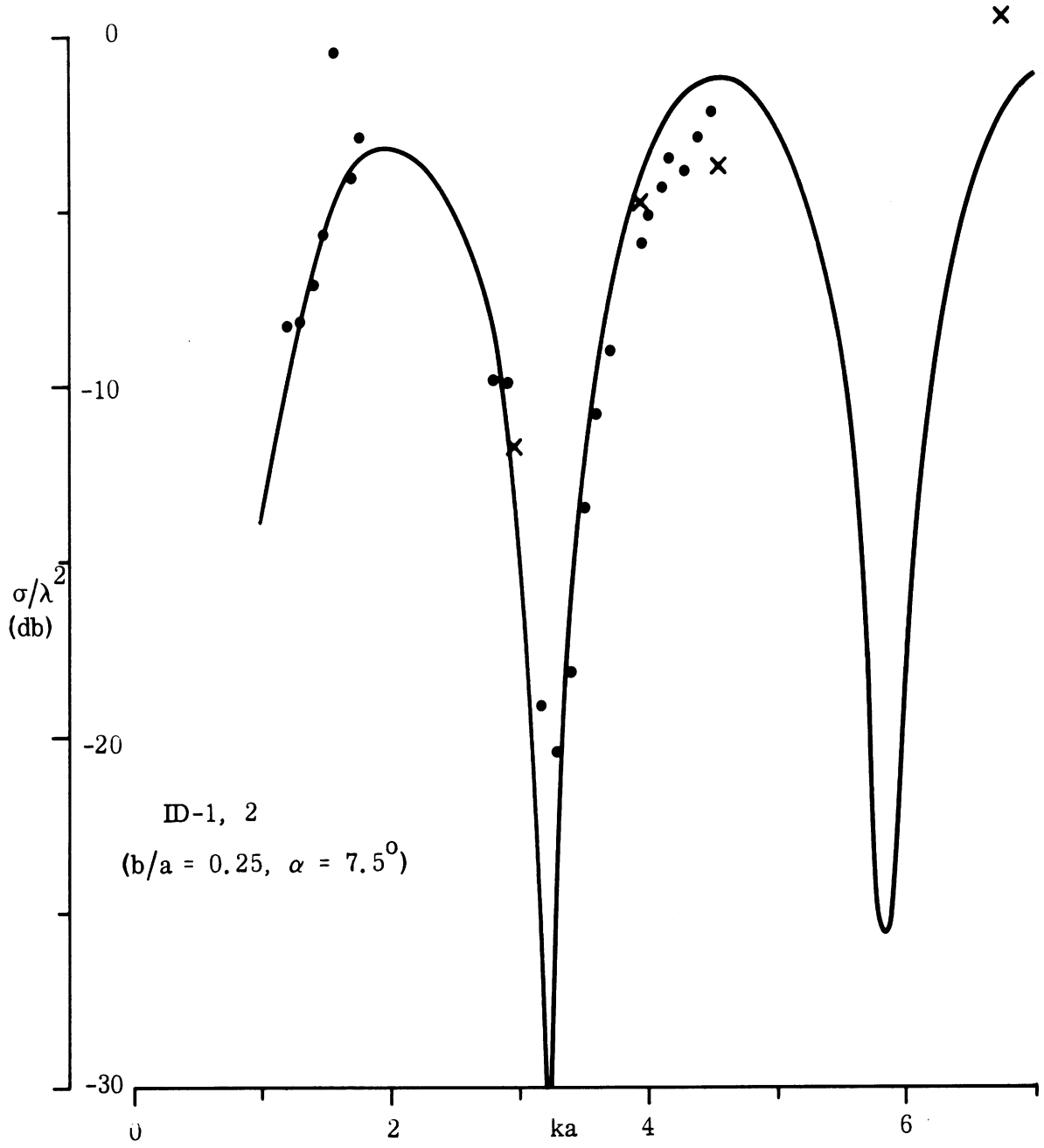

FIG. 3-11: COMPARISON BETWEEN THEORY (—) AND EXPERIMENT FOR NOSE-ON BACKSCATTERING FROM ID-1 (xxx) AND ID-2 (●●●).

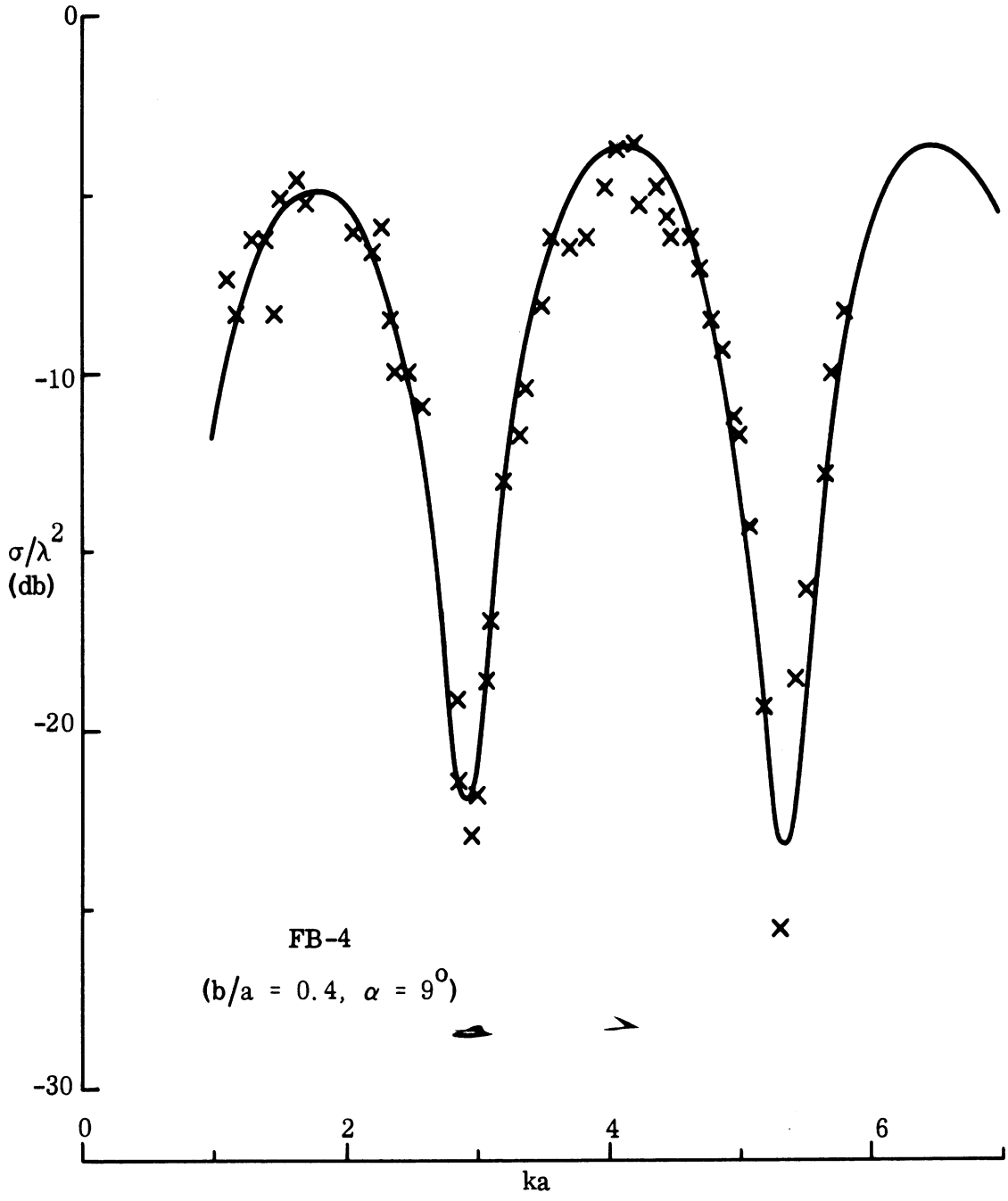

FIG. 3-12: COMPARISON BETWEEN THEORY (——) AND EXPERIMENT (xxx) FOR NOSE-ON BACKSCATTERING FROM MODEL FB-4 (b/a = 0.4, $\alpha = 9^{o}$).

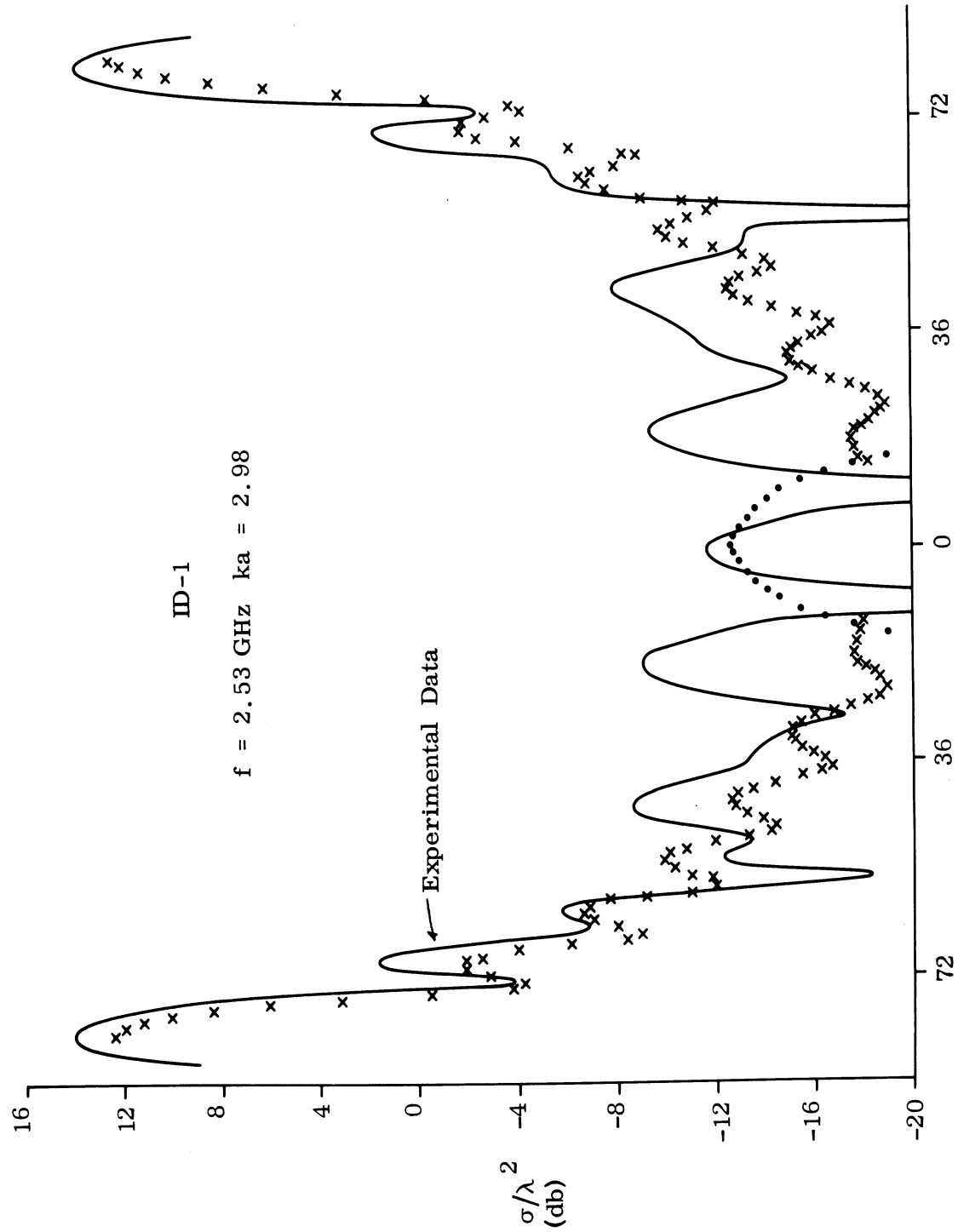

FIG. 3-13: COMPARISON BETWEEN THEORY AND EXPERIMENT.

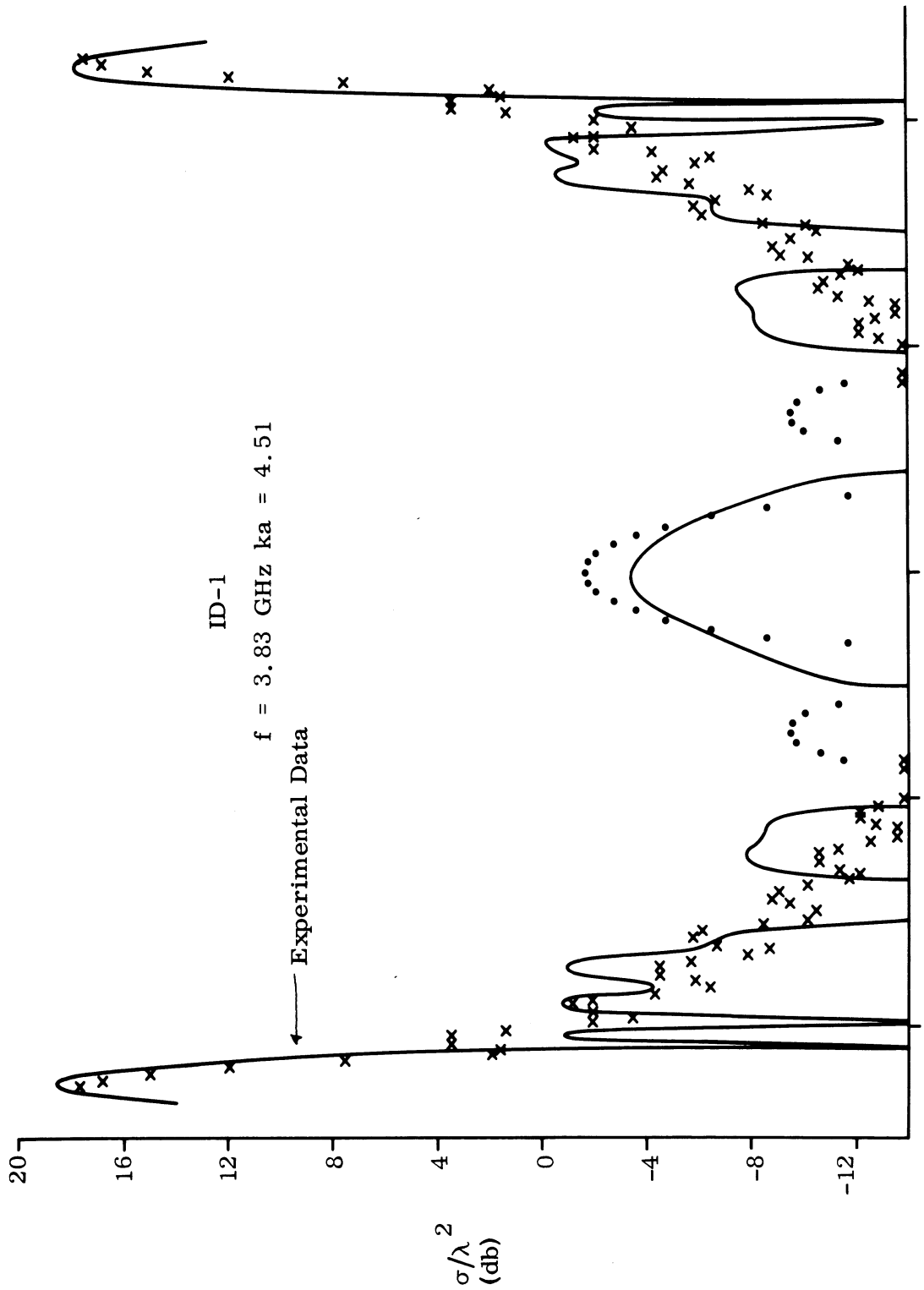

FIG. 3-14: COMPARISON BETWEEN THEORY AND EXPERIMENT.

3.2.4. Nose Tip Antenna (LSP) Model

(U) The LSP (Lucite spacer point) model is a bare cone-sphere of half angle $\alpha = 7.5^{o}$ and base radius a = 2.210 inches from which a segment 1/4 inch thick centered 3-3/8 inches from the tip has been removed and replaced by a lucite insert of the same size, so that the resulting model has the same dimensions as the original cone-sphere. The lucite disc is meant to simulate a nose-tip antenna.

(U) In order to provide a rigorous derivation of the effect of the lucite on either the surface or far fields, it is necessary to measure or compute the complex far field amplitude of the spacer regarded as a ring antenna excited in those modes appropriate to the incident field, the radiation impedance of the antenna so excited, and the loading impedance provided by the lucite and measured at the surface. Such an analysis would be tedious, though relatively straightforward, and would be similar in all respects to the approach generally adopted in the consideration of problems involving the reactive loading technique; and in view of the extremely close agreement between theory and experiment in such reactive loading problems, the accuracy of the far field specification for the LSP model resulting from this analysis could be expected to be very high.

(U) The purpose of "reactive loading" applied to scattering problems is the control of the scattered field by appropriate choice of the loading impedance, and a feature of this technique is that relatively small variations in the applied load can produce large changes in cross sections. Ergo, any practical antenna must be modeled most precisely, including simulations of the feed and line impedances, for the measured data to be truly indicative of the cross section that would be realized. In contrast, the LSP model is only a very crude simulation which can at most indicate the type of cross section changes

that could occur, and because of this there was neither reason nor justification for undertaking the detailed analysis that could have led to an entirely theoretical and rigorous prediction of the backscattered field. Rather was it our intent to investigate the modifications to the surface field which might result from the presence of the antenna (a full description of these can be found in Goodrich et al, 1967) and, in the present note, to compare a formula for the cross section with measured data. In such a formula there is one parameter, representing the excitation strength of the antenna, which is unspecified; and in the absence of a general analysis of the form described above, it is necessary to deduce this parameter as best we can from the surface field data.

(U) The far field amplitude in the backscattering direction associated with the spacer alone can, for angles of incidence not greatly different from nose-on, be written as

$$S_{sp} = \frac{2\sqrt{3}}{9} ka_s \Gamma e^{i\phi} J_o(2ka_s \sin\theta) e^{-2ik(a - a_s \cos\alpha)\operatorname{cosec}\alpha \cos\theta} \qquad (3.22)$$

where a_s is the radius of the spacer at its mid-point, $\Gamma e^{i\phi}$ is the complex excitation strength, and the phase is referred to an origin at the shadow boundary of the cone-sphere. Inasmuch as surface field measurements at points beyond the spacer show the field to be relatively unaffected by its presence, it is concluded that the join and shadow boundary contributions will remain those which are appropriate to a pure cone-sphere, and accordingly, Eq. (3.22) is but an additive effect. S_{sp} must be included (and may be dominant) in the aspect range $0 \leq \theta \leq \beta$, where β is the limiting angle defined following Eq. (3.12). Depending on Γ and ka_s, it may still be significant outside this region but, for practical purposes (and computational convenience) can be neglected outside this range in view of the rapidly increasing side lobes of the specular flash.

(U) The far field prescription is now as follows: $0 \leq \theta \leq \beta$:

$$\frac{\sigma}{\lambda^2} = 1/\pi \left| S_1 + S_2 + S_3 J_o (2 \text{ ka } \sin \theta) + S_{sp} \right|^2 \qquad (3.23)$$

(see Eq. 3.11), where S_1, S_2, and S_3 are as defined in Eqs. (3.2), (3.3) and (3.5) respectively, and S_{sp} is given in Eq. (3.22); $\beta \leq \theta \leq \pi/2 - \alpha$

$$\frac{\sigma}{\lambda^2} = 1/\pi \left| S_{spec} \right|^2 \qquad (3.24)$$

(see Eq. 3.12).

(U) Both Γ and ϕ could be estimated from measured data for the amplitude and phase of the surface field on model LSP at the appropriate frequencies. Unfortunately, only amplitude data is available, but from this the curve of Γ versus ka shown in Fig. 3-15 has been constructed. We observe that for ka = 2.98, Γ = 1.0, whereas for ka = 4.51, Γ = 2.9.

(U) Comparisons between the measured and computed values for the backscattering cross section of the LSP model at near nose-on aspects with frequencies 2.53 and 3.83 GHz corresponding to ka = 2.98 and 4.51 respectively, are shown in Figs. 3-16 and 3-17; and to illustrate the large variations that can result from changes in the phase ϕ of the spacer excitation, we have in each case computed σ/λ^2 with ϕ chosen such that the spacer contribution is in-phase or out-of-phase with the remaining contributors to the cross section. This entailed the choice $\phi = -42.846^\circ$ (in-phase) and $\phi = 137.154^\circ$ (out-of-phase) for ka = 2.98, and $\phi = -108.952^\circ$ (in-phase) and $\phi = 71.048^\circ$ (out-of-phase) for ka = 4.51. At each frequency, the two curves are the extreme ones as regards the nose-on lobe, and these bracket the

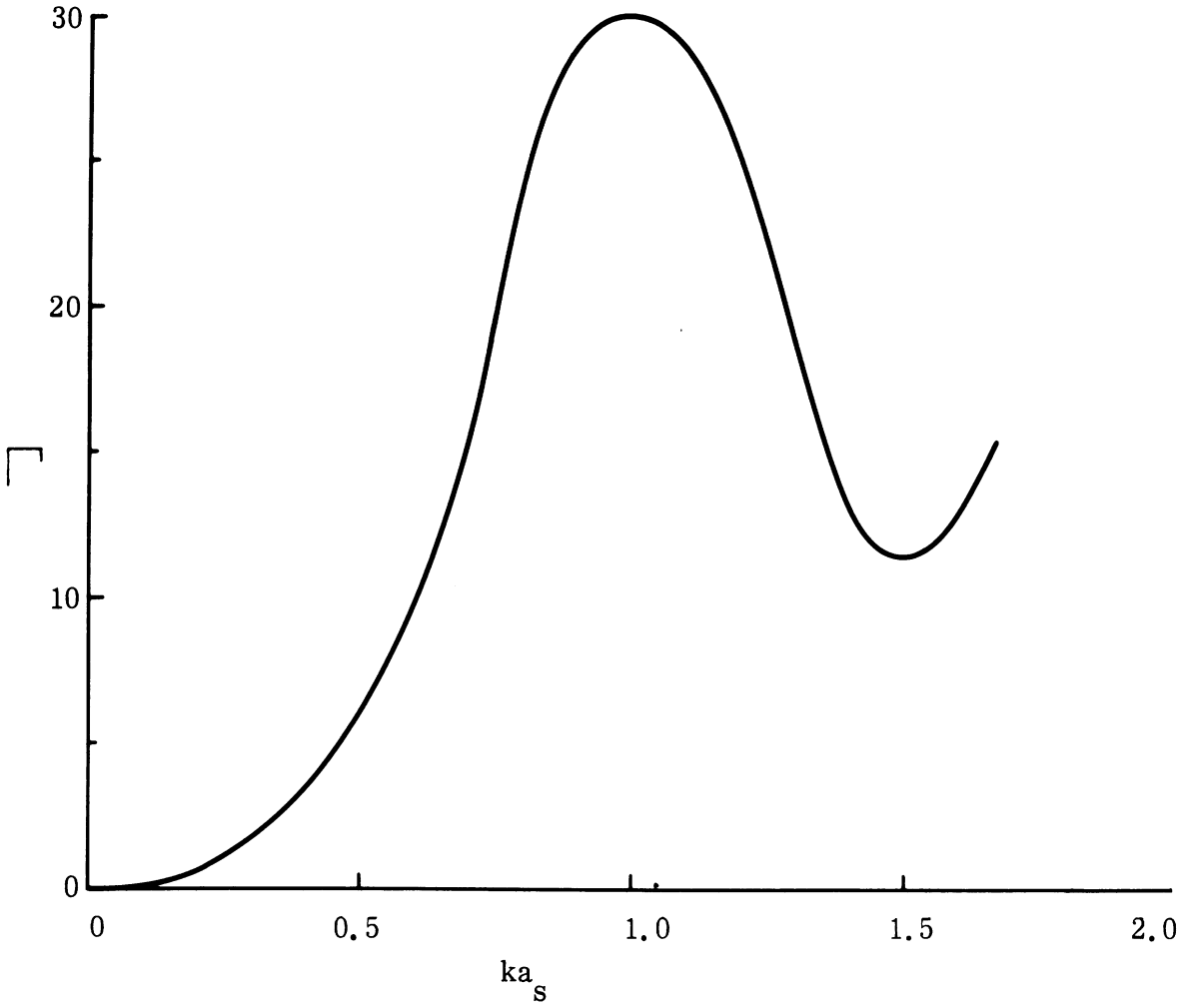

FIG. 3-15: AMPLITUDE Γ OF EFFECTIVE RING EXCITATION FACTOR FOR LSP MODEL, INFERRED FROM SURFACE FIELD DATA.

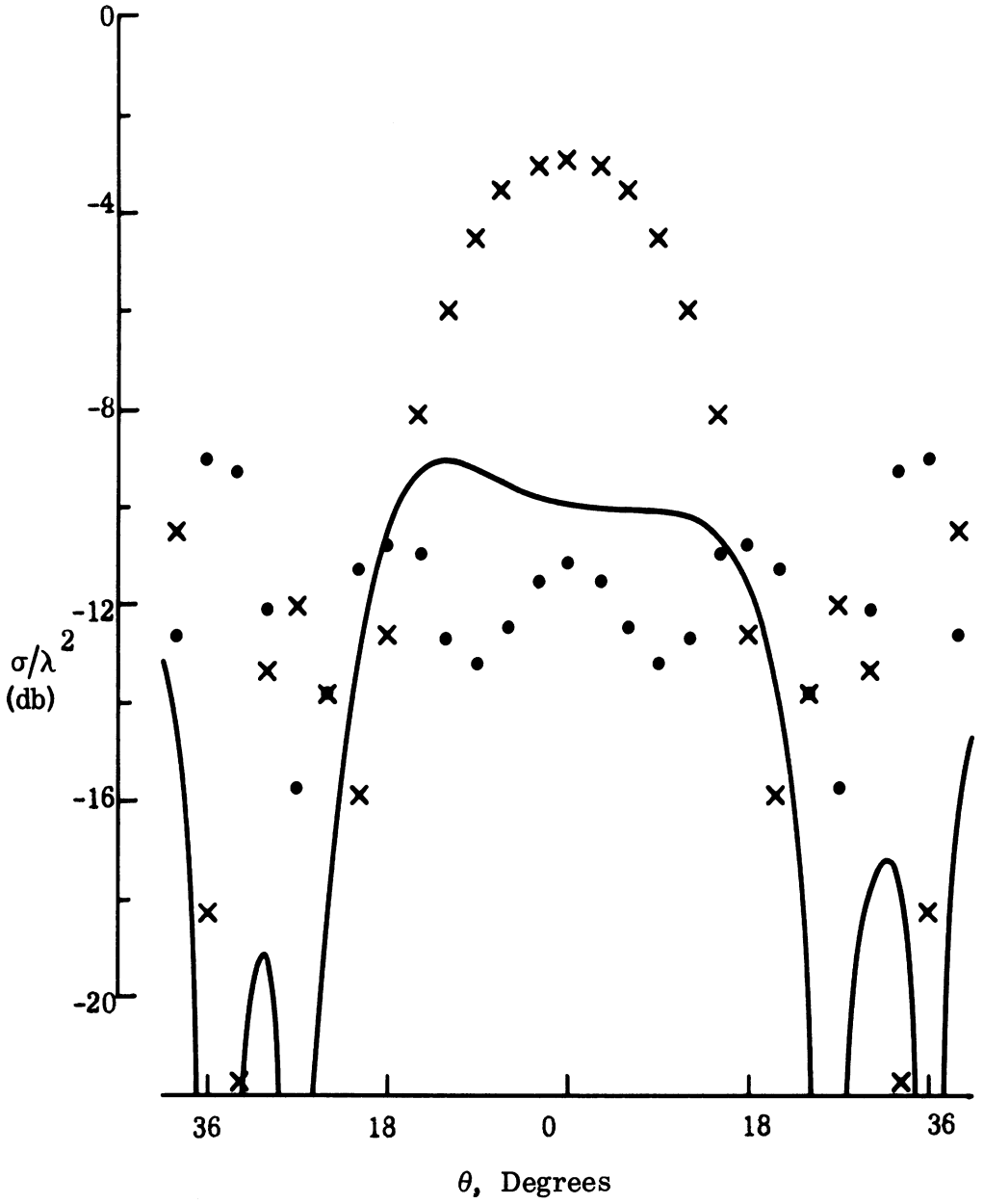

FIG. 3-16: COMPARISON BETWEEN THEORY AND EXPERIMENT (——) FOR THE LSP MODEL WITH ka = 2.8. The Theoretical Values are Computed from Eq. (3.23) with Γ = 10 and ϕ = 42.846° (in-phase, xxx) and ϕ = 42.846° + 180° (Out-of-phase, ●●●).

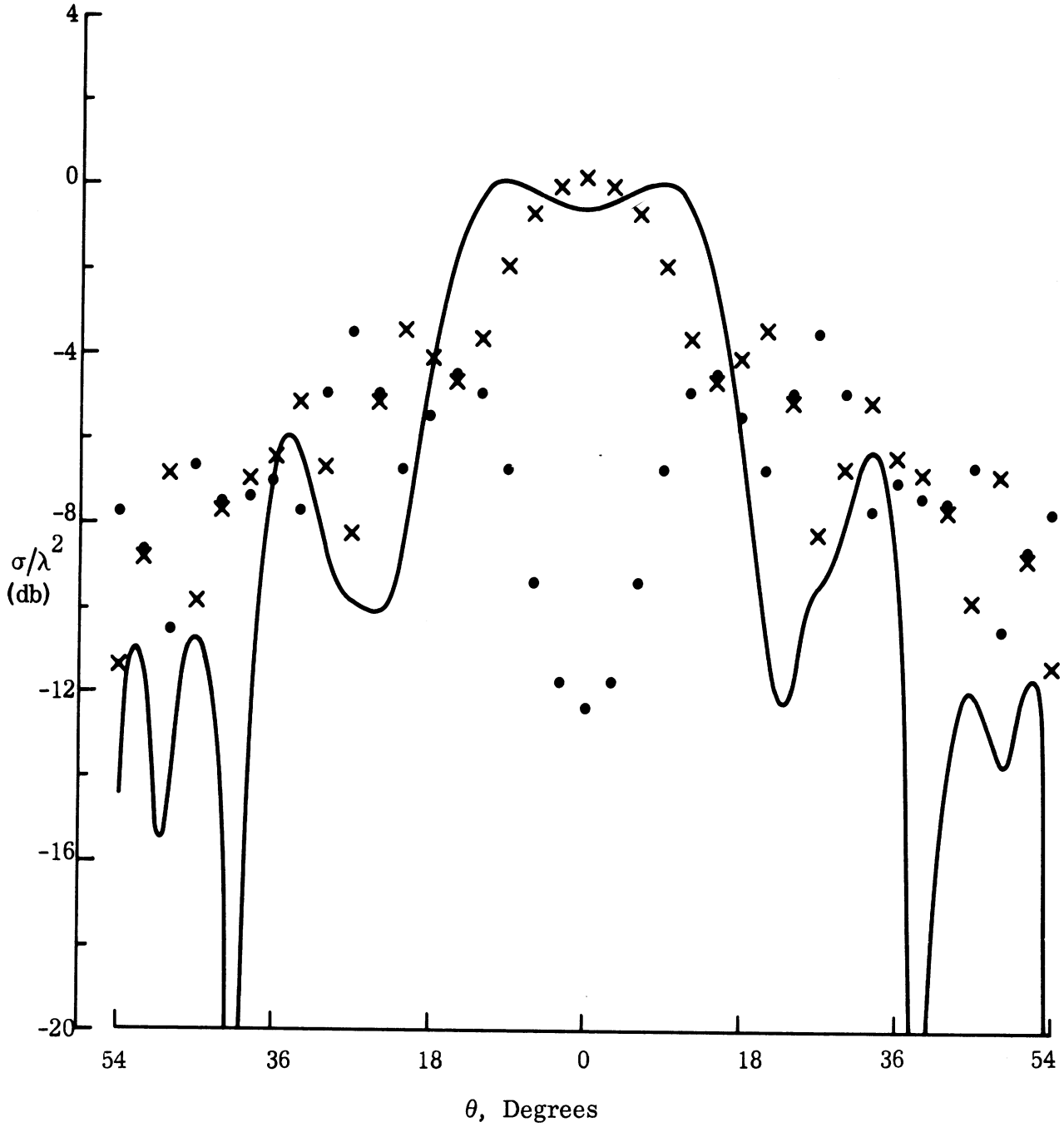

FIG. 3-17: COMPARISON BETWEEN THEORY AND EXPERIMENT (——) FOR THE LSP MODEL WITH ka = 4.51. The theoretical values are computed from Eq. (3.23) with $\Gamma = 2.9$ and $\phi = 108.952^{\circ}$ (in-phase, xxx) and $\phi = -108.952^{\circ}$ (out-of-phase, ●●●).

measured data. Using only the lobe shape and magnitude as a guide it would appear that to fit the data at the lower frequency, ϕ should be chosen near to, but somewhat distinct from, its value corresponding to the out-of-phase condition, and for the purposes of the subsequent comparison we selected $\phi = -42.846^{o} + 225^{o}$. In contrast, at the higher frequency it would appear that we can do little better than to choose ϕ corresponding to the in-phase condition, that is, $\phi = -108.952^{o}$. Note that these values are not necessarily the optimum, and since the nature of the side lobes in a scattering pattern is quite critically dependent on ϕ, it is entirely possible that other values of ϕ would lead to a better overall fit to the measured data.

(U) The theoretical backscattering patterns for ka = 2.98 and 4.51 computed from Eqs. (3.23) and (3.24), using the above values of ϕ, are shown along with the measured patterns in Figs. 3-18 and 3-19. The agreement is rather good, and though there are some discrepancies in the "sensitive" aspect ranges midway between nose-on and specular, it is probable that these are attributable partly to a less-than-optimum choice of ϕ and partly to a failure of the Bessel function $J_0(2\,ka\,\sin\theta)$ to adequately diminish the creeping wave contribution at wide aspects.

3.2.5 Coated Cone-spheres

(U) Although the scattering behavior of a metallic cone-sphere-like body is by no means simple, the presence of one or more non-metallic coatings complicates the problem by many orders of magnitude, and it is only in such trivial cases as the sphere or infinite circular cylinder that even the case of uniform homogeneous and isotropic coatings has received rigorous consideration. In order to make progress with the cross section prediction problem when coatings are present, it is therefore necessary to adopt some approach which builds on the information gained from the study of the corresponding

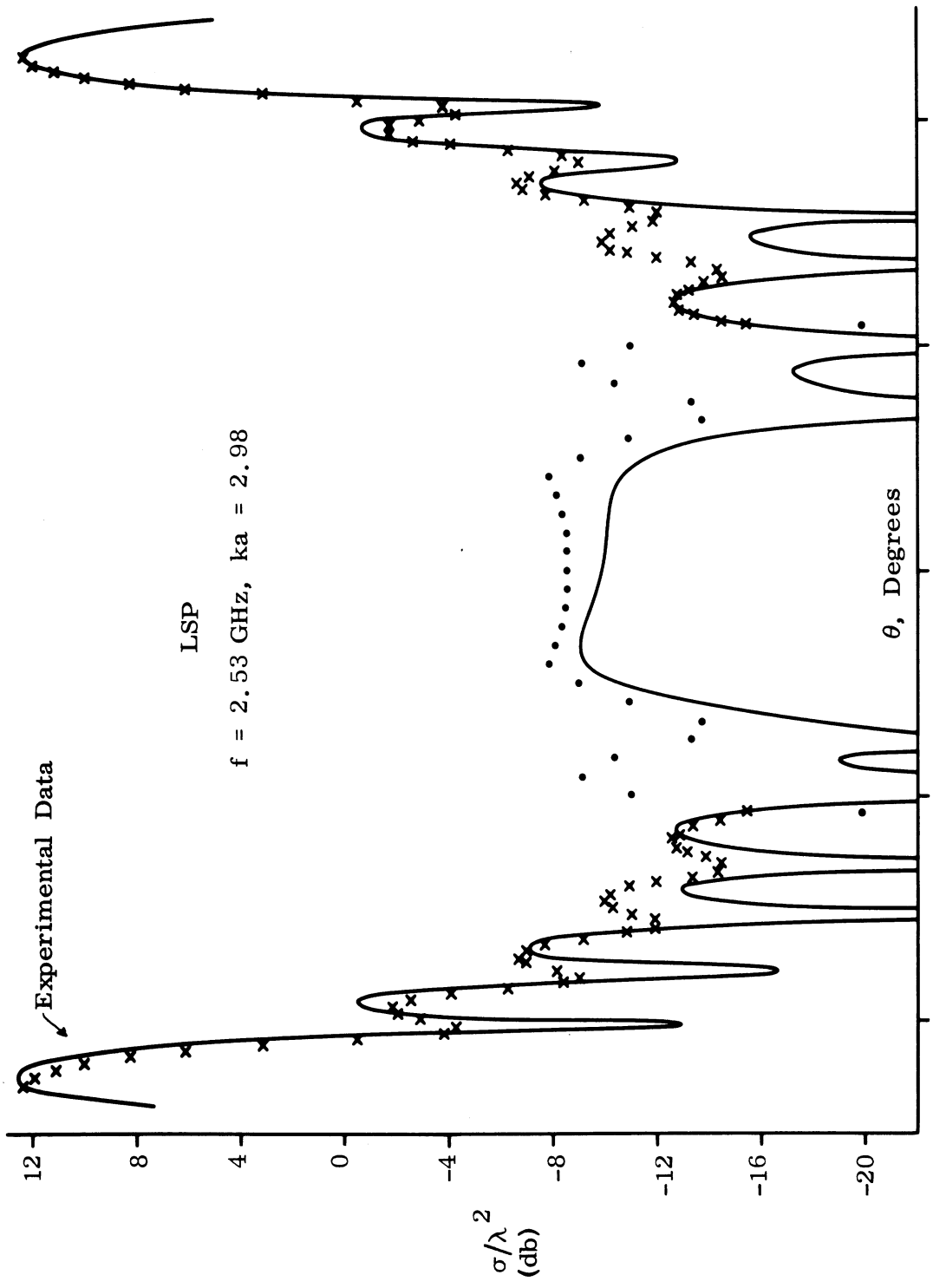

FIG. 3-18: COMPARISON BETWEEN THEORY AND EXPERIMENT USING $\Gamma = 1.0e^{i(225 - 42.845)^{\circ}}$.

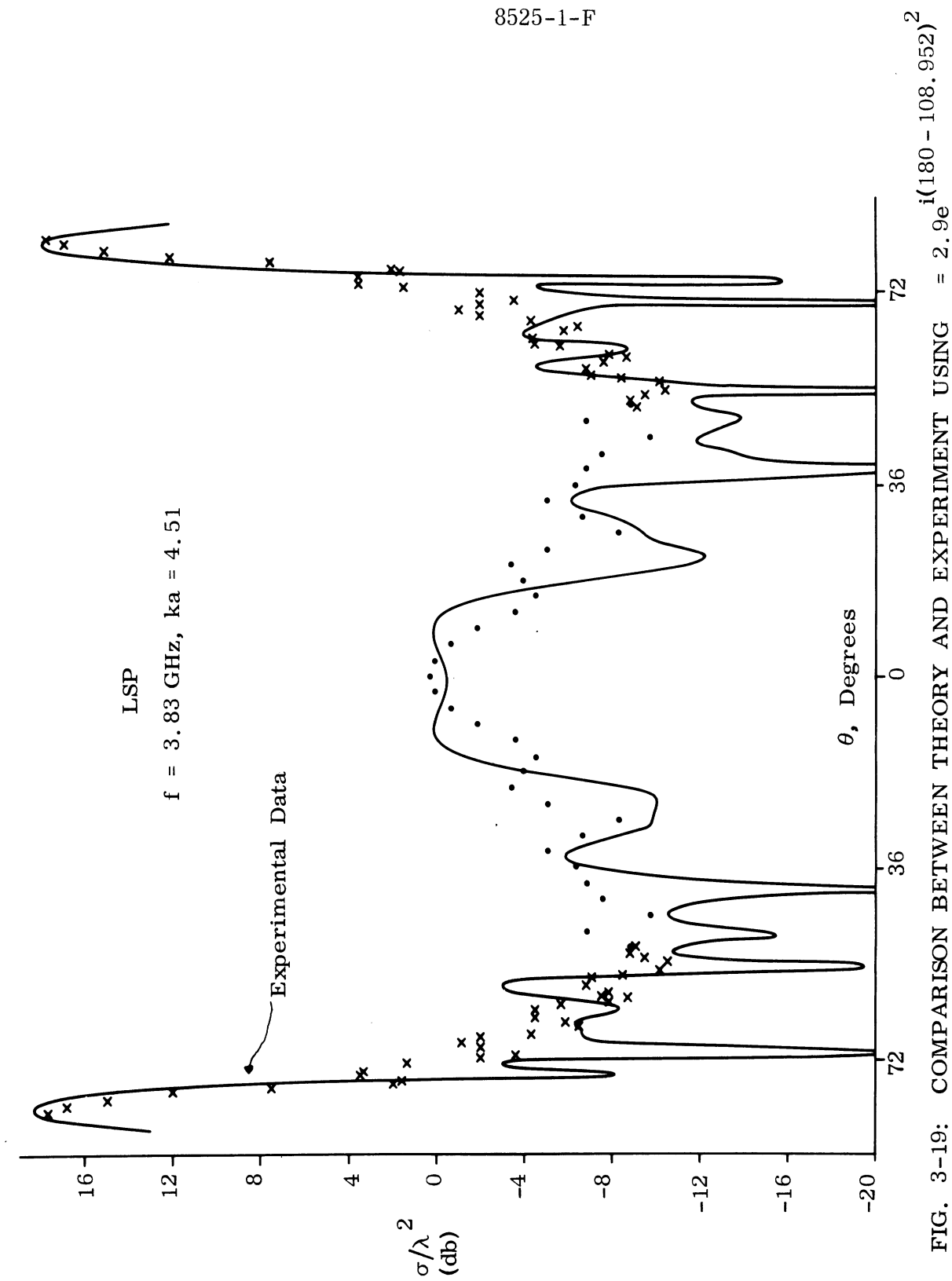

FIG. 3-19: COMPARISON BETWEEN THEORY AND EXPERIMENT USING $= 2.9e^{i(180-108.952)^2}$

metallic shape, but yet enables us to take the coating into account, and for this purpose the impedance boundary condition is almost ideal. Such a boundary condition simulates the effect of the entire coating (which, in practice, may be intentionally variable in its properties as a function of depth, and unintentionally variable in the transverse directions) by means of a single boundary condition,

$$\underline{E} - (\hat{n} \cdot \underline{E})\hat{n} = \eta \sum \hat{n} \times \underline{H} \qquad (3.25)$$

applied at the outer surface, where $\underline{E}$, $\underline{H}$ are the total (incident plus scattered) fields, n is a unit vector normal in the outwards direction, and $\sum$ is the intrinsic impedance of free space. η is the parameter representing the effective impedance of the coating relative to that of free space, and is zero for a perfect conductor -- in which case, the boundary condition (3.25) reduces to that used heretofore.

(U) For a single homogeneous coating composed of a material of relative (complex) permeability μ, and of depth large compared to the skin depth at the frequency of interest, η is simply the bulk impedance of the material and is

$$\eta = \sqrt{\mu/\epsilon} \quad . \qquad (3.26)$$

If the depth, δ, of the layer is not that large, so that a significant amount of energy returns to the surface after reflection at the (metallic) substrate, the expression for η required for use in (3.25) becomes

$$\eta = -i \sqrt{\frac{\mu}{\epsilon}} \tan\left(\sqrt{\epsilon\mu}\, k\, \delta\right), \qquad (3.27)$$

where k is the free space propagation constant, and in the limit $k\delta \rightarrow \infty$, Eq. (3.27) reduces to the form shown in (3.26). It is convenient to refer to (3.27) as the tangent approximation.

(U) The formal conditions under which the impedance boundary condition (3.25) can be justified are fairly restricted, but from an examination of surface field measurements for a variety of shapes and coatings, it is believed that the condition has a much wider practical applicability provided only that adequate estimates of the effective surface impedance can be arrived at. It certainly affords the only feasible method for estimating scattering when non-uniform coatings are present and/or when the body is not of trivial shape. It also enables multiple coatings to be taken into account via a simple (computable) modification to the postulated impedance and, last but not least, makes possible the computation of both the surface and far fields for a class of non-trivial shapes by a development of those same techniques that have proved efficacious for the corresponding metallic bodies. The condition (3.25) is therefore basic to all our analyses of coated bodies, and because of the generally small thickness of the coatings that have been considered, the required surface impedance must be computed from (3.27) using the bulk properties of the material determined from coaxial line measurements (see Goodrich, et al, 1966, Section 2.1.6).

(U) From surface measurements on pointed non-metallic bodies it has been concluded that at points not too close to the tip the surface field can be estimated using the known fields on a infinitely-long circular cylinder of the appropriate radius (see Senior 1966) and composed of the same material; and as we recede still further from the tip, the field components reduce to what they would have been had the surface at that point been part of an infinte

tangent plane. In practice this limiting behavior is almost always* attained prior to the cone-sphere join being reached, and for near nose-on incidence it is therefore sufficient to modify the join contribution by the Fresnel reflection coefficient. Moreover, as we go to more oblique angles, for which the incidence is more nearly normal to the side of the cone, this limiting behavior is attained more early, and over an ever greater percentage of the illuminated side the field behavior is that obtained by invoking the Fresnel reflection coefficient in conjunction with the fields that would have existed had the cone been metallic. It is therefore trivial to derive the expression for wide-angle scattering from that which has already been given for a metallic body.

(U) It will be recalled that the other main contributor to the scattering from a metallic cone-sphere is the creeping wave, and that its expression is derivable from a consideration of a sphere in isolation. The same is true when the surface has an impedance η associated with it, but whereas the sphere creeping wave had a simple asymptotic expression which was accurate even down to very small values of ka ($<< 1$: see Section 3.4) this is unfortunately not true for $\eta \neq 0$. Creeping waves of both the electric and magnetic type can now be excited, and even if we postulate ka $>> 1$ (as was done in the original derivation of the creeping wave expression for a metallic sphere), the computation of the corresponding result for a coated sphere still requires the solution of two transcendental equations. Thus, for a sphere coated with a material of surface impedance η, the far field amplitude produced by the creeping waves in the backscattering direction is

$$S_{cw} = S^{(e)} + S^{(m)} \tag{3.28}$$

* The exception is for very small values of ka.

with

$$S^{(e)} = \left(\frac{ka}{2}\right)^{4/3} e^{i\pi\, ka - i\pi/6} \sum_s \frac{1}{\left\{Ai(-\beta_s)\right\}^2 \left\{\beta_s - e^{-i\pi/3} q_e^2\right\}} \tag{3.29}$$

where

$$q_e = (ka/2)^{1/3}\, \eta \tag{3.30}$$

and the β_s are the roots of

$$Ai'(-\beta_s) - q_e\, Ai(-\beta_s) = 0 \ ; \tag{3.31}$$

and

$$S^{(m)} = (ka/2)^{4/3} e^{i\pi\, ka - i\pi/6} \sum_s \frac{q_m^2}{Ai(-\alpha_s)\left\{e^{i\pi/3}\alpha_s - q_m^2\right\}} \tag{3.32}$$

where

$$q_m = -(ka/2)^{1/3}\ \frac{1}{\eta} \tag{3.33}$$

and the α_s are the roots of

$$Ai'(-\alpha_s) - q_m\, Ai(-\alpha_s) = 0 \quad . \tag{3.34}$$

Since η is, in general, complex, the roots of Eq. (3.31) and (3.34) are similarly complex. Although no difficult should arise the determination of these roots in any given case, the computation will almost certainly be tedious and has not been attempted.

(U) The only other contributor to the scattering from a cone-sphere is the tip, and this is quite inconsequential for an infinitely sharp (ideal) cone-sphere. For completeness, however, its contribution will be included in the estimate of the scattering, and from a consideration of surface field data it is believed to be unaffected by the coating. The resulting prescription for the backscattering cross section of a cone-sphere or half-angle α, radius a and surface impedance η is now as follows: $0 \leq \theta \leq \beta$:

$$\frac{\sigma}{\lambda^2} = 1/\pi \left| S_1 + S_2 + S_3 J_o (2 ka \sin 2\theta) \right|^2 \tag{3.35}$$

where S_1 is the tip contribution given in Eq. (3.2), S_2 is the join contribution, namely

$$S_2 = R(\theta) S_{join} \tag{3.36}$$

with

$$R(\theta) = \frac{1 - \eta \sin(\theta + \alpha)}{1 + \eta \sin(\theta + \alpha)} \tag{3.37}$$

and S_{join} as given in Eq. (3.3), and S_3 is the creeping wave contribution shown in Eq. (3.28). $\beta \leq \theta \leq \pi/2 - \alpha$:

$$\frac{\sigma}{\lambda^2} = 1/\pi \left| R(\theta) S_{spec} \right|^2 \tag{3.38}$$

where $R(\theta)$ is as given in Eq. (3.36) and S_{spec} as given in Eq. (3.8).

(U) For a specified surface impedance η, the computation of the expression (3.38) for the wide angle scattering is entirely trivial. But such is not the case for nose-on and near nose-on scattering to which the creeping waves

form a dominant contributor. The expression for S_{cw} given in Eq. (3.28) incorporates not only the influence of the magnetic waves, but also the change in the contribution of the (dominant) electric waves resulting from the changes in birth and launch weights, as well as in decay rates, attendant on the coating. Inasmuch as these effects can be rigorously determined only by laborious computation of Eq. (3.28), and the digital programming necessary for this has not been carried out, it is fortunate that alternative and physically-motivated approximations to S_{cw} are possible to those limiting cases called for in this Agreement Item.

(U) Since all coatings of interest are electrically thin, and since the tangent approximation which must then be used for η introduces a pseudo-attenuation effect which attributes a "loss" component η as a consequence of the thickness, it is unrealistic to label a coating "lossless" or "lossy" from an examination only of the real and imaginary parts of the effective surface impedance. Indeed, were we to do so, it would be found (see Table III-2) that all of the coatings employed were lossy. In contrast, surface field measurements strongly support the contention that some of the coatings were lossless at least some of the frequencies considered, and to provide a more unambiguous categorization of the coatings it is necessary to examine the extent to which power incident on the coating is actually absorbed. A measure of this effect is provided by the power reflection coefficient, $\left|R(\theta)\right|^2$; if this is almost unity, the coating clearly behaves as an almost lossless one, but if it is much less than unity (< 0.5, say) it would seem safe to regard the coating as a lossy one. Inasmuch as this distinction is maximized at normal incidence on the surface, the following definition will be adopted:

lossless:

$$\left|\frac{1-\eta}{1+\eta}\right|^2 \sim 1$$

lossy:

$$\left|\frac{1 - \eta}{1 + \eta}\right|^2 << 1 \quad .$$

(U) A listing of the cases for which coated cone-sphere backscatter patterns had been measured as of March 1967 is given in Table III-2. It will be observed that three different coating materials were employed: LS-22, LS-24 and LS-26, and each is a lossy poly-urethane foam impregnated with graphite particles. The LS-22 coating averaged 0.1875 inches in thickness, but the other two were somewhat thicker (δ = 0.25 inches). In general the effect of each coating was measured at 7 different frequencies (see Table III-1), but since the highest frequency (8.43 GHz) is considerably beyond the range for which the bulk electrical properties of the coating materials were determined (Goodrich et al, 1966), it is necessary to confine ourselves to the lower six frequencies in the selection of patterns for the thoeretical comparison.

(U) Table III-2 gives a listing of the bulk parameters of the coatings at these six frequencies deduced, where necessary, by interpolation from the coaxial line data, together with the corresponding values of the real and imaginary parts of the surface impedance η computed using Eq. (3.27), and the power reflection coefficients at normal incidence. It will be observed that η has a significant imaginary part in every case, and that the variation with frequency is more or less the same for each coating. Indeed, the general impression is that each coating appears relatively lossless at the lowest frequency, but as the frequency increases, leading to an increase in the electrical thickness of the layer, the loss increases substantially.

(U) According to our previous criterion of "lossless", only the LS-22 coating at the lowest frequency (2.53 GHz) unquestionably fulfills it, and since the associated value of ka is 2.98, it is convenient to select this as the loss-

TABLE III-2: Coating Parameters.

LS-22

	2.53 GHz	3.37 GHz	3.77 GHz	3.83 GHz	5.73 GHz	5.83 GHz
$\lvert\epsilon\rvert$	3.11	2.42	2.43	2.45	2.01	2.04
$\arg\epsilon$	1.05	0.948	0.942	0.946	0.649	0.631
$\lvert\mu\rvert$	1.00	1.04	1.00	0.985	0.998	0.983
$\arg\mu$	0.0438	0.0577	0.0009	-0.0115	0.0942	0.0698
Re. η	0.0273	0.0524	0.0410	0.0372	0.185	0.173
Im. η	-0.259	-0.364	-0.399	-0.400	-0.643	-0.658
$\left\lvert\frac{1-\eta}{1+\eta}\right\rvert^2$	0.903	0.831	0.868	0.879	0.593	0.617

LS-24

	2.53 GHz	3.37 GHz	3.77 GHz	3.83 GHz	5.73 GHz	5.83 GHz
$\lvert\epsilon\rvert$	7.81	6.32	6.01	5.98	4.39	4.37
$\arg\epsilon$	1.65	1.21	1.04	1.05	1.08	1.14
$\lvert\mu\rvert$	1.00	0.994	1.10	1.13	0.952	0.966
$\arg\mu$	0.0191	0.0716	0.0113	-0.0073	0.0290	0.0156
Re. η	0.0884	0.213	0.343	0.361	0.496	0.483
Im. η	-0.298	-0.388	-0.482	-0.491	-0.429	-0.427
$\left\lvert\frac{1-\eta}{1+\eta}\right\rvert^2$	0.722	0.474	0.326	0.310	0.181	0.189

LS-26

	2.53 GHz	3.37 GHz	3.77 GHz	3.83 GHz	5.73 GHz	5.83 GHz
$\lvert\epsilon\rvert$	7.81	5.77	5.72	5.76	4.25	4.26
$\arg\epsilon$	1.73	1.41	1.52	1.60	1.42	1.48
$\lvert\mu\rvert$	0.997	1.05	0.965	0.950	0.9693	1.00
$\arg\mu$	0.0292	0.0463	-0.0441	- 0.0665	-0.0029	-0.0216
Re. η	0.0858	0.187	0.168	0.153	0.353	0.353
Im. η	-0.291	-0.400	-0.407	-0.401	-0.468	-0.456
$\left\lvert\frac{1-\eta}{1+\eta}\right\rvert^2$	0.729	0.523	0.561	0.590	0.311	0.307

less case for the comparison of theory with experiment. To typify lossy behavior, either of the coatings LS-24 or LS-26 at any of the higher frequencies would suffice, but since the ka values 2.98 and 4.51 are the preferred ones, attention is naturally directed at the LS-24 coating at the frequency 3.83 GHz (for which the power reflection coefficients is 0.310).

[A] Low Loss Coating

(U) For any type of coating the theoretically correct prescription of the scattering is that given in Eq. (3.35) (for $0 \leq \theta \leq \beta$) or Eq. (3.38) (for $\beta \leq \theta \leq \pi/2 - \alpha$). As previously remarked, however, the computation of the creeping wave contribution presents some difficulty (or, at least, tedium) and here and in the next section we offer alternative, practically-motivated, estimates of this particular contribution which are appropriate to the cases of low- and high-loss coatings respectively.

(U) For a coating which is essentially lossless, the fields induced on the surface of the body are of the same character as in the case of the metallic body, with only their magnitudes differing somewhat. In particular, the magnetic creeping waves are insignificantly excited (because $q_m >> q_e$, implying very rapid damping of the magnetic waves). Moreover, $|q_e| << 1$ due to the smallness of $|\eta|$ in most practical cases, and it therefore appears reasonable to postulate an electric creeping wave which is identical to that supported by the metallic body, which suffers no additional decay due to the coating, and which even has its amplitude unchanged since the field is incident at grazing angles at the shadow boundary.

(U) The resulting prescription for the far field scattering is then as follows: $0 \leq \theta \leq \beta$:

$$\frac{\sigma}{\lambda^2} = 1/\pi \left| S_1 + S_2 + S_3 J_o (2ka \sin \theta) \right|^2 \qquad (3.39)$$

(see Eq. 3.35), where S_1 and S_2 are as defined in Eqs. (3.2) and (3.36) respectively, and

$$S_3 = S_{cw} \qquad (3.40)$$

where S_{cw} is as given in Eq. (3.4). $\beta \leq \theta \leq \pi/2 - \alpha$:

$$\frac{\sigma}{\lambda^2} = 1/\pi \left| R(\theta)\, S_{spec} \right|^2 \qquad (3.41)$$

(see Eq. 3.38).

(U) The best example of lossless behavior that is available is coating LS-22 at 2.53 GHz for which ka = 2.98. Even for normal incidence on the surface the power reflection coefficient is only - 0.45 db. This is the amount by which the peak of the specular lobe is reduced by the coating, with the reduction being less away from the specular angle. Near nose-on the reduction in the cross section is infinitesimal since only the join contribution is affected by the coating, and this is smaller than, and almost in-phase with, the creeping wave contribution at 2.53 GHz. The comparison of theory with experiment is shown in Fig. 3-20, and overall the agreement is quite good.

[B] Lossy Coating

(U) As the loss increases one must expect that the contribution of the magnetic creeping wave will increase relatively to that of the electric one and may, in fact, exceed it. But at the same time, however, the contribution of both is decreasing as a result of the higher decay rates associated with the coating and for coatings of sufficiently high loss the creeping wave contribution will be negli-

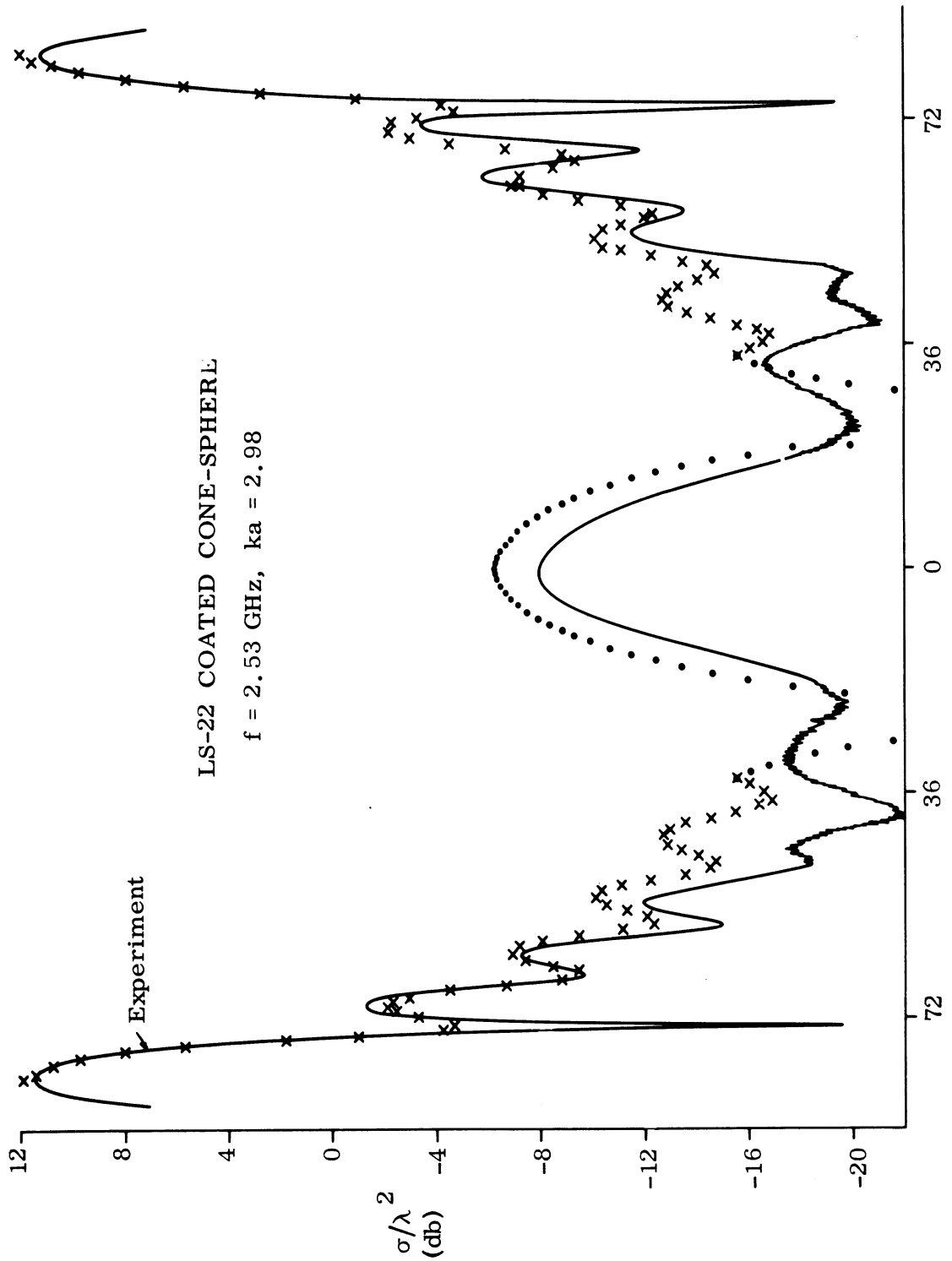

FIG. 3-20: COMPARISON BETWEEN THEORY AND EXPERIMENT.

gible compared with the join contribution. The creeping waves can then be neglected in their entirety, and an examination of surface field data suggests that this is a reasonable approximation for many of the cases examined.

(U) A rough (very rough) estimate of how much the creeping wave contribution is reduced by the coating can be had by likening the wave to a surface wave traveling over a plane surface characterized by a surface impedance q_e or q_m depending on which type of creeping wave is considered. The net reduction obtained in this manner is then $\left| e^{i\pi\, ka\, \sqrt{1 - q^2}} \right|^2$ which, for the LS-24 coating at 3.83 GHz, amounts to -33.3 db. This certainly supports the contention that we may neglect the creeping wave, in which case the cross section prediction becomes: $0 \leq \theta \leq \beta$:

$$\frac{\sigma}{\lambda^2} = 1/\pi \left| S_1 + S_2 \right|^2 \tag{3.42}$$

where S_1 and S_2 are as defined in Eqs. (3.2) and (3.36) respectively.
$\beta \leq \theta \leq \pi/2 - \alpha$:

$$\frac{\sigma}{\lambda^2} = 1/\pi \left| R(\theta)\, S_{spec} \right|^2 \tag{3.43}$$

(see Eq. 3.38).

(U) The predicted cross section obtained in this manner is compared with the measured pattern for coating LS-24 at 3.83 GHz in Fig. 3-21. Once again the agreement is quite good, and though there is a tendency for the theoretical formula to slightly underestimate the return at near nose-on aspects, the discrepancy is a good deal less than that between the two measured patterns for this one case.

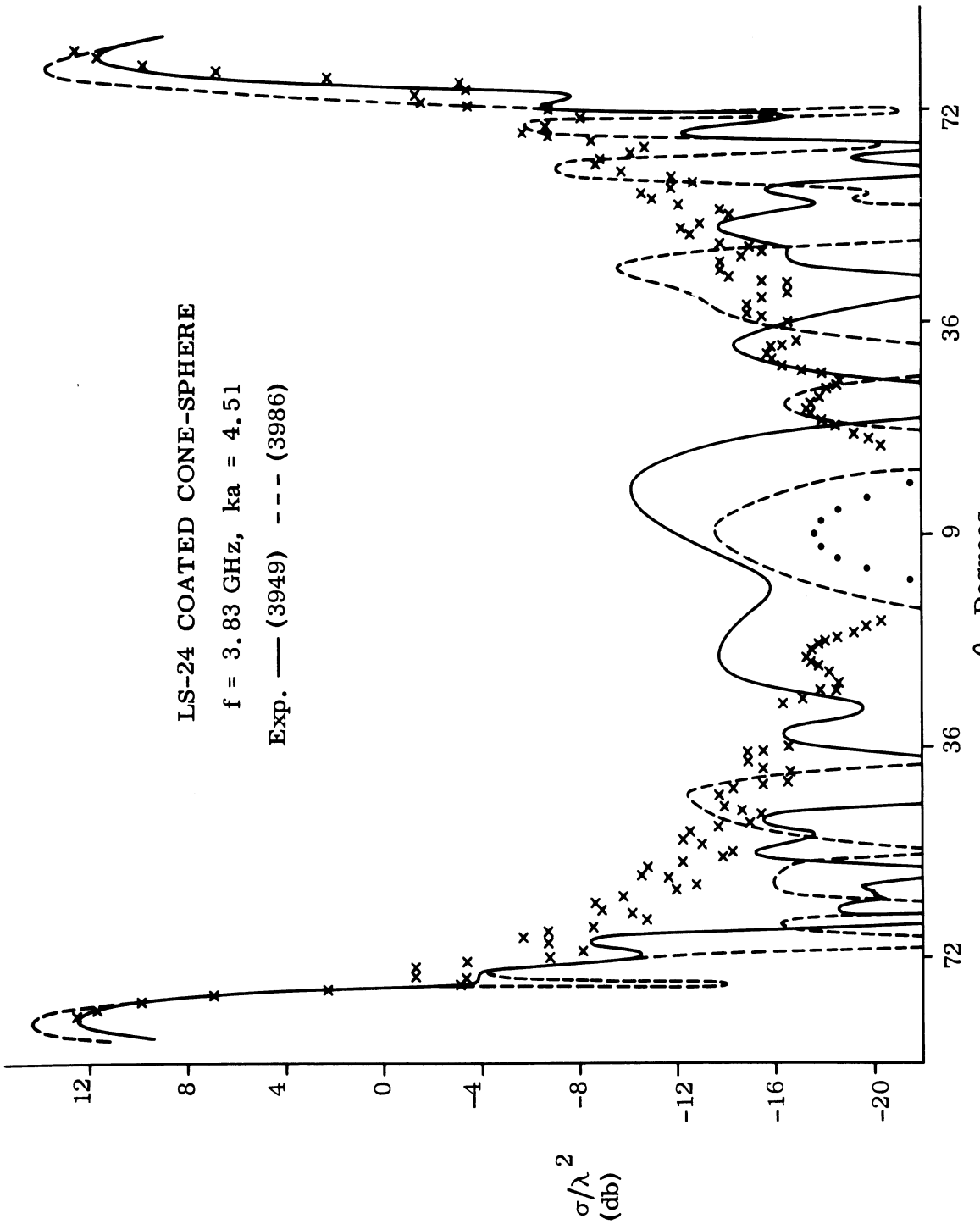

FIG. 3-21: COMPARISON BETWEEN THEORY AND EXPERIMENT.

3.3 Backscattering Behavior of Model LSP

(U) The LSP (lucite spacer point) model discussed in Section 3.2.4 is a bare cone-sphere of half-angle 7.5^{o} and base radius a = 2.210 inches from which a segment 1/4 inch thick centered 3-3/8 inches from the tip has been removed and replaced by a lucite insert of the same size, so that the resulting model has the same dimensions as the original cone-sphere. The lucite disc is meant to simulate a nose-tip antenna.

(U) Complete backscattering patterns have been measured at a series of 43 S- and C-band frequencies spanning the range $2.5 \leq ka \leq 6.8$, and from these patterns, values of the cross sections at nose-on, specular and rear-on incidence have been read. Corresponding patterns have been obtained for the pure cone-sphere of identical dimensions and it is the purpose of this Section to examine the effect of the spacer at these particular angles of incidence, and to compare the resulting cross sections with the theoretical estimates based on formulae given heretofore.

(U) The measured values of the rear-on cross sections of the pure cone-sphere and LSP models are plotted as functions of ka in Fig. 3-22 where, for clarity of presentation, we have displaced the values for the latter model by 10 db. Taking first the cone-sphere data, the theoretical estimate of the cross section is based on the existence of only a specular contribution provided by the spherical rear, and using the formula (Senior, 1965) for the specular return from a sphere, we have

$$\frac{\sigma}{\lambda^2} = 1/4\pi \ (ka)^2 \left\{ 1 + \frac{1}{(2\ ka)^2} \right\} . \qquad (3.44)$$

Inasmuch as the second term in braces gives the correction of less than 0.17 db over the range of ka covered by the measurements, we can neglect it for

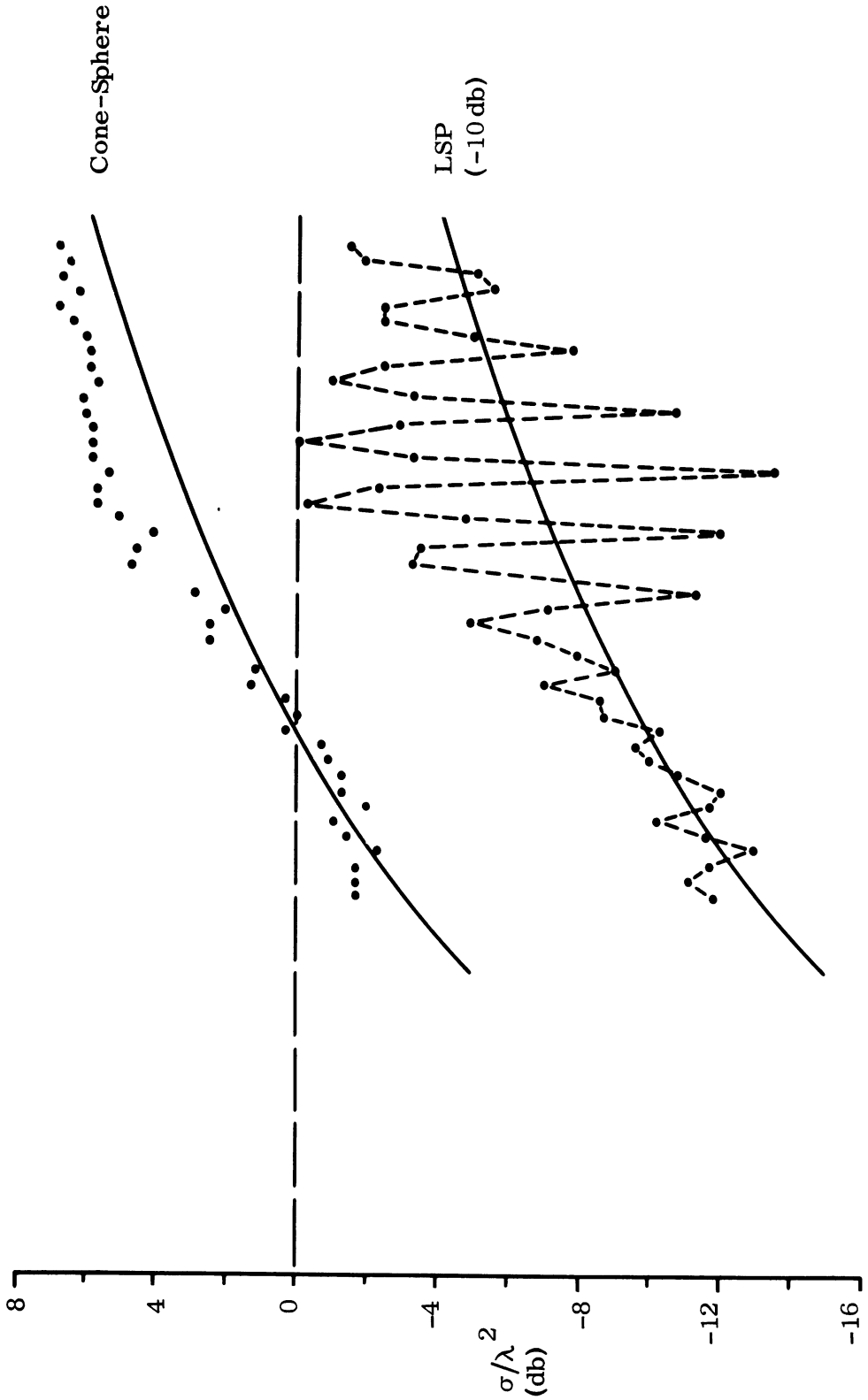

FIG. 3-22: MEASURED VALUES OF REAR-ON CROSS SECTIONS OF PURE CONE-SPHERE AND MODEL LSP.

all practical purposes and take

$$\frac{\sigma}{\lambda^2} = 1/4\pi\ (ka)^2 \quad . \tag{3.45}$$

The curve computed from this equation has been included in Fig. 3-22, and is seen to be in excellent agreement with the measured data for ka less than (about) 4, but for larger values of ka the formula appears to underestimate the cross section by as much as 3 db. The nature of the discrepancy is more clearly seen in Fig. 3-23 where we have plotted the ratio of measured and predicted cross sections. There is some evidence that the error is oscillatory in character, with quite long period, and though a likely explanation is the existence of a traveling wave contribution associated with a reflection at the tip, the period is incompatible with this. We note in passing that the theoretical estimate of such a traveling wave return is based on the concept of a long thin wire and, in consequence, provides no effect at end-on incidence. Only away from, but near, end-on incidence is a contribution predicted, but because of the significant "thickness" of the present body, a return at rear-on incidence would not be unexpected.

(U) For the LSP model the specular return at rear-on incidence is the same as for the cone-sphere, and the corresponding curve has been superimposed on the LSP data in Fig. 3-22. Quite large discrepancies of as much as 7 db are evident, particularly for ka in the vicinity of 5, and to throw some light on their nature, we have plotted in Fig. 3-23 the ratios of the measured to the theoretical (specular) cross sections. The result is a high frequency oscillation or remarkably regular period constrained within a slowly varying envelope. There is no doubt but what this is the consequence of a traveling wave effect whose reflection is provided by the ring antenna. On

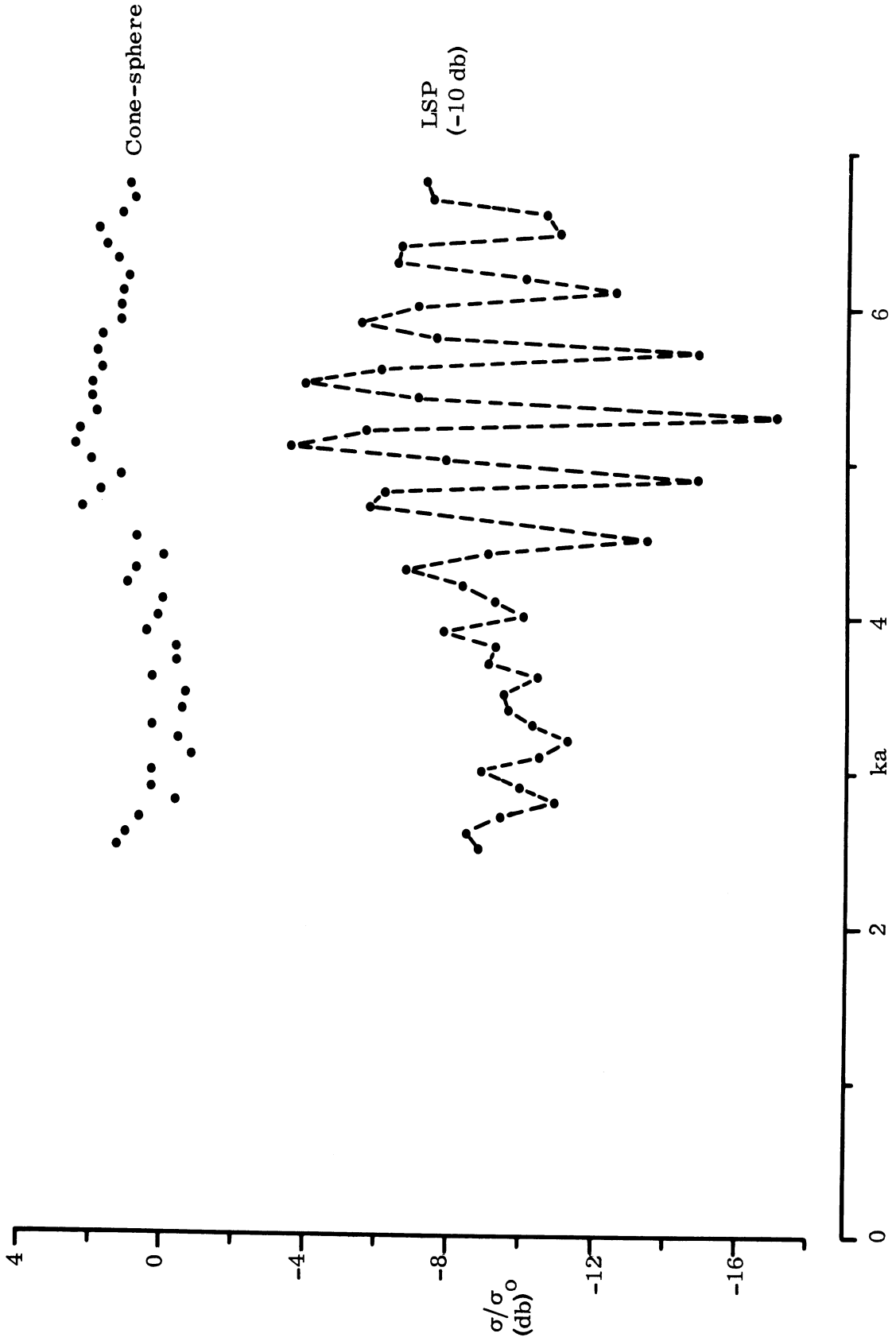

FIG. 3-23: RATIOS OF MEASURED TO THEORETICAL (OPTICS) CROSS SECTIONS OF PURE CONE-SPHERE AND MODEL LSP FOR REAR-ON INCIDENCE.

the assumption of a wave which proceeds directly the the shadow boundary and thereafter follows the surface back to the ring, traveling with the velocity of light throughout, the resulting interference with the specular returns leads to an oscillation in the cross section of (uniform) period 0.44 in ka, compared with the period 0.41 evident in the measured data. The difference could be attributable to an effective phase velocity of the traveling wave smaller than c by about 7 percent. Since the mean of the data for the LSP model in Fig. 3-23 is near unity, it is apparent that the other (specular) contribution is accurately predicted by theory. We therefore postulate

$$\frac{\sigma}{\sigma_o} = \left| 1 + A(ka) \exp \left\{ i(\alpha\, ka + \phi) \right\} \right|^2 \qquad (3.46)$$

where the exponential arises from the phase difference between the traveling wave and specular returns, and A(ka) is proportional to the amplitude of the former. Some of the values of A(ka) determined from the envelope of the oscillations in Fig. 3-23 are as follows:

ka	A(ka)	ka	A(ka)
3.5	0.10	5.5	1.04
4.0	0.30	6.0	0.68
4.5	0.66	6.5	0.32
5.0	1.09	7.0	0.10

A(ka) is, of course, proportional to the amplitude of the (voltage) reflection coefficient at the ring antenna. We observe that it displays a characteristic resonance phenomena centered on the frequency for which the circumference of the ring is one wavelength. Such resonance was previously observed in studies of the cross section of the LSP model at nose-on incidence.

(U) Turning now to incidence in the specular direction, the measured data for the cross sections of the cone-sphere and LSP models are shown in Fig. 3-24, where for clarity, the values for the latter model have been reduced by 10 db. The differences between the cross sections are quite miniscule, implying that the ring spacer has no effect at this aspect. This is in accordance with theory in which the cross section is likened to that of a cylinder whose length is the slant length of the cone and whose radius is $4/9$ $a \sec\alpha$ (Senior, 1967). Regardless of the presence of any ring, the theoretical estimate of the cross section is therefore

$$\frac{\sigma}{\lambda^2} = \frac{\operatorname{cosec}^2 \alpha \sec \alpha}{9\pi^2} (ka)^3$$

$$= 0.6667\,(ka)^3 \qquad \text{for} \quad \alpha = 7.5^\circ ,$$

and the curve computed from this formula has been included in Fig. 3-24. The agreement is good, a fact which is more clearly shown in Fig. 3-25, where the ratios of the measured to the theoretical cross sections have been plotted, but even so we do notice a tendency for the measured values to fall below the theoretical ones for ka greater than (say) b, with the discrepancy increasing as ka increases. As remarked on previous occasions, such a discrepancy is often an experimental error attributable to a near-field effect and caused by the necessity of bringing the model closer to the antenna in order to measure accurately the nose-on cross section.

(U) The measured data for nose-on incidence is given in Fig. 3-26, with the upper sequence of points showing the values for a cone-sphere, and the lower sequence showing the corresponding values for the LSP model. The latter have been reduced by 20 db to permit a clearer presentation of the data. Whereas the cone-sphere cross section displays the regular sinusoidal

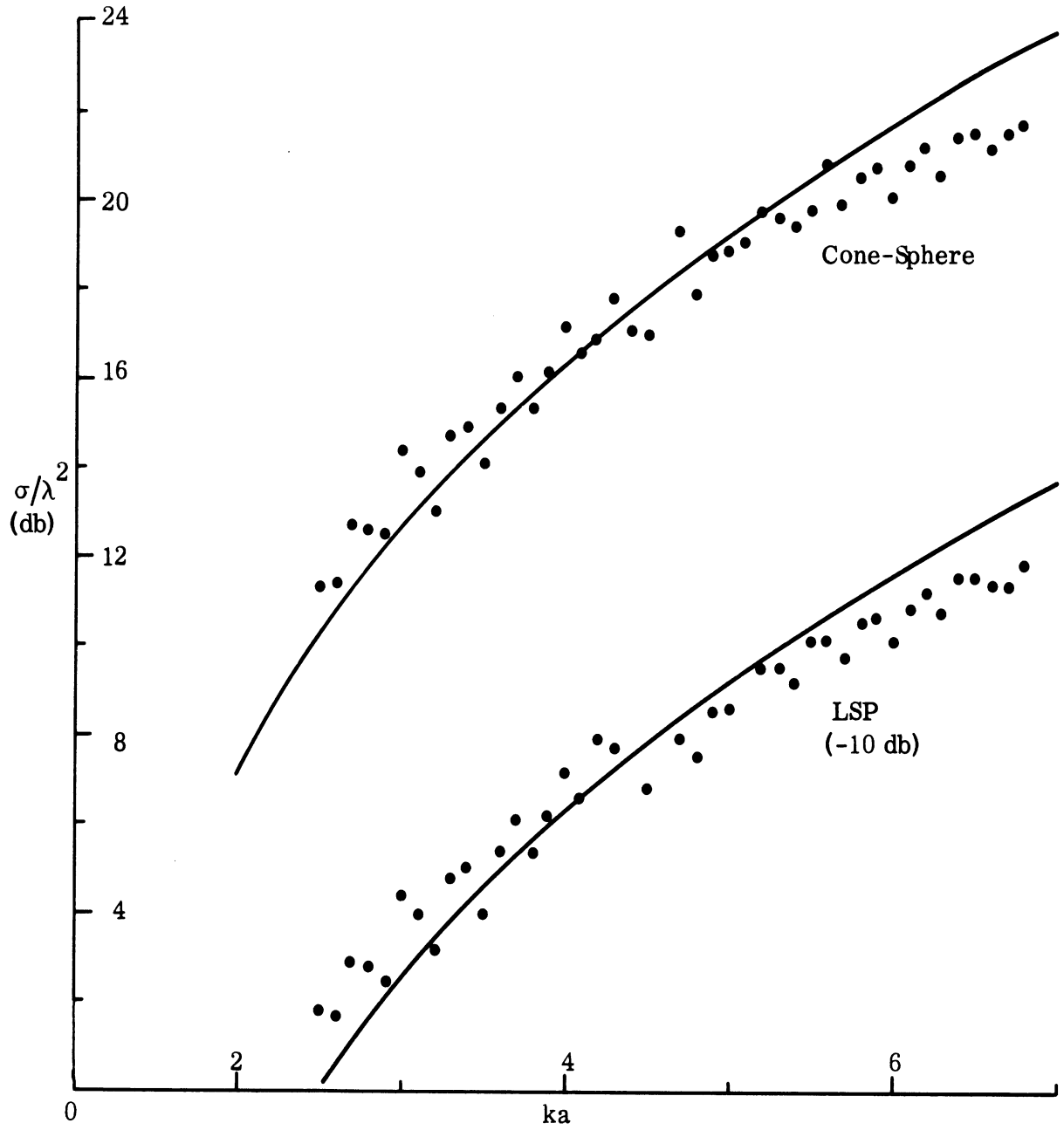

FIG. 3-24: MEASURED VALUES OF SPECULAR FLASH CROSS SECTION OF PURE CONE-SPHERE AND MODEL LSP.

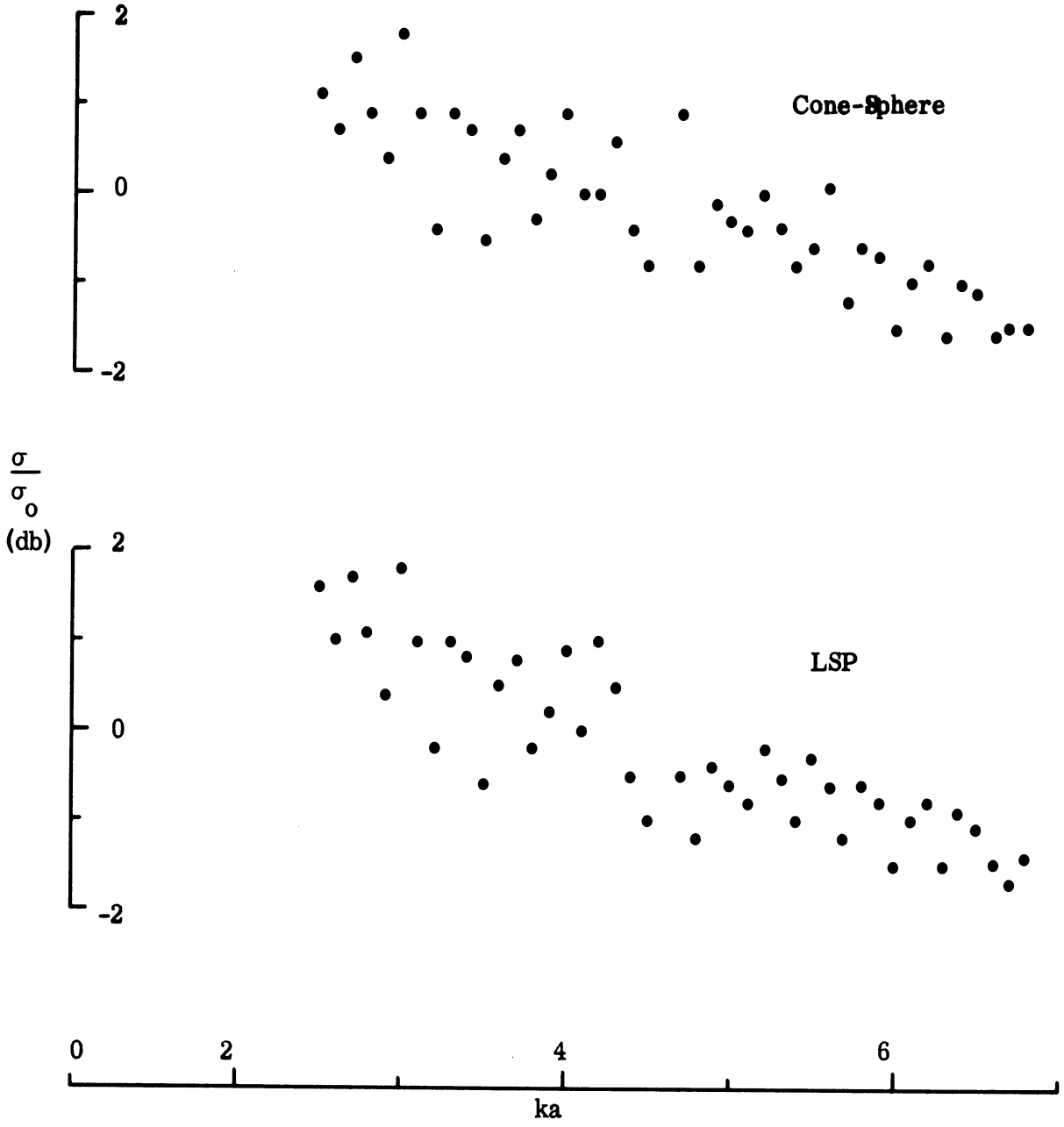

FIG. 3-25: RATIOS OF MEASURED TO THEORETICAL (OPTICS) CROSS SECTIONS OF PURE CONE-SPHERE AND MODEL LSP FOR INCIDENCE AT THE SPECULAR ANGLE.

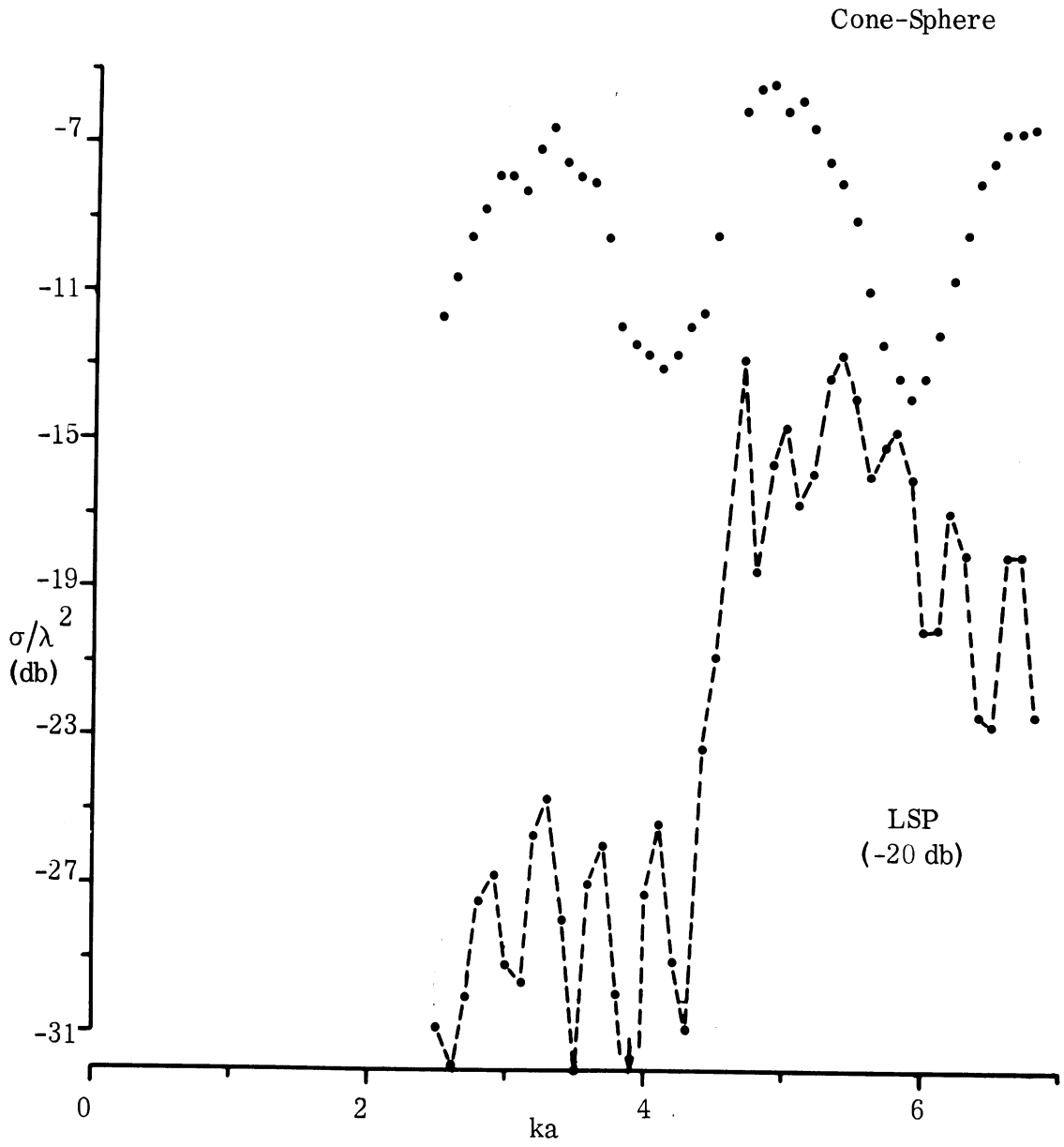

FIG. 3-26: MEASURED VALUES OF NOSE-ON CROSS SECTIONS OF PURE CONE-SPHERE AND MODEL LSP.

oscillation that is expected, the values for the LSP model follow a much more irregular pattern composed of a high frequency oscillation of period approximately 0.4 in ka superimposed on a slowly varying curve. For $ka < 3.5$ this mean curve is indistinguishable from the cone-sphere curve, but for $ka > 3.5$ the mean LSP cross section departs considerably from its cone-sphere value, and exceeds the latter by almost 20 db for ka in the range 4.5 to 6.0.

(U) A comparison between the measured data for the pure cone-sphere and the theoretical formula for the cross section is shown in Fig. 3-27. The computed curve has been taken directly from Fig. 3-3 of "The Agreement Item," using the asymptotic formula for the creeping wave enhancement factor. We note in passing that the empirical factor (see Fig. 3-2 of Section 3.2) gives better agreement with the cross section data in the vicinity of the peak near ka = 3.1, but leads to somewhat deeper minima near ka = 4.0 and 5.8. We also observe that a value for the enhancement factor even greater than that provided by the asymptotic formula would improve the agreement with experiment for $ka \geq 4.0$, but in spite of these comments, the agreement between theory and experiment evident in Fig. 3-27 is more than satisfactory.

(U) According to the theory for the LSP model outlined in "The Agreement Item," the cross section for nose-on incidence is

$$\frac{\sigma}{\lambda^2} = 1/\pi \left| S_{cs} + S_{sp} \right|^2 \tag{3.47}$$

where S_{cs} is the far field amplitude for a pure cone-sphere and

$$S_{sp} = \frac{2\sqrt{3}}{9} ka_s \Gamma e^{i\phi - 2ik(a - a_s \cos\alpha) \operatorname{cosec}\alpha} \tag{3.48}$$

is the far field amplitude of the ring (spacer) antenna. Here, $a_s (= a/5)$ is the

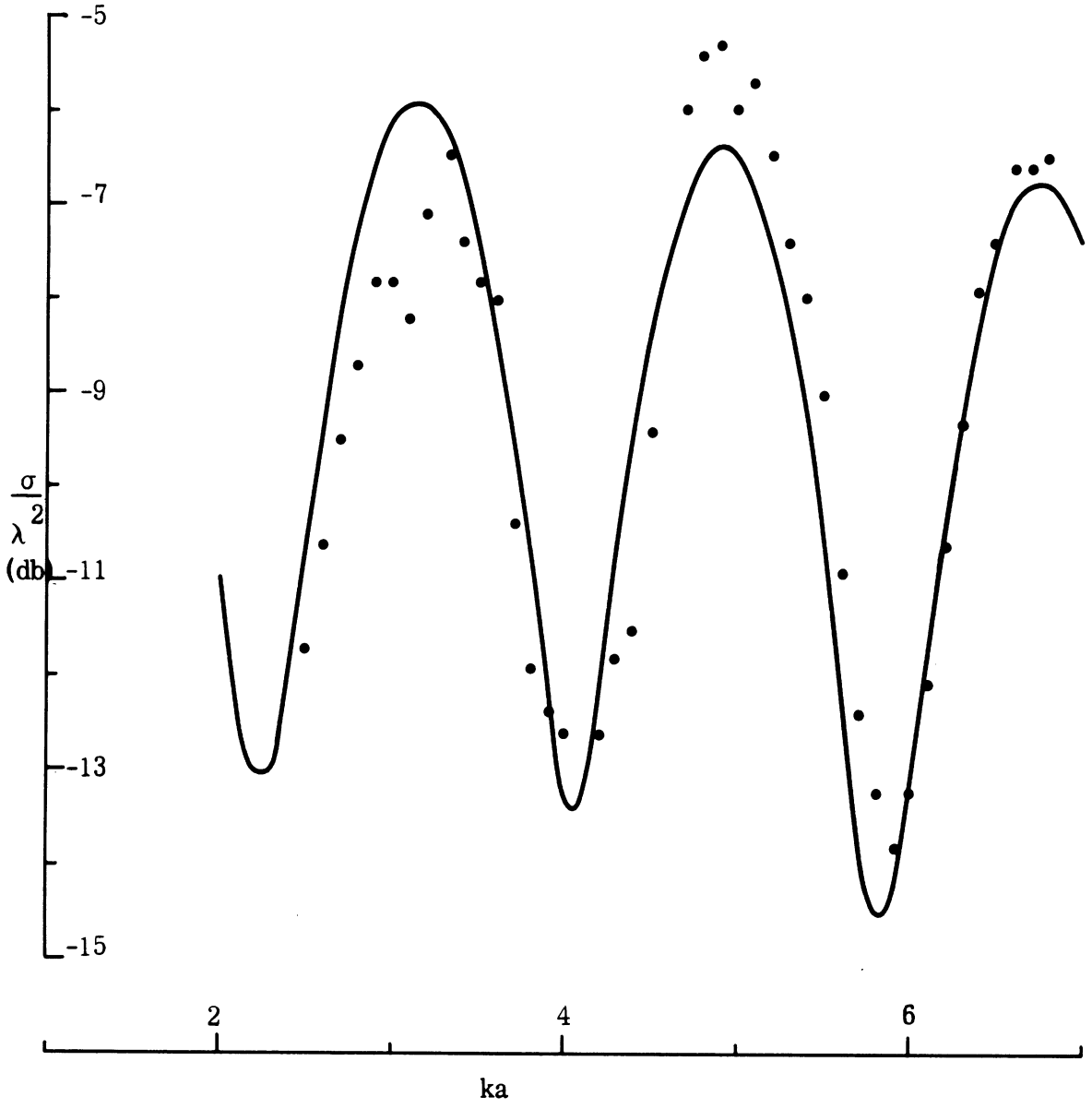

FIG. 3-27: COMPARISON OF MEASURED AND THEORETICAL NOSE-ON CROSS SECTIONS FOR A PURE CONE-SPHERE.

(center) radius of the ring and $\Gamma e^{i\phi}$ is the excitation strength. Assuming Γ and ϕ are, at most, slowly varying functions of ka, S_{sp} will beat in and out of phase with S_{cs} as a consequence of the large phase possessed by S_{sp} and the resulting period of oscilllation is in excellent agreement with that of the high frequency oscillation displayed by the cross section of model LSP. If, therefore we average out these oscillations to obtain a mean cross section, $\bar{\sigma}$, for model LSP, it now follws from Eq. (3.47) that

$$\frac{\bar{\sigma}}{\lambda^2} = \frac{\sigma_{cs}}{\lambda^2} + 1/\pi \left| S_{sp} \right|^2 = \frac{\sigma_{cs}}{\lambda^2} + \frac{4}{27\pi} \left| ka_s \Gamma \right|^2 \qquad (3.49)$$

enabling us to deduce Γ as a function of ka from the measured data. The resulting curve for Γ is shown in Fig. 3-28 along with the curve previously deduced from four isolated sets of measurements of the surface field behavior. Using the curve now obtained, the measured data for the LSP cross section can be reproduced precisely, and though the curve for Γ does differ in several particulars from that used in "The Agreement Item," the two are reasonably close at the two frequencies (corresponding to ka = 2.98 and 4.51) which were considered in detail there.

3.4 Effective Estimates for the Nose-on Backscattering of Flat-Back (FB) Models.

(U) In the light of the analyses given in Section 3.2 of Goodrich et al, 1967b, the expression for the nose on backscattering cross section of an FB (or ID) model is now as follows:

$$\frac{\sigma}{\lambda^2} = 1/\pi \left| S_1 + S_2 + S_3 \right|^2 \qquad (3.50)$$

where

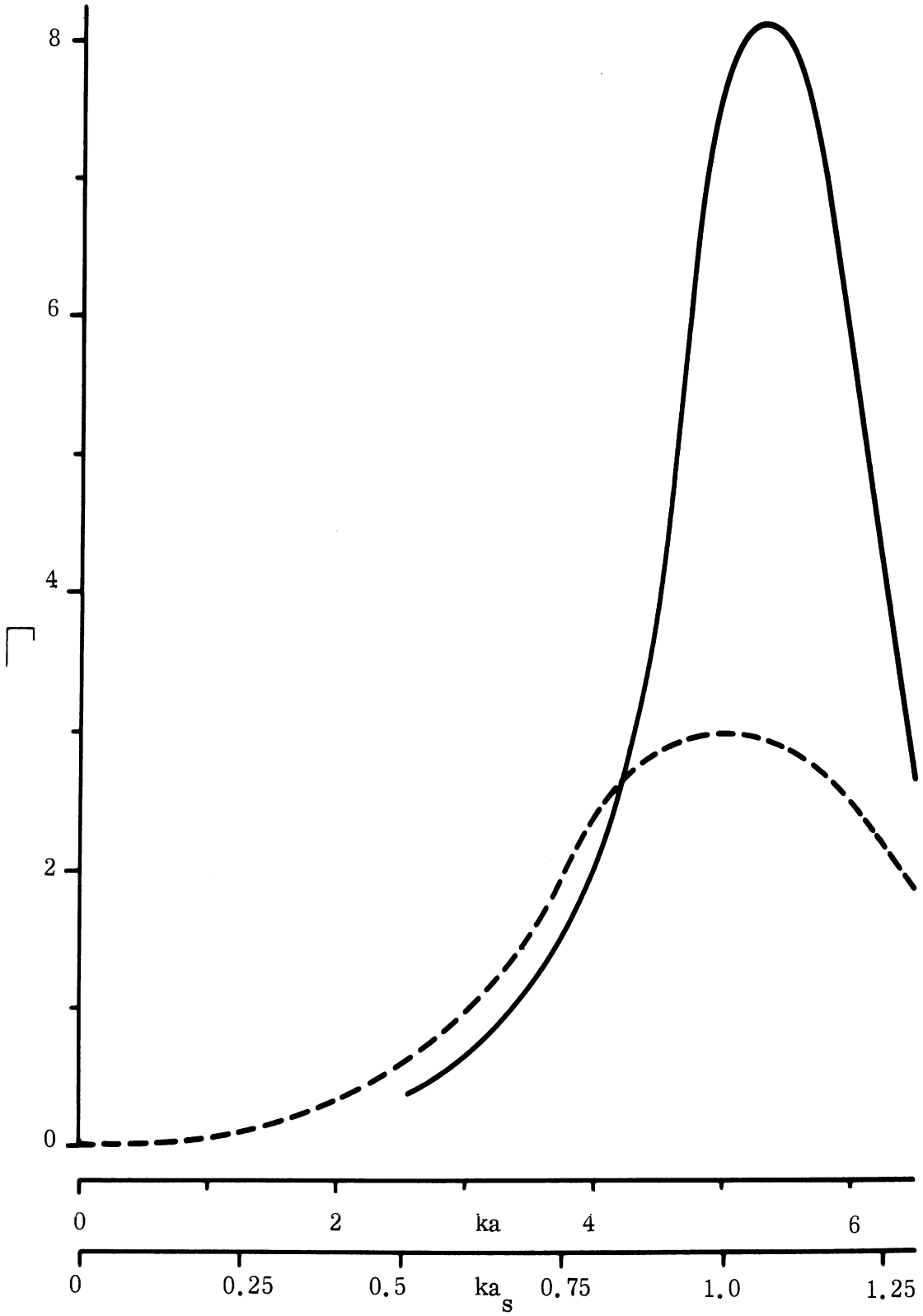

FIG. 3-28: EXCITATION STRENGTH Γ OF RING SPACER FOR NOSE-ON INCIDENCE. Deduced (—) from present far field data; postulated (— — —) from isolated surface field measurements.

$$S_1 = -i/4 \tan^2 \alpha \, e^{-2ik(a \cot \alpha \cos \alpha + b \sin \alpha)} \tag{3.51}$$

is the tip contribution;

$$S_2 = i/4 \sec^2 \alpha \, e^{-2ikb \sin \alpha} A(kb) \tag{3.52}$$

is the join contribution, with the factor $A(kb)$ as given in Section 3.1.3 of Goodrich et al, 1967b: and S_3 is the net creeping wave contribution which differs from the function discussed and computed in Section 5.2 of the present report only in an enhancement factor, viz.

$$S_3 = \gamma S_{cw} \tag{3.53}$$

$$S_{cw} = \frac{a}{2b}\left(\frac{kb}{2}\right)^{1/3} \frac{e^{2ik(a-b)+i\pi/12}}{\sqrt{2k(a-b)}} \frac{1}{\beta_1 \left\{Ai(-\beta_1)\right\}^2} S^{(1)}. \tag{3.54}$$

$S^{(1)}$ is here the creeping wave contribution for a sphere of radius b, and is computed from the formula

$$S^{(1)} = \tau^4 e^{i\pi/3} \left\{1 + \frac{e^{i\pi/3}}{60\tau^2\beta_1^2}(32\beta_1^3 + 9)\right\} \frac{1}{\beta_1 \left\{Ai(-\beta_1)\right\}^2}$$

$$\cdot \exp\left\{i\pi kb - e^{-i\pi/6}\tau\pi\beta_1 - e^{i\pi/6}\frac{\pi}{60\tau\beta_1}(\beta_1^3 - 9)\right\} \tag{3.55}$$

(see Senior 1965), where $\tau = (kb/2)^{1/3}$. Extensive tables of $S^{(1)}(x)$ have been given in the above-mentioned report and in Section 5.3, and have since been extended down to $x = 0.05$.

(U) It would seem natural to take the creeping wave enhancement factor γ to be the same as for a cone-sphere, and that is what is advocated. However, the purpose of the present Section is merely to investigate the general

character of the cross section predicted by (3.50) to determine the effectiveness of this formula. To these ends we shall:

(a) Ignore any creeping wave enhancement, i.e. take $\gamma = 1$; and

(b) omit the tip contribution S_1.

From an examination of the magnitudes of the terms in (3.50), it is clear that the effect of S_1 would be noticable only near deep minima in the cross section.

(U) The join factor A(kb) was discussed in Section 3.1.3 of Goodrich et al, 1967b, and asympotic expansions for large and small kb were there presented. There is the question as to which of these to employ for the values of kb near unity that are of most interest to us; and as to how many terms to retain in the expansion in order to achieve the most effective numerical values. From the initial computations that have been performed it appears probable that the best (numerical) extimates are obtained by using only the leading term in the high frequency (large kb) expansion, and to begin with we shall therefore take

$$A(kb) = a/b \ . \tag{3.56}$$

The resulting formula for the nose-on cross section is now

$$\frac{\sigma}{\lambda^2} = 1/\pi \left| S_2 + S_3 \right|^2 \tag{3.57}$$

with

$$S_2 = \frac{i}{4}\frac{a}{b} \sec^2 \alpha \, e^{-2\, ikb \sin \alpha} \tag{3.58}$$

and

$$S_3 = \frac{a}{2b}\left(\frac{kb}{2}\right)^{1/3} \frac{e^{2ik(a-b)+i\pi/12}}{\sqrt{2k(a-b)}} \frac{1}{\beta_1\left\{Ai(-\beta_1)\right\}^2} S^{(1)}(kb). \qquad (3.59)$$

(U) The computation of the above expression for σ/λ^2 is quite straightforward, and is facilitated using the values for $\left|S^{(1)}(kb)\right|$ computed from Eq. (3.55) and listed in Table III-3. Observe that the modulus and phase maintain their smooth character even down to $ka = 0.1$ and beyond. $S^{(1)}(kb)$ is graphed in Fig. 3-29 and in Fig. 3-30 $|S_3|$ is plotted as a function of ka for $b/a = 0.5$, 0.25, and 0.1. Formally at least, these three curves are identical to the corresponding ones in Fig. 4-7 of Section 4.2 over the ranges of ka for which they are shown in the latter Figure, but in contrast to the roundabout method of computation there adopted, the present curves have been obtained directly from Eq. (3.59). Notice that for small ka the moduli tend to increase with decreasing ka, with the up-swing setting in at a larger value of ka as b/a decreases. It becomes apparent at about $kb = 0.1$ regardless of b/a. The lowest curve in Fig. 3-30 is for $b/a = 1$, and is simply $S^{(1)}(ka)$ transcribed from Fig. 3-29.

(U) Even at this stage and without more detailed computations it is possible to get a general impression about the behavior of the cross section σ/λ^2 for different b/a, and for this purpose we shall henceforth take $\alpha = 9^o$ as appropriate to the FB (but not the ID) models. We then have

$$S_2 = 0.25627\,\frac{a}{b}\ , \qquad (3.60)$$

which is independent of ka for fixed b/a. The values corresponding to $b/a = 1$, 0.5, 0.25 and 0.1 are indicated by the horizontal lines in Fig. 3-30, and whereas for $b/a = 0.1$ the join contribution always exceeds the creeping

TABLE III-3

kb	$S^{(1)}$(kb)	arg $S^{(1)}$(kb), degrees
0.05	0.32065	190.017
0.10	0.33389	194.682
0.15	0.34615	202.183
0.20	0.35629	210.555
0.25	0.36488	219.320
0.30	0.37230	228.296
0.40	0.38462	246.592
0.50	0.39459	265.128
0.60	0.40286	283.796
0.70	0.40988	302.537
0.80	0.41588	321.321
0.90	0.42107	340.136
1.00	0.42558	358.963
1.10	0.42950	377.802
1.20	0.43291	396.645
1.30	0.43590	415.490
1.40	0.43849	434.333
1.50	0.44075	453.178
1.60	0.44268	472.009
1.70	0.44435	490.837
1.80	0.44576	509.663
1.90	0.44696	528.481
2.00	0.44794	547.295

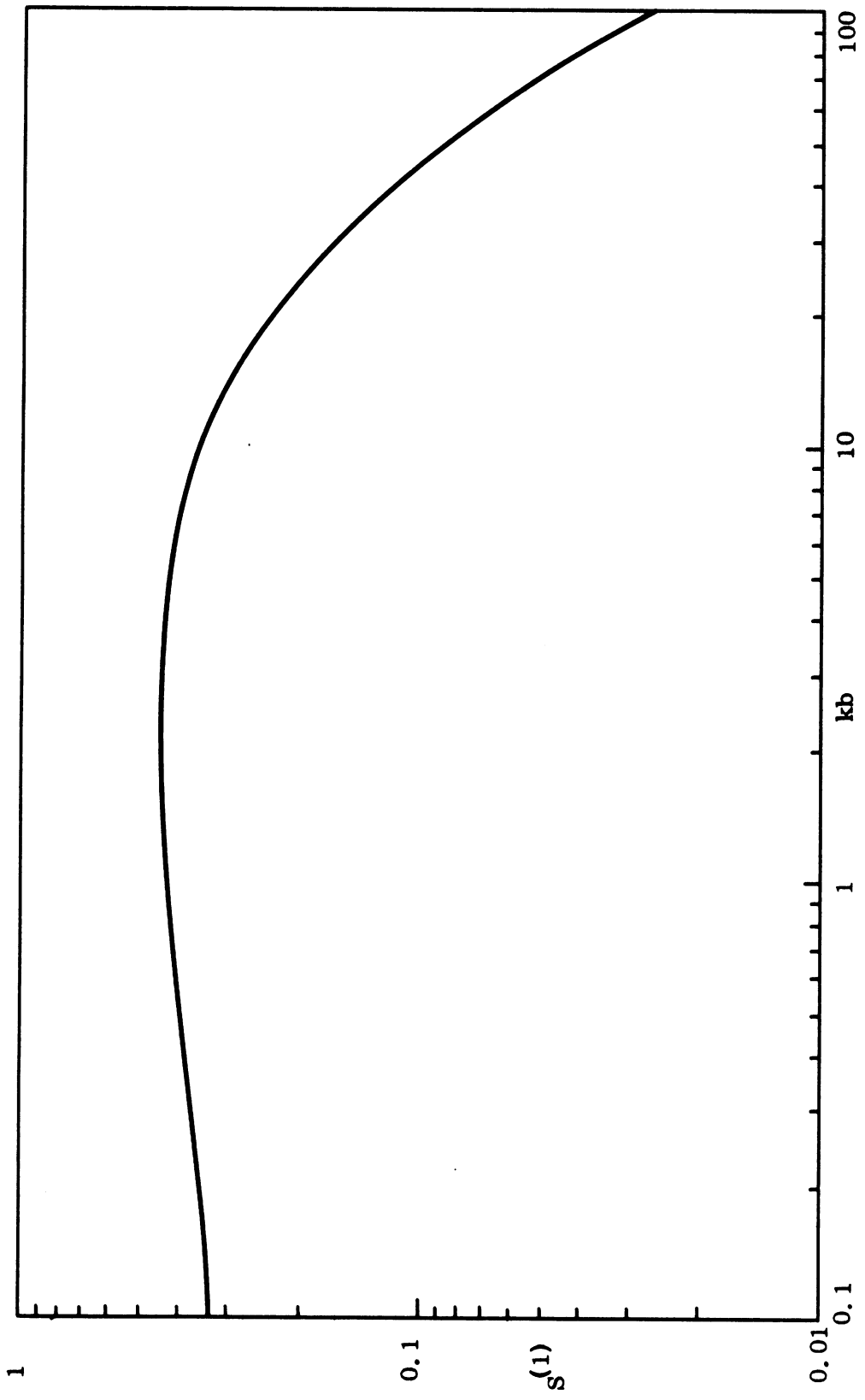

FIG. 3-29: THE MODULUS OF THE SPHERE CREEPING WAVE CONTRIBUTION.

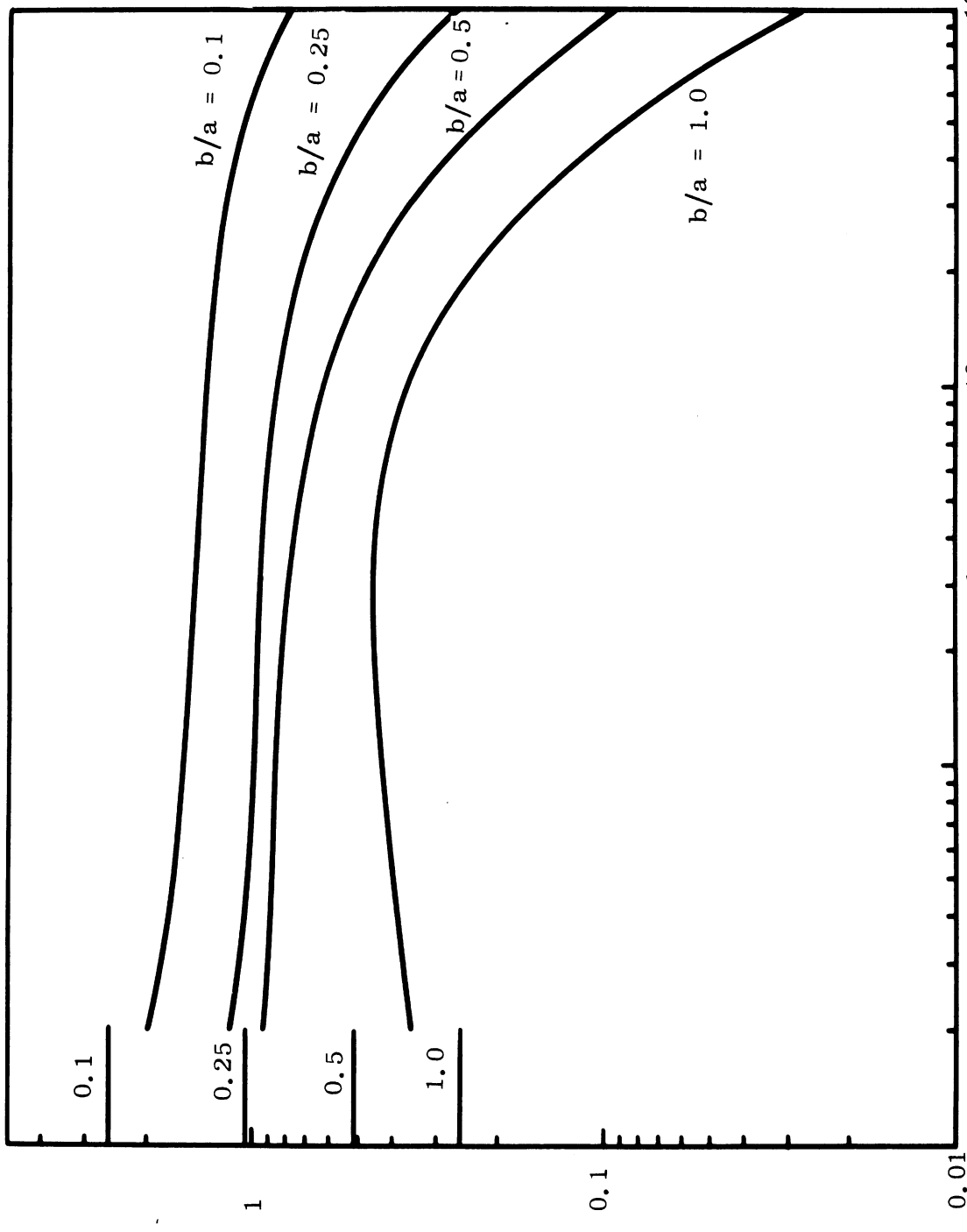

FIG. 3-30: $|S_3|$ FOR VARIOUS b/a COMPUTED FROM EQ. (3.59); THE LOWEST CURVE IS $|S^{(1)}|$ APPROPRIATE TO A SPHERE, AND THE LINES AT LEFT SHOW $|S_2|$ COMPUTED FROM EQ. (3.58).

wave one, and does so by almost a factor 2 in the range $1 \leq ka \leq 10$ (implying relatively shallow minima), the two contributions are almost identical in this range (implying very deep minima) for $b/a = 0.25$. If b/a is increased still further, the creeping wave contribution dominates until such time as the exponential decay characteristic of the larger ka has reduced it magnitude to that of the (constant) join return.

(U) The locations of the maxima and minima can be determined using the almost-linear phase variation of $S^{(1)}(kb)$ as a function of kb. Thus, for $0.3 \leq kb \leq 3.0$ $\arg S^{(1)}(kb) = 187.916kb + 171.312$ (degrees) with a maximum error of 0.6 degrees. The formula is also effective, with only slightly greater error, for kb outside this range, and using it we have $\arg S_3 = (114.592 + 73.424\, b/a)\, ka + 186.312$ (degrees). Hence $\arg S_3 - \arg S_2 = (114.592 + 91.350\, b/a)\, ka + 96.312$ (degrees), and the maxima and minima in the cross section occur at those values of ka for which this is an even or odd multiple of 180 (degrees) respectively. Some locations are as follows:

	$b/a = 0.5$	$b/a = 0.25$	$b/a = 0.1$
max.	$ka = 1.677$	$ka = 1.919$	$ka = 2.131$
min.	$= 2.821$	$= 3.228$	$= 3.586$
max.	$= 3.966$	$= 4.538$	$= 5.041$
min.	$= 5.110$	$= 5.848$	$= 6.496$
max.	$= 6.255$	$= 7.158$	$= 7.950$
min.	$= 7.399$	$= 8.467$	$= 9.405$

(U) By direct computation of the expression given in Eq. (3.57) at a sequence of values of ka, and using also our knowledge of the precise locations of the maxima and minima, the cross sections shown in Figs. 3-31

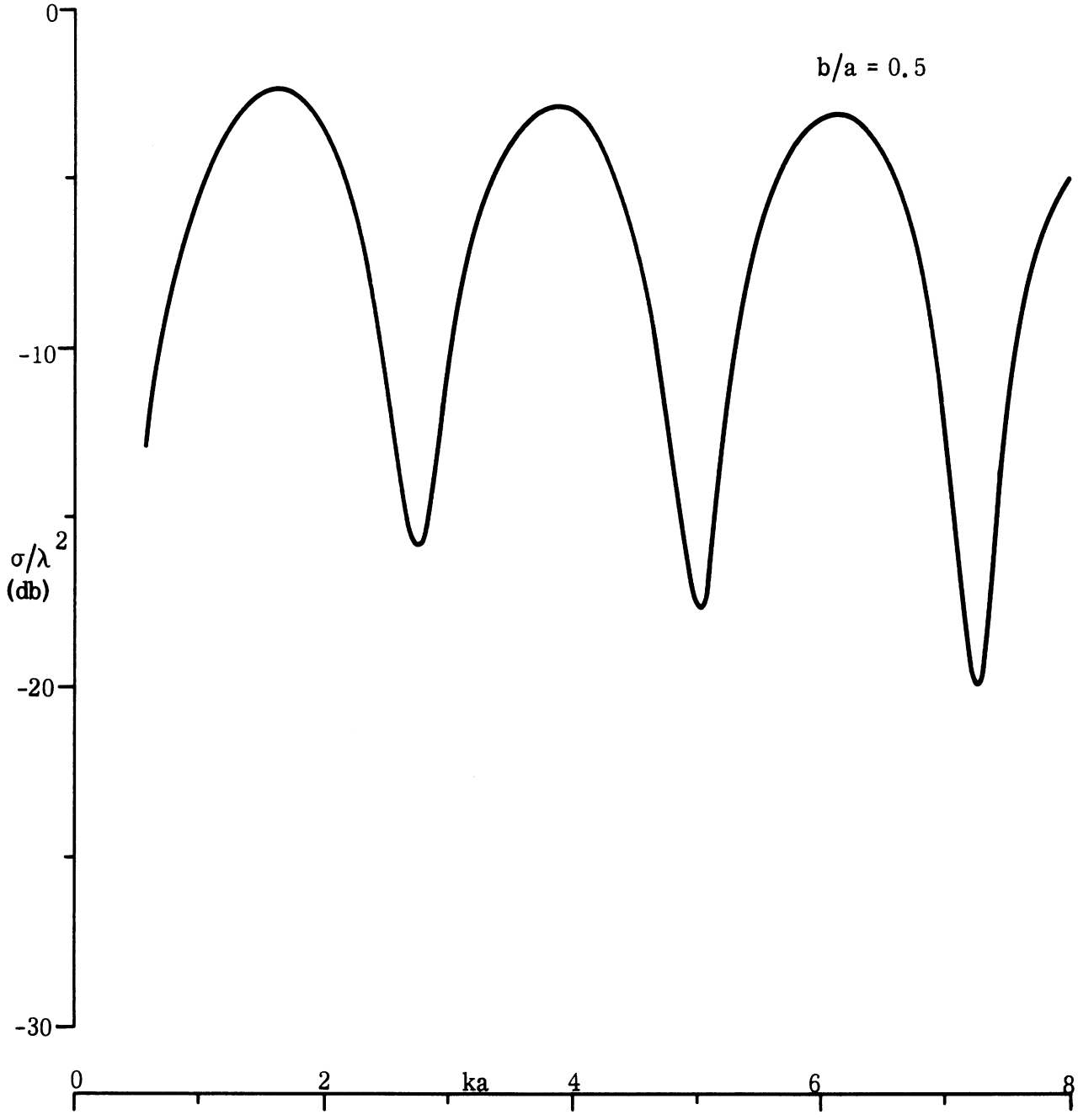

FIG. 3-31: σ/λ^2 FOR FB MODEL WITH b/a = 0.5, COMPUTED FROM EQ: (3.57).

through 3-33 are obtained. The associated values of b/a are here 0.5, 0.25 and 0.1 respectively. The curves certainly have the character necessary to fit the measured cross section data for the FB models (see Section 3.2.2 of Goodrich et al, 1967b), and both the positions and depths of the minima vary with b/a in the manner displayed by that data. But there is some discrepancy in the heights of the first one or two peaks, particularly for small b/a, and to illustrate this fact we show in Figs. 3-34 and 3-36 respectively the theoretical curves for b/a = 0.4 (corresponding to model FB-4) and b/a = 0.1 (corresponding to model FB-1), along with the measured data for the cross sections. In Fig. 3-35 the theoretical curve of Fig. 3-32 for an FB model with b/a = 0.25 is compared with the measured data for ID-1 and ID-2. Both of these experimental models have b/a = 0.25 and, in consequence, the formula should give a valid* estimate for these. For purposes of comparison, we have also included in each figure and theoretical curve for a flat-backed (right circular) cone.

(U) Taking first the comparison between the theoretical and experimental values for model FB-4 shown in Fig. 3-34, we observe the fact noted above, namely, that the theoretical curve overestimates the cross section, and does so to a degree which decreases with increasing ka. Thus, to fit the first maximum and minimum, a reduction of approximately 3 db is called for, but at the second maximum the required reduction has decreased to about 1.5 db. Such a changing reduction of the theoretical values would, indeed, lead to a better fit to the experimental data at all values of ka, not merely those corresponding to the maxima and minima, and we further observe that for ka less than that of the first maxima, the data points are closer to the curve of the flat backed cone than they are to the FB model curve.

---

* The slight displacement of the minima is undoubtedly due to the fact that we have used $\alpha = 9^{o}$ in the computation, rather than the value 7.5^{o} appropriate to ID-1 and ID-2.

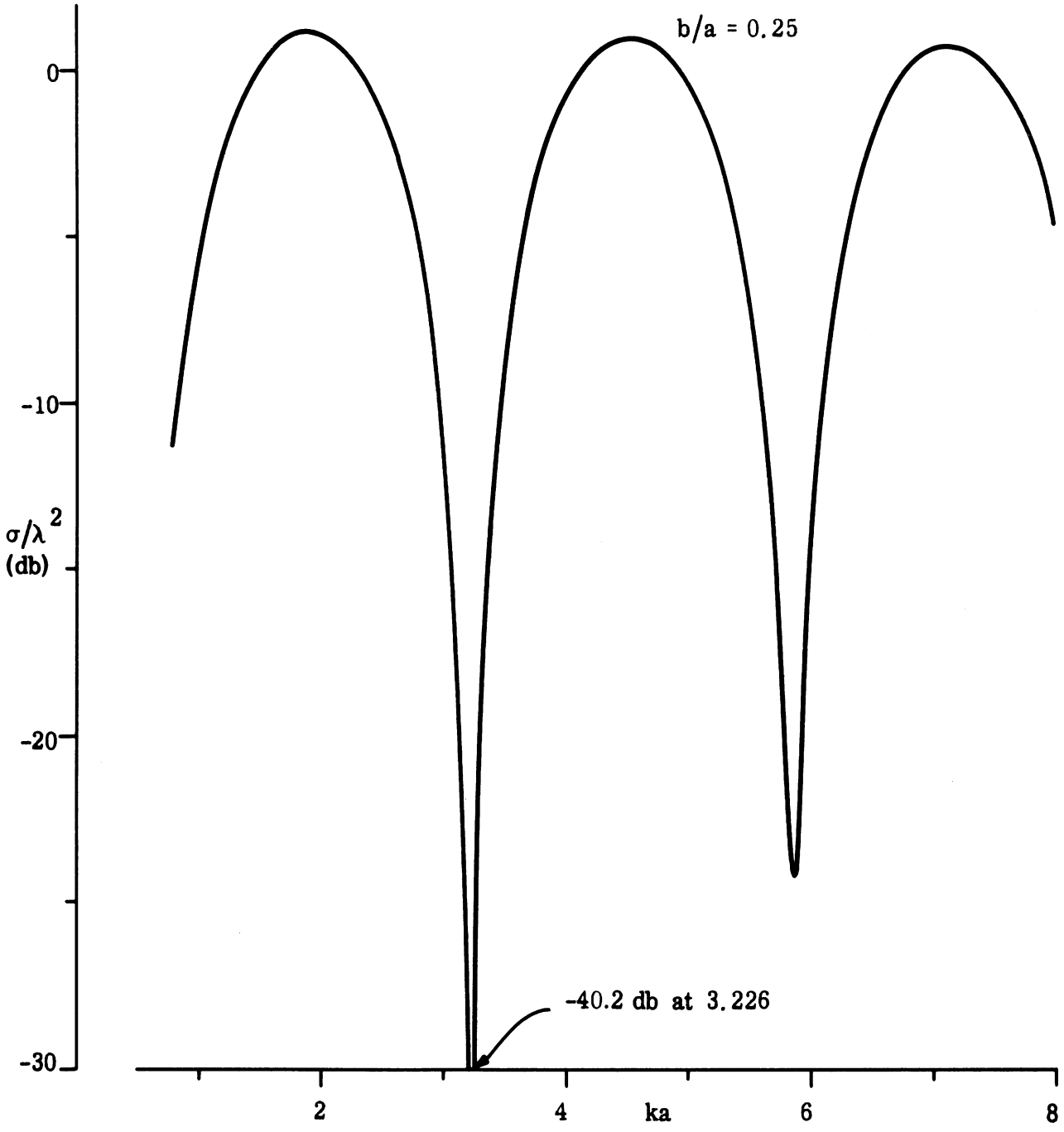

FIG. 3-32: σ/λ^2 FOR FB MODEL WITH b/a = 0.25, COMPUTED FROM EQ. (3.57).

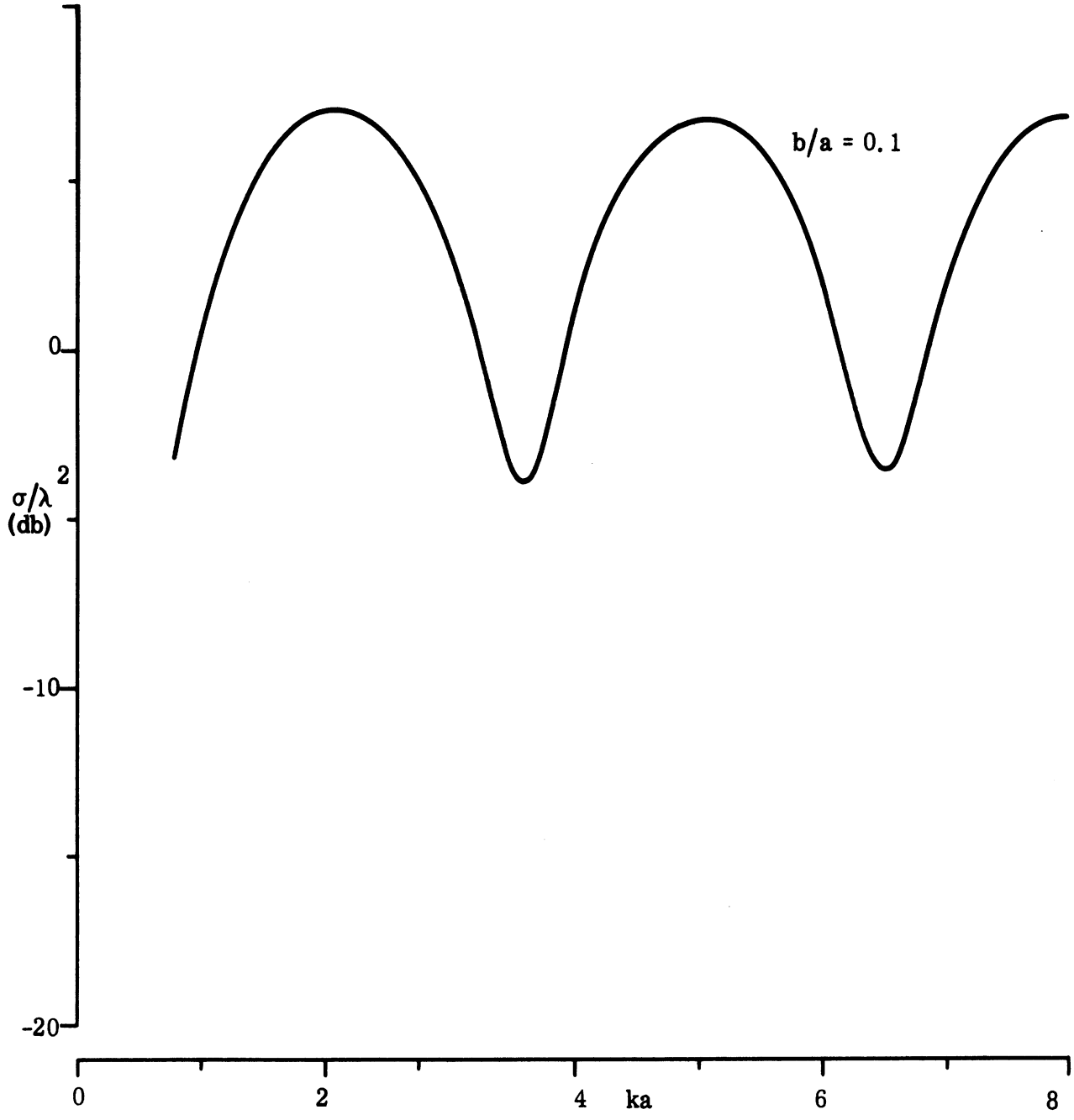

FIG. 3-33: σ/λ^2 FOR FB MODEL WITH b/a = 0.1, COMPUTED FROM EQ: (3.57).

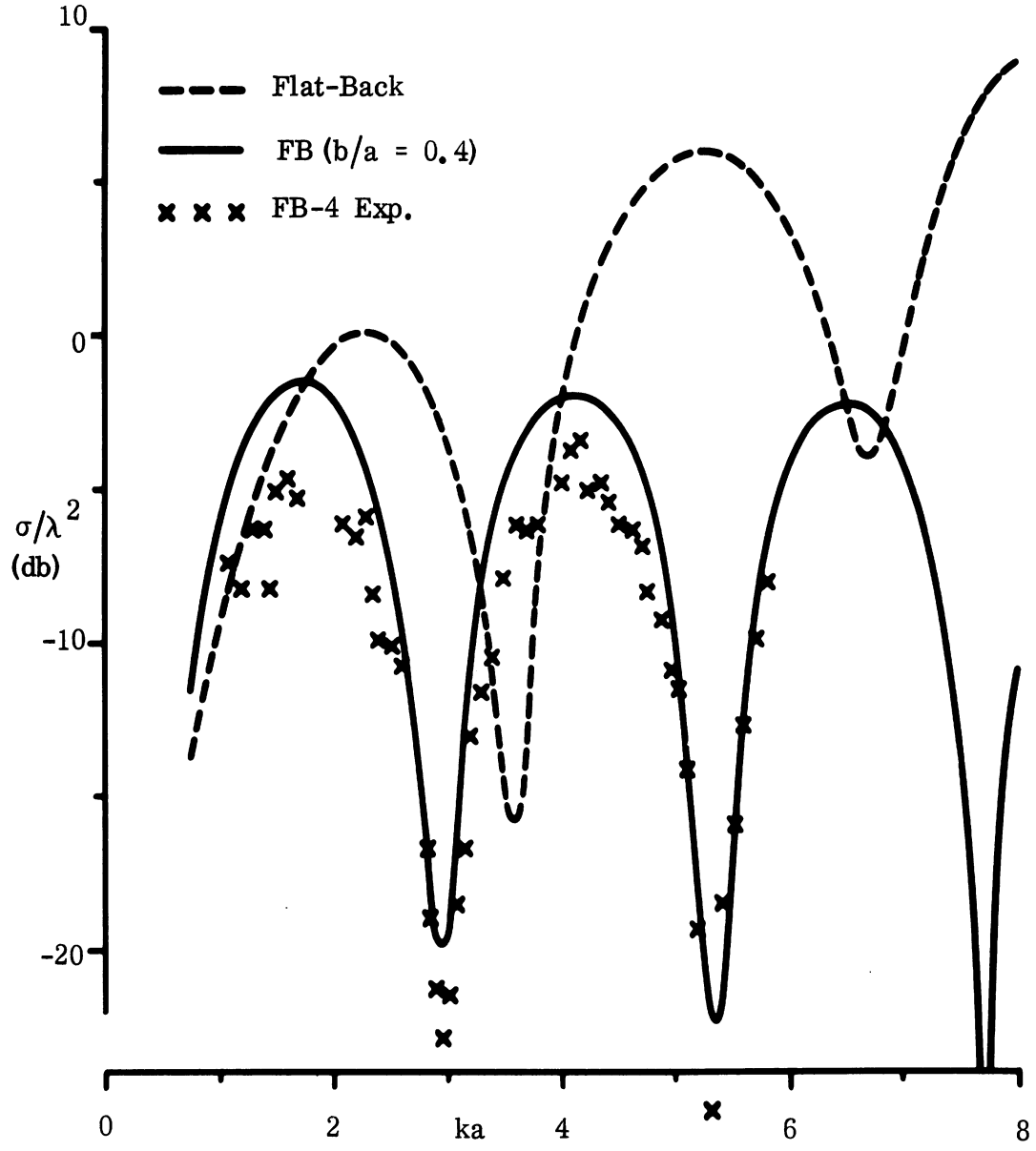

FIG. 3-34: MEASURED DATA (xxx) FOR THE BACKSCATTERING CROSS SECTION OF MODEL FB-4, COMPARED WITH THE THEORETICAL PREDICTION (EQ. 3.57) FOR THIS MODEL (——) AND FOR A FLAT-BACKED CONE (----).

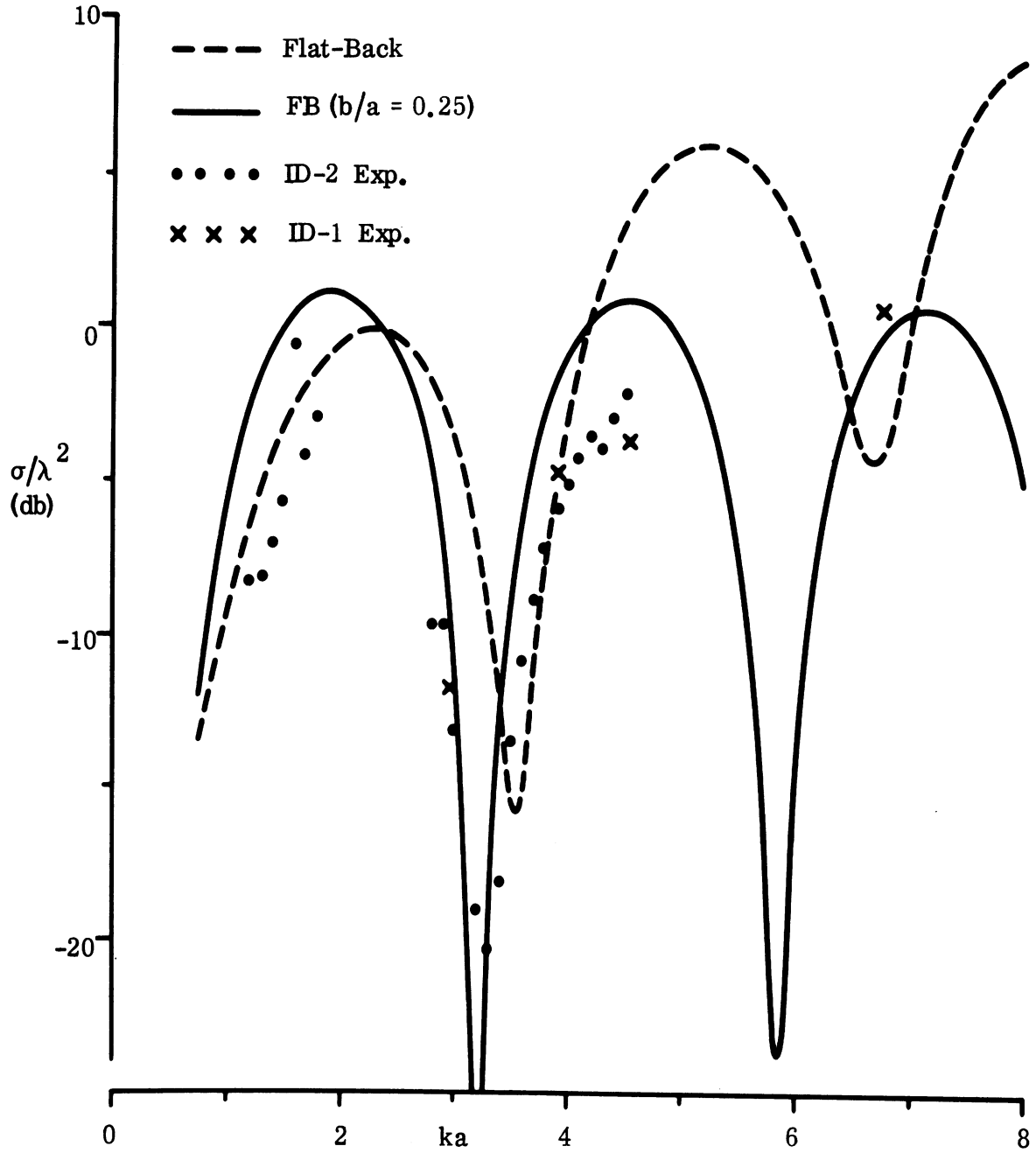

FIG. 3-35: MEASURED DATA FOR THE BACKSCATTERING CROSS SECTION OF MODELS ID-1 (xxx) AND ID-2 (●●●), COMPARED WITH THE THEORETICAL PREDICTION (EQ. 3.57) FOR AN FB MODEL WITH b/a = 0.25 (——) AND FOR A FLAT-BACKED CONE (---).

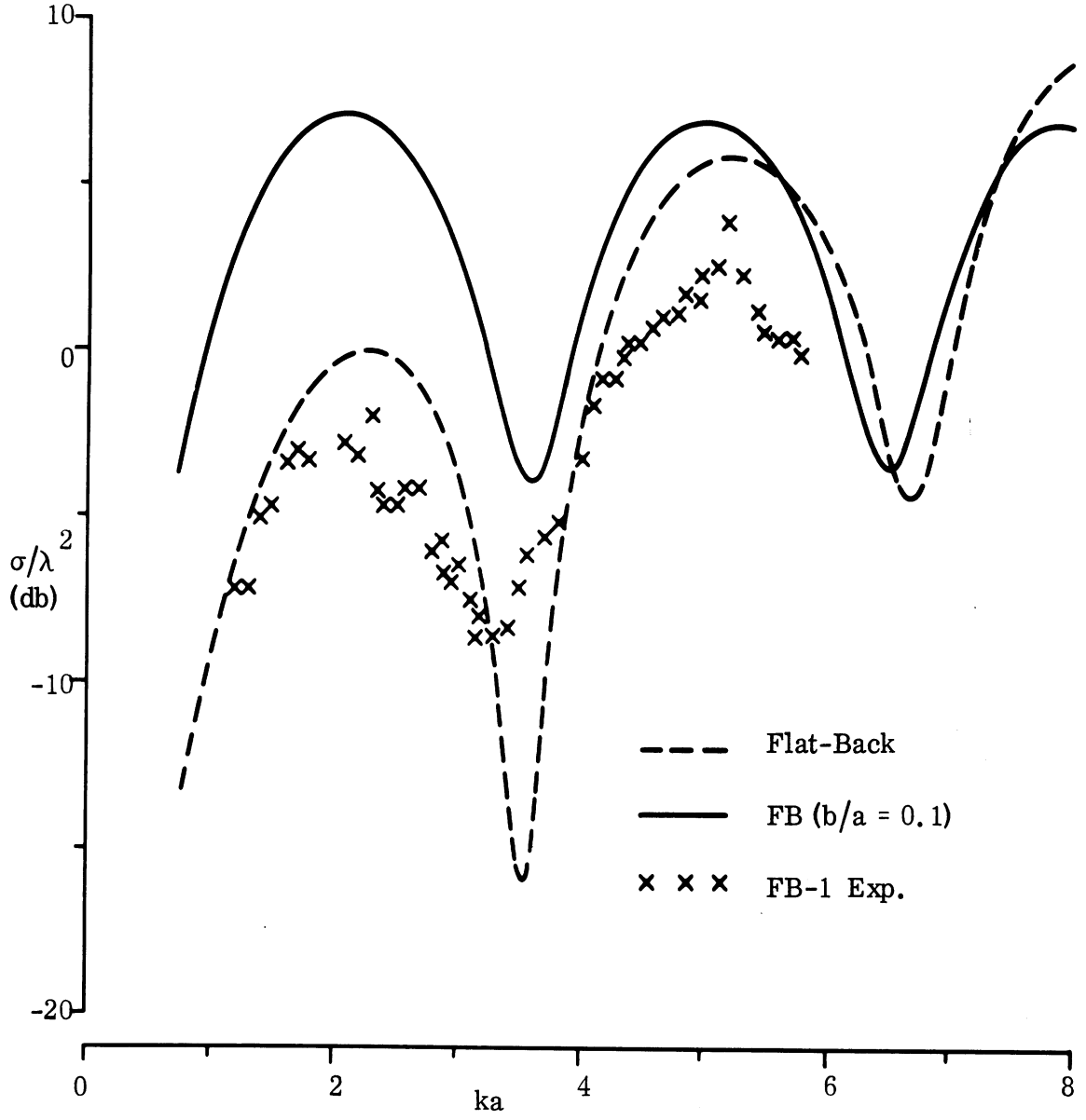

FIG. 3-36: MEASURED DATA (xxx) FOR THE BACKSCATTERING CROSS SECTION OF MODEL FB-1, COMPARED WITH THE THEORETICAL PREDICTION (EQ. 3.57) FOR THIS MODEL (——) AND FOR A FLAT-BACKED CONE (---).

(U) The same conclusions apply to the comparison shown in Fig. 3-35, but because of the unusually deep theoretical first minimum, whose depth would undoubtedly be changed were the tip contribution to be considered, we can only derive reduction factors based on the first two maxima. Note, however, the tendency of the experimental data points to follow the curve for the flat-backed cone, and this is even more clearly seen in Fig. 3-36, where the comparison for model FB-1 is given. Substantial reductions of the theoretical FB values are now required throughout the range of ka covered by the experimental data, reaching as much as 10 db in the vicinity of the first maximum.

(U) Similar comparisons of the predicted and measured values of the cross sections at the maxima and minima have been carried out for models FB-2 and FB-3, and when the required reduction factors thus obtained are examined in toto, it is found that these factors are functions of kb alone, and are more or less independent of ka. From the levels of the maxima and minima for all the bodies for which experimental data is available, and excluding only those few minima where it is clear that the full depth was not plumbed experimentally or where the theoretical depth would be markedly changed were the tip scattering to be included, we obtain the voltage (or amplitude) reduction factors shown in Fig. 3-37. The quantity plotted here is the factor that must be applied to the net (join plus creeping wave) scattering amplitude in order to best fit the experimental data. Denoting this factor by B(kb) and re-plotting log (1 - B) versus log kb, we find only a small amount of scatter about a linear variation. A visual fit to the points leads to the empirical curve

$$B(kb) = 1 - \frac{0.25}{(kb)^{0.6}} \quad , \tag{3.61}$$

and this has been included in Fig. 3-37.

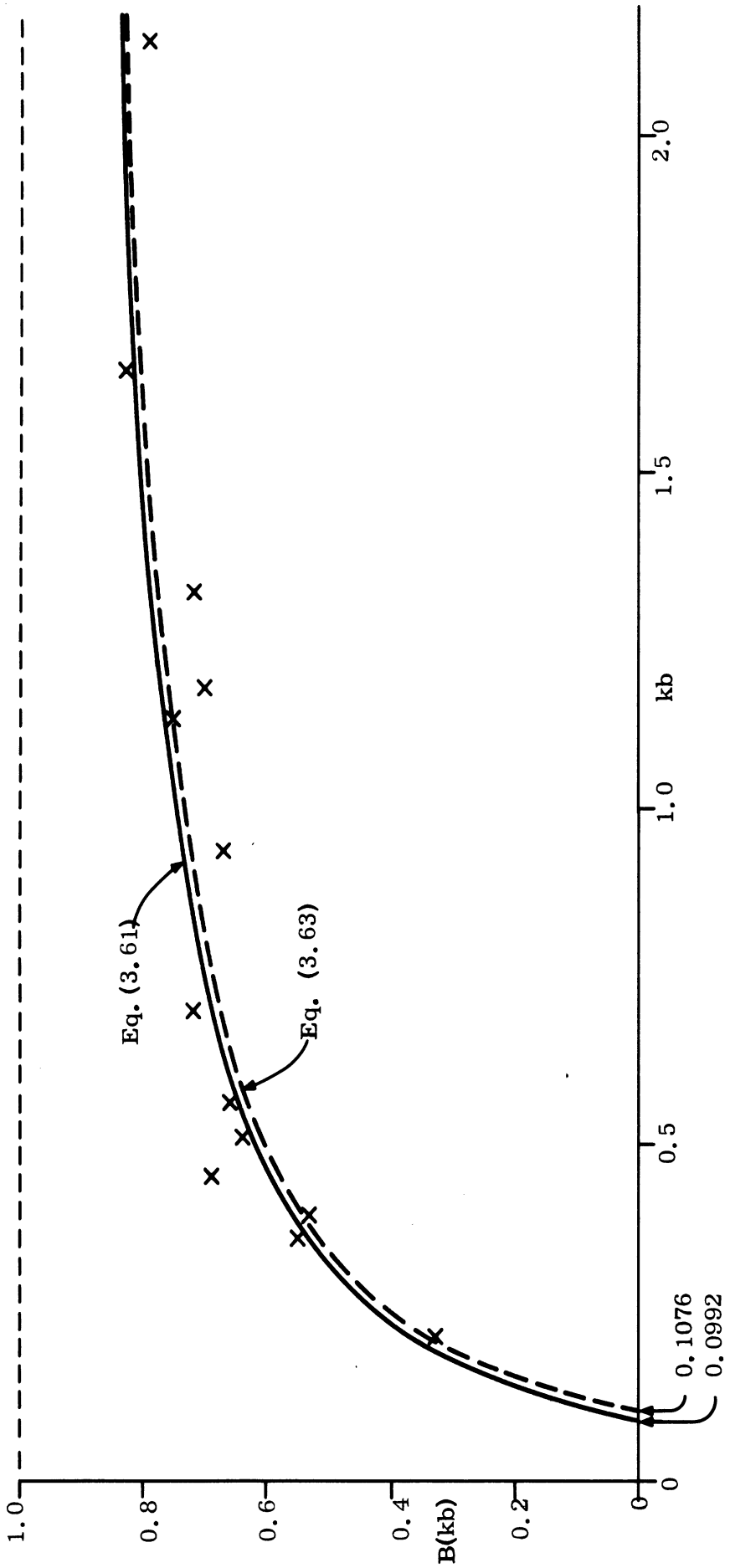

FIG. 3-37: EXPERIMENTALLY DEDUCED (xxx) VOLTAGE REDUCTION FACTORS FOR NET FAR FIELD AMPLITUDE. The solid line is a functional fit to the data points (see Eq. (3.61) of text), whilst the broken line is the function defined in Eq. (3.63).

(U) Since $B(kb) < 0$ for $kb < 0.9921$, it is legitimate to ask what happens to the join contribution, for example, as kb approaches (and goes beyond) this value. To answer this, we show in Fig. 3-38 the moduli of the join contributions for bodies with $b/a = 0.1, 0.2, 0.5$ and 1.0 as modified by the reduction factor $B(kb)$. It is observed that each curve, as a function of ka, approaches the line corresponding to the join contribution for a flat-backed cone, namely

$$S_j = -\frac{ka}{2n} \operatorname{cosec} \frac{2\pi}{n} \cdot \left(n = \frac{3}{2} + \frac{\alpha}{\pi}\right)$$

$$= 0.40793 \qquad \text{for } \alpha = 9^o \quad , \tag{3.62}$$

becomes almost tangent to this line, and then falls away from it. This is just the sort of behavior that we were seeking in Section 3.5, and clearly the required join contribution is that obtained by following each curve down to its first intercept with the flat-backed value, and then following the latter line thereafter. This first intercept occurs at $kb = 0.312$ regardless of b/a.

(U) The prescription would, of course, be tidier if the reduced join contribution curves were truly tangent to the flat-backed one, and we note that merely by changing the formula for $B(kb)$ from that given in Eq. (3.61) to

$$B(kb) = 1 - \frac{0.2625}{(kb)^{0.6}} \tag{3.63}$$

the tangency is assured, with the point of tangency occuring at $kb = 0.236$. Such a change in $B(kb)$ in no way affects the quality of the fit shown in Fig. 3-37, but to some extent the aesthestic improvement obtained thereby is illussory. Although the particular formulae (3.61) and (3.63) were deduced from an examination of measured data for bodies having $\alpha = 9^o$, both the formulae

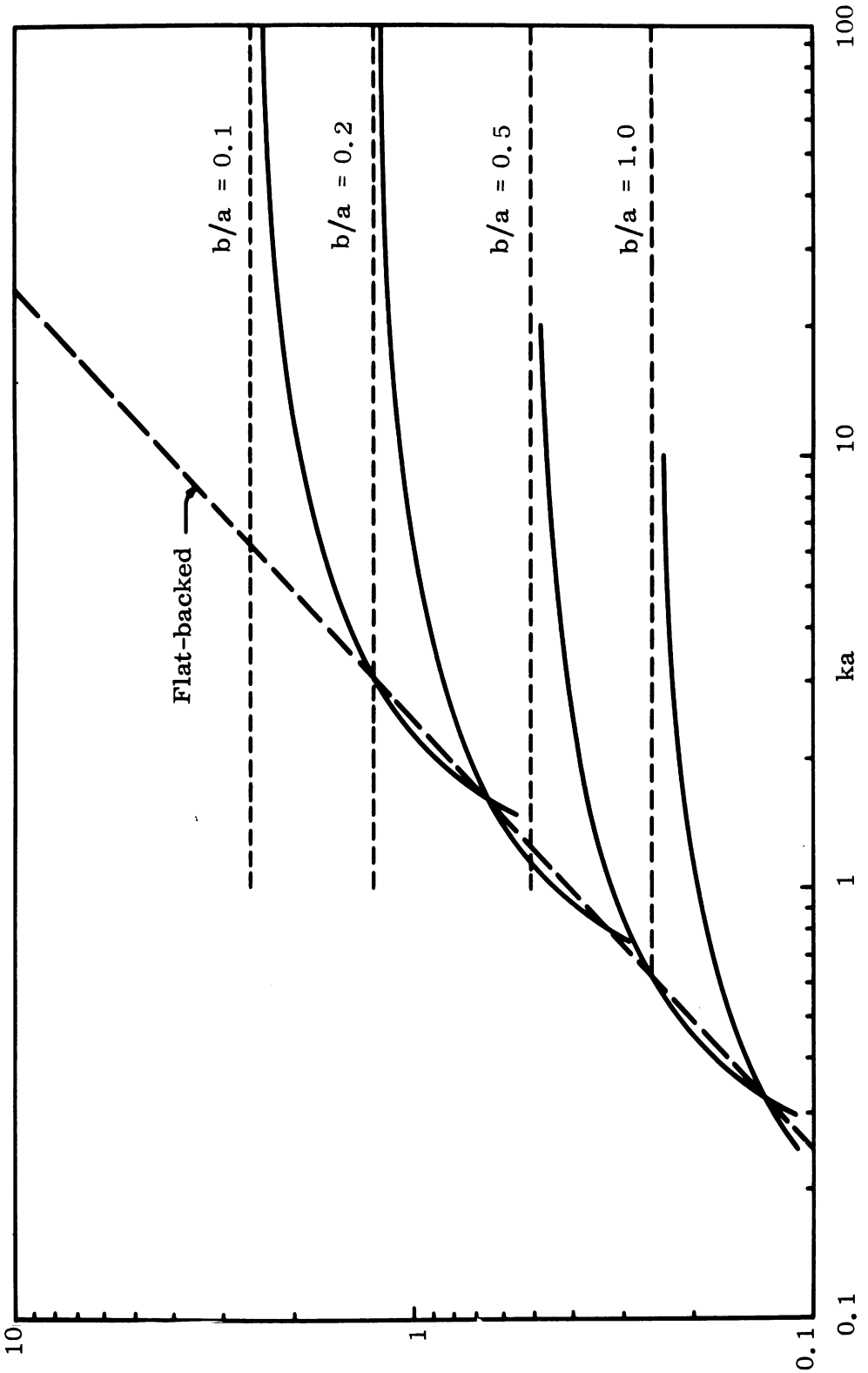

FIG. 3-38: MODIFIED JOIN CONTRIBUTIONS COMPUTED USING EQ. (3.61).

themselves and the technique by which they were derived are believed valid for all pointed objects of small included angle. Since the proportionality factor in the expression (3.62) for S_j is a function of α, albeit a very slowly varying one, the above expression for B(kb) will produce tangency only when α is 9^o. We can, however, generalize it as follows:

$$B(kb) = 1 - \frac{C}{(kb)^{0.6}} \tag{3.64}$$

where

$$C = \frac{5}{64}\left(-\frac{6n \sin\frac{2\pi}{n}}{\cos^2\alpha}\right)^{0.6} \tag{3.65}$$

and with this value of C, the curve for the join contribution modified using the factor B given in Eq. (3.64) is tangent to the curve for the flat-backed join contribution at $kb = kb_1$ with

$$kb_1 = -\frac{3n \sin\frac{2\pi}{n}}{16 \cos^2\alpha} \tag{3.66}$$

for all α. Typical values are:

α	C	kb_1
7.5^o	0.2631	0.2366
9^o	0.2625	0.2356
15^o	0.2615	0.2341

For $\alpha = 9^o$ the resulting formula for B(kb) is, of course, identical to that in Eq. (3.63), and computed data based on this expression are given in Table III-4.

TABLE III-4

kb	B(kb)	(db)
0.1	-0.0451	—
0.15	0.1806	-14.86
0.2	0.3105	-10.16
0.25	0.3968	-8.03
0.3	0.4594	-6.76
0.4	0.5451	-5.27
0.5	0.6020	-4.41
0.6	0.6433	-3.83
0.7	0.6748	-3.42
0.8	0.6999	-3.10
0.9	0.7203	-2.85
1.0	0.7375	-2.64
1.2	0.7647	-2.33
1.5	0.7942	-2.00
1.8	0.8155	-1.77
2.0	0.8268	-1.65
2.5	0.8485	-1.43
3.0	0.8642	-1.27
4.0	0.8857	-1.05
5.0	0.9000	-0.92
8.0	0.9246	-0.69
10.0	0.9341	-0.59

(U) As a result of these studies, the prescription for the join contribution is

$kb_1 \leq kb < \infty$:

$$S_j = \frac{i}{4} \sec^2 \alpha \, e^{-2\, ikb \sin \alpha} \cdot \frac{a}{b} B(kb) \qquad (3.67)$$

where B(kb) is given in Eq. (3.64).

$$kb < kb_1: \quad S_j = -i \frac{ka}{2n} \operatorname{cosec} \frac{2\pi}{n} e^{-2\, ikb \sin \alpha} \qquad (3.68)$$

Observe the phase factor $ie^{-2\, ikb \sin \alpha}$ that has been inserted, at least temporarily, into Eq. (3.68). This has been done to preserve continuity of phase through the point $kb = kb_1$, but the same effect could have been achieved as regards the total scattering by having the creeping wave contribution discontinuous in phase at $kb = kb_1$ in such a way as to counterbalance a discontinuity in S_j.

(U) If the reduction factor B(kb) as given in Eq. (3.64) were to be applied only to the join contribution, with the creeping wave contribution S_3 (see Eq. 3.59) left unchanged, the predicted cross sections would still depart somewhat from the measured data. This is illustrated by Figs. 3-39 and 3-40 for $b/a = 0.4$ and 0.1 respectively in which the original predictions (with no reduction factor included) are shown as solid lines, and the predictions with only the join contribution reduced as broken lines.

(U) Nevertheless, the factor B(kb) was originally derived on the premise that it would be applied to both the join and creeping wave contributions, and when this is done we arrive at the predictions shown as broken lines in

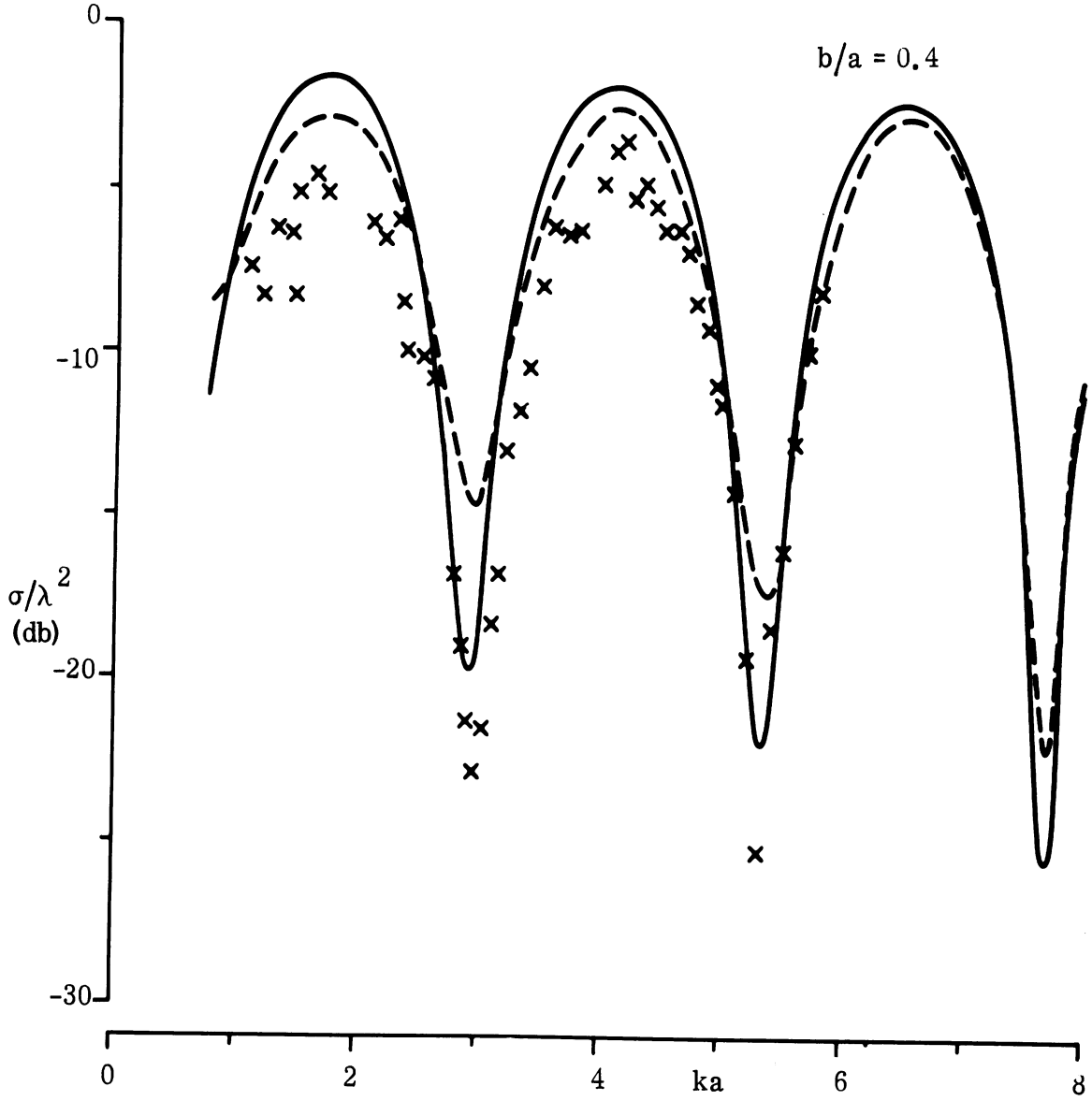

FIG. 3-39: PREDICTED CROSS SECTIONS FOR b/a = 0.4 WITHOUT REDUCTION FACTOR (——), AND WITH REDUCTION FACTOR APPLIED TO JOIN CONTRIBUTION ONLY (---), COMPARED WITH EXPERIMENTAL DATA (xxx).

in Figs. 3-41 through 3-45 for $b/a = 0.4, 0.3, 0.25, 0.2$ and 0.1 respectively.* The agreement with the measured data is hearteningly close in each case and for all values of ka. The solid lines again show the original predictions with no reduction factor applied, and in the case of the broken lines we have, for convenience only, terminated each at the value of ka corresponding to the transition value of $kb = kb_1$, namely at $ka = kb_1 \frac{a}{b}$.

(U) The factor B(kb) applied to the join contribution was found to have the desirable effect of smoothing the transition from the values appropriate to a smoothly-terminated cap to that corresponding to a flat-backed cone, but when we come to examine the creeping wave contribution, with or without the factor B(kb) incorporated, we find a peculiar and somewhat distressing behavior. When the original (unreduced) creeping wave contribution is plotted as a function of k for fixed b/a, we obtain the moduli shown in Fig. 3-30 and each curve intersects the straight line representing the creeping wave modulus for a flat-backed cone at an acute angle. Application of the factor B(kb) to these curves has the effect of bending each one over the lower end of the ka range, with the bending being greatest the smaller b/a is, and the resulting curves no longer reach the flat-backed one. Undesirable as this is, the trouble may not seem unsurmountable, but a far more graphic illustration of the shortcomings of the creeping wave expression is obtained by plotting S_3 as a function of b/a for fixed ka. The results are shown in Fig. 3-46 for the case in which no reduction is applied, and in Fig. 3-47 for the case in which the factor B(kb) is incorporated. On the left of each graph are the values appropriate to a flat-backed cone, namely 0.61569 ka, and on the right are the values of $S^{(1)}$ appropriate to a sphere, Taking

---

*In Fig. 3-43 the prediction has again been based on the choice $\alpha = 9^\circ$ rather than the value 7.5° appropriate to the ID models.

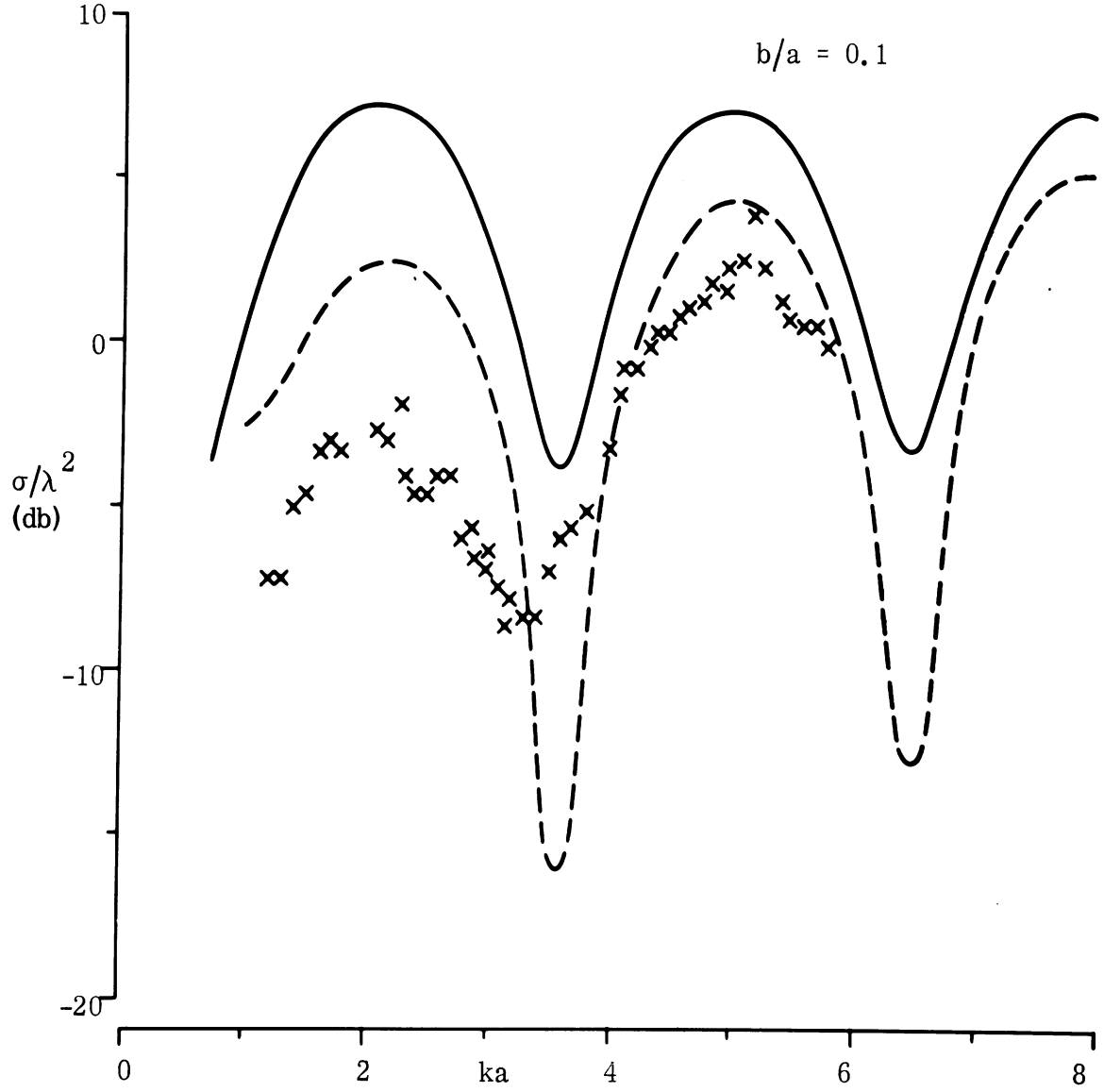

FIG. 3-40: PREDICTED CROSS SECTIONS FOR b/a = 0.1 WITHOUT REDUCTION FACTOR (——), AND WITH REDUCTION FACTOR APPLIED TO JOIN CONTRIBUTION ONLY (---), COMPARED WITH EXPERIMENTAL DATA (xxx).

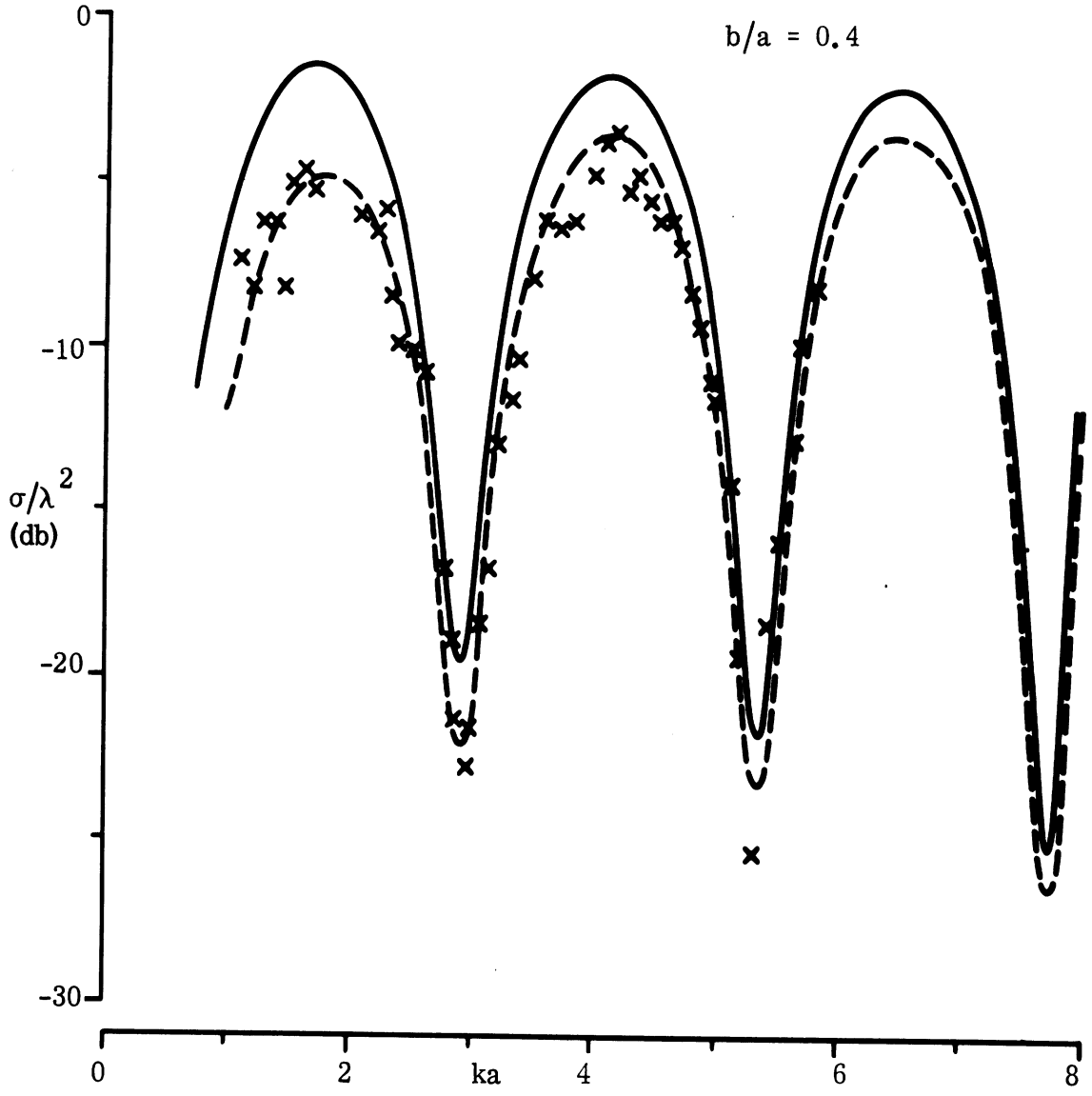

FIG. 3-41: PREDICTED CROSS SECTIONS FOR b/a = 0.4 WITHOUT (——) AND WITH REDUCTION FACTOR B(kb) FULLY INCORPORATED, COMPARED WITH EXPERIMENTAL DATA (xxx).

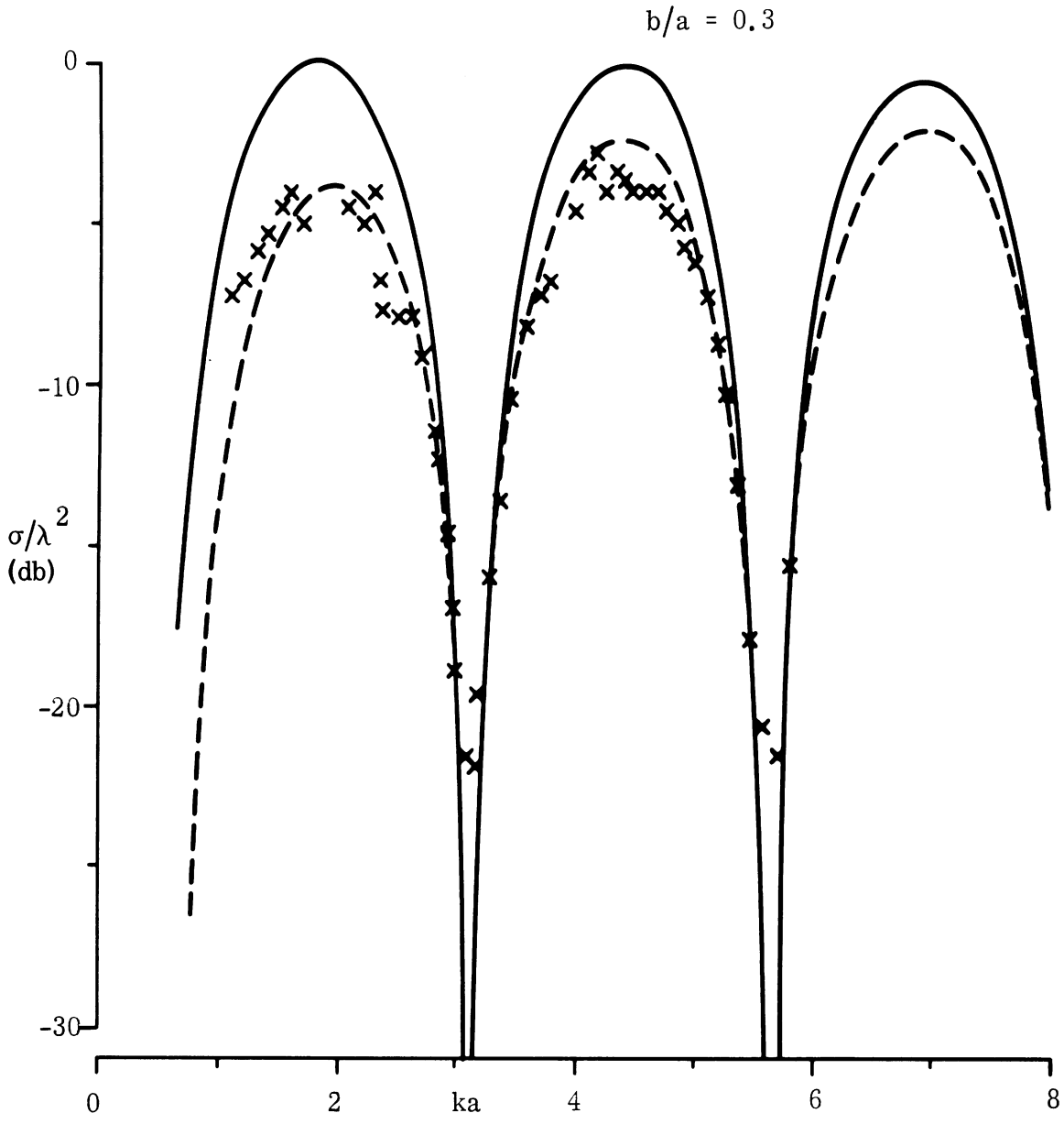

FIG. 3-42: PREDICTED CROSS SECTIONS FOR b/a = 0.3 WITHOUT (——) AND WITH (---) REDUCTION FACTOR B(kb) FULLY INCORPORATED WITH EXPERIMENTAL DATA (xxx).

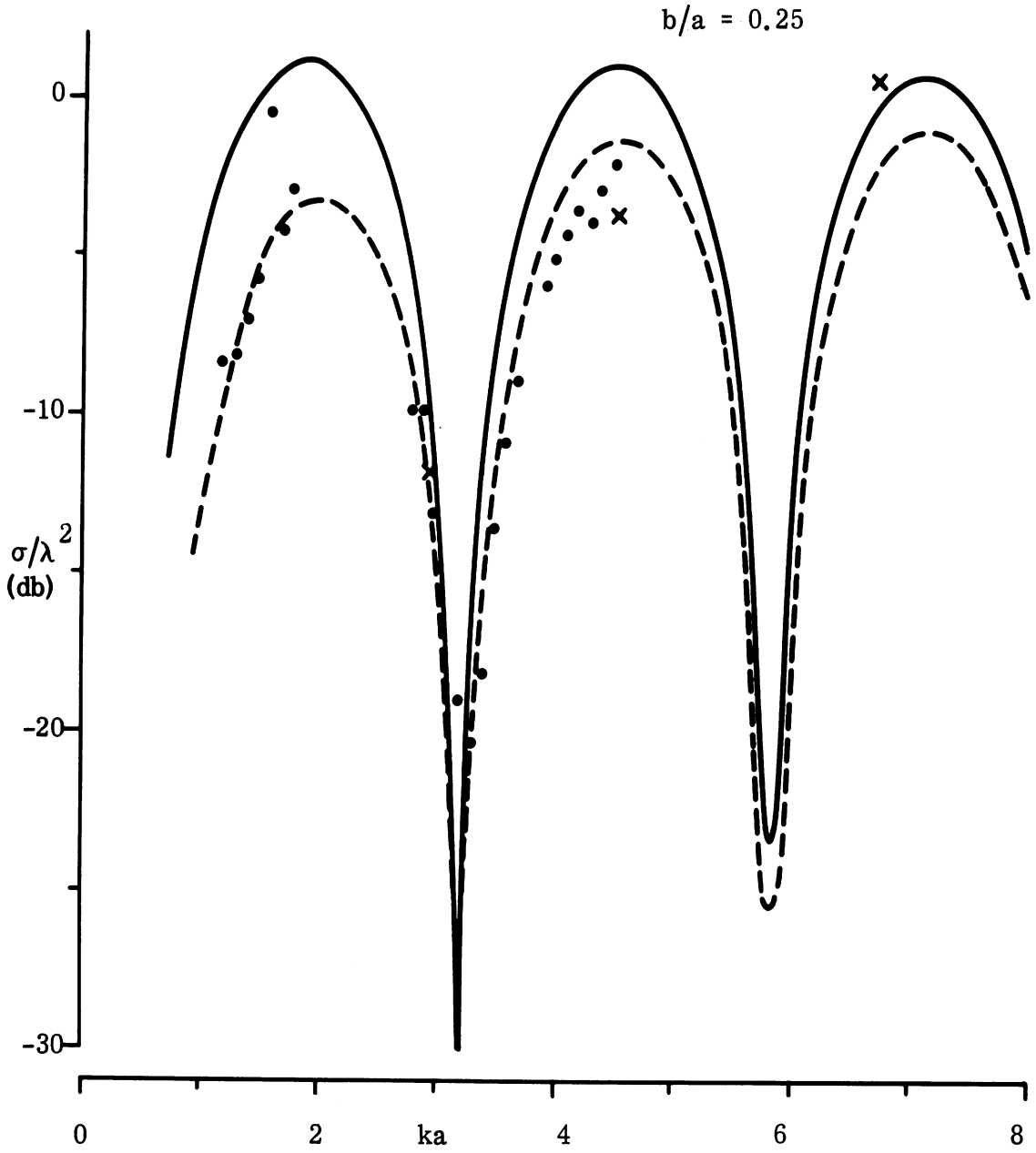

FIG. 3-43: PREDICTED CROSS SECTIONS FOR b/a = 0.25 WITHOUT (——) AND WITH (---) REDUCTION FACTOR B(kb) FULLY INCORPORATED, COMPARED WITH EXPERIMENTAL DATA FOR MODEL ID-1 (xxx) AND ID-2 (●●●).

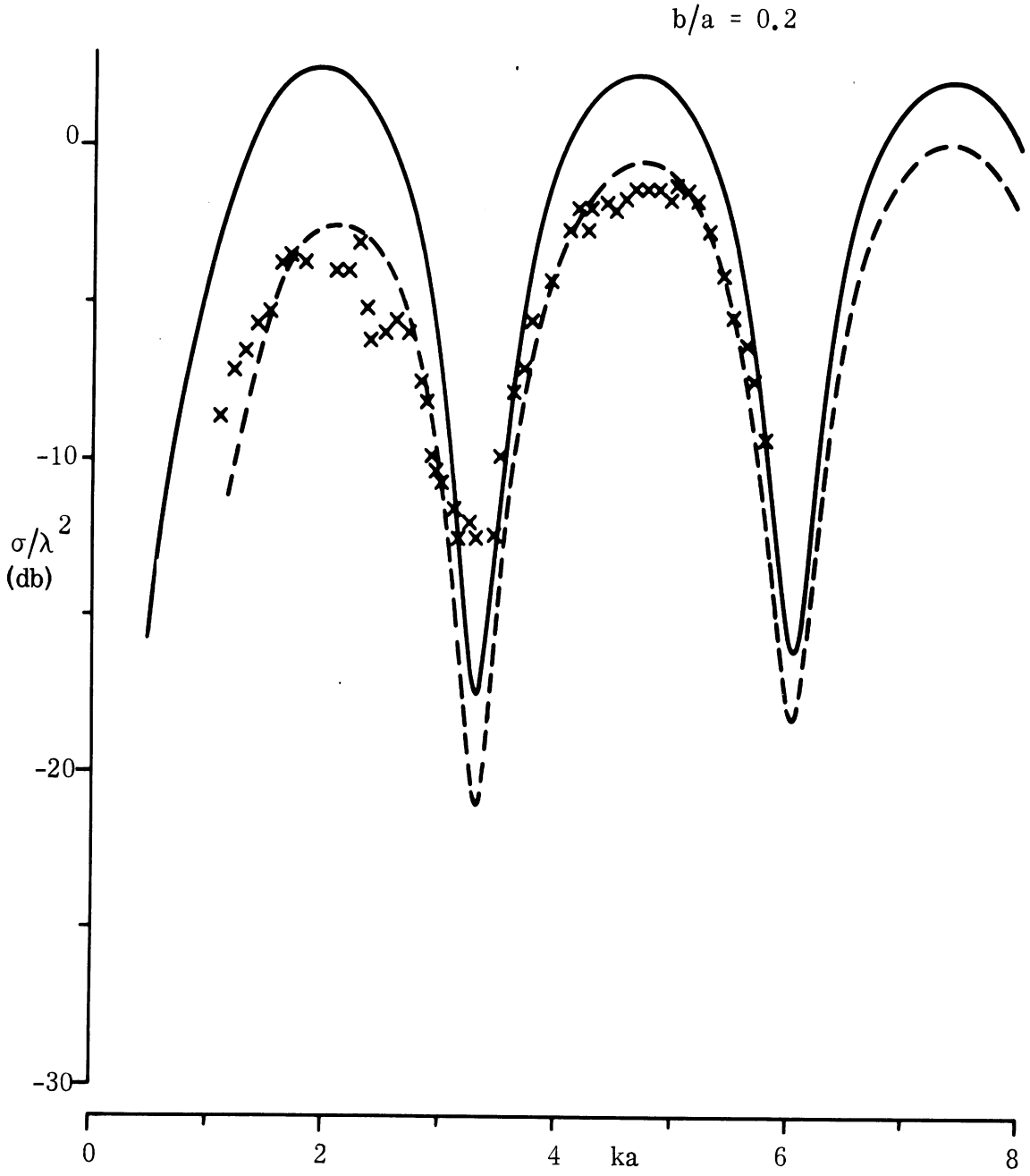

FIG. 3-44: PREDICTED CROSS SECTIONS FOR b/a = 0.2 WITHOUT (——) AND WITH (---) REDUCTION FACTOR B(kb) FULLY INCORPORATED, COMPATED WITH EXPERIMENTAL DATA (xxx).

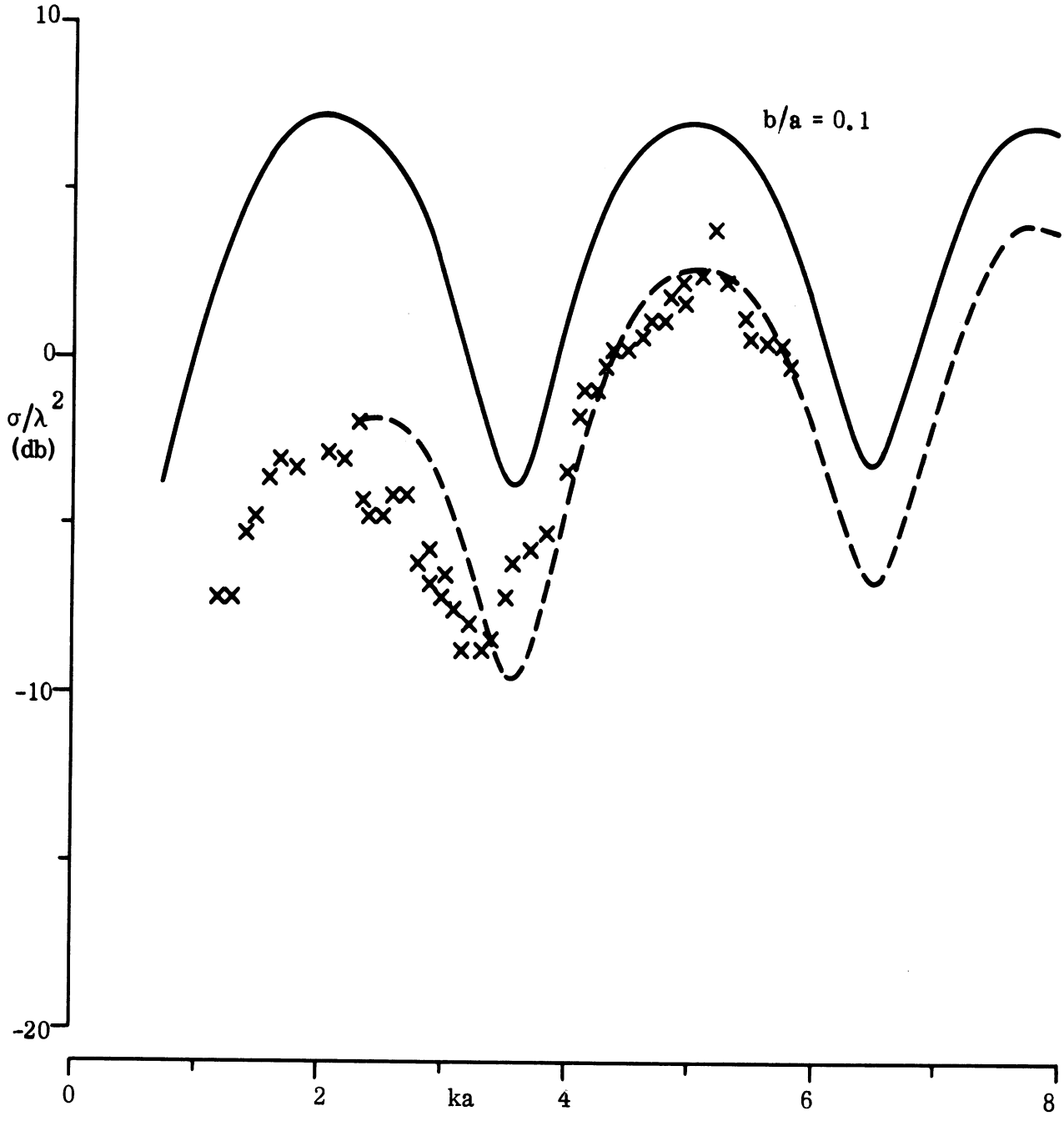

FIG. 3-45: PREDICTED CROSS SECTIONS FOR b/a = 0.1 WITHOUT (——) AND WITH (---) REDUCTION FACTOR B(kb) FULLY INCORPORATED, COMPARED WITH EXPERIMENTAL DATA (xxx).

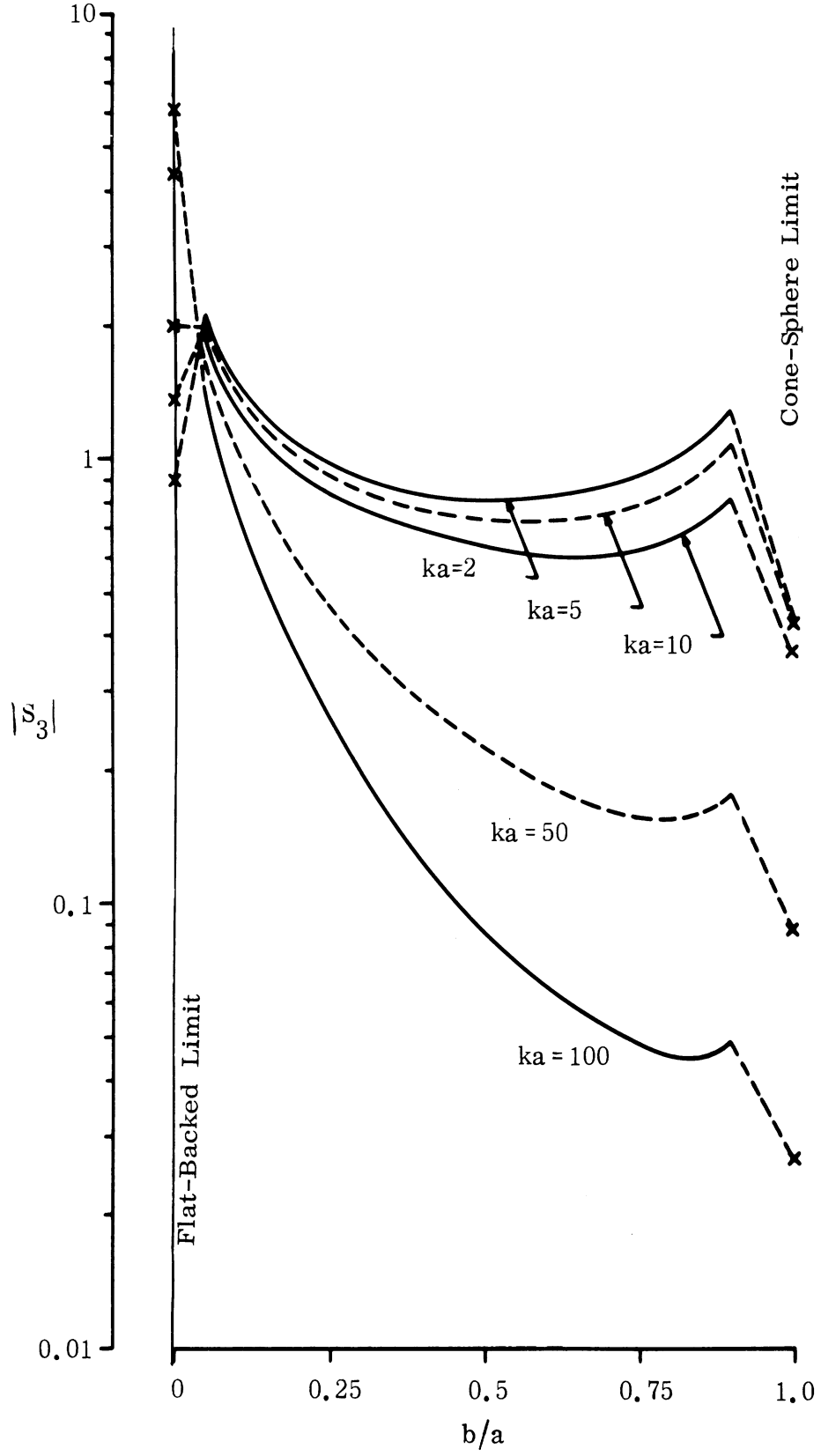

FIG. 3-46: THE MODULUS OF THE CREEPING WAVE CONTRIBUTION WITH NO REDUCTION; COMPUTED FROM EQ. (3.59).

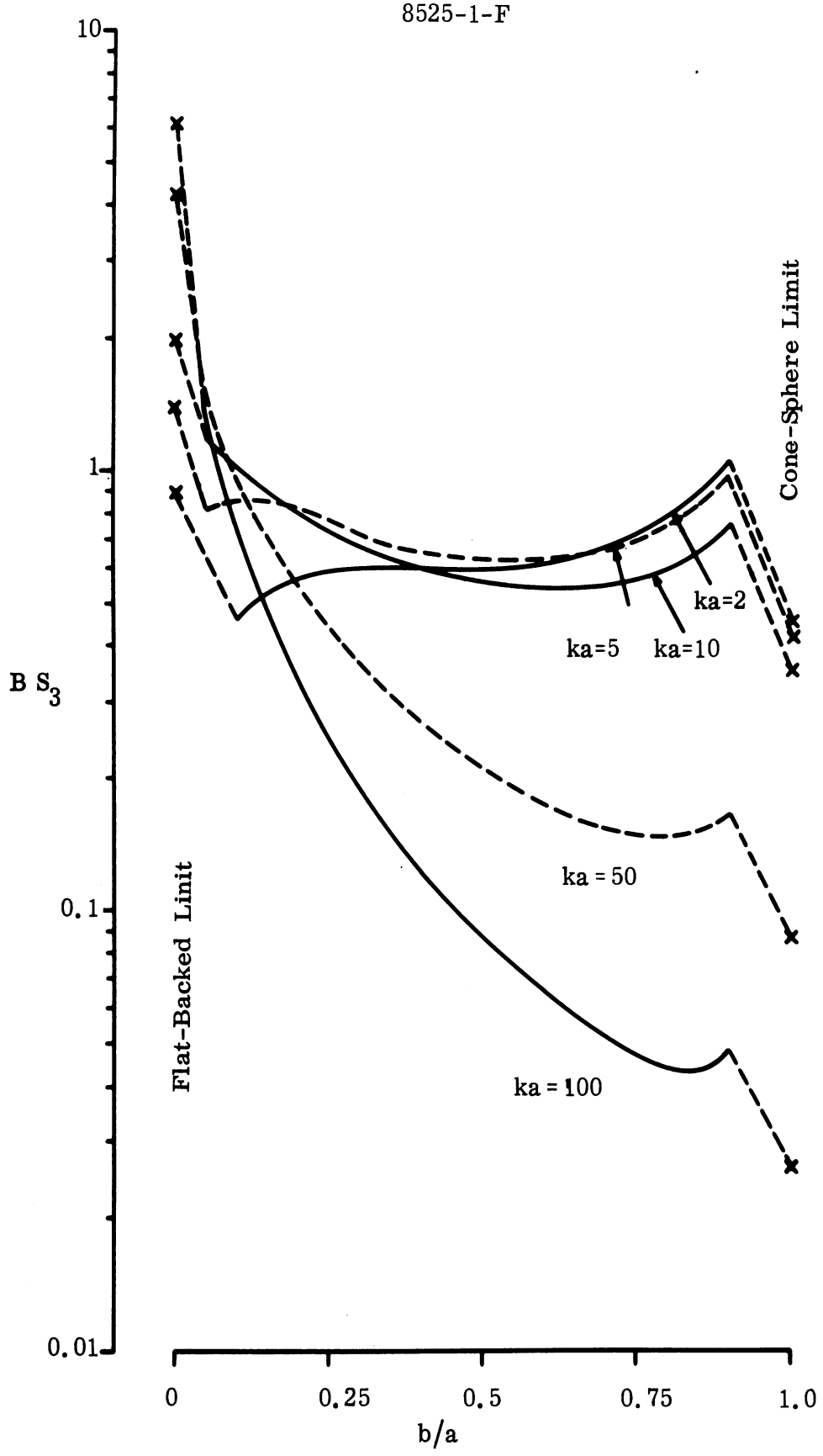

FIG. 3-47: THE MODULUS OF THE CREEPING WAVE CONTRIBUTION WITH THE REDUCTION FACTOR B(kb) INCORPORATED FOR $0 < b/a < 1$.

first Fig. 3-46 we observe that only for the very largest ka ($\geq$ 50 say) is there any evidence of a natural continuation into the flat-backed cone value. But much more distressing is the upswing in each curve that occurs as b/a approaches unity, and that takes place for b/a as low as 0.5 for ka as small as 2. Such an upswing occurs no matter how large ka is, and in view of the factor $\sqrt{2k(a-b)}$ in the denominator of the expression for S_3, it was predictable that it would do so. Not expected, however, was the fact that it would be significant at such low values of b/a. It occurs, for example, at $b/a \simeq 0.84$ for ka = 100, and here $2k(a-b) \simeq 32$. This is certainly large compared with unity.

(U) Incorporation of the reduction factor B(kb) (see Fig. 3-47) does nothing to diminish these undesirable trends in behavior and does, in fact, accentuate them. The curves for ka = 5 and 2 now show a reverse turn-over for small b/a which further complicates the task of arriving at a smooth transition to the flat-backed cone results. Indeed, the entire curve for ka = 2 is now most peculiar, and is almost the mirror image of what one would prefer.

(U) In spite of all these difficulties, the theoretical cross section prediction that we have given is numerically acceptable providing $b/a \lesssim 0.5$ (as it was in all cases that we examined), and the peculiarities that are evident in the behavior of the creeping wave estimates for small b/a are entirely masked by the large join contributions that then occur. It is, however, incumbent upon us to produce a theoretically tenable estimate of the creeping wave contribution, not only to permit cross section estimates for $0.5 < b/a < 1.0$, but also to explain (and almost certainly remove) the pecularities evident in Figs. 3-46 and 3-47. Indeed, these figures cast some doubt even on the validity of Eq. (3.59) on an asymptotic basis for large ka, kb and k(a - b), and using the numerical 'feel' obtained from them, one is tempted to believe

that a viable expression for the creeping wave modulus could be obtained using smooth parabolic-shaped lines joining the extreme values representing the results for the flat-backed cone and the cone-sphere.

3.5 A Quantitative Failure of a Scattering Estimate

(U) In Section 3.1.4 of Goodrich et al, 1967b we examined the nose-on scattering from models ID-1 and -2 and derived an expression for the back-scattering cross section based on the 'corrected' formulae for the join and creeping wave contributions given in Sections 3.1.3 and 3.1.2 (of the same report) respectively. As is true with most of our results, however, this expression is an asymptotic one, valid only for large kL where L is the smallest 'effective' dimension of the body, and in order to justify its use, it was conceded that kL may have to exceed (say) 5. Nevertheless, we often have to stretch the limit with asymptotic formulae, and in some cases at least (e.g. a sphere, or a cone-sphere) it has been found possible to obtain results which are quantitively accurate for values of kL as small as unity (or even less).

(U) The ID models are characterised by two effective radii of curvature: the longitudinal radius, b, at the shadow boundary, and the transverse radius, a (which is tantamount to the maximum radius). For both ID models, $a = 4b$. We note in passing that for the FB models subsequently measured, a/b varies from 2.5 for model FB-4 to 10 for model FB-1.

(U) Since $b < a$, kb is the parameter that can be expected to limit the validity of the asymptotic expansion for the join and creeping wave contributions, but if we were to demand that $kb > 5$, this would, for the ID models, exclude all of the range out to $ka = 20$, and thereby exclude the range of most practical interest, Indeed, for the ID models, the available experimental data for the nose-on cross section is confined to the range $1.2 \leq ka \leq 4.5$, corresponding to kb satisfying $0.3 \leq kb \leq 1.125$, and to believe

that the formulae will provide accurate estimates in the range may be no more than a pious hope. This is particularly true of the join contribution, which undergoes a marked change of character as kb approaches

$$\sqrt{\frac{3(a-b)}{4a}} \qquad \left(= \frac{3}{4} \text{ for } a = 4b \right) ,$$

but the absence of any rapid change in the creeping wave contribution is no criterion for judging the accuracy of its formula as kb approaches unity or less.

(U) These facts notwithstanding, computations of the nose-on cross section of the ID model for $0.25 \leq kb \leq 1.25$ were performed and, as shown in Section 3.1.4 of Goodrich et al, 1967b the results are in tolerable (but by no means good) agreement with the experimental data. In brief, our feeling was that all qualitative features of the experimental data were predicted by the formula, and that any quantitative shortcomings in this range of kb would rapidly disappear with increasing kb. However, when we came to apply the same analytical prescription to the estimation of oblique angle scattering from an ID model, even the qualitative features of the measured pattern were not reproduced, and it appeared that any agreement with experiment for this range of kb was little more than coincidental. And when the more extensive measured data for the FB models became available, it was found that the formula which, for given ka and b/a, is the same regardless of whether the back is flat or indented, was quite inadequate for the estimation of the nose-on behavior even for kb as large as 2 with $a = 2.5\ b$.

(U) In order to try to pinpoint the reasons for these shortcomings, let us survey some of the successes and failures of the theoretical prescription for backscattering by a body with smooth non-spherical termination. In the first place, the theory predicts that for nose-on and near nose-on incidence on

an indented-back model, the scattering is a function of ka and a/b, and is independent of c. This is confirmed by the identity of the measured nose-on cross sections of models ID-1 and 2 (see Section 3.1.3 of Goodrich et al, 1967b) Since the parameter c does not enter into the formula, the cross section should remain unchanged if we allow c to become infinite whilst keeping a and a/b fixed. The resulting model is of the FB type, and to show that the scattering is still the same, we show in Fig. 3-48 the measured nose-on cross sections of models FB-2 and 3 (for which a/b = 5 and 3.33 respectively) and of model ID-2 (for which a/b = 4). As required, the measured values for the FB models effectively bracket the data for ID-2.

(U) The nature of the formula for the creeping wave contribution S_{cw} for a body with non-spherical rear is such that over the range $1 \leq ka \leq 10$ the magnitude of S_{cw} is almost independent of a/b and smaller than the analogous quantity for a flat-backed cone by a factor 4 or more. The consequences of this are two-fold: (a) the character of the predicted oblique angle scattering more closely resemble the behavior of a cone-sphere rather than a flat-backed cone over this range of ka. In contrast, the measured data for the ID models, for example, is more closely akin to the data for a flat-backed cone, as is evident from Fig. 3-49 where we show the measured patterns for ID-2, a flat-backed cone* (Keys and Primich, 1959) and a cone-sphere for ka = 2.98 and 4.51; (b) the formula is unable to reproduce the correct magnitudes for the peaks in the nose-on backscattering cross section of the FB models as a function of ka, and, in particular, fails completely to predicted the increasing depth of the minimum near ka = 5.5 as b/a decreases from 10 to 2.5. The fact that the formula did lead to tolerable agreement with the nose-on data for ID-2 in the vicinity of the minimum near ka = 3.3 was entirely a consequence of the rapid variation in the join contribution taking

* The actual ka - values for the flat-backed cone are 3.08 and 4.56.

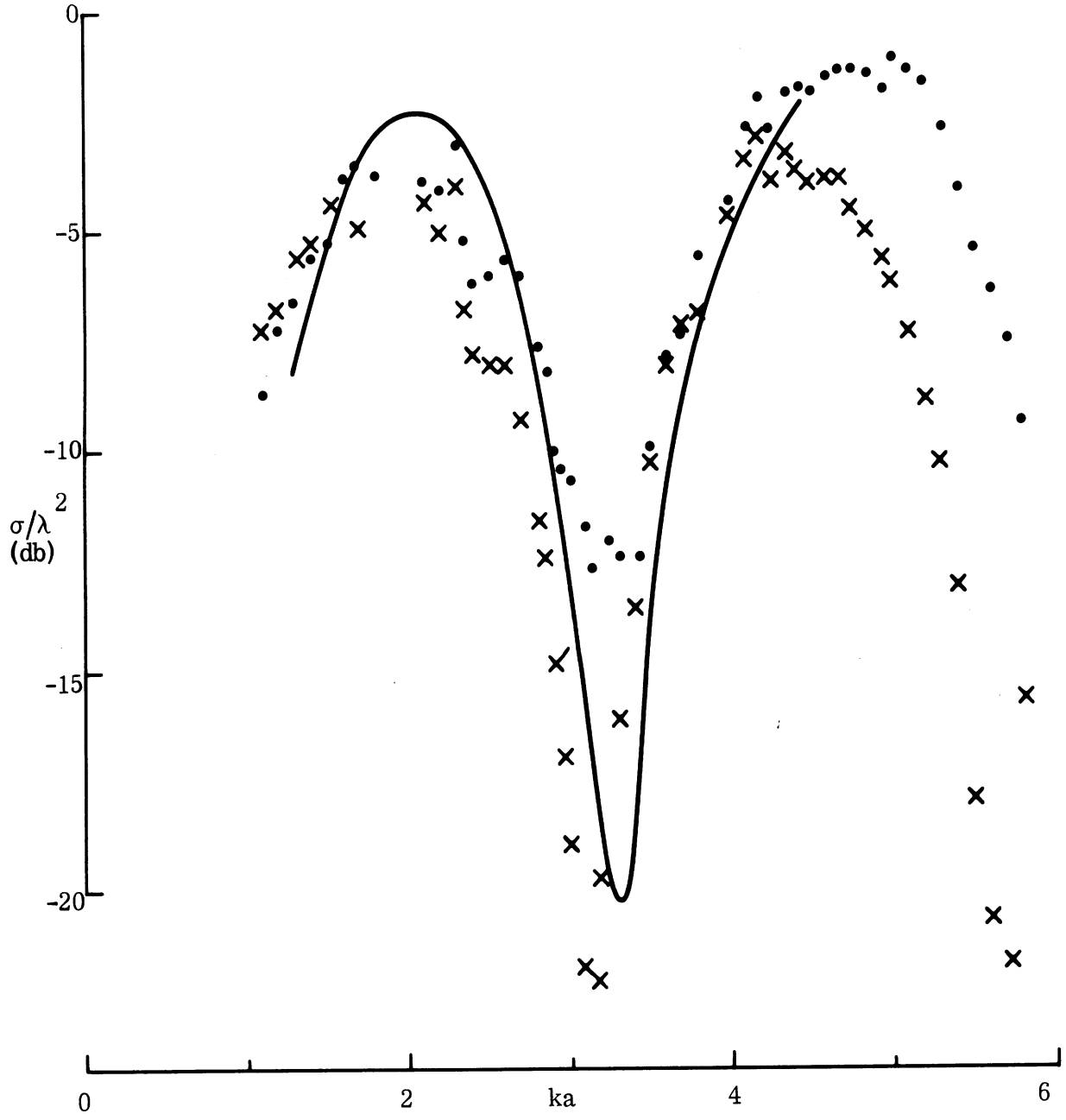

FIG. 3-48: COMPARISON OF MEASURED DATA FOR MODELS ID-2, —— (a/b = 4), FB-2 ●●● (a/b = 5) AND FB-3, xxx (a/b = 3.33°).

FIG. 3-49: COMPARISON OF MEASURED SCATTERING PATTERNS FOR MODEL ID-2 WITH THOSE OF FLAT-BACKED CONES AND CONE-SPHERES.

place near kb = 0.8, and the more one studies the measured data (see Fig. 3-50), the more one is led to believe that the agreement was merely fortuitious.

(U) Because of the tendency for the measured data to approach the flat-backed cone behavior as a/b increases, and to approach it quite closely for even small values of a/b (> 1) for ka in the range 1 to 10, it is of interest to examine the formula for nose-on scattering from a flat-backed cone. It is known (Kleinman and Senior, 1963) that the formula based on Keller's second order theory is in close agreement with measured data even for ka as small as unity (or less), particularly for small values of the half-cone angle α. The resulting expression for the far field amplitude in the backscattering direction for nose-on incidence is

$$S = -\frac{ka}{2n}\operatorname{cosec}\frac{2\pi}{n} - \frac{ka}{4n^2}\sec\frac{\pi}{n}\frac{\cos\frac{\pi}{n} - \cos\frac{3\pi}{n}}{\left(\cos\frac{\pi}{n} - \cos\frac{3\pi}{2n}\right)^2}\frac{e^{2ika - \frac{\pi}{4}}}{\sqrt{\pi\, ka}} \qquad (3.69)$$

with $n = 3/2 + \alpha/\pi$. The first term on the right hand side of (3.69) is clearly the degenerate form of the join contribution as $b \to 0$, where as the second term is the degenerate form of the creeping wave return. Denoting these by $\tilde{S}_j$ and $\tilde{S}_{cw}$ respectively, we have, for* $\alpha = 9^o$

$$\left|\tilde{S}_j\right| = 0.40793 \quad , \quad \arg \tilde{S}_j = 0$$

$$\left|\tilde{S}_{cw}\right| = 0.61569\sqrt{ka} \quad , \quad \arg \tilde{S}_{cw} = 2ka + 3\frac{\pi}{4} \; . \qquad (3.70)$$

* Whereas $\alpha = 7.5^o$ for most of our previous models, the FB series have $\alpha = 9^o$. The change in the numerical constants in (3.70) on going to $\alpha = 7.5^o$ is small, with the first being replaced by 0.40339 and the second 0.63348.

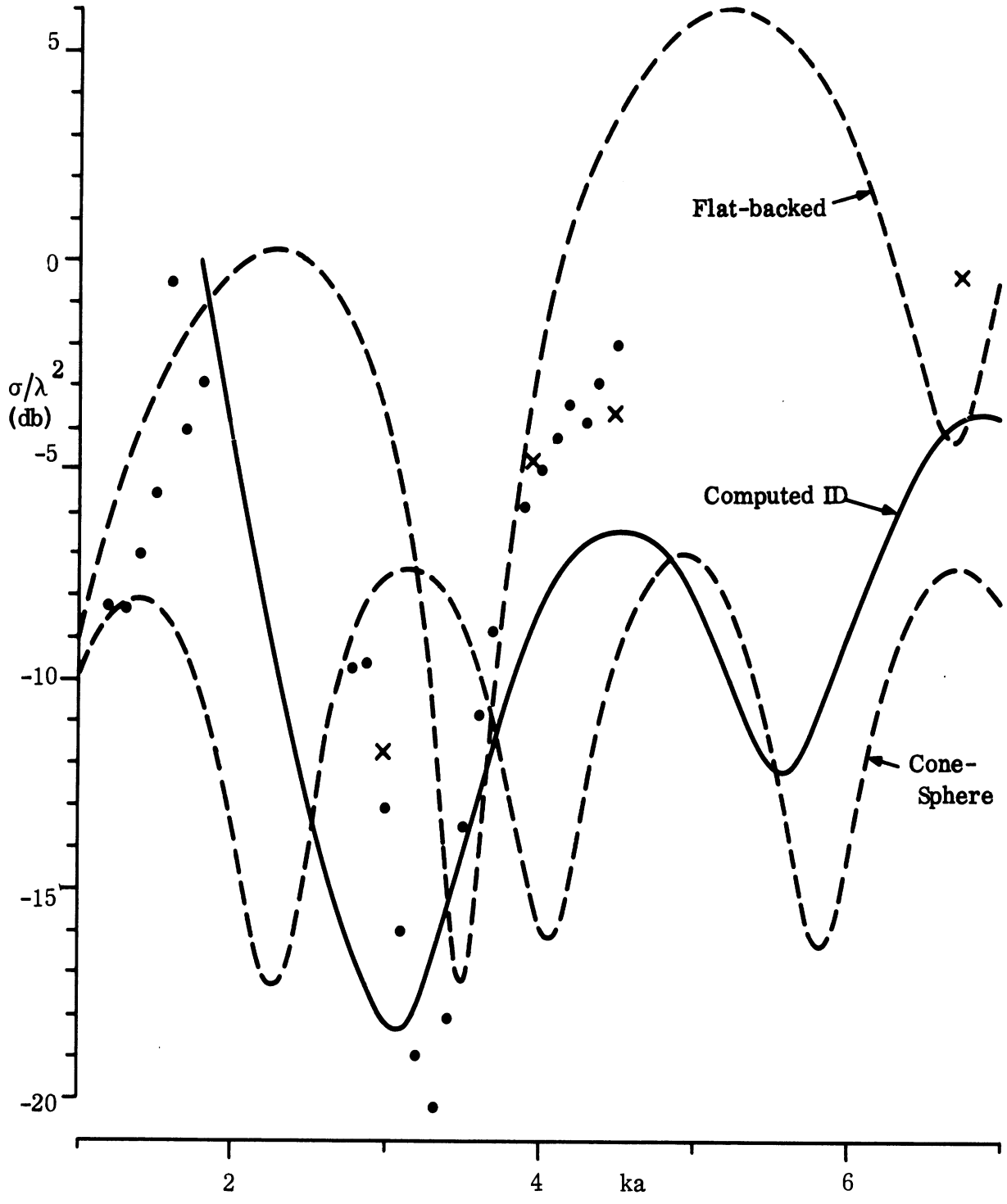

FIG. 3-50: COMPARISON OF MEASURED DATA FOR NOSE-ON BACKSCATTERING OF MODEL ID-1 (xxx) AND ID-2 (ooo) WITH COMPUTED CURVES FOR ID MODEL (——), FLAT-BACKED CONE (— — —) AND CONE-SPHERE (— — —).

(U) The modulus of the degenerate creeping wave contribution for a flat-backed cone (b/a = 0) is plotted as a function of ka in Fig. 3-51, along with the corresponding quantity for a cone-sphere (b/a = 1). For simplicity, we have omitted any enhancement factor from the latter, and have taken the results directly from Senior (1967b), supplemented by new computations for ka > 10. It will be observed that the sphere curve is almost asymptotic to the curve for a flat-backed cone for ka small, and the latter provides a natural continuation of the former for ka < 0.3, say.

(U) It is a most reasonable assumption that for any body having b/a < 1 the curve of the creeping wave modulus as a function of ka will lie between the bounds established by the flat-backed cone and sphere, and this is regardless of whether we insist that b remain constant, or allow b/a to be held fixed; and we further expect that as b/a decreases, the value of ka at which the curve for the creeping wave modulus 'breaks away' from the curve for a flat-backed cone will increase.

(U) Using asymptotic analyses, a formula for the creeping wave contribution associated with an ID or FB model has been derived. This was presented in Section 3.1.2 of Goodrich et al, 1967b, and has been computed as a function of ka for b = 0.25 a (appropriate to the ID models). From an inspection of the formula it can be seen that, for a body having b = αa, the creeping wave contribution is

$$S_{cw}(ka/4\alpha) = \frac{1}{4}\sqrt{\frac{3}{\alpha(1-\alpha)}}\; e^{i(1-4\alpha)\frac{ka}{2\alpha}} \left[S_{cw}\right]_{\alpha = 0.25}, \qquad (3.71)$$

where the last factor on the right hand side is the quantity already computed for the body having b = 0.25 a, and this enables us to trivially deduce the creeping wave return for bodies having other (fixed) ratios of b to a. In

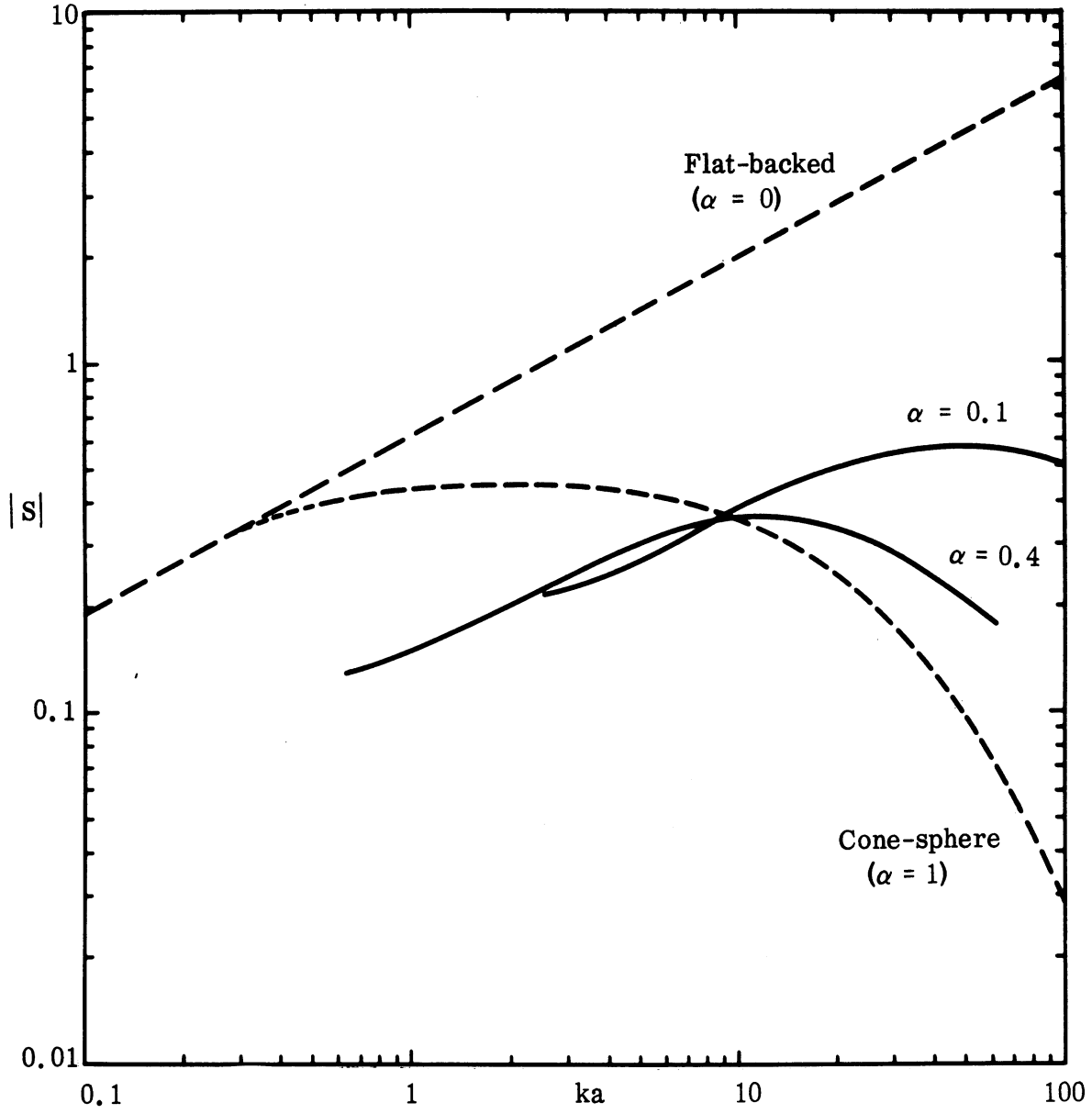

FIG. 3-51: COMPUTED MODULI FOR CREEPING WAVE CONTRIBUTION FOR BACKSCATTERING AT NOSE-ON INCIDENCE.

this manner we have computed the modulus of the creeping wave contribution for bodies having α = 0.1, 0.2, 0.3 and 0.4, and two of the resulting curves are included in Fig. 3-51. They do not in any manner conform to the guide-lines given above, and, for ka less than (about) 9, the moduli are even less than for a cone-sphere (for which α = 1). What is more, for ka < 9, the moduli are relatively independent of α, and this has been found true for all the values of α considered. It is clear that such values for the creeping wave contribution are not likely to be consistent with the marked dependence on α of the nose-on cross sections of the FB models.

(U) In attempting to improve the theoretical estimate of the creeping wave contribution for a body with non-spherical rear, particularly for values of kb not much greater than unity, it should be borne in mind that the formula is, without doubt, correct for sufficiently large kb. For kb >> 1, we can replace the function $\hat{q}(\xi)$ appearing in Eq. (3.1) of Goodrich et al, 1967b, by the leading term in its asymptotic expansions for large argument, viz.

$$\hat{q}(\xi) \sim \frac{e^{5i\frac{\pi}{6}}}{2\sqrt{\pi}} \frac{1}{\beta_1 \left\{A_i(-\beta_1)\right\}^2} e^{i\xi\beta_1 e^{i\frac{\pi}{3}}}, \qquad (3.72)$$

and thereby obtain

$$S \sim \frac{ka}{4} \left(\frac{kb}{2}\right)^{2/3} \frac{e^{2ik(a-b)+i\pi kb}}{\sqrt{2k(a-b)}} \cdot$$

$$\cdot \frac{1}{\beta_1^2 \left\{A_i(-\beta_1)\right\}^4} e^{i\pi\beta_1(\frac{kb}{2})^{1/3} e^{i\frac{\pi}{3}}}, \qquad (3.73)$$

which is in accordance with the result provided by the geometrical theory of diffreaction. Using this asymptotic approximation, we have

$$\left|\frac{S(ka,\ \alpha_1\ ka)}{S(ka,\ \alpha_2\ ka)}\right| = (\alpha_1/\alpha_2)^{2/3}\sqrt{\frac{1-\alpha_2}{1-\alpha_1}}$$

$$\exp\left\{-\frac{\sqrt{3}}{2}\ \pi\ \beta_1\ (ka/2)^{1/3}\quad\left(\alpha_1^{1/3} - \alpha_2^{1/3}\right)\right\} \qquad (3.74)$$

with $b = \alpha a$, and for sufficiently large ka, the right hand side of (3.74) is less than unity for $\alpha_2 < \alpha_1$. Thus, at high enough frequencies, the magnitude of the creeping wave contribution increases with decreasing α, as expected. This is otherwise evident from the computations of the original formula for S: for ka large (near, say, 100), the curves correctly ordered as a function of α, being closest to the sphere curve for α near unity, and tending upwards towards the flat-backed cone curve as α decreases. Note that the relation (3.74) does not, unfortunately, enable us to deduce the creeping wave amplitude for general α from its known values for either of the limiting cases $\alpha = 0$ or 1.

(U) Even though the formula for S_{cw} is asymptotically correct for large kb, and can therefore be expected to yield an accurate numerical estimate of the creeping wave return for kb large enough, inspection of Fig. 3-51 suggests that for ka as large as 50 with $\alpha = 0.4$ (implying kb = 20) the estimated modulus is beginning to depart from the behavior expected of it. The slope of the curve here is somewhat different from that desired, and this is certainly true of the curve for $\alpha = 0.1$ when ka = 100. It seems probable that we are, in fact, seeking two refinements of theory: one which is significant even for kb as large as 10 or 20, and which is doubtless associated with the higher order attenuation effects that have been neglected in the deri-

vation of the creeping wave expression: and one which is only of concern for kb quite small (less than 2, say), and has as its origin the rapid transition in the birth and launch weights as the radius of curvature of the shadow boundary decreases. The investigation of the latter is a relatively basic study, and is already in progress using a parabolic cylinder as the model. However, the first refinement may be the more significant one for practical purposes, and though a rigorous derivation of the correction would be a lengthy task, it may still be possible to arrive at an empirical and numerically effective correction.

IV

THEORETICAL STUDIES (SURF)

4.1 Introduction

(U) In analyzing the surface field data and the backscatter data obtained experimentally, it was necessary to carry out theoretical studies of the physical factors which contribute to the observed effects. Where an exact theoretical description could not be constructed and where approximate methods did not give sufficiently accurate results, empirical modifications of formulas were obtained from the experimental data itself. Where a synthesis of a cross section formula for a specific shape could not be developed by a direct solution of the scattering problem for that shape, the formula was obtained by the extension of the solution for similar shape. This section reports on studies of this nature.

4.2 An Empirical Correction to the Estimated Creeping Wave Contribution for a Non-Spherical Body.

(U) In Section 3.1.2 of Goodrich et al 1967b, the 'corrected' asymptotic expression* was given for the far field amplitude attributable to the creeping wave excited on a non-spherical body at symmetrical incidence. Specifically, for a body whose transverse radius of curvature at the shadow boundary is a, and whose longitudinal radius is b, with the latter radius remaining the same up to or beyond the point at which the profile is perpendicular to the axis of symmetry, the expression quoted there is*

$$S_{cw} = -\pi\, ka\, e^{i\pi kb}\, \frac{e^{2ik(a-b)-i\pi/4}}{\sqrt{2k\,(a-b)}}\, \left(\frac{kb}{2}\right)^{2/3} \left[\hat{q}(\xi) + \frac{e^{i\pi/6}}{30\sqrt{\pi}}\, \frac{2^{1/3}}{(kb)^{2/3}} \cdot \sum_s \frac{1}{\left\{A_i(-\beta_s)\right\}^2} \left(1 + \frac{3}{\beta_s^3}\right) \exp\left(-\xi\beta_s e^{-i\pi/6}\right)\right]^2 \qquad (4.1)$$

* There is one additional correction over and above those previously described. This amounts to the removal of a factor $e^{i\pi/2}$ from the space factor and, hence, from the overall expression for S_{cw}, and is necessitated by the fact that we are dealing with the (electric) field component normal to the surface.

where

$$\xi = \pi/2\ (kb/2)^{1/3} \quad , \tag{4.2}$$

the β_s are the zeros of the Airy function derivative, and $q(\xi) = q^{(o)}(\xi)$ is the function tabulated on pp. 8-18 and 8-19 of Logan (1959). Detailed computations have been made as a function of ka, $1 \leq ka \leq 100$, for a body having $b = 0.25a$, and using the fact that for a body having $b = \alpha a$,

$$S_{cw}(ka/4\alpha) = \frac{1}{4}\sqrt{\frac{3}{\alpha(1-\alpha)}}\ e^{i(1-4\alpha)\frac{ka}{2\alpha}} \left[S_{cw}\right]_{\alpha = 0.25} , \tag{4.3}$$

where the last factor is the quantity already computed, it is a trivial matter to deduce the creeping wave contribution for a body having $\alpha \neq 0.25$.

(U) The above expression for S_{cw} was derived under the assumption that $kb >> 1$ and, as such, is not valid in the limiting case of a flat-backed cone ($kb \equiv 0$). It also breaks down in the limiting case of a sphere ($b \equiv a$) due to the 'space' factor involving $a - b$ in the denominator, and we therefore cannot investigate either of these cases directly using (4.1). However, it is believed that these cases, whose creeping wave effects can be determined by alternative methods, provide effective bounds on the creeping wave contribution that the present class of bodies can produce; and as shown in Section 3.5 the results computed using (4.1) violate these bounds, and do not lead to good agreement with the measured data for backscattering from cones with non-spherical terminations (e.g. the ID and FB models).

(U) There are probably two main sources of these numerical discrepancies: firstly, the inaccuracy of the high frequency expression for the birth and launch weights of the creeping waves when kb is not large, and secondly, the failure of the expression (4.1) to take into account the higher order attenuation factors which are known to be important even at relatively high fre-

quencies (Senior, 1965). In this present section we shall endeavor to provide an empirical (or numerical) correction to the formula for S_{cw} sufficient to remove some of the numerical inadequacies, and in so doing will concentrate on the higher order attenuation factors as the main source of the correction.

(U) Figure 4-1 shows the modulus of the creeping wave contribution for α = 0.1, 0.25 and 0.5 computed from Eq. (4.1). The results for α = 0.1 and 0.5 have been deduced from those for α = 0.25 using (4.3), and this accounts for the reduced spans of the curves in these cases. Note the close agreement between the computed values for all three values of α when ka is less than (about) 9. The broken curve in Fig. 4-1 is for a sphere (α = 1), and will be discussed in a moment.

(U) The effect of omitting the infinite sum from the right hand side of Eq. (4.1), i.e., replacing the interior of the square bracket by $q(\xi)$ alone, is illustrated in Fig. 4-2 for the same three values of α. It will be observed that the main result is an increase in the level of each curve, with the bend that formerly characterized each curve for small ka being somewhat reduced. The broken curve is again that for a sphere.

(U) To emphasize the increase that occurs with the deletion of the series, the results obtained with and without the series included for α = 0.25 are replotted in Fig. 4-3. It is seen that the increase can be as much as 33 percent (for ka in the vicinity of 2), and is still in excess of 10 percent at ka = 20 (implying kb = 5). This change is surprising as much in its direction as in its magnitude. The origin (and intent) of the series is a correction to take into account the finite transverse radius of curvature of the body and, as such, would be expected to include, at least in part, the effect of higher order attenuation factors. Certainly the expression with the series included should be more accurate than with the series deleted. As a result of our previous work, however, it was concluded (see Section 3.5) that Eq.

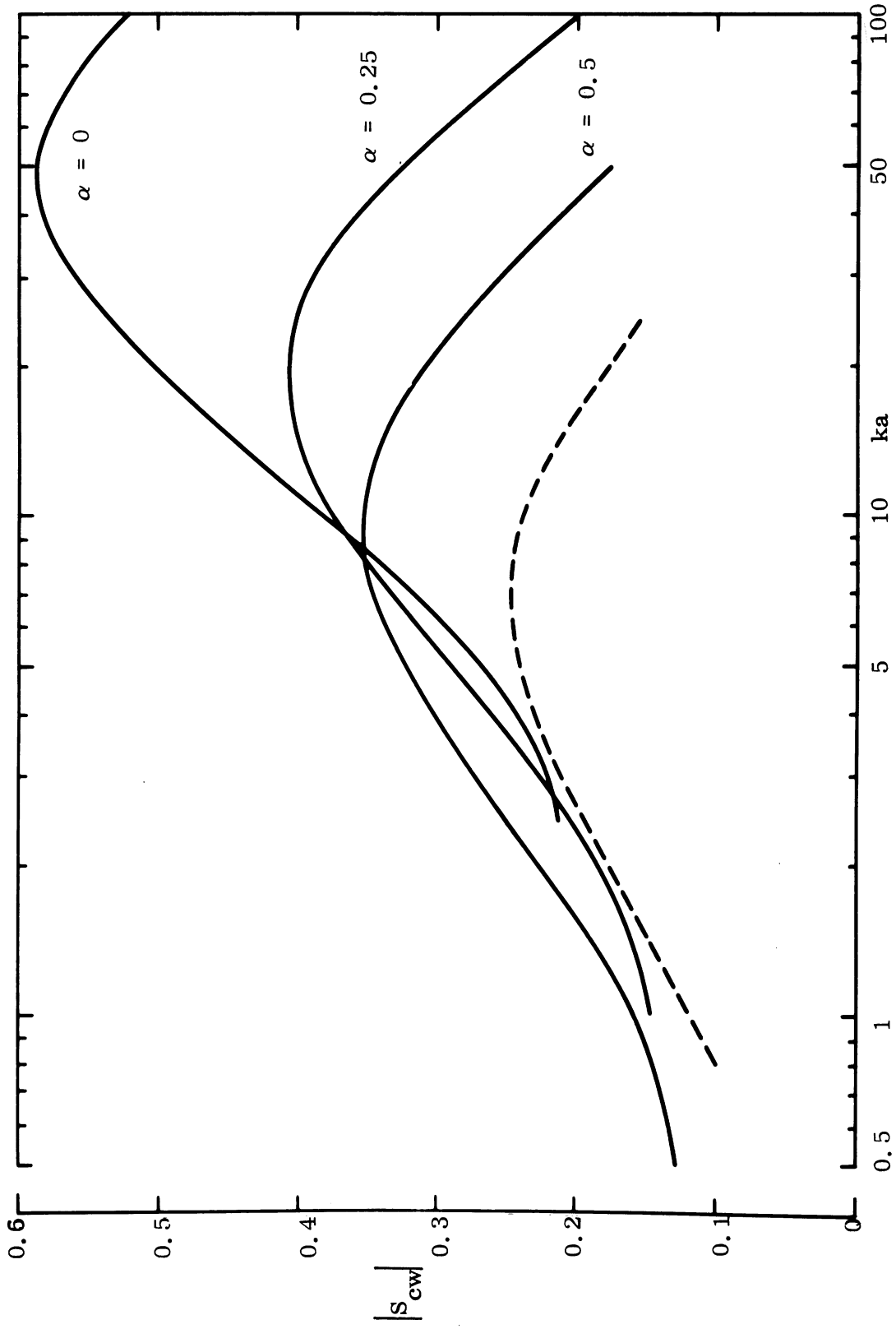

FIG. 4-1: MODULI OF THE CREEPING WAVE CONTRIBUTION FOR BODIES HAVING b = α a COMPUTED FROM EQ. (4.1) COMPARED WITH A SPHERE CURVE (---) COMPUTED FROM EQ: (4.9).

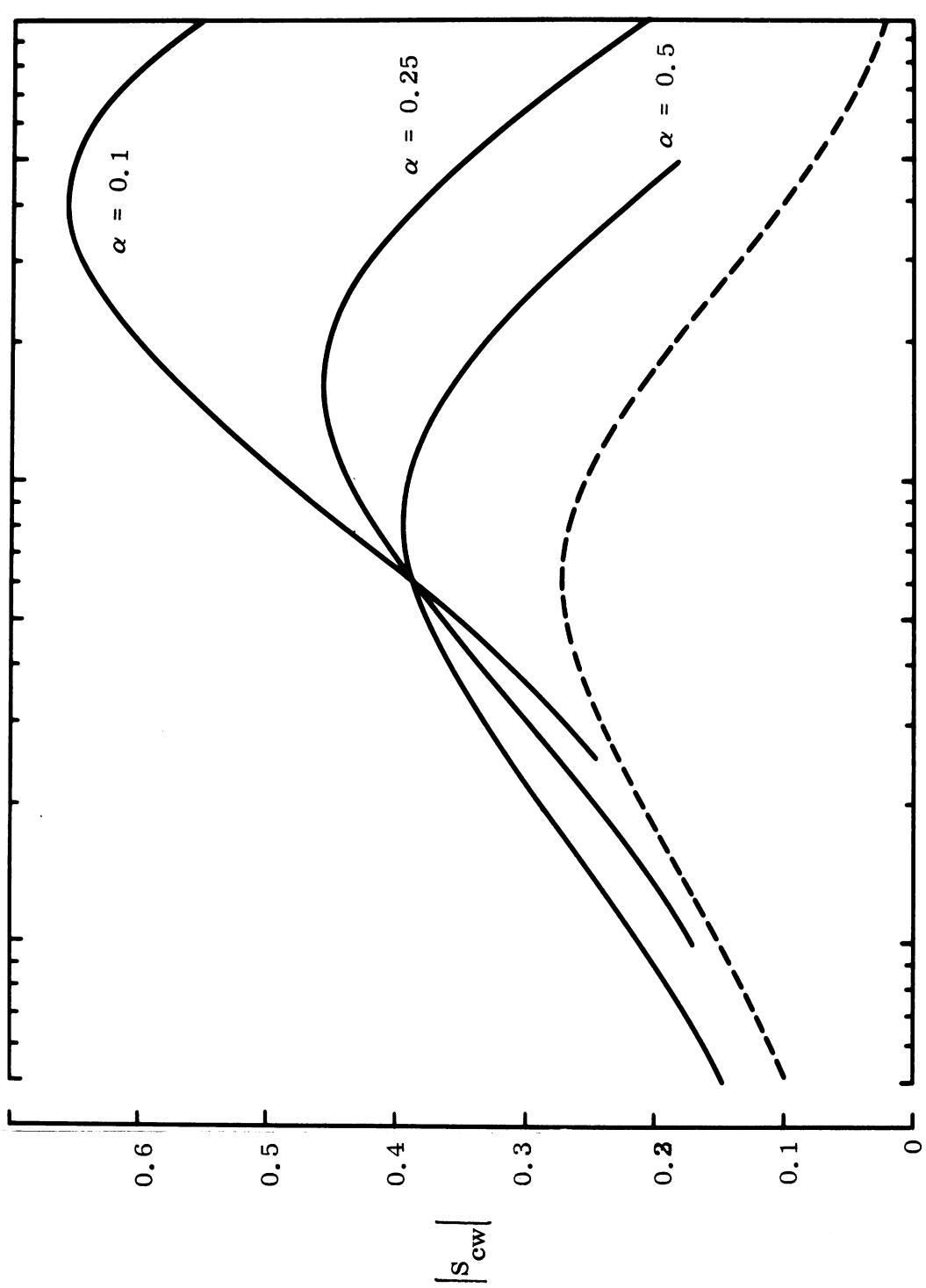

FIG. 4-2: MODULI OF THE CREEPING WAVE CONTRIBUTION FOR BODIES HAVING b = αa COMPUTED FROM EQ. (4.1) WITH THE SERIES DELETED, COMPARED WITH A SPHERE CURVE (---) COMPUTED FROM EQ. (4.7).

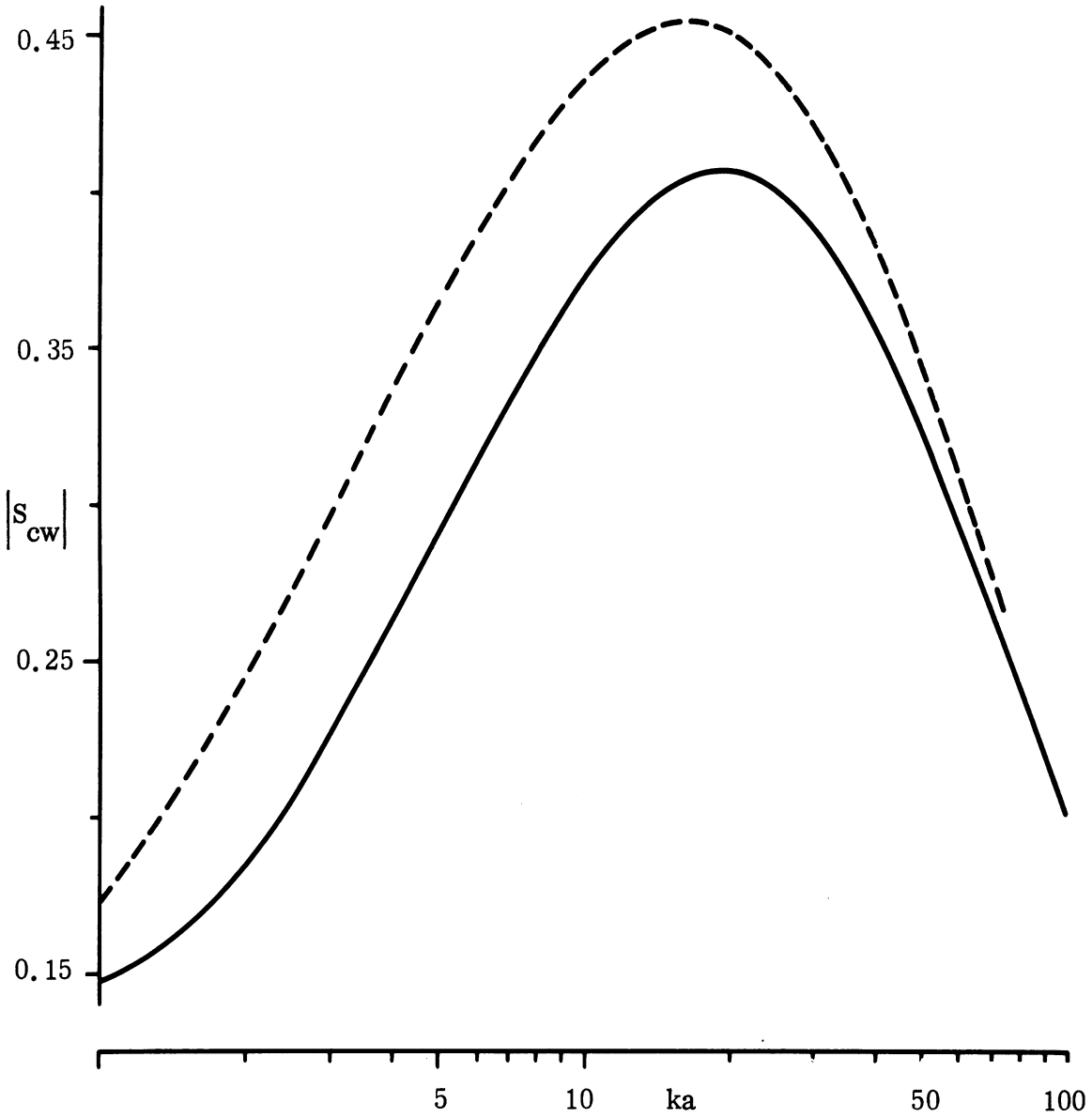

FIG. 4-3: MODULUS OF CREEPING WAVE CONTRIBUTION FOR BODY HAVING b = 0.25a, COMPUTED FROM EQ. (4.1) WITH (——) AND WITHOUT (---) THE SUMMATION INCLUDED.

(4.1) under-estimated the true magnitude of the creeping wave effect, particularly for $ka \lesssim 10$, and it would therefore seem most natural were the deletion of the series to reduce (rather than increase) the magnitude.

(U) Although the creeping wave contribution for a sphere is not immediately derivable from Eq. (4.1), we can obtain one or more expressions for comparison with (4.1) by going back to the basic analysis for a sphere given by Senior (1965). If we retain only the dominant term for high frequencies in the expression for S_{cw} given in Eq. (90) of the above reference, we have

$$S_{cw} \sim \left(\frac{ka}{2}\right)^{4/3} e^{i\pi\,(ka + 1/3)} \frac{1}{\beta_1 \left\{Ai\,(-\beta_1)\right\}^2}$$

$$\exp\left\{i\pi\ \beta_1\,(ka/2)^{1/3}\ e^{i\frac{\pi}{3}}\right\} \qquad (4.4)$$

and if we now introduce the effect of all higher order ($s > 1$) creeping waves, then $S_{cw} \sim S_{cw}^{L}$, where

$$S_{cw}^{L} = 2\sqrt{\pi}\ (ka/2)^{4/3}\ e^{i\pi\,(ka - 1/2)}\ \hat{q}(\xi_1) \qquad (4.5)$$

with

$$\xi_1 = \pi\,(ka/2)^{1/3} \quad . \qquad (4.6)$$

Alternatively, the exponential in Eq. (4.4) can be written as the product of two exponentials, each with half the exponent shown in (4.4). To introduce the effects of additional creeping waves into each exponential separately now entails the physical assumption of the waves being launched and re-born at some point, and is mathematically justifiable only at such high frequencies that the leading term in each sum above suffices, but if we do sum in this

manner over each exponential separately, we can arrive at an approximate expression for S_{cw} in the form $S_{cw} \simeq S^{p}_{cw}$, where

$$S^{p}_{cw} = -4\pi \left(\frac{ka}{2}\right)^{4/3} e^{i\pi(ka - 1/3)} \beta_1 \left\{Ai(-\beta_1)\right\}^2 \left[\hat{q}(\xi_2)\right]^2 \qquad (4.7)$$

with

$$\xi_2 = \pi/2\ (ka/2)^{1/3} \quad . \qquad (4.8)$$

This is analogous to Eq. (4.1) with the series deleted, and it was using Eq. (4.7) that the sphere curve given in Fig. 4-2 was computed. We note in passing that for all $ka > 0.5$, S^{L}_{cw} and S^{p}_{cw} differ by less than 6 percent. This reinforces somewhat our acceptance of the reasoning leading up to Eq. (4.7) and certainly demonstrates the insignificance of all higher order creeping wave contributions.

(U) In line with the analysis leading up to Eq. (4.1), we can seek to 'improve' the estimate S^{p}_{cw} of the sphere creeping wave by incorporating the series expansion contained in (4.1), and in this way we obtain

$$S^{s}_{cw} = -4\pi \left(\frac{ka}{2}\right)^{4/3} e^{i\pi(ka - 1/3)} \beta_1 \left\{Ai(-\beta_1)\right\}^2 \Bigg[q(\xi_2) + \frac{e^{i\frac{\pi}{6}}}{30\sqrt{\pi}} \frac{2^{1/3}}{(ka)^{2/3}} \sum_s \frac{1}{\left\{Ai(-\beta_s)\right\}^2} \left(1 + 3/\beta_s^3\right) \exp\left(-\xi_2 \beta_s e^{-i\pi/6}\right) \Bigg]^2 \qquad (4.9)$$

where ξ_2 is as given in Eq. (4.8). This is, of course, a function of ka only, and its modulus is shown as the broken line in Fig. 4-2. It bears about the same relationship to the results for $\alpha \neq 1$ as does the sphere curve based on Eq. (4.7) to the computations of Eq. (4.1) with the series deleted.

(U) Having transfered our attention to the sphere creeping wave, we are in a position to estimate the accuracy of numerical data obtained from Eqs. (4.5), (4.7) or (4.9) by using our knowledge of the true creeping wave contribution for this body (Senior, 1965), and in Fig. 4-4 the moduli computed from Eqs. (4.7) and (4.9) are compared with the exact values. As suspected from our studies of Figs 4-1 through 4-3, the incorporation of the 'correction' provided by the infinite series actually worsens the accuracy of the numerical approximation, and Eq. (4.7) provides a somewhat better approximation than does (4.9). Even (4.7), however, does not yield a good approximation at those values of ka of most practical interest. At ka = 5, for example, the estimated modulus is in error by almost 60 percent, and the error is still of order 10 percent for ka approaching 100. This in spite of the fact that (4.8) furnishes the correct leading term in the asymptotic expansion for large ka, and is numerically equivalent to Eq. (4.4). This is, in turn, the approximation furnished by the geometrical theory of diffraction, and its inadequacy for ka < 10 has previously been commented upon (Senior, 1965). Moreover, the primary source of the discrepancy is known to be the neglect of higher order terms in the expansion for the 'true' creeping wave decay factor.

(U) Inasmuchas the exact expression for the sphere creeping wave contribution is available, it is a trivial matter to find the numerical factor which, when applied to Eq. (4.7) (or, indeed, Eq. (4.9)), will yield the correct estimate for the creeping wave. Confining ourselves henceforth to the situation in which the infinite series is omitted, we show in Figs. 4-5 and 4-6 the modulus and phase respectively of the ratio of the true creeping wave contribution for a sphere to that computed using Eq. (4.7), i.e.

$$\Gamma(ka) = \left|\Gamma(ka)\right| \; e^{i\phi(ka)} = \left| \frac{S_{cw}}{S^{P}_{cw}} \right| .$$

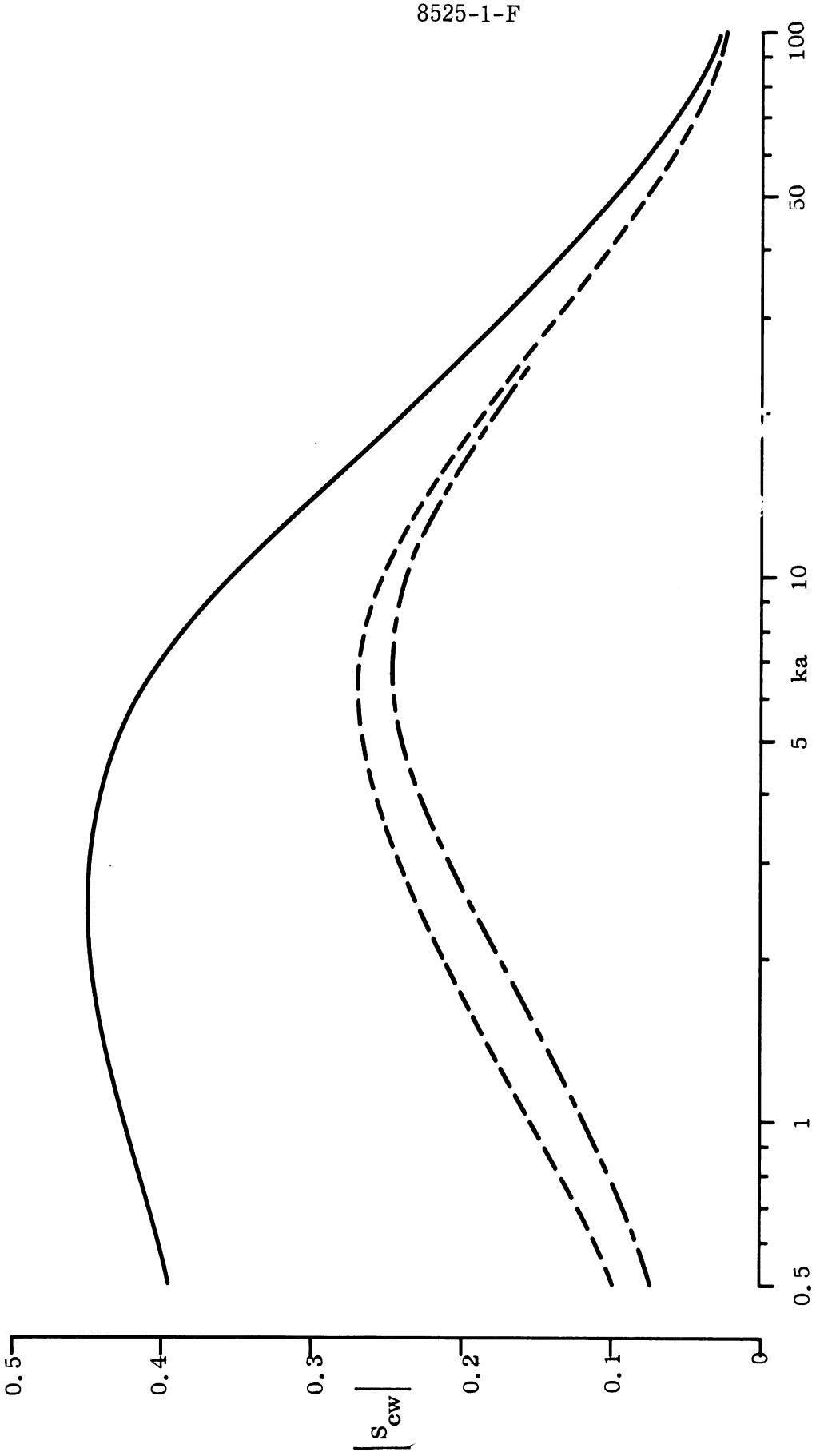

FIG. 4-4: MODULUS OF THE CREEPING WAVE CONTRIBUTION FOR A SPHERE COMPUTED USING EQ. (4.9) (– – –) AND EQ. (4.7) (– – –), COMPARED WITH THE EXACT VALUES (——).

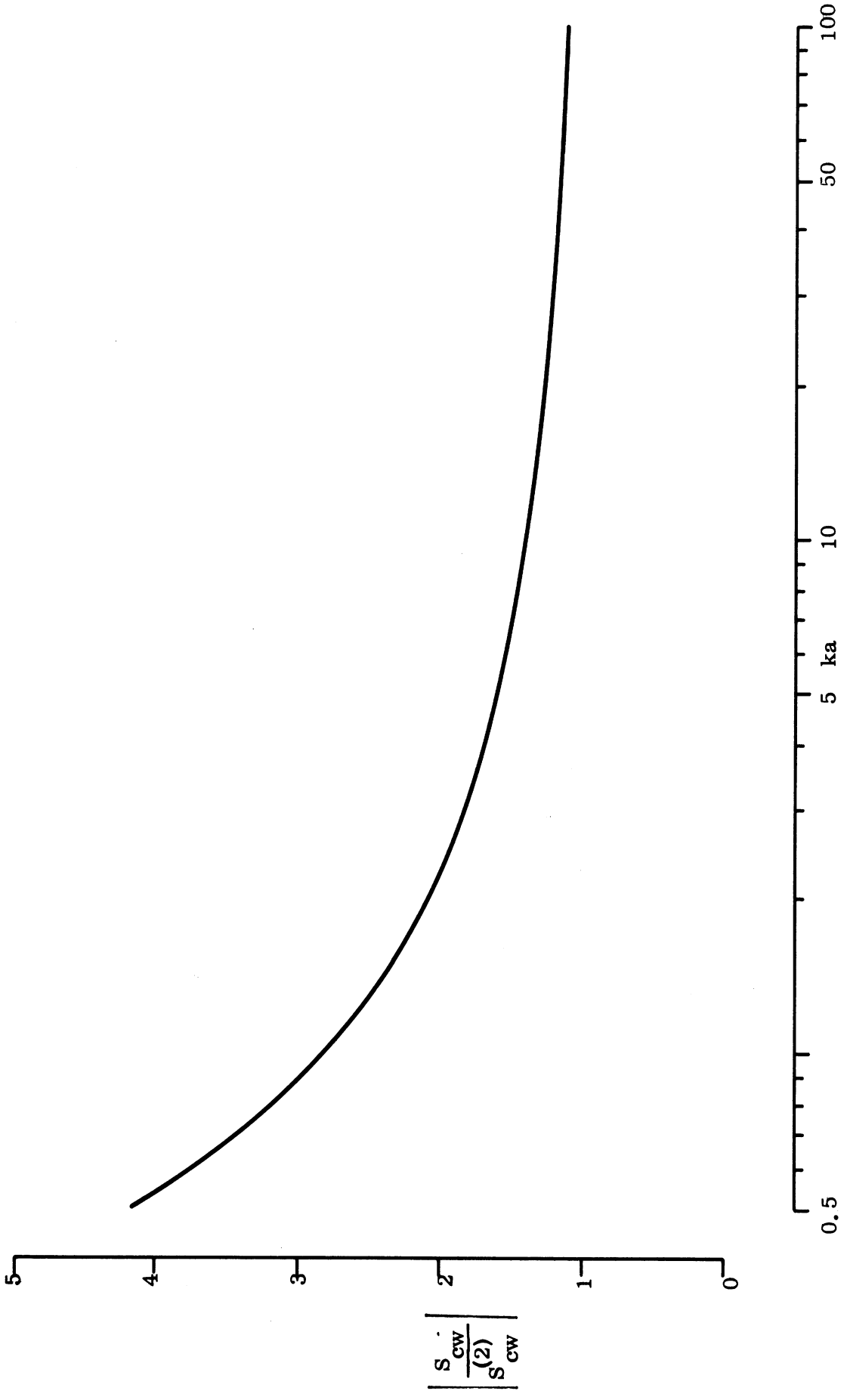

FIG. 4-5: RATIO OF EXACT CREEPING WAVE AMPLITUDE FOR A SPHERE TO THAT COMPUTED USING EQ. (4.7).

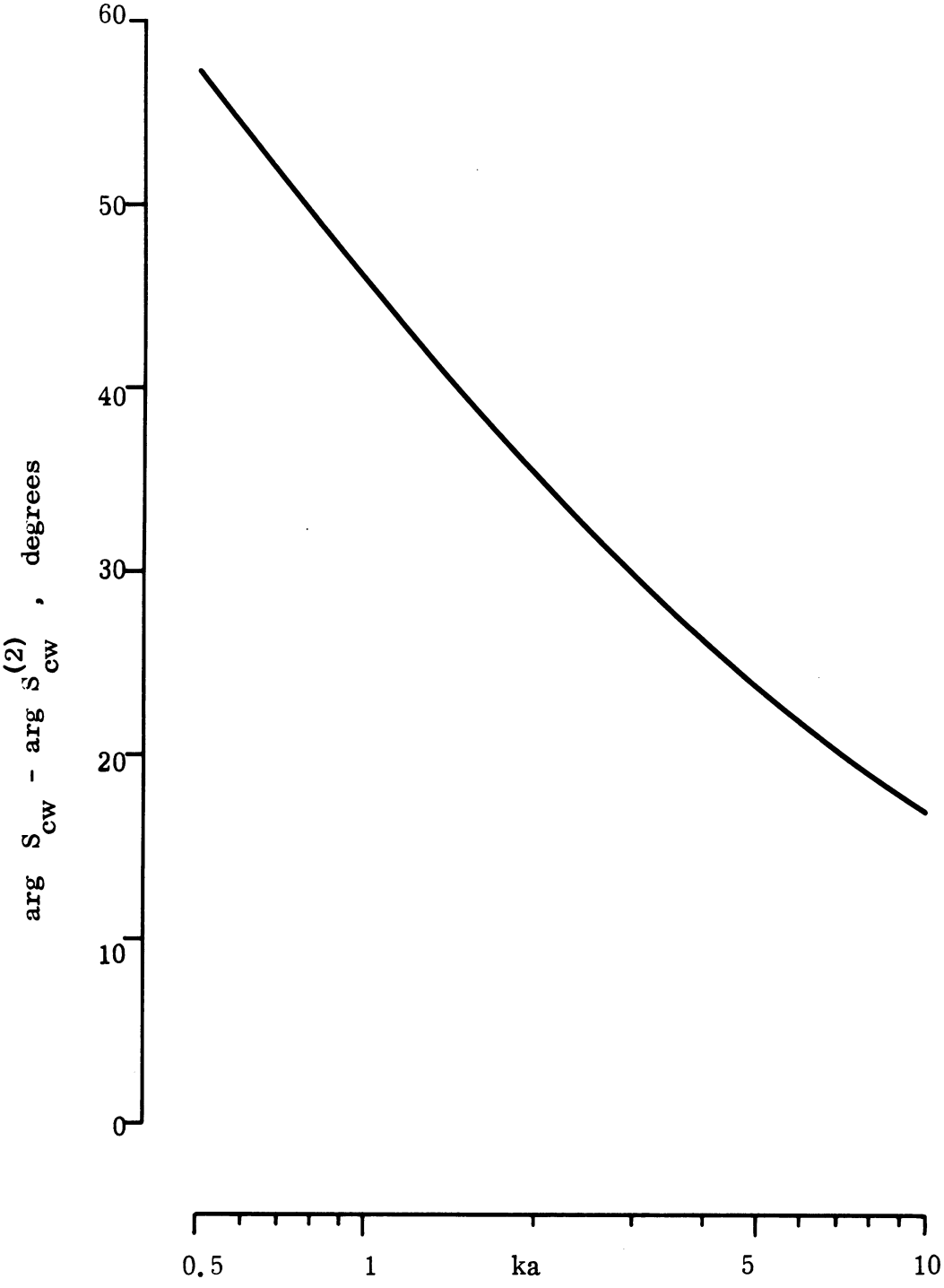

FIG. 4-6: PHASE DIFFERENCE BETWEEN EXACT AND APPROXMATE (EQ. 4.7) CREEPING WAVE CONTRIBUTION FOR A SPHERE.

Clearly, such a factor is of no practical utility if it relates only to a sphere, and we must next ask ourselves whether it can be used to correct the estimates for the creeping wave contributions of non-spherical terminations given in Fig. 4-2. To apply the factor $\Gamma(x)$ with the argument x equal to ka implies that the correction is primarily determined by the transverse radius at the shadow boundary, and it is found that this does not lead to a change in the modulus of the type satisfying the intuitive guidelines discussed in Section 3.5. On the other hand, it would seem most natural that the longitudinal, rather than the transverse, radius should be the relevent parameter, and if we use the factor $\Gamma(x)$ with $x = kb$, the resulting moduli of the creeping wave contribution for bodies having various $\alpha = b/a$ are as shown in Fig. 4-7, along with the bounding curves provided by a flat-backed cone and a cone-sphere. The curves now have much more the character expected of them. Their levels increase uniformly with decreasing α and, providing the curves are duly cut off at their intercepts with the curve for the flat-backed cone return, all are contained within the bounds set by the cone-sphere and flat-backed cone. It is therefore suggested that for a cone with non-spherical termination a reasonable estimate for the modulus of the creeping wave return should be obtained by following the flat-backed curve out to its intercept with the curve for the appropriate (non-zero) value of α, and thereafter following the latter curve. The estimate is, of course, only an approximation whose effectiveness for cross section purposes has yet to be determined. In particular, the abrupt change of slope at the intercept is obviously non-physical, and a better approximation should reveal a fairing-in of each higher-frequency curve as its intercept point is approached from above. We note in passing that with the four curves shown in Fig. 4-7 for $\alpha \neq 0, 1$, the point of intercept increases from $ka \simeq 1.8$ to $ka \simeq 20$ as α decreases from

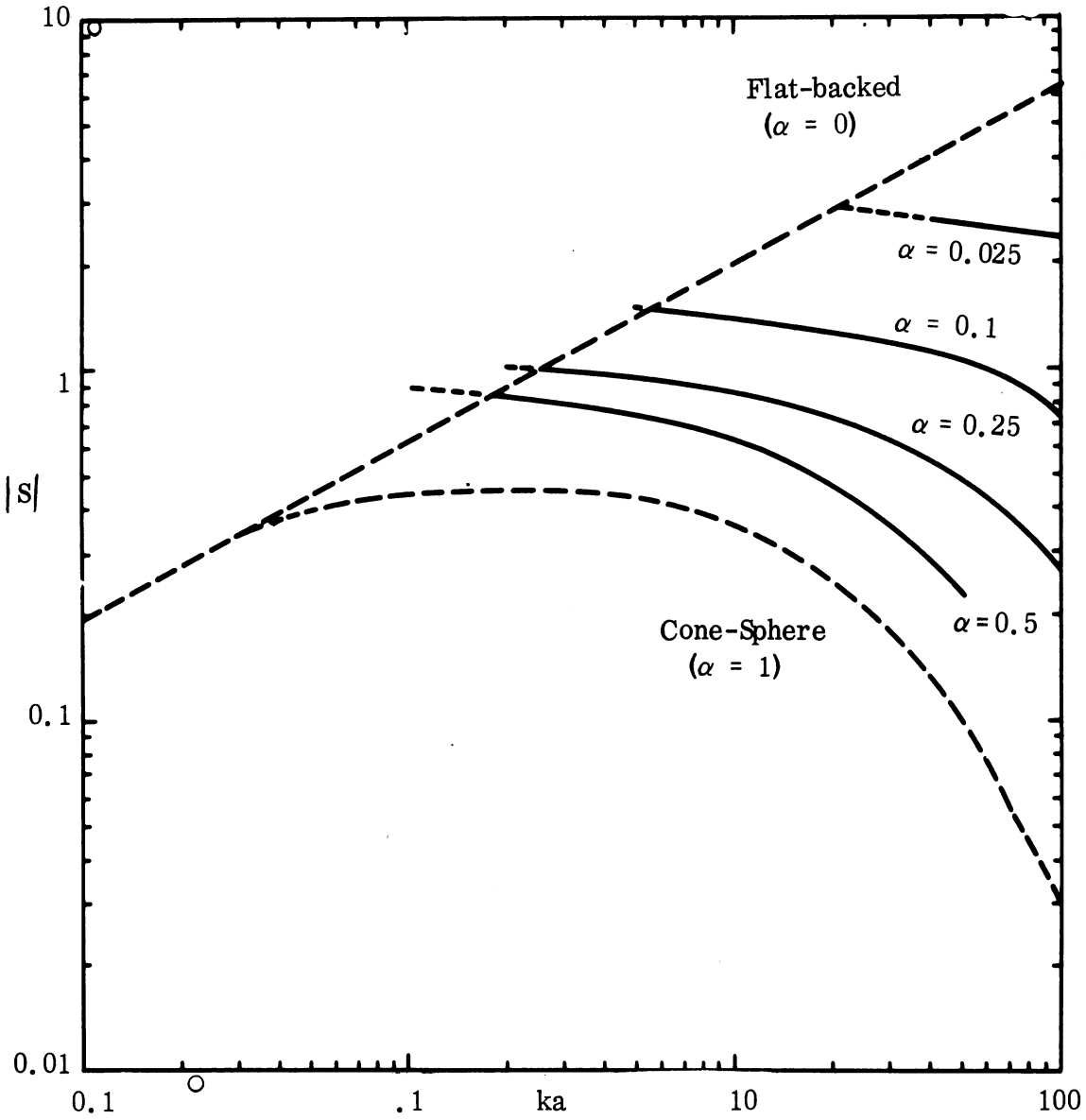

FIG. 4-7: AMPLITUDES OF THE CREEPING WAVE CONTRIBUTIONS FOR VARIOUS FB MODELS, DEDUCED FROM EQ. (4.7) AND USING THE CORRECTION FACTOR $\Gamma(kb)$.

0.5 to 0.025, corresponding to kb decreasing from 0.9 to 0.5. Values of $ka < 1$ are just those where we would expect a fairly rapid change in the nature of the scattering, with changes in the nature of the birth and launch weights of the creeping waves and, perhaps, some direct backscatter. Such transitional behavior is presently being studied using the parabolic cylinder as a model.

In spite of the round-about manner in which the curves in Fig. 4-7 have been derived, their theoretical basis is relatively simple. Bearing in mind that what we have really done is to 'correct' the estimate in Eq. (4.7) or, equivalently, Eq. (4.9) using the 'true' values for the creeping wave contribution of a sphere, it follows that for an FB model

$$S_{cw} = \frac{a}{2b} (kb/2)^{1/3} \frac{e^{2ik(a-b) + i\pi/12}}{\sqrt{2k(a-b)}} \times$$

$$\times \frac{1}{\beta_1 \left\{Ai(-\beta_1)\right\}^2} S^{(1)}(kb) \qquad (4.10)$$

where $S^{(1)}(kb)$ is the true far field amplitude of the creeping wave for a sphere of radius b. In effect we have used the function $S^{(1)}(kb)$ to account for the influence of the curved portion of the path, and modified the result by the space factor and differing birth and launch weights demanded by the FB model. The function $S^{(1)}(kb)$ has a relatively simple (asymptotic) expression which is numerically accurate over a very wide range of kb, and a selection of the available computed values was listed in Table IV-1 of Section 4.3.

(U) The amplitude of the function S_{cw} defined in Eq. (4.10) is certainly very close to that required for reproducing the measured backscatter for the

FB models. Moreover, since arg $S^{(1)}(kb)$ is almost a linear function of kb over a substantial range of kb, it is trivial to estimate arg S_{cw}. In particular, for $0.3 \leq kb \leq 3.0$ arg $S_{cw} = (114.592 + 73.42\,\alpha)\,ka + 186.312$ (degrees) with a maximum error of 0.6 degrees, and this phase is in excellent agreement with that demanded by the positions of the maxima and minima in the FB data when ka is large. In Section 3.4 we shall attempt to predict the nose-on scattering behavior of these models using the above expression for the creeping wave contribution.

4.3 Various Approximations for the Creeping Wave Contribution of a Sphere.

(U) In the course of our attempts to provide a numerically effective expression for the creeping wave contribution of the rear of a non-spherically terminated cone (e.g. one of the FB models), it has proved desirable to investigate various approximations for the creeping wave contribution of a sphere.

(U) For this purpose, consider a sphere of radius a illuminated with a plane wave. One of the major contributors to the far field amplitude is the creeping wave, and if we confine ourselves to the backscattering direction, then, as shown in Senior (1965), a highly accurate approximation to the creeping wave return is $S(ka) = S^{(1)}(ka)$ where*

$$S^{(1)}(ka) = \tau^4 e^{i\pi/3} \left\{ 1 + \frac{e^{i\pi/3}}{60\tau^2\beta_1^2} (32\beta_1^3 + 1) \right\} \cdot \frac{1}{\beta_1 \left\{ Ai(-\beta_1) \right\}^2}$$

$$\cdot \exp\left\{ i\pi\, ka - e^{-i\pi/6} \tau\pi\, \beta_1 - e^{i\pi/6} \frac{\pi}{60\tau\beta_1} (\beta_1^3 - 9) \right\} \qquad (4.11)$$

with $\tau = (ka/2)^{1/3}$ $\beta_1 = 1.01879297\ldots$,

* Note the omission of a factor π from the third terms in the exponents of Eqs. (90) and (91) of Senior (1965).

and $Ai(-\beta) = 0.53565666\ldots$. The phase origin has been taken at the center of the sphere (or, equivalently, at the shadow boundary) and a time factor $e^{-i\omega t}$ has been suppressed.

(U) The asymptotic approximations leading up to Eq. (4.11) are fully detailed in the above-referenced Report and computed values of $2/ka\, S^{(1)}(ka)$ are given in Table 10. As a result of the checks that have been carried out, it is concluded that for $ka \geq 0.7$, and certainly for $ka \geq 1.0$, the estimate of the creeping wave contributed provided by Eq. (4.11) is accurate enough for all practical purposes. Indeed, it is so accurate that throughout the rest of this section we shall regard Eq. (4.11) as giving an exact expression for the creeping wave amplitude.

(U) A selection of the computed values listed in Table 10 of Senior (1965) are reproduced in Table IV-1 along with the results of some later computations of the same expression for both larger and smaller values of ka. Although there can be no question of the meaningfulness of the results when ka is large, it is by no means certain that the same is true when $ka < 0.7$.

(U) An alternative, but inferior, approximation to the creeping wave contribution is that provided by the geometrical theory of diffraction. For numerical purposes, the associated expression can be obtained from Eq. (4.11) by omitting all higher order terms in the amplitude factor and in the exponent. If we denote the resulting expression by $S^k(ka)$, where the affix k is short for Keller, we have $S(ka) \simeq S^k(ka)$ where

$$S^k(ka) = \tau^4 e^{i\pi/3} \frac{1}{\beta_1 \left\{Ai(-\beta_1)\right\}^2} \exp\left\{i\pi\, ka - e^{-i\pi/6}\tau\pi\beta_1\right\}. \quad (4.12)$$

Computed values based on this expression were also given in Senior (1965).

TABLE IV-1

ka	$S^{(1)}(ka)$	arg $S^{(1)}(ka)$, degrees
0.3	0.372297	228.296
0.4	0.384624	246.592
0.5	0.394588	265.128
0.8	0.415880	322.146
1.0	0.425575	358.963
1.5	0.440747	453.178
2.0	0.447937	547.295
2.5	0.450308	641.232
3.0	0.449529	734.981
4.0	0.442182	921.945
5.0	0.430490	1108.302
8.0	0.386793	1664.667
10.0	0.357137	2033.961
15.0	0.291536	2953.574
20.0	0.239536	3869.785
25.0	0.198751	4783.771
50.0	0.088872	9335.938

A selection of this, together with some later ones, are shown in Table IV-2. The last two columns give the amplitude and phase of the factor

$$\Gamma^k(ka) \left[\equiv \frac{S^{(1)}(ka)}{S^k(ka)} \right]$$

by which $S^k(ka)$ must be multiplied to yield the exact creeping wave values. Observe the considerable error inherent in Eq. (4.12) for small values of ka, and the fact that the discrepancy (particularly in modulus) is still quantitively significant for ka as large as 10.

(U) We might seek to remove the part of this discrepancy by incorporating the effect of creeping waves other than the first, but still neglecting higher order terms in both the amplitude and exponential factors. In this way we obtain $S(ka) \simeq S^L(ka)$ where

$$S^L(ka) = 2\sqrt{\pi}\, \tau^4\, e^{i\pi(ka - 1/2)}\, \hat{q}(\xi_1), \qquad (4.13)$$

with $\xi_1 = \pi\tau$. The function

$$\hat{q}(\xi_1) = q^{(o)}(\xi_1) \sim \frac{1}{2\sqrt{\pi}\,\beta_1 \left\{ Ai(-\beta_1) \right\}^2} \exp\left\{ i\xi_1\beta_1 e^{i\pi/6} + 5\, i\pi/6 \right\}$$

has been tabulated by Logan (1959) for $\xi_1 = 0.5(0.1)8.0$ (see Table T of this reference) and the affix L used above is short for Logan. Computed values based on Eq. (4.13) are given in Table IV-3, and these are seen to be almost indistinguishable from the corresponding values of $S^k(ka)$ even for small ka. It therefore follows that Γ^L and Γ^k are almost identical, implying that the higher order creeping waves are not responsible [+] for the discrepancy between the exact and approximate values for the creeping wave.

[+] This is, of course, otherwise obvious from the fact that the so-called exact expression (4.11) involves only the lowest order creeping wave.

TABLE IV-2

ka	$\lvert S^k(ka)\rvert$	arg $S^k(ka)$	$\lvert \Gamma^k(ka)\rvert$	arg $\Gamma^k(ka)$
0.3	0.062515	162.718	5.9553	65.578
0.4	0.079104	185.621	4.8623	60.971
0.5	0.093985	207.762	4.1984	57.366
0.8	0.130797	271.559	3.1796	50.587
1.0	0.150426	312.775	2.8291	46.188
1.5	0.187865	413.307	2.3461	39.871
2.0	0.213971	511.691	2.0934	35.604
2.5	0.232604	608.771	1.9359	32.461
3.0	0.246002	704.960	1.8273	30.021
4.0	0.262324	895.524	1.6856	26.421
5.0	0.269735	1084.444	1.5960	23.858
8.0	0.266684	1645.551	1.4504	19.116
10.0	0.255656	2016.790	1.3969	17.171
15.0	0.221080	2939.480	1.3187	14.094
20.0	0.187926	3857.543	1.2746	12.242
25.0	0.159565	4772.797	1.2456	10.974
50.0	0.075535	9328.107	1.1765	7.831

TABLE IV-3

ka	$\lvert S^L(ka)\rvert$	arg $S^L(ka)$	$\lvert \Gamma^L(ka)\rvert$	arg $\Gamma^L(ka)$
0.3	0.062094	163.735	5.9957	64.560
0.4	0.078555	186.301	4.8962	60.291
0.5	0.093357	208.221	4.2267	56.907
0.8	0.130187	271.698	3.1945	50.448
1.0	0.149859	312.838	2.8398	46.125
1.5	0.187596	413.237	2.3494	39.941
2.0	0.213874	511.607	2.0944	35.688
2.5	0.232548	608.710	1.9364	32.522
3.0	0.245921	704.926	1.8279	30.055
4.0	0.262442	895.452	1.6849	26.493
5.0	0.269890	1084.382	1.5951	23.920
8.0	0.266701	1645.518	1.4503	19.149
10.0	0.255784	2016.737	1.3962	17.224
15.0	0.223762	2939.402	1.3029	14.172
20.0	0.187782	3857.461	1.2756	12.324
25.0	0.159842	4772.684	1.2434	11.087
50.0	Beyond range of Logan's table.			

(U) Still another approximation to the sphere creeping wave follows from Eq. (4.12) on rewriting the right hand side as

$$\tau^4 e^{i\pi\left(ka + \frac{1}{3}\right)} \beta_1 \left\{Ai(-\beta_1)\right\}^2 \left[\frac{1}{\beta_1 \left\{Ai(-\beta_1)\right\}^2} \right.$$

$$\left. \exp\left\{ -e^{-i\pi/6} \frac{\tau\pi\beta_1}{2} \right\} \right]^2$$

and if we now insert the effect of higher order creeping waves using Logan's function $\hat{q}(\xi)$, we have $S(ka) \simeq S^p(ka)$ where

$$S^p(ka) = -4\pi\tau^4 e^{i\pi(ka - 1/3)} \beta_1 \left\{Ai(-\beta_1)\right\}^2 \left[\hat{q}(\xi_2)\right]^2 \qquad (4.14)$$

with $\xi_2 = \pi\tau/2$. The affix p denotes a product form, and Eq. (4.14) can be visualized as resulting from the instantaneous launch and re-birth of all creeping waves after they have traversed only half their path.

(U) In view of our earlier finding about the numerical insignificance of the higher order creeping waves, it is to be expected that the approximation (4.14) will do little to remove the discrepancies inherent in S^k and S^L, and rather is it our aim to see if the incorporation of the product has worsened the approximation to any extent. This is important because of the role played by an expression analogous to (4.14) in our estimation of the creeping wave return for a non-spherical body.

(U) Computed values based on Eq. (4.14) are shown in Table IV-4. Observe that the differences between S^p and S^L or S^k are quite small except when ka is small; but what differences there are are such as to de-

TABLE IV-4

ka	$\lvert S^p(ka)\rvert$	arg $S^p(ka)$	$\lvert \Gamma^p(ka)\rvert$	arg $\Gamma^p(ka)$
0.3	0.070167	175.424	5.3059	52.872
0.4	0.085564	196.468	4.4952	50.124
0.5	0.099293	217.236	3.9740	47.892
0.8	0.133481	278.307	3.1156	43.839
1.0	0.151664	318.380	2.8060	40.583
1.5	0.186599	417.112	2.3620	36.066
2.0	0.211430	514.416	2.1186	32.879
2.5	0.229226	610.847	1.9645	30.385
3.0	0.242272	706.567	1.8555	28.414
4.0	0.258837	896.442	1.7083	25.503
5.0	0.266692	1084.974	1.6142	23.328
8.0	0.264679	1645.614	1.4614	19.053
10.0	0.254356	2016.774	1.4041	17.187
15.0	0.220739	2939.339	1.3207	14.235
20.0	0.187841	3857.420	1.2752	12.365
25.0	0.159657	4772.631	1.2449	11.140
50.0	0.075584	9328.035	1.1758	7.903

crease somewhat the discrepancy between the approximate and exact values for the creeping wave. This is presumed to be fortuitous.

(U) The final approximation that we wish to consider is one in which we attempt to account for some of the effect of the transverse curvature of the sphere (all previous approximations take into account only the curvature along the creeping wave path), thereby incorporating to some extent the contributions of the higher order terms in the exponential factor that were neglected in Eqs. (4.12) through (4.14). The result is analogous to S^p but differs in the presence of a series correction to Logan's function, namely $S(ka) \simeq S^s(ka)$ where

$$S^s(ka) = -4\pi\tau^4 e^{i\pi(ka - \frac{1}{3})} \beta_1 \left\{Ai(-\beta_1)\right\}^2 \left[\hat{q}(\xi_2)\right.$$

$$+ \frac{e^{i\pi/6}}{30\sqrt{\pi}} \frac{2^{1/3}}{(ka)^{2/3}} \sum_n \frac{1}{\left\{Ai(-\beta_n)\right\}^2} \left(1 + \frac{3}{\beta_n^3}\right)$$

$$\left. \exp\left(-\xi_2 \beta_n e^{-i\pi/6}\right)\right]^2 \qquad (4.15)$$

The affix s indicates the incorporation of the series, which series has been hand-computed for the required range of ka.

(U) Computations based on Eq. (4.15) are shown in Table IV-5, and the fact that immediately stands out is that the series does not carry out its intended function and does, indeed, increase the discrepancy between the approximate and exact values for the creeping wave contribution. The increase in the discrepancy is particularly noticeable for small ka, but is still evident for ka as large as 50. It must therefore to concluded that the approximation $S^s(ka)$ is numerically (if not mathematically) inviable.

TABLE IV-5

ka	$\lvert S^S(ka)\rvert$	arg $S^S(ka)$	$\lvert \Gamma^S(ka)\rvert$	arg $\Gamma^S(ka)$
0.3	0.056553	86.944	6.5832	141.352
0.4	0.065129	123.058	5.9056	123.534
0.5	0.074435	155.131	5.3011	109.997
0.8	0.101880	234.316	4.0821	87.830
1.0	0.118096	281.049	3.6036	77.914
1.5	0.151450	390.642	2.9102	63.536
2.0	0.176681	491.883	2.5353	55.412
2.5	0.195578	591.645	2.3024	49.587
3.0	0.207634	688.957	2.1650	46.024
4.0	0.228700	882.474	1.9335	39.471
5.0	0.240164	1073.220	1.7925	35.082
8.0	0.243499	1636.958	1.5885	27.709
10.0	0.234364	2008.934	1.5239	25.027
15.0	0.207960	2933.564	1.4019	20.010
20.0	0.179458	3852.819	1.3348	16.966
25.0	0.153791	4768.751	1.2923	15.020

(U) There is one overwhelming conclusion that can be reached as a result of our study, namely, that the higher order terms in the exponential factor and, perhaps, the amplitude factor of the creeping wave expression are numerically important for all but the very highest values of ka. Failure to include them, or to provide an adequate simulation of them, leads to estimates which are unsatisfactory for detailed computations of scattering behavior, and compared with these terms, higher order creeping wave contributions are comparatively insignificant.

(U) If the surface over which the creeping waves travel is not spherical, and cannot be decomposed into portions which are either planar or spherical, we have no alternative but to use one or other of the approximations (4.12) through (4.15). The approximation $S^{s}(ka)$ given in Eq. (4.15) is distinctly inferior to the other three, but of the others it would seem to matter little which we use. Based on computational convenience, $S^{k}(ka)$ given in Eq. (4.12) is the more attractive, and we would then have no alternative but to accept the error that this approximation entails. On the other hand, if we can incorporate the 'exact' expressions $S^{(1)}(ka)$, it is clearly to our advantage to do so, and one such 'non-spherical' shape for which this is possible is the rear of an FB model. Such an application is discussed in Section 3.4.

(U) There is one final point that can be made in regard to $S^{(1)}(ka)$ that is of some convenience in cross section estimation. Over substantial ranges of ka, $\arg S^{(1)}(ka)$ is almost a linear function of ka. Using the method of least squares, the following fits have been obtained:

$0.3 \leq 3.0$ (16 values):

$\arg S^{(1)}(ka) = 187.916\,ka + 171.312$

maximum underestimate is 0.610 degrees
maximum overestimate is 0.316 degrees

$1.0 \leq ka \leq 10.0$ (23 values)

$\arg S^{(1)}(ka) = 186.033\, ka + 176.327$

maximum underestimate is 1.810 degrees
maximum overestimate is 3.397 degrees.

4.4 Surface Current in the Illuminated Region on a Parabolic Cylinder. (Focal length is comparable to the incident wavelength).

4.4.1 Introduction

(U) The surface current in the shadow region had been studied earlier and the results of the study were reported in Section 3.3.2 of Goodrich et al, 1967c. In the illuminated region, the surface current may be represented by the summation of a geometrical optics term and a residue series which may be defined as the reflected creeping waves. In the penumbra region, the surface current may be obtained by the series expansion of the integral representation about a point on the shadow boundary.

4.4.2 Integral Representation for the Surface Current.

(U) In Section 3.3.2 of Goodrich et al, 1967c, the surface currents were shown to be

$$J_D = \frac{ik}{2\pi r} \frac{e^{-ikr}}{2} \sec\frac{\psi}{2} \int_{C_2} \frac{(i \tan\frac{\psi}{n})^n}{\sin \pi n} \frac{U_n(z)}{W_n(z'_o)}\, dn \qquad (4.16)$$

and

$$J_N = \frac{1}{\pi} \frac{e^{-ikr}}{2} \sec\frac{\psi}{2} \int_{C_2} \frac{(i \tan\frac{\psi}{2})^n}{\sin \pi n} \frac{U_n(z)}{W'_n(z'_o)}\, dn \qquad (4.17)$$

for Dirichlet and Neumann problems respectively. If we consider the region $x < 0$ where ξ is negative, we have the following relations

$$U_n(-z) = -i^{2n} V_n(z) - i^{-2n} W_n(z) \tag{4.18}$$

$$U_n(z) + V_n(z) + W_n(z) = 0 \tag{4.19}$$

$z = \sqrt{ik\xi}$ where $U_n(z)$ and $W_n(z)$ are defined by Eqs. (4.18) and (4.19).

(U) Following Rice's (1954) derivation, the leading terms in the asymptotic expansion for $U_n(-z)$ along the contour C_2 are obtained as follows:

$$U_n(-z) = (i^{-2n} - i^{2n}) A'_o + i^{-2n} A'_1 \tag{4.20}$$

$$A'_o = \frac{\sqrt{t'_o}\, e^{f(t'_o)}}{2i\sqrt{\pi}\,(ik\xi^2 - 2m)^{1/4}} \tag{4.21}$$

$$A'_1 = \frac{\sqrt{t'_i}\, e^{f(t'_i)}}{2\sqrt{\pi}\,(ik\xi^2 - 2m(^{1/4}} \tag{4.22}$$

$$f(t') = zt' + m/2 - m \ell n\, t' \tag{4.23}$$

$$t'_o = \frac{1}{2}\left[\sqrt{ik}\,\xi + \sqrt{ik\,\xi^2 - 2m}\right] \tag{4.24}$$

$$t'_1 = \frac{1}{2}\left[\sqrt{ik}\,\xi - \sqrt{ik\,\xi^2 - 2m}\right] \tag{4.25}$$

$$m = n + 1$$

$$z = \sqrt{ik}\,\xi\,, \qquad \xi > 0\,.$$

In fact, the asymptotic expressions of the function $U_n(-z)$ in the various

regions of the m-plane are listed in the following table when $z = i^{1/2}\sqrt{k}\,\xi$, $\sqrt{k}\,\xi > 0$.

Region in m - plane m = n + 1	$U_n(-z)$
I_a	$(i^{-2n} - i^{2n})\,A'_o + i^{-2n}\,A'_1$
II	$-i^{2n}\,A'_o + i^{-2n}\,A'_1$
I_b	$(i^{-2n} - i^{2n})(A'_o + A'_1)$
III	$(i^{-2n} - i^{2n})\,A'_o$

The contour C_2 passes through regions I_a and II in which $U_n(-z)$ has different asymptotic forms (Fig. 4-8). Because the stationary phase point is found within the region I_a, i.e.

$$\frac{-i\eta_o^2}{2} < \alpha_o < \frac{i\xi^2}{2} \quad ,$$

we may use the asymptotic form in I_a for $U_n(-z)$ along the entire contour C_2. When (4.20) is substituted back into (4.16) and (4.17) we obtain

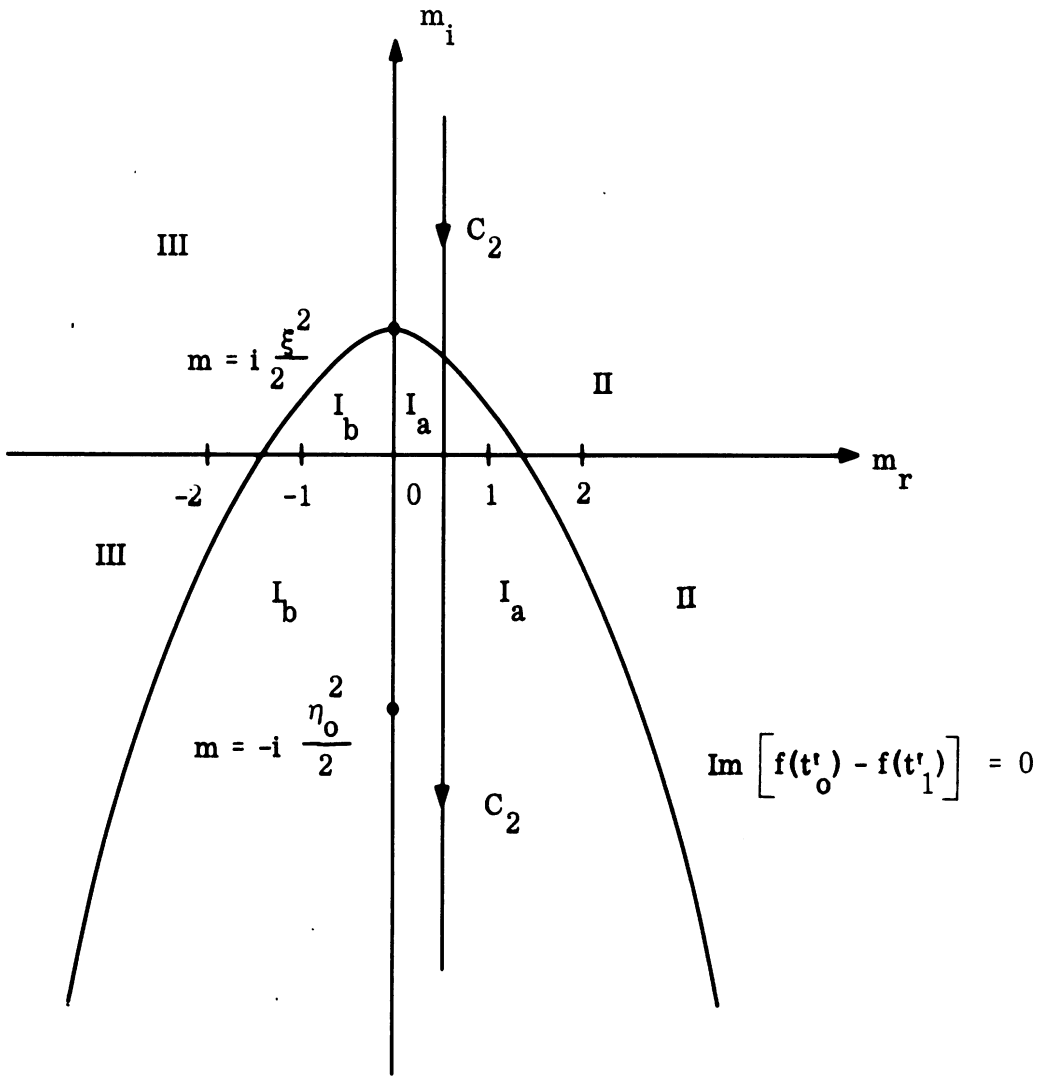

FIG. 4-8: REGION IN THE COMPLEX m-PLANE CORRESPONDING TO DIFFERENT ASYMPTOTIC EXPRESSIONS WHEN $\xi = \sqrt{ik}\,\xi$.

$$J_D = -2i\,M_o \int_{C_2} (i\omega)^n \frac{A'_o}{W_n(z'_o)}\,d_n + M_o \int_{C_2} \left(\frac{\omega}{i}\right)^n \cdot \frac{A'_1\,dn}{\sin \pi n\, W_n(z'_o)} \tag{4.26}$$

and

$$J_N = -2i\,N_o \int_{C_2} (i\omega)^n \frac{A'_o}{'W_n(z'_o)}\,dn + N_o \int_{C_2} (\omega/i)^n \frac{A'_1\,dn}{\sin \pi n\, 'W_n(z'_o)} \tag{4.27}$$

where $\omega = \tan \frac{\psi}{2}$,

$$M_o = \sqrt{\frac{ik}{2\pi r}}\,\frac{e^{-ikr}}{2} \sec \frac{\psi}{2} \quad \text{and} \quad N_o = \frac{e^{-ikr}}{2\sqrt{\pi}} \sec \frac{\psi}{2} .$$

In the following sections, we will see that the first term may be recognized as the geometrical optics term. The second term may be expressed by a residue series which represents creeping waves launched from the shadow boundary and traveling along the surface of the parabolic cylinder into the illuminated region. It may be called the reflected creeping waves (Fig. 4-9).

4.4.3 The Method of Geometrical Optics.

(U) The first term of (4.26) and (4.27) may be calculated by the stationary phase method when $k \to \infty$. The asymptotic forms of the functions $W_n(z'_o)$ and $'W_n(z'_o)$ along the contour C_2 are given by

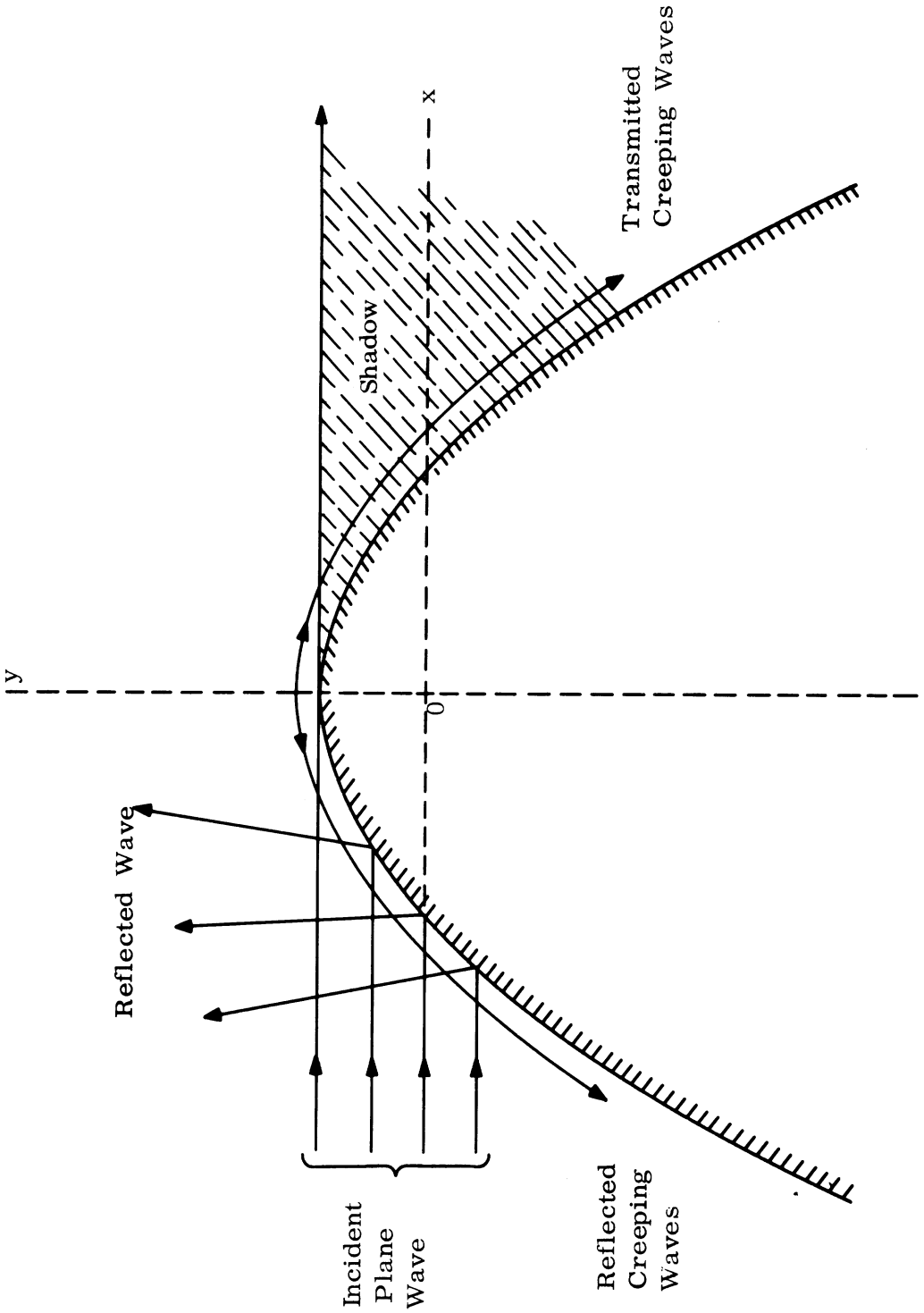

FIG. 4-9: GEOMETRICAL OPTICS AND CREEPING WAVES.

$$W_n(z'_o) = A_o \tag{4.28}$$

and

$$'W_n(z'_o) = \sqrt{(z'_o)^2 - 2m}\ A_o \tag{4.29}$$

where

$$A_o = \frac{\sqrt{t_o}\ e^{f(t_o)}}{-2i\sqrt{\pi}\ (-i\rho^2 - 2m)^{1/4}} \tag{4.30}$$

$$t_o = \frac{1}{2}\left[\sqrt{-i}\ \rho + \sqrt{-i\rho^2 - 2m}\right] \tag{4.31}$$

$$f(t_o) = z'_o t_o + \frac{m}{2} - m\ 1_n t_o \tag{4.32}$$

$$z'_o = \sqrt{-i}\ \rho = \sqrt{-i\ k}\ \eta_o = \sqrt{-2i\,k\,h}\ .$$

Therefore, the first term (4.26) and (4.27) becomes

$$J_{D_o} = -2i\,M_o \int_{C_2} (i\omega)^n \frac{A'_o}{A_o}\ dn \tag{4.33}$$

$$J_{N_o} = -2i\,N_o \int_{C_2} \frac{(i\omega)^n}{\sqrt{-i\rho^2 - 2m}}\ \frac{A'_o}{A_o}\ dn \tag{4.34}$$

where

$$\frac{A'_o}{A_o} = -\sqrt{\frac{t'_o}{t_o}}\left[\frac{-i\rho^2 - 2m}{ik\xi^2 - 2m}\right]^{1/4} e^{f(t'_o) - f(t_o)} \tag{4.35}$$

$$f(t'_o) - f(t_o) = ikr - ik\left\{\frac{\xi}{2}\sqrt{\xi^2 + 2i\,(m/k)} + \frac{\eta_o}{2}\sqrt{\eta_o^2 - 2i(m/k)} - \right.$$

$$\left. - i\,(m/k)\,\ell n\left[(-i)\,\frac{\eta_o + \sqrt{\eta_o^2 - 2i\,(m/k)}}{\xi + \sqrt{\xi^2 + 2i\,(m/k)}}\right]\right\} \qquad (4.36)$$

$\omega = \tan \psi/2.$

Introducing the new variable of integration $\alpha = i\,(m/k)$, we obtain

$$J_{D_o} = \frac{-ik}{\sin\frac{\psi}{2}}\sqrt{\frac{ik}{2\pi r}}\int_{C_2}\left[\frac{\xi + \sqrt{\xi^2 + 2\alpha}}{\eta_o + \sqrt{\eta_o^2 - 2\alpha}}\right]^{1/2}$$

$$\left[\frac{\eta_o^2 - 2\alpha}{\xi^2 + 2\alpha}\right]^{1/4} e^{-ik\,\Phi\,(\alpha)}\,d\alpha \qquad (4.37)$$

and

$$J_{NZ_o} = \frac{1}{\sin\frac{\psi}{2}}\sqrt{\frac{ik}{\pi}}\int_{C_2}\left[\frac{\xi + \sqrt{\xi^2 + 2\alpha}}{\eta_o + \sqrt{\eta_o^2 - 2\alpha}}\right]^{1/2}$$

$$\frac{e^{-ik\,\Phi\,(\alpha)}\,d\alpha}{\left[(\xi^2 + 2\alpha)\,(\eta_o^2 - 2\alpha)\right]^{1/4}} \qquad (4.38)$$

where

$$\Phi\,(\alpha) = \frac{\xi}{2}\sqrt{\xi^2 + 2\alpha} + \frac{\eta_o}{2}\sqrt{\eta_o - 2\alpha} -$$

$$- \alpha\,\ell n\left[\omega\left(\frac{\eta_o + \sqrt{\eta_o^2 - 2\alpha}}{\xi + \sqrt{\xi^2 + 2\alpha}}\right)\right] \qquad (4.39)$$

The stationary point of the phase $\bar{\Phi}(\alpha)$ is obtained from

$$\bar{\Phi}'(\alpha) = \ell n \left[\omega \left(\frac{\eta_o + \sqrt{\eta_o^2 - 2\alpha}}{\xi + \sqrt{\xi^2 + 2\alpha}} \right) \right] = 0$$

as

$$\omega \left(\eta_o + \sqrt{\eta_o^2 - 2\alpha} \right) = \xi + \sqrt{\xi^2 + 2\alpha} \quad . \tag{4.40}$$

The Eq. (4.40) has a real root if $\eta_o \omega < \sqrt{\xi^2 + 2\alpha} + \xi$. On solving this inequality, we find $\xi > -\eta_o \cot \psi$. The point $\xi = -\eta_o \cot \psi$ is the boundary of the shadow and the points $\xi > -\eta_o \cot \psi$ are located in the illuminated region (Fig. 4-10). Thus the stationary point of the phase $\bar{\Phi}(\alpha)$ exists only if the point of observation is situated in the illuminated region. Solving (2.40), the stationary point is found as

$$\alpha_o = \sin \psi \left(\frac{\eta_o^2 - \xi^2}{2} \sin \psi - \xi \eta_o \cos \psi \right) \quad . \tag{4.41}$$

Substituting α_o int the phase function $\bar{\Phi}(\alpha)$ we have

$$\bar{\Phi}(\alpha) = \xi \eta_o \sin \psi - \frac{\eta_o^2 - \xi^2}{2} \cos \psi \quad . \tag{4.42}$$

$$= x \sin \psi - y \cos \psi$$

and also

$$\sqrt{\xi^2 + 2\alpha_o} = \eta_o \sin \psi - \xi \cos \psi$$

$$\sqrt{\eta_o^2 - 2\alpha_o} = \eta_o \cos \psi + \xi \sin \psi$$

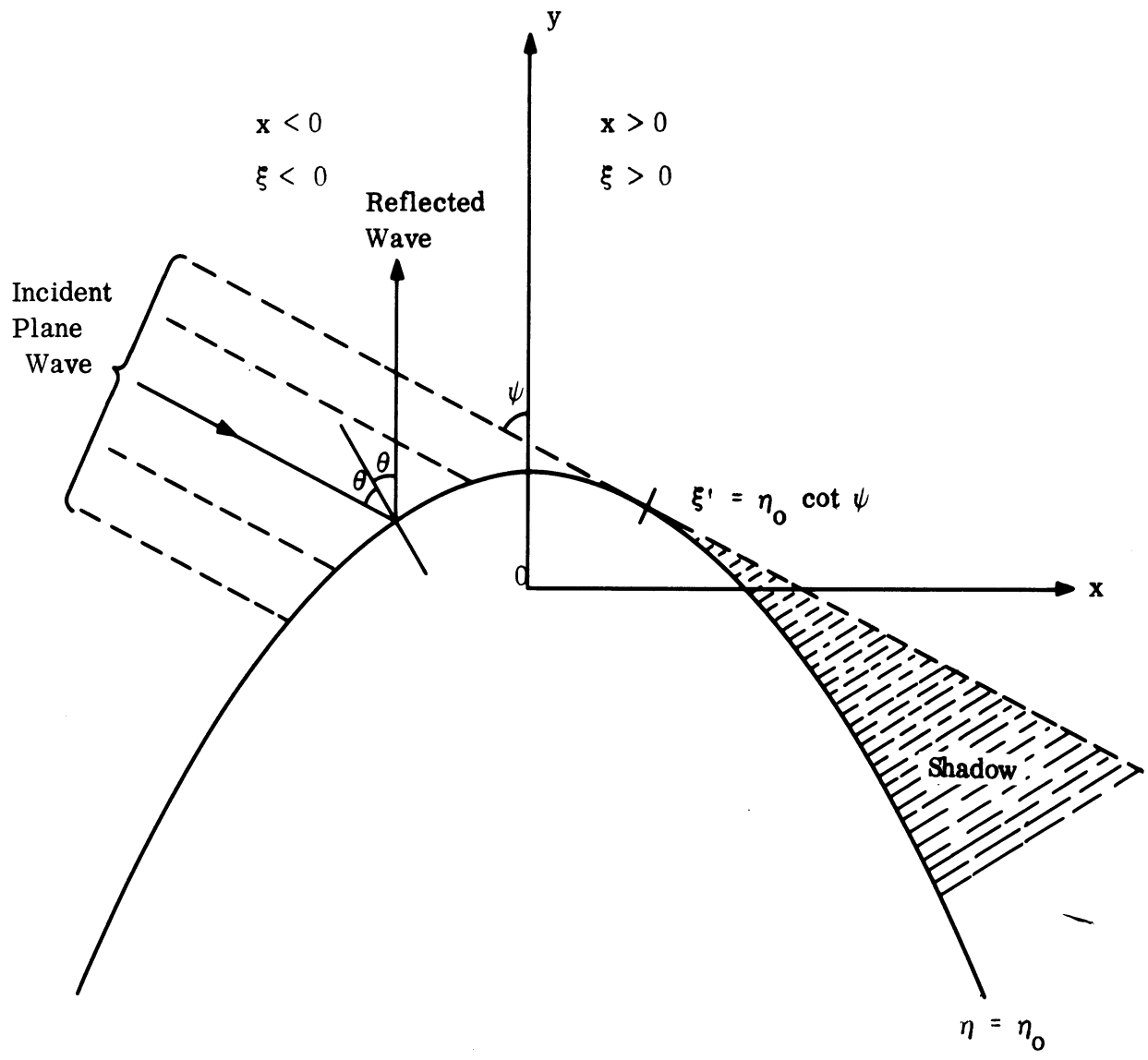

FIG. 4-10: GEOMETRICAL OPTICS.

$$\Phi''(\alpha_o) = \frac{-1}{\sin\psi\,(\eta_o \cos\psi + \xi \sin\psi)\,(\eta_o \sin\psi - \xi \cos\psi)}$$

$$r = \frac{1}{2}\,(\eta_o^2 + \xi^2).$$

Now the asymptotic expressions of the surface current in the illuminated region are obtained as follows:

$$J_{D_o} = -2ik \frac{\eta_o \cos\psi + \xi \sin}{\sqrt{\xi^2 + \eta_o^2}} \exp\left\{-ik\,(x \sin\psi - y \cos\psi)\right\} \quad (4.43)$$

$$J_{N_o} = 2 \exp\left\{-ik\,(x \sin\psi - y \cos\psi)\right\}. \quad (4.44)$$

It can be shown that the quantity $(\eta_o \cos\psi + \xi \sin\psi)/\sqrt{\xi^2 + \eta_o^2}$ in (4.43) is the cosine of the angle of incidence θ (Fig. 4-10), and the exponential factor is the incident plane wave U_o (Ivanov, 1963). Thus,

$$J_{D_o} = -2ik \cos\theta\, U_o \quad (4.45)$$

$$J_{N_o} = 2\, U_o \quad (4.46)$$

i.e. the distribution of current in the illuminated region is described asymptotically by geometrical optics.

4.4.4 Reflected Creeping Waves.

(U) The second term of (4.26) and (4.27) may be calculated by the sum of the residues at poles given by $W_n(z'_o) = 0$ and $'W_n(z'_o) = 0$. In Section 3.3.2 of Goodrich et al, 1967c, it has been shown that all zeros of both functions $W_n(z'_o)$ and $'W_n(z'_o)$ are located in the third quadrant of the n-

plane. The contour C_2 may be deformed into C_3 containing all poles (as in the above reference). Thus the asymptotic behavior of the integral is defined by the poles of the integrand. Therefore, we obtain

$$J_{D_c} = -2\pi i M_o \sum_{s=1}^{\infty} \left[\frac{(\omega/i)^n A'_1}{\sin \pi n \frac{\partial}{\partial n} W_n(z'_o)} \right]_{n = n_s} \tag{4.47}$$

and

$$J_{N_c} = -2\pi i N_o \sum_{s=0}^{\infty} \left[\frac{(\omega/i)^n A'_i}{\sin \pi n \frac{\partial}{\partial n} {}'W_n(z'_o)} \right]_{n = n'_s} \tag{4.48}$$

where n_s and n'_s are zeros of the functions $W_n(z'_o)$ and ${}'W_n(z'_o)$ respectively, and they are obtained as follows:

$$m_p = n_s + 1 = -\frac{1}{2}\left[(\rho + 2.8) + i(\rho^2 + \rho + 1.4)\right] \tag{4.49}$$

$$m'_p = n'_s + 1 = -\frac{1}{2}\left[\left(\frac{2}{\pi}\rho + \frac{1}{5}\right) + i(\rho^2 + \rho)\right] \tag{4.50}$$

and also we have

$$\frac{\partial}{\partial n} W_n(z'_o)\Big|_{n=n_s} = -\left[\ell n\,(t_o/t_1)\right] A_o \tag{4.51}$$

$$\frac{\partial}{\partial n} {}'W_n(z'_o)\Big|_{n=n'_s} = -\sqrt{-i\rho^2 - 2m'_p}\left[\ell n\,(t_o/t_1)\right] A_o\,. \tag{4.52}$$

Let us assume a plane wave impinges upon the parabolic cylinder at an angle

$\psi = \frac{\pi}{2}$, then we have $\omega = \tan\frac{\psi}{2} = 1$. If we consider the leading terms of the residue series, the reflected creeping waves are given by

$$J_{D_c} = 2\pi\, i\, M_o \frac{A'_1/A_o}{(i)^{n_s} \sin \pi\, n_s\, \ell n\,(t_o/t_1)} \tag{4.53}$$

$$J_{N_c} = 2\pi\, i\, N_o \frac{A'_1/A_o}{(i)^{n'_s} \sin \pi\, n'_s \sqrt{-i\rho^2 - 2m'_p}\; \ell n\,(t_o/t_1)} \tag{4.54}$$

here

$$\frac{A'_1}{A_o} = i\sqrt{\frac{t'_1}{t_o}} \left[\frac{-\rho^2 - 2m}{ik\xi^2 - 2m}\right] e^{f(t'_1) - f(t_o)}$$

$m = m_p$ for Dirichlet problem

$= m'_p$ for Neumann problem.

Simplifying the expressions in (4.53) and (4.54), we obtain

$$J_{D_c} = 2k\sqrt{\frac{\pi}{kr}} \left[\frac{-i\rho^2 - 2m_p}{ik\xi^2 - 2m_p}\right]^{\frac{1}{4}} \frac{\exp\left[\bar{\Phi}(\xi)\right]}{e^{i\pi m_p}(1 - e^{i2\pi m_p})\ell n(t_o/t_1)} \tag{4.55}$$

$$J_{N_c} = \frac{2\sqrt{2\pi}\; i^{3/2} \exp\left[\bar{\Phi}(\xi)\right]}{\left[(ik\xi^2 - 2m'_p)(-i\rho^2 - 2m'_p)\right]^{1/4} e^{i\pi m'_p}(1 - e^{i2\pi m'_p})\ell n\,(t_o/t_1)} \tag{4.56}$$

where the phase $\bar{\Phi}(\xi)$ is expressed by

$$\Phi(\xi) = (m - \tfrac{1}{2})\,\ell n\left[\frac{\sqrt{k}\xi + \sqrt{k\xi^2 + 2\,im}}{\sqrt{-2\,im}}\right] + i\frac{\sqrt{k}\xi}{2}\sqrt{k\xi^2 + 2\,im} +$$

$$+ i\frac{\rho}{2}\sqrt{\rho^2 - 2im} + (m - \tfrac{1}{2})\,\ell n\left[\frac{\rho + \sqrt{\rho^2 - 2\,im}}{\sqrt{-2\,im}}\right] . \qquad (4.57)$$

(U) Let S be length of the arc of the parabola between the point $\xi = 0$ and $\xi = \xi$, and

$$D = (2h)^{1/3}\,\ell n\left[\frac{\xi + \sqrt{\xi^2 + 2h}}{\sqrt{2h}}\right] ,$$

then (4.55) and (4.56) reduce to

$$J_{D_c} \approx kA(\xi)\exp\left\{-ikS - \frac{k^{1/3}}{2}\left[(\rho + 3.8) + i(\rho + 1.4)\right]\frac{D}{\rho^{2/3}}\right\} \qquad (4.58)$$

$$J_{N_c} \approx A'(\xi)\exp\left\{-ikS - \frac{k^{1/3}}{2}\left[(\frac{2}{\pi}\rho + 1.2) + i\rho\right]\frac{D}{\rho^{2/3}}\right\} \qquad (4.59)$$

where $A(\xi)$ and $A'(\xi)$ are amplitude functions, and they are given by

$$A(\xi) = 2\sqrt{\frac{\pi}{kr}}\left[\frac{-i\rho^2 - 2m_p}{ik\xi^2 - 2m_p}\right]^{1/4}\frac{1}{\ell n\,(t_o/t_1)}\left[\frac{e^{-i\pi m_p}}{1 - e^{i2\pi m_p}}\right]$$

$$A'(\xi) = \frac{2\sqrt{2\pi}\; i^{3/2}}{\left[(ik\xi^2 - 2m'_p)(-\rho^2 - 2m'_p)\right]^{1/4}\ell n(t_o/t_1)}\left[\frac{e^{-i\pi m'_p}}{1 - e^{i2\pi m'_p}}\right] \qquad (4.60)$$

(U) The reflected creeping waves are exactly the same as the transmitted creeping waves in the shadow region except for a constant factor

$$e^{-m\pi} / (1 - e^{i2m\pi}) .$$

Both are launched from the shadow boundary. One propagates into the illuminated region and the other into the shadow region. Let us define this constant factor as the ratio of reflection to transmission, then we have

$$C(m) = \frac{e^{-i m\pi}}{1 - e^{i2m\pi}} \tag{4.61}$$

where $m = m_p$ for Dirichlet problem, $m = m'_p$ for Neumann problem. In general, $|C(m)|$ is negligibly small for $\rho > 1$ (Fig. 4-11). Therefore, reflected creeping waves may be neglected in the case of large parabolic cylinders.

4.4.5 The Surface Current in the Region of Penumbra.

(U) The function $U_n(z)$ in (4.16) and (4.17) may be expanded into a series about a point on the shadow boundary. If we expand exp (2zt) in the following integral

$$U_n(z) = \frac{1}{2\pi i} \int_u \exp\left\{-t^2 + 2zt - (n+1)\ell n\, t\right\} dt \tag{4.62}$$

and integrate termwise, then the function $U_n(z)$ becomes

$$U_n(z) = -\frac{\sin \pi n}{2\pi} \sum_{\ell=0}^{\infty} (-2z)^{\ell} \Gamma(\ell - n/2)/\ell! \tag{4.63}$$

Therefore, we obtain the surface current in the following forms

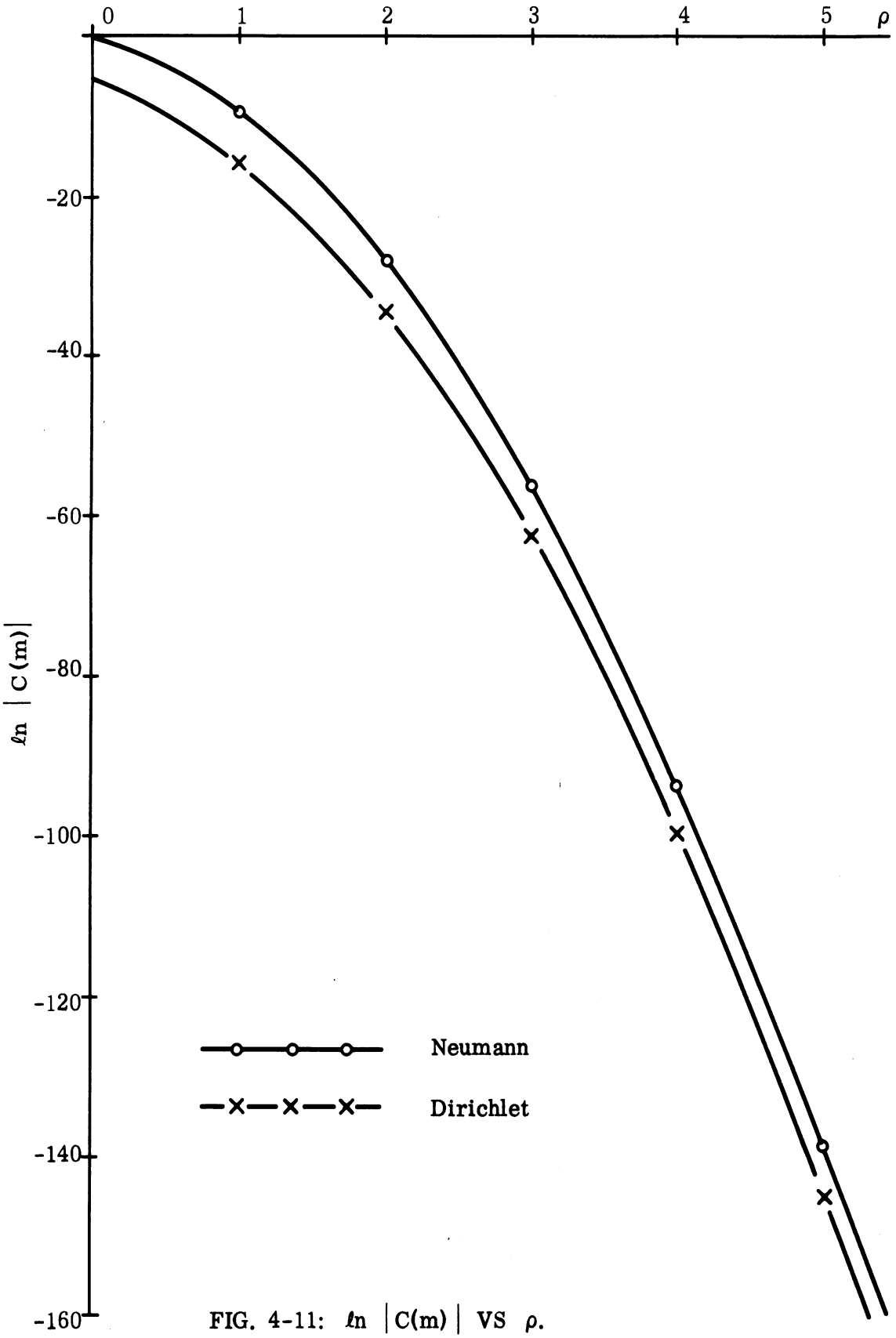

FIG. 4-11: ℓn |C(m)| VS ρ.

$$J_D = -\frac{M_o}{2\pi} \sum_{\ell=0}^{\infty} \frac{(-2z)^\ell}{\ell!} \int_{C_2} \frac{(i\omega)^n \Gamma(\ell - n/2)}{W_n(z'_o)}\, dn \qquad (4.64)$$

$$J_N = -\frac{N_o}{2\pi} \sum_{\ell=0}^{\infty} \frac{(-2z)^\ell}{\ell!} \int_{C_2} \frac{(i\omega)^n \Gamma(\ell - n/2)}{'W_n(z'_o)}\, dn \,. \qquad (4.65)$$

Now (4.64) and (4.65) may be evaluated by the residue series. If only leading terms are considered, we obtain

$$J_D = -M_o \frac{2\sqrt{\pi}\,(-i\rho^2 - 2m_p)^{1/4}\,(i\omega)^{n_s}}{\ell n\,(t_o/t_1)\,\sqrt{t_o}\,e^{f(t_o)}} \sum_{\ell=0}^{\infty} \frac{(-2z)^\ell}{\ell!}\,\Gamma\left(\frac{\ell - n_s}{2}\right)$$

$$\approx i M_o \frac{2\pi\sqrt{2}\,(-i\rho^2 - 2m_p)^{1/4}(\omega)^{n_s}}{\ell n(t_o/t_1)\,\Gamma(-n_s/2)(2m_p)^{1/4}}$$

$$\exp\left\{(m_p - \tfrac{1}{2})\,\ell n\,\frac{t_o}{\sqrt{2m_p}} - \sqrt{-i\rho}\,t_o\right\} \sum_{\ell=0}^{\infty} \frac{(-2z)^\ell}{\ell!}\,\Gamma\left(\frac{\ell - n_s}{2}\right) \qquad (4.66)$$

$$J_N = -N_o \frac{2\sqrt{\pi}\,(i\omega)^{n'_s} e^{-f(t_o)}}{\ell n(t_o/t_1)\sqrt{t_o}(-i\rho^2 - 2m'_p)^{1/4}} \sum_{\ell=0}^{\infty} \frac{(-2z)^\ell}{\ell!}\,\Gamma\left(\frac{\ell - n'_s}{2}\right)$$

$$\approx i N_o \frac{2\pi\sqrt{2}\,(\omega)^{n'_s}}{\ell n(t_o/t_1)(2m'_p)^{1/4}\,\Gamma(-n'_s/2)\,(-i\rho^2 - 2m'_p)^{1/4}}$$

continued

$$\exp\left\{(m'_p - \tfrac{1}{2})\ln\frac{t_o}{\sqrt{2m'_p}} - \sqrt{-i}\,\rho t_o\right\}\sum_{\ell=0}^{\infty}\frac{(-2z)^\ell}{\ell!}\,\Gamma\left(\frac{\ell - n'_s}{2}\right), \quad (4.67)$$

where $z = \sqrt{ik}\,\xi$, n_s and n'_s are zeros of $W_n(z'_o)$ and $'W_n(z'_o)$, respectively, and $m = n + 1$.

(U) When $\omega = 1$, we have $\xi > 0$ for the shadow region, $\xi < 0$ for the illuminated region. Equations (4.65) and (4.66) converge absolutely for all values of ξ. They are especially useful in calculating the surface current near the shadow boundary where $\xi = 0$. At $\xi = 0$, (4.65) and (4.66) are identical with (3.72) and (3.73) in Goodrich et al, 1967c.

4.5 Zeros of Parabolic Cylinder Functions

(U) In the study of creeping waves, surface currents in the shadow region are represented by the residue series which are evaluated from poles (see Section 4.4 of this report and Section 3.3.2 of Goodrich et al, 1967c). It is desirable to investigate the location of poles in order to see how far the high frequency approximation can be extended into the low frequency region.

(U) For this purpose, let us consider a perfectly conducting parabolic cylinder $x^2 = 4h(h - y)$ of focal length h illuminated with a plane wave $e^{ik(x\sin\psi - y\cos\psi)}$ with the time factor $e^{i\omega t}$. Then surface current densities are

$$J_D = \sqrt{\frac{k}{2\pi ri}}\,\frac{e^{-ikr}}{2}\sec\frac{\psi}{2}\int_c \frac{(i\tan\frac{\psi}{2})^n}{\sin\pi n}\,\frac{U_n(\sqrt{ik}\,\xi)}{W_n(\sqrt{-ik}\,\eta_o)}\,dn \quad (4.68)$$

$$J_N = \frac{1}{\pi}\,\frac{e^{-ikr}}{2}\sec\frac{\psi}{2}\int_c \frac{(i\tan\frac{\psi}{2})^n}{\sin\pi n}\,\frac{U_n(\sqrt{ik}\,\xi)}{'W_n(\sqrt{-ik}\,\eta_o)}\,dn \quad (4.69)$$

where J_D and J_N indicate respectively the Dirichlet problem and the Neumann problem. The contour c encloses all positive zeros of sin π n. The parabolic coordinates $x = \xi\eta$, $y = 1/2\,(\eta^2 - \xi^2)$ in which the surface of given cylinder is defined by $\eta_o = \sqrt{2h}$. When $h = 0$ the cylinder reduces to the half plane $x = 0$, $y \leq 0$.

(U) In the shadow region we obtain creeping waves by deforming the contour c and taking to account all zeros of the function $W_n(\sqrt{-i\,2kh})$ or the function $'W_n(\sqrt{-2ikh})$. It has been shown that all zeros are located in third quadrant of the n-plane (Rice, 1954). These functions are related to the parabolic cylinder function $D_n(z)$ (Whittaker and Watson, 1927) through the equations

$$U_n(z) = 2^{n/2}\, e^{z^2/2}\, D_n(\sqrt{2}\,z) \,/\, \Gamma(n+1) \tag{4.70}$$

$$W_n(z) = -\,i^n\, 2^{n/2}\, e^{z^2/2}\, D_{-n-1}(i\sqrt{2}\,z)/\sqrt{2\pi} \tag{4.71}$$

$$'W_n(z) = -\,\frac{i^n 2^{n/2}}{\sqrt{2\pi}}\, e^{z^2/2}\, \frac{\partial}{\partial z}\left[D_{-n-1}(i\sqrt{2}\,z)\right] \tag{4.72}$$

Now zeros may be obtained asymptotically from the following three cases:

Case 1: If $kh \to 0$, then the expansions of the parabolic cylinder function $D_n(z)$ are given by the formula (Erdelyi, et al 1954)

$$D_n(z) = \frac{2^{-\frac{1}{2}n-1}}{\Gamma(-n)}\, e^{-\frac{1}{4}z^2} \sum_{s=0}^{\infty} (-1)^s\, \frac{\Gamma(\frac{1}{2}s - \frac{1}{2}n)}{s!}\, (\sqrt{2}\,z)^s \tag{4.73}$$

where $z = i\sqrt{2}\sqrt{-i2kh} = e^{i\pi/4}\sqrt{4kh}$. Therefore the condition $W_n(\sqrt{-i2kh}) = 0$ implies that

$$\frac{1}{\Gamma(1 - \alpha/2)} - \frac{2\, e^{i\pi/4}\sqrt{2kh}}{\Gamma(-\alpha/2)} = 0 \tag{4.74}$$

where $\alpha = -n - 1 = -m$.

When $kh \to 0$, the values of α for which the above expression vanishes are clearly near the poles of $\Gamma(1 - \alpha/2)$. Therefore α may be given by the formula

$$\frac{1 - \alpha}{2} = -(s + \epsilon) \tag{4.75}$$

where $s = 0, 1, 2, \ldots$ and $|\epsilon|$ is a small value.

(U) Substituting (4.75) into (4.74) ϵ may be obtained approximately from the equations

$$\frac{1}{\Gamma(1 - \alpha/2)} = -s\,\Gamma(s)\,\frac{\sin \pi(s + \epsilon)}{\pi} \simeq -(-1)^s\, s!\, \epsilon$$

$$= \frac{2\, e^{i\pi/4} \sqrt{2kh}}{\Gamma(-s - \frac{1}{2})} \,. \tag{4.76}$$

Now the asymptotic behavior of the zeros of $W_n(\sqrt{-2ikh})$ in the complex n-plane are given by

$$m_s = n_s + 1 = -(2s + 1) + \frac{4\, e^{(4s+1)\pi \frac{i}{4}} \sqrt{2kh}}{s!\, \Gamma(-s - \frac{1}{2})} \tag{4.77}$$

When $kh = 0$, we have

$$W_n(0) = \frac{-i^n}{2\,\Gamma(1 + \frac{n}{2})} \,.$$

Then zeros are given by poles of $\Gamma(1 + n/2)$ that is

$$m_s = n_s + 1 = -(2s + 1) \quad (s = 0, 1, 2, 3, \ldots) \tag{4.78}$$

This is the limit case of (4.77). Similarly the equation which determines the asymptotic behavior of the zeros of $'W_n(\sqrt{-2ikh})$ is

$$\frac{1}{\Gamma(-\alpha/2)} + \frac{(\alpha + \frac{1}{2})\ e^{i\pi/4}\ \sqrt{2kh}}{\Gamma(1 - \alpha/2)} = 0 \tag{4.79}$$

For $kh \to 0$ the zeros are very near the poles of $\Gamma(-\alpha/2)$. Let us assume the solution as

$$-\alpha/2 = -(s + \epsilon) \tag{4.80}$$

where $s = 0, 1, 2, 3, \ldots$ and ϵ is a small value. Then we have

$$\epsilon \simeq e^{(4s+1)\frac{\pi i}{4}}\ \frac{(2s + \frac{1}{2})\sqrt{2kh}}{s!\,\Gamma(-s + \frac{1}{2})} \tag{4.81}$$

From (4.80) and (4.81), the asymptotic behavior of the zeros of $'W_n(\sqrt{-2ikh})$ in the complex n-plane are obtained by

$$m'_s = n'_s + 1 = -2S - e^{(4s+1)\frac{\pi i}{4}}\ \frac{(4s+1)\sqrt{2kh}}{s!\,\Gamma(-s+\frac{1}{2})} \tag{4.82}$$

When $kh = 0$, we have

$$'W_n(0) = \frac{-i^{n-1}}{\Gamma(n + 1/2)} \tag{4.83}$$

Then zeros are given by

$$m'_s = n'_s + 1 = -2S \quad (s = 0, 1, 2, 3, \ldots) \tag{4.84}$$

The result is the limit case of (4.82).

Case 2: If $kh \to \infty$, the asymptotic expression of the function $W_n(z)$ and $'W_n(z)$ may be obtained by the saddle-point method (Rice, 1954; Ivanov, 1960). The function $W_n(z)$ is expressed by the integral.

$$W_n(z) = \frac{1}{2\pi i} \int_W \exp\left[-u^2 + 2uz - (n+1)\ell nu\right] du \qquad (4.85)$$

where W is the contour which runs from $+\infty$ to $-\infty$ with $-\pi < \arg u < 0$ in the complex u - plane.

(U) It is well known that for large kh the zeros n_s are also large (Rice, 1954)

$$n_s \simeq -ikh + O\left\{(kh)^{1/3}\right\} .$$

Thus, to obtain the zeros of smallest moduli of $W_n(\sqrt{-i2kh})$, the asymptotic expression will be obtained in the case $n_s \simeq -ikh$. It has been shown that the asymptote of this function is expressed by the Airy function (Rice, 1954; Ivanov, 1960). From Ivanov's result we obtain

$$W_n(\sqrt{-2ikh}) = \frac{i}{2}\sqrt{\frac{B}{2\pi}}\, e^{f_o + t\frac{B}{2}\ell n\frac{B^3}{2}} \left\{\omega(t) + \frac{1}{B}\left[\frac{\omega^{(IV)}(t)}{4} - \frac{t}{2}\omega''(t)\right] + O(B^{-2})\right\} \qquad (4.86)$$

where $B = (-ikh)^{1/3}$, $f_o = B^3/2\,(3 - \ell n\frac{B^3}{2})$ and $t = \frac{1}{B}\left[B^3 - (n+1)\right]$. The Airy function $\omega(t)$ is defined by

$$\omega(t) = 1/\pi \int_{\Gamma} \exp\left(\tau t - \frac{\tau^3}{3}\right) d\tau \qquad (4.87)$$

where the contour of integration Γ runs from $\infty\, e^{-2\pi(i/3)}$ to 0 and further along the real axis to infinity.

(U) The zeros of $W_n(\sqrt{-2ikh})$ are clearly near the zeros of $\omega(t)$ due to the large parameter B. Denoting the sth zero of the Airy function by t_s and assuming the zero of $W_n(\sqrt{-2ikh})$ by $t = t_s + \frac{C}{B} + O(B^{-2})$, we determine $C = -\frac{1}{2}$ from (4.85). Transforming the zero from the t-plane to the complex n-plane, we obtain

$$n_s = -ikh - (-ikh)^{1/3} t_s - \frac{1}{2} + O(B^{-1}) \qquad (4.88)$$

(U) From the definition of the function $'W_n(z)$ we obtain

$$'W_n(z) = e^{z^2/2} \frac{\partial}{\partial z}\left[e^{-z^2/2} W_n(z)\right]$$

$$= \frac{1}{2\pi i} \int_W (2u - z)\, e^{-u^2 + 2uz - (n+1)\ell n}\, du \qquad (4.89)$$

The asymptote of this function is

$$'W_n(\sqrt{-2ikh}) = \frac{i}{2}\frac{B}{\pi} e^{f_o + t\frac{B}{2} \ell n \frac{B^3}{2}} \left\{ \omega'(t) + \frac{1}{B}\left[\frac{\omega^{(V)}(t)}{4} - \frac{t}{2}\omega'''(t)\right] + O(B^{-2}) \right\} \qquad (4.90)$$

Similary we assume the zero of $'W_n(\sqrt{-2ikh})$ by $t = t'_s + \frac{C'}{B} + O(B^{-2})$ where t'_s is the sth zero of the function $\omega'(t)$. From (4.90) we determine $C' = -\frac{1}{2}$.

In the complex n-plane zeros are located at

$$n'_s = -ikh - (-ikh)^{1/3} t'_s - \frac{1}{2} + O(B^{-1}) \quad . \tag{4.91}$$

(U) We note that one may use Rice's results (Eqs. 13.21 and 13.24) to calculate the zeros in the complex t-plane asymptotically. If zeros in the complex n-plane are requested, the Rice's asymptotic expansions should be modified to include the term of order (1/B). The reason is that it involves a large parameter B multiplication in mapping the zeros from the complex t-plane to complex n-plane. Therefore one should not neglect the term of order (1/B) in evaluating the zeros. Finally instead of the -1 in Rice's results we obtain $-\frac{1}{2}$ in (4.88) and (4.91) (Keller, 1956; Ivanov, 1960).

(U) The zeros of the Airy function $\omega(t_s)$ and its derivative $\omega'(t'_s)$ occur when t_s and t'_s are negative. The first five zeros are tabulated below

s	t_s	t'_s
1	-2.3381	-1.0188
2	-4.0879	-3.2482
3	-5.5206	-4.8201
4	-6.7867	-6.1633
5	-7.9441	-7.3722

Equations (4.88) and (4.91) can be rewritten as follows

$$m_s = n_s + 1 = 0.866\, t_s (\rho^2/2)^{1/3} + \frac{1}{2} - \frac{i}{2}\left[\rho^2 - t_s(\rho^2/2)^{1/3}\right] \tag{4.92}$$

$$m'_s = n'_s + 1 = 0.866\, t'_s (\rho^2/2)^{1/3} + \frac{1}{2} - \frac{i}{2}\left[\rho^2 - t'_s (\rho^2/2)^{1/3}\right] \qquad (4.93)$$

where $\rho = \sqrt{2kh}$.

(U) For the case of the zeros of largest moduli of $W_n(\sqrt{-2ikh})$ and $'W_n(\sqrt{-2ikh})$, i.e., $kh/|n| << 1$, Rice obtained

$$W_n(\sqrt{-i}\,\rho) \simeq A(i^{-n}\theta_1 - i^n \theta_o) = -2iA \sin\left(\frac{n\pi}{2} + i\rho\sqrt{2im}\right) \qquad (4.94)$$

$$'W_n(\sqrt{-i}\,\rho) \simeq \sqrt{-i\rho^2 - 2m}\; A(i^{-n}\theta_1 + i^n \theta_o)$$

$$= 2\sqrt{-i\rho^2 - 2m}\; A \cos\left(\frac{n\pi}{2} + i\rho\sqrt{2im}\right) \qquad (4.95)$$

where

$$A = 2^{-3/2}\, \pi^{-1/2} \exp\left[m/2\,(1 - \ell n\, \frac{m}{2}) - i\rho^2/2\right]$$

$$\theta_1 = \exp\left[\rho\sqrt{2im}\right] = 1/\theta_o$$

$$m = n + 1 \ .$$

Thus the location of the zeros of largest moduli are obtained from the trigonometrical function. If s is a large positive integer such that $2S >> \rho^2$, zeros of $W_n(\sqrt{-i}\,\rho)$ are

$$m_s = -\left[(2s - 1) + 4(\rho/\pi)\sqrt{s/2}\right] - i4\,(\rho/\pi)\,(\sqrt{s/2} + \rho/\pi) \qquad (4.96)$$

and zeros of $'W_n(\sqrt{-i}\,\rho)$ are

$$m'_s = -\left[2s + 2(\rho/\pi)\sqrt{2s+1}\right] - 2i(\rho/\pi)\left(\sqrt{2s+1}\right) + 2(\rho/\pi) \qquad (4.97)$$

From the condition $2s >> \rho^2$, we know that (4.96) and (4.97) will be useful in locating the zeros of large moduli when $\rho = \sqrt{2kh}$ is small.

case 3: If $kh \approx 1$, that is the case of the incident wavelength comparable to the focal length, zeros may be obtained graphically from Rice's results. The asymptotic expression of $W_n(\sqrt{-i}\,\rho)$ in the third quadrant of the complex n-plane is

$$W_n(\sqrt{-i}\,\rho) = A_o - A_1 \qquad (4.98)$$

where

$$A_o = \frac{\sqrt{t_o}\; e^{f(t_o)}}{-2i\sqrt{\pi}\,(-i\rho^2 - 2m)^{1/4}} \qquad (4.99)$$

$$A_1 = \frac{\sqrt{t_1}\; e^{f(t_1)}}{2\sqrt{\pi}\,(-i\rho^2 - 2m)^{1/4}} \qquad (4.100)$$

$$t_o = 1/2\left[\sqrt{-i}\,\rho + \sqrt{-i\rho^2 - 2m}\right] \qquad (4.101)$$

$$t_1 = 1/2\left[\sqrt{-i}\,\rho - \sqrt{-i\rho^2 - 2m}\right] \qquad (4.102)$$

$$f(t_o) = m/2\left(1 - \ell n \frac{m}{2} - \ell n \frac{t_o}{t_1}\right) + \sqrt{-i}\,\rho\, t_o \qquad (4.103)$$

$$f(t_1) = m/2 \ (1 - \ell n \frac{m}{2} - \ell n \frac{t_1}{t_o}) + \sqrt{-i}\,\rho \ t_1 \qquad (4.104)$$

$$m = n + 1$$

$$-3\pi/2 \leq \arg m < \pi/2$$

$$-3\pi/2 \leq \arg (-i\rho^2 - 2m) < \pi/2$$

$$-3\pi/4 \leq \arg t_o < \pi/4$$

$$-5\pi/4 \leq \arg t_1 < 3\pi/4$$

therefore zeros of $W_n(\sqrt{-i}\,\rho)$ are located at

$$W_n(\sqrt{-i}\,\rho) = A_o - A_1 = 0 \qquad (4.105)$$

or

$$\exp\left[f(t_o) - f(t_1)\right] = \frac{1}{i\sqrt{t_o/t_1}} \quad . \qquad (4.106)$$

Using the following transformation

$$w = \ell n \ (t_o/t_1) = u + iv \qquad (4.107)$$

$$m = \frac{z^2}{\cosh w + 1} \qquad (4.108)$$

$$f(t_o) - f(t_1) = m \ (\sinh w - w) = \frac{z^2 \ (\sinh w - w)}{\cosh w + 1} \quad , \qquad (4.109)$$

the complex m-plane is mapped into the w-plane in the region $u \geq 0$; $v \leq \pi$. Thus in w-plane (4.106) becomes

$$-i\,\rho^2\,\frac{\sinh w - w}{\cosh w + 1} = -\left[\frac{w}{2} + i\,\frac{\pi}{2}(1 - 4s)\right] \tag{4.110}$$

where $s = 1, 2, 3, \ldots$. By separating the real part and the imaginary part of (4.110), we obtain two simultaneous equations

$$\rho^2\left[(\cos v + \cosh u + u \sinh u)\sin v - (\cosh u \cos v + 1)\, v\right]$$

$$= -\frac{1}{2}\, u\left[(\cosh u \cos v + 1)^2 + (\sinh u \sin v)^2\right] \tag{4.111}$$

$$\rho^2\left[(\cos v + \cosh u - v \sin v)\sinh u - (\cosh u \cos v + 1)\, u\right]$$

$$= \frac{1}{2}\left[v + (1 - 4s)\pi\right]\left[(\cosh u \cos v + 1)^2 + (\sinh u \sin v)^2\right] \tag{4.112}$$

Let (4.111) be divided by (4.112), we obtain

$$\frac{(\cos v + \cosh u + u \sinh v)\sin v - (\cosh u \cos v + 1)v}{(\cos v + \cosh u - v \sin v)\sinh u - (\cosh u \cos v + 1)u} = \frac{-u}{v - (1 - 4s)\pi} \tag{4.113}$$

This equation is independent of the parameter ρ. Settings $s = 1$, we calculate the first zero as the following:

(U) First, Eq. (4.112) may be approximated by a circle in the w-plane as

$$\left[u - (r - a)\right]^2 + \left[v - \frac{\pi}{2}\right]^2 = r^2 \tag{4.114}$$

where

$$r = \frac{a^2 + (\pi/2)^2}{2a} \tag{4.115}$$

$$a = u_{v = \pi/2} = 0.575, \quad s = 1$$

$$0 < u < a < 1.$$

Second, for $u < 1$, (4.112) can be evaluated approximately by

$$-\rho^2 uv \sin v = \frac{1}{2}(v - 3\pi)\left[(\cos v + 1)^2 + (u \sin v)^2\right] \tag{4.116}$$

The location of zeros may be obtained by graphical means. If we plot (4.114) and (4.116) on the w-plane, the points of intersection between the two curves determine the zeros. A typical plot is given in Fig. 4-12. Mapping the zeros from the auxilliary w-plane with the help of $m = -i\rho^2/(\cosh w + 1)$ gives the location of zeros on the m-plane. If we consider ρ as the variable parameter, the locus of the first zero in the m-plane is expressed approximately by

$$m_s = -\frac{1}{2}\left[(\rho + 2.8) + i(\rho^2 + \rho + 1.4)\right] \tag{4.117}$$

where we limit the range of ρ as $0 < \rho < 10$. Re m_s and Im m_s are plotted in Fig. 4-13. Similarly, loci for $s = 2, 3, 4, \ldots$ may be obtained by the graphical method.

(U) Similarly the asymptotic expression of the function $'W_n(\sqrt{-i}\,\rho)$ in the third quadrant of the n-plane is

$$'W_n(\sqrt{-i}\,\rho) = \sqrt{-i\rho^2 - 2m}\left[A_o + A_1\right] \tag{4.118}$$

Therefore, the zeros are located at

$$A_o + A_1 = 0 \tag{4.119}$$

or

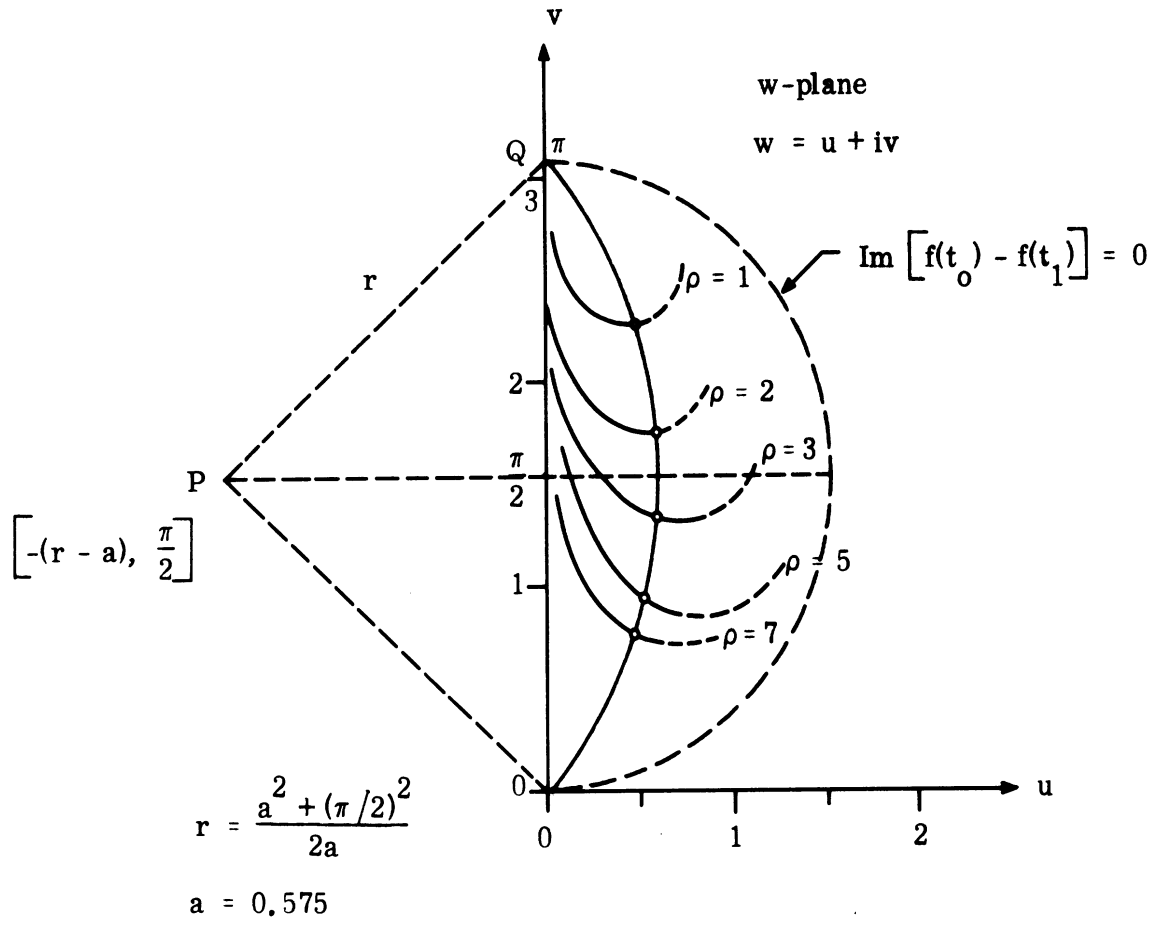

FIG. 4-12: GRAPHICAL SOLUTION FOR ZEROS OF $W_n(z)$ WHEN $z = \sqrt[4]{-i}\,\rho$.

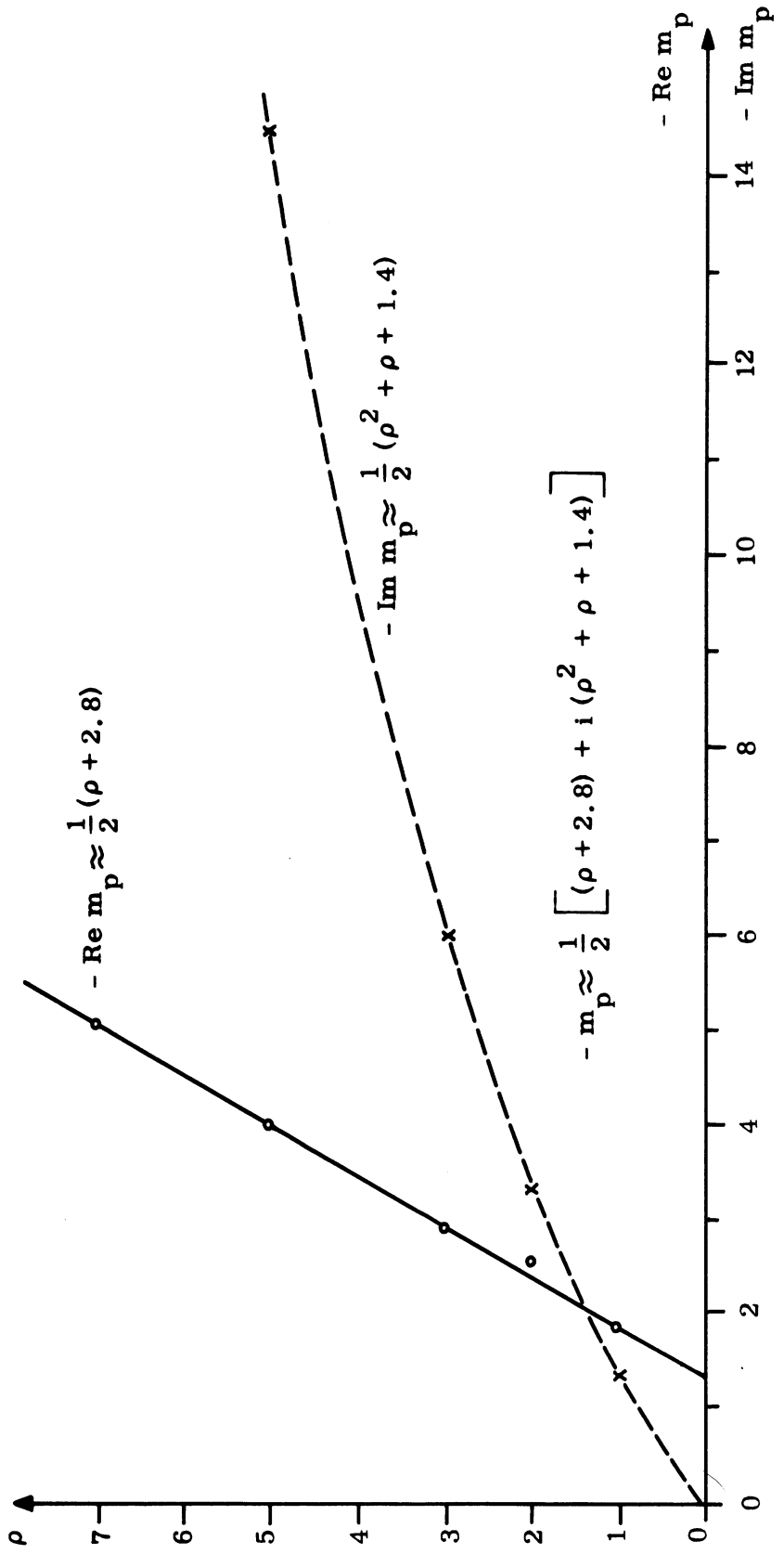

FIG. 4-13: LOCUS OF THE FIRST ZERO OF $W_n(z)$ IN THE m-PLANE WHEN $z = e^{-i\frac{\pi}{4}} \rho$.

$$\exp\left[f(t_o) - f(t_1)\right] = i/\sqrt{t_o/t_1} \quad ; \tag{4.120}$$

Using the transformation $w = \ell n\,(t_o/t_1) = u + iv$, we obtain

$$-i\,\rho^2\,\frac{\sinh w - w}{\cosh w + 1} = i\,\frac{\pi}{2}\,(1 + 4s) - \frac{w}{2} \tag{4.121}$$

where $s = 0, 1, 2, 3, \ldots$. By separating the real part and the imaginary part of (4.121) we obtain two simultaneous equations

$$\rho^2\left[(\cos v + \cosh u + u \sinh u)\sin v - (\cosh u \cos v + 1)\,v\right]$$

$$= -\frac{1}{2}\,u\left[(\cosh u \cos v + 1)^2 + (\sinh u \sin v)^2\right] \tag{4.122}$$

$$\rho^2\left[(\cosh v + \cosh u - v \sin v)\sinh u - (\cosh u \cos v + 1)\,u\right]$$

$$= \frac{1}{2}\left[v - \pi\,(1 + 4s)\right]\left[(\cosh u \cos v + 1)^2 + (\sinh u \sin v)^2\right] \tag{4.123}$$

Dividing (4.122) by (4.123) we have

$$\frac{(\cos v + \cosh u + u \sinh u)\sin v - (\cosh u \cos v + 1)v}{(\cos v + \cosh u - v \sin v)\sinh u - (\cosh u \cos v + 1)u} = \frac{-u}{v - \pi\,(1+4s)} \tag{4.124}$$

Setting $s = 0$, (4.124) may be approximated by a circle in the w-plane

$$\left[u - (r - a)\right]^2 + \left[v - \pi/2\right]^2 = r^2 \tag{4.125}$$

where

$$r = \frac{a^2 + (\pi/2)^2}{2a}$$

$$a = u_{v = \pi/2} = 0.48$$

$$0 < u < a < 1 \quad .$$

For $u < 1$, (4.123) may be approximated by

$$-\rho^2 uv \sin v = \frac{1}{2} (v - \pi) \left[(\cos v + 1)^2 + (u \sin v)^2 \right] \quad . \qquad (4.126)$$

The location of zeros are determined by the graphical method from (4.125) and (4.126). A typical plot is shown in Fig. 4-14. Mapping the zeros from the w-plane to m-plane gives approximately the locus of the first zero as

$$m'_s = - \left(\frac{1}{\pi} \rho + \frac{1}{10} \right) - i \frac{1}{2} \rho (\rho + 1) \qquad (4.127)$$

where ρ is limited in the range $0 < \rho < 10$. Re m'_s and Im m'_s are plotted in Fig. 4-15. Similarly, loci for $s = 1, 2, 3, \ldots,$ may be obtained by the graphical method.

(U) From the results (4.77), (4.82), (4.92), (4.93), (4.95), (4.96), (4.117) and (4.127), we plot zeros as the function of ρ in Fig. 4-16 to Fig. 4-19. They show that the high frequency approximation may be pushed down to very low frequency region for the imaginary part of zeros (Fig. 4-17 and 4-19). For the real part of zeros the high frequency approximation may be extended down to $\rho = 3$ for the first zero (Fig. 4-16 and 4-18).

(U) For zeros near the boundary $2s = \rho^2$, they may be determined by the graphical means. In the region $2s < \rho^2$, the high frequency approximation may be applied.

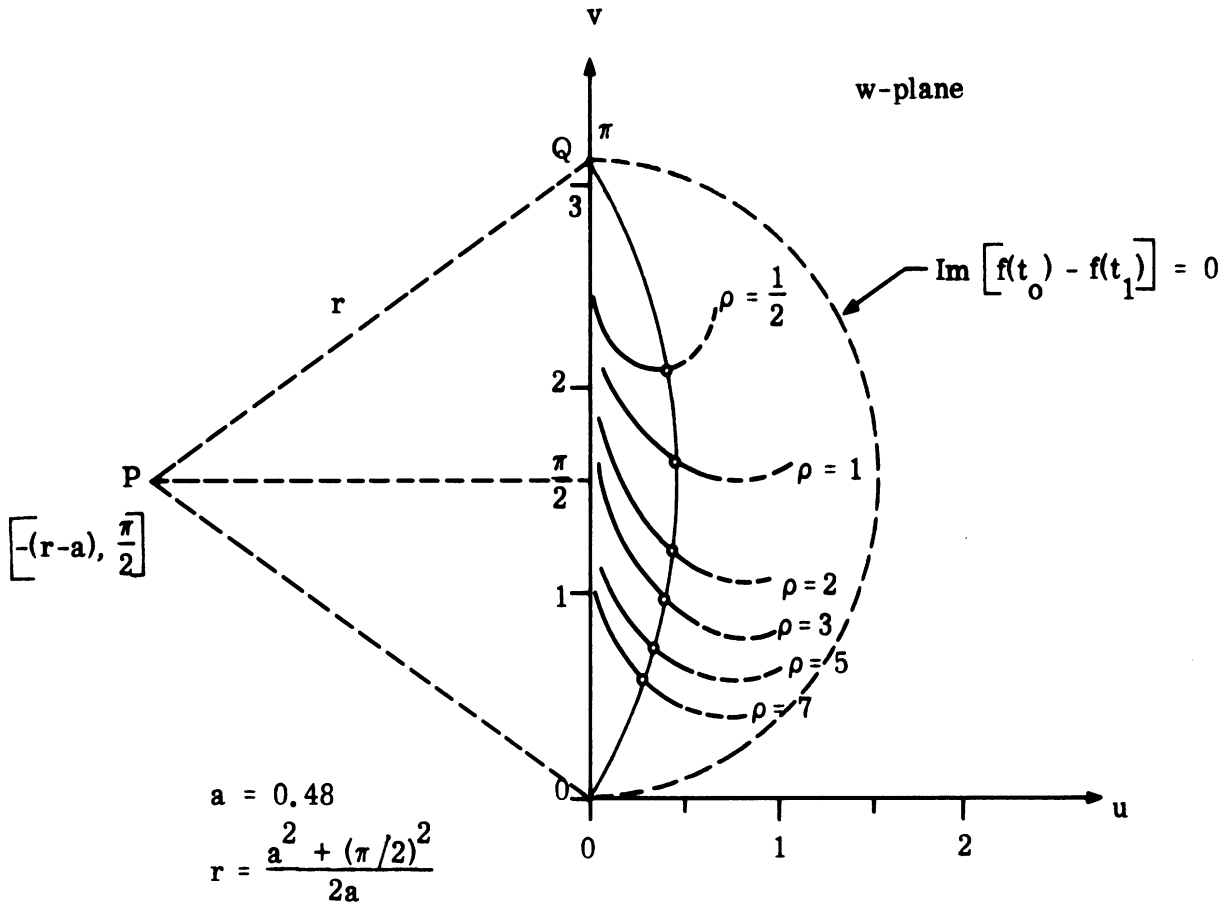

FIG. 4-14: GRAPHICAL SOLUTION FOR ZEROS OF $'W_n(z)$ WHEN $z = \sqrt{-i}\,\rho$.

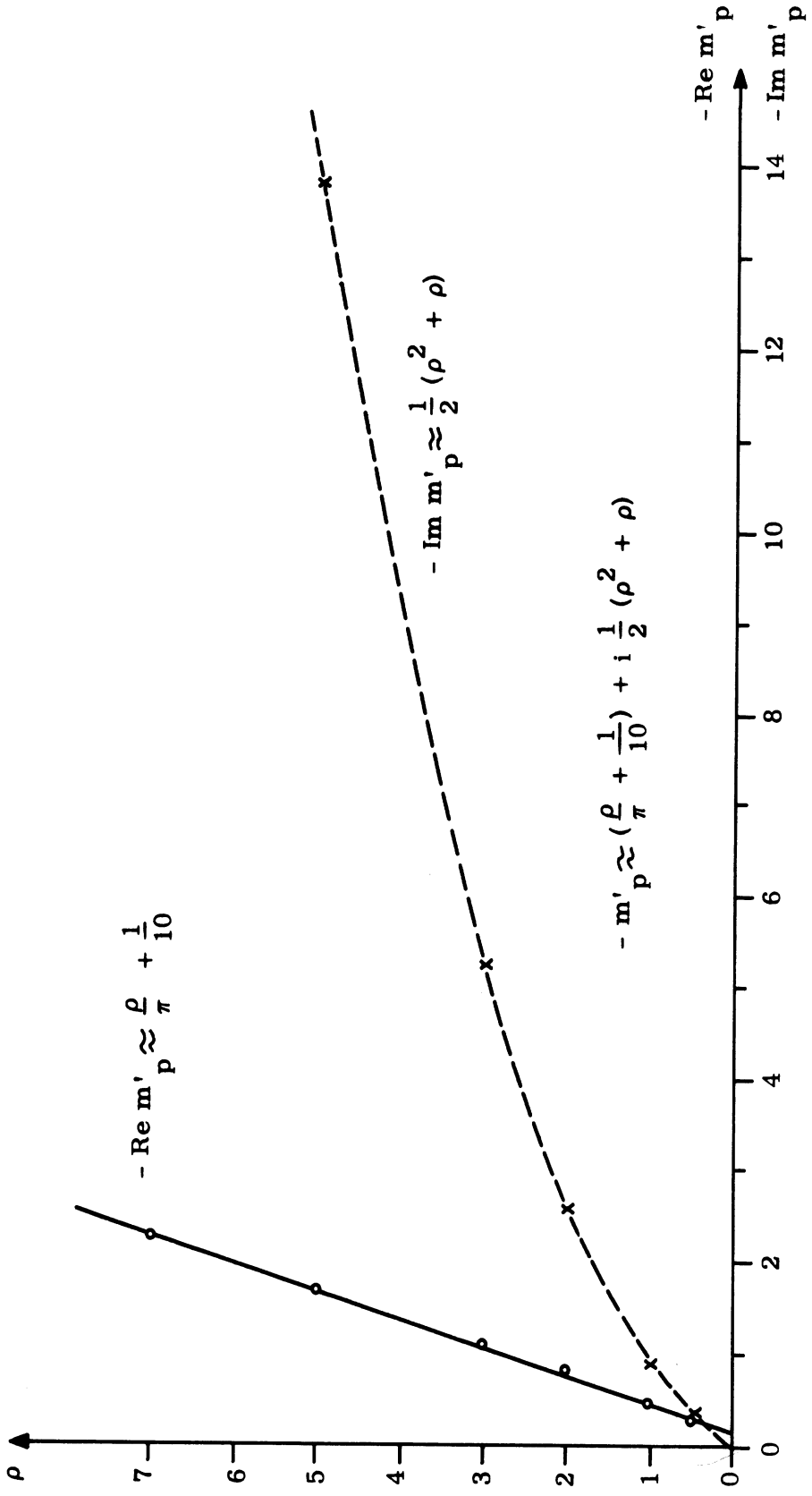

FIG. 4-15: LOCUS OF THE FIRST ZERO OF $W_n(z)$ IN THE m-PLANE WHEN $z = \sqrt{-i}\,\rho$.

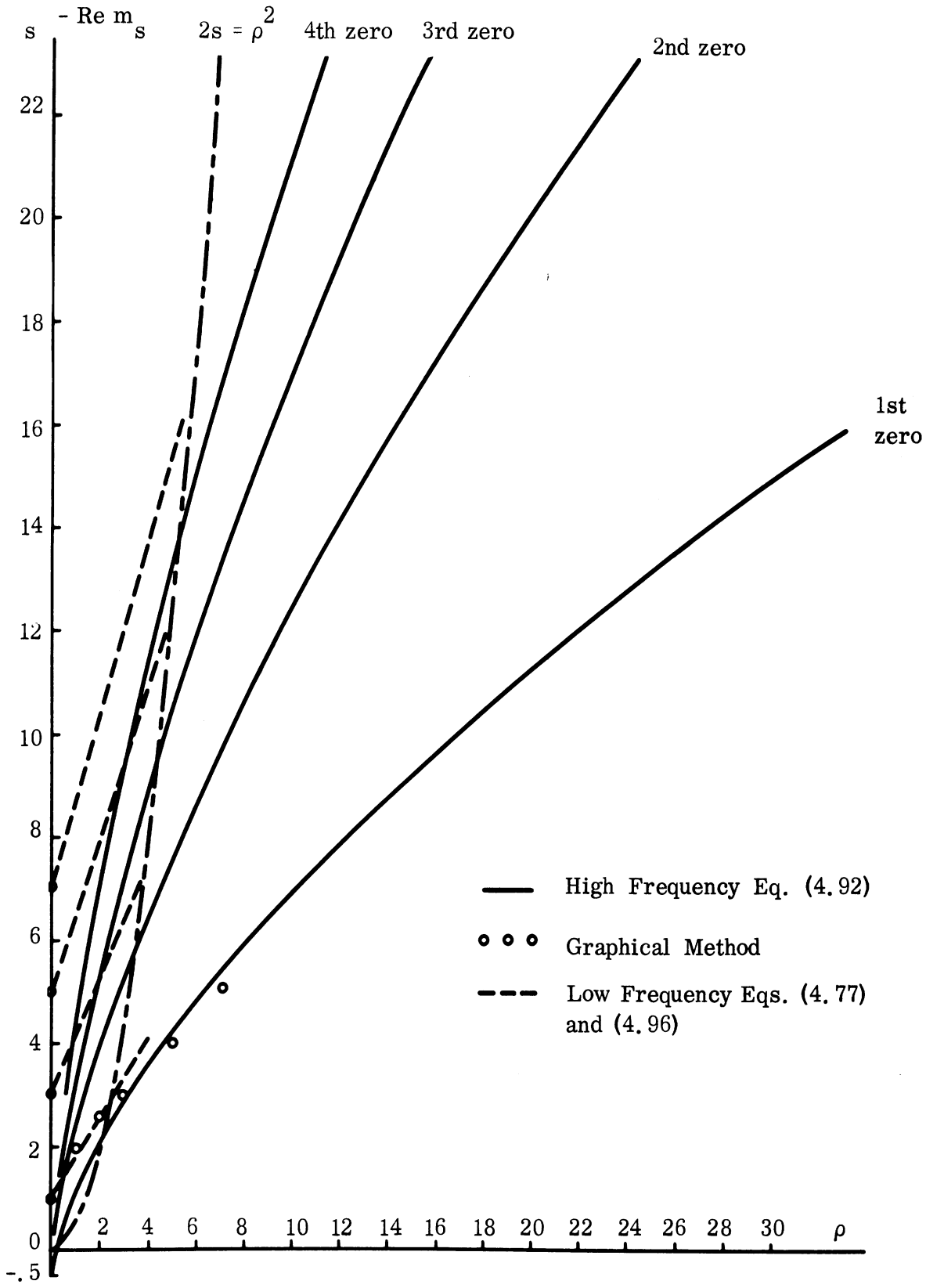

FIG: 4-16: REAL PART OF ZEROS OF $W_n(\sqrt{-i}\,\rho)$, $\rho = \sqrt{2kh}$. (Dirichlet's Problem).

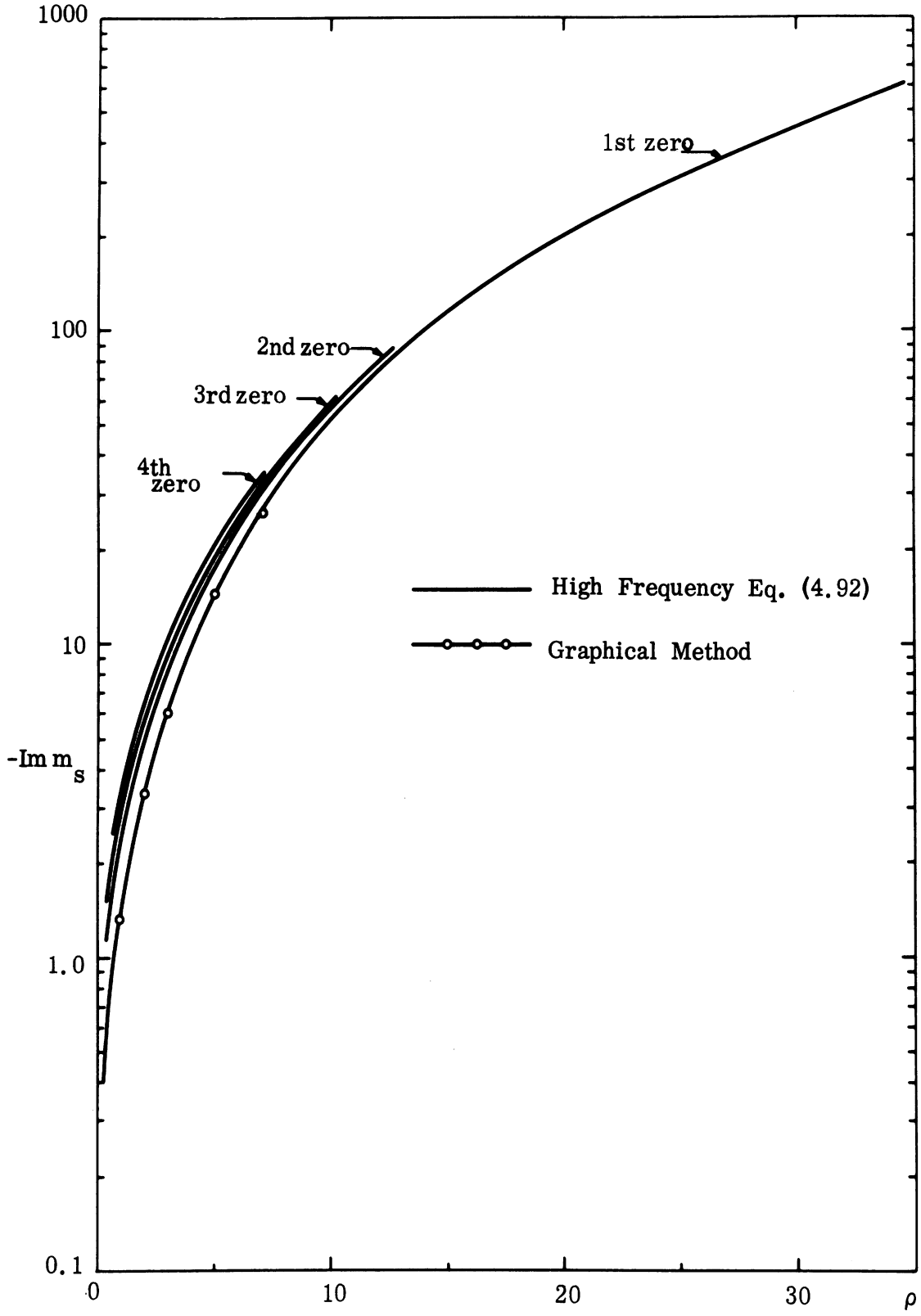

FIG. 4-17: IMAGINARY PART OF ZEROS OF $W_n(\sqrt{-i}\rho)$, $\rho = \sqrt{2kh}$. (Dirichlet's Problem).

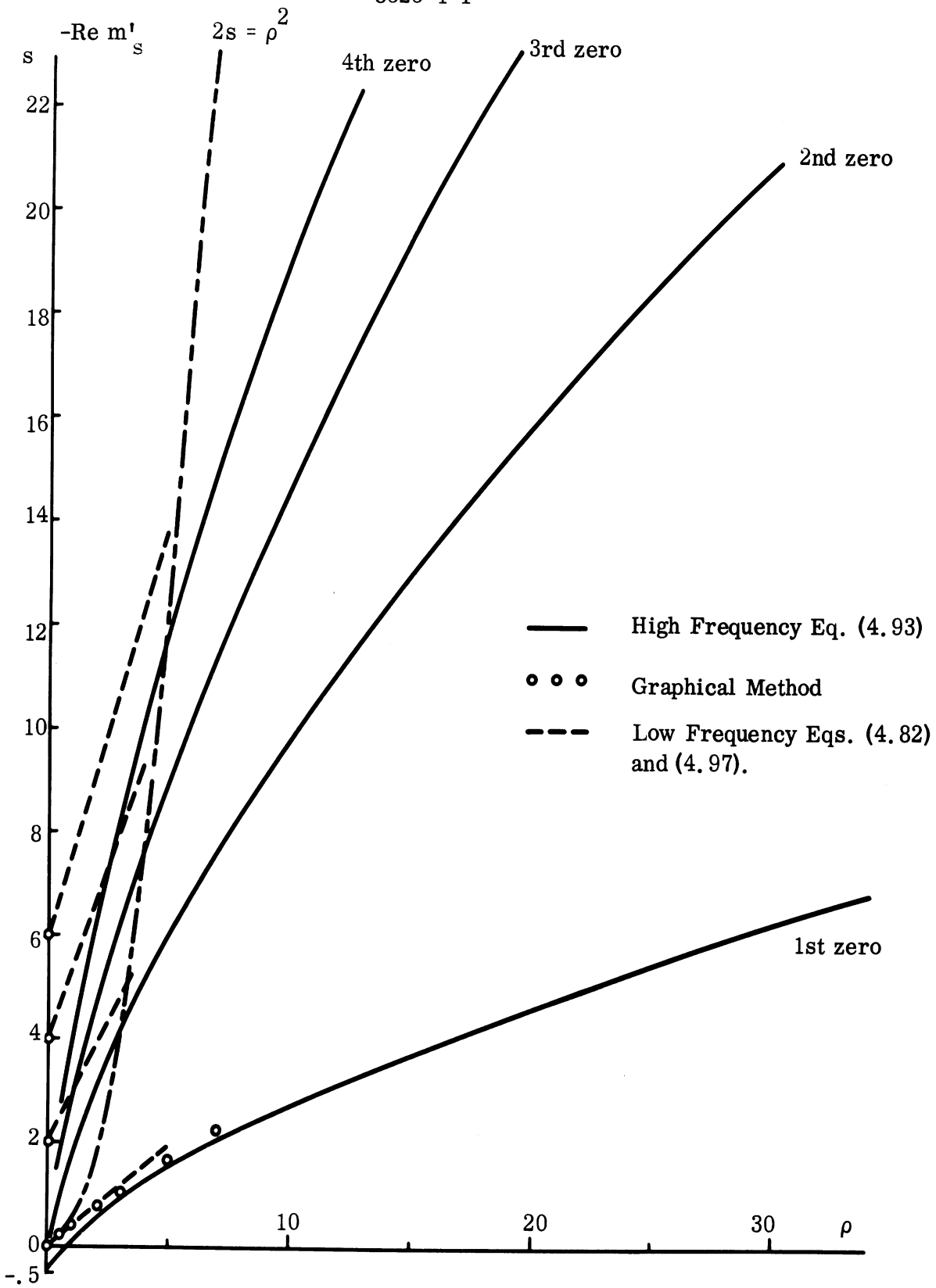

FIG. 4-18: REAL PART OF ZEROS OF $'W_n(\sqrt{-i}\,\rho)$, $\rho = \sqrt{2kh}$. (Neumann's Problem).

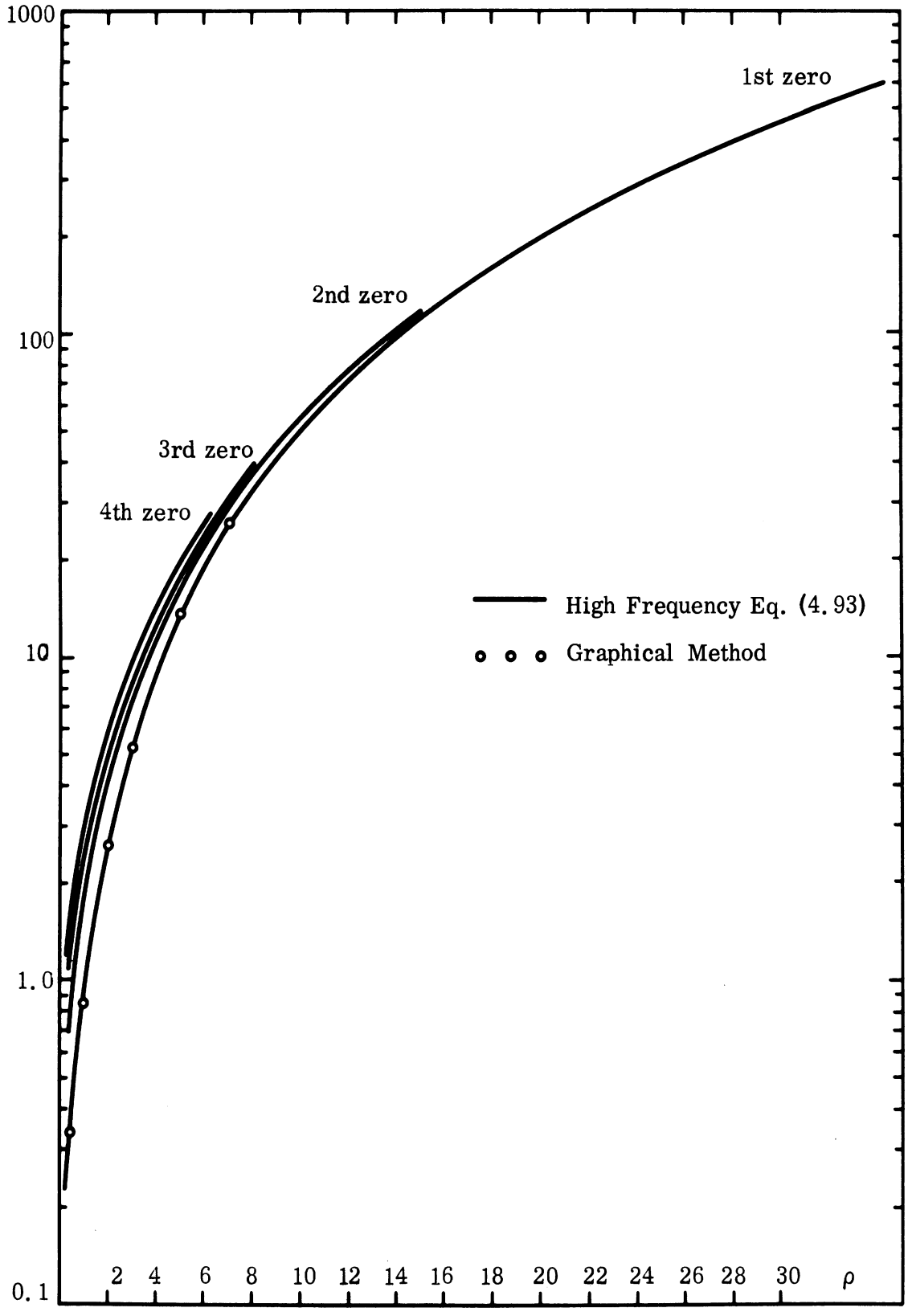

FIG. 4-19: IMAGINARY PART OF ZEROS OF $'W_n(\sqrt{-i}\,\rho)$, $\rho = \sqrt{2kh}$. (Neumann's Problem).

V

RADAR CROSS SECTION IN THE PLASMA RE-ENTRY ENVIRONMENT

5.1 Introduction

(S) The emphasis in the theoretical and experimental investigations during the last two quarters has been shifted towards the determination of the back-scattered return from a plasma sheathed conical vehicle for nose-on incidence. Apart from the return from the tip which becomes blunted due to ablation effects, the key problem is the determination of the return from the base of the vehicle which for the exo-atmosphere case is the dominant return for most sharp nose re-entry bodies. The plasma will partially or completely shield the base thus reducing its cross-section.

(U) The treatment of the electromagnetic scattering problem depends upon proper knowledge of the electrical properties of the sheath, which in turn depends upon knowledge of the flow fields. Because of lack of such information for a rounded base, the study was limited to the flat-backed base vehicle, although it was anticipated that with the advent of additional information that the rounded base could be properly treated in an extended program.

(U) For a flat-backed base the flow fields have been computed by Weiss and Weinbaum (1966), who point out there is a rapid expansion and separation of the hypersonic boundary layer at the rear shoulder of a blunt based re-entry body. In the outer portion of this expansion region (the free shear layer) the electron density will rapidly decrease beyond the shoulder, whereas, in the inner portion and the recirculation region the electron density may be quite large (see Fig. 5-1). Due to the complexity of the problem, some simplications of the electromagnetic problem have been made. For the direct backscattered return from the rear edge, the effect of the electron density in the recirculation region and the free inviscid layer adjacent to it, has been assumed to play a minor role. Such regions are important when multiple scattering across the

base are to be taken into account. With the above in mind, attention is focussed upon the spatial behavior of the electron density in the vicinity of the rear shoulder of the vehicle, and the outer portion of the expansion region beyond it. Again here, further approximations are made in the model, which lead to three separate cases, which are described below.

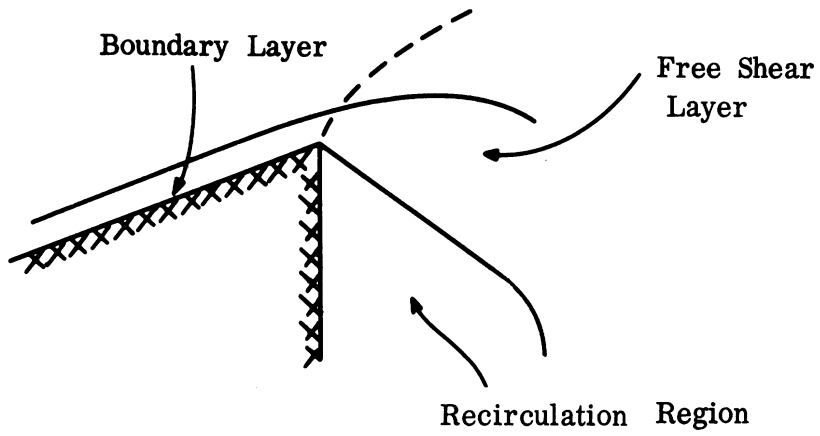

FIG. 5-1: HYPERSONIC BOUNDARY LAYER SEPARATION FOR FLAT-BACKED CONES.

(U) In the first case it is assumed that the expansion is sufficiently rapid in the outer portion of the free shear layer, such that the electron density becomes insignificant a short distance (compared to wavelength) back of the rear shoulder or edge. If N_s is the mean relative index of refraction of the boundary layer at the shoulder, and δ_s is a boundary layer thickness at the shoulder, and θ is the angle typical of the divergence of the flow in expansion region, then on assuming frozen flow the mean relative index of refraction N at a distance D beyond the shoulder is given by

$$(N - 1) = (N_s - 1)\,\delta_s/(D\theta) = (N_s - 1)k\,\delta_s/\left[D/\lambda\ 2\pi\,\theta\right] \quad .$$

Hence it is seen that if $(N_s - 1)\, k\delta_s << 1$, $\theta - \pi/4$, then $(N - 1) << 1$, at a distance $D = \lambda/4$ from the shoulder. This implies that for thin penetrable plasmas, the sheath in the neighborhood of the shoulder can be modeled by a terminated slab. Such a model will be useful in practice at lower operating frequencies, and higher altitudes where the sheath is less dense.

(S) For the cases where the sheath is too thick or overdense, such that the electron density in the expansion region remains significant well beyond the shoulder, alternative models must be employed since the sheath can not be abruptly terminated at the shoulder. There are two separate cases, an impenetrable sheath at the shoulder and a penetrable sheath at the shoulder. In the former, the sheath effectively hides the inner conducting wedge. In this case the backscattered return will arise from the discontinuity in electrical properties located in the vicinity of the shoulder. There the rapid expansion of the flow field will cause an abrupt charge in the electrical properties. In the later case there will still be some return arising from the inner conducting edge, but it will be reduced due to absorption.

(U) Only the first case (thin penetrable sheath) has been treated both theoretically and experimentally. It had been expected that the remaining cases would be treated in the follow-on program. A detailed discussion on a theoretical approach based upon the concept of an anisotropic impedance sheet along with comparison to the physical optics approximation is given in the next section. The associated experimental model is treated in Section 5.3.

5.2 Anisotropic Impedance Boundary Condition Approach to the Base Return for a Thin Plasma Sheath.

(U) The backscattered return for nose-on incidence to the plasma coated flat-backed cone is comprised of the tip and base returns. The base returns (neglecting multiple diffraction effects) is calculated using well-known techniques of diffraction theory, wherein the base is approximated by wedge segments.

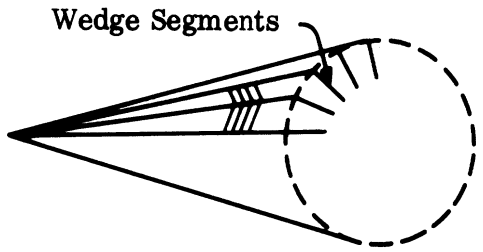

FIG. 5-2: ILLUSTRATION OF WEDGE SEGMENT APPROXIMATION.

The total field is the sum of the individual returns from the edges of the wedge segments. It can be shown that the total backscattered field for nose-on incidence for a base of radius a, is given by

$$\sigma = \pi a^2 \left| R_{||} - R_{\perp} \right|^2 , \qquad (5.1)$$

where $R_{||}$ and $R_{\perp}$ are local reflection coefficients associated with the two-dimensional wedge return. To be explicit, if $\underline{E}^i$ is the plane wave incident upon the wedge, the backscattered return from the edge has the form

$$\underline{E}^s = \frac{e^{i(kr + \pi/4)}}{\sqrt{2\pi kr}} \left[\underline{E}^i_{||} R_{||} - \underline{E}^i_{\perp} R_{\perp} \right] \qquad (5.2)$$

where r is the distance from the edge, and $\underline{E}^i_{||}$ and $\underline{E}^i_{\perp}$ are the components of the incident field parallel and perpendicular to the edge, respectively. Thus the problem reduces to solving the two-dimensional wedge problem.

(U) For a special class of coatings (magnetic absorbers, good conductors) the electrical properties of the coating may be expressed in terms of a boundary condition on the outer surface, i.e., the effect of the coating upon incident radiation can be represented in terms of the impedance boundary condition involving the tangential components of the total field on the surface $\underline{E} - (\underline{E} \cdot \underline{n})\underline{n} =$

$\sqrt{\mu_o/\epsilon_o}\ \eta\ \underline{n} \times \underline{H}$. In this expression, $\underline{n}$ is the unit outward normal to the surface, and η is a function of the electrical properties of the coatings as well as its thickness, being zero for a perfect conductor. For this case of coatings, η is independent of polarization and angle of incidence of the incident radiation.

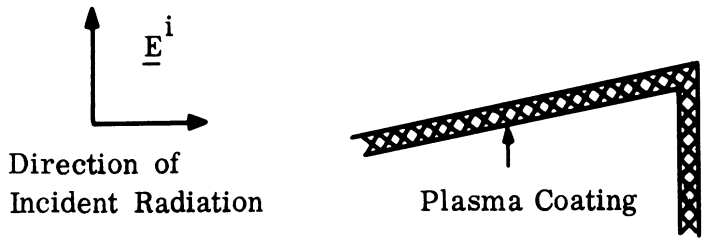

FIG. 5-3: LOCAL WEDGE GEOMETRY.

(U) To obtain approximate results for thin plasma sheaths, the concept of impedance will be modified, with η taken to be a function of polarization. Except for very overdense plasmas, the appropriate choice of η can not be made independent of the angle of incidence.

(U) For a uniform plasma sheath of thickness d and index of refraction N, an appropriate choice for η, based upon the flat plane results, is given by

$$\eta_{||} = -i \frac{\tan\left[kd\,(N^2 - \cos^2\delta)^{1/2}\right]}{(N^2 - \cos^2\delta)^{1/2}}\ , \qquad (5.3)$$

$$\eta_{\perp} = -\frac{i}{N^2}\,(N^2 - \cos^2\delta)^{1/2} \tan\left[kd\,(N^2 - \cos^2\delta)^{1/2}\right], \qquad (5.4)$$

where δ is the angle of incidence measured from the locally flat surface and will turn out to be equal to the (small) interior half-angle of the cone. The index of refraction will be based upon the cold plasma result

$$N^2 = 1 - \frac{\omega_p^2/\omega^2}{1 + i\,(f_c/f).} \qquad (5.5)$$

(U) Several observations can be made here. In the very overdense case, such that $|N| >> 1$ and $\mathrm{Im}(Nkd) >> 1$, the impedances become $\eta_{||} \sim \eta_{\perp} \sim 1/N \sim 0$ and the sheath appears effectively as a good conductor. On the other hand, for thin sheaths, such that $kd << 1$ and $|Nkd| << 1$, the impedances are approximately given by

$$\eta_{||} \sim -i\,kd \sim 0\,,$$

$$\eta_{\perp} \sim -i\,kd\,\frac{N^2 - \cos^2\delta}{N^2}\,.$$

Again, the sheath appears as a conductor for the $\eta_{||}$ impedance; however, the $\eta_{\perp}$ impedance can profoundly change the characteristics of the scattering process. For operating frequencies well above the plasma frequency, such that $N \sim 1$, the impedance $\eta_{\perp}$ behaves as $\eta_{\perp} \sim -i\,kd\sin^2\delta \sim 0$, and the sheath appears again as a conductor. Contrarywise, for operating frequencies close to the plasma frequency, such that $N \sim 0$, the impedance $\eta_{\perp}$ behaves as $\eta_{\perp} \sim ikd\cos^2\delta/N^2 \sim \infty$, and the sheath now appears as a magnetic conductor. The result is that near the plasma frequency, the two reflection coefficients $R_{\perp}$ and $(-R_{||})$ appearing in Eq. (5.1) will cancel each other and greatly diminish the backscattering cross section. This effect will be made more quantitative later.

(U) For non-uniform plasma sheaths, the appropriate choice for the impedances is given by

$$\eta_{||} = \frac{1}{\sin\delta}\,\frac{1 + R_1}{1 - R_1}\,, \qquad \eta_{\perp} = \sin\delta\,\frac{1 + R_2}{1 - R_2} \qquad (5.6)$$

where R_1 and R_2 are voltage reflection coefficients for a plane wave incident upon an infinite non-uniform plasma slab. Such reflection coefficients were calculated last year on the basis of the plasma profiles supplied by Aerospace. In the present notation, R_1 and R_2 correspond to electric polarization perpendicular to, and parallel to, the plane of incidence, respectively. Some quantitative results for the laminar flow case at 150 K ft, will be presented.

(U) The above representation of the sheath in terms of an anisotropic impedance boundary condition greatly simplifies the scattering problem. The two-dimensional scalar scattering problem can be expressed as follows; to find the scattered field u^s such that the total field $u = u^i + u^s$, where u^i is the incident field, satisfies the Helmhotz equation $\nabla^2 u + k^2 u = 0$ and the boundary condition on the outer surface of the coating

$$\frac{\partial u}{\partial n} = -ik \begin{Bmatrix} \eta_\perp \\ 1/\eta_{||} \end{Bmatrix} u$$

The appropriate boundary condition on the rear face of the wedge may be taken to be that which corresponds to a perfect conductor i.e., $u = 0$ and $\frac{\partial u}{\partial n} = 0$, for polarization parallel to the edge and perpendicular to the edge, respectively.

(U) Fortunately, this problem has been solved by Milinzhinets (1958), and his solution appropriate to our geometry is, for backscattering:

$$u = \left[e^{i(kr + \frac{\pi}{4})} \Big/ \sqrt{2\pi kr} \right] R$$

where

$$R = \frac{\sin \frac{2\pi\delta}{2\delta + 3\pi}}{\left(\frac{\delta}{\pi} + \frac{3}{2}\right) \psi\left(-\frac{\delta}{2} + \frac{3\pi}{4}\right)} \left[\frac{\psi\left(-\frac{\delta}{2} - \frac{\pi}{4}\right)}{\cos \frac{2\pi(\delta - \pi)}{2\delta + 3\pi} - \cos \frac{2\pi\delta}{2\delta + 3\pi}} \right.$$

$$\left. - \frac{\psi\left(-\frac{\delta}{2} + \frac{7\pi}{4}\right)}{\cos \frac{2\pi(\delta - \pi)}{2\delta + 3\pi} - \cos \frac{2\pi\delta}{2\delta + 3\pi}} \right] \qquad (5.8)$$

with δ representing the angle of incidence.

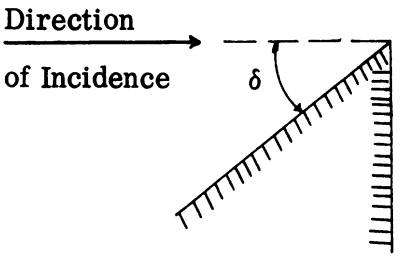

The function ψ is given in terms of a special meromorphic function $\psi_{\bar{\Phi}}$ by

$$\psi(\alpha) = \psi_{\bar{\Phi}}(\alpha + \bar{\Phi} + \theta_1)\psi_{\bar{\Phi}}(\alpha - \bar{\Phi} - \theta_1)\psi_{\bar{\Phi}}(\alpha - \bar{\Phi} + \theta_2)\psi_{\bar{\Phi}}(\alpha - \bar{\Phi} - \theta_2), \quad (5.9)$$

with $\bar{\Phi} = \frac{\delta}{2} + \frac{3\pi}{4}$ and

$$\psi_{\bar{\Phi}}(\alpha) = \sqrt{\cos \frac{\pi\alpha}{4\bar{\Phi}}} \exp\left[\frac{1}{2\pi} \int_{-\infty}^{\infty} \log\left(1 - i \tan \frac{\pi\alpha}{4\bar{\Phi}}\right.\right.$$

$$\left.\left. \times \tanh \frac{\pi\nu}{4\bar{\Phi}}\right) \frac{d\nu}{\cosh \nu} \right] = \psi_{\bar{\Phi}}(-\alpha) \quad . \qquad (5.10)$$

This solution contains both polarization cases at the same time and they are to be distinguished by the relationships between the (complex) angles $\theta_{1,2}$ and

the impedances; in particular, on the illuminated face:

$$\eta = \frac{1}{\cos \theta_1^{||}} \quad , \tag{5.11}$$

$$\eta = \cos \theta_1^{\perp} \quad , \tag{5.12}$$

and for the shadowed (or rear) face, later taken to be perfectly conducting:

$$\eta = \frac{1}{\cos \theta_2^{||}} \quad , \tag{5.13}$$

$$\eta = \cos \theta_2^{\perp} \quad . \tag{5.14}$$

Thus, at present, the solution contains four complex impedances for two polarization cases in the single formal expression (5.8).

(U) It turns out that for the particular geometry at hand, Eq. (5.8) can be vastly simplified, at least to the extent that the definite integral in Eq. (5.10) does not enter into the final results. We begin with the ψ functions in Eq. (5.8):

$$\psi\left(-\frac{\delta}{2}-\frac{\pi}{4}\right) = \psi_{\bar{\Phi}}\left(\frac{\pi}{2}+\theta_1\right)\psi_{\bar{\Phi}}\left(\frac{\pi}{2}+\theta_1\right)\psi_{\bar{\Phi}}\left(2\bar{\Phi}-\frac{\pi}{2}+\theta_2\right)\psi_{\bar{\Phi}}\left(2\bar{\Phi}-\frac{\pi}{2}-\theta_2\right),$$

$$\psi\left(-\frac{\delta}{2}+\frac{3\pi}{4}\right) = \psi_{\bar{\Phi}}\left(\frac{3\pi}{2}-\theta_1\right)\psi_{\bar{\Phi}}\left(\frac{3\pi}{2}-\theta_1\right)\psi_{\bar{\Phi}}\left(2\bar{\Phi}-\frac{3\pi}{2}+\theta_2\right)\psi_{\bar{\Phi}}\left(2\bar{\Phi}-\frac{3\pi}{2}-\theta_2\right), \tag{5.15}$$

$$\psi\left(-\frac{\delta}{2}+\frac{7\pi}{4}\right) = \psi_{\bar{\Phi}}\left(\frac{5\pi}{2}+\theta_1\right)\psi_{\bar{\Phi}}\left(\frac{5\pi}{2}-\theta_1\right)\psi_{\bar{\Phi}}\left(2\bar{\Phi}-\frac{5\pi}{2}+\theta_2\right)\psi_{\bar{\Phi}}\left(2\bar{\Phi}-\frac{5\pi}{2}-\theta_2\right) .$$

Now, from Malinzhinets (1958), we have

$$\psi_{\bar{\Phi}}(\pi/2+\alpha)\psi_{\bar{\Phi}}(\pi/2-\alpha) = \psi^2_{\bar{\Phi}}(\pi/2)\cos\pi\alpha/4\bar{\Phi} \tag{5.16}$$

and by means of this formula, we find

$$\psi_{\bar{\Phi}}\left(\frac{3\pi}{2}+\alpha\right)\psi_{\bar{\Phi}}\left(\frac{3\pi}{2}-\alpha\right) = \psi^2_{\bar{\Phi}}(\pi/2)\ \frac{\cos\frac{\pi(\alpha+\pi)}{4\bar{\Phi}}\ \cos\frac{\pi(\alpha+\pi)}{4\bar{\Phi}}}{\cos\frac{\pi\alpha}{4\bar{\Phi}}}\ , \tag{5.17}$$

$$\psi_{\bar{\Phi}}\left(\frac{5\pi}{2}+\alpha\right)\psi_{\bar{\Phi}}\left(\frac{5\pi}{2}-\alpha\right) = \psi^2_{\bar{\Phi}}(\pi/2)\ \frac{\cos\frac{\pi\alpha}{4\bar{\Phi}}\ \cos\frac{\pi(\alpha+2\pi)}{4\bar{\Phi}}\ \cos\frac{\pi(\alpha-2\pi)}{4\bar{\Phi}}}{\cos\frac{\pi(\alpha+\pi)}{4\bar{\Phi}}\ \cos\frac{\pi(\alpha-\pi)}{4\bar{\Phi}}} \tag{5.18}$$

With these we may simplify the various ratios of $\psi_{\bar{\Phi}}$ functions involving θ_1 in Eq. (5.15) and the quantity $\psi^2_{\bar{\Phi}}(\pi/2)$ gets cancelled out. Similar considerations apply to the $\psi_{\bar{\Phi}}$ functions involving θ_2, only first the relation (Malinzhinets, 1958)

$$\frac{\psi_{\bar{\Phi}}(\alpha+2\bar{\Phi})}{\psi_{\bar{\Phi}}(\alpha-2\bar{\Phi})} = \cot\left(\frac{\alpha}{2}+\frac{\pi}{4}\right) \tag{5.19}$$

is employed to bring the $\psi_{\bar{\Phi}}$ functions involving θ_2 to the appropriate form applicable to Eqs. (5.16) through (5.18).

(U) Without entering into any more algebraic details, we found that the quantity R in Eq. (5.7) can be written in closed form as:

$$R = \frac{1}{2\nu}\ \frac{\sin(3\pi/2\nu)}{\sin(\pi/2\nu)}\ \left[\frac{A}{\sin(\pi/\nu)} + \frac{B}{\sin(2\pi/\nu)}\right] \tag{5.20}$$

where

$$A = \frac{1 + \cos(\theta_1/\nu)}{\cos(\pi/\nu) + \cos(\theta_1/\nu)} \frac{1 - \cos(\theta_2/\nu)}{\cos(\pi/\nu) - \cos(\theta_2/\nu)} \frac{1+\cos\theta_2}{1-\cos\theta_2} \tag{5.21}$$

$$B = A \frac{\cos(2\pi/\nu) + \cos(\theta_1/\nu)}{\cos(\pi/\nu) + \cos(\theta_1/\nu)} \frac{\cos(2\pi/\nu) - \cos(\theta_2/\nu)}{\cos(\pi/\nu) - \cos(\theta_2/\nu)} , \tag{5.22}$$

and $\nu = (\delta/\pi + 3/2)$. The nose-on backscattering cross section for the flat back impedance cone is then

$$\sigma = \pi a^2 \left| R_{||} - R_{\perp} \right|^2 \tag{5.23}$$

where a is the base radius, $R_{||}$ is obtained from Eq. (5.20) upon employing the definitions in Eqs. (5.11) and (5.13), and $R_{\perp}$ is obtained from Eq. (5.20) upon employing Eqs. (5.12) and (5.14). For a perfectly conducting finite cone, $\theta_1^{||} = \theta_2^{||} = i\infty$, $\theta_1^{\perp} = \theta_2^{\perp} = \pi/2$, and

$$R_{||} - R_{\perp} = -\frac{1}{\nu} \csc\frac{2\pi}{\nu} , \sigma = \frac{\pi a^2}{\nu^2} \csc^2(2\pi/\nu) , \tag{5.24}$$

in agreement with Siegel et al, (1959a), (1959b). On the other hand, for a perfectly absorbing finite cone (all impedances equal to unity) $\theta_1^{||}\ \theta_1^{\perp} = 0$, $\theta_2^{||} = \theta_2^{\perp} = 0$ and $R_{||} = R_{\perp}$, $\sigma = 0$, in agreement with Weston's (1963) general theorem concerning absorbers.

(U) We now specialize to the case where the rear face is perfectly conducting, $\theta_2^{||} = i\infty$, $\theta_2^{\perp} = \pi/2$, and the illuminated surface is governed by the impedances $\eta_{||}$, $\eta_{\perp}$. The following explicit results are obtained:

$$A = \frac{1 + u^{-1/\nu}\left[2 + u^{-1/\nu}\right]}{1 + u^{-1/\nu}\left[2\cos\frac{\pi}{\nu} + u^{-1/\nu}\right]} , \tag{5.25}$$

$$B_{||} = A_{||} \frac{1 + u_{||}^{-1/\nu}\left[2\cos\frac{2\pi}{\nu} + u_{||}^{-1/\nu}\right]}{1 + u_{||}^{-1/\nu}\left[2\cos\frac{\pi}{\nu} + u_{||}^{-1/\nu}\right]} , \tag{5.26}$$

$$A_{\perp} = \frac{1 + u_{\perp}^{-1/\nu}\left[2 + u_{\perp}^{-1/\nu}\right]}{1 + u_{\perp}^{-1/\nu}\left[2\cos\frac{\pi}{\nu} + u_{\perp}^{-1/\nu}\right]} \frac{\sin(\pi/4\nu)}{\sin(3\pi/4\nu)} , \tag{5.27}$$

$$B_{\perp} = A_{\perp} \frac{1 + u_{\perp}^{-1/\nu}\left[2\cos\frac{2\pi}{\nu} + u_{\perp}^{-1/\nu}\right]}{1 + u_{\perp}^{-1/\nu}\left[2\cos\frac{\pi}{\nu} + u_{\perp}^{-1/\nu}\right]} \frac{\sin(5\pi/4\nu)}{\sin(\pi/4\nu)} , \tag{5.28}$$

where

$$u_{||} = 1/\eta_{||} + \sqrt{1/\eta_{||}^2 - 1} , \tag{5.29}$$

$$u_{\perp} = \eta_{\perp} + \sqrt{\eta_{\perp}^2 - 1} ,$$

and the square roots have non-negative real parts.

(U) The corresponding physical optics result for backscattering from a finite coated cone may be taken normalized to a perfectly conducting cone as

$$\frac{\sigma_{\text{coated}}}{\sigma_{\text{p.c.}}} = 1/4 \left| R_1 + R_2 \right|^2 \tag{5.30}$$

where R_1 and R_2 are the voltage reflection coefficients defined in Eq. (5.6).

(U) The backscattering cross section in the wedge approximation (5.23), where $R_{||}$ and $R_{\perp}$ are obtained from (5.20) with (5.25) through (5.29), has been programmed for the computer. The output of the program gives the cross section of the plasma sheathed finite cone normalized to the cross of the perfectly conducting finte cone; this ratio is denoted by $\sum$, where

$$\sum = \sigma_{\text{coated}}/\sigma_{\text{p.c.}} . \tag{5.31}$$

(S) The first results obtained are for the laminar flow case at 150Kft, for a sharp 11^{o} cone of length 104". The plasma profiles were supplied by Aerospace (profile No. 3) and the appropriate reflection coefficients, amplitude and phase, were calculated in last year's effort. These are tabulated in Table V-1. The resultant cross sections are also included. It will be noted that the reduction in cross section is greatest for those frequencies close to the plasma frequency $f_p = 6.10^8$. Unfortunately, experimental data for this case are not available. Some data are contained in de Ridder and White, (1966), for a flat-back cone of angle 8^{o}, length 110", although the cone tip is slightly blunted, and this can alter the flow field characteristics significantly. It is difficult to obtain an accurate measure of the cross section reduction from their report; nevertheless, some data of interest are reproduced in Table V-2.

TABLE V-1: Amplitude and Phase of Reflection Coefficients for Profile No. 3, and Nose-on Backscattering Cross Section $\delta = 11^{o}$, $\ell = 104"$.

f	R_1	ϕ_1	R_2	ϕ_2	$\sum$
10^8	.999	3.183	:877	-2.140	- 3.3 db
$5 \cdot 10^8$	.992	3.338	.638	- .303	-23.2 db
10^9	.990	3.529	.682	.852	-19.4 db

TABLE V-2: Measured Cross Section Reduction (de Ridder and White, 1966)

Altitude	Frequency	$\sum$
45 -50 km	UHF	-10 db
50 55 km	L-band	-20 db

(U) The cross section reduction in either the wedge approximation or the physical optics approximation is quite sensitive to changes in the various parameters, especially when these changes occur for frequencies close to the plasma frequency. In order to assess these effect, computations were conducted for a uniform plasma sheath, where the impedances are given by Eqs. (5.3) through (5.5). A thickness $d = 1/4''$ was chosen, although other thicknesses can significantly alter the results. The cross section reduction, both in the wedge approximation ($\sum$) and the physical optics approximation ($\sum_{p.o.}$), was calculated for a sequence of values $0.4 \leq (\omega_p/\omega) \leq 2.5$, $10^8 \leq f \leq 5.10^9$; for several values of the collision frequency f_c; and for $\delta = 11^o$, 8^o. Some of the results are presented in Figs. 5-3 through 5-10.

(S) Figures 5-4 through 5-7 present results for the wedge approximation. Generally the reduction for $\delta = 8^o$ is greater than for $\delta = 11^o$, as expected. Further, the reduction for $f_c = 10^8$ is greater than that for $f_c = 10^9$, and, in addition, the effects for the lower collision frequency are much more severe. This is expected since one approaches a sharper resonance effect as the losses are reduced. It will be noticed that at the higher frequencies, the curves change shape, and in some cases display a kind of double resonance effect. At present, this phenomenon is not completely understood, the equations being too complicated to pinpoint the cause; however, at the higher frequencies the plasma layer is thick and one may question the validity of the wedge model.

(U) Figures 5-8 through 5-11 present results for the physical optics approximation. The physical optics cross sections are consistently larger than the corresponding cross sections based on the wedge approximation -- this is also true in the case of a perfectly conducting finite cone.

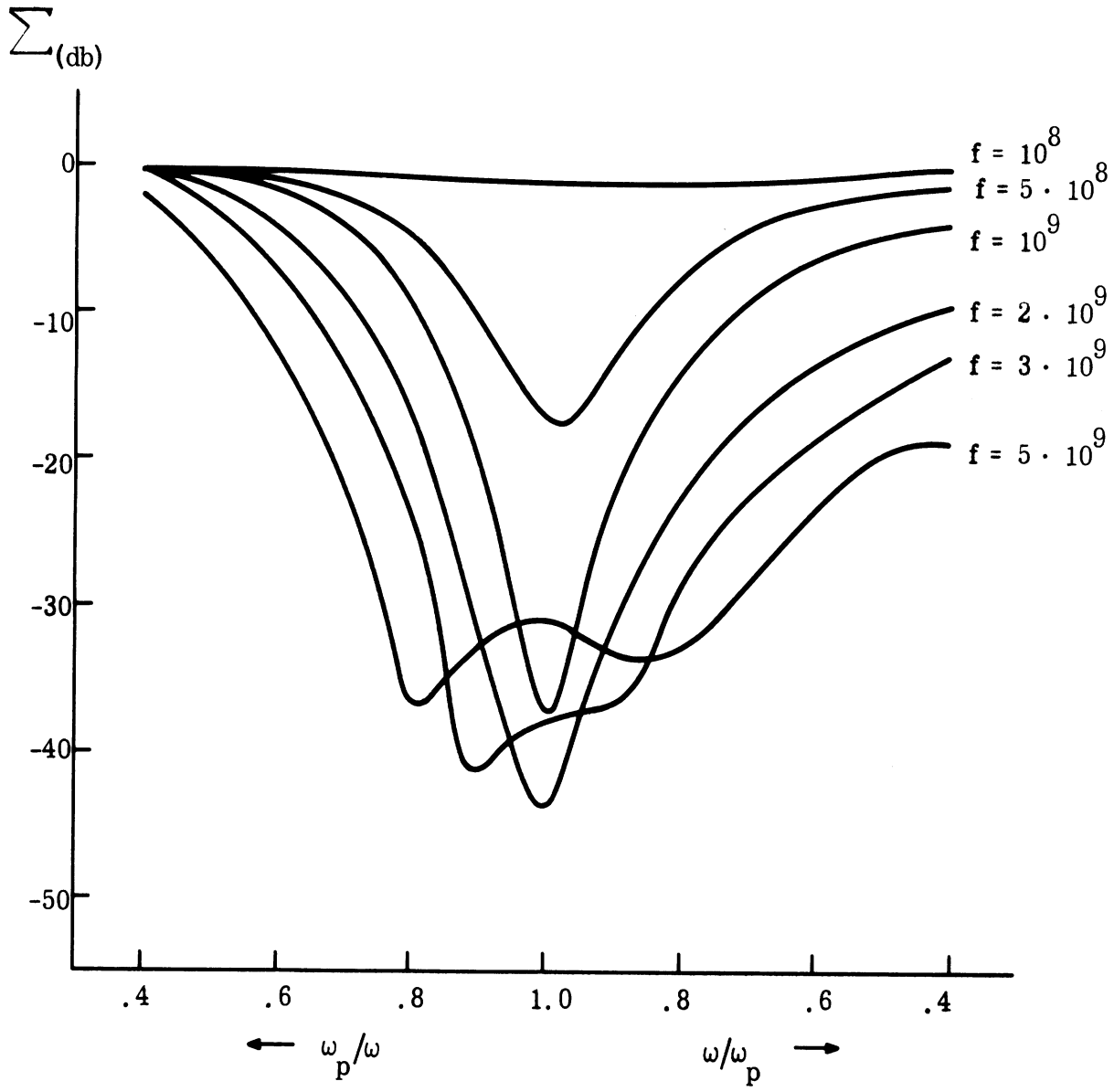

FIG. 5-4: NOSE-ON CROSS SECTION ($\delta = 11^o$, $f_c = 10^8$).

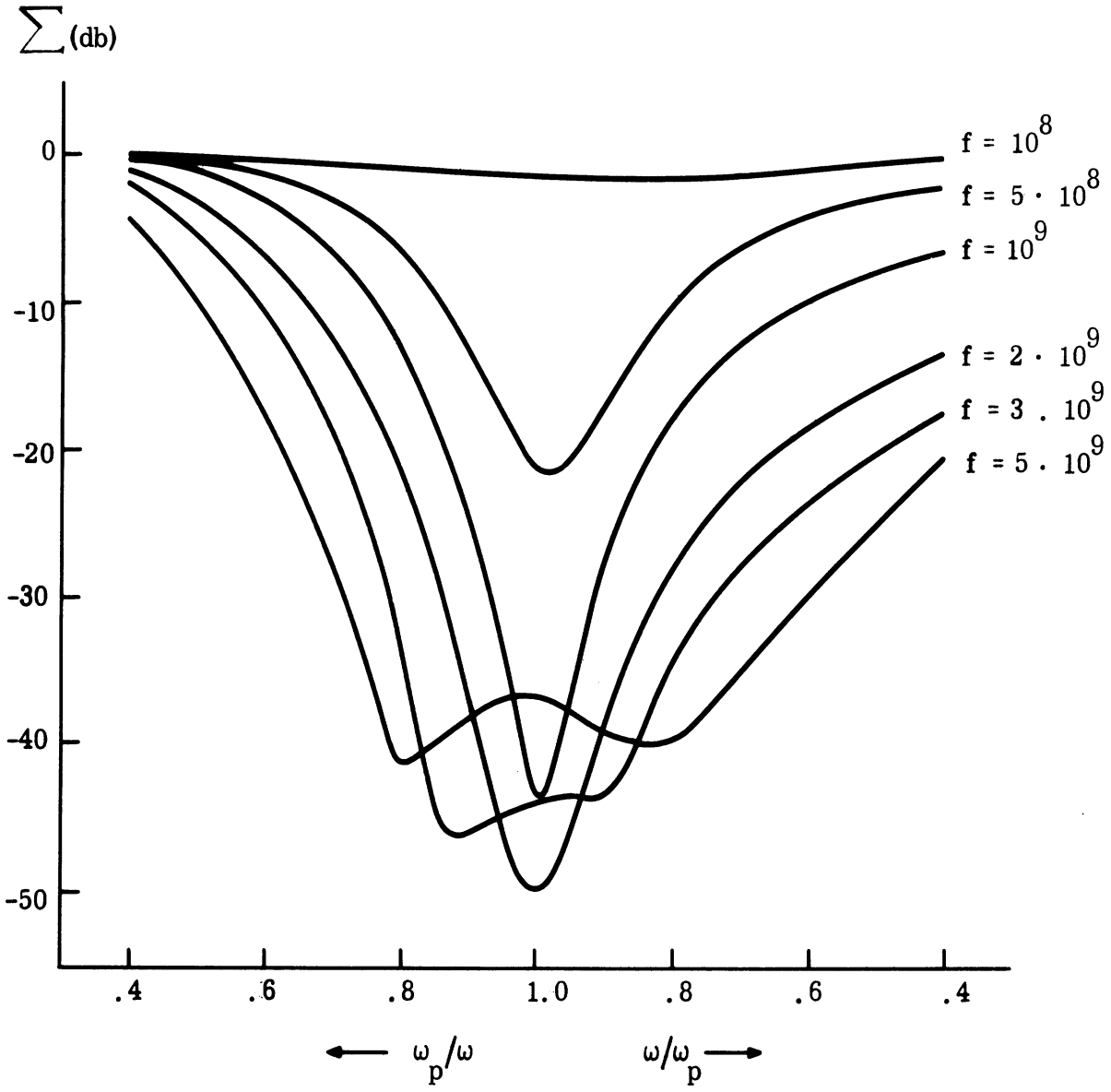

FIG. 5-5: NOSE-ON CROSS SECTION ($\delta = 8^o$, $f_c = 10^8$).

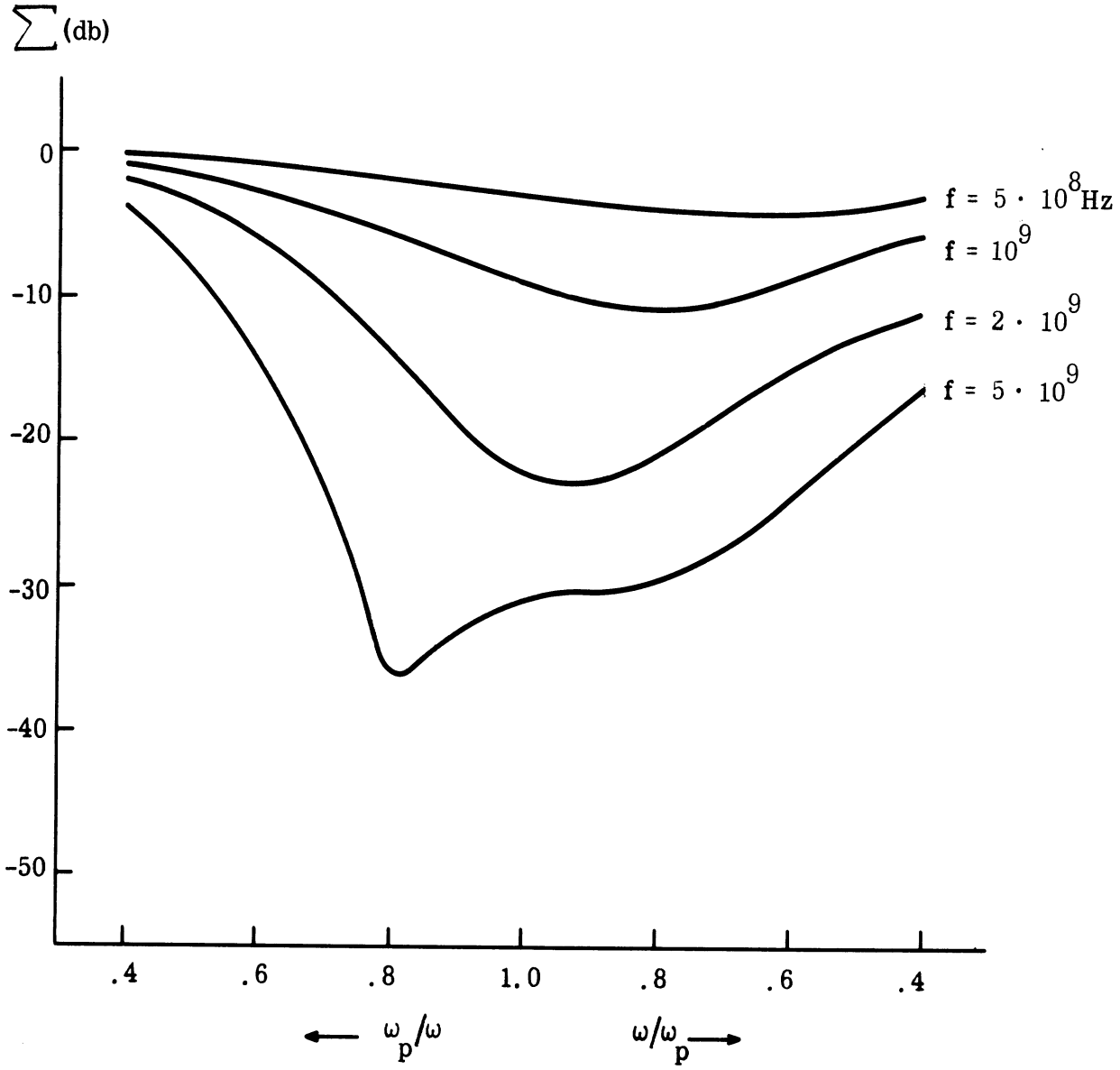

FIG. 5-6: NOSE-ON CROSS SECTION ($\delta = 11^{o}$, $f_c = 10^9$).

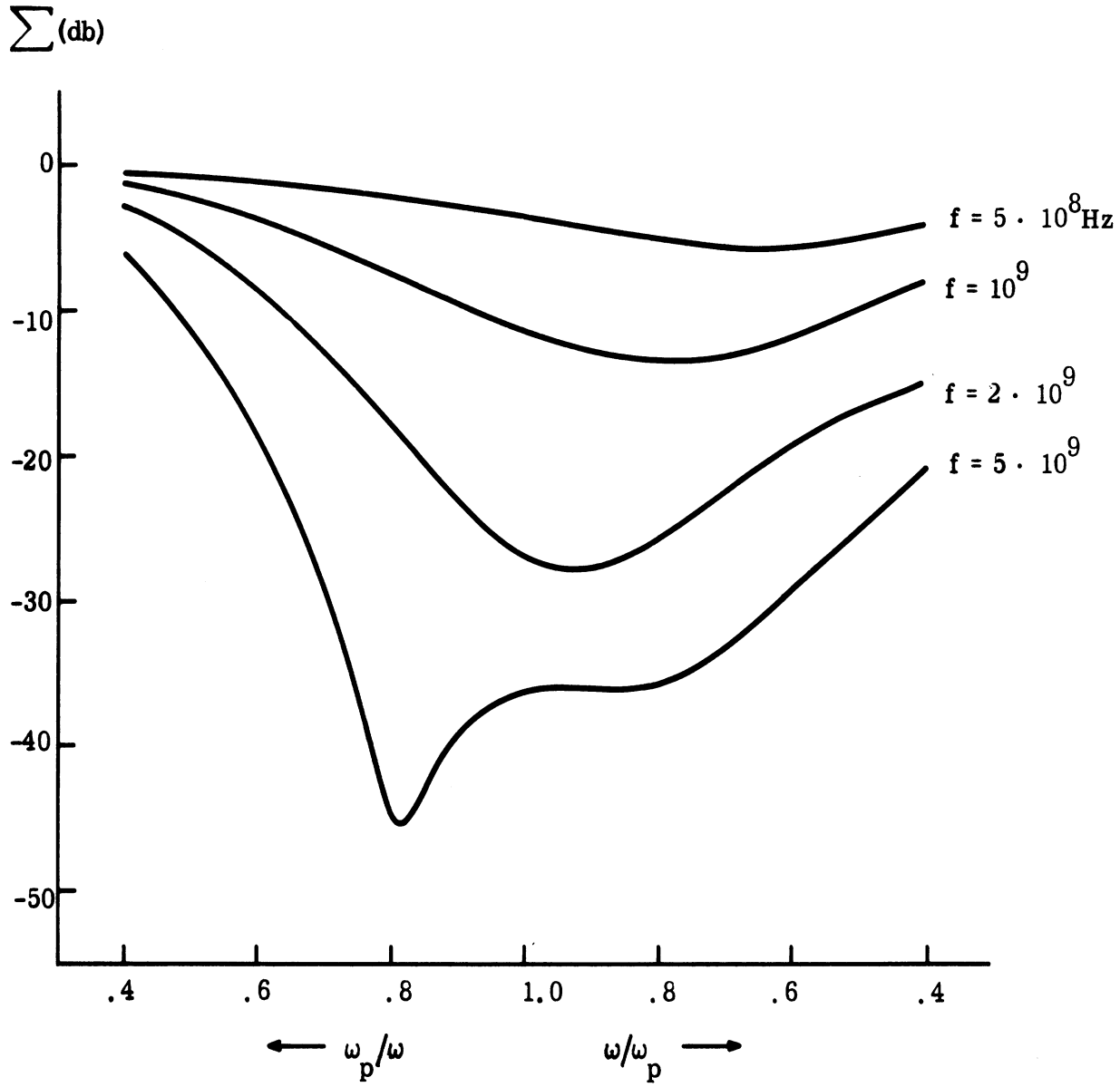

FIG. 5-7: NOSE-ON CROSS SECTION ($\delta = 8^{o}$, $f_c = 10^9$).

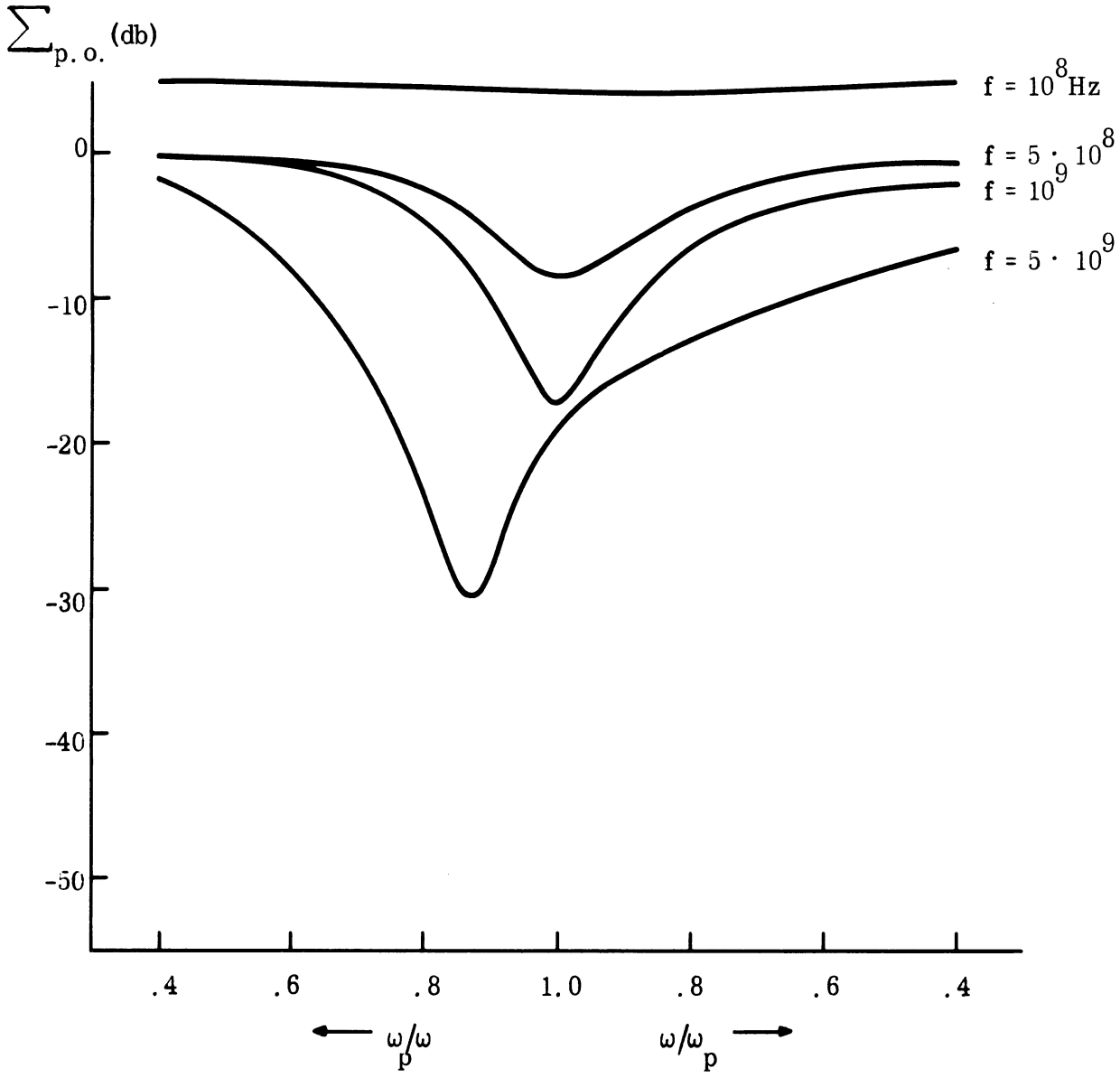

FIG. 5-8: PHYSICAL OPTICS NOSE-ON CROSS SECTION ($\delta = 11^o$, $f_c = 10^8$).

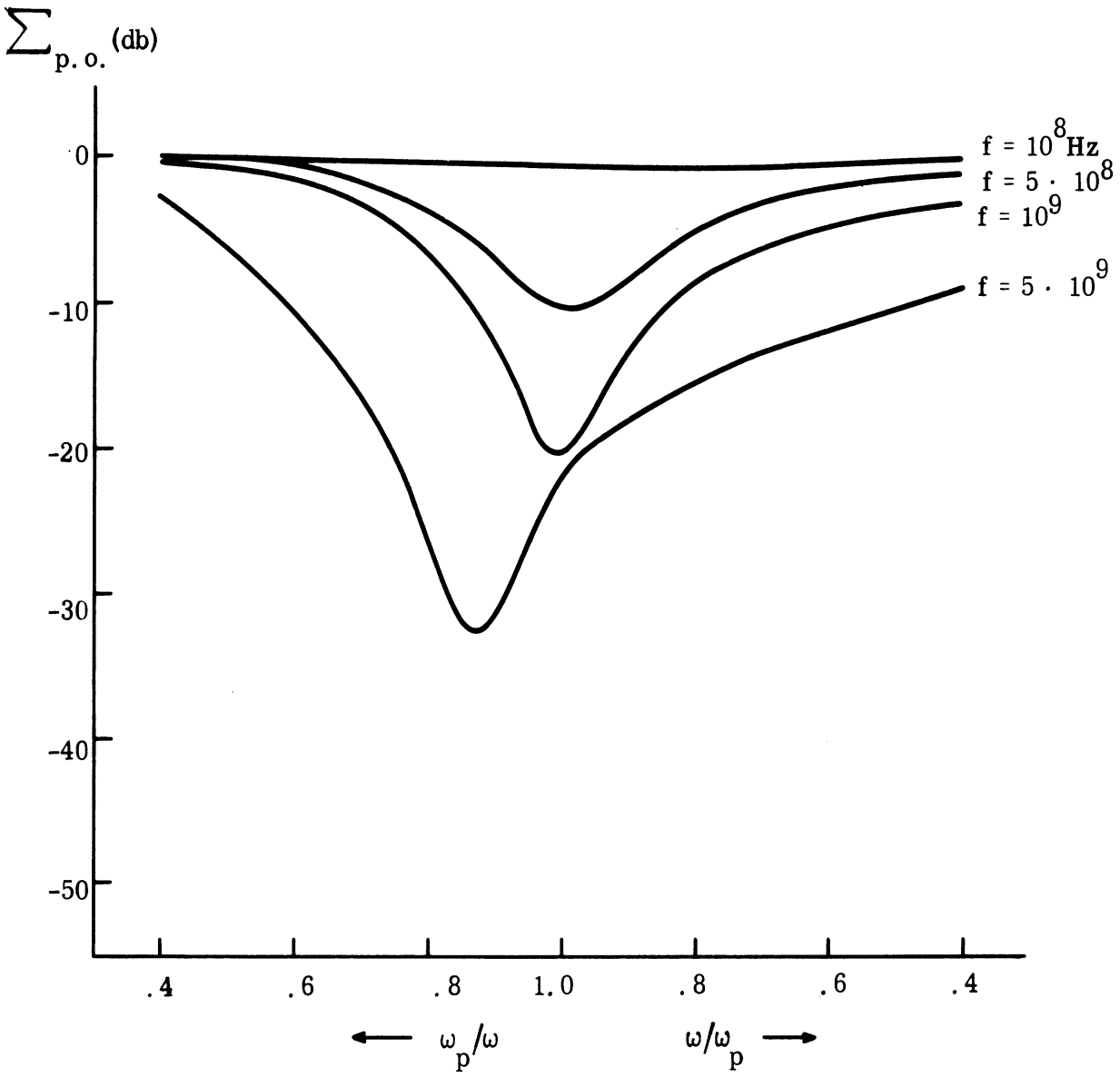

FIG. 5-9: PHYSICAL OPTICS NOSE-ON CROSS SECTION ($\delta = 8^o$, $f_c = 10^8$).

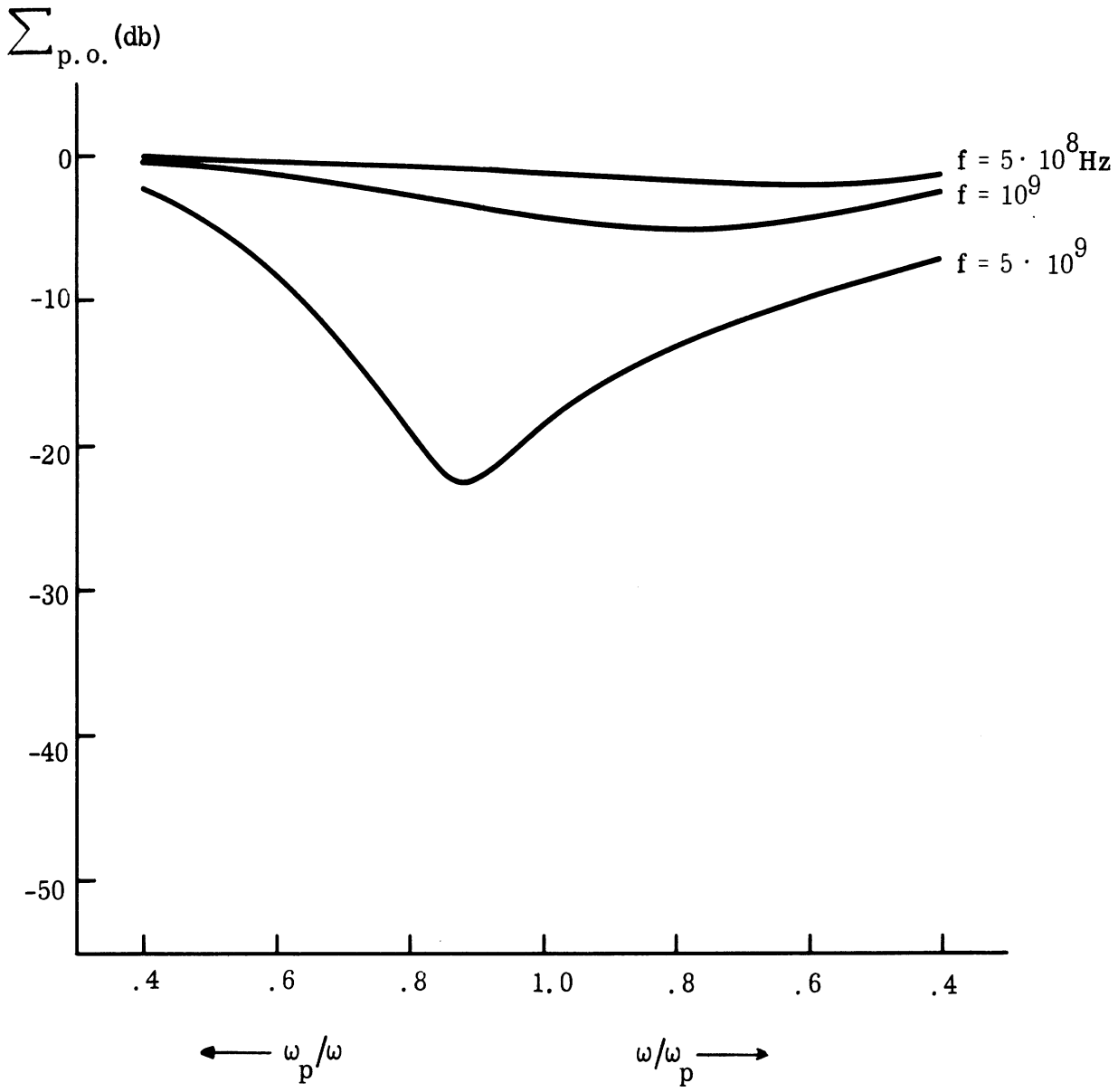

FIG. 5-10: PHYSICAL OPTIC NOSE-ON CROSS SECTION ($\delta = 11^o$, $f_c = 10^9$).

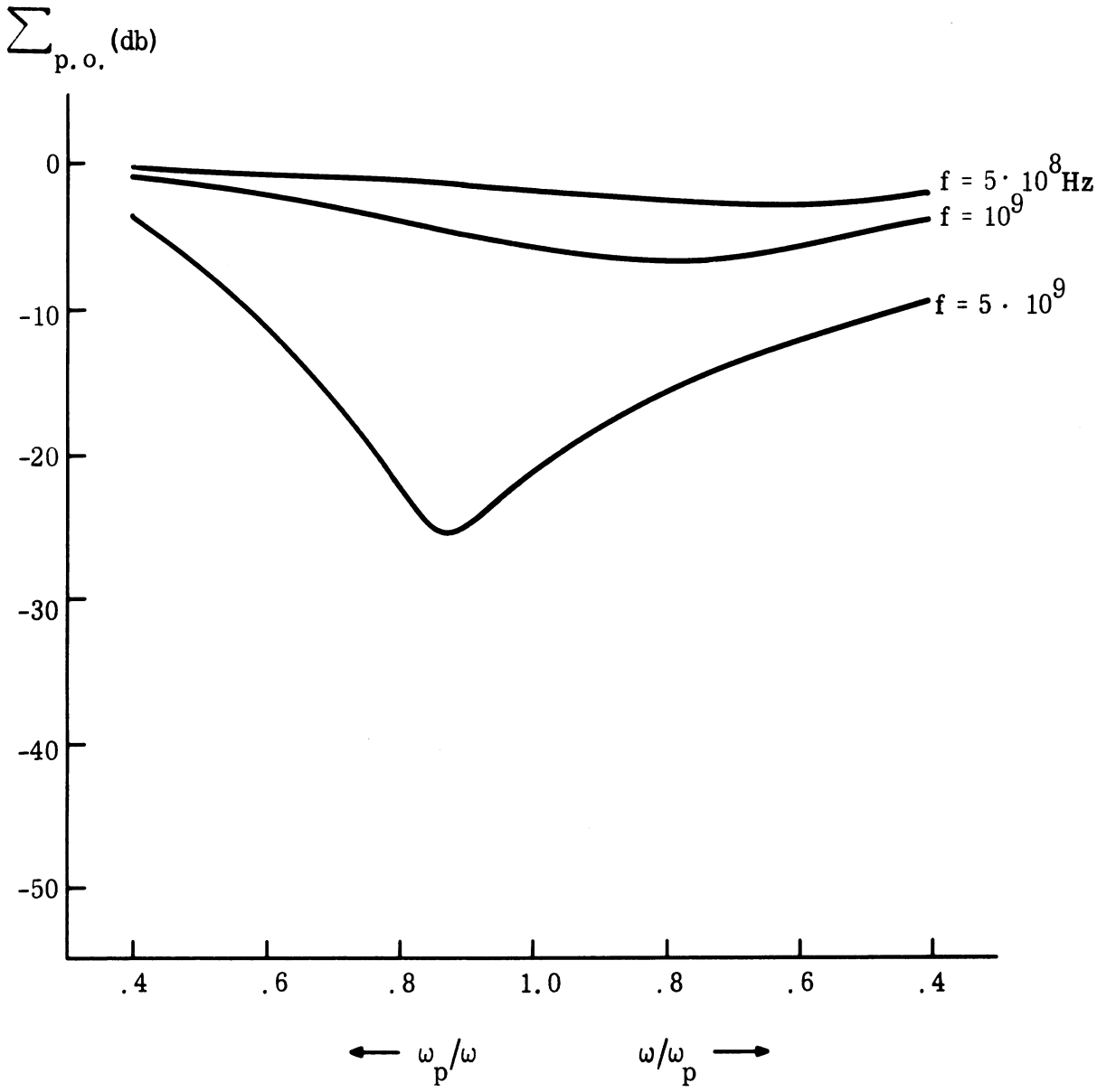

FIG. 5-11: PHYSICAL OPTICS NOSE-ON CROSS SECTION ($\delta = 8^o$, $f_c = 10^9$).

(U) It is clear from the results that the nose-on backscattering cross sections of plasma sheathed finite cones are very sensitive to variations in the plasma sheath properties. No attempt has been made to account for secondary diffraction effects, due to the lack of information concerning the flow field in the base region on the cone. For those cases where the primary diffraction cross sections are very small, secondary effects can be of utmost importance.

5.3 Re-entry Plasma Experiment (Task 2.1.5)

5.3.1 Introduction

(U) Experimental re-entry plasma studies were undertaken during the third year (1967) of the SURF program in order to examine the effect of thin plasma sheaths on the backscattering (radar cross section) from simple geometries, i.e. flat plates, flat back cones, and cylinders. Wire grid structures, with wire spacings less than a half wavelength, were used to simulate the thin plasma sheaths. Previously wire grid structures were successfully employed to simulate plasmas in propagation and antenna studies (Smith and Golden, 1965a, b), but our present investigation for backscattering has uncovered limitations to this technique which were not noticed in earlier work. For example surface field measurements are difficult to interpret because the discrete rather than the continuous properties of the grid structure are more dominant in the near field. Also at oblique angles of incidence the transmission and reflection coefficients for thin sheaths of infinite extent do not appear to be as accurate as at and near normal incidence due to the edge of effects of the finite structure.

(U) The plasma sheath study has met with only limited success, especially so far as theoretical models to support the experiments are concerned. One of the primary goals of this part of the program was to determine the validity of a physical optics model for describing the behavior of backscattering

from plasma clad bodies. Experimental results indicate that a theoretical model based on the physical optics approximations is valid only near normal incidence on coated bodies which have large dimensions and radii of curvature compared to the incident wavelength. As the angle of incidence becomes more oblique complex surface waves are excited and cause the scattered fields to depart noticably from the ordinary physical optics model. It also should be noted that the physical optics model becomes less accurate even for perfectly conducting, flat bodies as the angle of incidence becomes more oblique (Ross, 1966).

(U) Attempts have been made to explain the effects of complex surface waves on the monostatic radar cross section of a thin current sheet (a grid of wires) in free space without any conducting backing. For this case the complex waves reduce to ordinary surface waves (the type which propagate along the surface and exponentially decay away from the surface) which are easier to work with analytically than the more general complex waves. This model is discussed in more detail later.

(U) Before describing last quarters work on the current sheet, a brief review is presented for the work done on the flat plate and flat back cone covered with thin sheaths. For these two coated bodies, the mathematical representations yielded only a limited amount of information, particularly for the coated cone case. Experimental results from both the plate and cone geometries indicate that the composite reflection coefficients for the wire grid backed by a perfect conductor are not accurate for large oblique angles of incidence and it is believed that this is the cause of our poor match between theory and experiment, particularly for the coated cone at nose-on incidence.

5.3.2 The Plasma Covered Flat Plate

(U) In Goodrich et al, 1967c experimental and limited theoretical results were presented for the radar cross section behavior of a grid of wires backed by the conducting flat plate. This model was designed to simulate a thin plasma sheath separated from a plate by an air gap. When the wire grid is fabricated from copper wires the sheath is purely inductive and can be described by a surface impedance $Z_s = j X_s$. For the wire grid the normalized inductance is approximately

$$X_s/Z_o \approx \frac{c}{\lambda} \ln(c/2\pi r) \qquad (5.32)$$

where λ is the wavelength and r and c are the wire radius and spacing. For the plasma sheath the approximate inductance of the sheath is (Smith, 1963)

$$X_s/Z_o \approx (\omega/\omega_p)^2 \frac{1}{kd} \qquad (5.33)$$

where k is the free space wave number, d the sheath thickness, ω_p and ω the plasma and incident frequencies, and $Z_o = 377\,\Omega$ for free space.

(U) Experimental measurements for the flat geometry and VV and HH polarizations have two noticable features:

1) In the vicinity of normal incidence the backscattering for the plate coated with a lossless sheath has the same return as a conducting plate and theoretically follows the physical optics model. If losses (collisions) are introducted the composite refelction coefficient will be reduced and in turn the scattering cross section is also reduced as indicated by the physical optics formulation described in Section 2.5.2 of Goodrich et al, 1967c.

2) For large oblique angles of incidence usually large lobes, which are dependent on the size of the air gap and the sheath impedance, appear in the scattering patterns. These lobes are due to complex waves generated by edge diffraction and are not part of the usual physical optics model.

(U) The approximate location of the large lobes in these patterns can be determined from the poles of the composite reflection coefficients. Unfortunately as the angle of incidence increases these reflection coefficients become more inaccurate and therefore the precise location of the pattern peaks becomes less predictable. For an infinte flat plate with a thin sheath placed a distance ℓ in front of it, the composite reflection coefficients $R_\perp$ and $R_{||}$ are

$$R_\perp = - \frac{Z_o(e^{j\,2k\,\ell\cos\theta_\perp} - 1) + 2\,Z_s\cos\theta_\perp}{Z_o(1 - e^{-j\,2k\,\ell\cos\theta_\perp}) + 2\,Z_s\cos\theta_\perp} \tag{5.34}$$

for VV polarization and

$$R_{||} = \frac{Z_o\cos\theta_{||}(e^{j\,2k\,\ell\cos\theta_{||}} - 1) + 2\,Z_s}{Z_o\cos\theta_{||}(1 - e^{-j\,2k\,\ell\cos\theta_{||}}) + 2\,Z_s} \tag{5.35}$$

for HH polarization. Z_o and Z_s are the free space and surface impedance, $\theta_\perp$ and $\theta_{||}$ are the angles of incidence for the two polarizations, and k is the free space wavenumber. These coefficients become inaccurate for finite plates as $\theta_\perp$ or $\theta_{||}$ increase (depart from normal incidence).

(U) For the sake of completeness let the surface impedance $Z_s = R + jX$ and allow the angle θ to take on complex values $\sigma + j\eta$. Then if the denominators in (5.34) and (5.35) are set equal to zero and one solves for X_V and X_H, the sheath inductances for the VV and HH polarizations, it is

found that

$$X_V = \frac{R_V\left[S\cos(2k\ell C) - C\sin(2k\ell C)\right] - \frac{1}{2}\sin(2k\ell C)}{S\sin(2k\ell C) + C\cos(2k\ell C)} \qquad (5.36)$$

and

$$X_H = \frac{R_H\left[S\cos(2k\ell C) + C\cos(2k\ell C)\right] + \frac{1}{2}(S^2 + C^2)\sin(2k\ell C)}{S\sin(2k\ell C) - C\cos(2k\ell C)} \qquad (5.37)$$

where $S = \sin\sigma\sinh\eta$ and $C = \cos\sigma\cosh\eta$. Solutions to (5.36) and (5.37) indicate the presence of pattern peaks located at angles of incidence σ for corresponding values of X, R, $k\ell$ and η. These solutions are poles of the reflection coefficients given in (5.34) and (5.35). Physically these poles result in complex surface waves which are excited by the edges of the sheath and propagate along it giving rise to large extraordinary pattern lobes at oblique angles. As η becomes small the amplitude of the extraordinary lobe increases.

(U) For a purely inductive sheath $R_V = R_H = 0$ and if we look for poles when $\eta \simeq 0$, then (5.36) and (5.37) reduce to

$$X_V = \frac{-1}{2\cos\theta}\tan(2k\ell\cos\theta) \qquad (5.38)$$

and

$$X_H = \frac{-\cos\theta}{2}\tan(2k\ell\cos\theta) \qquad (5.39)$$

where σ has been replaced by θ since $\eta = 0$. Roots do exist for these equations for various values of θ, X_V and X_H so long as $k\ell$ is large enough to cause the expressions to become positive. Negative roots for these equations indicate that a capacitive sheath is necessary and physically the wire grid or current sheath is never capacitive.

(U) Lack of time has prevented this part of our study to be carried any further. Theoretical techniques such as those found in Chapter 11 of Collin (1960), Chapter 4 of Brekhovskikh (1961), and Chapter 3 of Clemmow (1966) regarding treatment of poles near saddle points and complex surface wave propagation would be useful in seeking a more complete answer to the behavior of the problem. Some of these techniques will be demonstrated in the section on the thin current sheet.

5.3.3 Plasma Coated Flat Back Cone

(U) Radar cross section measurements were made on a flat back cone with and without a wire grid sheath covering the cone, the results of which were described in Goodrich et al, (1967b). Measurements for the perfectly conducting cone (without the grid sheath) agreed well with theory for nose-on, broadside, and end-on incident angles. When the wire grid is covering the cone the broadside and end-on cross sections are the same as the perfectly conducting case as expected, but the nose-on return is reduced by 5 to 13 db depending on the incident wavelength.

(U) So far two theoretical models have been examined in an attempt to explain the nose-on cross section with the wire grid present and both models only predict reduction of approximately 1 db compared to the uncoated cone case. The two theoretical models (the physical optics approximation and the coated wedge approximation) are discussed in Section 5.2 of this report. The weak point in both of these models for this particular experiment is that they depend upon the composite flat plate reflection coefficients given in (5.34) and (5.35). Near nose-on these coefficients are being applied at steep angles of incidence where their validity is questionable. In addition traveling wave modes can be supported by the grid coated cone and they are not considered in these models, in fact it may be these modes which are causing the reflection coefficients to appear erroneous.

(U) The flat back cone measurements with and without the wire grid produced consistent experimental results even though we cannot explain what is happening at and near nose-on incidence. One way of gaining more insight into this problem is to study the scattering from a cylinder coated by a sheath at oblique angles of incidence, a problem which should be easier to examine theoretically. A few experimental measurements were made on a rough model of a cylinder with a wire grid sheath surrounding it. No time remained to examine or extend this work on the cylinder model, although our limited cross section tests indicated that surface wave modes were having noticable effects on the patterns at oblique angles of incidence.

5.3.4 Backscattering by a Current Sheet.

5.3.4.1 Introduction

(U) During the final quarter of the 1967 program efforts were made to gain a better understanding of the radar cross section characteristics of a thin current sheet (flat wire grid) alone in free space. This is the primary component of our physical system and a clear understanding of its behavior is essential in order to explain the effects of a wire grid in the presence of conducting bodies such as cones and plates. A distinction is made here between the words "sheet" and "sheath". Both words are used to describe a thin layer of material such as a wire grid or a thin plasma, but "sheet" means a flat layer alone and "sheath" refers to the same material surrounding a body. Both theoretical and experimental results are discussed for the sheet problem. In the experiment a uniform wire grid is used to represent the current sheet while in the theory the current sheet is any thin layer of material which can be described electrically by its surface impedance (Smith and Golden, 1965a, b)

$$Z_s = 1/\sigma d \qquad (5.40)$$

where σ is the complex conductivity and d the thickness of the sheet. Results are given for the two linear polarizations, vertical (VV) and horizontal (HH).

(U) The main difference in the monostatic radar cross sections for the two polarizations is that the HH case supports surface waves and the VV case does not. The effects of the surface waves become evident for aspect angles beyond 30^{o} where the lobes of HH patterns increase in amplitude and beam width somewhat like the pattern of a traveling wave antenna (Wolff, 1966). Otherwise the backscattering for aspect angles between 0^{o} and 30^{o} for both polarizations has the same characteristics as that for a perfectly conducting flat plate of the same dimensions with the amplitude reduced by an amount equal to the power reflection coefficients.

(U) The feature which distinguishes the sheet from a perfect conductor is that part of the incident field is transmitted through and part is reflected by the sheet whereas all of the incident field is reflected by the conductor. Because the sheet is thin its analytic solution yields to a simplified form of the Stratton-Chu Equations which is no more difficult to handle than the conducting plate problem with the exception of accounting for the surface wave in the HH case.

5.3.4.2 Formulation of the Problem

(U) Consider the geometry given in Fig. 5-12 where a plane wave of either vertical or horizontal polarization is incident obliquely on a square current sheet which is very thin compared to the wavelength in the sheet material. It is assumed that the length and width, a, of the sheet are large compared to the incident wavelength ($a >> \lambda$) to such a degree, that locally the transmission and reflection coefficients $T_{||}$, $T_{\perp}$, $R_{||}$, and $R_{\perp}$ are those for sheet of infinite extent along the x and y axes; this is essentially the physical optics

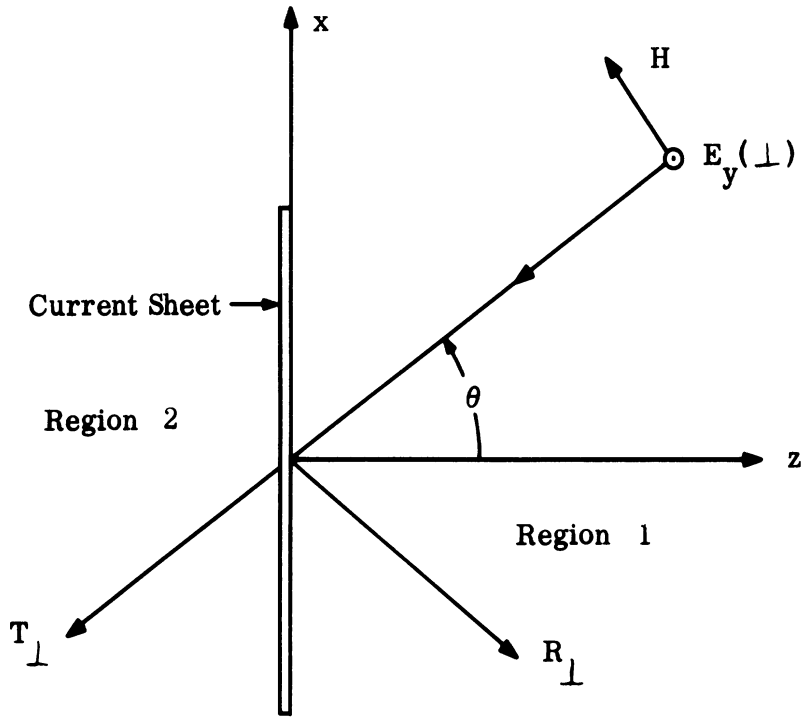

(a) Vertical Polarization

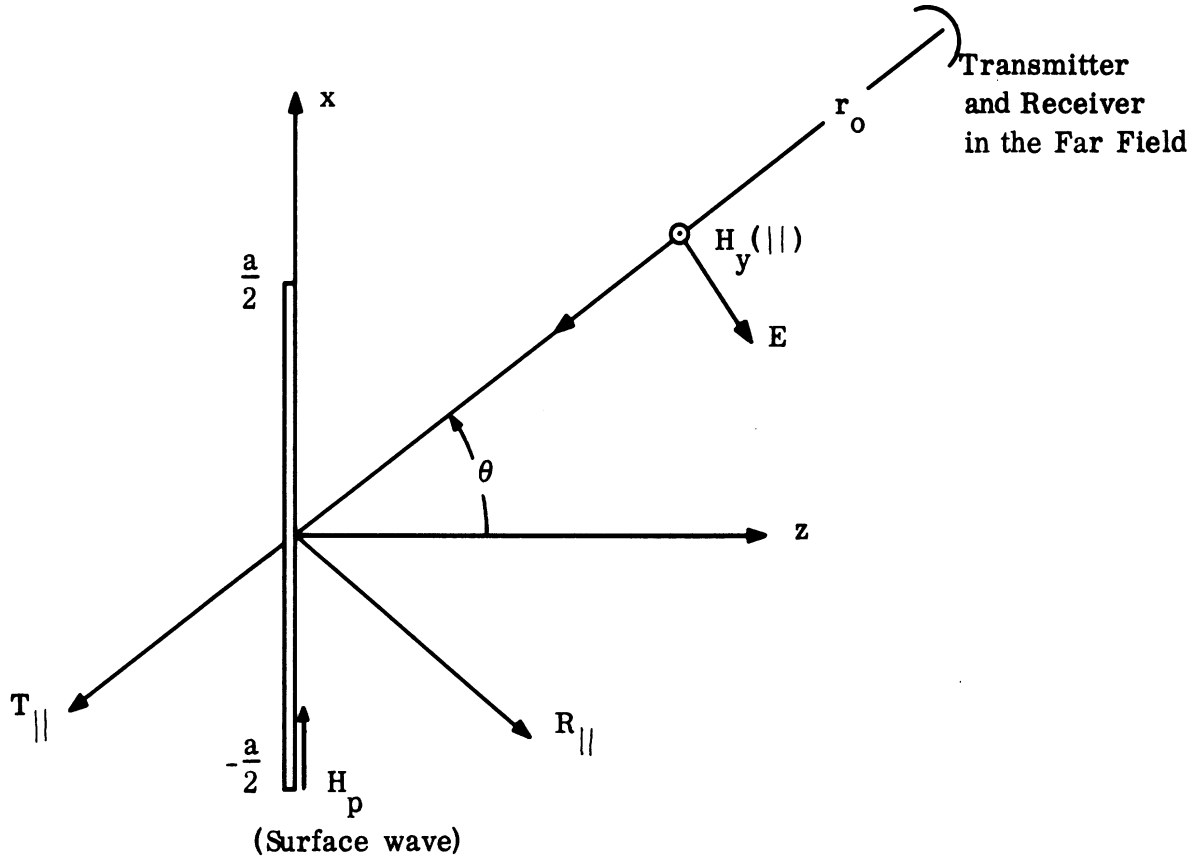

(b) Parallel Polarization

FIG. 5-12: SCATTERING GEOMETRY FOR THE CURRENT SHEET.

assumption. At the sheet surface, $z = 0$, the Poeverlein-Wait jump conditions are used to describe the sheet behavior (Wait, 1960; and Smith, 1965a)

$$\hat{z} \times (\bar{E}_1 - \bar{E}_2) = 0 \tag{5.41}$$

$$\hat{z} \times (\bar{H}_1 - \bar{H}_2) = \bar{J}_s \tag{5.42}$$

where $\hat{z}$ is the unit vector normal to the surface, $\bar{J}_s$ is the surface current (amps per meter) and the subscripts 1 and 2 refer to the electric ($\bar{E}$) and magnetic ($\bar{H}$) fields in regions 1 and 2. The surface current is related to the electric fields and the surface impedance in (5.40) by

$$\bar{J}_s = \frac{1}{Z_s} \left[\bar{E}_2 - (\hat{z} \cdot \bar{E}_2)\, \hat{z} \right] \tag{5.43}$$

on considering (5.41)

$$\bar{J}_s = \frac{1}{Z_s} \left[\bar{E}_1 - (\hat{z} \cdot \bar{E}_1)\, \hat{z} \right] . \tag{5.44}$$

(U) For two-dimensional, flat geometries with homogeneous and isotropic materials the VV and HH polarizations may be examined separately and the entire E and H fields can be expressed as

$$\bar{E}_1 = \hat{y}\, E_o (e^{jkz\cos\theta} + R_\perp\, e^{-jkz\cos\theta})\, e^{jkx\sin\theta} \tag{5.45}$$

$$\bar{E}_2 = \hat{y}\, E_o\, T_\perp\, e^{jk(z\cos\theta + x\sin\theta)} \tag{5.46}$$

for VV polarization and

$$\bar{H}_1 = \hat{y}\, H_o (e^{jkz\cos\theta} + R_{||}\, e^{-jkz\cos\theta})\, e^{jkx\sin\theta} \tag{5.47}$$

$$\bar{H}_2 = \hat{y}\ H_o\ T_{||}\ e^{jk\,(z\,\cos\,\theta\,+\,x\,\sin\,\theta)} \tag{5.48}$$

for HH polarization where E_o and H_o are the intensities of the incident fields for the two cases. The remaining E and H fields can be derived from Maxwell's two curl equations. No surface wave fields are included in the above, but they will be considered later.

(U) An application of the Poeverlein-Wait jump conditions (5.41) and (5.42) to the total fields in regions 1 and 2 leads to the following transmission and reflection coefficients (Poeverlein, 1958)

$$T_{\perp} = \frac{1}{1 + \dfrac{Z_o}{2\,Z_s\,\cos\,\theta}}, \qquad R_{\perp} = \frac{1}{1 + \dfrac{2\,Z_s\,\cos\,\theta}{Z_o}} \tag{5.49}$$

for VV, and

$$T_{||} = \frac{1}{1 + \dfrac{Z_o\,\cos\,\theta}{2\,Z_s}}, \qquad R_{||} = \frac{1}{1 + \dfrac{2\,Z_s}{Z_o\,\cos\,\theta}} \tag{5.50}$$

for HH polarization, where $Z_o = \sqrt{\mu_o/\epsilon_o}$ and $Z_s = 1/\sigma d$ according to (5.40) or more generally $Z_s = R_s + j\,X_s$.

(U) In order to determine the monostatic radar cross section, where the transmitter and receiver are located together at the same far field point, it is necessary to find the scattered fields. The Stratton-Chu equations (Stratton, 1941), which are a vector form of the Kirchhoff-Huggens principle, are evaluated in the physical optics approximation to obtain the scattered far fields. Assuming a time harmonic form $e^{j\omega t}$, the scattered $\bar{E}^s$ and $\bar{H}^s$ fields can be expressed by a surface integration over the total fields $\bar{E}(\perp,||)$ and $\bar{H}(\perp,||)$

at the surface of the scatterer (Johnson, 1965),

$$\bar{E}_{\perp}^{s} = -\int_{S_1}\int \left[(\hat{z} \times \bar{E}_{\perp}) \times \nabla G + (\hat{z} \cdot \bar{E}_{\perp}) \nabla G - \right.$$

$$\left. - j k_o Z_o G (\hat{z} \times \bar{H}_{\perp})\right] d S_1 \qquad (5.51)$$

$$\bar{H}_{\perp}^{s} = -\int_{S_1}\int \left[(\hat{z} \times \bar{H}_{||}) \times \nabla G + (\hat{z} \cdot \bar{H}_{||}) \nabla G + \right.$$

$$\left. + j \frac{k_o}{Z_o} G (\hat{z} \times \bar{E}_{||})\right] d S_1 \qquad (5.52)$$

where $d S_1 = dx\, dy$ is the differential surface element on the region 1 side of the sheet, and G is the spherical Green's function

$$G \approx - \frac{e^{-jkr_o}}{4\pi r_o} e^{jk(\hat{z} \cos\theta + \hat{x} \sin\theta)} \qquad (5.53)$$

and in the far field

$$\nabla G \approx - (jk) (\hat{z} \cos\theta + \hat{x} \sin\theta) G \qquad (5.54)$$

where r_o is shown in Fig. 5-12. The fields at the surface in (5.51) and (5.52) are related to those in (5.45) through (5.48) by

$$\left.\begin{aligned} \bar{E}_{\perp} &= \bar{E}_1 - \bar{E}_2 \\ \text{and} \\ \bar{H}_{||} &= \bar{H}_1 - \bar{H}_2 \end{aligned}\right\} \qquad (5.55)$$

5.3.4.3 Radar Cross Section of Current Sheet-Excluding Surface Waves

(U) Since the surface integrations in (5.51) and (5.52) take place at the sheet, the Poeverlein-Wait jump conditions are applied to the surface fields and only the difference in tangential magnetic field components, which are equal to the surface currents J_s remain; thus

$$\bar{E}_{\perp}^{s} = - \int_{S_1}\int jk_o Z_o G \hat{z} \times \left[\frac{1}{j\omega\mu} \nabla \times (\bar{E}_1 - \bar{E}_2)\right] dx\, dy \qquad (5.56)$$

and

$$\bar{H}_{||}^{s} = - \int_{S_1}\int \left[\hat{z} \times (\bar{H}_1 - \bar{H}_2)\right] \times \nabla G \; dx\, dy \qquad (5.57)$$

where (5.55) and $\bar{H} = 1/j\omega\mu \; \nabla \times \bar{E}$ have been substituted. Upon further substitution of (5.45) through (5.48), (5.53) and (5.54) and integrating over the sheet, it is found that

$$E_{\perp}^{s} = y\, E_o \left(\frac{jk_o a^2 \cos\theta}{2\pi r_o}\right) \left[R_{\perp} \frac{\sin(ka \sin\theta)}{ka \sin\theta}\right] e^{-jkr_o} \qquad (5.58)$$

and

$$H_{||}^{s} = y\, H_o \left(\frac{jk_o a^2 \cos\theta}{2\pi r_o}\right) \left[R_{||} \frac{\sin(ka \sin\theta)}{ka \sin\theta}\right] e^{-jkr_o} \qquad (5.59)$$

As the current sheet approaches a perfect conductor ($Z_s \rightarrow 0$) both $R_{\perp}$ and $R_{||}$ approach unity and the scattered fields for the two polarizations have the same form

$$\frac{j\,ka^2\cos\theta}{2\pi\, r_o}\;\frac{\sin(ka\sin\theta)}{ka\sin\theta}\;e^{-jkr_o}$$

which is the usual physical optics result showing polarization independence.

(U) Radar cross section is defined by

$$\sigma = 4\pi r_o^2\left|\frac{\bar{E}^s_{\perp}}{\bar{E}_o}\right|^2 = 4\pi r_o^2\left|\frac{\bar{H}^s_{||}}{\bar{H}_o}\right|^2 \qquad (5.60)$$

and for the case of a perfectly conducting, large, square plate, both the $\bar{E}^s$ and $\bar{H}^s$ formulations yield

$$\sigma_{pc} = \frac{a^2}{\pi}(ka\cos\theta)^2\left[\frac{\sin(ka\sin\theta)}{ka\sin\theta}\right]^2 . \qquad (5.61)$$

If the two polarization cross sections, $\sigma_{\perp}$ and $\sigma_{||}$ are normalized to σ_{pc} and the Z_s is expressed in terms of a surface resistance R_s and inductance X_s then

$$\frac{\sigma_{\perp}}{\sigma_{pc}} = R_{\perp}\,R^*_{\perp} = \frac{1}{1+4(R_s/Z_o)\cos\theta+4\left(\frac{R_s^2+X_s^2}{Z_o^2}\right)\cos^2\theta} \qquad (5.62)$$

and

$$\frac{\sigma_{||}}{\sigma_{pc}} = R_{||}\,R^*_{||} = \frac{\cos^2\theta}{\cos^2\theta+4(R_s/Z_o)\cos\theta+4\left(\frac{R_s^2+X_s^2}{Z_o^2}\right)} \qquad (5.63)$$

where the * quantities are the complex conjugates of the reflection coefficients

in (5.49) and (5.50). In the case of VV polarization (5.62) is as good an approximation for a sheet of arbitrary Z_s as σ_{pc} is for a large conducting plate. Beyond an aspect angle of $\theta = 30^o$ all physical optics models increase in error with increasing θ as indicated in an article by Ross (1965).

(U) For small aspect angles θ through the first few sidelobes off broadside $\sigma_{||}/\sigma_{pc}$ in (5.63) is also accurate, but as θ increases and depending on the value of Z_s, the shape and amplitude of the scattering pattern depart noticeably from ordinary physical optics behavior. This is due to the excitation of surface waves by the edges and the support of these waves by the sheet for HH polarization. A rough model is presented to account for the surface wave, but it is only a qualitative model which shows that the lobe amplitude and beamwidth increase, but the agreement with experimental data is poor. This is to be expected because the physical optics model is poor in this aspect region independent of whether or not surface waves exist. The larger the inductance X_s is compared to R_s, the more noticeable the surface wave contribution is to the pattern.

5.3.4.4 Surface Wave Contribution

(U) Actually two surface waves are excited for HH incidence one originating from the edge at $X = a/2$ and the other at $X = -a/2$. If these surface waves are treated like traveling wave antennas, ignoring any multiple reflections, then the edge at $X = -a/2$ will contribute considerably more to the monostatic scattering than the $a/2$ edge; it is the only surface wave analyzed at this time (Fig. 5-12). Our model is based on the work of Tamir and Oliner (1963), although J.R. Wait (1960) also has looked at this problem. In order to formulate an expression for the surface wave, assume the sheet in Fig. 5-12b is extended to $\pm\infty$ along the X axis and that a magnetic line source

is located at $y = -a/2$ and $z = 0^+$ which is just on the region 1 side of the sheet. According to Tamir and Oliner (1963), the surface wave contribution from such a source is of the form

$$\bar{H}_p = - y\, j\, L \frac{R_{||}^2 (\phi_p)}{\frac{dR_{||}(\phi_p)}{d\phi}} e^{-jk(x + a/2)\cos(\phi_p - \pi/2)} \tag{5.64}$$

where L is the launch factor representing the strength of the line source generated by the edge at $x = -a/2$ and ϕ_p is the complex pole of the reflection coefficient,

$$R = \frac{\cos\phi}{\cos\phi + 2\frac{Z_s}{Z_o}} . \tag{5.65}$$

This last equation is actually (5.50) after $\phi = \sigma + j\eta$ has been substituted for θ, the aspect angle. To find the pole location ϕ_p, set the denominator of (5.65) equal to zero and expand ϕ and Z_s in their complex forms to

$$\cos(\sigma + j\eta) = -\frac{2}{Z_o}(R_s + j X_s) \tag{5.66}$$

which leads to two expressions upon setting real and imaginary parts equal to one another.

$$\cos\sigma \cosh\eta = -\frac{2}{Z_o} R_s$$

$$\sin\sigma \sinh\eta = \frac{2}{Z_o} X_s . \tag{5.67}$$

Returning once again to (5.64), the term

$$\frac{R_{||}^2(\phi_p)}{\frac{dR_{||}(\phi_p)}{d\phi}} = \frac{-Z_o \cos^2 \phi_p}{2 Z_s \sin \phi_p} \tag{5.68}$$

is the residue for the pole contribution.

(U) In the experiment the current sheet is purely inductive with $R_s = 0$; thus Eq. (5.67) indicates $\sigma = \pi/2$ or $\phi_p = \pi/2 + j\eta$ which leads to

$$\sinh \eta = 2 X_s/Z_o \quad \cosh \eta = \sqrt{1 + (2 X_s/Z_o)^2} \tag{5.69}$$

and after further substitution

$$\frac{R_{||}^2(\phi_p)}{R'_{||}(\phi_p)} = \frac{-Z_o \sinh^2 \eta}{2(jX_s)\cosh \eta} = \frac{j\,2\,X_s}{\sqrt{Z_o^2 + 4 X_o^2}}. \tag{5.70}$$

Therefore the surface wave in (5.64) is approximately

$$\bar{H}_p \approx \hat{y}\, L \left[\frac{2X_s}{Z_o b}\right] e^{-jk(x + a/2)b} \tag{5.71}$$

where $b = \left[1 + 4(X_s^2/Z_o^2)\right]^{1/2}$ and the approximation sign is used to indicate that the launch factor L is unknown. This is to say the amount of the incident energy which is converted into line source energy is unknown.

(U) When $\bar{H}_1 - \bar{H}_2$ in (5.56) is replaced by $\bar{H}_p$ in (5.71), the integration over the current sheet gives the scattered field $\bar{H}_p^s$ due to the surface wave

$$\bar{H}_p^s = \hat{y}\left(\frac{jk_o a^2 \cos\theta}{2\pi r_o}\right)\left[\frac{2X_s L}{Z_o b} \cdot \frac{\sin k\frac{a}{2}(b - \sin\theta)}{k\frac{a}{2}(b - \sin\theta)}\right] e^{-jk\left(r_o - \frac{ab}{2}\right)} \tag{5.72}$$

Now H_p^s and $H_{||}^s$ can be combined as phasors and after using the definition in (5.60) the total HH cross section $\sigma_{||}^T$ can be expressed as

$$\sigma_{||}^T = 4\pi r_o \frac{\left| \bar{H}_{||}^s + \bar{H}_p^s \right|^2}{H_o} \tag{5.73}$$

where $\bar{H}_{||}^s$ and $\bar{H}_p^s$ are given in (5.59) and (5.72). This expression which atempts to account for surface wave contributions in the HH scattering patterns only gives a rough indication of this behavior as will be shown in Fig. 5-13.

(U) Before going on a word is in order to explain why the VV polarization case does not support any surface waves. If the denominator $R_\perp$ in (5.49) is equated to zero in the same fashion as in (5.66), then

$$\cos(\sigma + j\eta) = \frac{-Z_o}{2(R_s + jX_s)}$$

and after equating real and imaginary parts

$$\text{(real)} \qquad \cos\sigma \cosh\eta = \frac{-Z_o X_s}{2(R_s^2 + X_s^2)}$$

$$\text{(imaginary)} \qquad \sin\sigma \sinh\eta = \frac{-Z_o X_s}{2(R_s^2 + X_s^2)} \tag{5.75}$$

The last equation indicates that for VV polarization the sheet will support surface waves only when it is capacitive reactive. Under most circumstances thin over dense plasmas, especially cold ones, are inductive reactive. More discussion on this topic is found in Wait (1960) and in Collin (1961).

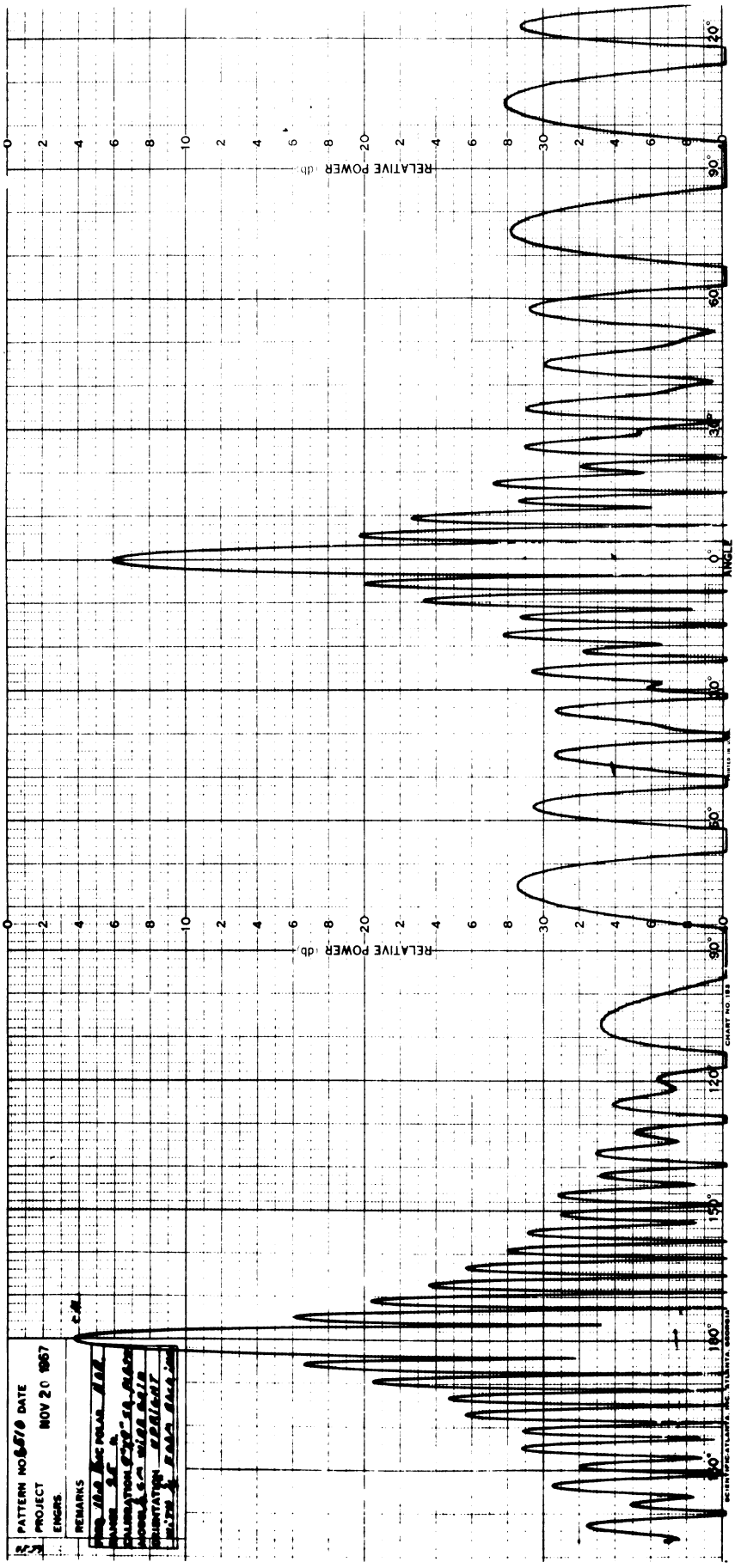

Wire Grid

Aluminum Plate

FIG: 5-13: RCS PATTERNS OF 9" x 9" GRID AND PLANE FOR HH POLARIZATION, 10 GHz, AND $X_s/Z_o = 0.37$.

5.3.4.5 The Current Sheet Experiment

(U) In the experiment, wire grids with two mesh sizes were measured at four X-band frequencies. Table V-1 displays the frequencies, wavelengths, sheet sizes normalized to a wavelength, and surface inductances for the tests.

TABLE V-1

f (GHz)	λ (cm)	a/λ	X_s/Z_o	
			C = 1/2 cm	C = 1 cm
8.5	3.53	6.48	.31	.82
9.5	3.16	7.25	.35	.92
10.0	3.0	7.62	.37	.96
10.5	2.86	8.0	.39	1.0

The sheets are 9" x 9" and the mesh spacings c are 1/2 and 1 cm. Equation (5.32) is used to calculate the wire grid inductance and is valid for $c/\lambda < 1/2$ (Golden and Smith, 1964). The grids were made by gluing No. 33 gauge wire (dia = .007") to 1/4" sheets of styrafoam. These models were measured on an indoor scattering range 25' from the transmitter-receiver location.

(U) Four experimental patterns are displayed in Figs. 5-13 through 5-16 for tests made at 10 GHz, VV and HH polarizations, and grid surface inductances X_s/Z_o equal to 0.37 and 0.96. In each of these patterns the right hand portion, θ between 0^o and 90^o, is the wire grid results and the left hand portion, θ between 90^o and 180^o, is the calibration reference, an aluminum flat plate. Both the grid and the plate are 9" x 9". The broadside peak for the plate has an absolute cross section in db compared to one square meter of

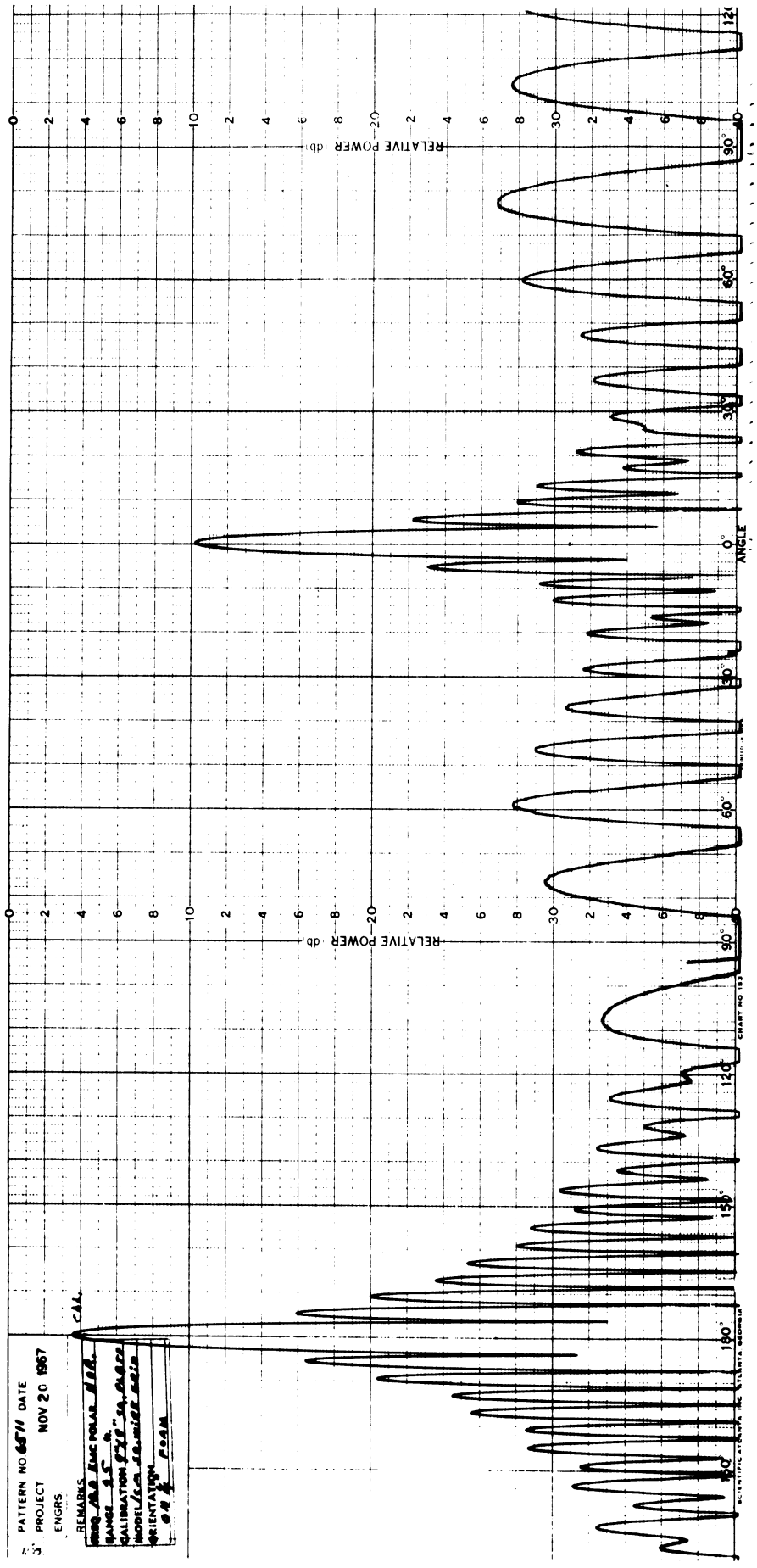

FIG. 5-14: RCS PATTERNS OF 9" x 9" GRID AND PLATE FOR HH POLARIZATION, 10 GHz, AND $X_s/Z_o = 0.96$.

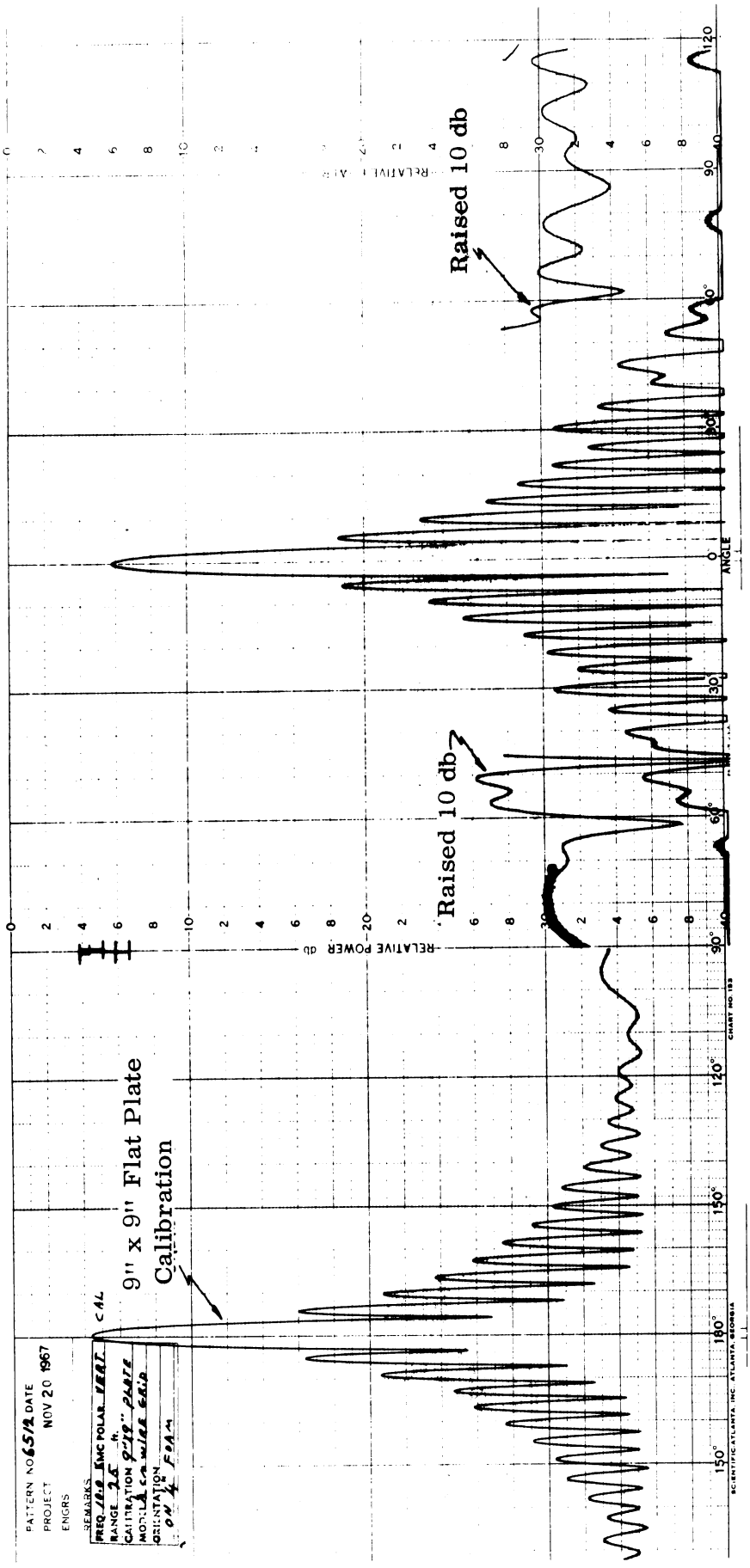

FIG. 5-15: RCS PATTERNS OF 9" x 9" GRID AND PLATE FOR VV POLARIZATION, 10 GHz AND $X_s/Z_o = 0.37$.

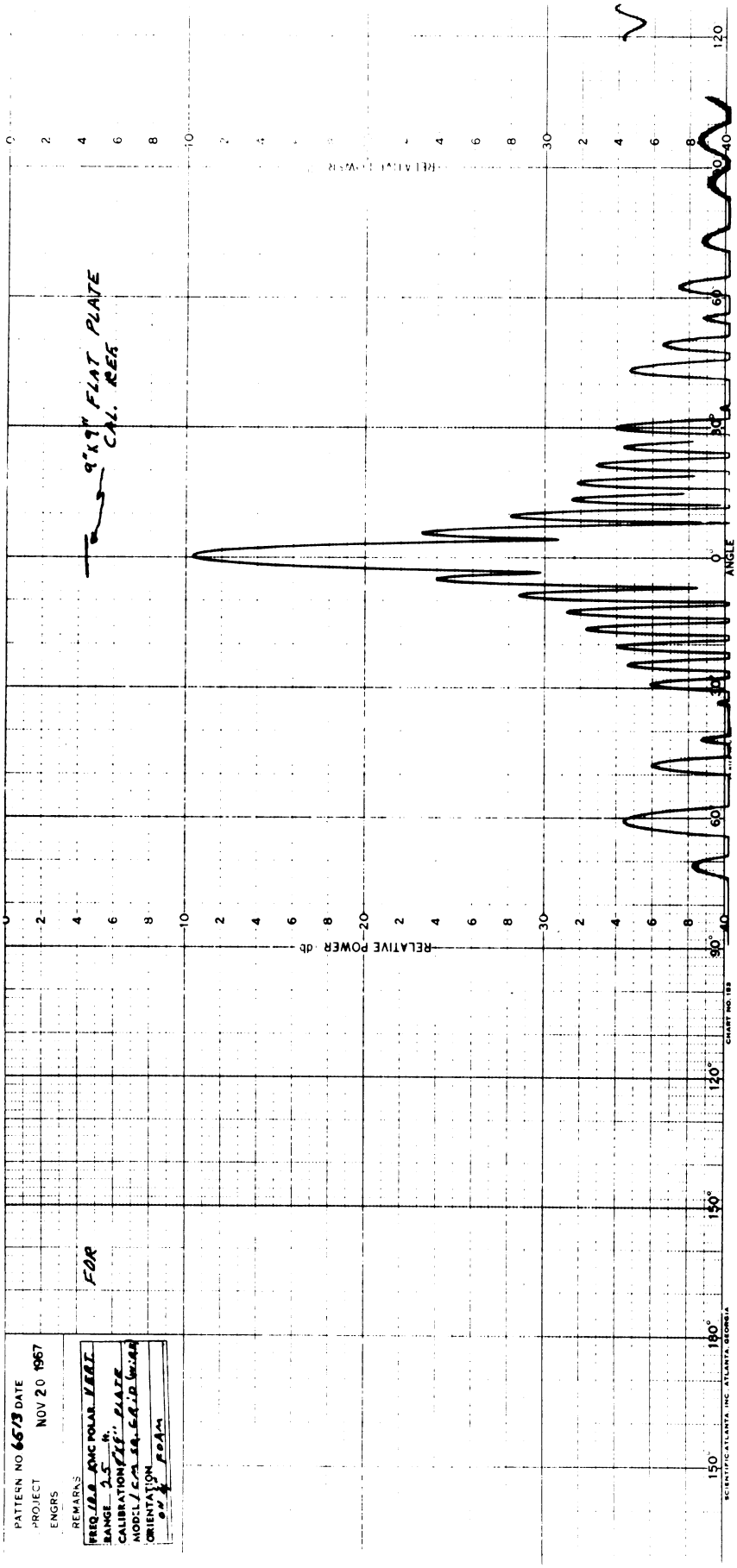

Wire Grid

FIG. 5-16: RCS PATTERNS OF 9" x 9" GRID AND PLATE FOR VV POLARIZATION, 10 GHz and $X_s/Z_o = 0.96$.

$$\sigma_{pc} = \frac{a^2}{\pi} (ka)^2 = +15.8 \text{ db} . \tag{5.76}$$

This recipe is obtained by setting $\theta = 0$ in (5.60).

(U) These measurements show clearly that the HH grid patterns produce large, broad lobes beyond 30^o aspect angles compared to VV grid patterns or either polarization results for the aluminum plates. These broader lobes resemble the pattern structure of a traveling wave antenna (Wolff, 1966) especially in Fig. 5-14. Surface wave behave in the same was as traveling wave antennas and it is reasonable to attribute these scattering pattern characteristics to surface waves excited by edge diffraction and supported by the grid sheet particularly since theory predicts this type of action. For the most part the VV grid patterns tend to follow the aluminum plate tendencies with one exception; the nulls are sharper for the grid at larger aspect angles.

(U) Figures 5-17 and 5-18 are comparisons between theory and experiment for the 1/2 cm mesh grid and aluminum plate. In all these patterns the solid line is theory and the XX marks are the experimental lobe peaks taken from Figs. 5-13 and 5-15. Part (a) of Fig. 5-17 is the HH pattern for the grid with $X_s/Z_o = 0.37$. The theory for this pattern is obtained by renormalizing (5.75) to the form

$$\frac{\pi \sigma^T_{||}}{a^2 (ka)^2} = \cos^2\theta \left| R_{||} \frac{\sin (ka \sin\theta)}{ka \sin\theta} + \frac{2X_s L}{Z_o b} \cdot \right.$$
$$\left. \cdot \frac{\sin k\frac{a}{2}(b - \sin\theta)}{k\frac{a}{2}(b - \sin\theta)} e^{j\frac{kab}{2}} \right|^2 \tag{5.77}$$

such that for $\theta = 0$, (5.77) is $\left|R_{||}\right|^2$ or - 2 db compared to the plates. For

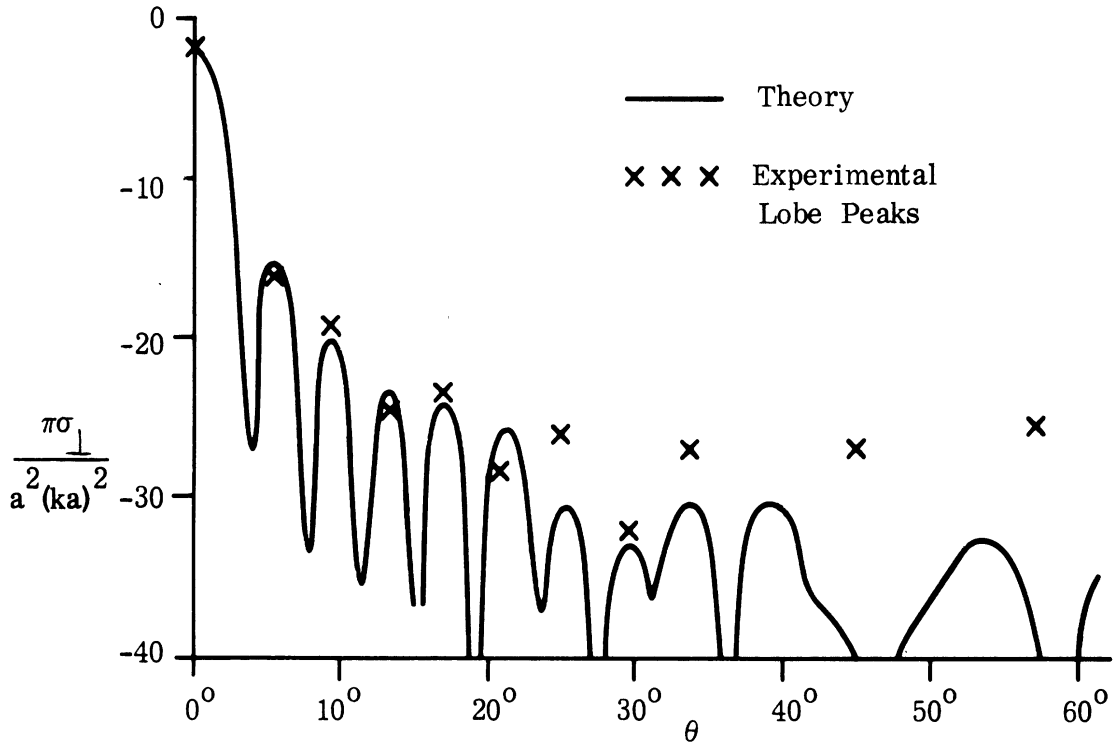

(a) Wire Grid

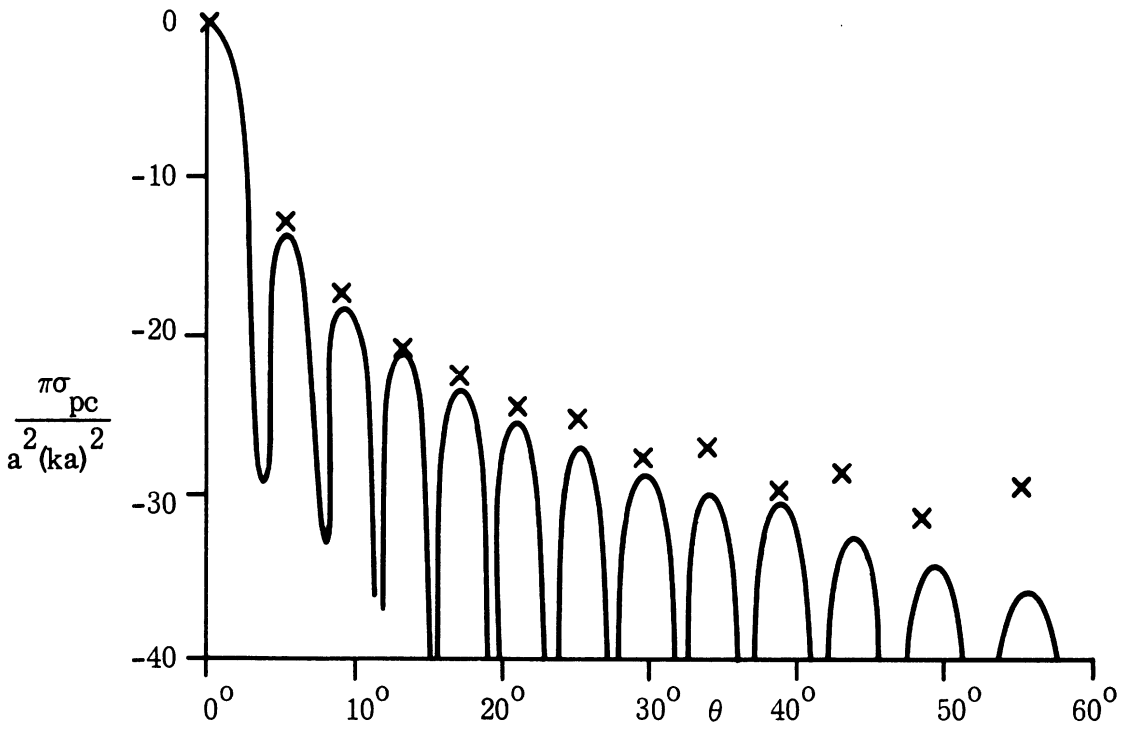

(b) Aluminum Plate

FIG. 5-17: COMPARISON BETWEEN THEORY AND EXPERIMENT FOR HH POLARIZATION AT 10 GHz.

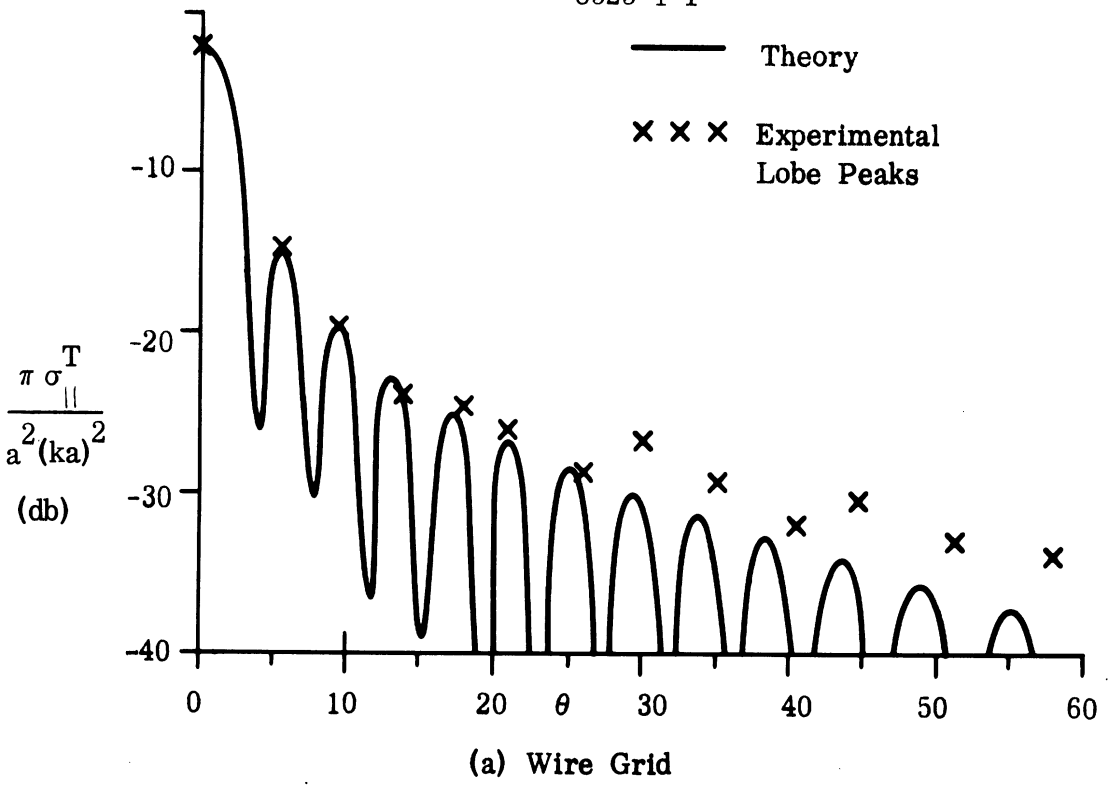

(a) Wire Grid

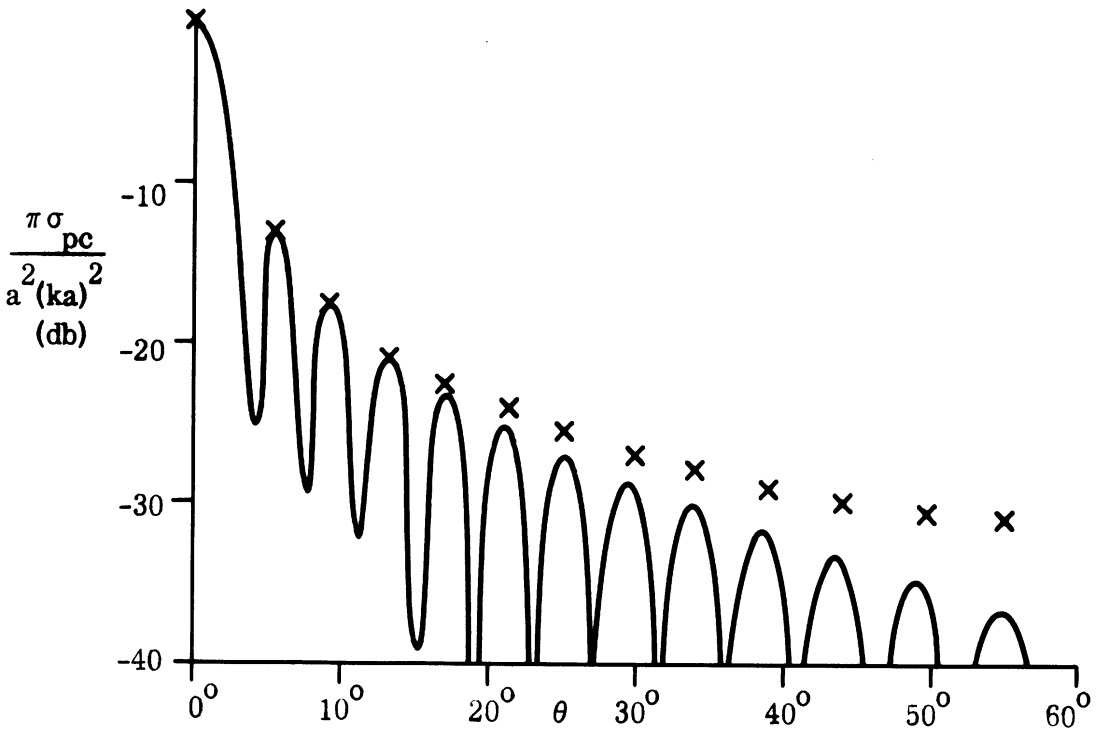

(b) Aluminum Plate

FIG. 5-18: COMPARISON BETWEEN THEORY AND EXPERIMENT FOR VV POLARIZATION AT 10 GHz.

the case in Fig. 5-17 L, the unknown launch factor was arbitrarily set equal to b in (5.77) to produce the best fit near 30^{o}. The lower pattern in part (b) is for the aluminum plate and the theory is taken from (5.61) and put into the form

$$\frac{\pi\sigma_{pc}}{a^2(ka)^2} = \cos^2\theta \left| \frac{\sin(ka \sin\theta)}{ka \sin\theta} \right|^2 \qquad (5.78)$$

and for $\theta = 0$, (5.78) is unity or 0 db.

(U) The theory for part (a) of Fig. 5-18 which is the VV polarization pattern for the grid is derived from (5.62) and is

$$\frac{\pi\sigma_{\perp}}{a^2(ka)^2} = \cos^2\theta \left| R_{\perp} \frac{\sin(ka \sin\theta)}{ka \sin\theta} \right|^2 \qquad (5.79)$$

which also reduced to $|R_{\perp}|^2$ for $\theta = 0^{o}$ or - 2 db compared to a perfectly conducting plate. Equation (5.78) holds for the VV aluminum plate case in Fig. 5-18b. More agreement is found in the VV than the HH pattern for the grid. This is mostly due to the qualitative rather than quantitative model used to describe the surface waves. More effort is needed to develop a more accurate formulation for the surface wave behavior.

(U) Figure 5-19 is a comparison between theory and experiment for all the test cases in Table V-1 at normal incidence as a function of the grid inductance. At $\theta = 0$ the theory for both polarization reduces to

$$\frac{\pi\sigma}{a^2(ka)^2} = |R|^2 = \frac{1}{1 + 4(X_s/Z_o)^2} \qquad (5.80)$$

where the second term in (5.77) is taken to be zero compared to the first. Good agreement is found between theory and experiment in Fig. 5-19 where all errors are less than 1 db.

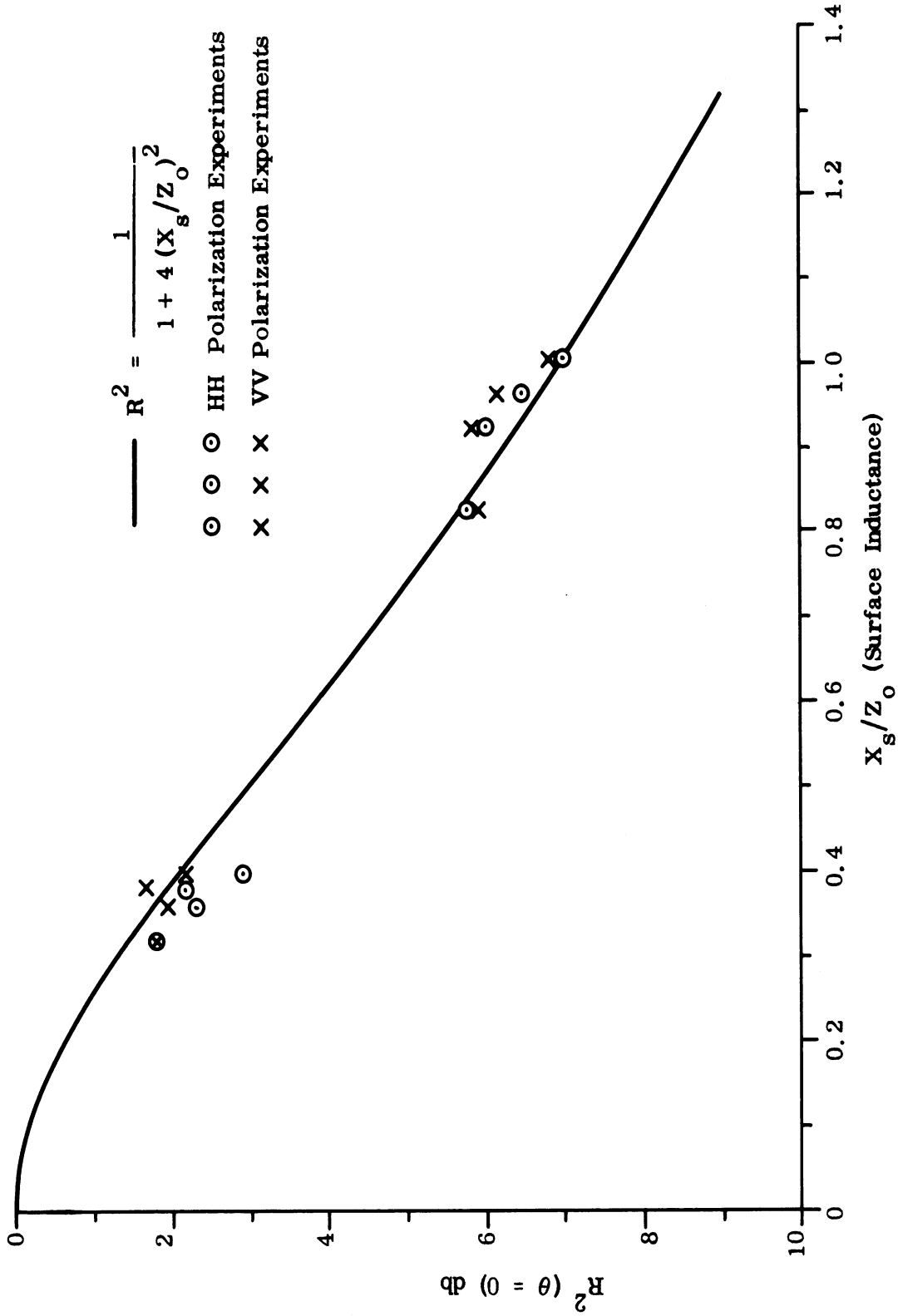

FIG. 5-19: COMPARISON BETWEEN THEORY AND EXPERIMENT FOR THE RCS OF THE WIRE GRID AS A FUNCTION OF X_s/Z_o AT NORMAL INCIDENCE:

5.3.5 Conclusion

(U) The work done on scattering by current sheets in the final quarter of 1967 shows that theoretically and experimentally physical optics assumptions do not hold for HH polarization at aspect angles greater than 30^{o}. Beyond 30^{o} surface wave, which are excited by edge diffraction, propagate well along the sheet and add a significant contribution to the scattering pattern. Vertical polarization follows the physical optics model more closely and no surface waves are supported by the sheet in this case.

(U) For coated body scattering problems with curvature such as cylinders and cones, both VV and HH polarizations must be considered together no matter what the incident polarization is. Therefore the surface wave, which will be more generally complex than not, must be accounted for at oblique angles of incidence if a reasonably accurate model is desired. This is demonstrated by the poor agreement between theory and experiment for the wire grid coated at nose-on incidence where surface waves have been neglected.

(U) If and when time and money permit, experimental and theoretical research should be done on the finite cylinder surrounded by a wire grid. This analysis will lead to a better understanding of how VV and HH polarizations couple and what types of surface propagation they produce. Once the coated cylinder is better understood, the coated cone difficulties should be reduced.

VI

SHORT PULSE INVESTIGATION-TASK 4.0

6.1 Introduction

(U) All aspects of the problem discussed in the Third Quarterly Report (Goodrich et al, 1967b) were continued, and the new work performed in the final quarter is described under the same section headings used in that report.

(U) The work to date on this task represents completed significant research on preliminary, relatively simple problems and on finding productive formulations of more physically interesting but difficult problems. In the course of studying the physically simple problems various interesting and unexpected limitations on the methods to handle pulses were uncovered. Some more specific descriptions and evaluations of aspects of the work are as follows.

(U) The work on this task which we feel has the greatest potential for providing knowledge of short pulse returns from relatively complex targets is the integral equation numerical approach formulated in Goodrich et al, 1967b Section 4.3. One part of these equations have been developed in the present report's Section 6.3 to a form very nearly ready to be programmed for a computer. These equations give the time dependant surface fields. The remaining equations give the fields off the surface and can be reduced in a directly analogous manner for numerical computation. This method is fundamentally different than the CW method used in Section 4.4; it is much better adapted to handling arbitrary pulse excitations, since no Fourier super-position of CW results is needed and there is no limitation to symmetrical geometries. We forsee no special numerical analysis difficulties in the method. Although written up in our work only for perfectly conducting bodies, the method is applicable to bodies with general impedance boundary conditions; however, the details are more complex.

(U) The formulas and numerical results of Sections 4.4 and 4.6 of Goodrich et al, 1967b and of 6.4 and 6.6 of the present report are quite specialized though they do illustrate the possibilities of pulse distortion. Some of them, primarily the perfectly conducting sphere results, are not basically different from results in the literature (Rheinstein, 1966) and were meant as trial problems to get us started prior to doing similar work on coated bodies. However a simple side investigation stimulated by these sphere results brought to light some pronounced effects of bandwidth on pulse reception which were not anticipated. These results are described in Section 6.7, below and are not limited to particular shapes or materials for the radar scatterers. In addition the simplicity of the formulas in the flat-backed cone section (6.5) brought to light certain unexpected theoretical difficulties in the general approach of synthesizing pulse returns from approximate CW responses by superposition. These are discussed in a separate section, Section 6.4 since they are in fact of concern for the treatment of any shape of scatterer which supports creeping waves.

(U) The investigation of pulse diffraction by means of the pulse phase fronts, their normal trajectories (rays) and transport equations for the discontinuities of fields and their derivatives has proven far more difficult than anticipated.

(U) Various approaches to the problems which arose have been tried (as reported in the previous quarterly reports under the heading Ray Optical Techniques, and in the present Section (6.2). While progress has been made we are far from having applicable results. To a large extent it turns out that we cannot avoid, by these methods, the difficulties which occur also in the CW high-frequency asymptotic diffraction theory. These difficulties are tied up with

divergences of the electromagnetic fields on the surfaces of the diffracting bodies. These divergences are in fact unphysical, but more refined theory than we have previously presented is needed to remove them from the formulas.

(U) A somewhat different and promising approach to the determination of the time dependent surface fields has therefore been tried in the last quarter. In particular an extension was made of the Fock method (1965) to treat the surface CW fields. This extension is reported in Section 6.2. As carried out it is limited to a fairly restricted class of pulse shapes incident on a smooth perfectly conducting parabolic cylinder. It is felt that further work could result in suitable generalizations.

6.2 Transient Surface Fields

(U) In this section an attempt is made to extend Fock's (1965) analysis of the launching and propagation of surface fields at and into the shadow side of an irradiated smooth obstacle to include an incident plane pulse with arbitrary time dependence. It was found that for a certain class of pulse shapes the method of Fock could be used to obtain the propagation of the pulse along the surface of a smooth perfectly conducting parabolic cylinder.

(U) For the two dimensional problem we desire to the solution of

$$\frac{\partial^2 u}{\partial x^2} + \frac{\partial^2 u}{\partial y^2} - \frac{1}{c^2}\frac{\partial^2 u}{\partial t^2} = 0 \ ,$$

in the neighborhood of the origin or coordinates as shown in Fig. 6-1. The assumed solution will be of the form

$$u(x, y, t) = \sum_n g_n(x, y)\, f_n(x - ct)$$

which we choose as satisfying the wave equation term by term. Substituting

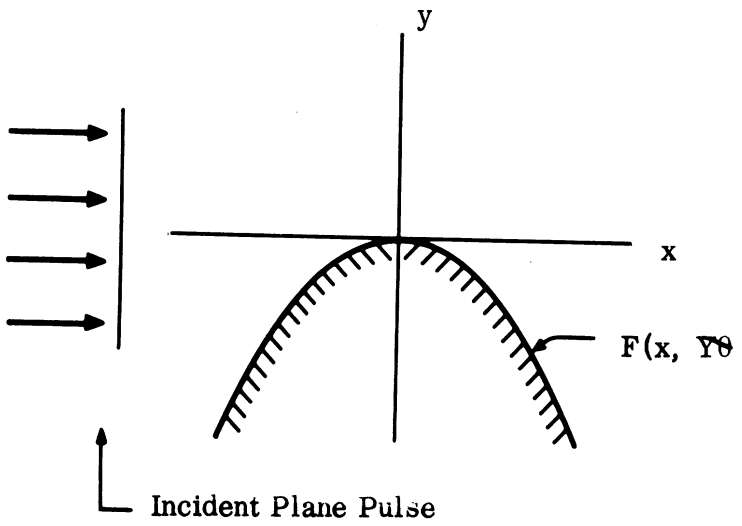

FIG. 6-1: COORDINATE SYSTEM.

$g(x, y)\ f(\phi)$; $\phi = x - ct$ into the wave equation we obtain

$$2\, g_x f_\phi + (g_{xx} + g_{yy})\, f = 0 .$$

Using Fock's order argument that

$$g_y >> g_x \Rightarrow g_{yy} >> g_{xx}$$

we obtain the equation

$$g_{yy} + \frac{2 f_\phi}{f}\, g_x = 0 .$$

Making a change of variables

$$\xi = \alpha x \qquad \eta = \beta\, F(x, y)$$

and letting

$$F(x, y) = y + \frac{x^2}{2R_o}$$

where R_o is the radius of curvature of the cylinder at the origin and α, β are constants we obtain

$$G_{\eta\eta} + \frac{2f_\phi}{f}\left[\frac{\alpha}{\beta^2} G_\xi + \frac{1}{\alpha\beta R_o}\,\xi\, G_\eta\right] = 0 .$$

Letting

$$\Phi = \frac{2f_\phi}{f}$$

and

$$G(\xi, \eta) = A\, e^{\frac{\beta^2}{\alpha}\int \frac{d\xi}{\Phi\xi} + \frac{1}{4\alpha^3 R_o^2}\int \xi^2 \Phi(\xi)\, d\xi}\, v(\xi\eta) ,$$

we obtain for $v(\xi\,\eta)$ the equation

$$v_{\eta\eta} + 2\left[\frac{\beta^2 P}{\alpha} + \frac{\xi\Phi}{2\alpha\beta R_o}\right] v_\eta + \left[\eta + \left(\frac{\beta^2 P}{\alpha} + \frac{\Phi\xi}{2\alpha\beta R_o}\right)^2\right] v = -\frac{\alpha\Phi}{\beta^2} v_\xi$$

where

$$P = \frac{d\xi}{\Phi(\xi)} .$$

To obtain Fock's equation we set

$$\frac{\beta^2 P}{\alpha} + \frac{\xi\,\Phi}{2\alpha\beta R_o} = 0$$

which becomes

$$\frac{d\Phi}{d\xi} + \frac{1}{\xi}\,\Phi + \frac{2\alpha\beta R_o}{\xi}\,\frac{\beta^2}{\alpha}\,\Phi^{-1} = 0$$

which is recognized as Bernoulli's equation. The solution for $\Phi(\xi)$ is given by

$$\Phi(\xi) = \frac{1}{\xi}\left[c_1 - 2\beta^2 R_o \xi^2\right]^{1/2} .$$

Noting that $\xi = \alpha x$ and $\Phi = \frac{2f'(x - ct)}{f(x - ct)}$ we solve for f and obtain a class of functions:

$$f_{c_1}(\phi) = e^{\frac{\beta}{\alpha^2}\sqrt{\frac{R_o}{2}}\sqrt{\frac{c_1\alpha^2}{2\beta^2 R_o} - \phi^2}\left[\frac{\sqrt{\frac{c_1\alpha^2}{2\beta^2 R_o}} + \sqrt{\frac{c_1\alpha^2}{2\beta^2 R_o} - \phi^2}}{\phi}\right] - \sqrt{\frac{c_1\alpha^2}{2\beta^2 R_o}}}$$

for which the equation

$$v_{\eta\eta} + \eta v = -\frac{\alpha\Phi}{\beta^2} v_\xi$$

defines $v(\xi\ \eta)$.

(U) The solution of this equation is

$$v(\xi\ \eta) = -\frac{\beta^2}{\alpha}\lambda \int \frac{d\xi}{\Phi}\ w^{(i)}(\lambda - \eta)$$

where $w^{(i)}(\lambda - \eta)$ is an Airy function which satisfies

$$w^{(i)}(\lambda - \eta) = (\lambda - \eta)\, w(\lambda - \eta)$$

and λ is an eigenvalue of this equation.

(U) To satisfy the Neumann Boundary Condition for $u(x, y, t)$ requires that

$$\partial v/\partial \eta \Big|_{\eta = 0} = 0 .$$

Satisfying both the boundary and initial conditions on $v(\xi\ \eta)$ we obtain

$$v(\xi\ \eta) = \int_c e^{-\frac{\beta^2}{\alpha}\lambda \int \frac{d\xi}{\Phi}} \left[w_1(\lambda - \eta) - \frac{w_1'(\lambda)}{w_2'(\lambda)} w_2(\lambda - \eta) \right] d\lambda$$

where c is a contour to be chosen. Thus $v(\xi\ \eta)$ is known and hence $G(\xi\ \eta)$ and $g(x, y)$. Depending upon the values of α and β the function $f_{c_1}(\phi)$ is also determined and thus $u(x, y, t)$ is specified. Now we may write

$$G(\xi\ \eta) = A\, e^{\frac{\beta^2 \eta}{\alpha} \int \frac{d\xi}{\Phi} + \frac{1}{4\alpha^3 R_o^2} \int \xi^2 \Phi(\xi)\, d\xi}$$

$$v(\xi,\ \eta)$$

which reduces on the surface of the cylinder, $\eta = 0$, to the expression.

$$G(\xi,\ 0) = A\, e^{\frac{1}{4\alpha^3 R_o^2} \int \xi^2 \Phi\, d\xi} \int_c \frac{e^{-\frac{\beta^2}{\alpha}\lambda \int \Phi\, d\xi}\, d\lambda}{w'(\lambda)}$$

Thus, for the given f which is a member of the above determined class of function we have determined $u(x, y, t)$ on the surface of the cylinder and in the neighborhood of the origin. The resulting integral over c is not explicitly the representation of the Fock functions but it is hoped that the integrand could be represented in such a way as to make $G(\xi, 0)$ given by a

series of Fock functions. This is yet to be done. It is noted that the function f is real only for the interval $\phi = x - ct \leq \sqrt{(c_1\alpha^2)/(2\beta^2 R_o)}$ which means that this technique will only yield the result for a certain predetermined period of time after the passage of the pulse front.

(U) By repeated application of this procedure at successive locations along the surface, the propagation of the pulse along the surface of the cylinder can be found and at the point of reradiation of the creeping wave it would appear that the radiated component of the creeping wave could be found.

(U) Additional work must yet be done on the details of this procedure which when worked out will provide an analysis for the surface diffracted field, which would be combined with our previous ray-optical work. Finally it is noted that the case $c_1 = 0$ represents Fock's assumed time dependence for the incident field.

6.3 Integral Equation Formulation of Time Dependant Scattering Problem

(U) In this section an integral equation is derived which governs the electromagnetic field when an electromagnetic pulse is incident on a smooth perfectly conducting object in three-space. A numerical solution of this equation for the unknown tangential components of the magnetic field on the surface; i.e., the surface current is outlined. The resulting expression is of the form

$$n_j \times \vec{\mathcal{H}}_{j,m} = \frac{1}{A_j} \left\{ 4\pi\, \hat{n}_j \times \mathcal{H}^i_{j,m} + \hat{n}_j \times \sum_{k=1}^{K}{}' \sum_q \vec{B}^q_{jk} \times \left(\hat{n}_k \times \vec{\mathcal{H}}_{k,m-q} \right) \right\} \qquad 1 \leq j \leq K$$

where the surface is divided in K small subdivisions over which the field is

assumed constant,

$\hat{n}_j$ is the outward unit normal at the j^{th} subdivision,

$\vec{\mathcal{H}}_{j,m}$ is the magnetic field on the j^{th} subdivision at the time $m\tau$ after some initial time,

τ is the increment in time, m an integer, and

A_j and B^q_{jk} are constant "influence" coefficients which are known functions of the surface geometry and independent of the field and time.

The summation over q always begins with $q > 0$ so that the field on subdivision j at time $t_o + m\tau$ is always expressed in terms of the incident fields and the total field in other subdivisions at previous times.

(U) The method outlined in this section provides a basis for the numerical solution of electromagnetic scattering of pulses by perfectly conducting objects. It is recommended that the following tasks be undertaken in a program concerned with scattering of electromagnetic pulses.

(U) 1. Carry out the calculation of the surface current for a particular incident pulse and a particular object. This first example should be chosen to be as simple as possible to demonstrate the workability of the method, or more to the point, the absence of any fundamental errors in the derivation.

(U) 2. Derive a numerical method for finding the field at any point in space and demonstrate its validity in a particular case. This appears to be directly analogous to the expression of the surface current but the details should be carefully considered.

(U) 3. Investigate alternate methods of solving the pulse scattering problem numerically. The present method appears workable but is not neces-

sarily the best. The idea here is that it may be possible to carry out some of the iteration analytically and arrive at a simpler, i.e., more economical, numerical problem.

(U) 4. Attempt to extend the above techniques to find the numerical solution of pulse scattering problems involving imperfectly conducting objects.

(U) As derived in Goodrich et al, (1967b) Section 4.3, the scattered pulse, $\mathscr{H}^s(r, t)$ due to an incident pulse $\vec{\mathscr{H}}^i(r, t)$ in the presence of a smooth perfectly conducting surface B is

$$\vec{\mathscr{H}}^s(\hat{r}, t) = \frac{Y}{4\pi} \nabla \times \int_B \frac{\hat{n}}{R} \times (\hat{\alpha} \times \hat{a}) \mathscr{F}^i\left(t - \frac{R}{c} - \frac{\hat{\alpha} \cdot \vec{r}_B}{c}\right) da$$

$$+ \frac{\nabla}{4\pi} \times \int_B \frac{\hat{n}}{R} \times \vec{\mathscr{H}}^s\left(\vec{r}_B, t - \frac{R}{c}\right) da, \ \vec{r} \text{ ext } B \qquad (6.1)$$

where the incident field propagating in the $\hat{a}$ direction is of the form

$$\vec{\mathscr{H}}^i(r, t) = Y \cdot (\hat{\alpha} \times \hat{a}) \mathscr{F}^i\left(t - \frac{\hat{a} \cdot \vec{r}}{c}\right)$$

$\hat{\alpha}$ is a constant vector such that $\hat{\alpha} \times \hat{a} = 0$,

$\vec{r}$ is a radius vector to a field point,

$\vec{r}_B$ is a radius vector to a point on the surface B,

$R = \left| \vec{r} - \vec{r}_B \right|$, is the distance between them,

$Y = \sqrt{\epsilon/\mu}$ is the intrinsic admittance of free space, and

$\mathscr{F}_i$ is an arbitrary function.

An alternate and more complete form of this integral representation is

$$\frac{1}{4\pi} \nabla \times \int_B \frac{\hat{n}}{R} \times \vec{\mathcal{H}}(\vec{r}_B,\ t - \frac{R}{c})\, da + \vec{\mathcal{H}}^i(\vec{r},\ t) = \vec{\mathcal{H}}(\vec{r}, t),\ \vec{r} \text{ ext } B$$

$$= \frac{1}{2}\vec{\mathcal{H}}(\vec{r}, t)\ \vec{r} \in B$$

$$= 0\ ,\quad \vec{r} \text{ int } B \qquad (6.2)$$

where $\vec{\mathcal{H}}$ denotes the total magnetic field (incident plus scattered).

(U) This expression results from Eq. (4.23) of Goodrich et al, (1967b) which may be written, again more completely, as

$$\frac{1}{4\pi} \nabla \times \int_B \frac{\hat{n}}{R} \times \vec{\mathcal{H}}(\vec{r}_B,\ t - \frac{R}{c})\, da = \vec{\mathcal{H}}^s(\vec{r}, t)\ \ \vec{r} \text{ ext to } B$$

$$= -\vec{\mathcal{H}}^i(\vec{r}, t)\ \vec{r} \text{ int to } B$$

or adding $\vec{\mathcal{H}}^i$ to both sides,

$$\frac{1}{4\pi} \nabla \times \int_B \frac{\hat{n}}{R} \times \vec{\mathcal{H}}(\vec{r}_B,\ t - \frac{R}{c})\, da + \vec{\mathcal{H}}^i(\vec{r}, t) = \vec{\mathcal{H}}(\vec{r}, t)\ \vec{r} \text{ ext to } B$$

$$= 0 \quad \vec{r} \text{ int to } B \qquad (6.3)$$

When $\vec{r}$ is on B we take the principal value and arrive at Eq. (6.2).

(U) By bringing the curl operator under the integral sign in (6.2) the integrand becomes

$$\nabla \times \left[\frac{\hat{n}}{R} \times \vec{\mathcal{H}}(\vec{r}_B,\ t - \frac{R}{c}) \right]$$

where ∇ operates on the variable $\vec{r}$. Then

$$\nabla \times \left[\frac{\hat{n}}{R} \times \vec{\mathcal{H}}(\vec{r}_B, t - \frac{R}{c})\right] = \nabla \frac{1}{R} \times \left[\hat{n} \times \vec{\mathcal{H}}(\vec{r}_B, t - \frac{R}{c})\right]$$

$$+ \frac{1}{R} \nabla \times \left[\hat{n} \times \vec{\mathcal{H}}(\vec{r}_B, t - \frac{R}{c})\right] \qquad (6.4)$$

but, since $\hat{n}$ depends only on $\vec{r}_B$ and is independent of $\vec{r}$,

$$\nabla \times \left[\hat{n} \times \vec{\mathcal{H}}(\vec{r}_B, t - \frac{R}{c})\right] = i_x \times \left[\hat{n} \times \frac{\partial}{\partial x} \vec{\mathcal{H}}(\vec{r}_B, t - \frac{R}{c})\right]$$

$$+ i_y \times \left[\hat{n} \times \frac{\partial \vec{\mathcal{H}}}{\partial y}(\vec{r}_B, t - \frac{R}{c})\right] + i_z \left[\hat{n} \times \frac{\partial \vec{\mathcal{H}}}{\partial z}(\vec{r}_B, t - \frac{R}{c})\right] \qquad (6.5)$$

Furthermore,

$$\frac{\partial \vec{\mathcal{H}}}{\partial x}(\vec{r}_B, t - \frac{R}{c}) = \frac{\partial \vec{\mathcal{H}}}{\partial t}(\vec{r}_B, t - \frac{R}{c})(-1/c) \frac{\partial R}{\partial x}$$

$$\frac{\partial \vec{\mathcal{H}}}{\partial y}(\vec{r}_B, t - \frac{R}{c}) = \frac{\partial \vec{\mathcal{H}}}{\partial t}(\vec{r}_B, t - \frac{R}{c})(-1/c) \frac{\partial R}{\partial y}$$

$$\frac{\partial \vec{\mathcal{H}}}{\partial z}(\vec{r}_B, t - \frac{R}{c}) = \frac{\partial \vec{\mathcal{H}}}{\partial t}(\vec{r}_B, t - \frac{R}{c})(-1/c) \frac{\partial R}{\partial z}$$

Thus, Eq. (6.5) may be written

$$\nabla \times \left[\hat{n} \times \vec{\mathcal{H}}(\vec{r}_B, t - \frac{R}{c})\right] = -\frac{1}{c} \nabla R \times \left[\hat{n} \times \frac{\partial \vec{\mathcal{H}}}{\partial t}(\vec{r}_B, t - \frac{R}{c})\right] . \qquad (6.6)$$

In addition

$$\nabla \frac{1}{R} = -\frac{1}{R^2} \nabla R \qquad (6.7)$$

Substituting (6.6) and (6.7) in (6.4) we obtain

$$\nabla \times \left[\frac{\hat{n} \times \vec{\mathcal{H}}}{R}(\vec{r}_B,\ t - \frac{R}{c})\right] = -\frac{1}{R^2}\nabla R \times \left[\hat{n} \times \vec{\mathcal{H}}(\vec{r}_B,\ t - \frac{R}{c})\right]$$

$$- \frac{1}{cR}\nabla R \times \left[\hat{n} \times \frac{\partial \vec{\mathcal{H}}}{\partial t}(\vec{r}_B,\ t - \frac{R}{c})\right] \qquad (6.8)$$

Finally, we note that $\nabla R = -\nabla_B R$ where ∇_B operates on $\vec{r}_B$ and use this fact together with (6.2) and (6.8) we obtain

$$\vec{\mathcal{H}}^i(\vec{r},\ t) + \frac{1}{4\pi}\int_B \frac{1}{R^2}\nabla_B R \times \left[\hat{n} \times \left\{\vec{\mathcal{H}}(\vec{r}_B,\ t - \frac{R}{c}) + \right.\right.$$

$$\left.\left. + \frac{R}{c}\frac{\partial \vec{\mathcal{H}}}{\partial t}(\vec{r}_B,\ t - \frac{R}{c})\right\}\right] da$$

$$= \vec{\mathcal{H}}(\vec{r},\ t), \qquad \vec{r} \text{ ext } B$$

$$= \frac{1}{2}\vec{\mathcal{H}}(\vec{r}, t), \qquad \vec{r} \in B$$

$$= 0 \quad , \qquad \vec{r} \text{ int } B \qquad (6.9)$$

(U) It is this form of the integral equation for the magnetic field which is most analogous to the scalar equation treated in Soules and Mitzner (1966). They proposed a numerical solution which may be extended to include the vector problem. An outline of this procedure for the vector case is presented next.

(U) The idea involves decomposing the surface into zones in which the field is taken as constant. The best way to effect this decomposition is not necessarily the simplest, according to Soules and Mitzner; however, this question will not be treated here.

(U) The surface is subdivided into K zones. If we think of these as being formed by the intersection of the surface with a set of parallel planes, see Fig. 6-2 , then in order to make sure that the field is relatively constant in each zone, there must be a further subdivision (see Fig. 6-3).

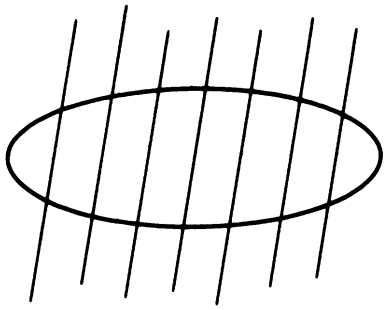

FIG. 6-2: ZONING THE SURFACE.

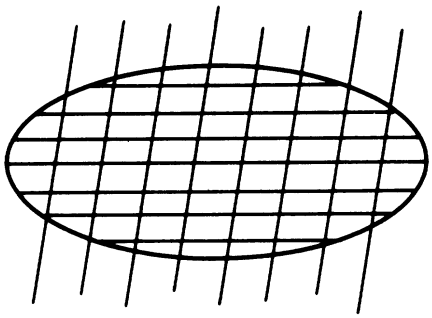

FIG. 6-3: ZONES OF CONSTANT FIELD.

This was done in Soules and Mitzner and is probably convenient if B is a surface of revolution. On the other hand, it requires two subscripts to denote one zone and this is tiresome in formulae that are cumbersome at best.

Furthermore it is not necessary if we think of Fig. 6-3 as representing the zoning of B. This is essentially a matter of notation and is in no way a change in method.

(U) Thus we assume that B is subdivided into K zones, each one small enough so that $\vec{\mathcal{H}}$ may be considered constant. Furthermore, the surface must be smooth enough so that n may also be taken as constant in each zone. Then, with equation (6.9), it follows that

$$\frac{1}{2}\vec{\mathcal{H}}(\vec{r}_j, t) = \vec{\mathcal{H}}^i(r_j, t) + \frac{1}{4\pi}\sum_{k=1}^{K}\int_{B_k}\frac{1}{R_j^2}\nabla_B R_j \times \left[\hat{n} \times \left\{\vec{\mathcal{H}}(\vec{r}_B, t - \frac{R_j}{c}) + \frac{R_j}{c}\frac{\partial\vec{\mathcal{H}}}{\partial t}(\vec{r}_B, t - \frac{R_j}{c})\right\}\right] da \qquad (6.10)$$

and with the assumed constancy within zones

$$\frac{1}{2}\vec{\mathcal{H}}(\vec{r}_j, t) \sim \vec{\mathcal{H}}^i(\vec{r}_j, t) - \frac{1}{4\pi}\sum_{k=1}^{K}\left[\hat{n}_k \times \left\{\vec{\mathcal{H}}(\vec{r}_k, t - \frac{R_{jk}}{c}) + \frac{R_{jk}}{c}\frac{\partial\vec{\mathcal{H}}}{\partial t}(\vec{r}_k, t - \frac{R_{jk}}{c})\right\}\right] \times \int_{B_k}\frac{1}{R_{jk}^2}\nabla_{B_k} R_{jk}\, da \,, \qquad (6.11)$$

where $R_{jk} = \left| r_j - r_k \right|$ and $1 \leq j \leq K$.

(U) Furthermore the remaining integral may be evaluated * and is a constant vector: i.e., let

---

* Section 6.3.1 shows how to handle the term involving the singular integral (6.12) in the final expression (6.33).

$$\vec{\Omega}_{jk} = \int_{B_k} \frac{1}{R_{jk}^2} \nabla_{B_k} R_{jk} \, da \qquad (6.12)$$

then

$$\frac{1}{2} \vec{\mathcal{H}}(\vec{r}_j, t) = \vec{\mathcal{H}}^i(\vec{r}_j, t) + \frac{1}{4\pi} \sum_{k=1}^{K} \vec{\Omega}_{jk} \times \left[\hat{n}_k \times \vec{\mathcal{H}}(\vec{r}_k, t - \frac{R_{jk}}{c}) \right.$$

$$\left. + \hat{n}_k \times \frac{R_{jk}}{c} \frac{\partial \vec{\mathcal{H}}}{\partial t} (\vec{r}_k, t - \frac{R_{jk}}{c}) \right] \qquad (6.13)$$

$$1 \leq j \leq K .$$

(U) In these formulae, $\vec{r}_j$ denotes a radius vector to a point in B_j. B_j is to be small hence $\vec{r}$ is essentially constant over B_j. Since the precise zoning rule has not been formulated, neither can a precise rule be given for choosing $\vec{r}_j$, given B_j. However, roughly speaking, $\vec{r}_j$ should be taken as the radius vector to some interior point of B_j, probably the "center" if one can be easily defined. The reason for this is that it is necessary to choose a time increment, τ, and it is convenient to do so in a way which quarantees that

$$R_{jk} \geq c\tau \text{ for } j \neq k \qquad (6.14)$$

In general R_{jk}/c will not be an integral multiple of τ but may be written as

$$R_{jk}/c = (n_{jk} + \gamma_{jk}) \tau \quad , \qquad (6.15)$$

where n_{jk} is an integer (≥ 1 unless $j = k$) and $0 < \gamma_{jk} < 1$. If $j = k$ then $n_{jk} = 0$ and $\gamma_{jk} = 0$. With this notation

$$\vec{\mathcal{H}}(\vec{r}_k,\ t - \frac{R_{jk}}{c}) = \vec{\mathcal{H}}(\vec{r}_k,\ t - n_{jk}\,\tau - \gamma_{jk}\,\tau) \tag{6.16}$$

which is approximated by

$$\vec{\mathcal{H}}(\vec{r}_k,\ t - \frac{R_{jk}}{c}) \sim (1 - \gamma_{jk})\vec{\mathcal{H}}(\vec{r}_k,\ t - n_{jk}\tau) +$$

$$+\ \gamma_{jk}\vec{\mathcal{H}}\left[\vec{r}_k,\ t - (n_{jk} + 1)\,\tau\right] \tag{6.17}$$

(Note that the approximation is exact if $\gamma_{jk} = 0$ or $\gamma_{jk} = 1$.) Similarly

$$\frac{\partial\vec{\mathcal{H}}}{\partial t}(\vec{r}_k,\ t - \frac{R_{jk}}{c}) \sim (1 - \gamma_{jk})\,\frac{\partial\vec{\mathcal{H}}}{\partial t}\,(\vec{r}_k,\ t - n_{jk}\,\tau) +$$

$$+\ \gamma_{jk}\vec{\mathcal{H}}\left[\vec{r}_k,\ t - (n_{jk} + 1)\,\tau\right] \quad . \tag{6.18}$$

Now assume that time progresses in integral multiples of τ, i.e.

$$t = t_o + m\,\tau\,, \quad m \text{ integer} \tag{6.19}$$

and rewrite Eq. (6.13) using Eqs. (6.17) (6.18) and (6.19) obtaining

$$\frac{1}{2}\,\vec{\mathcal{H}}(\vec{r}_j,\ t_o + m\tau) = \vec{\mathcal{H}}^i(\vec{r}_j,\ t_o + m\tau) + \frac{1}{4\pi}\sum_{k=1}^{K}\Omega_{jk}\ x\left\{(1 - \gamma_{jk})\,\hat{n}_k\right.$$

$$x\vec{\mathcal{H}}\left[\vec{r}_k,\ t_o + (m - n_{jk})\,\tau\right] + \gamma_{jk}\,\hat{n}_k\ x\,\vec{\mathcal{H}}\left[\vec{r}_k,\ t_o + (m - n_{jk} - 1)\,\tau\right]$$

Continued

$$+ (n_{jk} + \gamma_{jk})\tau(1 - \gamma_{jk})\,\hat{n}_k \times \frac{\partial}{\partial t}\vec{\mathcal{H}}\left[\vec{r}_k,\ t_o + (m - n_{jk})\,\tau\right]$$

$$+ (n_{jk} + \gamma_{jk})\tau\,\gamma_{jk}\,\hat{n}_k \times \frac{\partial}{\partial t}\vec{\mathcal{H}}\left[\vec{r}_k,\ t_o + (m - n_{jk} - 1)\,\tau\right]\Bigg\} \qquad (6.20)$$

(U) The next step is to replace the derivative with a backwards difference formula. Let

$$\frac{\partial}{\partial t}\vec{\mathcal{H}}\left[\vec{r}_k,\ t_o + p\tau\right] \sim \frac{1}{\tau}\sum_{q=0}^{Q} c_q \vec{\mathcal{H}}\left[\vec{r}_k,\ t_o + (p - q)\tau\right] \quad . \qquad (6.21)$$

The constants c_q and the number of terms, Q, will depend on the particular approximation, e.g., if Q = 1 then $c_o = 1$ and $c_1 = -1$ so that

$$\frac{\partial}{\partial t}\vec{\mathcal{H}}\left[r_k,\ t_o + p\,\tau\right] \sim \frac{1}{\tau}\left\{\vec{\mathcal{H}}(\vec{r}_k,\ t_o + p\tau) - \vec{\mathcal{H}}\left[r_k,\ t_o + (p - 1)\tau\right]\right\} \qquad (6.22)$$

Soules and Mitzner give an example of a three term approximation. The constants c_q are subject to the restriction

$$\sum_{q=0}^{Q} c_q = 0 \qquad (6.23)$$

Introducing the general approximation, Eq. (6.21) into Eq. (6.20), leads to the equation

$$\frac{1}{2}\vec{\mathcal{H}}(\vec{r}_j,\ t + m\,\tau) = \vec{\mathcal{H}}^{i}(\vec{r}_j,\ t + m\,\tau) + \frac{1}{4\pi}\sum_{k=1}^{K}\vec{\Omega}_{jk} \times$$

Continued

$$\Big\{(1-\gamma_{jk})\,\hat{n}_k \times \vec{\mathcal{H}}\left[\vec{r}_k,\ t_o + (m - n_{jk})\,\tau\right] + \gamma_{jk}\,\hat{n}_k \times$$

$$\vec{\mathcal{H}}\left[\vec{r}_k,\ t_o + (m - n_{jk} - 1)\,\tau\right] + (n_{jk} + \gamma_{jk}) \sum_{q=0}^{Q} c_q \hat{n}_k \times$$

$$\vec{\mathcal{H}}\left[\vec{r}_k,\ t_o + (m - n_{jk} - q)\,\tau\right] + (n_{jk} + \gamma_{jk})\,\gamma_{jk} \sum_{q=0}^{Q} c_q \hat{n}_k \times$$

$$\vec{\mathcal{H}}\left[\vec{r}_k,\ t + (m - n_{jk} - 1 - q)\,\tau\right]\Big\}. \qquad (6.24)$$

To simplify notation somewhat, let

$$\vec{\mathcal{H}}_{j,p} = \vec{\mathcal{H}}(r_j,\ t_o + p\,\tau) \qquad (6.25)$$

that is, the field at subdivision B_j after p increments of time after t_o. Then (6.24) becomes

$$\frac{1}{2}\vec{\mathcal{H}}_{j,m} = \vec{\mathcal{H}}^{i}_{j,m} + \frac{1}{4\pi} \sum_{k=1}^{K} \Omega_{jk} \times \Big\{(1-\gamma_{jk})\,\hat{n}_k \times \vec{\mathcal{H}}_{k,\,m-n_{jk}}$$

$$+ \gamma_{jk}\,\hat{n}_k \times \vec{\mathcal{H}}_{k,\,m-n_{jk}-1} + (n_{jk} + \gamma_{jk})(1-\gamma_{jk}) \sum_{q=0}^{Q} c_q \hat{n}_k$$

$$\times \vec{\mathcal{H}}_{k,\,m-n_{jk}-q} + (n_{jk} + \gamma_{jk})\,\gamma_{nk} \sum_{q=0}^{Q} c_q\,\hat{n}_k$$

$$\times \vec{\mathcal{H}}_{k,\,m-n_{jk}-1-q}\Big\}. \qquad (6.26)$$

Further, denote by $\sum_{k=1}^{K}{}'$ the summation with the term $j = k$ deleted, re-

calling that $R_{jk} = 0$ if $j = k$ which with Eq. (6.15) implies that $n_{jk} = 0$ and $\gamma_{jk} = 0$ if $j = k$. Then Eq. (6.26) becomes

$$\frac{1}{2}\vec{\mathcal{H}}_{j,m} = \vec{\mathcal{H}}^{i}_{j,m} + \frac{1}{4\pi}\sum_{k=1}^{K}{}' \Omega_{jk} \times \Big\{(1-\gamma_{jk})\hat{n}_k \times \vec{\mathcal{H}}_{k,m-n_{jk}} + \gamma_{jk}\hat{n}_k \times \vec{\mathcal{H}}_{k,m-n_{jk}-1} + (n_{jk}+\gamma_{jk})(1-\gamma_{jk})\sum_{q=0}^{Q} c_q \hat{n}_k \times \vec{\mathcal{H}}_{k,m-n_{jk}-q} + (n_{jk}+\gamma_{jk})\gamma_{jk}\sum_{q=0}^{Q} c_q \hat{n}_k \times \vec{\mathcal{H}}_{k,m-n_{jk}-1-q}\Big\} + \frac{1}{4\pi}\Omega_{jj} \times (\hat{n}_j \times \vec{\mathcal{H}}_{j,m}) \quad . \tag{6.27}$$

The awkward sum in Eq. (6.27) may be simplified by writing

$$(1-\gamma_{jk})\hat{n}_k \times \vec{\mathcal{H}}_{k,m-n_{jk}} + \gamma_{jk}\hat{n}_k \times \vec{\mathcal{H}}_{k,m-n_{jk}-1} + (n_{jk}+\gamma_{jk})(1-\gamma_{jk})\sum_{q=0}^{Q} c_q \hat{n}_k \times \vec{\mathcal{H}}_{k,m-n_{jk}-q} + (n_{jk}+\gamma_{jk})\gamma_{jk}\sum_{q=0}^{Q} c_q \hat{n}_k \times \vec{\mathcal{H}}_{k,m-n_{jk}-1-q}$$

$$= \sum_{q=0}^{Q}\left[(n_{jk}+\gamma_{jk})(1-\gamma_{jk})c_q + (1-\gamma_{jk})\delta^{o}_{q}\right]\hat{n}_k \times \vec{\mathcal{H}}_{k,m-n_{jk}-q} + \sum_{q=0}^{Q}\left[(n_{jk}+\gamma_{jk})\gamma_{jk}c_q + \gamma_{jk}\delta^{o}_{q}\right]\hat{n}_k \times \vec{\mathcal{H}}_{k,m-n_{jk}-1-q}$$

(continued)

$$= \sum_{q=n_{jk}}^{Q+n_{jk}} \left[(n_{jk} + \gamma_{jk})(1 - \gamma_{jk})\, c_{q-n_{jk}} + (1 - \gamma_{jk})\, \delta^{o}_{q-n_{jk}} \right] \hat{n}_k$$

$$\times \vec{\mathcal{H}}_{k,\, m-q} + \sum_{q=n_{jk}+1}^{Q+n_{jk}+1} \left[(n_{jk} + \gamma_{jk})\gamma_{jk}\, c_{q-n_{jk}-1} \right.$$

$$\left. + \gamma_{jk}\, \delta^{o}_{q-n_{jk}-1} \right] \hat{n}_k \times \vec{\mathcal{H}}_{k,\, m-q}$$

$$= \sum_{q=n_{jk}}^{Q+n_{jk}+1} B^{q}_{jk}\, \hat{n}_k \times \vec{\mathcal{H}}_{k,\, m-q} \qquad (6.28)$$

where

$$B^{q}_{jk} = (n_{jk} + \gamma_{jk})(1 - \gamma_{jk})\, c_o + 1 - \gamma_{jk}\,, \quad q = n_{jk}$$

$$= (n_{jk} + \gamma_{jk})\ \gamma_{jk}\, c_Q\,, \quad q = n_{jk} + 1 + Q \qquad (6.29)$$

$$= (n_{jk} + \gamma_{jk}) \left[(1 - \gamma_{jk})\, c_{q-n_{jk}} + \gamma_{nk}\, c_{q-n_{jk}-1} \right]$$

$$+ \gamma_{jk}\, \delta^{o}_{q-n_{jk}-1}\,, \quad n_{jk} < q < Q + n_{jk} + 1$$

and

$$\delta^{o}_{q} = 0 \quad q \neq 0$$

$$= 1 \quad q = 0.$$

With this result Eq. (6.27) may be written as

$$\frac{1}{2}\vec{\mathcal{H}}_{j,m} - \frac{1}{4\pi}\,\vec{\Omega}_{jj} \times (\hat{n}_j \times \vec{\mathcal{H}}_{j,m}) = \vec{\mathcal{H}}^{i}_{j,m}$$

$$+ \frac{1}{4\pi} \sum_{k=1}^{K}{}' \sum_{q=n_{jk}}^{Q+n_{jk}+1} B^{q}_{jk}\, \vec{\Omega}_{jk} \times (\hat{n}_k \times \vec{\mathcal{H}}_{k,m-q}) \quad . \qquad (6.30)$$

(U) Note that since $j \neq k$ in the sum, $n_{jk} \neq 0$ which means $q \neq 0$ hence all terms in the sum are evaluated at a time less than $t = t + m\tau$.

(U) In actuality, it is only the tangential components of $\mathcal{H}$ which are unknown. An equation for these components is found by forming the vector product of Eq. (6.30) with n_j, the unit normal to the j^{th} zone on the surface, B, as follows

$$\frac{1}{2}\,\hat{n}_j \times \vec{\mathcal{H}}_{j,m} + \frac{1}{4\pi}\vec{\Omega}_{jj} \cdot \hat{n}_j\hat{n}_j \times \vec{\mathcal{H}}_{j,m} = \hat{n}_j \times \vec{\mathcal{H}}^{i}_{j,m} + \frac{1}{4\pi}\,\hat{n}_j$$

$$\times \sum_{k=1}^{K} \sum_{q=n_{jk}}^{Q+n_{jk}+1} B^{q}_{jk}\, \vec{\Omega}_{jk} \times (\hat{n}_k \times \vec{\mathcal{H}}_{k,m-q}) \qquad (6.31)$$

where the identity

$$\hat{n}_j \times \left[\vec{\Omega}_{jj} \times (n_j \times \vec{\mathcal{H}}_{j,m})\right] = \hat{n}_j \times \left[\vec{\Omega}_{jj} \cdot \vec{\mathcal{H}}_{j,m} n_j - \vec{\Omega}_{jj} : \hat{n}_j \vec{\mathcal{H}}_{j,m}\right]$$

$$= -\vec{\Omega}_{jj} \cdot \hat{n}_j\hat{n}_j \times \vec{\mathcal{H}}_{j,m} \qquad (6.32)$$

has been used. This may also be written

$$\hat{n}_j \times \vec{\mathcal{H}}_{j,m} = \frac{4\pi\, \hat{n}_j \times \vec{\mathcal{H}}^{i}_{j,m} + \hat{n}_j \times \sum_{k=1}^{K}{}' \sum_{q=n_{jk}}^{Q+n_{jk}+1} B^{q}_{jk}\, \vec{\Omega}_{jk} \times (\hat{n}_k \times \vec{\mathcal{H}}_{k,m-q})}{2\pi + \vec{\Omega}_{jj} \cdot \hat{n}_j} \qquad (6.33)$$

$$1 \leq j \leq K$$

(U) This is the vector analogue of the scalar formulation of the pulse scattering problem as developed by Mitzner (1966). It expresses the tangential components of the total magnetic field in zone B_j in the scattering surface at time $t_o + m\tau$ in terms of the incident field in the same zone at the same time and the total field in other zones at previous times. If the surface is zoned so that the incident pulse reaches zone B_1 at $m = 0$ and has not yet reached any other zones. Then

$$\hat{n}_j \times \vec{\mathcal{H}}_{j,o} = \frac{4\pi\, \hat{n}_1 \times \vec{\mathcal{H}}^{i}_{1,0}}{2\pi + \vec{\Omega}_{11} \cdot \hat{n}_1} \qquad j = 1$$

$$= 0 \qquad j \neq 1 \qquad (6.34)$$

and the field at successive times may be computed using (6.33). Since (6.33) is a vector equation, it is perhaps more convenient for computational purposes to write it in scalar component form. In any particular case it is undoubtedly most efficient to employ a surface coordinate system in which one coordinate varies along normals to the surface and the other two vary on the surface. Only two component equations will then result, though proper care must be exercised in distinguishing contravariant and covariant components should the coordinate system be non-orthogonal. In rectangular components, three scalar equations will be generated. Introducing the notation

$$\hat{n}_j \times \vec{\mathcal{H}}_{j,m} = h^{x_1}_{j,m}\,\hat{x}_1 + h^{x_2}_{j,m}\,\hat{x}_2 + h^{x_3}_{j,m}\,\hat{x}_3 = \vec{h}_{j,m} \tag{6.35}$$

$$\vec{\Omega}_{jk} = \Omega^{x_1}_{jk}\,\hat{x}_1 + \Omega^{x_2}_{jk}\,\hat{x}_2 + \Omega^{x_3}_{jk}\,\hat{x}_3 \tag{6.36}$$

these scalar equations are

$$h^{x_p}_{j,m} = \frac{4\pi h^{ix_p}_{j,m} + \sum_{k=1}^{K}{}' \sum_{q=n_{jk}}^{Q+n_{jk}+1} B^q_{jk}\left[\hat{n}_j \cdot \vec{h}_{k,m-q}\,\Omega^{x_p}_{jk} - \hat{n}_j \cdot \vec{\Omega}_{jk}\,h^{x_p}_{k,m-q}\right]}{2\pi + \vec{\Omega}_{jj} \cdot \hat{n}_j} \tag{6.37}$$

$$p = 1, 2, 3$$

(U) To obtain the magnetic field off the surface, an expression comparable to the scalar equation derived in Mitzner may be derived in a manner following the method described above. The details of this analysis are not yet complete.

6.3.1 Addendum on the Evaluation of $\vec{\Omega}_{jk}$.

(U) The numerical solution of Eq. (6.33) is dependent upon the knowledge of the geometric quantities, Ω_{jk} defined in Eq. (6.12) as

$$\vec{\Omega}_{jk} = \int_{B_k} \frac{1}{R^2_{jk}} \nabla_{B_k} R_{jk}\, da \quad .$$

This may be a serious problem since any numerical integration must cope with a highly singular integrand. A method of treating this is considered here.

(U) The straight forward application of a vector identity yields

$$\vec{\Omega}_{jk} = -\int_{B_k} \nabla_{B_k} \frac{1}{R_{jk}}\, da = -\int_{B_k} \hat{n}_k \cdot \nabla_{B_k} \frac{1}{R_{jk}}\, \hat{n}_k\, da + \int_{B_k} \hat{n}_k \times (\hat{n}_k \times \nabla_{B_k} \frac{1}{R_{jk}})\, da .$$

Since $\hat{n}_k$ is assumed to be constant over B_k this is rewritten as

$$\vec{\Omega}_{jk} = -\hat{n}_k \int_{B_k} \hat{n}_k \cdot \nabla_{B_k} \frac{1}{R_{jk}}\, da + \hat{n}_k \times \int_{B_k} \hat{n}_k \times \nabla_{B_k} \frac{1}{R_{jk}}\, da .$$

(U) The first integral is precisely that which occurred in the scalar problem. It is the solid angle subtended by zone k at $\vec{r}_j$ and was evaluated approximately by Soules and Mitzner. The second integral remains to be evaluated. However, with Stokes' theorem, this may be written

$$\hat{n}_k \times \int_{B_k} \hat{n}_k \times \nabla_{B_k} \frac{1}{R_{jk}}\, da = \hat{n}_k \times \int_{C_k} \frac{d\vec{r}_k}{R_{jk}}$$

where C_k is the curve enclosing zone B_k. In this form, there is still a singularity in the integrand. However it is seen in Eq. (6.33) that the quantity which occurs is not $\vec{\Omega}_{jk}$ but

$$\hat{n}_j \times \left[\vec{\Omega}_{jk} \times (\hat{n}_k \times \vec{\mathcal{H}}_{k,m-q})\right] .$$

Thus the possibly troublesome terms are

$$\hat{n}_j \times \left[(\hat{n}_k \times \int_{C_k} \frac{d\vec{r}_k}{R_{jk}}) \times (\hat{n}_k \times \vec{\mathcal{H}}_{k,m-q}) \right] .$$

For convenience, call this expression I and let $\vec{K} = \hat{n}_k \times \vec{\mathcal{H}}_{k,m-q}$,

$$\vec{I} = \hat{n}_j \times \left[(\hat{n}_k \times \int_{C_k} \frac{d\vec{r}_k}{R_{jk}}) \times \vec{K} \right] .$$

(Note that $\hat{n}_k \cdot \vec{K} = 0$) since $\hat{n}_j = (\hat{n}_j \cdot \hat{n}_k)\hat{n}_k - \hat{n}_k \times (\hat{n}_k \times \hat{n}_j)$,

$$\vec{I} = \left[(\hat{n}_j \cdot \hat{n}_k)\hat{n}_k - \hat{n}_k \times (\hat{n}_k \times \hat{n}_j) \right] \times \left[(\hat{n}_k \times \int_{C_k} \frac{d\vec{r}_k}{R_{jk}}) \times \vec{K} \right]$$

but

$$\left[\hat{n}_k \times (\hat{n}_k \times \int \frac{d\vec{r}_k}{R_{jk}}) \times \vec{K} \right] = 0$$

thus

$$\vec{I} = - \left[\hat{n}_k \times (\hat{n}_k \times \hat{n}_j) \right] \times \left[(\hat{n}_k \times \int_{C_k} \frac{d\vec{r}_k}{R_{jk}}) \times \vec{K} \right]$$

Since

$$(\hat{n}_k \times \int_{C_k} \frac{d\vec{r}_k}{R_{jk}}) \times \vec{K} = - \vec{K} \cdot \int_{C_k} \frac{d\vec{r}_k}{R_{jk}} \hat{n}_k ,$$

$$\vec{I} = \left[\hat{n}_k \times (\hat{n}_k \times \hat{n}_j)\right] \times \hat{n}_k \; \vec{K} \cdot \int_{C_k} \frac{d\vec{r}_k}{R_{jk}}$$

$$= \hat{n}_k \times \hat{n}_j \; \vec{K} \cdot \int_{C_k} \frac{d\vec{r}_k}{R_{jk}} \quad ,$$

which may be rewritten as

$$\vec{I} = \frac{\hat{n}_k \times \hat{n}_j}{\left|\hat{n}_k \times \hat{n}_j\right|} \; \vec{K} \cdot \int_{C_k} \frac{\left|\hat{n}_k \times \hat{n}_j\right| d\vec{r}_k}{R_{jk}}$$

or in dyadic form

$$\vec{I} = \int_{C_k} \frac{\hat{n}_k \times \hat{n}_j}{R_{jk}} \, d\vec{r}_k \cdot \vec{K} \quad .$$

In either case the integrand is non singular. Since $\left|\hat{n}_j \times \hat{n}_k\right| = \sin \theta_{jk}$ where θ_{jk} is the angle between $\hat{n}_j$ and $\hat{n}_k$, it follows from the law of sines (see Fig. 6-4) that

$$\frac{\left|\hat{n}_j \times \hat{n}_k\right|}{R_{jk}} = \frac{\sin \theta_{jk}}{R_{jk}} = \frac{\sin \alpha}{A}$$

where, even though R_{jk} is small (the troublesome case) A will be large (hence the integrand bounded) provided only that the surface is smooth.

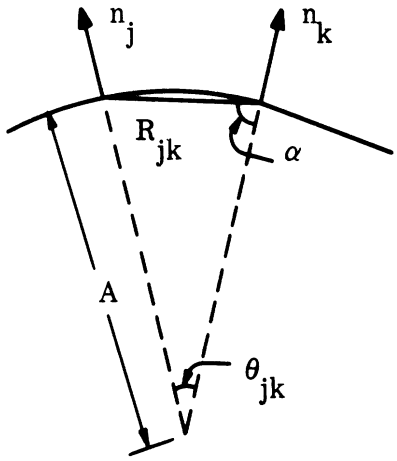

FIG. 6-4: ZONAL GEOMETRY.

6.4 Causality and Reality in the Synthesis of Pulse Responses.

(U) In the previous reports on this contract we have used the procedure of building up the response to a pulsed input by superposition of the CW responses. This method is valid in the sense that it yields (a) a causal response; i.e., zero response at a distance r from a point on the target until a time r /c after that point is first irradiated, and (b) a real response (zero imaginary part) to a real excitation.

(U) Conditions (a) and (b) are satisfied automatically when the exact CW solutions are used. However, an exact CW solution is known only for the sphere. One may wish to approximate the complicated solution for the sphere and for all other shapes exact analytic solution are not available. One then uses approximate formulas such as those of geometric optics, physical optics, creeping waves and Rayleigh theory. A dilemma then appears since one can verify that both (a) and (b) cannot both be satisfied when the

creeping wave or Rayleigh CW formulas are used. In addition if an approximate CW response is constructed by patching together different solutions in different frequency ranges, there will of necessity be discontinuities in the function or its derivatives with respect to ν. These will be translated as physically unreal contributions in the time response. To illustrate the latter point let $\mathcal{F}$ represent the Fourier transformation operation. Then

$$\mathcal{F} f''(\nu) = (2\pi\ i\ ct)^2\ \mathcal{F} f(\nu)$$

Thus if $f(\nu)$ has a discontinuity at $\nu = \nu_a$, $f''(\nu)$ has the form $f_2(\nu) + A\delta(\nu_a)$. $\mathcal{F}\ \delta(\nu_a) = A \exp(-2\pi\ i\nu_a t)$ and so

$$\mathcal{F} f(\nu) = \frac{A\, e^{-2\pi\ i\nu_a t}}{(2\pi\ i\ ct)^2} + \mathcal{F} f_2(\nu).$$

(U) In Section 6.5 we illustrate these remarks by the simple formulas for the flat-backed cone derived in Goodrich et al, (1967b). We first realized these difficulties when treating this case. However, Kennaugh, Moffat and Schafer (1967) have also observed an example of this phenomenon in the creeping wave expression for a sphere. They point out that if the sphere creeping wave expression is multiplied by $-i = -\sqrt{-1}$, superposition then yields a causal response. They obtained the creeping wave expression from Levy and Keller (1960) who derived it be using Keller's generalized geometric optics approach and inserting a phase change of $e^{i\pi/2}$ along each geodesic (ray path) as it passed through the common intersection of the ray paths on the shadowed side of the sphere. Kennaugh et al, pointed out that a phase shift independant of frequency ν, $0 < \nu < \infty$, is physically unrealizable and hence questioned Keller's formula. However, we feel that this is not the root of the difficulty since, for the sphere, one can derive a result comparable to

Keller's formula by purely mathematical high frequency asymptotic approximation applied to the exact (Mie) solution for the diffracted field. This is done in Senior (1965) where the creeping wave solution which is derived to $O\left[(a/\lambda)^{-4/3}\right]$ coincides with Keller's result to $O\left[(a/\lambda)^{-1/3}\right]$. Thus, an arbitrary multiplication of the creeping wave terms by a constant phase factor is not permissible. Another way to see that this is not possible is to note that the CW sphere (and also cone) formulas, which combine creeping wave and optics results taking into account their relative phases, agree very well with experimental results. We refer to Kleinman and Senior (1963) for the cone case. We have verified that the agreement is destroyed for the cone results if the relative phase is so changed as to make the flat-backed cone creeping wave term causal in the manner advocated by Kennaugh et al, (1967).

(U) The problem lies deeper. Our CW results are for positive frequency ($\nu > 0$) only. To evaluate the transform

$$F(\tau) = \int_{-\infty}^{\infty} f(\nu)\, e^{-2\pi i \nu \tau}\, d\nu$$

ν must be known over the entire real axis. One might make an analytic continuation of $f(\nu)$ into the complex ν plane. Then if $\tau = t - r/c$ causality requires $F(\tau) = F(\tau)\, H(\tau)$ where $H(\tau)$ is the unity step function i.e., the response at a distance r is zero when $t < r/c$. This requires that all poles of $f(\nu)$ lie in the half plane $\mathrm{Im}\,\nu < 0$ or, more precisely, below the point of integration. Then, for $\tau < 0$, when the integral along the real axis is replaced, using Cauchy's theorem, by an infinite arc in the upper half plane plus the sum of residues of the poles enclosed, the result is zero. For $\tau > 0$ one must use an infinite arc below the axis in order to have a convergent integral along the arc. The integral on the infinte arc is in fact zero so that $F(\tau)$ is then $-2\pi i \sum$ residues.

(U) The continuation of $f(\nu)$, $\nu > 0$ into the complex plane must, however, satisfy $f(-\nu) = f^*(\nu)$, $\nu > 0$ when $F(\tau)$ is real. This is evident from the inverse transform formula

$$f(\nu) = \int_{-\infty}^{\infty} F(\tau)\, e^{2\pi i \nu t}\, d\tau$$

In Goodrich et al, 1967b we made use of this fact to write

$$F(\tau) = 2\,\mathrm{Re} \int_{0}^{\infty} f(\nu)\, e^{-2\pi i \nu \tau}\, d\nu \quad .$$

However, when the asymptotic creeping wave formulas derived for ν positive, real are analytically continued to the negative real axis one finds that $f(-\nu) = -f^*(\nu)$ so that one is led to an imaginary function $F(\tau)$.

(U) On the other hand if one requires $f(-\nu) = f^*(\nu)$, the function of complex ν which accomplishes this is not an analytic function of ν alone but depends on ν and ν^*. One can for example start with $f(\nu)$ defined for $\nu \geq 0$ and replace ν by $|\nu|$, i by i sgn ν. One is then led to a real $F(\tau)$ which, however, is not causal.

(U) We do not know how to get out of this dilemma; until it is resolved, it is necessary to use only exact results or purely numerical approximations to them. Geometrical and physical optics formulas, while not causing difficulties in satisfying (a) and (b) are too crude by themselves to be truly useful. This is evident from, say, Kennaugh and Moffat (1965).

(U) An alternate approach to the problem would consist of using the moment method suggested in that paper. This is based on the fact that the existence of a convergent low frequency expansion of the CW result in powers of the frequency puts requirements on the time moments

$$\int_0^\infty t^n F(t)\, dt \quad ,$$

(n an integer) of the time response F(t). These requirements can presumably be used to modify the high frequency physical optics CW response to take into account low frequency effects without an objectionable "patching" procedure. Kennaugh and Moffat did not pursue this approach in their paper. It has been investigated in this laboratory (not on this contract) without very favorable results).

(U) As an illustration of the extent to which we satisfied causality in using a numerical approximation to the Mie sieries we reproduce here graphs of the field backscattered from a sphere when irradiated by an impulse and by a square pulse of length 4 carrier cycles. Both graphs are extensions to negative τ of figures given in Goodrich et al (1967b), section 4.0. The small non-zero responses for $\tau < 0$ are due to truncation of the Mie series and using a numerical approximation to the contribution by the remainder in the series.

6.5 Pulse Scattering from a Perfectly Conducting Flat Back Cone.

(U) In this section we use the rather simple formulas derived in Goodrich et al, (1967b) to illustrate the points brought out in 6.4. The formulas give the backscatter response to a δ function excitation $\overline{E} = \hat{x}\, E_o \delta(x + ct)$. They are rewritten here in a normalized form. Cone length is included in the normalization of the independant parameter $\tau_3 = c/a\,(\frac{z}{c} - t)$.

$$\frac{\mathcal{E}^s(\frac{z}{c} - t)}{c\, E_o/z} = \frac{c_1}{4\pi}\, \delta(\tau_1) + I_1 - I_2 + I_3$$

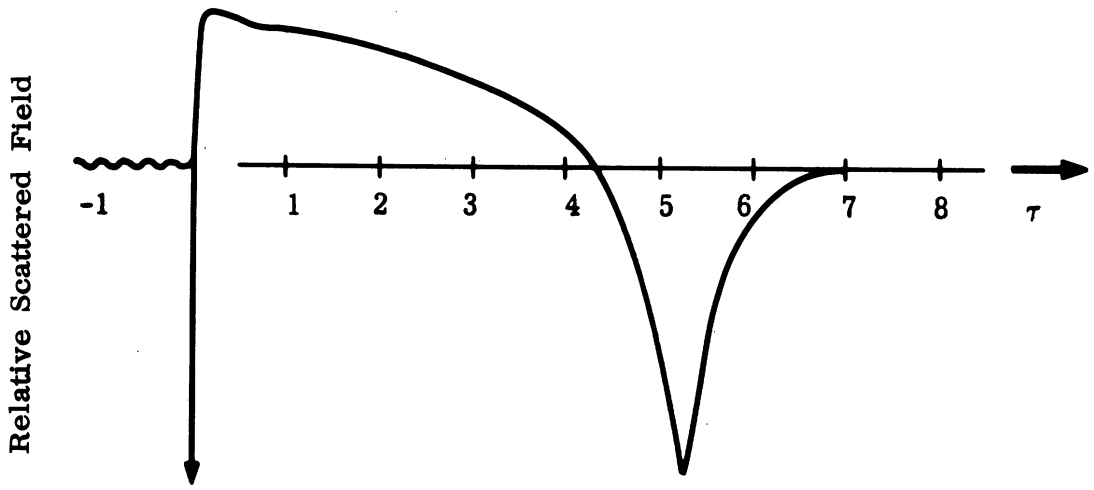

Fig. 6-5: IMPULSE RETURN.

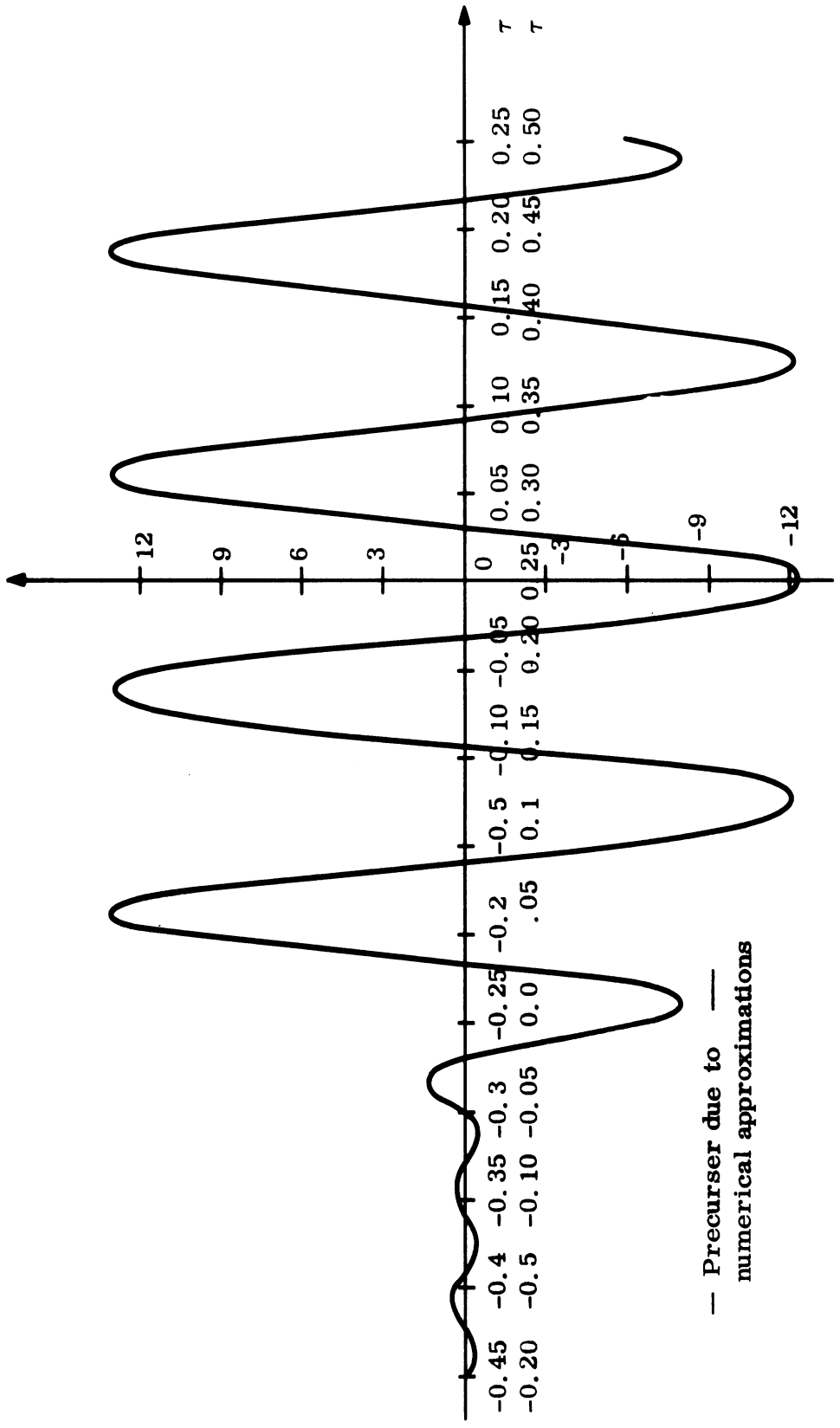

FIG. 6-6: SPECULAR RETURN, n = 4, ℓ = 1/4.

$$I_1 = \frac{c_2}{2} \frac{1}{\sqrt{|\tau_2|}} (1 \pm \text{sgn } \tau_2)$$

$$I_2 = \frac{c_1}{\tau_1} \sin 2\pi u_c \tau_1 + \frac{c_2}{|\tau_2|} \left\{ C(2\sqrt{u_c |\tau_2|}) + \text{sgn } \tau_2 \, S(2\sqrt{u_c |\tau_2|}) \right\}$$

$$I_3 = \frac{c_3}{|\tau_3|^3} \left\{ 4\pi u_c |\tau_3| \cos(2\pi u_c \tau_3 + (4\pi^2 u_c^2 \tau_3^2 - 2) \sin(2\pi u_c |\tau_3|) \right\}$$

where

$$C(x) = \int_0^x \cos\left(\frac{\pi}{2} t^2\right) dt$$

$$S(x) = \int_0^x \sin\left(\frac{\pi}{2} t^2\right) dt$$

$$C_1 = -\frac{2\pi}{\text{Ⓗ}} \text{ cosec } \frac{2\pi}{\text{Ⓗ}}$$

$$C_2 = C_1 \frac{\sqrt{2}}{H\pi} \sin\frac{\pi}{H} \frac{\cos\frac{\pi}{\text{Ⓗ}} - \cos\frac{3\pi}{\text{Ⓗ}}}{\left(\cos\frac{\pi}{\text{Ⓗ}} - \cos\frac{3\pi}{2\text{Ⓗ}}\right)^2}$$

$$C_3 = \frac{4}{3}(-\pi \cot\theta_o + 4\, e^{\cot\theta_o/4})$$

$$\text{Ⓗ} = \frac{5}{2} - \theta_o/\pi$$

$$\tau_1 = \tau_3 + 2\omega$$

$$\tau_2 = \tau_1 + 2$$

$$\tau_3 = \frac{c}{a}\left(\frac{z}{c} - t\right).$$

(U) In these formulas $C_1/4\pi\ \delta(\tau_1) + I_1$, I_2 and I_3 are simply the normalized versions of the integrals I_1, I_2 and I_3 respectively in Goodrich et al, (1967b). The derivation assumed $f(-\nu) = f^*(\nu)$ and really yielded the + sign in the $\pm$ factor in I_1 and I_2; the (-) sign is inserted arbitrarily in the discussion to follow. The physical source of the terms is as follows. By using a formula valid for frequencies $\nu > \nu_c$, $\nu_c = 0(1)$ for the response integral (which is evaluated over all frequencies $\nu \geq 0$) one gets $(C_1/4\pi)\delta(t_1)$ as the direct return from the cone base and I_1 as the return from radiation which travels across the base and then back as sketched. I_2 is the result of integrating the same formulas only over $0 < \nu < \nu_c$. This was subtracted from I_1 and replaced by adding the presumably more correct integral I_3 which is obtained by integration over $0 < \nu < \nu_c$ of the scattering formula valid in that range, the Rayleigh scattering formula.

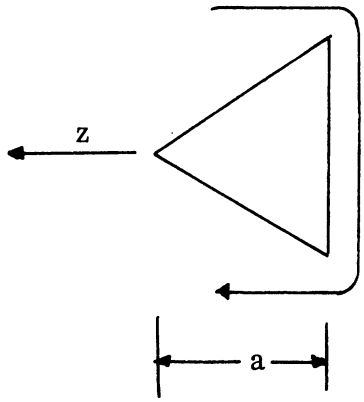

(U) Thus $-I_2 + I_3$ is intended to be a correction of the approximate result $I_1 + (C_1/4\pi)\,\delta(T_1)$. For a fixed observation distance z one would expect $I_1 = 0$ for all time for which $\tau_2 = 1/a\,(z + 2a - ct) > 0$. Yet this is not true for the formula as derived, in fact it is zero for $\tau_2 < 0$. If the arbitrary minus sign were used this violation of causality would be rectified, but one cannot of course simply do this arbitrarily. Examination of the CW equation from which I_1 comes, via.

$$\vec{E}^s = \hat{x}\,\frac{E_o C}{2\pi}\,\frac{e^{i(kz-\omega t)}}{z}\left[C_1 e^{iB_1\nu} + C_2\nu^{-1/2}\,e^{iB_2\nu}\,e^{-i\pi/4}\right]$$

with C_1 and C_2 real, shows that this change amounts to inserting a factor i in the second term (which accounts for waves diffracting about the cone base the "creeping waves" of this problem). While this term is an approximate result (due to Keller) its phase relative to the term representing the CW return directly from the edge, (the first term) is crucial in the CW response. This is the formula mentioned in 6.4 for which Kleinman and Senior (1963) have verified the accuracy by extensive comparison of numerical and experimental fixed frequency results. We have checked that insertion of a factor i in the second term gives results which do not agree well with experiment.[+] As an alternate to having a non-causal creeping wave result, we could make the result causal (use $-$), but imaginary, by the use of true analytic continuation into the complex ν plane as discussed in 6.3.

(U) The difficulties with the Rayleigh region, which result here appears as symmetric in τ and hence non-causal, are best avoided by realizing that in practice one uses frequency bands about high frequency carriers which

[+] Kennaugh and Moffat (1965) apparently treated the ramp response wave form from a flat-back cone using the same Keller formula that we have used. They do not mention the causality difficulty there, but discuss other physically unreal aspects of the results.

exclude the low frequencies. This does not of course solve the basic theoretical problem. It does indicate that it is folly to try to use the impulse or ramp responses and the convolution method to solve problems of high frequency pulsed excitations. One merely brings in the difficulty which could be avoided, of a proper handling of the low frequencies.

6.6 Pulse Scattering from a Perfectly Conducting Cone-Sphere.

(U) This section is a revision and extension of the analysis in Goodrich et al, (1967b) Section 4.5 of backscattering from a perfectly conducting cone-sphere irradiated nose-on by a pulsed CW wave. The present analysis differs from the former one in using more accurate formulas for the creeping wave contribution and for the creeping wave enhancement factor γ. These are formulas derived recently by Senior (1967a,b). However, the result of this creeping wave part is not valid (it is not causal) as discussed in Section IV. On the other hand the terms in the following which represent the tip and join returns are indeed causal and real. They are manipulated into a form, Eq. (6.52c) where this is clearly evident. This and the fact that we have written the formulas in a manner more closely resembling the earlier analyses of spheres are the main reasons for this section being included in spite of the difficulty with the creeping waves; to be closer to the sphere analyses. In addition to this, the presentation follows more closely that of the earlier analysis of spheres, the integrals have been rewritten in terms of a variable involving the base radius a, namely, $y = \omega a/c$ instead of ω. Also the variables

$$\ell = cT/2a \quad \text{and} \quad n = T\omega_o/2\pi \tag{6.38}$$

are used instead of the pulse length T and center frequency ω_o.

(U) We are considering backscattering from a cone-sphere irradiated nose-on by a pulse

$$\bar{f}^i(r, t) = \hat{x} \cos \omega_o t \qquad |t| < T/2$$
$$= 0 \qquad |t| > T/2 \tag{6.39}$$

which in the normalized frequency domain corresponds to

$$\bar{F}^i(y) = \hat{x} \frac{T}{4\pi} \left\{ \frac{\sin(\ell y + n\pi)}{\ell y + n\pi} + \frac{\sin(\ell y - n\pi)}{\ell y - n\pi} \right\} \tag{6.40}$$

(U) To compute the scattered field we will assume a linear time invariant system so that in the frequency domain, the response to (6.40) will be

$$\bar{F}^s(r, y) = \hat{x} F^i(y) E^s(r, y) \tag{6.41}$$

where $E^s(r, y)$ is the impulse response of the cone-sphere and is given by Senior (1965) as

$$\bar{E}^s(r, y) = \hat{x} \frac{a}{r} \frac{e^{i\frac{r}{a}y}}{y} S \tag{6.42}$$

and S is the scattering amplitude.

(U) Thus, from (6.39b) and (6.42) we get that

$$\bar{F}^s(r, y) = \hat{x} \frac{aT}{4\pi r} \left\{ \frac{\sin(\ell y + n\pi)}{\ell y + n\pi} + \frac{\sin(\ell y - n\pi)}{\ell y - n\pi} \right\} \frac{e^{i\frac{r}{a}y}}{y} S \tag{6.43}$$

Using the inverse Fourier transform, we can write

$$\bar{F}^s(r, t) = \frac{c}{2\pi a} \int_{-\infty}^{\infty} \bar{F}^s(r, y) e^{-i\frac{tc}{a}y} dy \tag{6.44}$$

Since $f(t)$ is real, it follows that $F^s(r,y) = \left[F^s(-y)\right]^*$, and

$$\bar{f}^s(r,\,t) = \frac{c}{\pi a}\,\mathrm{Re}\int_0^\infty \bar{F}^s(r,\,y)\; e^{-i\frac{tc}{a}y}\,dy \qquad (6.45)$$

The scattering amplitude S is given by (Senior, 1965)

$$S = \frac{i}{4}\sec^2\alpha\,\exp\left\{-2\,iy\sin\alpha\right\} - \frac{i}{4}\tan^2\alpha\,\exp\left\{-2iy\csc\alpha\right\} + \gamma S_c \qquad (6.46)$$

where γS_c is the creeping wave contribution. Normalizing $\bar{f}^s(r,\,t)$,

$$\bar{f}_n^s(r,\,t) = \mathrm{Re}\left\{\int_0^\infty \left[\frac{\sin(\ell y + n\pi)}{\ell y + n\pi} + \frac{\sin(\ell y - n\pi)}{\ell y - n\pi}\right] e^{-i\tau y}\,S(y)\;\frac{dy}{y}\right. \qquad (6.47a)$$

$$= \int_0^\infty \left\{\frac{\sin(\ell y + n\pi)}{\ell y + n\pi} + \frac{\sin(\ell y - n\pi)}{\ell y - n\pi}\right\} \mathrm{Re}\left\{e^{-i\tau y}\,S(y)\right\}\frac{dy}{y} \qquad (6.47b)$$

where

$$\bar{f}_n^s(r,\,t) = \frac{4\pi^2 r}{cT}\;\bar{f}^s(r,\,t) \qquad (6.48a)$$

and

$$\tau = \frac{ct - r}{a}\,. \qquad (6.48b)$$

(U) By substituting (6.46) in (6.47b) we get:

$$\bar{f}_n^s(r,\,t) = \hat{x}\;\frac{\sec^2\alpha}{4}\int_0^\infty \left\{\frac{\sin(\ell y + n\pi)}{\ell y + n\pi} + \right.$$

Continued

$$+ \frac{\sin(\ell y - n\pi)}{\ell y - n\pi} \Bigg\} \sin(2y \sin\alpha) \cos\tau y +$$

$$+ \cos(2y \sin\alpha) \sin\tau y \Bigg\{ \frac{dy}{y} - \hat{x} \frac{\tan^2\alpha}{4} \int_0^\infty \Bigg\{ \frac{\sin(\ell y + n\pi)}{\ell y + n\pi} +$$

$$+ \frac{\sin(\ell y - n\pi)}{\ell y - n\pi} \Bigg\} \Bigg\{ \sin(2y \csc\alpha) \cos\tau y +$$

$$+ \cos(2y \csc\alpha) \sin\tau y \frac{dy}{y} + \hat{x}\, \mathrm{Re} \int_0^\infty \Bigg\{ \frac{\sin(\ell y + n\pi)}{\ell y + n\pi} +$$

$$+ \frac{\sin(\ell y - n\pi)}{\ell y - n\pi} \Bigg\} \gamma S_c(y)\, e^{-i\tau y} \frac{dy}{y} \qquad (6.49a)$$

$$= \hat{x} \frac{\sec^2\alpha}{4} \int_0^\infty \Bigg\{ \frac{\sin(\ell y + n\pi)}{\ell y + n\pi} + \frac{\sin(\ell y - n\pi)}{\ell y - n\pi} \Bigg\} \sin\Big[(2\sin\alpha +$$

$$+ \tau)y\Big] \frac{dy}{y} - \hat{x} \frac{\tan^2\alpha}{4} \int_0^\infty \Bigg\{ \frac{\sin(\ell y + n\pi)}{\ell y + n\pi} +$$

$$+ \frac{\sin(\ell y - n\pi)}{\ell y - n\pi} \Bigg\} \sin\Big[(2\csc\alpha + \tau)\Big] \frac{dy}{y} +$$

$$+ x\, \mathrm{Re} \int_0^\infty \Bigg\{ \frac{\sin(\ell y + n\pi)}{\ell y + n\pi} + \frac{\sin(\ell y - n\pi)}{\ell y - n\pi} \Bigg\} \gamma S_c(y) e^{-i\tau y} \frac{dy}{y} \qquad (6.49b)$$

S_c is given approximately be Senior (1967a) as

$$S(y) = \tau_c^4\, e^{i\pi/3} \left\{ 1 + \frac{e^{i\pi/3}}{60\,\tau_c^2 \beta_1^2} (32\beta_1^3 + a) \right\} \frac{1}{\beta_1 \left\{ \mathrm{Ai}(-\beta_1) \right\}^2}$$

$$\exp\left\{ i\pi y - e^{-i\pi/6} \tau_c \pi \beta_1 - e^{i\pi/6} \frac{\pi}{60\tau_c \beta_1} (\beta_1^3 - a) \right\} \qquad (6.50)$$

with $\tau_c = (y/2)^{1/3}$, $\beta_1 = 1.01879297\ldots$, and $Ai(-\beta_1) = 0.53565666\ldots$. Equation (6.50) is a highly accurate approximation to the creeping wave return.

(U) An asymptotic approximation for γ (Hong and Weston, 1965) valid for large y, is given by

$$\gamma \approx \left[2\left(1/3 + \int_0^{\beta_1} Ai(-x)\,dx\right)\left\{1 + \frac{1}{2}(y/2)^{2/3}\alpha^2\beta_1^2 e^{-i\pi/3}\right\} + (y/2)^{2/3}\alpha^2 e^{-i\pi/3} Ai(-\beta_1)\right] \exp\left\{-(y/2)^{1/3}\alpha\beta_1 e^{-i\pi/6}\right\} \quad (6.51)$$

(U) Equations (6.49b), (6.50) and (6.51) may be used to get numerical results, but instead an empirical relation for γ (Goodrich, et al, 1967b) will be used. The integrations will then be carried out using an analytical curve which is fitted to the empirical one.

Computations for $n = 4$, $\ell = 1/4$

(U) Computations were carried out using $n = 4$, $\ell = 1/4$ in Eq. (6.49b)

$$\bar{f}_n^s(r,t) = \hat{x}\frac{\sec^2\alpha}{4}\int_0^\infty \sin(y/4)\left(\frac{1}{\frac{y}{4}+4n} + \frac{1}{\frac{y}{4}-4n}\right)\sin\left[(2\sin\alpha+\tau)y\right]\frac{dy}{y} - \hat{x}\frac{\tan^2\alpha}{4}\int_0^\infty \sin(y/4)\left(\frac{1}{\frac{y}{4}+4n} + \frac{1}{\frac{y}{4}-4n}\right)\sin\left[(2\csc\alpha+\tau)y\right]\frac{dy}{y} + \hat{x}\,\mathrm{Re}\int_0^\infty \sin(y/4)\left(\frac{1}{\frac{y}{4}+4n} + \frac{1}{\frac{y}{4}-4n}\right)\gamma S_c e^{-i\tau y}\frac{dy}{y} \quad (6.52a)$$

$$f_n^s(r,t) = \hat{x}\, 2\sec^2\alpha \int_0^\infty \frac{\sin(y/4)}{y^2-(16\pi)^2} \sin\left[(2\sin\alpha+\tau)y\right] dy$$

$$- \hat{x}\, 2\tan^2\alpha \int_0^\infty \frac{\sin(y/4)}{y^2-(16\pi)^2} \sin\left[(2\csc\alpha+\tau)y\right] dy$$

$$+ \hat{x}\, 8\,\mathrm{Re}\int_0^\infty \frac{\sin(y/4)}{y^2-(16\pi)^2}\, \gamma S_c\, e^{-i\tau y}\, dy \qquad (6.52b)$$

$$= \hat{x}\,\frac{1}{8\pi}\sec^2\alpha \sin\left[16\pi(2\sin\alpha+\tau)\right]\int_0^\infty \left\{\sin\left[(\tfrac{1}{4}-\tau_1)y\right]\right.$$

$$\left. + \sin\left[(\tfrac{1}{4}+\tau_1)y\right]\right\}\frac{dy}{y} - \hat{x}\,\frac{1}{8\pi}\tan^2\alpha \sin\left[16\pi(2\csc\alpha+\tau)\right]$$

$$\int_0^\infty \left\{\sin\left[(\tfrac{1}{4}-\tau_2)y\right] + \sin\left[(\tfrac{1}{4}+\tau_2)y\right]\right\}\frac{dy}{y}$$

$$+ \hat{x}\, 8\,\mathrm{Re}\int_0^\infty \frac{\sin(y/4)}{y^2-(16\pi)^2}\, \gamma S_c\, e^{-i\tau y}\, dy \qquad (6.52c)$$

with $\tau_1 = 2\sin\alpha + \tau$, and $\tau_2 = 2\csc\alpha + \tau$. The first and second integrals clearly exhibit the causal property of the response from the tip and the join respectively. This is evident on using

$$\int_0^\infty \frac{\sin my}{y}\, dy = \begin{cases} \pi/2\,, & m > 0 \\ -\pi/2, & m < 0 \end{cases}.$$

The third integral does not give a causal response as we have discussed in Section 6.4 and as numerical checks verify. Once we learn how to handle the creeping wave properly we can use the correct creeping wave expression together with the first two terms in (6.52c).

6.7 Bandwidth Effects on Pulse Return

6.7.1 General

(U) The purpose of this memo is to show how the effect of frequency pass band and the dispersive characteristics of radar echos particularly the creeping waves, combine to affect the shape of pulsed radar returns. It is shown that considerable care must be used in trying to infer information on the scatterer from comparison of incident and creeping wave pulse shapes. However, when sufficient bandwidth is allowed, the creeping wave pulse shape can be an indicator of the target structure which will not be easily duplicated by returns from other targets, regardless of whether the other structures yield the same time delay between geometric optics and creeping wave echoes.

(U) Assume incident fields of the form

$$\bar{E} = f(t - z/c)\,\hat{x} \tag{6.53}$$

Then the resulting backscattered field will be

$$\vec{\mathcal{E}}^{s}(z/c - t) = \frac{\hat{x}c}{\pi z}\,\mathrm{Re}\int_0^{\infty} e^{i2\pi\nu(z/c - t)}\,\tilde{S}(\nu)\,F(\nu)\,d\nu$$

where

$$F(\nu) = \int_{-\infty}^{\infty} f(\tau)\,e^{-i2\pi\nu\tau}\,d\tau \tag{6.54}$$

and $\tilde{S}$ is defined in terms of the CW backscattered field $\bar{E}^s$

$$\bar{E}^s = \frac{\hat{x}c}{2\pi z}\,\tilde{S} \quad . \tag{6.55}$$

(U) If now the "desired" incident pulse shape (6.53) is modified by a rectangular bandpass or if the return is so bandlimited in the receiver then

$$\vec{\mathcal{E}}^s\left(\frac{z}{c} - t\right) = \frac{\hat{x}c}{\pi z}\,\mathrm{Re}\int_{\nu_o(1-\theta)}^{\nu_o(1+\theta)} e^{i2\pi\nu(z/c - t)}\tilde{S}(\nu)\,F(\nu)\,U(\nu)\,d\nu \tag{6.56}$$

where $2\nu_o\theta$ is the bandwidth and $U(\nu) = \begin{cases} 1, & \nu > 0 \\ 1, & \nu < 0 \end{cases}$. Three ranges of θ can be distinguished.

(U) (i) <u>θ very small (approach to CW)</u>. In this case θ is so small that $F(\nu)\,S(\nu) \sim$ constant in the integration range. In this case the output is,

$$\vec{\mathcal{E}}^s(\tilde{t}) = \hat{x}\,\frac{2c}{\pi z}\,\tilde{S}(\nu_o)\,F(\nu_o)\cos 2\pi\,\nu_o\,\tilde{t}\,\sin 2\pi\,\nu_o\,\theta\,\tilde{t} \tag{6.57}$$

where $\tilde{t} = z/c - t$. This is a modulated cosine wave of carrier frequency ν_o and modulating frequency $\theta\nu_o$. Thus the pulse aspects of the response are completely lost. In the limit as $\theta \to 0$, the modulation frequency goes to zero. The field given in this way also goes to zero in the limit because the power per unit frequency interval is bounded; in the limit as $\delta\nu = 2\theta\nu_o \to 0$ there is zero flux. The idealized non-zero single frequency CW case requires a δ function term $\delta(\nu - \nu_o)$ in the spectrum.

(U) (ii) <u>Intermediate θ</u>: This case will be concerned with situation which may arise, in which $\tilde{S}(\nu) = \tilde{S}(\nu_o)\,e^{-i\eta\nu}$ in the interval $2\theta_c\nu_o$ whereas $F(\nu)$ has no such representation (except for the trivial case obtained by multiplying and dividing by common factors).

$$\vec{\mathcal{E}}^{s}(\tilde{t}) = \frac{\hat{x}c}{\pi z}\,\tilde{S}(\nu_o)\,\mathrm{Re}\int_{\nu_o(1-\theta_o)}^{\nu_o(1+\theta_o)} e^{-i\eta\nu}\, e^{i2\pi\nu\tilde{t}}\, F(\nu)\, U(\nu)\, d\nu$$

$$= \frac{\hat{x}c}{2\pi z}\,\tilde{S}(\nu_o)\, F(\tilde{t}-\eta) \quad . \tag{6.58}$$

The response is simply a demagnified time delayed replica of the original pulse.

(U) This is the situation considered by Hong (1967), for convex bodies. He writes that $S(\nu) = S^{g}(\nu) + S^{c}(\nu)$ where $S^{c}(\nu)$ is the creeping wave response and $S^{g}(\nu)$ the geometric optics part. Then he states that $S^{c}(\nu)$ can be written in the form $S^{c}(\nu_o)\, e^{-i\eta\nu}$ over the radar bandwidths considered. Our computations however show that this assumption does not apply to the bandwidths used in present day short pulse radars.

(U) (iii) Neither of the Above Two Cases for θ_c. In this case the dispersive character of the creeping wave due to varying creeping speed of each frequency component will be able to show up without excessive masking by the band pass characteristics of the receiver. Creeping wave pulse shape is then an indicator of the target characteristics.

6.7.2 Examples: Sphere Computations

(U) The analysis of Goodrich et al, (1967c) can be used to illustrate the above remarks. The target was a perfectly conducting sphere of radius c. The functional form of $f(t - z/c)$ was taken to be

$$f^{i}(\Lambda) = e(\Lambda)\cos 2\pi\nu_o \qquad |\Lambda| < T/2$$

$$= 0 \qquad |\Lambda| > T/2 \tag{6.59}$$

Then Eq. (6.54) becomes

$$\vec{\mathcal{E}}^{s}(\tau) = \hat{x}\,\frac{cT}{4\pi z}\,\mathrm{Re}\int_{\kappa_o(1-\theta)}^{\kappa_o(1+\theta)} \Phi(\kappa;\ell,n)\; G^{*}(\kappa)\,U(\kappa)\,e^{-i\kappa\tau}\,d\kappa \qquad (6.60)$$

where

$$\kappa = 2\pi\nu\, a/c \qquad , \quad \tau = (ct - z)/a + 2$$

$$\Phi(\kappa;\ell,n) = \mathrm{sinc}\,(n + \kappa\ell/\pi) - \mathrm{sinc}\,(n - \kappa\ell/\pi)$$

$$n = \nu_o T\,, \qquad \ell = cT/(2a)$$

$$G^{*}(\kappa) = i\,\frac{e^{i2\kappa}}{\kappa}\sum_{n=1}^{\infty}(-)^{n}(2n+1)\left\{\frac{j_n(\kappa)}{h_m^{(1)}(\kappa)} - \frac{\left[\kappa\, j_n(\kappa)\right]'}{\left[\kappa\, h^{(1)}(\kappa)\right]'}\right\} \qquad (6.61)$$

Here $\mathrm{sinc}\ x = \sin\pi x/(\pi x)$ is the so called filtering function while $j_n(x)$ and $h_n^{(1)}(x)$ are the spherical Bessel and Hankel functions respectively.

(U) If $\theta\nu_o$ exceeds the frequency range from ν_o to the first zero of $\mathrm{sinc}\,(n - \kappa\ell/\pi)$ the bandwidth is then determined by the zero. The zero occurs $n - \kappa\ell/\pi = 1$ i.e., $T(\nu - \nu_o) = 1$ giving a fractional bandwidth

$$\textcircled{H} = 1/n \qquad (6.62)$$

In Goodrich et al, (1967c) the variable θ was not introduced explicitly; (alternatively one could say that θ was infinite). The computational results given there, Figs. (4-7) and (4-8) for $\ell = 1/4$, $n = 4$ thus correspond to a 25 percent bandwidth. This is a bandwidth which is considerably exceeded by

actual short-pulse radars*. One observes the considerable distortion of the pulse shape in the creeping wave. This is an example of case (iii) above. Such a pulse shape could be considered as an identifying indicator of the target since the natural pulse distortion is pretty well reproduced and would not be at all the same for other targets.

(U) The opposite extreme (case i) is given by setting $\theta = 0.5$ in what is otherwise the same example. Numerical evaluation of Eq. (6.58) yields Fig. 6-7 which illustrates clearly the predicted modulated cosine response. Clearly the pulse distortion effects are submerged.

*See, for example, Milburn, J. (1967) "Short Pulse Model Measurement Studies," Aerosystems Laboratory General Dynamics, RADC-TR-66-785. Vol. 1 which cites a 50 percent bandwidth as typical.

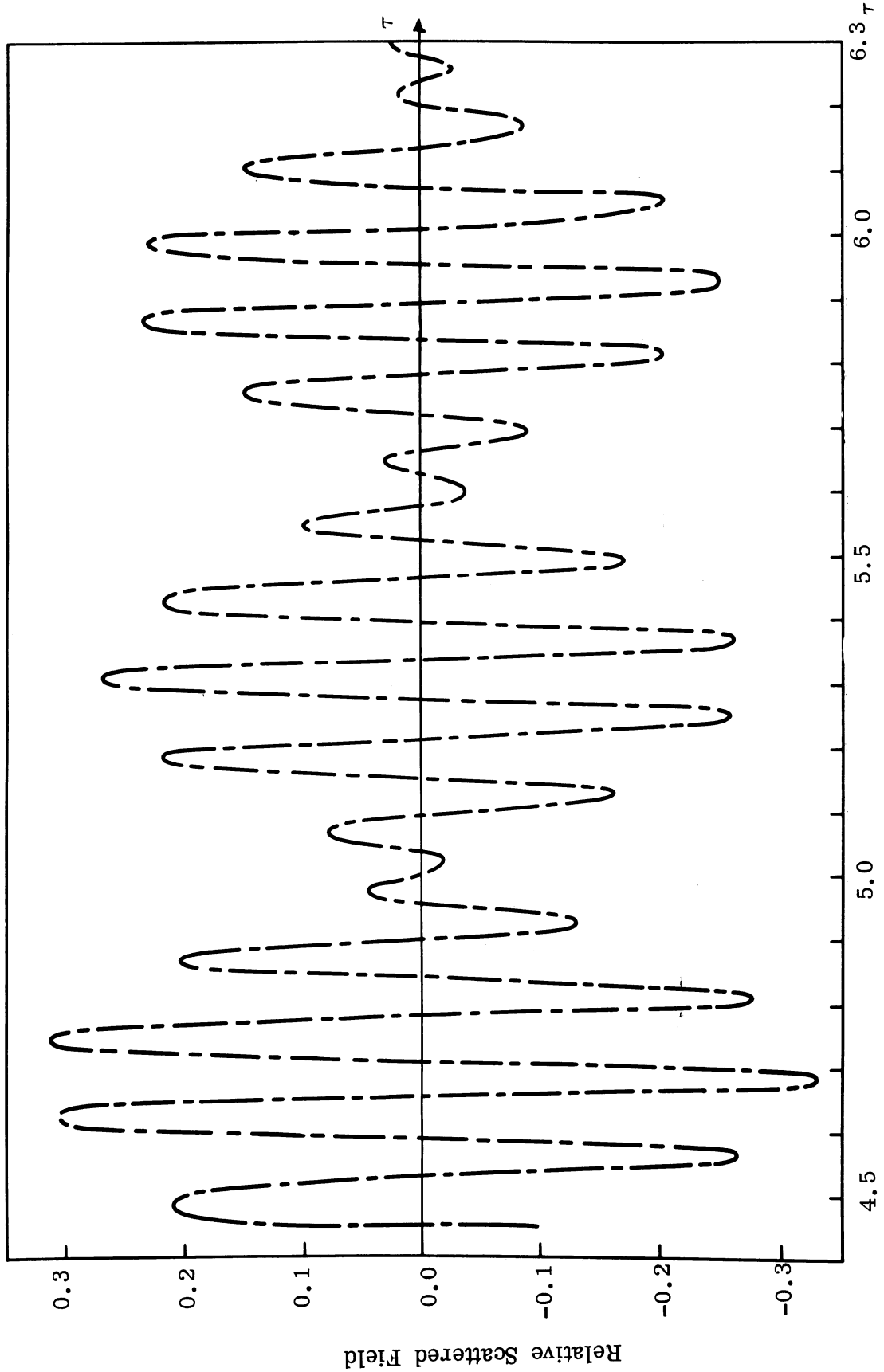

FIG. 6-7: BAND LIMITED CREEPING WAVE RETURN CREEPING WAVE. n = 4, ℓ = 1/4, 10 percent bandwidth.

VII

HANDBOOK OF RADAR CROSS SECTION FORMULAS

7.1 Introduction

(U) For convenience, the radar cross section formulas for the various basic shapes studies under SURF have been listed in "handbook" form in the final reports at the end of each year's work. (See Goodrich et al, 1965 and 1967) This report is the third in this series. In this Section, are given the formulas for:

a) Cone-sphere with indented base (revised),

b) flat backed cone (radius of curvature at the join is a parameter),

c) coated cone-sphere with indented base,

d) coated cone-sphere with annular slots (representing slot antennas) near the tip of the cone and near the cone-sphere join, and

e) coated cone-sphere with longitudinal slots.

In Goodrich et al, (1967), formulas have been given for two other coated shapes. These were the coated cone-oblate spheroid and the coated cone-prolate spheriod. Formulas were also given for the cone-sphere with an indented base (such as is to be found in the Mark-12 re-entry vehicle). A revised formula for this latter shape is given in this Section reflecting improvements in accuracy obtained from further analysis in 1967.

7.2 Indented Cone Sphere (revised)

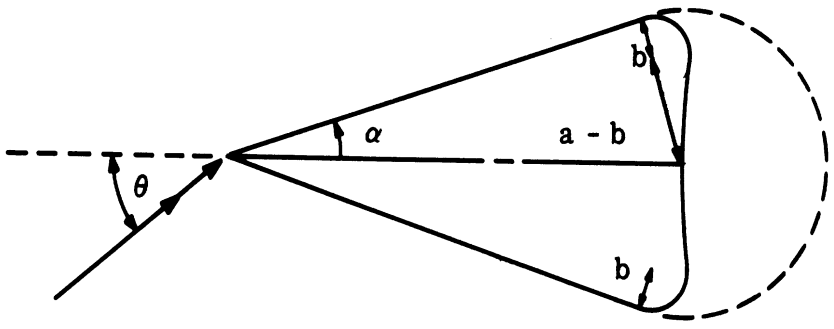

FIG. 7-1: CONE-SPHERE WITH CONCAVE INDENTATION IN REAR CAP.

$$\frac{\sigma}{\lambda^2} = 1/\pi \left| S_1 + S_2 + S_3 J_o (2 ka \sin \theta) \right|^2 \quad 0 \leq \theta \leq \beta \tag{7.1}$$

$$\frac{\sigma}{\lambda^2} \doteq 1/\pi \left| S_{spec} \right|^2 , \quad \beta \leq \theta \leq \frac{\pi}{2} - \alpha \tag{7.2}$$

where

$$S_1 = - \frac{i}{4} \frac{\tan^2 \alpha \exp\left[-2 i ka \operatorname{cosec} \alpha \cos \theta\right]}{(1 - \sin^2 \theta \sec^2 \alpha)^{3/2}} \tag{7.3}$$

$$S_2 = \frac{i}{4} \sec^2 \alpha \frac{a}{b} B (kb) J_o (2 ka \cos \alpha \sin \theta) e^{-2ikb \sin\alpha \cos \theta}, \quad b \geq b_1$$

$$= - i \frac{ka}{2n} \operatorname{cosec} \frac{2\pi}{n} J_o (2 ka \cos \alpha \sin \theta) e^{-2ikb \sin \alpha \cos \theta}, \quad b \leq b_1 \tag{7.4}$$

$$n = (3/2) + (\alpha/\pi) \tag{7.5}$$

$$kb_1 = - \frac{3n \sin \frac{2\pi}{n}}{16 \cos^2 \alpha} \tag{7.6}$$

$$B (kb) = 1 - \frac{5}{64} \left(- \frac{6n \sin \frac{2\pi}{n}}{kb \cos^2 \alpha} \right)^{0.6} \tag{7.7}$$

$$S_3 = \gamma (ka) B(kb) S_{cw} \tag{7.8}$$

$$\gamma(ka) = \left\{\left(\frac{1}{3} + \int_0^{\beta_1} \mathrm{Ai}(-x)\,dx\right)\left(2 + (ka/2)^{2/3}\,\alpha^2\beta_1^2\,e^{-i\pi/3}\right)\right.$$

$$\left. + (ka/2)^{2/3}\,\alpha^2\,e^{-i\pi/3}\mathrm{Ai}(-\beta_1)\right\} \exp\left[-\left(\frac{ka}{2}\right)^{1/3}\alpha\beta_1 e^{-i\pi/6}\right] \quad ,(7.9)$$

$$ka > 3$$

$$\gamma(ka) = 1, \quad ka < 3$$

$$S_{cw} = \frac{a}{2b}(kb/2)^{5/3}\,\frac{e^{2ik(a-b)+i\,5\pi/12}}{\sqrt{2k(a-b)}\,\beta_1\left\{\mathrm{Ai}(-\beta_1)\right\}^4}\left\{1 + \frac{e^{i\pi/3}(32\beta_1^3+9)}{60\tau^2\beta_1^2}\right\} \cdot$$

$$\cdot \exp\left\{i\pi\,kb - e^{-i\pi/6}\,\tau\pi\beta_1 - \frac{e^{i\pi/6}}{60\tau\beta_1}\,(\beta_1^3 - 9)\right\} \qquad (7.10)$$

$$\tau = (kb/2)^{1/3} \qquad (7.11)$$

$$\beta_1 = 1.018793\ldots. \qquad (7.12)$$

$$\mathrm{Ai}(-\beta_1) = 0.535656\ \ldots\ (\mathrm{Ai\ is\ the\ Airy\ function}) \qquad (7.13)$$

$$S_{spec} = \frac{1}{4}\,e^{i\pi/4}\sqrt{\frac{ka\cos\alpha}{\pi\sin\theta}}\,\tan(a+\theta)\,e^{2ika\cot\alpha\cos(\alpha+\theta)}$$

$$\left\{1 - F\left(\sqrt{2\,ka\cot\alpha\cos(\alpha+\theta)}\right)\right\} \quad , \ \theta < \pi/2 - \alpha$$

$$= \frac{ka\,\mathrm{cosec}\,\alpha}{3}\sqrt{\frac{ka\sec\alpha}{\pi}} \quad , \quad \theta = \pi/2 - \alpha \qquad (7.14)$$

$$F(x) = \frac{e^{-ix^2}}{x} \int_0^x e^{it^2}\, dt \qquad (7.15)$$

The angle β at which transition between (7.1) and (7.2) is made is the smallest value of θ where (7.1) and (7.2) intersect which is larger than the first zero of $J_o(2\,ka \sin\theta)$ i.e. $\beta > \sin^{-1} \frac{2.405}{2\,ka}$.

7.3 Flat Backed Cone

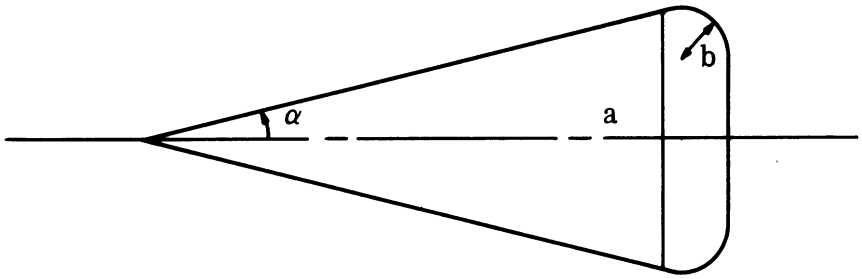

FIG. 7-2: BASIC FB SHAPE.

$$\frac{\sigma}{\lambda^2} = 1/\pi \left| S_1 + S_2 + S_3\, J_o(2\,ka \sin\theta) \right|^2 , \quad 0 \le \theta \le \beta \qquad (7.16)$$

$$\frac{\sigma}{\lambda^2} = 1/\pi \left| S_{spec} \right|^2 , \quad \beta \le \theta \le \pi/2 - \alpha \qquad (7.17)$$

where

S_1 is given by (7.3)

S_2 is given by (7.4) with b now the radius in Fig. 7-2

S_3 is given by (7.8) with b as above

S_{spec} is given by (7.14) .

The angle β at which transition between (7.16) and (7.16) is made is the smallest value of θ where (7.16) and (7.17) intersect which is larger than the first zero of $J_o(2\,ka\,\sin\theta)$ i.e. $\beta > \sin^{-1}\frac{2.405}{2\,ka}$.

7.4 Coated Cone Sphere with Indented Base.

$$\frac{\sigma}{\lambda^2} = 1/\pi \left| S_1 + R(\theta)\, S_2 + S_3\, J_o(2\,ka\,\sin\theta) \right|^2 , \quad 0 \le \theta \le \beta \tag{7.18}$$

$$\frac{\sigma}{\lambda^2} = 1/\pi \left| R(\theta)\, S_{spec} \right|^2 \quad \beta \le \theta \le \pi/2 - \alpha \tag{7.19}$$

where

S_1 is given by (7.3)

S_2 is given by (7.4)

$$S_3 = \frac{a}{2b}\,(kb/2)^{1/3}\,\frac{e^{2ik(a-b)+i\pi/12}\left(S^{(e)}_{(b)} + S^{(m)}_{(b)}\right)}{\sqrt{2\,k(a-b)}\;\beta_1\left[Ai\,(-\beta_1)\right]^2} \tag{7.20}$$

$$S^{(e)}(x) = (kx/2)^{4/3}\, e^{i\pi\, kx - i\pi/6} \sum_s \frac{1}{\left\{Ai(-\beta_s)\right\}^2 \left\{\beta_s - e^{i\pi/3} q_e^2\right\}} \tag{7.21}$$

$$S^{(m)}(x) = (kx/2)^{4/3}\, e^{i\pi\, kx - i\pi/6} \sum_s \frac{q_m^2}{Ai'(-\alpha_s)\left\{e^{i\pi/3}\alpha_s - q_m^2\right\}} \tag{7.22}$$

$$q_e = -\,(kx/2)^{1/3}\,\eta \tag{7.23}$$

$$q_m = -\,(kx/2)^{1/3}\,1/\eta \tag{7.24}$$

α_s are roots of $Ai'(-\alpha_s) - q_m Ai(-\alpha_s) = 0$

β_s are roots of $Ai'(-\beta_s) - q_e Ai(-\beta_s) = 0$

$$R(\theta) = \frac{1 - \eta \sin(\theta + \alpha)}{1 + \eta \sin(\theta + \alpha)} \qquad (7.25)$$

S_{spec} given by (7.14)

For lossless coatings, S_3 is given by (7.10)

For lossy coatings, $S_3 = 0$

The angle β at which transition between (7.18) and (7.19) is made is the smallest value of θ where (7.18) and (7.19) intersect which is larger than the first zero of $J_o(2\ ka \sin\theta)$ i.e. $\beta > \sin^{-1} \frac{2.405}{2\ ka}$.

$\eta = -i \sqrt{\mu/\epsilon} \tan(\sqrt{\epsilon\mu}\ k\delta)$

δ = coating thickness , ϵ, μ = coating permittivity and permeability

$\lim_{k\delta \to \infty} \eta = \sqrt{\mu/\epsilon}$

7.5 Coated Cone Sphere, LSP with Slotted Coating.

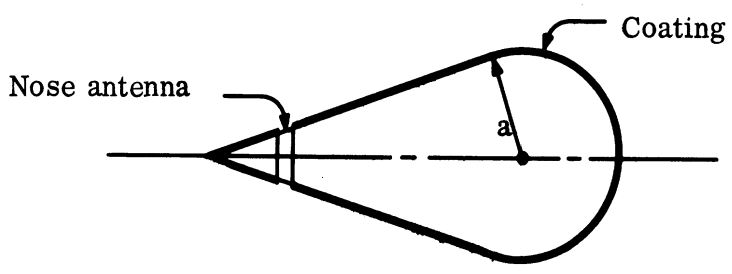

FIG. 7-3: COATED CONE-SPHERE WITH NOSE-TIP ANTENNA.

$$\frac{\sigma}{\lambda^2} = \frac{1}{\pi}\left|S_1 + R(\theta)\, S_2 + S_3\, J_o(2\,ka\,\sin\theta) + S_{sp}\right|^2, \quad 0 \le \theta \le \beta \tag{7.26}$$

$$\frac{\sigma}{\lambda^2} = 1/\pi \left|R(\theta)\, S_{spec}\right|^2, \quad \beta \le \theta \le \pi/2 - \alpha \tag{7.27}$$

where

S_1 is given by (7.3)

$R(\theta)$ is given by (7.25)

$$S_2 = \frac{i}{4}\sec^2\alpha\, J_o(2\,ka\,\cos\alpha\,\sin\theta)\, e^{-2ika\,\sin\alpha\,\cos\theta} \tag{7.28}$$

$$S_3 = S^{(e)}(a) + S^{(m)}(a) \tag{7.29}$$

$S^{(e)}(a)$ given by (7.21)

$S^{(m)}(a)$ given by (7.22)

$$S_{sp} = \frac{4\pi\, ka_s\, e^{2ika_s\,\mathrm{cosec}\,\alpha\,\cos\alpha\,\cos\theta}}{Y_\ell + Y_r}\, S(0)\, J_o(2\,ka_s\,\sin\theta) \tag{7.30}$$

Y_ℓ is slot load admittance

Y_r is slot radiation admittance

a_s is spacer radius at its midpoint

$$S(0) = \sum_n \frac{(2\nu_n + 1)\, e^{i\nu_n \pi/2}}{\left[\frac{\partial}{\partial \nu} P_\nu^1 (\cos\alpha)\right]_{\nu=\nu_n}} \psi_{\nu_n} (ka_s \operatorname{cosec}\alpha) - i \sum_m$$

$$\frac{(2\mu_m + 1)\, e^{i\mu_m \pi/2}\, \psi_{\mu_m} (ka_s \operatorname{cosec}\alpha)\, \zeta'_{\mu_m} (ka_s \operatorname{cosec}\alpha)}{\sin^2\alpha \left[\frac{\partial}{\partial\mu\partial\alpha} P_\mu^1 (\cos\alpha)\right]_{\mu=\mu_m} \zeta_{\mu_m} (ka_s \operatorname{cosec}\alpha)} \qquad (7.31)$$

ν_n are the roots of $P_\nu^1 (\cos\alpha) = 0$

μ_m are the roots of $\frac{\partial}{\partial\alpha} P_\mu^1 (\cos\alpha) = 0$

$$\psi_\nu(x) = \sqrt{\frac{\pi x}{2}}\; J_{\nu + 1/2}(x)$$

$$\zeta_\mu (x) = \sqrt{\frac{\pi x}{2}}\; H^{(1)}_{\mu + 1/2}(x) \;,\quad \zeta'_\mu (x) = \frac{d}{dx}\, \zeta_\mu (x)$$

Alternatively

$$S_{sp} = \frac{2\sqrt{3}}{9}\, ka_s \Gamma e^{i\phi} J_o(2ka_s \sin\theta)\, e^{-2ik(a - a_s \cos\alpha)\operatorname{cosec}\alpha \cos\theta} \qquad (7.32)$$

$\Gamma e^{i\phi}$ is the complex excitation strength which may be evaluated from surface current measurements as discussed in Section 3.2.4.

S_{spec} is given by (7.14)

For lossless coatings, S_3 is given by

$$S_3 = (ka/2)^{4/3}\, e^{i\pi/3} \left\{ 1 + \frac{e^{i\pi/3}}{60\beta_1^2} (32\beta_1^3 + 9)\,(2/ka)^{2/3} \right\}$$

$$\frac{1}{\beta_1 \left\{ Ai(-\beta_1) \right\}^2} \cdot \exp \left\{ i\,\pi\, ka - e^{-i\pi/6}\, \pi\, \beta_1 (ka/2)^{1/3} \right.$$

$$\left. - e^{i\pi/6}\, \frac{\pi}{60\beta_1}\, (\beta_1^3 - 9)\,(2/ka)^{1/3} \right\} \qquad (7.33)$$

β_1 and $Ai(-\beta_1)$ given in (7.12) and (7.13)

For lossy coatings, $S_3 = 0$.

The angle β at which transition between (7.26) and (7.27) is made is the smallest value of θ where (7.26) and (7.27) intersect which is larger than the first zero of $J_o(2\,ka\,\sin\theta)$ i.e. $\beta > \sin^{-1} \frac{2.405}{2\,ka}$

7.6 Coated Cone Sphere, LSH with Slotted Coating.

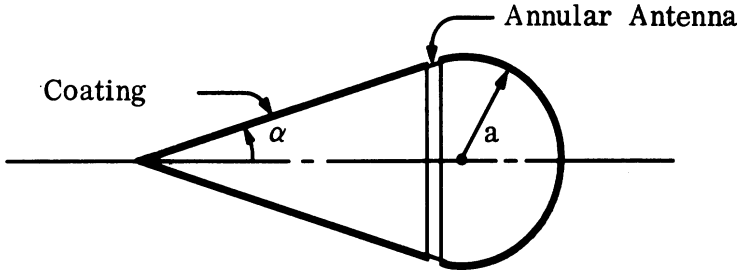

FIG. 7-4: COATED CONE-SPHERE WITH ANNULAR ANTENNA NEAR JOIN.

$$\frac{\sigma}{\lambda^2} = \frac{1}{\pi}\left|S_1 + R(\theta)\, S_2 + S_3 J_o\,(2\,ka \sin\theta) + S_{sp}\right|^2, \quad 0 \le \theta \le \beta \tag{7.34}$$

$$\frac{\sigma}{\lambda^2} = 1/\pi \left|R\,(\theta)\, S_{spec}\right|^2, \quad \beta \le \theta \le \pi/2 - \alpha \tag{7.35}$$

where

S_1 is given by (7.3)

$R(\theta)$ is given by (7.25)

S_2 is given by (7.28)

S_3 is given by (7.29)

$$S_{sp} = e^{2ika(\cot\alpha + \pi/2 - \theta_o)} \frac{\pi\,(ka)^3}{(Y_\ell + Y_r)\sin\theta_o} \left\{g\left[(ka/2)^{1/3}\,(\pi/2 - \theta_o)\right]\right\}^2 J_o(ka \sin\theta_o \sin 2\theta) \tag{7.36}$$

$$g(\xi) = 1/\sqrt{\pi} \int_{-\infty}^{\infty} \frac{e^{i\xi t}}{\omega'(t)}\, dt \tag{7.37}$$

$$\omega(t) = \sqrt{\pi}\left[Bi(t) + i\,Ai\,(t)\right] \tag{7.38}$$

θ_o is the angular distance from slot to join

Y_ℓ is slot load admittance

Y_r is slot radiation admittance

S_{spec} is given by (7.14)

For lossless coatings, S_3 is given in (7.33)

For lossy coatings, $S_3 = 0$

The angle β at which transition between (7.34) and (7.35) is made is the smallest value of θ where (7.34) and (7.35) intersect which is larger than the first zero of $J_o(2\,ka \sin\theta)$ i.e. $\beta > \sin^{-1} \frac{2.405}{2\,ka}$.

7.7 Coated Cone Sphere with Longitudinal Slots

(U) The effect of the slots is negligible and the formulae for the coated cone-sphere without slots apply, i.e.

$$\frac{\sigma}{\lambda^2} = 1/\pi \left| S_1 + R(\theta)\, S_2 + S_3\, J_o(2\,ka \sin\theta) \right|^2 \qquad 0 \le \theta \le \beta \qquad (7.39)$$

$$\frac{\sigma}{\lambda^2} = 1/\pi \left| R(\theta)\, S_{spec} \right|^2 \qquad \beta \le \theta \le \pi/2 - \alpha \qquad (7.40)$$

where

S_1 is given by (7.3)

$R(\theta)$ is given by (7.25)

S_2 is given by (7.28)

S_3 is given by (7.29)

S_{spec} is given by (7.14)

For lossless coatings S_3 is given by (7.33)

For lossy coatings $S_3 = 0$

The angle β at which transition between (7.39) and (7.40) is made is the smallest value of θ where (7.39) and (7.40) intersect which is larger than the first zero of $J_o(2\,ka \sin\theta)$ i.e. $\beta > \sin^{-1} \frac{2.405}{2\,ka}$.

VIII

COMPUTER PROGRAM FOR A ROTATIONALLY SYMMETRIC METALLIC BODY

8.1 Introduction

(U) Under other studies sponsored by Department of Defense agencies, attempts have been made to develop a computer program to calculate the radar cross section of rotationally symmetric metallic bodies. These attempts have met with some sucess but have serious drawbacks so far as application to the type of re-entry bodies investigated under SURF. They are characterized by the fact that either (a) the computer program is unavailable (b) the computer program is not sufficiently accurate when applied to pointed re-entry shapes and/or (c) the computer program is limited as regards electrical size of bodies to which it can be applied.

(U) It was a goal of the SURF study, under Task 3.1.3, to develop a computer program to calculate the surface currents and radar cross section of cone-sphere-like metallic shapes for all angles of incidence and extend the programming to handle coated shapes as well. This goal has not been realized. A computer program has been developed for the metallic body but the analytical problems which arose during the development have been difficult and obtuse and the program is not yet at a stage for practical application. Although worthwhile advances which should lead to the effective solution of this problem have been made in the state-of-art and a method of matrix inversion proposed by earlier investigators (Schweitzer, 1965) has, with some modification, proven to be practical, further programming work would be required to bring it into operation.

(U) Section 8.2 summarizes the numerical analysis of the problem. Section 8.3 describes the program at the stage of development which was reached at the conclusion of the SURF investigation. For a given metallic shape appropriately parameterized, the Fortran IV computer program calcu-

lates the surface current for an arbitrary number, N, of uniformly spaced sampling points. The output of the calculation is in the form of 2N complex numbers representing the values of the orthogonal surface current components at those sampling points. There is no inherent limitation on the number of sampling points that can be handled. The choice of N as ten sampling points for this version of the program was dictated by the desire to test the system with sufficient accuracy without incurring undue cost. The computer program described in Section 8.3 is capable of handling bodies larger than those treated in other available computer programs which attempt to solve a similar problem. Because of the column matrix inversion system which has been adopted, the number of sampling points and the size of the body which can be treated is limited only by the amount of computer storage available to the user and the necessity to obtain a computation of given accuracy at the least cost.

(U) The program described in Section 8.3 was written to test the programming development. It was devised to compute the surface currents on the smallest re-entry body to which the results of the SURF investigation might be applied. The example chosen is for a body for which ka is approximately 1.5. For bodies with cone half-angles of interest in the SURF study, L (see Fig. 8-1) would be approximately 6a. By the simple criteria stated below,

$$\frac{L}{N-1} \lesssim \lambda/6 = \frac{\pi}{3K_o} \simeq 1/K_o$$

$$N - 1 \gtrsim K_o L$$

a reasonable choice for the number of sampling points, N, is 10.

(U) In this test program, θ equals zero, i.e., the nose-on direction of incidence has been chosen and only one azimuthal mode is computed. The program is capable of extension to oblique incidence.

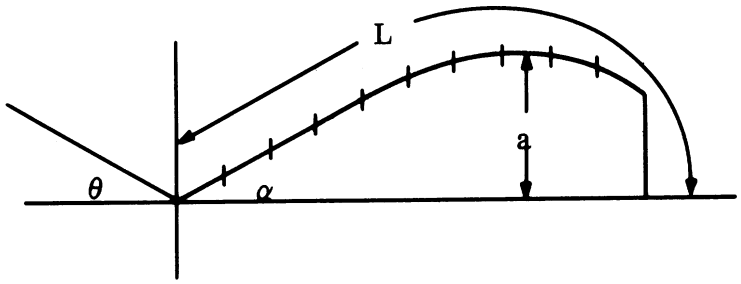

FIG. 8-1: REPRESENTATION FOR SAMPLING.

8.2 Description of the Numerical Analysis

8.2.1 Introduction

(U) This Section describes the solution of numerical analysis problems not solved in Schweitzer (1965) which outlined a method of solution of the Maue integral equation for the surface current on the surface of a metallic rotationally symmetric shape. In Schweitzer (1965) and Castellanos (1966) will be found the fundamental description of the earlier analysis which led to development of the program given in Section 8.3. This Section summarizes the continuation of the numerical analyses of problems which arose in devising a practical program.

(U) The input parameter is f(z). The function $\mathbf{f} = t(z)$ is then defined by (4.10) and (4.11) of Schweitzer (1965). The T_{ij}'s are then computed by use of formulas on page 26 of the Schweitzer report and quadrature scheme described in the present report.

(U) Next, the elements d_i^{mj} are computed by use of their definition on page 42 of the Schweitzer report, and methods of Section 8,2.4 of the present report, and the b_i^m's are expressed in terms of the d_i^m by use of (11.15) and (11.21) of the Schweitzer report.

(U) The T matrix is then inverted by use of the scheme described in Section 34 of Schweitzer report, and the system solved for the c_i^m as often as is desirable.

8.2.2 The Evaluation of G_m

(U) A. Definition of G_m: We begin with the definition of G_m given in Eq. (3.177) of Goodrich et al, 1967c

$$G_m = 2(-i)^m \int_0^{\pi/2} \frac{e^{i\Gamma R\sqrt{1 - k^2 \sin^2 \phi}}}{\Gamma R\sqrt{1 - k^2 \sin^2 \phi}} \cos 2m\phi \, d\phi \, . \qquad (8.1)$$

Letting

$$\phi = \pi/2 - \theta \qquad (8.2)$$

we get

$$G_m = 2(-i)^m \int_0^{\pi/2} \frac{e^{i\Gamma R\sqrt{1 - k^2 \cos^2 \phi}}}{\Gamma R\sqrt{1 - k^2 \cos^2 \phi}} \cos 2m\phi \, d\phi \, . \qquad (8.3)$$

Now let

$$x = \cos \phi \qquad (8.4)$$

in Eq. (8.3), to get

$$G_m = 2(i)^m \int_0^1 \frac{e^{i\Gamma R\sqrt{1 - k^2 x^2}}}{\Gamma R\sqrt{1 - x^2}\sqrt{1 - k^2 x^2}} T_{2m}(x) \, dx \qquad (8.5)$$

where $T_{2m}(x)$ is the Chebyshev polynomial of degree 2m.

(U) Using $e^{i\theta} = \cos\theta + i \sin\theta$ we write G_m in the form

$$G_m = 2\,(i)^m \left[\mathrm{Re}m + i\,\ell m\right] \tag{8.6}$$

where

$$\mathrm{Re}m = \int_0^1 \frac{\cos\left[\Gamma R \sqrt{1 - k^2 x^2}\right]}{\Gamma R \sqrt{1 - k^2 x^2}} \frac{T_{2m}(x)}{\sqrt{1 - x^2}}\, dx \tag{8.7}$$

$$\ell m = \int_0^1 \frac{\sin\left[\Gamma R \sqrt{1 - k^2 x^2}\right]}{\Gamma R \sqrt{1 - k^2 x^2}} \frac{T_{2m}(x)}{\sqrt{1 - x^2}}\, dx \quad . \tag{8.8}$$

(U) B. The Evaluation of T_{2m}: With

$$x = \cos\theta \;,\quad T_m(x) = \cos m\theta \;; \tag{8.9}$$

we have

$$\left.\begin{aligned} 2x^2 - 1 &= \cos 2\theta \\ 2(2x^2 - 1)(2x^2 - 2) &= \cos 4\theta \end{aligned}\right\} \tag{8.10}$$

or

$$\cos(m + 2)\theta = 2 \cos m\theta \cos 2\theta - \cos(m - 2)\theta \tag{8.11}$$

Thus, with

$$\left.\begin{aligned} T_o &= 1 \\ T_2 &= 2x^2 - 1 \\ T_{2r+2} &= 2\,T_2\,T_{2r} - T_{2r-2} \end{aligned}\right\} \qquad (8.12)$$

and (8.12) may be used to evaluate T_{2r+2} for all r.

(U) C. The Evaluation of ℓm: We evaluate ℓm in (8.8) by the use of Chebyshev quadrature:

$$\int_0^1 \frac{F(t)\,dt}{\sqrt{1-t^2}} = \frac{\pi}{2N} \sum_{j=1}^{N} F(t_j) + \mathcal{E}_N; \quad t_j = \cos\left[\frac{(2j-1)}{4N}\right] \qquad (8.13)$$

Note that the integrand in (8.8) is entire. Applying a result of Stenger (1966) we obtain an error bound

$$\left|\mathcal{E}_N\right| < 8 \cdot 2^{2m}\, e^{\Gamma R} \left[\frac{\Gamma R\, ke}{2(2N-m)}\right]^{2(2N-m)} \qquad (8.14)$$

upon evaluating (8.8) by use of (8.13).

(U) D. The Evaluation of Rem for all Cells not Bordering the Diagonal: We also use Chebyshev quadrature of (8.7) for all cells not touching the diagonal. Here the nearest singularity is a pole at the point x = 1/k. Upon again using (8.13) we get an error bounded by

$$8 \left(\frac{16\,e\,N}{k\sqrt{1-k^2}}\right)^{1/2} (2/k)^{2m} \left(\frac{k}{1+\sqrt{1-k^2}}\right)^{8N} \qquad (8.15)$$

(U) E. The Evaluation of G_m for Cells Bordering the Diagonal: For the cells touching the diagonal it becomes important to appropriately treat the

nature of the singularity of G_m. We thus write (8.7) in the form

$$\text{Rem} = \int_0^1 \frac{F_m(x)\ dx}{\sqrt{(1-x^2)(1-k^2x^2)}}$$

$$= \int_0^1 \frac{F_m(x)}{\sqrt{(1+x)(1+kx)}} \frac{dx}{\sqrt{(1-x)(1-kx)}}$$

$$= \int_0^1 \frac{H_m(x)\ dx}{\sqrt{(1-x)(1-kx)}} \qquad (8.16)$$

where

$$H_m(x) = F_m(x) / \sqrt{(1+x)(1+kx)}$$

$$= \frac{\cos\left[\Gamma R \sqrt{1-k^2x^2}\right] T_{2m}(x)}{\Gamma R \sqrt{(1+x)(1+kx)}} \qquad (8.17)$$

(U) Substituting

$$\int_x^1 \frac{dt}{\sqrt{(1-t)(1-kt)}} = \alpha \int_y^1 dt \qquad (8.18)$$

where as in Goodrich and Stenger (1967)

$$\alpha = \int_0^1 \frac{dt}{\sqrt{(1-t)(1-kt)}} \qquad (8.19)$$

in (8.16), or

$$\left.\begin{aligned} x &= 1 - \frac{1-k}{k}\,\sinh^2\left[\alpha\sqrt{k}\,(1-y)\right] \\ \alpha &= \frac{2}{\sqrt{k}}\sinh^{-1}\sqrt{\frac{k}{1-k}} = \frac{2}{\sqrt{k}}\,\ell n\left(\frac{1+\sqrt{k}}{\sqrt{1-k}}\right) \end{aligned}\right\} \tag{8.20}$$

Then

$$\text{Rem} = \alpha\int_0^1 H_m\left[x(y)\right]dy \tag{8.21}$$

where $x = x(y)$ is given by (8.16). This integral is now evaluated by Legendre-Gauss quadrature in the form

$$\text{Rem} = \alpha\left[\sum_{j=1}^{N} W_j H_m\left[x(y_j)\right] + E_N(H)\right] \tag{8.22}$$

$$\left|E_N(H)\right| < \frac{256\,N\,e^{1+2m}}{\alpha\sqrt{(1+k)(2-\eta)}}\left(\eta+\sqrt{\eta^2-1}\right)^{-4N}$$

$$\eta = -1 + 2\left(\frac{2\sinh^{-1}\sqrt{2k/(1-k)}}{\alpha k}\right)^2 \tag{8.23}$$

and where the y_j and W_j are the positive zeros and weights of 2N-point Gaussian quadrature.

(U) In all of the above approximate sums the error is approximately equal to the difference between two evaluations using N and N + 1 points.

8.2.3 The Evaluation of T_{ij}^{m}

(U) We split these into two parts, those not bordering the diagonal and those that do.

(U) A. Cells not Bordering the Diagonal: The T_{ij}'s for cells not bordering the diagonal are done by repeated Legendre-Gauss quadrature. The integrals are all of the form

$$I = \int_{a}^{a+h} \int_{b}^{b+h} F_1(s)\, F_2(t)\, G_m(s,\, t)\, ds\, dt \tag{8.24}$$

They are more explicitly described in Schweitzer page 73ff; there is no need to give their explicit form here.

(U) Putting

$$s = b + \frac{1}{2} h + \frac{h}{2} x\,, \quad t = a + \frac{1}{2} h + \frac{h}{2} y \tag{8.25}$$

the integral I becomes

$$I = \frac{h^2}{4} \int_{-1}^{1} \int_{-1}^{1} H_m(x,\, y)\, dx\, dy \tag{8.26}$$

where

$$H_m(x,y) = F_1\left(b + \frac{1}{2} h + \frac{1}{2} hx\right) F_2\left(a + \frac{1}{2} h + \frac{1}{2} h\, y\right)$$

$$\cdot\, G_m\left(b + \frac{1}{2} h + \frac{1}{2} hx\, a + \frac{1}{2} h + \frac{1}{2} h\, y\right) \tag{8.27}$$

and

$$I = \frac{h^2}{4} \sum_{i=j}^{M} \sum_{j=1}^{N} w_i^{(1)} w_j^{(2)} H_m(x_i, y_j) + \mathcal{E}_{M,N} \quad . \tag{8.28}$$

The error $\mathcal{E}_{M,N}$ satisfies, approximately

$$\mathcal{E}_{M+1,\,N+1} - \mathcal{E}_{M,N} \cong 2\left[\mathcal{E}_{M+1;N} - \mathcal{E}_{M,N}\right]$$

$$\cong 2\left[\mathcal{E}_{M+1,N+1} - \mathcal{E}_{M+1,\,N}\right]; \tag{8.29}$$

these results can be used to arrive at the correct choice of M and N. In (8.28) the x_i, $W_i^{(1)}$, y_j, $W_j^{(2)}$ are the corresponding zeros and weights for M and N-point Legendre-Gauss quadrature.

(U) B. The Cells Bordering the Diagonal Cells: We recall that G_m is of the form

$$G_m = 2\,(i)^m \left[\text{Rem} + i\,\ell m\right] \quad . \tag{8.30}$$

We now write

$$\text{Rem} = \log\left(\frac{1 + \sqrt{k}}{\sqrt{1 - k}}\right) \widetilde{G} \tag{8.31}$$

where $\widetilde{G}$ is a bounded function, in order to explicitly display the singularity. Thus to evaluate the integrals (8.24) we, for either a = b or a = b + h, split Rem up into two parts. We achieve this using

$$\log \frac{1+\sqrt{k}}{\sqrt{1-k}} = -\log\left|\frac{s-t}{h}\right| + \log\left[\frac{1+\sqrt{k}}{\sqrt{1-k}} \cdot \left|\frac{s-t}{h}\right|\right] \tag{8.32}$$

Letting

$$\text{Rem} = g^{(1)} + g^{(2)} \tag{8.33}$$

where

$$\int_a^{a+h}\int_b^{b+h} \text{Rem}\ F_1(s)\ F_2(t)\ ds\ dt = I_1 + I_2\ , \tag{8.34}$$

and where

$$I_1 = \int_a^{a+h}\int_b^{b+h} g^{(1)}\ F_1(s)\ F_2(t)\ ds\ dt \tag{8.35}$$

$$I_2 = \int_a^{a+h}\int_b^{b+h} g^{(2)}\ F_1(s)\ F_2(t)\ ds\ dt\ . \tag{8.36}$$

Of these the integral I_2 presents less difficulty; we can evaluate it directly using Gauss-Legendre quadrature, just as we evaluated (8.26) above.

(U) In evaluating I_1 we consider three cases:

1) $a = b$; 2) $a = b + h$; 3) $a = b = 0$, or $1 - h$.

(U) a. <u>The Case $a = b \neq 0,\ 1 - h$:</u> The integrals are of the form

$$I = \int_a^{a+h}\int_a^{a+h} F(s,\ t)\ \left|\frac{s-t}{h}\right|\ ds\ dt\ . \tag{3.37}$$

We set

$$\left.\begin{aligned} s &= a + \frac{1}{2}h + \frac{u - v}{\sqrt{2}} \\ t &= a + \frac{1}{2}h + \frac{u + v}{\sqrt{2}} \end{aligned}\right\} \qquad (8.38)$$

in (8.37) to get*

$$I = \int_{-h/\sqrt{2}}^{0} \int_{-(v + h/\sqrt{2})}^{v + h/\sqrt{2}} G(u, v)\, \ell n \left| \frac{\sqrt{2}}{h} v \right| du\, dv$$

$$+ \int_{0}^{h/\sqrt{2}} \int_{-(h/\sqrt{2} - v)}^{h/\sqrt{2} - v} G(u, v)\, \ell n \left| \frac{\sqrt{2}}{h} v \right| du\, dv \qquad (8.39)$$

In the first term on the right we replace v by $-v$, so that

$$I = \int_{0}^{h/\sqrt{2}} \int_{-(h/\sqrt{2} - v)}^{h/\sqrt{2} - v} \left[G(u, v) + G(u, -v) \right] \ell n \left| \frac{\sqrt{2}}{h} v \right| du\, dv \qquad (8.40)$$

Next we set

$$v = \frac{h}{\sqrt{2}}\, x \qquad (8.41)$$

$$u = \frac{h}{\sqrt{2}} (1 - x)\, y \qquad (8.42)$$

in (8.40) to get, finally

*Compare Goodrich et al, (1967c), pp. 111-112.

$$I = \frac{h^2}{2} \int_{x=0}^{1} \int_{y=-1}^{1} \left[F(s,t) + F(t,s) \right] (1-x) \ln x \, dy \, dx \tag{8.43}$$

where

$$\left.\begin{aligned} s &= h/2\,(1-x)(1+y) + a \\ t &= h/2 \left[(1-x)\,y + x + 1 \right] + a \end{aligned}\right\} \tag{8.44}$$

(U) We evaluate (8.43) by use of Legendre-Gauss quadrature in the variable y and Gauss quadrature with weight $\ln x$ in the variable x:

$$I = \sum_{i=1}^{M} \sum_{j=1}^{N} W_i^{(1)} W_j^{(2)} H(x_i, y_j) + \mathcal{E}_{M,N} \tag{8.45}$$

Where $\mathcal{E}_{M,N}$ again satisfies (8.29).

(U) b. <u>The Case a = b + h:</u> In this case we want to evaluate the integrals

$$I = \int_{s=a}^{a+h} \int_{t=a-h}^{a} F(s,t) \ln \left| \frac{s-t}{h} \right| dt \, ds \tag{8.46}$$

Let us make the transformation

$$s = a + \frac{u-v}{\sqrt{2}}, \quad t = a + \frac{u+v}{\sqrt{2}} \tag{8.47}$$

in (8.46), to get

$$I = \int_{-(h/\sqrt{2})}^{0} \int_{-v}^{v+\sqrt{2}h} G(u, v) \ln \left| \frac{\sqrt{2}}{h} v \right| du\, dv$$

$$+ \int_{0}^{h/\sqrt{2}} \int_{v}^{-v+\sqrt{2}h} G(u, v) \ln \left| \frac{\sqrt{2}}{h} v \right| du\, dv \qquad (8.48)$$

where $G(u, v) = F\left(a + \frac{u - v}{\sqrt{2}}, a + \frac{u + v}{\sqrt{2}}\right)$. We now replace v by -v in the first integral to get

$$I = \int_{0}^{h/\sqrt{2}} \int_{-v}^{v+\sqrt{2}h} \left[G(u, v) + G(u, -v)\right] \ln \left| \frac{\sqrt{2}}{h} v \right| du\, dv \qquad (8.49)$$

Finally, putting

$$v = \frac{h}{\sqrt{2}} x \quad , \qquad u = h/\sqrt{2} \left[(1 + x) y + 1\right] \qquad (8.50)$$

we arrive at the formula

$$I = \frac{h^2}{2} \int_{0}^{1} \int_{-1}^{1} \left[F(s, t) + F(t, s)\right](1 + x) \ln |x|\, dy\, dx \qquad (8.51)$$

where

$$\left.\begin{aligned} s &= \frac{1}{2} h \left[(1 + x) y + (1 - x)\right] + a \\ t &= \frac{1}{2} h (1 + x) (1 + y) + a \end{aligned}\right\} \qquad (8.52)$$

We evaluate the integral (8.51) just as we evaluated the integral (8.43).

(U) c. The Case When $a = b = 0$ or $a = b = 1 - h$: These are very important cases. They need special careful consideration, since of these cells T_{mn} approaches zero only as $O(h)$, whereas T_{mn} approaches zero as $O(h^2)$ at all other cells. Thus T_{mn} at these cells is $O(1/h)$ times as large as T_{mn} elsewhere.

(U) We assume $f'(0) \neq 0$, $f'(L) \neq 0$. In this case

$$G_m = O\left(\frac{1}{s+t}\ \ell n\ \left|\frac{s-t}{s+t}\right|\right) \tag{8.53}$$

or s or $t \longrightarrow 0$. As in the previous section, we therefore write

$$G_m = g^{(1)} + g^{(2)} = \frac{1}{s+t}\ \ell n\left(\frac{1+\sqrt{k}}{\sqrt{1-k}}\right)\tilde{G} = \frac{1}{s+t}\ \ell n\left|\frac{s-t}{s+t}\right|\tilde{G}$$

$$+ \frac{1}{s+t}\ \ell n\left|\frac{1+\sqrt{k}}{\sqrt{1-k}}\cdot\frac{s+t}{s-t}\right|\tilde{G} \tag{8.54}$$

where G is well-behaved.

(U) Let us first consider the case $a = b = 0$. By use of (8.54) we need to develop two quadrature formulas:

$$I^{(1)} = \int_0^h\int_0^h F_1(s,t)\ \frac{1}{s+t}\ \ell n\left|\frac{s-t}{s+t}\right|\ dt\ ds \tag{8.55}$$

$$I^{(2)} = \int_0^h\int_0^h F_2(s,t)\cdot\frac{1}{s+t}\ dt\ ds \tag{8.56}$$

(U) Let us first consider (8.55). On setting

$$s = \frac{u - v}{2} \quad , \quad t = \frac{u + v}{2} \tag{8.57}$$

we get

$$I^{(1)} = \int_0^{h/\sqrt{2}} \int_{-u}^{u} G(u, v) \cdot \frac{1}{\sqrt{2}\, u} \ln |v/u| \, dv \, du$$

$$+ \int_{h/\sqrt{2}}^{\sqrt{2}\,h} \int_{-(\sqrt{2}h-u)}^{(\sqrt{2}h+u)} G(u, v) \cdot \frac{1}{\sqrt{2}\, u} \ln \left| \frac{v}{\sqrt{2}} \right| du \, dv = I_1 + I_2 \tag{8.58}$$

where I_1 is the first integral in (8.55) and I_2 is the second. We next set

$$u = h\sqrt{2}\, x \quad , \qquad y = uy = \frac{h}{\sqrt{2}}\, xy \quad . \tag{8.59}$$

in I_1. Then*

$$I_1 = \frac{h}{2} \int_0^1 \int_0^1 \left[F_1(s, t) + F_1(t, s) \right] \ln |y| \, dy \, dx \tag{8.60}$$

where

$$s = \frac{h}{\sqrt{2}}\, x (1 - y) \quad , \quad t = \frac{h}{\sqrt{2}}\, x (1 + y) \tag{8.61}$$

Similarly, by setting

$$u = h(\sqrt{2} - 1/\sqrt{2}\, x) \quad , \quad v = h/\sqrt{2}\, xy \tag{8.62}$$

*Note the factor $h/2$, not $h^2/4$

in I_2, we get

$$I_2 = h/2 \int_0^1 \int_0^1 \left[F_1(s, t) + F_1(t, s)\right] \cdot \frac{1}{2 - x} \left[\ell n\, y + \ell n\, x + \ell n\, \frac{1}{2 - x}\right] x\, dy\, dx \qquad (8.63)$$

(U) Before collecting terms, let us digress for a moment and evaluate I_2:

$$I_2 = \int_0^h \int_0^h F_2(s, t) \cdot \frac{1}{s + t}\, ds\, dt \quad . \qquad (8.64)$$

(U) Upon setting

$$s = \frac{u + v}{\sqrt{2}} \quad , \quad t = \frac{u - v}{\sqrt{2}} \qquad (8.65)$$

we have

$$I^{(2)} = \left[\int_0^{h/\sqrt{2}} \int_{-u}^{u} + \int_{h/\sqrt{2}}^{\sqrt{2}\,h} \int_{-(\sqrt{2}h-u)}^{\sqrt{2}h-u}\right] G(u, v) \cdot \frac{1}{\sqrt{2}\,u}\, dv\, du \qquad (8.66)$$

where $G(u, v) = F_2(s, t)$ under (8.65). In the first integral on the right of (8.66) we put

$$v = ux \quad , \quad u = h/\sqrt{2}\; y \qquad (8.67)$$

and in the second

$$\sqrt{2}\ h - u = h/\sqrt{2}\ y\ ,\quad v = h/\sqrt{2}\ xy\ . \tag{8.68}$$

We then arrive at the formula

$$I^2 = \frac{h}{2}\int_0^1\int_{-1}^1 \left[G\left(\frac{h}{\sqrt{2}}\,y,\ \frac{h}{\sqrt{2}}\,xy\right) + \frac{y}{2-y}\ G\left(\frac{h}{\sqrt{2}}(2-y),\ \frac{h}{\sqrt{2}}\,xy\right)\right]\cdot dx\,dy$$

$$= \frac{h}{2}\int_0^1\int_{-1}^1 \left[F_2\left(\frac{h}{2}\,y\,(1+x),\ \frac{h}{2}\,y\,(1-x)\right)\right.$$

$$\left. + \frac{y}{2-y}\ F_2\left(\frac{h}{2}\,(2-y+xy),\ \frac{h}{2}\,(2-y-xy)\right)\right] dx\,dy \tag{8.69}$$

We are now in a position to collect terms:

$$I^{(1)} + I^{(2)} = h/2\int_0^1\int_0^1 \left\{F_1(s_1,\ t_1) + F_1(t_1,\ s_1)\right.$$

$$+ \frac{x}{2-x}\left[F_1(s_2,\ t_2) + F_1(t_2,\ s_2)\right] + \frac{y}{2-y}\left[F_1(s_3,\ t_3)\right.$$

$$\left.\left. + F_1(t_3,\ s_3)\right]\right\}\cdot \ln y\ dy\ dx \tag{8.70}$$

$$+ h/2\int_0^1\int_0^1 \left\{\frac{y}{2-y}\ \ln\frac{1}{2-y}\left[F_1(t_3,\ s_3) + F_1(t_3,\ s_3)\right]\right.$$

$$+ F_2(s_1,\ t_1) + F_2(t_1,\ s_1) + \frac{y}{2-y}\left[F_2(s_3,\ t_3)\right.$$

$$\left.\left. + F_2(t_3,\ s_3)\right]\right\} dx\ dy \tag{8.70}$$

where

$$\left.\begin{aligned} s_1 &= \frac{h}{2}\, x\,(1-y) \quad , \quad t_1 = \frac{h}{2}\, x\,(1+y) \\ s_2 &= \frac{h}{2}\left[2 - x\,(1-y)\right] , \quad t_2 = \frac{h}{2}\left[2 - x\,(1+y)\right] \\ s_3 &= \frac{h}{2}\left[2 - y\,(1-x)\right] , \quad t_3 = \frac{h}{2}\left[2 - y\,(1+x)\right] \end{aligned}\right\} \tag{8.71}$$

The first of (8.70) is evaluated by use of Gaussian quadrature with weight function $\ell n y$ in y, and weight function 2 (Legendre-Gauss) in x (compare 8.43). The second of (8.70) is evaluated by use of Gauss quadrature with weight 1 in both variables, x and y (compare 8.27).

(U) Near $s = t = 1$, the singular portion of G_m is of the form $G_m \frac{1}{2 - s - t} \ell n \left|\frac{s - t}{2 - s - t}\right|$. If we set $s' = 1 - s$, $t' = 1 - t$ we see that G_m satisfies (8.54) with s replaced by s' and t by t'. Thus we end up with (8.70) with s_i and t_i replaced by s'_i and t'_i. The s'_i and t'_i are then given by (8.71) together with the relation $s'_i = 1 - s_i$, $t'_i = 1 - t_i$.

8.2.4 The Evaluation of $d_i^{m_{ij}}$

(U) The formula for these is given in Eq. (9.3) of Castellanos; these take the form

$$I = \int_0^1 F(t)\, e^{ik_o z(t)}\, J_m\left(k_o f(z) \sin\theta_o\right) dt \quad . \tag{8.72}$$

(U) The Bessel function is evaluated by use of its truncated expansion

$$J_m(x) = \sum_{\mu=0}^{M} \frac{(-1)^\mu\, (x/2)^{2m+2\mu}}{\mu!\,(m+\mu)!} + \mathcal{E}_M \tag{8.73}$$

where

$$\mathcal{E}_M < \left[|x/2|^2 \, e^2 \, M(m+M) \right]^M < \left| \frac{|x| \, e}{2M} \right|^{2M} \quad . \qquad (8.74)$$

(U) The evaluation of I in (8.72) is then done by use of the mid-ordinate formula:

$$\int_0^1 f(x)\,dx = h \sum_{i=1}^{N} f\left(\frac{2i-1}{2} h\right) + \mathcal{E}_N \; ; \; h = 1/N \qquad (8.75)$$

which is suited to this type of integral. The error $\mathcal{E}_N$ satisfies the approximate relation $\mathcal{E}_N \cong \mathcal{E}_N - \mathcal{E}_{2N}$; this can be used as a test of when to stop the computations.

8.3 Description of Computer Programming

(U) This Section gives a listing of the computer programming. The main program is shown schematically in Fig. 8-1. The inputs to the program are as given in Table VIII-1. It will be noted that as shown in this particular listing, the angle of incidence alpha is set at zero, representing nose-on incidence and the number of modes is entered as one. These representative entries to the program were chosen so that the first test programs would be as simple as possible and still provide data for comparison with theoretical calculations or experimental data. This is not a fundamental restriction.

TABLE VIII-1: Main Listing Inputs

Read:

M	N	CIR	XKO	A	ALPHA
1	10	π^2	1	π	0
No. of modes	No. of sampling points	1/2 circumference			Angle of incidence

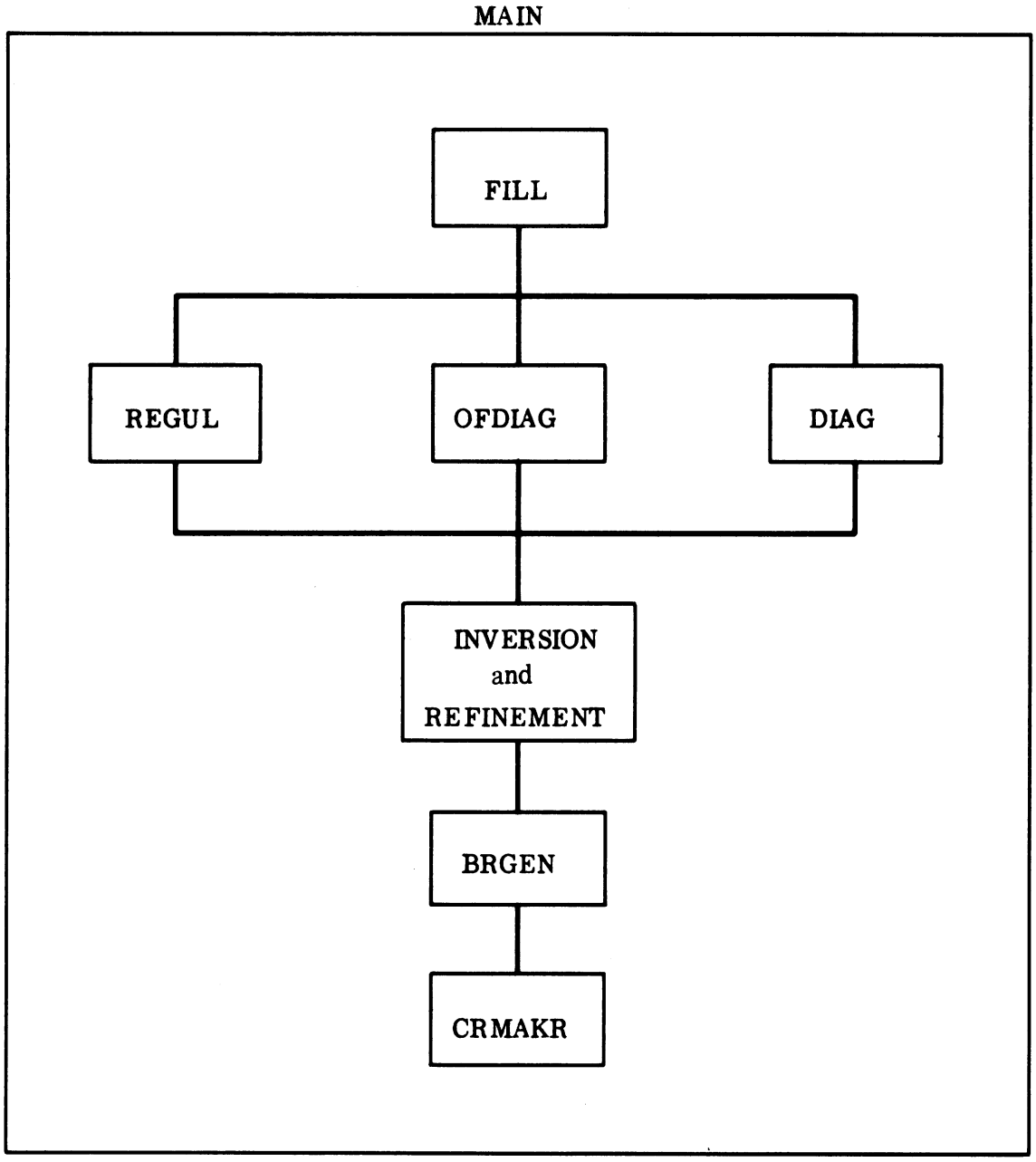

FIG. 8-2: SCHEMATIC REPRESENTATION OF COMPUTER PROGRAM.

MAIN

```
      IMPLICIT REAL*8(A-H,O-Z)
      COMMON FM,M,IM,CIR,XKO,A,ALPHA,T
      DIMENSION T(100),MAT(2,210),IMAT(2,210),TM(2,420)
      DIMENSION BRI(2,20),BRII(2,20),CRI(2,20),CRII(2,20)
      REAL*8 MAT,IMAT
3     READ (1,101,END=200) M,N,CIR,XKO,A,THETA
101   FORMAT (2I3,4D16.7)
      NN=N+N
      N1=N-1
      IM=M+2
      FACT=1.DO/(3.D1*CIR)
      T(1)=0.
      H=1.DO/N1
      DO 1 K=2,N1
1     T(K)=T(K-1)+H
      T(N)=1.DO
      FM=M
      NNO=NN*N+N
      DO 4 I=1,NNO
      DO 4 K=1,2
4     MAT(K,I)=0.DO
      CALL FILL(N1,MAT)
      WRITE (6,201) (MAT(1,K),K=1,NNO)
      WRITE (6,201) (MAT(2,K),K=1,NNO)
201   FORMAT (1H1(8D15.5))
      CALL DCIBS(MAT,IMAT)
      DO 2 K=3,NN
      CALL DCIVT
      IF ((K/5)*5 .EQ. K) CALL REFINE(MAT,IMAT,TM,K,1.D-5,20)
2     CONTINUE
      CALL BRGEN(N,THETA,BRI,BRII)
      WRITE (6,102) BRI,BRII
      CALL CRMAKR(CRI,CRII,BRI,BRII,IMAT,NN,FACT)
      WRITE (6,102) CRI,CRII
102   FORMAT ('1      REAL'12X,'IMAGINARY'/2(D17.7))
      GO TO 3
200   CALL SYSTEM
      END
```

The geometry of the shape to be studied is specified in the FMAKER listing. The parameter, T, ranges from zero to one and the parameterization in terms of this T for ρ, z and their derivatives is done in the FMAKER routine.

FILL

(U) All integrals are of the form

$$T_{k,\ell} = \int_a^{a+h} ds \int_b^{b+h} dt \; F(s, t)\, G_m(s, t)$$

The integral may be done three different ways depending on its relation to the singularity of the Greens function at s = t. If the range of integration is not near the singularity then the subroutine REGUL is used. If the integration goes up to the singularity the subroutine OFDIAG is used. If the integration goes across the singularity the subroutine DIAG is used. There is a subroutine FST which calculates the functions F(s, t). A subroutine GGEN calculates $G_m(s, t)$. There are subroutines G1MST, G2MST, HMST which calculate $g_m^{(1)}(s, t)$, $g_m^{(2)}(s, t)$, and $h_m(s, t)$ respectively which are used to handle the singularity.

REGUL $\int_a^{a+h} \int_b^{b+h}$ $\quad a \neq b \quad a + h \neq b$

$$T_{k,\ell} - \frac{h^2}{4} \sum_{i=1}^{N} \sum_{j=1}^{N} A_i A_j F(s_i, t_j)\, G_m(s_i, t_j)$$

$$s_i = a + \frac{h}{2}(1 + \alpha_i)$$

FILL

```
      SUBROUTINE FILL(N1,MAT)
      IMPLICIT REAL*8(A-H,O-Z)
      INTEGER D
      DIMENSION MAT(2,100)
      K=(N1/3)*2
      DO 2 KC=1,N1
      D=N1-KC
      DO 2 I=1,KC
      J=D+I
      IF (D-1) 11,12,13
11    CALL DIAG(I,J,MAT)
      GO TO 2
12    CALL OFDIAG(I,J,MAT)
      GO TO 2
13    KD=K-D
      IF (KD) 4,4,5
4     KD=0
      GO TO 6
5     KD=2**KD
6     NPTG=10+KD
      CALL REGUL(I,J,NPTG,MAT)
2     WRITE (6,101) I,J
101   FORMAT (5X,2I5)
      RETURN
      END
```

$$t_j = b + \frac{h}{2}(1 + \alpha_j)$$

A_i are the Legendre weights from Stroud and Secrest, Gaussian Quadrature Formulas, Table 1. α_i are the Legendre nodes from Stroud and Secrest, Table I.

(U) It has been determined that this quadrature converges but it has not been tested under these circumstances to see exactly how rapid the convergence is.

GGEN

$$G_m(s, t) = (-1)^m \frac{\pi}{n} \sum_{j=1}^{n} \frac{e^{i\Gamma R_j}}{\Gamma R_j} \cos m \left[\frac{2j - 1}{2n} \pi\right] \Gamma R_j$$

$$= \sqrt{\left[z(t) - z(s)\right]^2 + \rho^2(t) + \rho^2(s) + 2\rho(t)\,\rho(s) \cdot \cos\left(\frac{2j - 1}{2n}\pi\right)}$$

$z(t)$ and $\rho(t)$ are calculated by the subroutine FMAKER. The imaginary part of this quadrature is not affected by the singularity of G_m and has been found to converge rapidly for all s and t with an n of 10 being adequate for 8^+ digits of accuracy. For the real part the degree of convergence is determined by the proximity of the singularity as s approaches t. When $s << t$ an $n = 10$ is adequate for 7 - 8 digit accuracy. For $s - t = h$ it was determined that $n = 30$ was adequate for 7 - 8 digit agreement.

(Discussion continued on page 360.)

REGUL

```
      SUBROUTINE REGUL(I,J,NPTG,MAT)
      IMPLICIT REAL*8(A-H,O-Z)
      REAL*8 MAT(100),GM(10)
      DIMENSION FI(5),FJ(5),AJ(10),X(10)
      COMMON FM,M,IM,CIR,XKO,A,ALPHA,T
      DIMENSION T(100),F(9),LI(4),LJ(4),KK(4,4)
      DIMENSION GLW(10),GLN(10)
      DATA X  /.932469514203152,.6612093864662645,.2386191860831969,-.93
     12469514203152,-.6612093864662645,-.2386191860831969/
      DATA AJ/.1713244923791703,.3607615730481386,.467913934572691,.1713
     1244923791703,.3607615730481386,.46791393457269l0/
      DATA NPT/6/
      H=(T(2)-T(1))*.5D0
      H2=H*H
      CALL CELL(I,J,KK,K,LI,LJ)
      DO 2 KJ=1,NPT
      TJ=T(J)+H*(1.+X(KJ))
      CALL FMAKER (TJ,FJ)
      DO 2 KI=1,NPT
      TI=T(I)+H*(1.+X(KI))
      CALL FMAKER(TI,FI)
      Q=FI(2)-FJ(2)
      Q=Q*Q+FI(1)*FI(1)+FJ(1)*FJ(1)
      R=2.*FI(1)*FJ(1)
      CALL GGEN(Q,R,NPTG,GM)
      MG=1
      DO 7 JQ=1,IM
      DO 7 IQ=1,2
      GM(MG)=GM(MG)*AJ(KI)*AJ(KJ)*H2
7     MG=MG+1
      DO 3 L=1,K
      CALL FST(TI,TJ,LI(L),LJ(L),FI,FJ,F)
      KK1=2*KK(1,L)-1
      KK2=2*KK(2,L)-1
      KK3=2*KK(3,L)-1
      KK4=2*KK(4,L)-1
      MG=2*M+1
      DO 3 IQ=1,2
      SUM=(GM(MG-2)+GM(MG+2))*.5D0
      DIF=(GM(MG-2)-GM(MG+2))*.5D0
      MAT(KK1)=MAT(KK1)+(F(1)+F(3))*GM(MG)+F(2)*SUM
      MAT(KK2)=MAT(KK2)+F(4)*DIF+F(5)*GM(MG)
      MAT(KK3)=MAT(KK3)+F(6)*SUM+F(7)*GM(MG)
      MAT(KK4)=MAT(KK4)+F(8)*DIF+F(9)*GM(MG)
      KK1=KK1+1
      KK2=KK2+1
      KK3=KK3+1
      KK4=KK4+1
3     MG=MG+1
2     CONTINUE
      RETURN
      ENTRY CHGRG(NN,GLW,GLN)
      NPT=NN
      DO 1 L=1,NN
      AJ(L)=GLW(L)
1     X(L)=GLN(L)
      RETURN
      END
```

GGEN

```
      SUBROUTINE GGEN(Q,B,NPT,GM)
      IMPLICIT REAL*8(A-H,O-Z)
      COMMON FM,M,IM,CIR,XKO,A,ALPHA,T
      DIMENSION GM(2,3),T(100)
      DIMENSION TM(15)
      DATA PI/3.141592653589793/
      TN=4*NPT
      DO 10 K=1,IM
      GM(1,K)=0.
10    GM(2,K)=0.
      DO 1 K=1,NPT
      X=2*K-1
      X=X/TN*PI
      X=DCOS(X)
      CALL CHEB (X,IM,TM)
      R=DSQRT(Q+B*TM(2))*CIR
      GR=DCOS(R)/R
      GI=DSIN(R)/R
      DO 2 KM=1,IM
      GM(1,KM)=GR*TM(KM)+GM(1,KM).
2     GM(2,KM)=GI*TM(KM)+GM(2,KM)
1     CONTINUE
      X=PI/NPT
      DO 3 K=1,IM
      GM(1,K)=GM(1,K)*X
      GM(2,K)=GM(2,K)*X
3     X=-X
      RETURN
      END
```

CHEB

```
      SUBROUTINE CHEB(X,IM,TM)
      IMPLICIT REAL*8(A-H,O-Z)
      DIMENSION TM(3)
      TM(1)=1.
      T=2.*X*X-1.
      TM(2)=T
      DO 1 M=3,IM
    1 TM(M)=2.*T*TM(M-1)-TM(M-2)
      RETURN
      END
```

FST

```
      SUBROUTINE FST(S,T,I,J,FS,FT,F)
      IMPLICIT REAL*8(A-H,O-Z)
      COMMON FM,M,N,CIR
      DIMENSION FS(5),FT(5),F(9)
      CALL KMAKER(S,I,FKI,FKID)
      CALL KMAKER(T,J,FKJ,FKJD)
      YI=(FKID+FS(5)+FKI)/CIR
      C=FS(1)*FKI*FT(1)*FKJ
      YJ=(FKJD+FT(5)+FKJ)/CIR
      F(1)=C*FS(4)*FT(4)
      F(2)=C*FS(3)*FT(3)
      F(3)=-FS(1)*YI*FT(1)*YJ
      F(4)=C*FS(3)
      F(5)=FKJ*FS(1)*YI/(FM*CIR)
      F(6)=C
      F(7)=-FKJ*FKI/(FM*FM*CIR*CIR)
      F(8)=C*FT(3)
      F(9)=FT(1)*YJ*FKI/(CIR*FM)
      RETURN
      END
```

KMAKER

```
      SUBROUTINE KMAKER(T,I,FK,FKD)
      IMPLICIT REAL*8(A-H,O-Z)
      COMMON FM,M,N,DIR,XKO,A,ALPHA,TT,Q,B
      DIMENSION TT(100)
      X=T-TT(I)
      D=1./(TT(2)-TT(1))
      FK=1.-DABS(X)*D
      IF (FK) 1,2,2
1     FKD=0.
      FK=0.
      RETURN
2     IF (X)3,4,5
3     FKD=D
      RETURN
5     FKD=-D
      RETURN
4     PRINT 101,T,X
101   FORMAT (22H ****K IS ON THE SPIKE2020.8)
      RETURN
      END
```

·FMAKER

```
      SUBROUTINE FMAKER(T,F)
      IMPLICIT REAL*8(A-H,O-Z)
      DIMENSION F(5)
      DATA PI/3.14159265358979 3/
      IF (T-1.E-5) 1,1,2
2     IF (.99999-T) 1,1,3
1     F(1)=0.
      F(2)=0.
      F(3)=1.
      F(4)=0.
      RETURN
3     X=PI*T
      C=DCOS(X)
      S=DSIN(X)
      F(1)=S/PI
      F(2)=(1.-C)/PI
      F(3)=C
      F(4)=S
      F(5)=PI*C/S
      RETURN
      END
```

DIAG $\int_a^{a+h} \int_a^{a+h}$

$$\mathrm{Re}\,(T_{k,\ell}) = \frac{h^2}{2}\left\{\sum_{i=1}^{N}\sum_{j=1}^{N} L_i A_j (1-\ell_i) g_m^{(1)}(s_{ij}, t_{ij})\left[F(s_{ij}, t_{ij}) + F(t_{ij}, s_{ij})\right] + \frac{1}{2}\sum_{i=1}^{N}\sum_{j=1}^{N} A_i A_j F(s_i, t_j) g_m^{(2)}(s_i, t_j)\right\}$$

$$\mathrm{Im}\,(T_{k,\ell}) = \frac{h^2}{4}\sum_{i=1}^{N}\sum_{j=1}^{N} A_i A_j F(s_i, t_j)\,\mathrm{Im}\,(G_m(s_i, t_j))$$

$$s_i = a + \frac{h}{2}(1+\alpha_i)$$

$$t_j = a + \frac{h}{2}(1+\alpha_j)$$

$$s_{ij} = h/\sqrt{2}\,(1-\ell_i)(1+\alpha_j) + a$$

$$t_{ij} = h/\sqrt{2}\left[(1-\ell_i)\alpha_j + 1 + \ell_i\right] + a$$

A_i and α_i defined as above and L_i are the log weights from Stroud and Secrest, Table 9. ℓ_i are the log nodes from Stroud and Secrest, Table 9.

(U) These quadratures have been demonstrated to converge but have not been tested in these circumstances to determine how great an N is needed to assure 7 digit accuracy.

G1MST

$$g_m^{(1)}(s,t) = \frac{2(-1)^m}{CR}\,\frac{1}{\sqrt{k}}\,h_m(s,t)$$

DIAG

```
      SUBROUTINE DIAG(I,J,MAT)
      IMPLICIT REAL*8(A-H,O-Z)
      REAL*8 MAT ,LAM
      COMMON EM,M,IM,CIR,XKO,A,ALPHA,T
      DIMENSION T(100),MAT(100)  ,FSI(5),FTJ(5),FTIJ(5),FSIJ(5),FS(9),FT
     1I(9),F(9),AJ(10),AL(10),ALF(10),LAM(10),G1M(10),G2M(10),GM(2,10)
      DIMENSION GLW(10),GLN(10),T9W(10),T9N(10)
      DIMENSION LI(4),LJ(4),KK(4,4)
      DATA NPTG/10/,NPT/6/
      DATA LAM/.21634005844116950-1,.1295833911549508,.3140204499147655,
     1.5386572173518021,.7569153373774029,.9226688513721202/
      DATA AL/.2387636625785476,.3082865732739468,.2453174265632104,.142
     100875656647 67,.5545462232488629D-1,.1016895869293228D-1/
      DATA ALF/.9324695142031 52,.6612093864662645,.2386191860831969,-.93
     1246951420315 2,-.6612093864662645,-.2386191860831969/
      DATA AJ/.1713244923791703,.3607615730481386,.467913934572691,.1713
     1244923791703,.3607615730481386,.4679139345726910/
      H=T(2)-T(1)
      H2=H*.5D0
      HS04=H2*H2
      HSO=H2*H
      HSO2=H2*1.4142135623730 95
      A=T(J)
      CALL CELL(I,J,KK,K,LI,LJ)
      DO 1 JK=1,NPT
      TJ=H2*(ALF(JK)+1.D0)+A
      CALL FMAKER(TJ,FTJ)
      DO 1 IK=1,NPT
      SI=H2*(ALF(IK)+1.D0)+A
      SIJ=H2*(1.D0-LAM(IK))*(1.D0+ALF(JK))+A
      TIJ=H2*((1.D0-LAM(IK))*ALF(JK)+1.D0+LAM(IK))+A
      AV=DABS(SI-TJ)/H
      CALL FMAKER(SI,FSI)
      CALL FMAKER(TIJ,FTIJ)
      CALL FMAKER(SIJ,FSIJ)
      CALL G1MST(FSIJ,FTIJ,G1M)
      CALL G2MST(AV,FSI,FTJ,G2M)
      Q=FSI(2)-FTJ(2)
      Q=Q*Q+FSI(1)*FSI(1)+FTJ(1)*FTJ(1)
      B=2.D0*FSI(1)*FTJ(1)
      CALL GGEN(Q,B,NPTG,GM)
      DO 2 L=1,IM
      G1M(L)=G1M(L)*AL(IK)*AJ(JK)*(1.D0-LAM(IK))*HSO
      GM(2,L)=GM(2,L)*AJ(IK)*AJ(JK)*HS04
2     G2M(L)=G2M(L)*AJ(IK)*AJ(JK)*HS04
      SUM1=(G1M(M)+G1M(M+2))*.5D0
      SUM2=(G2M(M)+G2M(M+2))*.5D0
      SUM=(GM(2,M)+GM(2,M+2))*.5D0
      DIF1=(G1M(M)-G1M(M+2))*.5D0
      DIF2=(G2M(M)-G2M(M+2))*.5D0
      DIF=(GM(2,M)-GM(2,M+2))*.5D0
      DO 3 L=1,K
      KK1=2*KK(1,L)
      KK2=2*KK(2,L)
      KK3=2*KK(3,L)
      KK4=2*KK(4,L)
      CALL FST(SI,TJ,LI(L),LJ(L),FSI,FTJ,F)
      CALL FST(SIJ,TIJ,LI(L),LJ(L),FSIJ,FTIJ,FS)
```

```
      CALL FST(TIJ,STJ,LI(L),LJ(L),FTIJ,FSIJ,FT)
      MAT(KK1-1)=MAT(KK1-1)          +(FS(1)+FT(1)+FS(3)+FT(3))*G1M(M+1)+(
     1FS(2)+FT(2))*SUM1+(F(1)+F(3))*G2M(M+1)+F(2)*SUM2
      MAT(KK1)=MAT(KK1)              +(F(1)+F(3))*GM(2,M+1)+F(2)*SUM
      MAT(KK2-1)=MAT(KK2-1)          +(FS(4)+FT(4))*DIF1+(FS(5)+FT(5))*G1M
     1(M+1)+F(4)*DIF2+F(5)*G2M(M+1)
      MAT(KK3-1)=MAT(KK3-1)          +(FS(6)+FT(6))*SUM1+(FS(7)+FT(7))*G1M
     1(M+1)+F(6)*SUM2+F(7)*G2M(M+1)
      MAT(KK2)=MAT(KK2)              +F(4)*DIF+F(5)*GM(2,M+1)
      MAT(KK3)=MAT(KK3)              +F(6)*SUM+F(7)*GM(2,M+1)
      IF (LI(L) .EQ. LJ(L)) GO TO 3
      MAT(KK4-1)=MAT(KK4-1)          +(FS(8)+FT(8))*DIF1+(FS(9)+FT(9))*G1M
     1(M+1)+F(8)*DIF2+F(9)*G2M(M+1)
      MAT(KK4)=MAT(KK4)              +F(8)*DIF+F(9)*GM(2,M+1)
3     CONTINUE
1     CONTINUE
      RETURN
      ENTRY CHGDG(NN,GLW,GLN,T9W,T9N)
      NPT=NN
      DO 7 L=1,NN
      AJ(L)=GLW(L)
      ALF(L)=GLN(L)
      AL(L)=T9W(L)
7     LAM(L)=T9N(L)
      RETURN
      END
```

C is half the circumference of the body

$$R = \sqrt{\left[z(s) - z(t)\right]^2 + \left[\rho(s) + \rho(t)\right]^2}$$

$$k = \frac{2\sqrt{\rho(s)\,\rho(t)}}{R}$$

G2MST

$$g_m^{(2)}(s, t) = \frac{2(-1)^m}{CR\sqrt{k}} \ln\left[\frac{|s - t|\,(1 + \sqrt{k})}{\sqrt{1 - k}\;h}\right] h_m(s, t)$$

note $\dfrac{|s - t|}{\sqrt{1 - k}} \xrightarrow[s \to t]{} 2\sqrt{2}\,\rho(t)$ C, R, k, ρ same as above $h_m(s, t)$ comes from the subroutine HMST.

HMST

$$h_m(s, t) = \int_{-1}^{1} dy \frac{\cos\left[CR\sqrt{1 - k^2x^2}\right]}{\sqrt{(1 + x)(1 + kx_i)}} T_{2m}(x)$$

$$= \sum_{i=1}^{N} A_i \frac{\cos\left[CR\sqrt{1 - k^2x_i^2}\right]}{\sqrt{(1 + x_i)(1 + kx_i)}} T_{2m}(x_i)$$

$$x_i = 1 - \frac{\sinh^2\left(\beta \dfrac{1 - \alpha_i}{2}\right)}{\sinh^2 \beta}$$

$$\beta = \ln \frac{1 + \sqrt{k}}{\sqrt{1 - k}}$$

$$\sinh \beta = \sqrt{\frac{k}{1 - k}} \quad .$$

G1MST

```
      SUBROUTINE G1MST(FS,FT,G1M)
      IMPLICIT REAL*8(A-H,O-Z)
      REAL*8 KST
      DIMENSION G1M(3),FS(5),FT(5)
      COMMON FM,M,IM,CIR
      R=FS(2)-FT(2)
      T1=FS(1)+FT(1)
      R=DSQRT(R*R+T1*T1)
      KST=2.DO*DSQRT(FS(1)*FT(1))/R
      CALL HMST(KST,R,G1M)
      T1=2.DO/(CIR*R*KST)
      DO 1 I=1,IM
      G1M(I)=G1M(I)*T1
      T1=-T1
      RETURN
      END
```

G2MST

```
      SUBROUTINE G2MST(AV,FS,FT,G2M)
      IMPLICIT REAL*8(A-H,O-Z)
      REAL*8 KST
      DIMENSION G2M(3),FS(5),FT(5)
      COMMON FM,M,IM,CIR,XKO,A,ALPHA,T
      DIMENSION T(100)
      R=FS(2)-FT(2)
      T1=FS(1)+FT(1)
      R=DSQRT(R*R+T1*T1)
      KST=2.D0*DSQRT(FS(1)*FT(1))/R
      IF (AV .GT. 1.D-8) GO TO 1
      T1=2.828427124746I9*FT(1)/(T(2)-T(1))
      GO TO 2
1     T1=AV/DSQRT(1.D0-KST)
2     SQK=DSQRT(KST)
      T1=T1*(1.D0+SQK)
      T1=2.D0/(CIR*R*SQK)*DLOG(T1)
      CALL HMST(KST,R,G2M)
      DO 3 I=1,IM
      G2M(I)=G2M(I)*T1
3     T1=-T1
      RETURN
      END
```

(U) A subroutine CHEB is provided to calculate the terms (T_{2m}) of the Tchebychev polynomial A_i, α_i, C, R, k all as above. It has been determined that this quadrature does converge but the size of the N needed to assure 7 digit accuracy has not been determined.

OFDIAG $\int_{a-h}^{a} \int_{a}^{a+h}$

$$\mathrm{Re}\,(T_{k,\ell}) = \frac{h^2}{2} \left\{ \sum_{i=1}^{N} \sum_{j=1}^{N} \ell_i L_i A_j F(s_{ij}, t_{ij}) g_m^{(1)}(s_{ij}, t_{ij}) + \right.$$

$$+ \frac{1}{2} \sum_{k=1}^{N} \sum_{k=1}^{N} A_k A_p (1 - \alpha_k) \ln \frac{2}{\alpha_k + 3} F(s_{kp}, t_{kp}) g_m^{(1)}(s_{kp}, t_{kp}) +$$

$$\left. + \frac{1}{2} \sum_{i=1}^{N} \sum_{j=1}^{N} A_i A_j F(s_i, t_j) g_m^{(2)}(s_i, t_j) \right\}$$

$$\mathrm{Im}\,(T_{k,\ell}) = \frac{h^2}{4} \sum_{i=1}^{N} \sum_{j=1}^{N} A_i A_j F(s_i, t_j)\, \mathrm{Im}\left[G_m(s_i, t_j)\right]$$

$$s_{ij} = \frac{h}{2} \ell_i (\alpha_j - 1) + a$$

$$t_{ij} = \frac{h}{2} \ell_i (1 + \alpha_j) + a$$

$$s_{kp} = \frac{h}{4} \left[\alpha_p (1 - \alpha_k) - \alpha_k - 3\right] + a$$

$$t_{kp} = \frac{h}{4} \left[\alpha_p (1 - \alpha_k) + \alpha_k + 3\right] + a$$

HMST

```
      SUBROUTINE HMST(KST,RST,HM)
      IMPLICIT REAL*8(A-H,O-Z)
      COMMON FM,M,IM,CIR
      REAL*8 KST
      DIMENSION GLW(20),GLN(20)
      DIMENSION SIG(2)
      DATA N/10/,SIG/1.D0,-1.D0/
      DIMENSION HM(3),TM(3),A(20),ALF(20)
      DATAALF/.9931285991850949,.9639719272779138,.9122344282513259,.839
     1116971822218 8,.7463319064601508,.6360536807265 5,.5108670019508271
     2,.3737060887154196,.2277858511416451,.7652652113349733D-1/
      DATA A /.1761400713915212D-1,.4060142980038694D-1,.6267204833410901
     16D-1,.8327674157670475D-1,.1019301198172404,.1181945319615184,.131
     2688638449176 ,.1420961093183821,.1491729864726037,.1527533871307258
     39/
      IF (KST .LT. 1.D0) GO TO 5
      DO 7 K=1,IM
7     HM(K)=1.D0
      RETURN
5     R=DLOG((1.D0+DSQRT(KST))/DSQRT(1.D0-KST) )
      DO 3 K=1,IM
3     HM(K)=0.D0
      DO 1 IS=1,2
      DO 1 I=1,N
      X=DSINH(R*(1.D0-SIG(IS)*ALF(I))*.5D0)
      X=1.D0-X*X/KST*(1.D0-KST)
6     CALL CHFR(X,IM,TM)
      R=A(I)*DCOS(CIR*RST*DSQRT(1.D0-RST*KST*X*X))/DSQRT((1.D0+X)*(1.D0+
     1KST*X))
      DO 2 K=1,IM
2     HM(K)=HM(K)+R*TM(K)
1     CONTINUE
      RETURN
      ENTRY CHGHM(NN,GLW,GLN)
      N=NN
      DO 4 L=1,N
      A(L)=GLW(L)
4     ALF(L)=GLN(L)
      RETURN
      END
```

OFDIAG

```
      SUBROUTINE OFDIAG(II,JJ,MAT)
      IMPLICIT REAL*8 (A-H,O-Z)
      COMMON FM,M,IM,CIR,SKZ,AA,ALPHA,TT(100)
      REAL*8 MAT(2,210),FSI(5),FTJ(5),FSIJ(5),FTIJ(5),FSKP(5),FTKP(5)
      REAL*8 FSTI(9),FSTIJ(9),FSTKP(9),G1IJ(8),G1KP(8),G2I(8)
      REAL*8 GMIJ(2,8),T(2,9),EQ(2,4),LRNI,LRWI,LGNI,LRNJ,LRWJ
      INTEGER KK(4,4),NN/6/,IP(4),JP(4),NPTG/20/
      REAL*8 LRN(20)/.9324695142031520,.661209386466264 5,.23961918608319
     &69,-.2386191860831969,-.6612093864662645,-.9324695142031520,14*0./
      REAL*8 LRW(20)/.1713244923791703,.3607615730481386,.46791393457269
     &10,.4679139345726910,.3607615730481386,.1713244923791703,14*0./
      REAL*8 LGN(20)/.0216340058441169 5,.0129583391154950 8,.031402044991
     &47655,.0538657217351802 1,.0756915337377402 9,.0922668851372120 2/
      REAL*8 LGW(20)/.2387636625785476,.3082865723729468,.24531742656321
     &04,.1420087565664767,.0554546223248862 9,.0101689586929322 8/
C
      A = TT(JJ)
      CALL CELL(II,JJ,KK,MM,IP,JP)
      H = TT(2)-TT(1)
      HOT = H*.5D0
      HOF = H*.25D0
      HS2 = H*HOT
      MM1 = M-1
      MP1 = M+1
C
      DO 100 I=1,NN
      LRNI = LRN(I)
      LRWI = LRW(I)
      LGNI = LGN(I)
      CI3 = 1.D0 - LRNI
      CI4 = LRNI + 3.D0
      CI1 = DLOG(2.D0/CI4)*CI3*LRW(I)
      CI2 = LGNI*LGW(I)
      SI = HOT*(LRNI+1.D0) + A
      CALL FMAKER(SI,FSI)
      DO 100 J=1,NN
      LRNJ = LRN(J)
      LRWJ = LRW(J)
      CJ1 = .5D0*LRWJ*LRWI
      TIJ = HOT*LGNI*(1.D0+LRNJ) + A
      SIJ = HOT*LGNI*(LRNJ-1.D0) + A
      TKP = HOF*(LRNJ*CI3 + CI4) + A
      SKP = HOF*(LRNJ*CI3 - CI4) + A
      TJ = HOT*(LRNJ-1.D0) + A
      CALL FMAKER(TIJ,FTIJ)
      CALL FMAKER(SIJ,FSIJ)
      CALL FMAKER(TKP,FTKP)
      CALL FMAKER(SKP,FSKP)
      CALL FMAKER(TJ,FTJ)
      Q = FSI(2) - FTJ(2)
      Q = Q*Q + FSI(1)**2 + FTJ(1)**2
      B = 2.D0*FSI(1)*FTJ(1)
      CALL GGEN(Q,B,NPTG,GMIJ)
      CALL G2MST(DABS(SI-TJ)/H,FSI,FTJ,G2I)
      CALL G1MST(FSIJ,FTIJ,G1IJ)
      CALL G1MST(FSKP,FTKP,G1KP)
C
      DO 90 NE=1,4
```

```
      CALL FST(SI,TJ,IP(NE),JP(NE),FSI,FTJ,FSTI)
      CALL FST(SIJ,TIJ,IP(NE),JP(NE),FSIJ,FTIJ,FSTIJ)
      CALL FST(SKP,TKP,IP(NE),JP(NE),FSKP,FTKP,FSTKP)
      DO 75 MM=1,9,2
      T(1,MM) = LRWJ*(CI2*FSTIJ(MM)*G1IJ(M) + CI1*FSTKP(MM)*G1KP(M))
     & + CJ1*FSTI(MM)*G2I(M)
75    T(2,MM) = CJ1*FSTI(MM)*GMIJ(2,M)
      SIGN = 1.D0
      DO 76 MM=2,8,2
      T(1,MM) = .5D0*(LRWJ*(CI2*FSTIJ(MM)*(G1IJ(MM1)+SIGN*G1IJ(MP1))
     & + CI1*FSTKP(MM)*(G1KP(MM1)+SIGN*G1KP(MP1))) + CJ1*FSTI(MM) *
     & (G2I(MM1)+SIGN*G2I(MP1)))
      T(2,MM) = CJ1*FSTI(MM)*.5D0*(GMIJ(2,MM1)+SIGN*GMIJ(2,MP1))
76    SIGN = -SIGN
C
      DO 85 IR=1,2
      EQ(IR,1) = T(IR,1) + T(IR,2) - T(IR,3)
      EQ(IR,2) = T(IR,4) + T(IR,4)
      EQ(IR,3) = T(IR,6) - T(IR,7)
      EQ(IR,4) = T(IR,8) + T(IR,9)
      IF (NE.NE.4) GO TO 79
      EQ(IR,1) = EQ(IR,1) + EQ(IR,1)
      EQ(IR,3) = EQ(IR,3) + EQ(IR,3)
C
79    DO 80 MM=1,4
      KM = KK(MM,NE)
80    MAT(IR,KM) = MAT(IR,KM) + EQ(IR,MM)*HS2
85    CONTINUE
90    CONTINUE
100   CONTINUE
      RETURN
C
C     USE ENTRY 'SETOFQ' TO CHANGE QUADRATURE CONSTANTS FOR REAL PART
      ENTRY SETOFQ(J,NLRN,NLRW,NLGN,NLGW)
      REAL*8 NLRN(20),NLRW(20),NLGN(20),NLGW(20)
      DO 300 I=1,J
      LRN(I) = NLRN(I)
      LRW(I) = NLRW(I)
      LGN(I) = NLGN(I)
300   LGW(I) = NLGW(I)
      NN = J
      RETURN
      END
```

A_i, L_i, α_i, ℓ_i all as above. It has been demonstrated that these quadratures do converge but the value of N needed to assure 7 digit accuracy in this situation has not been determined.

CELL

(U) The subroutine CELL performs the bookkeeping function of telling the integral calculating subroutines where in the matrix to store the results.

Enlargement (Bordering) Method

(U) The n x n matrix M, which is to be inverted, is partitioned in the form

$$M = \begin{bmatrix} A & B^T \\ C & D \end{bmatrix}$$

where A is of order m ($1 \leq m < n$) B and C have n - m rows and m columns. D is order n - m.

(U) If A^{-1} is known then the following identity gives M^{-1}

$$M^{-1} = \begin{bmatrix} A & B^T \\ B & D \end{bmatrix}^{-1} = \begin{bmatrix} A^{-1} + A^{-1}B^T F^{-1} CA^{-1} & -A^{-1}B^T F^{-1} \\ -F^{-1}CA^{-1} & F^{-1} \end{bmatrix}$$

where

$$F = D - CA^{-1} B^T$$

this process may be written

1) $E^T = A^{-1}B^T$

2) $F = D - CE^T$

3) compute F^{-1}

CELL

```
      SUBROUTINE CELL(I,J,KK,K,LI,LJ)
      DIMENSION KK(4,4),LI(4),LJ(4)
      K=4
      IF (I .EQ. J) K=3
      LI(1)=I
      LJ(1)=J
      LI(3)=I+1
      LJ(3)=J+1
      LI(2)=I
      LJ(2)=J+1
      LI(4)=I+1
      LJ(4)=J
      DO 1 L=1,K
      M=LI(L)
      N=LJ(L)
      M=2*M-1
      N=2*N-1
      IS=0
      DO 2 IK=1,N
    2 IS=IS+IK
      IM=IS-N+M
      KK(1,L)=IM
      KK(2,L)=IM+N
      KK(3,L)=IM+N+1
      KK(4,L)=IM+1
      IF (M .EQ. N) KK(4,L)=KK(2,L)
    1 CONTINUE
      RETURN
      END
```

4) $G^T = E^T F^{-1}$

5) $H = F^{-1} CA^{-1}$

6) $K = A^{-1} + E^T H$

then

$$M^{-1} = \begin{bmatrix} K & -G \\ -H & F^{-1} \end{bmatrix}$$

In particular if $m = n - 1$ so that B and C are vectors and D is a single element, then F is also a single element and $F^{-1} = 1/F$. Thus if A and A^{-1} are known it is easy to add one more row and column to the inverse. The process can be repeated to add as many rows/columns as needed.

Refinement Method

(U) Given a matrix M and some approximation to the inverse $(M^{-1})_n$. Then a better inverse $(M^{-1})_{n+1}$ may be found from the following

$$R = (M^{-1})_n M - I$$

$$(M^{-1})_{n+1} = (M^{-1})_n - R(M^{-1})_n$$

this can be repeated until the improvement at each step is satisfactorily small, as when

$$\left| \frac{RE\left[R(M^{-1})_n\right]_{ij}}{RE\left[(M^{-1})_n\right]_{ij}} \right| \leq TOL \quad \text{all } j, i$$

```
                DCIBS          04-17-68        19:11.39        PAGE 0001

      SUBROUTINE DCIBS(DCMTX,DCINV)
      IMPLICIT COMPLEX*16 (A-H,O-Z)
      DIMENSION DCMTX(3),DCINV(3)
C
C     ROUTINE TO INVERT A MATRIX BY ENLARGEMENT (BORDERING)
C     ENTRY 'DCIBS' ESTABLISHES LOC OF MATRIX ('DCMTX') AND ITS INVERSE
C       ('DCINV) AND ALSO INVERTS THE 2 X 2 SUB-MATRIX.
C     BOTH MATRICIES ARE SYMMETRIC WITH THE LOWER TRIANG. AND DIAG.
C       STORED PACKED BY ROWS.
C     EACH CALL ON DCINT ADDS ONE NEW ROW (& COL) TO INVERSE.
C     THE CONTENTS OF THE ORIGINAL MATRIX ARE NOT CHANGED.
C
      DT1 = DCMTX(1)*DCMTX(3) - DCMTX(2)*DCMTX(2)
      DCINV(1) = DCMTX(3)/DT1
      DCINV(3) = DCMTX(1)/DT1
      DCINV(2) = -DCMTX(2)/DT1
      N = 2
      RETURN
C
      ENTRY DCINT
      NC = (N*(N+1)/2)+1
      CALL VMPRCD(DCMTX(NC),DCINV,DCINV(NC),N)
      NCN = NC + N - 1
      DT1 = DCMTX(NCN+1)
      DO 100 I=NC,NCN
  100 DT1 = DT1 - DCMTX(I)*DCINV(I)
      DT1 = 1.DO/DT1
      DCINV(NCN+1) = DT1
      IJ = 1
      DO 200 J=NC,NCN
      DO 200 I=NC,J
      DCINV(IJ) = DCINV(IJ) + DCINV(I)*DT1*DCINV(J)
  200 IJ = IJ + 1
      DT1 = -DT1
      DO 300 I=NC,NCN
      DCINV(I) = DCINV(I)*DT1
  300 CONTINUE
      N = N + 1
      RETURN
      END
```

MMPRCD 04-17-68 19:11.44 PAGE 0001

```
      SUBROUTINE MMPRCD(M1,M2,MP,N,T)
      IMPLICIT COMPLEX*16(A-H,M,O-Z)
      DIMENSION M1(1),M2(1),MP(1),T(1)
C
C     'MMPRCD' COMPUTES THE PRODUCT OF TWO SYMMETRIC MATRICIES.
C     MP = M1*M2
C     M1 AND M2 ARE N X N SYMMETRIC STORED WITH LOWER TRIANG. AND DIAG.
C       PACKED BY ROWS.
C     MP IS N X N REGULAR MTX STORED BY ROWS
C     T IS SCRATCH VECTOR OF AT LEAST N ELEMENTS
C
      NIJ = 1
      IJS = 1
      DO 100 I=1,N
      IJ = IJS
      IJI = 1
      ISS = 0
      DO 75 J=1,N
      T(J) = M1(IJ)
      IF (J.NE.I) GO TO 20
      IJI = J
      ISS = 1
20    IJ = IJ + IJI
75    IJI = IJI+ISS
      CALL VMPRCD(T,M2,MP(NIJ),N)
      IJS = IJS + I
100   NIJ = NIJ + N
      RETURN
      END
```

```
PMPROC          04-17-68        19:11.48        PAGE 0001

      SUBROUTINE PMPROD(VEC,MTX,PROD,N,N1)
      IMPLICIT COMPLEX*16 (A-H,M,O-Z)
      DIMENSION VEC(1),MTX(1),PROD(1)
C
C     THIS ROUTINE COMPUTES THE PRODUCT OF A VECTOR AND A SYMM. MATRIX
C     PROD = VEC*MTX
C     VEC AND PROD ARE VECTORS OF LENGTH N
C     MTX IS N X N SYMM. MTX STORED PACKED BY ROWS
C     FOR ENTRY VMPROD, ALL N ELEMENTS OF PROD ARE COMPUTED
C     FOR ENTRY PMPROD ONLY FIRST N1 ELEMENTS ARE COMPUTED
C
      NP = N1
      IF (N1.GT.N) NP=N
      GO TO 3
C
      ENTRY VMPROD(VEC,MTX,PROD,N)
      NP = N
3     IJS = 1
      DO 100 I=1,NP
      S = 0.D0
      IJ = IJS
      IJI = 1
      ISS = 0
      DO 75 J=1,N
      S = S + VEC(J)*MTX(IJ)
      IF (J.NE.I) GO TO 20
      IJI = J
      ISS = 1
20    IJ = IJ + IJI
75    IJI = IJI + ISS
      PROD(I) = S
100   IJS = IJS + I
      RETURN
      END
```

REFINE 04-17-68 19:11.52 PAGE 0001

```
      SUBROUTINE REFINE(X,V,T,N,TOL,MXI)
      IMPLICIT REAL*8 (A-H,O-Z)
      DIMENSION X(1),V(1),T(1)
C
C     REFINE THE N X N MTX 'V' TO BE THE INVERSE OF THE MATRIX 'X' UNTIL
C       THE CORRECTION TO EACH ELEMENT IS LESS THAN 'TOL'.
C     'T' IS SCRATCH MTX OF AT LEAST N X (N+1) LOCATIONS
C     'MAXI' IS THE MAXIMUM NUMBER OF ITERATIONS ALLOWED
C     'X' AND 'V' ARE SYMMETRIC MATRICIES WITH LOWER TRIANG. AND DIAG
C       STORED BY ROWS, PACKED.
C     ALL ELEMENTS ARE DBL PREC CMPX EXCEPT: 'TOL' - DBL PREC REAL AND
C       'N' & 'MXI' - INTEGER
C
      IC = 1
      IS = 2*N*N
      IT = N*(N+1)
      NN = N + N
      IN = NN + 2
10    CALL MMPRDD(V,X,T,N,T(IS+1))
      DO 1CC I=1,IS,IN
1CC   T(I) = T(I) - 1.DO
      II = 1
      DO 2CC I=1,N
      CALL MMPRDD(T((I-1)*NN+1),V,T(II),N,I)
2CC   II = II + I + I
      K = C
      DO 3CC I=1,IT
      IF (V(I) .EQ. 0.DO) GO TO 170
      IF (DABS(T(I)/V(I)) .GT. TOL) K = K + 1
170   V(I) = V(I) - T(I)
3CC   CONTINUE
      IF (K.EQ.C) RETURN
      IC = IC + 1
      IF (IC .GT. MXI) RETURN 1
      GO TO 10
      END
```

$$\left| \frac{IM\left[R(M^{-1})_n\right]_{i,j}}{IM\left[(M^{-1})_n\right]_{i,j}} \right| \leq TOL \quad \text{all } i,j$$

Where TOL is the maximum allowable relative error in any element.

BRGEN

(U) Each integral is of the form

$$b_r = \int_0^1 dt\ F(t)\ K_i(t)\ \rho(t)\ J_m\left[\rho(t) \sin\theta\right]$$

F(t) is calculated for each integral, $K_i(t)$ is the trial function, θ is the angle of incidence. The subroutine BSLJ computes $J_n(x)$.

(U) The integration is done numerically using a midpoint rule. The interval is halved until 5 digits of agreement between successive tries is achieved.

BSLJ

$$J_m(x) = (x/2)^m \sum_{k=0}^{N} \frac{(-x^2/4)^k}{k!\,(m+k)!}$$

This series is summed until the individual term in absolute value is less than 10^{-12}.

CRMAKR

(U) This subroutine simply performs the matrix multiplication of b_r and T^{-1} involved in obtaining the final output.

BRGEN

```
      SUBROUTINE BRGEN(N,TH,BRI,BRII)
      IMPLICIT REAL*8 (A-H,O-Z)
      COMMON FM,M,IC,CIR,XKO,A,ALPH,TT
      DATA S1/.1D-2/,S2/.2D-4/,TOL/1.D-5/
      DIMENSION TT(100),BRI(2,10),BRII(2,10),F(5),D(10,2),DD(10,2),
     & FKI(2),FV(6)
      STH = DSIN(TH)
      CTH = DCOS(TH)
      NM1 = N-1
      NN = N+N
      DO 100 I=1,NN
      DO 100 J=1,2
      BRI(J,I) = 0.
100   BRII(J,I) = 0.
      DO 200 I=1,NM1
      DT = TT(I+1)-TT(I)
      S = S1
198   NI = DT/S + .5
      FNI = NI
      H = DT/FNI
      HT = H/2.
      DO 199 J=1,2
      DO 199 JJ=1,10
199   DD(JJ,J) = 0.
      DO 201 K=1,NI
      FK = K
      DDT = FK*H - HT
      T = TT(I) + DDT
      CALL FMAKER(T,F)
      FKI(2) = H*DDT*F(1)/DT
      FKI(1) = H*F(1)-FKI(2)
      TP = F(2)*CIR*CTH
      FV(1) = .5*DCOS(TP)
      FV(2) = .5*DSIN(TP)
      FV(3) = FV(1)*F(3)
      FV(4) = FV(2)*F(3)
      FV(5) = (FV(1)+FV(1))*F(4)
      FV(6) = (FV(2)+FV(2))*F(4)
      TP = F(1)*STH
      BJ1 = BSLJ(TP,M-1)
      BJ2 = BSLJ(TP,M)
      BJ3 = BSLJ(TP,M+1)
      DO 202 J=1,2
      DO 203 JJ=1,4
      TP = FV(JJ)*FKI(J)
      DD(JJ,J) = DD(JJ,J) + TP*BJ1
203   DD(JJ+6,J) = DD(JJ+6,J) + TP*BJ3
      DD(5,J) = DD(5,J) + FKI(J)*BJ2*FV(5)
202   DD(6,J) = DD(6,J) + FKI(J)*BJ2*FV(6)
201   CONTINUE
      IF (S1-S) 75,75,76
75    DO 204 J=1,2
      DO 204 JJ = 1,10
204   D(JJ,J) = DD(JJ,J)
205   S = S*.5
      IF (S2-S) 198,198,211
76    K = 0
      DO 210 J=1,2
```

```
      BRGEN
      DO 210 JJ=1,10
      IF (DABS((DD(JJ,J)-D(JJ,J))/DD(JJ,J))-TOL) 210,210,77
   77 K = K + 1
  210 D(JJ,J) = DD(JJ,J)
      IF (K) 205,211,205
  211 DO 225 J=1,2
      II = 2*(I+J-1)
      III = II-1
      BRI(1,III) = BRI(1,III) + D(3,J)+D(9,J)
      BRI(2,III) = BRI(2,III) + D(4,J)+D(10,J)
      BRI(1,II) = BRI(1,II) + D(1,J)-D(7,J)
      BRI(2,II) = BRI(2,II) + D(2,J)-D(8,J)
      BRII(1,III) = BRII(1,III) - STH*D(6,J) - CTH*(D(3,J)-D(9,J))
      BRII(2,III) = BRII(2,III) + STH*D(5,J)-CTH*(D(4,J)-D(10,J))
      BRII(1,II) = BRII(1,II) + CTH*(D(1,J)+D(7,J))
  225 BRII(2,II) = BRII(2,II) + CTH*(D(2,J)+D(8,J))
      II = I+I-1
      III = II+3
  200 CONTINUE
      RETURN
      END
```

BSLJ

```
      FUNCTION BSLJ(X,M)
      IMPLICIT REAL*8 (A-H,O-Z)
      DATA TOL /1.D-12/
      IF (X) 53,50,53
50    IF (M) 52,51,52
51    BSLJ = 1.
      RETURN
52    BSLJ = 0.
      RETURN
53    FM = M
      XT = X/2.
      FAC = XT**M
      C = 1.
      IF (M) 75,75,74
74    DO 100 I=1,M
      FI = I
100   C = C/FI
75    XT = -XT*XT
      BSLJ = C
      DO 101 I=1,30
      FI = I
      C = C*XT/(FI*(FI+FM))
      BSLJ = BSLJ + C
      IF (DABS(C)-TOL) 80,80,101
101   CONTINUE
80    BSLJ = FAC*BSLJ
      RETURN
      END
```

CRMAKER

```
      SUBROUTINE CRMAKR (CRI,CRII,BRI,BRII,TI,NN,FACTOR)
      IMPLICIT REAL*8(A-H,O-Z)
      DIMENSION CRI(2,100),CRII(2,100),BRI(2,100),BRII(2,100),TI(2,5050)
      S=1.
      IDIAG = 0
      ILEGTH = 0
160   KLEGTH = 0
      ILEGTH = ILEGTH + 1
      IF (ILEGTH - NN)  170,170,240
170   I = IDIAG + 1
      IDIAG = IDIAG + ILEGTH
      J = 0
      SUMIA = 0.DO
      SUMRA = 0.DO
      SUMRB = 0.DO
      SUMIB = 0.DO
180   J = J + 1
      KLEGTH = KLEGTH + 1
      SUMRA = TI(1,I)*BRI(1,J) - TI(2,I)*BRI(2,J) + SUMRA
      SUMIA = TI(1,I)*BRI(2,J) + TI(2,I)*BRI(1,J) + SUMIA
      SUMRB = TI(1,I)*BRII(1,J) - TI(2,I)*BRII(2,J) + SUMRB
      SUMIB = TI(1,I)*BRII(2,J) + TI(2,I)*BRII(1,J) + SUMIB
      S=-S
      IF (I-IDIAG)  200,210,210
200   I = I + 1
      GO TO 220
210   I = I + KLEGTH
220   IF (J - NN)  180,230,230
230   CRI(1,ILEGTH) = -FACTOR*SUMIA
      CRI(2,ILEGTH) = FACTOR*SUMRA
      CRII(1,ILEGTH)= -FACTOR*SUMIB
      CRII(2,ILEGTH) = FACTOR*SUMRB
      S=-S
      GO TO 160
240   RETURN
      END
```

IX

ACKNOWLEDGEMENTS

(U) Experiments, analysis, interpretation and theorization are necessarily interrelated in a program of this complexity. It is possible therefore to indicate the gross catagories of specialization only for the individuals who took part in these studies.

(U) The program was under the supervision of Prof. Ralph E. Hiatt, Head of the Radiation Laboratory. The Principal Investigator for the SURF radar cross section investigation was Dr. Raymond F. Goodrich; for the SURF plasma re-entry environment investigation, Dr. Vaughan H. Weston; for the short pulse studies, Dr. Ralph E. Kleinman and Prof. Herschel Weil. The Program Manager for all of these studies was Burton A. Harrison.

(U) Dr. Thomas B.A. Senior was responsible for the analysis and interpretation of the surface field data and for the synthesis of the SURF radar cross section formulas. He was assisted in this work by Dr. Ralph Kleinman, Leon P. Zukowski and Bruce C. Vrieland.

(U) Eugene F. Knott was responsible for the experimental programs in surface field measurements and radar backscatter measurements. He was assisted by David W. Brandenburg, Larry L. Brown and Ernest C. Bublitz.

(U) The re-entry plasma experimental program was carried out by Thomas M. Smith who was assisted by Ernest C. Bublitz and Chester Grabowski. In the theoretical studies under the re-entry plasma program, Dr. Weston was assisted by John J. Bowman, David M. Levine, and Prof. Chai Yeh.

(U) In the theoretical SURF studies, Dr. Goodrich was assisted by Dr. Chi-Fu Den and by Dr. Shun-Jen Houng. Working with him on the computer program for the radar section of the rotationally symmetric metallic body were Dr. Robert F. Lyjack and Assistant Professor Frank Stenger, who aided in the analytical work, and Thomas L. Boynton and Peter H. Wilcox who were

responsible for the programming. Harold E. Hunter carried out supporting computational studies and the hand check of the computer program.

(U) Dr. Kleinman and Professor Weil were aided in the short pulse study by Nicholas G. Alexopoulos, Jose R. Moron-Borjas, and Jon A. Soper.

(U) The above named investigators were assisted by technicians and students. The preparation of memoranda, reports and manuscripts was carried out under the supervision of Mrs. Claire F. White.

(U) We would like to express our appreciation for the assistance of Dr. Paul J. Schweitzer of the Institute of Defense Analyses in consulting on the program for the cross section of the rotationally symmetric metallic body; for the cone-sphere backscatter data made available to us by James H. Pannell of MIT-Lincoln Laboratory; and the constructive suggestions of Dr. Sidney L. Borison and Dr. Soonsung Hong of the same organization. We wish to acknowledge the expediting assistance and practical suggestions of Capt. James Wheatley, Contract Monitor for the Space and Missile Systems Organization and the technical critiques of H.J. Katzman and his associates, Dr. William Botch, Dr. Eugene C. Brouillette, Dr. Fred F. Meyer, and Edward N. Skomal of the Aerospace Corporation. An economy to the government and a savings in time to the project was effected by Kurt E. Golden of the Aerospace Corporation/El Segundo who loaned the Radiation Laboratory a "coated cone" model for use in the plasma experiments.

X

SUPPORTING TECHNICAL STUDIES

(U) During the third phase of SURF, four technical reports were written. They are as follows:

1. "Some Facets of Surface Wave Behavior" by T.B.A. Senior, BSD-TR-67-142 University of Michigan, Radiation Laboratory Report No. 8525-1-T UNCLASSIFIED.

2. "Physical Optics Applied to Cone-sphere-like Objects," by T.B.A. Senior BSD-TR-67-143 University of Michigan Radiation Laboratory Report No. 8525-2-T UNCLASSIFIED.

3. "Diffraction by the Concave Surface of the Paraboloid of Revolution," by S. Stone, BSD-TR-67-143 AD 818382 University of Michigan Radiation Laboratory Report No. 8525-3-T. UNCLASSIFIED

4. "Surface Currents Induced by a Plane Wave on a Parabolic Cylinder with a Focal Length Comparable to the Incident Wavelength" by S-J Houng and R.F. Goodrich, University of Michigan Radiation Laboratory Report No. 8525-4-T. UNCLASSIFIED

The first of these reports deals with the types of surface waves excited by incident microwave radiation on metallic surfaces. It discusses plane waves, traveling and Goubau waves and creeping waves. The second report discusses techniques for estimating the scattering behavior of an object for which the 'effective' dimensions are large compared with the wavelength. The third and fourth reports deal with the surface currents induced on curved surfaces.

REFERENCES

Blore, W.E. (1964) "The Radar Cross Section of Ogives Double-backed Cones, Double-rounded Cones, and Cone-spheres," IRE Trans. AP-12, pp. 582-590.

Brekhovskikh, L. M. (1960) Waves in Layered Media, Academic Press, New York, Chapter IV.

Castellanos, D. (1966), "Notes on Electromagnetic Scattering from Rotationally Symmetric Bodies with an Impedance Boundary Condition," The University of Michigan Radiation Laboratory Report No. 7741-1-T.

Clemmow, P.C. (1966) The Plane Wave Spectrum Representation of Electromagnetic Fields, Pergamon Press, New York.

Collin, R.E. (1960) Field Theory of Guided Waves, McGraw-Hill Book Co., Inc. New York Chapter 11.

deRidder, C.M., and D.P. White (1966) "Plasma Effects on Body Cross Sections of Slender Vehicles," Project Report PPP-60, MIT Lincoln Laboratory.

Erdelyi, A., M. Kennedy and J.L. McGregor, (1954) "Parabolic Cylinder Function of Large Order," J. Rat. Mech. and Anal., 3, pp. 459-485.

Fock, V.A. (1965) Diffraction by Convex Surfaces, Pergamon Press, New York.

Golden, K.E. and T.M. Smith (1964) "Simulation of a Thin Plasma Sheath by a Plane of Wires," IEEE Trans. on Nuclear Science, NS-11, pp. 225-230.

Goodrich, R.F., E. Ar, B.A. Harrison, S. Hong, T.B.A. Senior and S.E. Stone, (1965) "Radar Cross Section of the Metallic Cone-sphere: Final Report (U) BSD-TR-66-112, The University of Michigan Radiation Laboratory Report No. 7030-5-T SECRET.

Goodrich, R.F., B.A. Harrison, E.F. Knott, T.B.A. Senior, and V.H. Weston, (1966) "Investigation of Re-entry Vehicle Surface Fields," (U) Quarterly Report No. 7741-3-Q, BSD-TR-66-355, The University of of Michigan Radiation Laboratory. SECRET

References (Cont'd)

Goodrich, R.F., B.A. Harrison, E.F. Knott, T.B.A. Senior, V.H. Weston and L.P. Zukowski (1967) "Investigation of Re-entry Vehicle Surface Fields," The University of Michigan Radiation Laboratory Report No. 7741-4-T SECRET

Goodrich, R.F., B.A. Harrison, E.F. Knott, T.B.A. Senior, T.M. Smith H. Weil and V.H. Weston (1967b) "Investigation of Re-entry Vehicle Surface Fields," The University of Michigan Radiation Laboratory Report No. 8525-3-Q, SECRET.

Goodrich, R.F., B.A. Harrison, R.E. Kleinman, E.F. Knott, and V.H. Weston (1967c) "Investigation of Re-entry Vehicle Surface Fields," (U) The University of Michigan Radiation Laboratory Report No. 8525-2-Q, BSD-TR-67-232, SECRET.

Goodrich, R.F. and F. Stenger, (1967), "Movable Singularities and Quadrature," To be published.

Hong, S. (1967) "Asymptotic Theory of Diffraction by Smooth Convex Surfaces of Non-constant Curvature," The University of Michigan Radiation Laboratory Report No. 7741-2-T.

Hong, S. and V.H. Weston (1965) "A Modified Fock Function for the Distribution of Currents in the Penumbra Region with Discontinuity in Curvature," Radio Science, 1., pp. 1045-1053.

Ivanov, V.I. (1960) "Shortwave Asymptotic Diffraction Field in the Shadow of an Ideal Parabolic Cylinder," Radiotekhnika i elektronika 5, No. 3, pp. 393-402.

Ivanov, V.I. (1963) "Diffraction of Short Plane Waves on a Parabolic Cylinder," USSR Computational Mathematical Physics, 2, p. 225.

Johnson, C.C. (1965) Field and Wave Electrodynamics, McGraw-Hill Book Co. Inc., New York, pp. 325-333.

Keller, J.B. (1956) "Diffraction by a Convex Cylinder," IRE Trans, AP-4, pp. 312-321.

References (Cont'd)

Kennaugh E.M., and D.L. Moffatt (1965) "Transient and Impulse Response Approximations," Proc. IEEE, 53, No. 8, pp 893-901.

Kennaugh, E.M., D.L. Moffatt, R.C. Schafer, (1967) "Research into the Scattering of Electromagnetic Energy from Highly Conducting Bodies," Final report on AF 19(628)-4002, prepared for AFCRL, The Ohio State University, ElectroScience Laboratory, Bedford, Massachusetts.

Keys, J.E., and R.I. Primich, (1959) "The Radar Cross Section of Right Circular Metal Cones-I," Defense Research Telecommunications Establishment, Ottowa, Canada Report No. 1010.

Kleinman, R.E. and T.B.A. Senior (1963), "Studies in Radar Cross Sections - XLVIII Diffraction and Scattering by Regular Bodies - II: The Cone," The University of Michigan Radiation Laboratory, Report No. 3648-2-T,

Knott, E.F. (1965) "Design and Operation of a Surface Field Measurement Facility," The University of Michigan Radiation Laboratory Report No. 7030-7-T.

Levy, B.R. and J.B. Keller, (1960) "Diffraction by a Spheroid," Canadian Journal of Physics, 38, pp. 128-144.

Logan, N.A. (1959) "General Research in Diffraction Theory, Vol. II," Lockheed Missiles and Space Division Technical Report No. 288088.

Malinzhinet, G.D. (1959), "Excitation, Reflection and Emmission of Surface Waves from a Wedge with Given Face Impedances," Soviet Physics-Doklady 3, pp. 752-755.

Mitzner, K.M. (1966) "An Integral Equation Approach to Scattering from a Body of Finite Conductivity," NOR 66-344.

Poeverlein, H. (1958), "Low-frequency Reflection in the Ionosphere- I," J. of Atmospheric and Terrestrial Physics, Vol. 12, pp. 126-139.

References (Cont'd)

Rheinstein, J. (1966) "Backscatter from Spheres: A Short Pulse View," Technical Report 414-MIT, Lincoln Laboratory.

Rice, S.O. (1954) "Diffraction of a Plane Wave by a Parabolic Cylinder," Bell Sys. Tech. Jour., pp. 417-504, 33.

Ross, R.A. (1965) "Radar Cross Section of Rectangular Flat Plates as a Function of Aspect Angle, IEEE Trans, AP-14, No. 3 pp 329-335.

Schweitzer, P. (1965) "Electromagnetic Scattering from Rotationally Symmetric Perfect Conductors," MIT-Lincoln Laboratory, PA-88.

Senior, T.B.A. (1965) "Analytic Numerical Studies of the Backscattering Behavior of Spheres," AF 04(694)-683, The University of Michigan Radiation Laboratory Report No. 7030-1-T

Senior, T.B.A. (1966) "An Approach to the Determination of the Surface Fields on a Coated Cone," The University of Michigan Radiation Laboratory Memorandum 7741-522-M.

Senior, T.B.A. (1967) "Physical Optics Applied to Cone-sphere-like Objects," The University of Michigan Radiation Laboratory Report No. 8525-2-T. BSD-TR-67-182 UNCLASSIFIED.

Senior, T.B.A. and L.P. Zukowski (1965), "The Interpretation of Some Surface Field Data," The University of Michigan Radiation Laboratory Report No. 7030-8-T, AD 374993, CONFIDENTIAL, 107 pp.

Siegel, K.M. (1959), "Far Field Scattering From Bodies of Revolution," Appl. Sci. Res. 7, pp. 293-328.

Siegel, K.M, R.F. Goodrich and V.H. Weston (1959) "Comments on Far Field Scattering from Bodies of Revolution," Appl Sci. Res. 8, pp. 8 - 12.

Smith, T.M. and K.E. Golden, (1963) "Surface Impedance of a Thin Plasma Sheet," TDR-269 (4280-10)-1, Aerospace Corporation, October

References (Cont'd)

Smith, T.M. and K.E. Golden (1965a) "Radiation Patterns of a Slot Covered by a Simulated Plasma Sheet," IEEE Trans., AP-13, No. 2 pp. 285-288, March

Smith, T.M. and K.E. Golden (1965b), "Radiation Patterns from a Slotted Cylinder Surrounded by a Plasma Sheath," IEEE Trans., AP-13 pp. 775-780, September

Soules, G.W. and K.H. Mitzner (1966), "Pulse in Linear Acoustics," Report ARD 66-60 R, Nortronics (Northrop), Part II by Mitzner alone contains the material referred to. November.

Stratton, J.A. (1941) Electromagnetic Theory, McGraw-Hill Book Company, Inc., New York, Chapter 8.

Stroud, A.H. and D. Secrest (1966) "Gaussian Quadrature Formulas, Prentice-Hall, Englewood Cliffs, New Jersey.

Tamir, T., and A.A. Oliner, (1963) "Guided Complex Waves: Part II, Relation to Radiation Patterns," Proc. IEEE, Vol. 10, No. 2.

Wait, J.R. (1960) "The Electromagnetic Fields of a Dipole in the Presence of a Thin Plasma Sheet." Appl. Sci. Res. No. 8, pp. 397-417.

Weiss, R.F. and S. Weinbaum, (1966) "Hypersonic Boundary-Layer Separation and the Base Flow Problem," AIAA Journal, Vol. 4, No. 8 . Aug.

Weston, V.H. (1963) "Theory of Absorbers and Scattering," IEEE Trans. AP-11.

Whittaker, E.T., and G.N. Watson (1927) Modern Analysis, Cambridge University Press, pp. 247-354.

Wolff, E.A. (1966) Antenna Analysis, Wiley and Sons, Inc., New York (Traveling Wave Antenna Chapter).

SECRET

Security Classification

DOCUMENT CONTROL DATA - R & D

(Security classification of title, body of abstract and indexing annotation must be entered when the overall report is classified)

1. ORIGINATING ACTIVITY *(Corporate author)*
The University of Michigan Radiation Laboratory, Dept. of Electrical Engineering, 201 Catherine Street, Ann Arbor, Michigan 48108

2a. REPORT SECURITY CLASSIFICATION
SECRET

2b. GROUP

3. REPORT TITLE

Investigation of Coated Re-entry Vehicle Cross Section (U)

4. DESCRIPTIVE NOTES *(Type of report and inclusive dates)*

Final Report

5. AUTHOR(S) *(First name, middle initial, last name)*

Raymond, F. Goodrich, John J. Bowman, Burton A. Harrison, Eugene F. Knott, Thomas B. A. Senior, Thomas M. Smith and Vaughan H. Weston

6. REPORT DATE
January 1968

7a. TOTAL NO. OF PAGES
391

7b. NO. OF REFS
53

8a. CONTRACT OR GRANT NO.
F 04694-67-C-0055

b. PROJECT NO.

c.

d.

9a. ORIGINATOR'S REPORT NUMBER(S)
8525-1-F

9b. OTHER REPORT NO(S) *(Any other numbers that may be assigned this report)*

10. DISTRIBUTION STATEMENT
In addition to security requirements which apply to this document and must be met, it may be further distributed by the holder only with specific prior approval of SAMSO, SMSDI, Air Force Station, Los Angeles, CA 90045

11. SUPPLEMENTARY NOTES

12. SPONSORING MILITARY ACTIVITY
Hq. Space and Missile Systems Organization
Air Force Systems Command
Norton AFB, California 92409

13. ABSTRACT

(S) This is the final report on Contract F 04694-67-C-0055, an investigation of re-entry vehicle radar cross section, the third phase of a program designated Project SURF. The objective of the SURF program is (1) to achieve the capability to determine the radar cross section of metallic and coated re-entry vehicles which are sphere-capped-cones in shape, or modifications of that basic shape, (2) to determine the effect on radar cross section of the plasma re-entry environment and (3) to study methods for countering short pulse discrimination of these re-entry shapes. Parts (1) and (2) of this program are based upon the interpretation of surface field data obtained on models illuminated by radar in a specially designed facility. Radar backscatter measurements and computer programs are used to check theoretical conclusions. This final report discusses the work carried out in the fourth quarter of this contract and such formulas for radar cross section as were developed and which extend the results previously reported.

DD FORM 1 NOV 65 1473

14. KEY WORDS	LINK A		LINK B		LINK C	
	ROLE	WT	ROLE	WT	ROLE	WT
Radar Cross Section						
Cone-Sphere Re-entry Vehicles						
Abosrber Coatings						
Surface Field Measurements						
Plasma Re-entry Environment						
Short Pulse Discrimination						